PREDICTION OF TEMPERATURES IN ORTHOGONAL MACHINING USING THE FINITE ELEMENT METHOD

A thesis submitted to

The Victoria University of Manchester

for the degree of

DOCTOR OF PHILOSOPHY

by

P.D. MURARKA, M. Tech.

Machine Tool Engineering Division,

Department of Mechanical Engineering,

The University of Manchester

Institute of Science and Technology.

April, 1977

ProQuest LLC.
789 East Eisenhower Parkway
P.O. Box 1346
Ann Arbor, MI 48106 – 1346

DECLARATION

No part of this work has been submitted in support of an application for another degree or qualification to this or any other university or other institution of learning.

ACKNOWLEDGEMENTS

The author wishes to thank Professor B.J. Davies and Professor F. Koenigsberger for permitting this work to be carried out in the Machine Tool Division of the Department of Mechanical Engineering, UMIST.

Very sincere gratitude is expressed to the author's supervisors, Dr. G. Barrow and Dr. S. Hinduja for their dynamic guidance and constant encouragement throughout the course of this work.

The author gratefully acknowledges the valuable co-operation by Mr. F. Kniveton, Mr. J. Hatton and other members of the technical staff of the Royce Laboratory. Sincere thanks are due to Mr. J.A. Nicholson for his helpful advice and patient assistance in programming matters.

The author is indebted to all those who helped in one way or another in the tedious job of preparing this thesis.

The author wishes to express his deep appreciation to his wife, Shanti for her encouragement, and help in the preparation of the diagrams.

THE AUTHOR

The author graduated in Mechanical Engineering from the Regional Institute of Technology, Jamshedpur, India in 1967 and immediately joined the Indian Institute of Technology (I.I.T), Kharagpur as an Associate Lecturer. After pursuing part-time studies for the degree of M. Tech. in Production Science and Technology, the degree was awarded in 1971 by I.I.T. Kharagpur.

The author was reappointed in the same Institute as a Lecturer in 1971 and was awarded the Commonwealth Scholarship in 1974 for a Doctorate Degree. This thesis is the outcome of his research carried out during the past two and a half years.

SUMMARY

This thesis deals with the determination of temperature distributions in the workpiece, tool and chip during orthogonal machining using the Galerkin approach of the finite element method for a wide range of cutting conditions. The finite element analysis (including the computing time) for one test condition has been carried out using linear as well as higher-order elements with different mesh patterns for optimising the choice of an element. Based on a compromise between accuracy and computing time, the remainder of the work was undertaken using quadratic quadrilateral elements.

The solution of the problem takes into account the actual geometries of chip and tool, experimentally obtained velocity and heat source distributions within the primary and secondary zones and the variation of density, thermal conductivity and specific heat with temperature. It also takes into consideration the variation of the flow stress with strain, strain-rate and temperature and the heat generation due to boundary friction on the rake face and along the flank face of the tool. The frictional stresses have been estimated on the rake face according to Zorev's suggested analysis of friction at the tool-chip interface and have been calculated along the flank face from experimentally obtained forces.

The action of coolants on the temperature has been included in the analysis. In addition to this, the effect of other process variables such as speed, feed, rake angle, tool flank wear and tool material properties on the temperatures has also been investigated. The computed results are compared with previous published work and, wherever possible, with experimental values obtained by the author.

CONTENTS

		Page
DECLARATION		ii
ACKNOWLEDGEMENTS		iii
THE AUTHOR		iv
SUMMARY		v
NOMENCLATURE		ix
LIST OF FIGURES		xiii
LIST OF TABLES		xvi
CHAPTER I	INTRODUCTION	1
CHAPTER II	THE FINITE ELEMENT METHOD	6
2.1	Introduction	6
2.2.1	Basic Formulation of the Problem	6
2.2.2	Boundary Conditions	10
2.3	Element Formulation	12
2.3.1	Element Thermal Matrix	12
2.3.2	Convergence Requirements	14
2.3.3	Temperature and Shape Functions	14
2.3.4	Evaluation of Element Matrices	21
2.4	Assembly and Solution of Equations	22
CHAPTER III	DETERMINATION OF TEST DATA AND HEAT GENERATION	25
3.1	Deformation and Heat Generation in Orthogonal Machining	25
3.2	Velocity, Strain and Strain-rate Distributions in the Primary Zone	26
3.2.1	Experimental Setup and Procedure	27
3.2.2	Method of Analysis	28
3.3	Velocity, Strain and Strain-rate Distributions in the Secondary Zone	34

3.4	Flow Stress in the Primary Zone	37
3.5	Flow Stress in the Secondary Zone	45
3.6	Material Properties of Workpiece and Cutting Tools	47
3.6.1	Workpiece Material	47
3.6.2	Tool Materials	48
3.7	Measured Input Data and Cutting Conditions	49
3.8	Experimental Measurement of Some Nodal Temperatures	50
3.9	Determination of the Heat Transfer Coefficient of Coolant	52
3.10	Heat Generation due to Plastic Deformation in the Primary Zone	55
3.11	Heat Generation in the Secondary Zone	55
3.12	Heat Generation over the Flank Face	56
CHAPTER IV	COMPUTATIONAL METHODS AND COMPUTER PROGRAMS	57
4.1	SRATE	58
4.2	ELDATGEN	60
4.3	ELDAT	68
4.4	DATA	69
4.5	FETC	73
4.5.1	Iterative Procedure	78
4.5.2	Evaluation of Element Matrices and Heat Loads and Injection of Boundary Conditions	78
4.5.2.1	Subroutine JACOBI	79
4.5.2.2	Subroutines BDB1/BDB	80
4.5.2.3	Element Subroutines	84
4.5.2.4	Boundary Subroutines	84
4.5.2.5	Subroutines for the Primary Zone Heat Loads	88
4.5.2.6	Subroutines for the Secondary Zone Heat Loads	89
4.5.2.7	Subroutine for the Flank Friction Heat Loads	92
4.5.3	Assembly of System Matrices	93

4.5.4	Solution of Assembled Matrices	96
4.6	TPLOT	98
4.6.1	Subroutine NODENO	100
4.6.2	Subroutine PLOTCO	102
4.6.3	Subroutine DRAW	102
4.7	PRPLOT	102
CHAPTER V	RESULTS AND DISCUSSION	105
5.1	Strain and Strain-rate Distribution in the Primary Zone	105
5.2	Flow Stress Distribution in the Primary Zone	108
5.3	Accuracy and Time Analysis of Finite Elements for Temperature Distribution	110
5.4	The Temperature Distribution	118
5.4.1	Shear Zone Temperatures	118
5.4.2	Tool-Face Temperatures	123
5.4.2.1	Location of the Point of Maximum Tool-Chip Interface Temperature	123
5.4.2.2	Effect of the Process Variables on Tool Temperatures	127
5.5	Comparison of Present Results with Previous Work	130
5.6	Comparison Between the Measured and Computed Temperatures	133
5.7	Influence of Input Data on the Accuracy of Computed Temperatures	135
CHAPTER VI	CONCLUSIONS AND SUGGESTIONS FOR FURTHER WORK	138
6.1	Conclusions	138
6.2	Suggestions for Further Work	141
REFERENCES		143
FIGURES FOR CHAPTER V		156
APPENDIX I	SIMPLIFICATION OF EQ.(2.9) FOR TRIANGULAR ELEMENTS	269
APPENDIX II	PROGRAM DATA	277

NOMENCLATURE

A	Area
C	Tool-Chip contact length
C_1	Sticking part of contact length
C'	Distance of the point of maximum temperature from the cutting edge
C_p	Specific heat
d_{cn}	Average thickness of the shear zone
D	Workpiece diameter
E_s	Deformation energy along the shear plane
$\{f\}$	Matrix representing the x- and y- co-ordinates of a point
$\{F\}$	Matrix, Eq. (2.10)
F	Frictional force along tool-chip contact length
F_F	Force component along the tool flank
F_H	Horizontal component of the resultant force
F_s	Shear force
F_v	Vertical component of the resultant force
$[G]^e$	Element thermal matrix (Eq. (2.13))
h	Heat transfer coefficient
$[H]$	Matrix, Eq. (2.10)
I_B	Boundary integral
$[J]$	Jacobian matrix
K	Thermal Conductivity
K_o	Material constant for shear flow stress
l_f	Length of the flank wear land
lx	Direction cosine of the normal and the x- axis
ly	Direction cosine of the normal and the y- axis
L_1, L_2, L_3	Area co-ordinates

n	Outward normal to the boundary; stress exponent
N	Shape function; Normal force to the tool-chip contact length
N_F	Force component perpendicular to the tool flank
N_h	Number of divisions along the tool-chip contact length
N_u	Nusselt number
P_r	Prandtl number
q	Heat flux (heat input per unit area per unit time)
$\dot{Q}$	Rate of heat input per unit volume per unit time
Q_s	Primary zone heat
R	Resultant cutting force
R_e	Renolds number
R_T	Thermal number
S	Surface
S_h	Boundary surface with known h
S_q	Boundary surface with known q
S_T	Boundary surface with specified temperature T_s
t_1	Feed
t_2	Deformed chip thickness
T	Temperature
T_∞	Ambient temperature
$\{T\}$	Matrix, Eq. (2.10)
$\{T\}^e$	Temperatures of the element nodes
T_f	Mean film temperature; Average rise of temperature given to the chip by the frictional heat source
T_m	Maximum rise of temperature in the chip
T_{max}	Maximum temperature
T_p	Temperature at a distance of 3.92 mm from tool edge along tool face
T_s	Surface temperature

u	x component of velocity
u_∞	Fluid velocity
U	Cutting speed (workpiece speed)
v	y component of velocity
V_c	Chip velocity
V_f	Velocity component along tool flank
V_s	Shear velocity
ω	Width of chip
W_s	Maximum width of secondary zone
$\{x\}^e$	x - co-ordinates of the element nodes
$\{y\}^e$	y - co-ordinates of the element nodes
x,y	Cartesian co-ordinates
α	Rake angle
α_T	Length of the heat source as a fraction of tool-chip contact length
β	Slope of streamline; Proportion of the primary zone heat conducted into the workpiece
γ	Shear strain
$\dot{\gamma}$	Shear strain-rate
ϵ	Effective strain
$\dot{\epsilon}$	Effective strain-rate
ξ, η, ζ	Normalized co-ordinates
μ	Overall coefficient of friction; viscosity of the fluid
μ_b	Coefficient of friction over the slidlng part of contact length
ρ	Density
σ	Effective stress
σ_m	Maximum normal stress
σ_n	Normal stress
τ	Shear stress
τ_f	Shear stress along tool flank

τ_s Maximum shear stress

τ_{sz} Average shear flow stress along the shear plane

ϕ Shear angle

θ Angle between R and the shear plane

Subscripts and Superscripts

c Chip

e Element

i,j Node

V Volume

S Surface

T Transpose of a matrix

LIST OF FIGURES

2.1 Boundaries of the problem region

2.2 Two-dimensional quadrilateral elements

2.3 Two-dimensional triangular elements

2.4 A two-dimensional isoparametric element

2.5 Solution of banded $[H]$ and $\{F\}$

3.1 Deformation and heat generation in Orthogonal machining

3.2 (a) A typical tracing of deformed grid

(b) Velocity diagram

1 (c) Enlarged view of streamline segment

(d) Co-ordinate system

3.3 Flow field tracing of secondary zone

3.4 Variation of lower yield stress with strain-rate at constant temperature (after Campbell and Ferguson (84))

3.5 Variation of shear flow stress with strain-rate (after Manjoine (85))

3.6 Variation of shear flow stress with shear strain (after Manjoine (85))

3.7 Forces and stresses acting in orthogonal machining

3.8 An experimental temperature record

3.9 Categorization of coolant surfaces for the calculation of h.

4.1 Schematic arrangement of finite element programs

4.2 Flow chart for SRATE

4.3 Co-ordinate mapping

4.4 Curved boundary element

4.5 Mesh grading

4.6 Work-tool-chip composite system (HSS tool)

4.7 Key diagram (HSS tool)

4.8 Work-tool-chip composite system (carbide tool)

4.9 Key diagram (carbide tool)

4.10 Flow chart for DATA

4.11 Flow chart for FETC

4.12 Flow chart for element subroutines

4.13 A linear three-dimensional element

4.14 Flow chart for the subroutines HQ12/HQ8

4.15 Distributed loading and equivalent nodal loads

4.16 Uniform distributed loading

4.17 Flow chart for subroutine ASSEMB

4.18 Assembed Matrix [H]

4.19 Flow chart for Subroutine EQSOL

4.20 Flow chart for TPLOT

4.21 Flow chart for PRPLOT

5.1(a) - 5.17(a) Strain distribution in the primary zone

5.1(b) - 5.17(b) Strain-rate distribution in the primary zone

5.1(c) - 5.17(c) Flow stress distribution in the primary zone

5.1(d) - 5.17(d) Temperature distributions in the primary zone

5.18 Work-tool-chip composite system for convergence analysis

5.19 Key diagram for Fig. 5.18

5.20 Mesh with quadrilateral elements

5.21 Mesh with triangular elements

5.22 Temperature distribution using QUAD12 elements

5.23 Isothermals using QUAD12 elements

5.24 Temperature distribution using QUAD8 elements

5.25 Isothermals using QUAD8 elements

5.26 Temperature distribution using QUAD4 elements

5.27 Temperature distribution using TRI3 elements

5.28 Convergence curve for T_p

5.29 Convergence curve for T_{max}

5.30 'EQSOL' Time versus N_h (no. of divisions along tool-chip contact length)

5.31 'FETC' time versus N_h

5.32 'EQSOL' Time versus the number of degrees of freedom

5.33 'FETC' Time versus the number of degrees of freedom

5.34 Convergence curve for T_p versus the number of iterations

5.35 Convergence curve for T_{max} versus the number of iterations

5.36 - 5.52 Temperature distribution and Isothermals for different cutting conditions

5.53 - 5.64 Temperature variations along the tool face and tool flank

5.65 Variation of β with $R_T \tan\phi$

5.66 Variation of T_m/T_f with R_T/α_T

A1.1 Division of the problem region into elements

A1.2 A typical assembly of two elements

PLATE I Experimental setup for scribing spiral grid lines on workpiece

PLATE II Experimental setup for flow line tests

PLATE III Photographs of deformed flow lines during orthogonal machining

PLATE IV Experimental setup for scribing radial grid lines on workpiece

PLATE V Secondary chip formation (Photographs)

PLATE VI Experimental setup for measuring cutting forces

PLATE VII Experimental setup for measuring temperatures

LIST OF TABLES

3.1 Measured and calculated co-ordinates for the streamlines in the Primary zone

3.2 Experimental and empirical flow stress values

3.3 Empirical flow stress and the average flow stress based on shear plane theory

3.4 Measured data and cutting conditions for all the tests

5.1 Shear zone strain analysis

5.2 Shear zone strain-rate analysis

5.3 Shear zone flow stress analysis

5.4 Temperature convergence with different elements

5.5 Computing time analysis

5.6 Temperature convergence with the number of iterations

5.7 Shear zone temperature analysis

5.8 Shear energy analysis

5.9 Maximum temperature analysis

5.10 Variation of forces with different tools

5.11 Proportion of shear zone heat conducted into the workpiece

5.12 Maximum and mean rise of temperature in chip

5.13 Comparison between computed and measured temperatures

CHAPTER I

INTRODUCTION

The importance of the chip-tool interface temperature distributions has been recognized by many investigators (1 - 8) for several purposes. These include the determination of the causes of the tool wear, estimation of tool-life and the analysis of metal flow on the rake-face of the tool. Temperature distributions in the workpiece are also necessary for studies of material properties where machining is used as a materials test (6, 7). It is not surprising, therefore, that considerable efforts have been made to assess temperature distributions by both experimental and theoretical means.

The classical tool-work thermocouple method was used by Gottwein(9), Shore(10) and Herbert(11) to measure the average temperature of the chip-tool interface. The temperature distributions were obtained experimentally by the technique of embedded thermocouples by Shaw et al (12), Hollander et al(13) and Reichenbach (14) in the workpiece and chip. Kusters (15) and Qureshi (16) embedded thermocouples in the tool and obtained three dimensional temperature distributions by extrapolation. But, the embedded thermocouples interfere with the normal heat flow; extrapolation involves inherent inaccuracies and, sometimes, the process is extremely time-consuming.

Radiation techniques have been used by many research workers including Lenz (17, 18), Prins (19) and Boothroyd (20) for determining the temperature distributions at the surfaces of the tool and workpiece. The problems associated here are the precise calibration of the pyrometers and the need of preheating the workpiece for infrared photography. Although these problems obviously affect the reliability of the results, useful information has been obtained.

In view of the limited accuracy and practicability of the experi-

mental methods, many attempts were made to solve the problem analytically. Trigger and Chao (21-23), Hahn (24), Leone (25), Loewen and Shaw (26), Weiner (27) and Rall and Giedt (28) made significant contributions to the analytical studies on the temperature distributions at the shear plane and tool-chip interface. All analytical attempts necessitated the use of an idealized model of the cutting process. Plane heat sources of uniform strength were assumed to represent the heat generation due to primary shear deformation as well as chip-tool interface friction. The secondary deformation zone has usually been neglected. Scrutton (29, 30) assumed the heat to be generated in two finite regions, the shear zone and the secondary deformation region near the chip-tool interface and derived the equations for the temperature distributions valid for the upper boundary of the shear zone only.

In the numerical analysis of the problem, Vieregge (31) used a finite difference method to compute the temperature distribution. Rapier (32) and Dutt and Brewer (33) used relaxation methods to compute the temperature distribution in the chip, tool and workpiece. All the analyses reported above have assumed plane and uniform heat sources which obviously influenced the accuracy of the results obtained. Altan, Ostafiev and Kobayashi (34) obtained the temperature distributions in the workpiece, chip and tool during orthogonal cutting by finite difference formulations based on an experimentally obtained flow field. They neglected the initial temperature increase of the workpiece due to the removal of layers before the chip was cut which seems to have resulted in predicting lower temperatures. Mansour et al (35) used a quasi-finite element approach to compute the temperature distribution based on some known nodal temperatures. However, the information about the heat sources is lacking and the precise experimental determination of the initial temperatures at some strategic nodes is

the necessary requirement. Tay, Stevenson and Davis (36) computed the temperature distributions in orthogonal machining using the variational approach of the finite element method based on experimentally determined flow stress and strain-rate distributions in the shear zones. Even though the method of Tay et al (36) takes substantial computer time for computation and the effect of coolants on temperatures has not been included in the analysis, it is a significant contribution to the numerical analysis of the problem. Recently, Shafto, Howes and Andrew (37) predicted workpiece temperature distributions in creep feed grinding using a finite element model.

It is evident from the process review above that the nature of the velocity and the heat source distributions and the complexity of the problem boundary preclude any accurate solution using analytical or finite difference methods. However, the finite element method (f.e.m.) has all the provisions for arbitrary geometry, orthotropic materials and arbitrary boundary conditions and has, therefore, been used here. Complex bodies composed of many different isotropic materials such as tool and workpiece with significant variations in specific heat and thermal conductivity with increasing temperature are easily handled by f.e.m. Temperature or heat flux boundary conditions may be specified at any point within the finite element system. Moreover, mathematically, the method can be shown to converge towards the exact solution as the number of elements is increased (38), provided the criteria for convergence is satisfied by the element.

Of the various approaches to finite element formulation, the minimization of a functional is the most widely accepted means of arriving at a finite element representation, but it is not the only and most efficient approach. The methods of weighted residuals permit consistent finite element representation to be obtained without recourse to variational theorems. These methods, based on the error distribution principle, aim at the minimization and distribution of the error with the help of a weighting function $W(x,y,z)$,

in such a manner that the net result will be zero, i.e.,

$$\iiint R(x, y, z) \cdot W(x, y, z)\, dx\, dy\, dz = 0$$

where $R(x, y, z)$ is an unknown function to be solved. There are various approaches to this technique depending upon the nature of the weighting function (54). The Galerkin process (38, 50, 53), a potential method of weighted residuals for the f.e.m. with a distribution function the same as the weighting function, leads in general to the best approximation (39) and has, therefore, been used for the present analysis.

In the present investigations the temperature distribution problem in orthogonal machining is formulated and solved in terms of the finite element process using the Galerkin approach. The finite element solution takes into account the actual geometries of the chip and tool, experimentally obtained velocity and heat source distributions within the primary and secondary zones and the variation of density, thermal conductivity and specific heat with temperature. It also takes into consideration the temperature increase due to boundary friction on the rake face and along the flank face of the tool. The frictional stresses have been estimated on the rake face according to Zorev's (40) suggested analysis of friction at the tool-chip interface and have been calculated along the flank face from experimentally obtained forces. The action of coolants on the temperatures has also been included in the analysis. The computed results are obtained for different cutting speeds, feeds and rake angles with high speed steel as well as carbide tools using higher-order quadrilateral plate elements and have been verified experimentally, wherever possible, However, for one test, simple and higher-order elements have been used to compare and assess in each case the accuracy that is obtained and the computational time that is required when the number of elements used in the idealization of the problem region is progressively increased.

The finite element formulations and the basic theory are described in the next chapter. To perform the analyses, some starting data are to be

determined experimentally and some are to be calculated based on certain assumptions as described in Chapter III. Computer programs are required which will determine the element matrices and the heat load vectors, generate the system matrices, determine the temperature distributions and represent them graphically. The programs which have been developed to perform these functions and the underlying computational methods are described in Chapter IV. The computational and experimental results are compiled and discussed in Chapter V. The concluding remarks are included in the final chapter.

CHAPTER II

THE FINITE ELEMENT METHOD

2.1 Introduction.

The matrix methods of analysis based upon the finite element idealisation have been applied to the analysis of a wide range of problems in mathematical physics in a number of ways. The phenomena studied have included heat transfer (36-38, 46-50, 59-68), torsion of a shaft (46) and various fluid flow problems (65-67) and the methods applied include Variational principles (36, 46, 49, 59-63, 68), Gurtin's approach (37, 47, 48, 64) and Galerkin's method (38, 50, 53, 65-68). Finlayson (54) has shown that Gurtin's approach is equivalent to Galerkin's method.

The process of finite element heat conduction is of particular interest because of its applicability to metal cutting. The treatment of a given type of problem by the finite element method consists of three major component aspects:

(i) basic formulation of the problem including the boundary conditions and assumptions,

(ii) the element formulation, and

(iii) the assembly and solution of the complete system.

2.2.1 Basic Formulation of the Problem.

The heat transfer phenomenon occurring during orthogonal machining is governed by the partial differential equation

$$K \frac{\partial^2 T}{\partial x^2} + K \frac{\partial^2 T}{\partial y^2} - \rho C_p \left(u \frac{\partial T}{\partial x} + v \frac{\partial T}{\partial y}\right) + \dot{Q} = 0 \qquad (2.1)$$

subject to boundary conditions

$$T = T_s \text{ on part of boundary } S_T, \qquad (2.2a)$$

$$- K \frac{\partial T}{\partial n} = q \text{ on part of boundary } S_q \qquad (2.2b)$$

and $-K \frac{\partial T}{\partial n} = h(T - T_\infty)$ on part of boundary S_h (2.2c)

where n is the outward normal to the boundary.

This is based on the following assumptions:

(i) The problem is two-dimensional:

If the depth of cut is much smaller than the width of chip, it may be assumed that the problem is two-dimensional. Such is the case in orthogonal machining.

(ii) The machining is a steady state process:

Force measurements confirm that for a continuous chip, machining can be assumed to be a steady state process.

(iii) The workpiece, tool and chip are homogeneous and isotropic and can be treated as one continuous medium.

In machining, the size of the deformation zone is much larger relative to the grain size of the work material and hence, this assumption is valid.

The spacewise discretization of the equation (2.1) can be accomplished via the steady-state variational form as shown in (36, 39). Here, a second alternative is presented which permits consistent finite element representation to be obtained without recourse to variational theorems. The necessary formulation follows the Galerkin principle (52, 54).

Let the unknown function T, throughout the solution domain, be approximated as

$$T = \sum_{1}^{n} N_i(x,y)\, T_i = [N] \{T\}^e \qquad (2.3)$$

where $[N] = [N_i, N_j, \ldots\ldots\ldots, N_m]$ and N_i, N_j, etc. are the "shape functions" (functions of the x-y co-ordinates) and T_i, T_j, etc. are the values of the temperatures $\{T\}^e$ at the element nodes i,j, etc. The shape functions are defined piecewise, element by element, and in the summation the appropriate function for the particular point in space must

be used. In the Galerkin process, the weighting function is made equal to the shape function N_i. The simultaneous equations, allowing the solution for n values of T_i, are obtained typically for point i by equating to zero the weighted and integrated residual, resulting from substitution of Eq. (2.3) into Eq. (2.1). Thus, the i_{th} equation is given by

$$\iint_V N_i \left[\left\{ K \left(\frac{\partial^2}{\partial x^2} + \frac{\partial^2}{\partial y^2} \right) \right\} \sum_1^n N_j T_j - \left\{ \rho C_p \left(u \frac{\partial}{\partial x} + v \frac{\partial}{\partial y} \right) \right\} \sum_1^n N_j \cdot T_j + \dot{Q} \right] dx.dy = 0 \qquad (2.4)$$

n such equations will allow in principle the complete solution of the problem if the integral can be evaluated. In the above form the integral would require continuity of slopes at all interface regions to avoid infinities in the second differentials and it is worthwhile to modify Eq. (2.4) by making use of Green's theorem. For instance,

$$\iint_V N_i \, K \left(\frac{\partial^2}{\partial x^2} \sum_1^n N_j T_j \right) dx.dy = \int_S N_i \, K \left(\sum_1^n \frac{\partial N_j}{\partial x} T_j \right) lx.ds$$
$$= \iint_V \frac{\partial N_i}{\partial x} \cdot K \left(\sum_1^n \frac{\partial N_j}{\partial x} \cdot T_j \right) dx.dy \qquad (2.5)$$

in which lx is the direction cosine of the outward normal and the x direction, and integral S is taken over the whole boundary.

Modification of the first two terms of Eq. (2.4) in this way results in

$$-\iint_V \left[K \frac{\partial N_i}{\partial x} \cdot \sum_1^n \frac{\partial N_j}{\partial x} + K \frac{\partial N_i}{\partial y} \cdot \sum_1^n \frac{\partial N_j}{\partial y} + \rho C_p \, u \, N_i \sum_1^n \frac{\partial N_j}{\partial x} + \rho C_p \cdot v N_i \sum_1^n \frac{\partial N_j}{\partial y} \right] T_j \, dx \, dy + \iint_V N_i \dot{Q} \, . \, dx \, dy +$$
$$\int_S K.N_i \left(\sum_1^n \frac{\partial N_j}{\partial x} lx + \sum_1^n \frac{\partial N_j}{\partial y} ly \right) T_j ds = 0 \qquad (2.6)$$

In matrix form, Eq. (2.6) can be written as

$$-\iint_V \left[K \frac{\partial N_i}{\partial x} \frac{\partial [N]}{\partial x} + K \frac{\partial N_i}{\partial y} \cdot \frac{\partial [N]}{\partial y} + \rho C_p \, u \, N_i \frac{\partial [N]}{\partial x} + \right.$$

$$\rho C_p \, v \, N_i \, \frac{\partial [N]}{\partial y} \Big] \Big\{T\Big\}^e \, dx \, dy + \iint_V N_i \dot{Q} \, . \, dx \, dy \, +$$

$$\int_S N_i \, . \, K \left(\frac{\partial [N]}{\partial x} \, . \, lx \, + \, \frac{\partial [N]}{\partial y} \, ly\right) \Big\{T\Big\}^e \, ds \, = \, 0 \qquad (2.7)$$

As a result, only the first-order derivatives have to be integrated and only the continuity of the shape functions N_i has to be imposed (39). On boundary points where the value of T is prescribed, the equation is not formed. The last integral in Eq. (2.7) does not contribute anything to the equations at internal boundary points (54) and arises only on the boundaries of type S_q (Eq. 2.2b) and S_h (Eq. 2.2c).

Introducing the boundary conditions of Eqs. (2.2b) and (2.2c), the surface integral of Eq. (2.7) becomes

$$\int_S N_i \, K \left(\frac{\partial [N]}{\partial x} \, lx \, + \, \frac{\partial [N]}{\partial y} \, ly\right) \Big\{T\Big\}^e \, ds$$

$$= \int_S N_i \, K \left(\frac{\partial T}{\partial x} \, . \, lx \, + \, \frac{\partial T}{\partial y} \, ly\right) ds$$

$$= \int_S N_i \, K \, \frac{\partial T}{\partial n} \, . \, ds$$

$$= -\int_{S_q} N_i \, q \, ds \, - \int_{S_h} N_i h [N] \Big\{T\Big\}^e \, ds \, + \int_{S_h} N_i h \, . \, T_\infty \, ds \qquad (2.8)$$

Substitution of Eq. (2.8) into Eq. (2.7) gives

$$\iint_V \Big[K \, \frac{\partial N_i}{\partial x} \, . \, \frac{\partial [N]}{\partial x} \, + \, K \, \frac{\partial N_i}{\partial y} \, . \, \frac{\partial [N]}{\partial y} \, + \, \rho C_p u \, N_i \, \frac{\partial [N]}{\partial x} \, +$$

$$\rho C_p \, v \, N_i \, . \, \frac{\partial [N]}{\partial y} \Big] \Big\{T\Big\}^e \, . \, dx \, dy \, - \iint_V N_i \, \dot{Q} \, . \, dx \, . \, dy \, +$$

$$\int_{S_q} N_i \, q ds \, + \int_{S_h} N_i h [N] \, . \, \Big\{T\Big\}^e \, . \, ds \, - \int_{S_h} N_i h T_\infty \, . \, ds \, = \, 0 \qquad (2.9)$$

The n equations (2.9) can be written down in matrix form as

$$\Big[H\Big] \, \Big\{T\Big\} \, + \, \Big\{F\Big\} \, = \, 0 \qquad (2.10)$$

in which

$$H_{ij} = \sum \iint_e \Big(K \, \frac{\partial N_i}{\partial x} \, . \, \frac{\partial N_j}{\partial x} \, + \, K \, \frac{\partial N_i}{\partial y} \, . \, \frac{\partial N_j}{\partial y} \, + \, \rho C_p \, u \, N_i \, \frac{\partial N_j}{\partial x}$$

$$+ \, \rho C_p \, v N_i \, \frac{\partial N_j}{\partial y} \Big) \, dx \, dy \, + \sum \int_{She} N_i h \, N_j ds \qquad (2.11a)$$

where summation covers contribution from each element and e is the element region and

$$F_i = -\sum\iint_e N_i \dot{Q}\, dx.dy + \sum\int_{Sqe} N_i\, q\, ds - \sum\int_{She} N_i h T_\infty\, ds \qquad (2.11b)$$

where Sqe and She refer only to elements with an external surface on which conditions (2.2b) and (2.2c) are specified respectively.

For nodes situated on boundary S_T (Eq. 2.2a)

$$H_{ij} = \begin{cases} 1 & \text{if } i = j \\ 0 & \text{if } i \neq j \end{cases} \qquad (2.11c)$$

and $$F_i = -T_s \qquad (2.11d)$$

and $\{T\}$ is the column matrix containing the nodal temperatures to be found.

Further simplification of Eq. (2.9) for a typical 3-node triangle is given in Appendix I.

2.2.2 Boundary Conditions.

The experiments have been conducted with and without coolants. In the present study, water has been used as a coolant for which the physical properties are known and hence, the heat transfer coefficient h could be calculated. For the experimental conditions, the heat transfer coefficient of the air is found to be negligibly small and hence, heat losses to the environment (when coolant is not used) are neglected. Thus, the surfaces of the chip, workpiece and tool that are surrounded by air are assumed to be insulated. When coolant is used, the heat transfer coefficient is calculated at the affected surface.

The geometrical boundaries (not to the scale) of the problem region are shown in Fig. 2.1. The chip curl is neglected; but beyond the tool-

chip interface SD, the chip and tool surfaces are isolated from each other. At the exit end EF of the chip, far away from the tool edge, the temperature gradients would be expected to diminish. Hence, at this boundary the condition $\partial T/\partial n = 0$ is applied. Along the workpiece boundaries AB and BC, the workpiece material is virtually at room temperature, being unaffected by the heat conducted and convected from the primary deformation zone. The chip exit boundary EF and the workpiece boundaries AB and BC are extended outwards from the tool edge until the isotherms obtained are essentially the same. When this state is reached, these

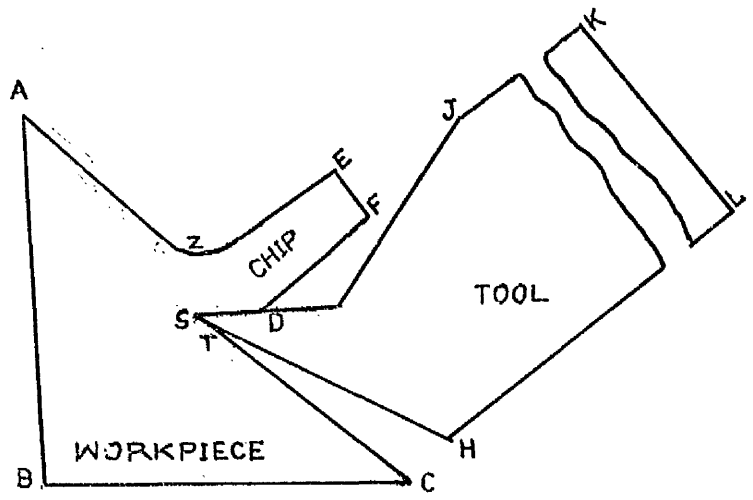

Fig. 2.1 Boundaries of the problem region.

three boundaries are correctly placed.

The actual size and shape of the tool are considered in the finite element model. The tool is clamped to the tool post with an overhang of 12.5 mm sandwiched with thin mica-sheets at the interfaces for heat insulation. Thus, at the upper and lower tool surfaces JK and HL, the condition $\partial T/\partial n = 0$ is imposed. The far end KL of the tool is assumed to be at room temperature.

It is assumed that along the tool-chip interface SD, the temperatures at the chip and the tool are equal. This is a reasonable assumption as contact pressures are very high at the interface. The amount of frictional heat generated is calculated for each node at the interface and the heat fluxes into the chip and the tool adjust themselves automatically according to the temperatures on both sides of the interface. The same treatment applies to the tool-work interface ST for the case of initial flank wear.

2.3 Element Formulation

2.3.1 Element Thermal Matrix.

From Eq. (2.10), the element equation, in general, can be written as

$$\left[H\right]^e \left\{T\right\}^e + \left\{F\right\}^e = 0 \qquad (2.12)$$

Where the matrix $\left[H\right]^e$ for the elements having no external boundary of type (Eq. 2.2c) is of the form

$$\left[H\right]^e = \int_V \left[G\right]^e \cdot dv \qquad (2.13)$$

In Eq. (2.13), $\left[G\right]^e$ can, for convenience, be called the element thermal matrix, a typical term of which is given by

$$G_{ij}^e = K\left(\frac{\partial N_i}{\partial x} \cdot \frac{\partial N_j}{\partial x} + \frac{\partial N_i}{\partial y} \cdot \frac{\partial N_j}{\partial y}\right) + \rho C_p \cdot N_i \left(u \frac{\partial N_j}{\partial x} + v \frac{\partial N_j}{\partial y}\right) \qquad (2.14)$$

For an element having n nodes, the thermal matrix can be written as

$$
\begin{aligned}
\left[G\right]^e = K &\begin{bmatrix}
\frac{\partial N_i}{\partial x}\cdot\frac{\partial N_i}{\partial x} & \frac{\partial N_i}{\partial x}\cdot\frac{\partial N_j}{\partial x} & \cdots & \frac{\partial N_i}{\partial x}\cdot\frac{\partial N_n}{\partial x} \\
 & \frac{\partial N_j}{\partial x}\cdot\frac{\partial N_j}{\partial x} & \cdots & \frac{\partial N_j}{\partial x}\cdot\frac{\partial N_n}{\partial x} \\
\text{Symmetrical} & & \cdots & \\
 & & & \frac{\partial N_n}{\partial x}\cdot\frac{\partial N_n}{\partial x}
\end{bmatrix} \\
+K &\begin{bmatrix}
\frac{\partial N_i}{\partial y}\cdot\frac{\partial N_i}{\partial y} & \frac{\partial N_i}{\partial y}\cdot\frac{\partial N_j}{\partial y} & \cdots & \frac{\partial N_i}{\partial y}\cdot\frac{\partial N_n}{\partial y} \\
 & \frac{\partial N_j}{\partial y}\cdot\frac{\partial N_j}{\partial y} & \cdots & \frac{\partial N_j}{\partial y}\cdot\frac{\partial N_n}{\partial y} \\
\text{Symmetrical} & & \cdots & \\
 & & & \frac{\partial N_n}{\partial y}\cdot\frac{\partial N_n}{\partial y}
\end{bmatrix} \\
+\rho C_p u &\begin{bmatrix}
N_i\frac{\partial N_i}{\partial x} & N_i\frac{\partial N_j}{\partial x} & \cdots & N_i\frac{\partial N_n}{\partial x} \\
N_j\frac{\partial N_i}{\partial x} & N_j\frac{\partial N_j}{\partial x} & & N_j\frac{\partial N_n}{\partial x} \\
\cdots & \cdots & \cdots & \cdots \\
N_n\frac{\partial N_i}{\partial x} & N_n\frac{\partial N_j}{\partial x} & & N_n\frac{\partial N_n}{\partial x}
\end{bmatrix} \\
+\rho C_p v &\begin{bmatrix}
N_i\frac{\partial N_i}{\partial y} & N_i\frac{\partial N_j}{\partial y} & \cdots & N_i\frac{\partial N_n}{\partial y} \\
N_j\frac{\partial N_i}{\partial y} & N_j\frac{\partial N_j}{\partial y} & \cdots & N_j\frac{\partial N_n}{\partial y} \\
\cdots & \cdots & \cdots & \cdots \\
N_n\frac{\partial N_i}{\partial y} & N_n\frac{\partial N_j}{\partial y} & \cdots & N_n\frac{\partial N_n}{\partial y}
\end{bmatrix}
\end{aligned}
\qquad (2.15)
$$

Or

$$[G]^e = K\frac{\partial[N]^T}{\partial x}\cdot\frac{\partial[N]}{\partial x} + K\frac{\partial[N]^T}{\partial y}\cdot\frac{\partial[N]}{\partial y} + \rho C_p u[N]^T\cdot\frac{\partial[N]}{\partial x} + \rho C_p v[N]^T\frac{\partial[N]}{\partial y} \quad (2.16)$$

2.3.2 Convergence Requirements.

As mentioned earlier, Eq. (2.9) is defined by the first-order derivatives of T, continuity of T is only necessary when choosing suitable shape functions. They have also to be such that constant values of any of the first derivatives exist throughout the element when suitable nodal values $\{T\}^e$ are assigned. Although the continuity of the first derivative is not essential for convergence, it is desirable for better accuracy (63).

2.3.3 Temperature and Shape Functions.

The temperature function T expresses the temperature of any point within or along the boundaries of the element as a function of the precise position of that point. It is the basic requirement to choose the shape of the element and the form of the approximating function T. A multiplicity of shapes shown in Figs. 2.2 and 2.3 are available and will be highlighted in the following discussion.

The choice of the approximating function T is far more difficult because of the abundance of closed-form mathematical functions available. In general, the function should be simple, should yield a well-conditioned matrix, and should be compatible. The compatability requires that if the temperature and desired derivative in one element are specified, they must be so specified that an adjoining element with a common set of nodal points will yield the same values on the common side. Probably, the most popular distributions are polynomials in x and y. Such polynomials may give rise to co-ordinate matrices which are difficult to invert accurately because of their ill-conditioning (69). However,

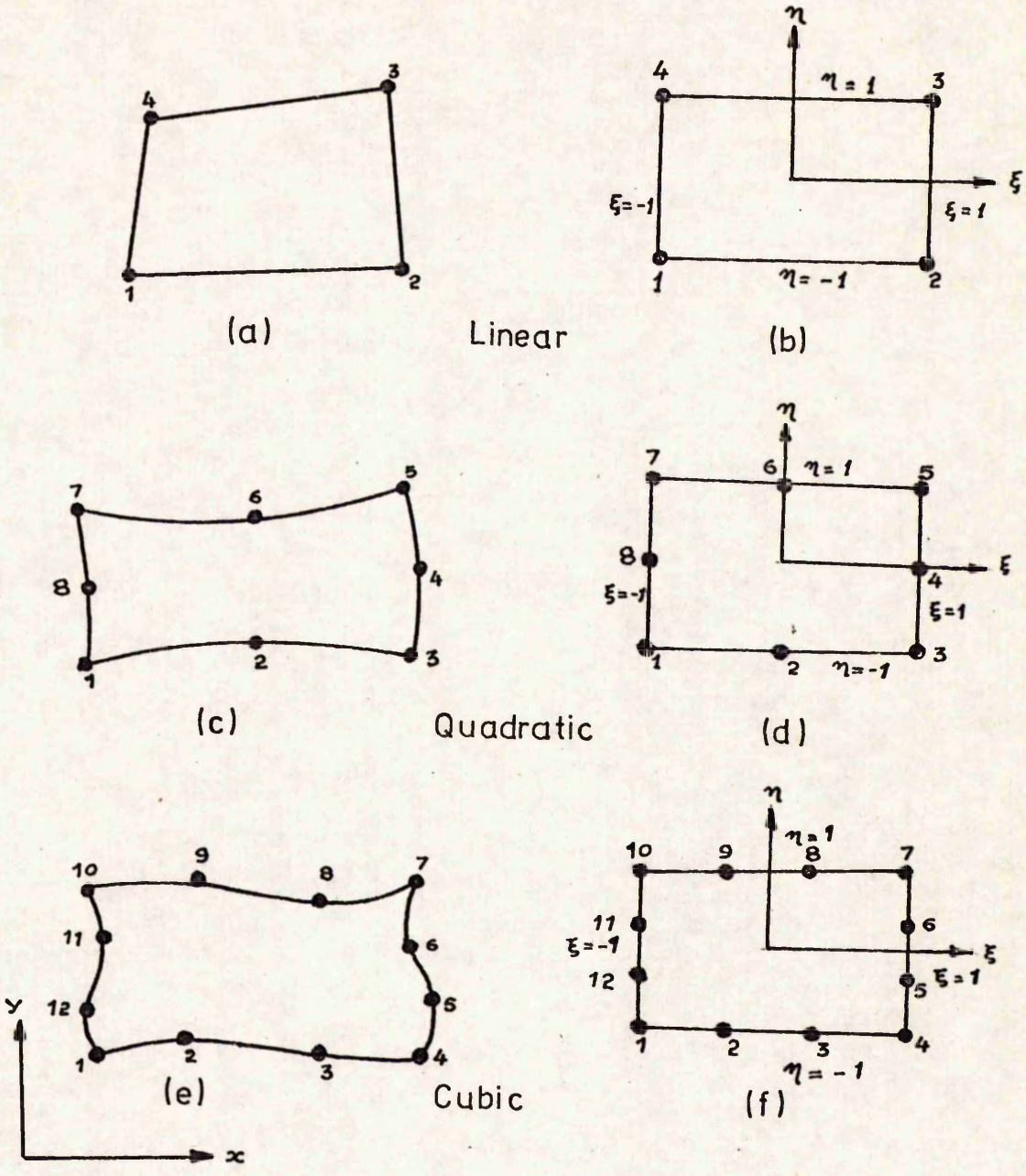

Fig. 2.2 TWO-DIMENSIONAL QUADRILATERAL ELEMENTS

AFTER REFERENCE (108)

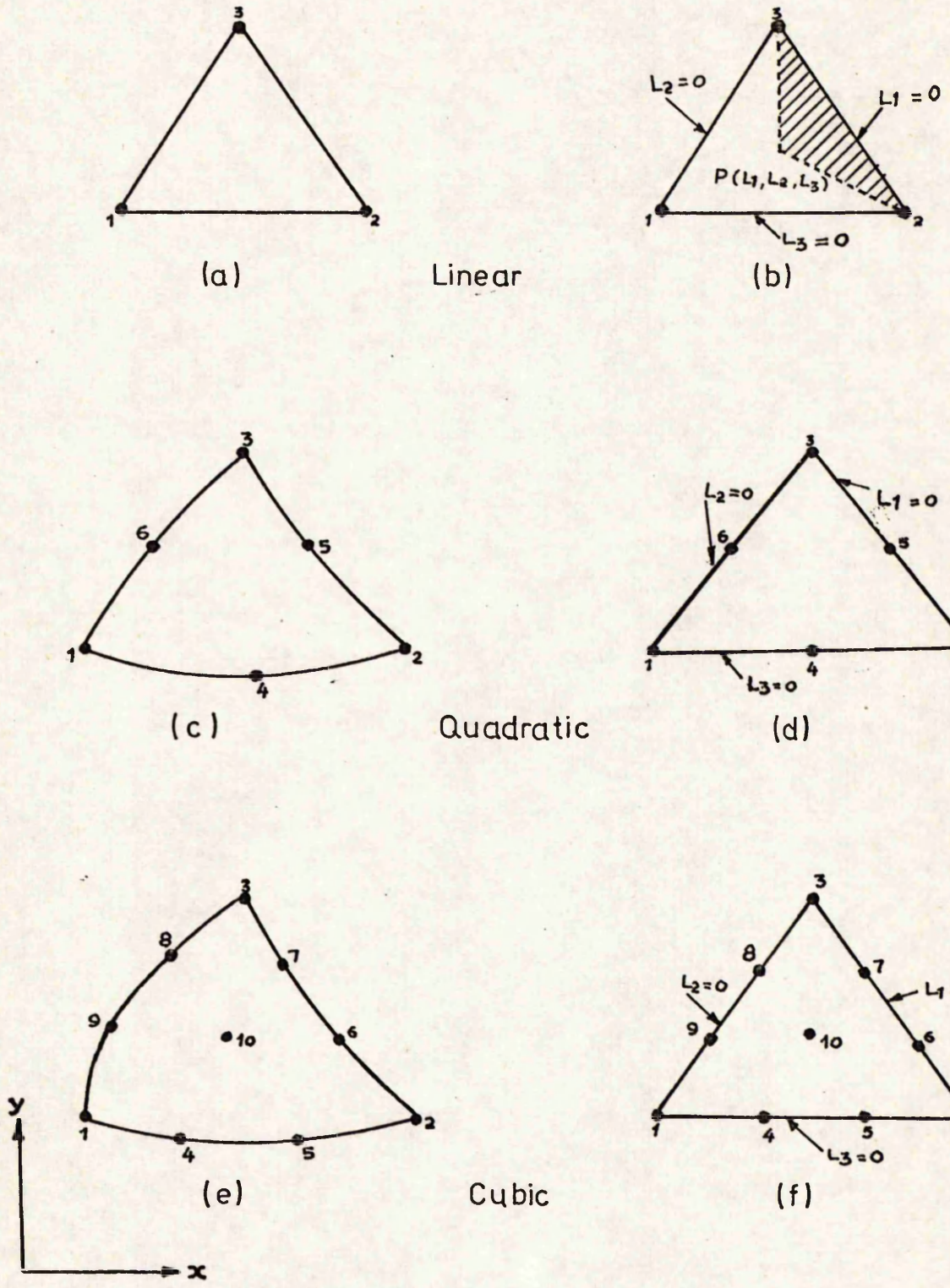

FIG. 2.3 TWO-DIMENSIONAL TRIANGULAR ELEMENTS

AFTER REFERENCE (63)

the order of such polynomials is rarely greater than the third, the inversion is usually straight forward and furthermore, the integration of $[G]^e$ is simple to carry out. For instance, for the 4-node quadrilateral element shown in Fig. 2.2(a), the possible function is

$$T = a_1 + a_2x + a_3y + a_4xy \tag{2.17}$$

The coefficients $a_1 \ldots\ldots a_4$ are determined by substituting successively the nodal temperatures and nodal co-ordinates into Eq.(2.17), such that

$$\begin{Bmatrix} T_1 \\ T_2 \\ T_3 \\ T_4 \end{Bmatrix} = \begin{bmatrix} 1 & x_1 & y_1 & x_1y_1 \\ 1 & x_2 & y_2 & x_2y_2 \\ \cdots & \cdots & \cdots & \cdots \\ 1 & x_4 & y_4 & x_4y_4 \end{bmatrix} \begin{Bmatrix} a_1 \\ a_2 \\ a_3 \\ a_4 \end{Bmatrix} = [A]\{a\} \tag{2.18}$$

and the inversion of $[A]$ multiplied by $\{T\}^e$ gives the values of $a_1 \ldots\ldots a_4$. Similarly, by taking the vertices of the triangle (Fig. 2.3(a)) to be the nodal points and the temperature variation within the element to be linear, the temperature function is

$$T = [f]\{a\} = \begin{bmatrix} 1 & x & y \end{bmatrix} \begin{Bmatrix} a_1 \\ a_2 \\ a_3 \end{Bmatrix} \tag{2.19}$$

where $[f]$ is a row vector representing the x- and y- co-ordinates of a point and $\{a\}$ is the column vector of unknown coefficients.

An alternative approach is to use shape functions $[N]$ which are defined as

$$T = \begin{bmatrix} N_1, N_2 \ldots\ldots \end{bmatrix} \begin{Bmatrix} T_i \\ T_2 \\ . \\ . \\ . \\ . \end{Bmatrix} = [N] \{T\}^e \tag{2.20}$$

Where $\{T\}^e$ is the vector of nodal temperatures and $[N]$ are, in general, functions of positions. They relate the temperature at any point inside the element to the nodal temperatures. It is apparent that they manifest

the following properties when the co-ordinates of the appropriate nodes are inserted.

$$\begin{aligned} \left[N_i \quad (x_i, y_i)\right] &= \left[I\right] \\ \left[N_i \quad (x_j, y_j)\right] &= \left[0\right] \qquad i \neq j \end{aligned} \tag{2.21}$$

That is, each shape function has a value of unity at its associated nodal points and vanishes at all other points. Usually, for the sake of convenience, they are expressed in terms of the normalized co-ordinates ξ, η (Fig. 2.2(b)). For instance, the shape functions (39) for the 4-node quadrilateral element are of the form

$$N_i = (1 + \xi_i \xi)(1 + \eta_i \eta)/4 \tag{2.22}$$

The normalized co-ordinates are, however, not convenient to be used for the triangular elements. Instead, a set of area co-ordinates, L_1, L_2 and L_3 (Fig. 2.3(b)) are used which can be defined by the following linear relations between these and the Cartesian system:

$$\begin{aligned} x &= L_1 x_1 + L_2 x_2 + L_3 x_3 \\ y &= L_1 y_1 + L_2 y_2 + L_3 y_3 \\ 1 &= L_1 + L_2 + L_3 \end{aligned} \tag{2.23}$$

For the 3-node triangular element, Fig. 2.3(b), the shape functions are, in fact, the area co-ordinates. Thus

$$N_i = L_i \tag{2.24}$$

It is evident that, for the linear elements, the temperature distribution given by Eq. (2.20) is compatible and represents the basis for nearly all thermal-inviscid-fluid and stress-finite-element programs. The basic drawback to this distribution is that the heat flux varies discontinuously from element to element and is not compatible. Furthermore, a large number of elements may be necessary in order to obtain sufficiently accurate results.

The quadratic elements are generated by establishing nodal points

at the mid-points of the sides. As a result, there will be six nodes per triangle (Fig. 2.3(c)) and eight nodes per quadrilateral (Fig. 2.2(c)) permitting the formulations

$$[f]_{\text{triangle}} = [1 \quad x \quad y \quad x^2 \quad xy \quad y^2] \tag{2.25}$$

$$[f]_{\text{quadrilateral}} = [1 \quad x \quad y \quad x^2 \quad xy \quad y^2 \quad x^2y \quad xy^2] \tag{2.26}$$

The shape functions (39) for the quadratic triangular element (Fig. 2.3(d)) can be expressed as follows:

For corner nodes 1, 2 and 3

$$N_i = 2(L_i - 1)\, L_i \tag{2.27}$$

For mid-side nodes

$$N_4 = 4L_1 L_2 \text{ etc.} \tag{2.28}$$

The shape functions for the quadratic quadrilateral element (Fig. 2.2(d)) are of the following form:

For corner nodes 1, 3, 5 and 7

$$N_i = 1/4\ (1 + \xi_o)\ (1 + \eta_o)\ (\xi_o + \eta_o - 1) \tag{2.29}$$

For mid-side nodes 2 and 6

$$N_i = \tfrac{1}{2}\ (1 - \xi^2)\ (1 + \eta_o) \tag{2.30}$$

For mid-side nodes 4 and 8

$$N_i = \tfrac{1}{2}\ (1 + \xi_o)\ (1 - \eta^2) \tag{2.31}$$

where $\xi_o = \xi_i \xi$ and $\eta_o = \eta_i \eta$

Again since the temperature variation is quadratic and it can be uniquely determined on each side from the three nodal temperatures on the side, adjoining elements are compatible. Furthermore, the heat flow will not be constant within each element and thus a value of the gradient may be associated with each nodal point. However, the heat flux is discontinuous and its value differs for each element and it is necessary to average all of the neighbouring element values to determine a value at the node. In addition, even if the degree of mesh refinement is the same for the linear and quadratic elements the size of the thermal matrix

is larger for the quadratic element because of the increased bandwidth. Thus, the core storage requirement and the computation times will be larger. Since these items are the principal drawbacks to the use of the finite element method, it is essential that the accuracy inherent in the higher-order method be sufficiently greater in order to reduce the overall number of nodal points required and thus to reduce the core storage requirements and execution time.

The cubic elements are obtained by increasing the number of mid-side nodes further. For a cubic variation, the polynomials for a 10-node triangle (Fig. 2.3 (e)) and for a 12-node quadrilateral (Fig. 2.2 (e)) are given by

$$[f]_{\text{triangle}} = \left[1 \quad x \quad y \quad x^2 \quad xy \quad y^2 \quad x^3 \quad x^2y \quad xy^2 \quad y^3\right] \tag{2.32}$$

$$[f]_{\text{quadrilateral}} = \left[1 \quad x \quad y \quad x^2 \quad xy \quad y^2 \quad x^3 \quad x^2y \quad xy^2 \quad y^3 \quad x^3y \quad y^3x\right] \tag{2.33}$$

The necessary shape functions (39) can be written down as follows:

(i) The cubic triangular element (Fig. 2.3 (f))

For corner nodes

$$N_i = \tfrac{1}{2}(3L_i - 1)\,(3L_i - 2)\,L_i \tag{2.34}$$

For mid-side nodes

$$N_4 = 9/2\; L_1\, L_2\, (3L_1 - 1), \text{ etc.} \tag{2.35}$$

For the internal node 10

$$N_{10} = 27 L_1 L_2\, L_3 \tag{2.36}$$

(ii) The cubic quadrilateral element (Fig. 2.2 (f))

For corner nodes 1, 4, 7 and 10

$$N_i = 1/32(1 + \xi_o)\,(1 + \eta_o)\left[-10 + 9\,(\xi^2 + \eta^2)\right] \tag{2.37}$$

For mid-side nodes 5, 6, 11 and 12

$$N_i = 9/32\,(1 + \xi_o)\,(1 - \eta^2)\,(1 + 9\eta_o) \tag{2.38}$$

For mid-side nodes 2, 3, 8 and 9

$$N_i = 9/32\,(1 + \eta_o)\,(1 - \xi^2)\,(1 + 9\xi_o) \tag{2.39}$$

As for the quadratic element, the temperature but not the heat flux is compatible. The formulation by Eq. (2.32) may be regarded as either the adjoining of three 6-node triangles or combining nine 3-node triangles. In either case, the number of non-zero elements in the thermal matrix increases proportionately. Thus, the core storage requirements and the computation times will be proportionately larger.

2.3.4 Evaluation of Element Matrices.

To perform a finite element analysis, the matrices $[H]^e$ and $\{F\}^e$ defining the element characteristics have to be determined. It is evident from Eqs. (2.13) and (2.11) that these matrices depend on N or its derivatives with respect to global co-ordinates. The exact integration of these could be cumbersome and in higher-order isoparametric elements even impossible; therefore, numerical integration has to be resorted to.

The concept of 'isoparametric' formulation in a two-dimensional space is fully discussed elsewhere (70 - 71). In order to summarize the essentials, a general two-dimensional isoparametric element is shown in Fig. 2.4 with positions defined within it by normalized co-ordinates (which take up, conveniently, values of $\pm$ 1 on opposite faces).

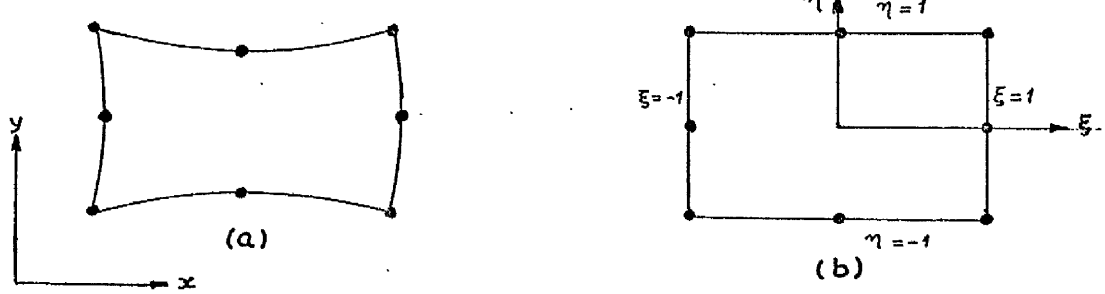

Fig. 2.4 A two-dimensional isoparametric element in (a) x, y space (b) ξ, η space (parent element parabolic)

Let the normalized co-ordinates be related to the Cartesian x, y by the expressions

$$x = [N] \{x\}^e$$
$$y = [N] \{y\}^e \qquad (2.40)$$

Where $\{x\}^e$, $\{y\}^e$ are column vectors containing the x- and y- nodal co-ordinates and $[N]$ is a given shape function in terms of ξ, η. Simultaneously, the unknown function T is prescribed in terms of the normalized co-ordinates by Eq. (2.20).

If the shape functions are so chosen that T satisfies continuity and 'constant derivative' criteria of convergence in the ξ, η space (mapped in x-y co-ordinates), then (i) element faces will be continuous and (ii) all the convergence criteria are satisfied (70-71). Now to derive matrices $[H]^e$ and $\{F\}^e$ in the Cartesian co-ordinate system, a few simple transformations are needed. Thus all derivative components transform as

$$\begin{Bmatrix} \frac{\partial N_i}{\partial x} \\ \\ \frac{\partial N_i}{\partial y} \end{Bmatrix} = [J]^{-1} \begin{Bmatrix} \frac{\partial N_i}{\partial \xi} \\ \\ \frac{\partial N_i}{\partial \eta} \end{Bmatrix} \tag{2.41}$$

in which $|J|$ is the Jacobian matrix which becomes

$$[J] = \begin{bmatrix} \frac{\partial x}{\partial \xi} & \frac{\partial y}{\partial \xi} \\ \\ \frac{\partial x}{\partial \eta} & \frac{\partial y}{\partial \eta} \end{bmatrix} = \begin{bmatrix} \frac{\partial [N]}{\partial \xi} \\ \\ \frac{\partial [N]}{\partial \eta} \end{bmatrix} \begin{bmatrix} \{x\}^e & \{y\}^e \end{bmatrix} \tag{2.42}$$

Elements of volume for unit thickness become

$$dxdy = \det [J] \, d\xi \, . \, d\eta \tag{2.43}$$

With these transformations and following numerical integration the matrices $[H]^e$ and $\{F\}^e$ can be evaluated easily.

2.4 Assembly and Solution of Equations.

The equations to be solved for the complete system are represented by Eq. (2.10) i.e.,

$$[H] \{T\} + \{F\} = 0 \tag{2.44}$$

The matrices $[H]$ and $\{F\}$ contain contributions from all the elements

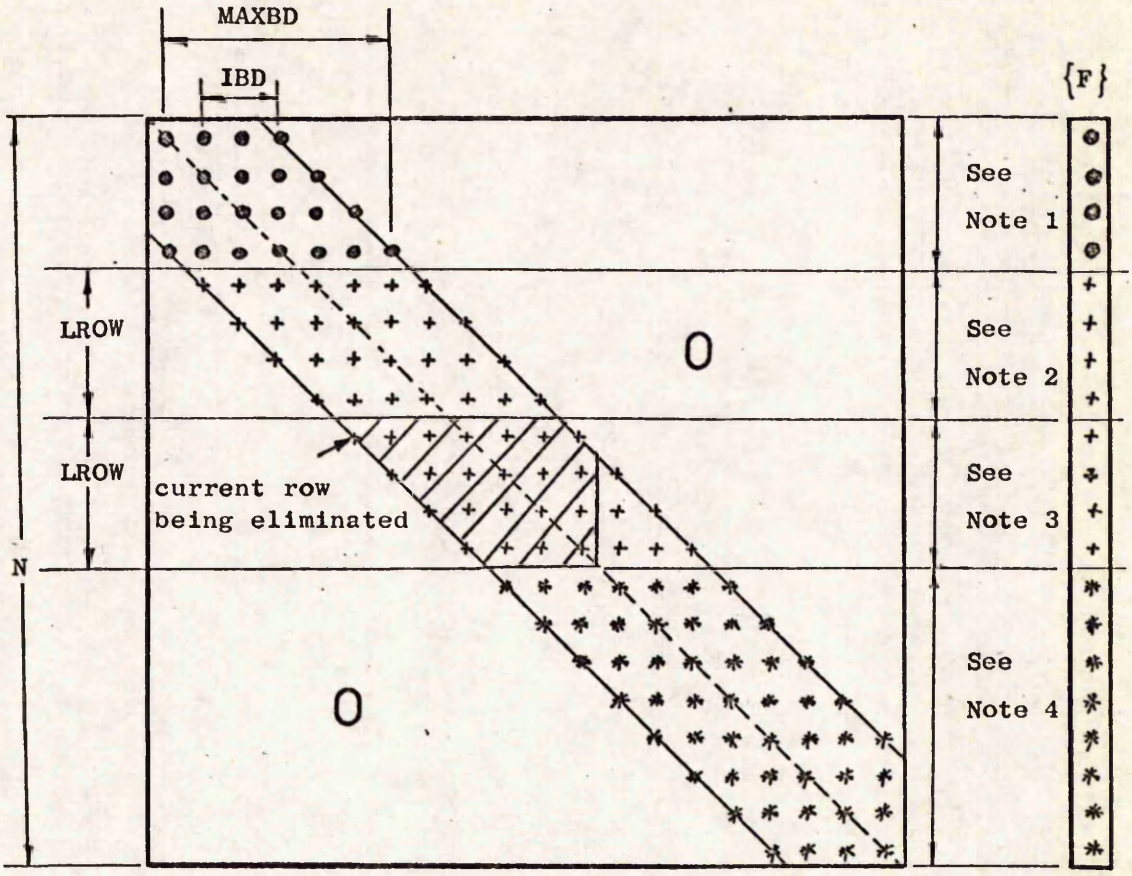

Fig. 2.5 Solution of banded [H] and {F}

Ref. - Kark (107)

IBD = Semi-bandwidth.

MAXBD = 2 * IBD + 1 = Overall Bandwidth.

LROW = Number of rows in each part.

N = Total no. of equations.

\+ Coefficients in core.

* Coefficients on disc.

● Coefficients transferred on magnetic tape.

▨ Coefficients affected.

NOTE 1 Forward elimination completed and coefficients transferred to magnetic tape.

NOTE 2 Forward elimination completed, coefficients waiting in core store A1 to be transferred to magnetic tape.

NOTE 3 Coefficients being eliminated in core store A2.

NOTE 4 Coefficients on disc.

of the system. The matrix $[H]$ is banded centrally about the diagonal (56) as shown in Fig. 2.5 provided the nodes are numbered judiciously. Generally, the width of the band will vary from row to row. However, the overall bandwidth is equal to twice the maximum difference between the largest and smallest nodal numbers for any row because $[H]$ is unsymmetric for the problem under consideration.

The efficiency of the finite element method hinges importantly upon the existence of reliable and efficient solution procedure. Tay and Davis (59) solve the asymmetric system (Eq. 2.44) directly, using a general, banded Gaussian elimination procedure. The solution routine developed herein is also based on Gaussian elimination technique and the zeroes of $[H]$ outside the band are not operated upon and are actually not stored (56). One important feature of the solution routine is that it can handle both large and small problems.

For small problems, the matrix $[H]$ is stored in the computer working core as a whole and the forward elimination is performed in one operation. For large problems (which can not be solved without the aid of external devices like tapes, discs, etc.), the matrix $[H]$ is read into the core from a disc file in parts. The forward elimination is performed in stages. Each stage contains a part of the matrix $[H]$. As the forward elimination is accomplished in each stage, the resulting coefficients are stored on an auxiliary tape. When a new stage is loaded in core, all the previous stages whose diagonal coefficients are required to eliminate the coefficients on it, are successively read from tape, and the elimination performed. The last coefficients to be eliminated are those that require diagonal elements from inside the presently considered stage (Fig. 2.5). Back substitution is affected in a similar manner to the forward elimination except that the stages (or parts) are loaded in reverse order. Further details are given in Chapter IV.

CHAPTER III

DETERMINATION OF TEST DATA AND HEAT GENERATION.

3.1 Deformation and Heat Generation in Orthogonal Machining.

The operation of orthogonal machining where the straight cutting edge of a wedge-shaped tool is perpendicular to the direction of relative motion of the tool and workpiece is shown in Fig. 3.1. Basically, this operation is one of shearing the work material to form the chip and subsequent sliding of the chip along the rake face of the cutting tool. It has now been well established from studies of deformed flow line

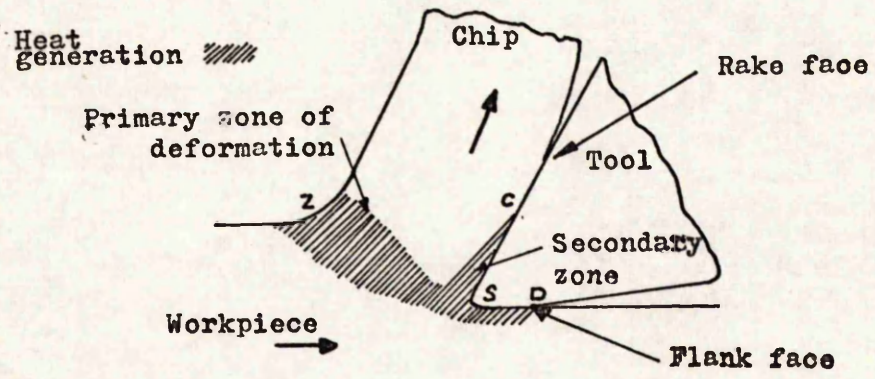

Fig. 3.1. Deformation and heat generation in orthogonal machining.

patterns(72 - 75) that plastic deformation takes place over two main regions: the region SZ around the so-called shear plane, known as the 'primary zone', and the region SC adjacent to the rake face of the tool, known as the 'secondary zone'. Thus, the heat due to deformation is generated in the two zones SZ and SC. Some heat is also generated due to sliding friction along the rake face. When a tool wears, an additional source of heat due to interfacial friction is present at the worn flank SD.

The pattern of heat generation as depicted in Fig. 3.1 leads to

temperature gradients along the rake face, and also into the chip, tool and workpiece. It is evident, therefore, that for complete assessment of temperature distributions, the information about the distributions of heat generation rate within the deformation zones and along the tool-chip and work-tool interfaces is necessary.

In order to calculate the distribution of heat generation rate within the deformation zones, the velocity, flow stress and strain-rate distributions are required. The calculation of the flow stress distributions in the primary deformation zone necessitates the knowledge of strain distributions. The strain, strain-rate and velocity distributions for all tests were obtained directly from experimental studies. Empirical expressions for the flow stress in terms of the strain, strain-rate and temperature were obtained from published literature. The heat input due to interfacial friction was calculated by estimating the frictional stresses on the rake face and along the flank face of the tool. These estimations were made from experimentally obtained force measurements combined with Zorev's (40) suggested analysis of friction at the tool-chip interface. The detailed description is given below.

3.2 Velocity, Strain and Strain-rate Distributions in the Primary Zone.

It is necessary to establish the flow line pattern under steady-state cutting for calculating the velocity, strain and strain-rate distributions. Stevenson and Oxley (74) used a printed grid and an explosive quick-stopping technique for obtaining the flow fields under machining conditions. Childs (72-73) inscribed the grid on the workpiece using a micro-hardness testing equipment and the deformed grid was recorded by photographing through a microscope. Goriani and Kobayashi (75) and Nakayama (5) used a simple mechanical technique to scribe the grid lines on the workpiece. For the present investigations, owing to the simplicity and convenience of the process, the grid lines on the workpiece were

scribed mechanically using a sharp carbide tool.

3.2.1 Experimental Setup and Procedure.

Circular discs of the workpiece material were parted off from a 100 mm diameter bar, turned down to 98.0 mm in diameter, and fine ground to a width of 6.35 mm. The side face of each disc was first polished with fine emery papers, and then a spiral line up to a depth of 10 mm was scribed with a feed t_1 of 0.0711 mm/rev. as shown in Plate I.

After scribing the lines, the side face of the specimen was cross-lapped in order to remove burrs and then polished with # 300 and # 600 emery papers until all scratches were removed. The specimen was mounted to a fixture which was held by the chuck of a Dean, Smith & Grace lathe. Orthogonal machining with a selected tool and selected cutting conditions was carried out and after the steady state was reached the cutting was quick-stopped using an explosive quick-stop device. The experimental set-up is shown in Plate II. The explosive quick-stop device used in the tests was developed by Ellis, Barrow and Kirk at UMIST and is described elsewhere (76). After quick-stopping, each test specimen was photographed on a polaride film using a photomicroscope. Some of these photographs are shown in Plate III. Enlarged prints of these photographs were made and the lines were traced and thus a total enlargement of about 250 times was obtained. These magnified streamlines were used for the determination of velocity, strain and strain-rate distributions in the primary zone. The x-y co-ordinates of a number of points on the stream-lines for all tests were measured on d-mac digitiser with solartron interface unit to an accuracy of 0.02 mm. The co-ordinates were simult-aneously punched on paper-tape and then transferred to a magnetic disc to be stored in the computer for further analysis.

3.2.2 Method of Analysis.

There are various methods for calculating the velocity, strain and strain-rate from known streamlines. Palmer and Oxley (77) and Goriani and Kobayashi (75) constructed orthogonal curves to the streamlines and then calculated the velocities along the streamlines. This method is based on a trial and error approach and takes a long time for calculations and hence, it is not suitable for the present analysis where a large number of flow fields have to be analysed. Stevenson and Oxley (74) and Kececioglu (78) calculated the strain-rate distribution based on the parallel sided shear zone model of chip formation and assumed a definite direction of maximum shear strain-rate. This process is relatively quick and seems to be sufficiently accurate. For the present analysis, a method similar to that of Stevenson and Oxley (74) was used.

A typical enlarged tracing of the deformed grid is shown in Fig. 3.2(a). It is assumed that the smooth curves representing the grid lines initially parallel to the work velocity are stream lines of flow although these do not represent paths of particular particles but show the instantaneous positions of many particles following approximately the same path. As the experiments were designed to approximate to steady-state conditions the errors involved in this assumption should not be large. From Fig. 3.2(a) it can be seen that the plastic deformation starts well in advance of the tool and the shear zone is of substantial width. Within the shear zone the streamlines are very similar to each other although there is some increase in curvature of those streamlines nearest to the cutting edge. These observations are similar to those made by Stevenson and Oxley (74).

The velocity diagram for the streamlines is shown in Fig. 3.2(b). The velocity triangle ASZ is defined by the rake angle α, the chip

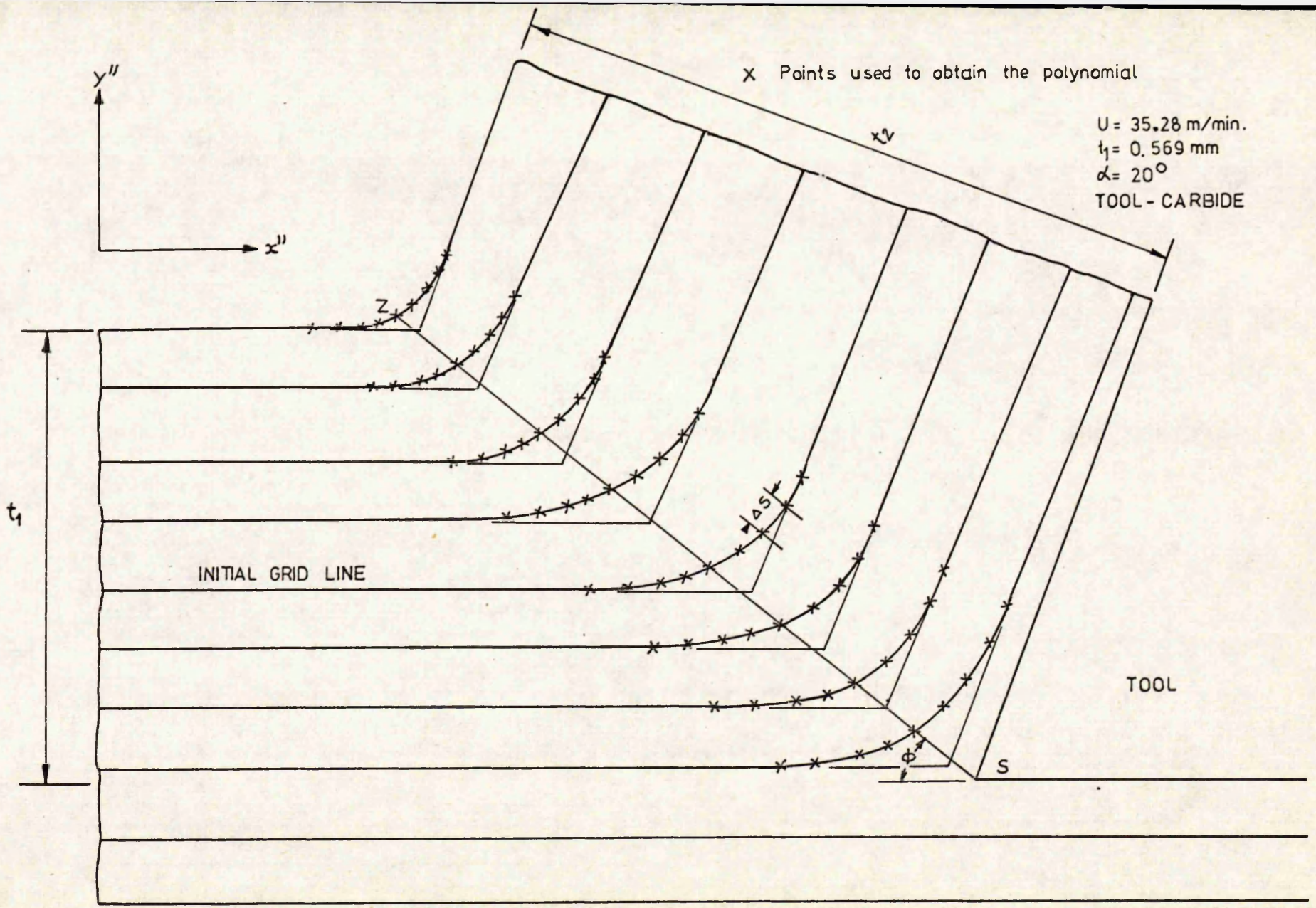

FIG. 3.2(a) A typical tracing of deformed grid

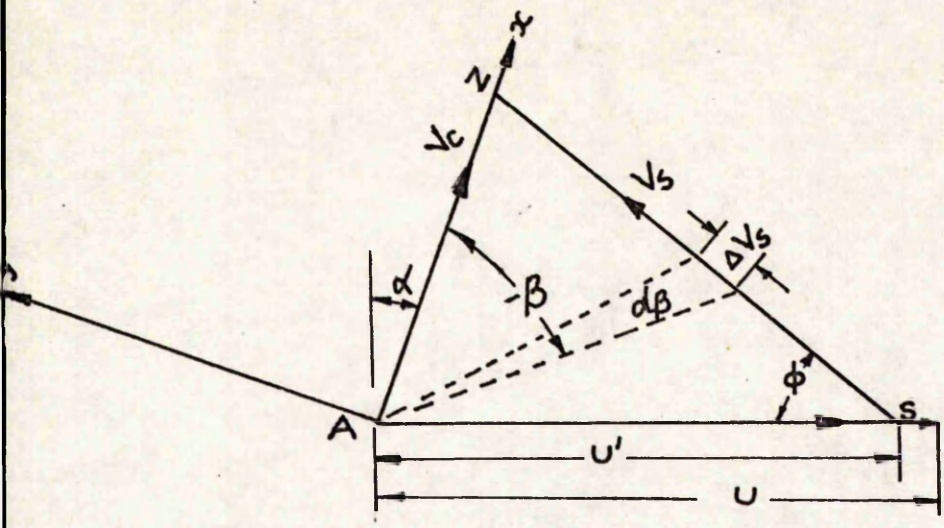

Fig. 3.2(b) Velocity Diagram

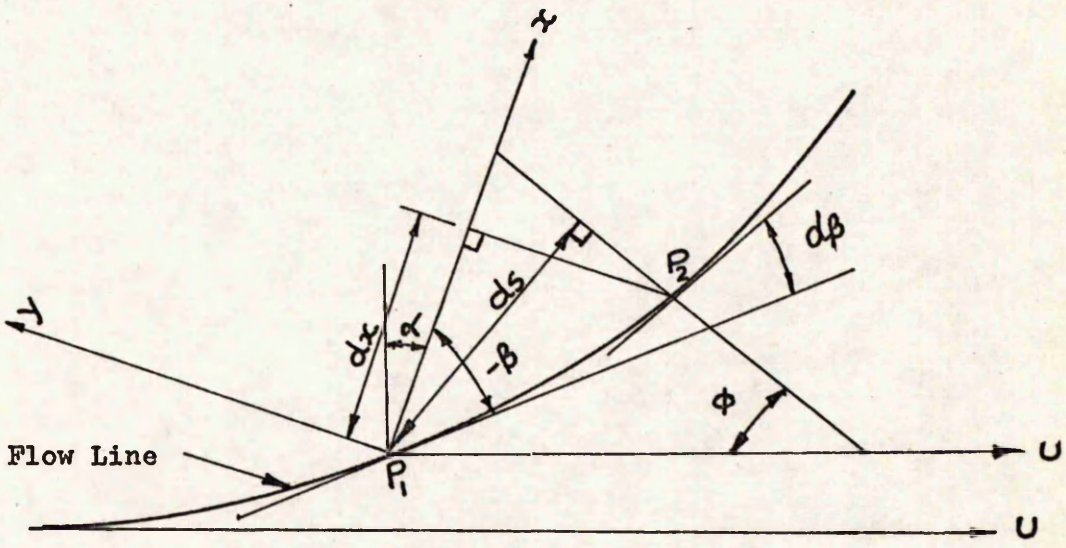

Fig. 3.2(c) Enlarged View of Streamline Segment.

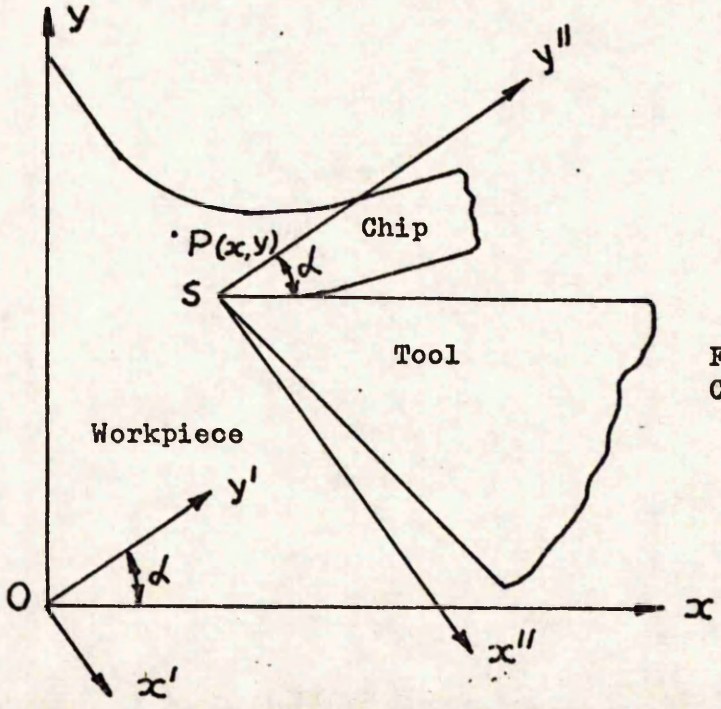

Fig. 3.2(d)
Cordinate System

velocity V_c and the shear angle ϕ . The chip velocity was found by the change in width between streamlines and the angle ϕ was found from the construction (Fig. 3.2(a)). The velocity magnitude V_β on a streamline at a point where the streamline has turned an angle β from the chip velocity V_c may then be determined from the velocity triangle and thus

$$V_\beta = \frac{V_c \ \text{Cos}(\phi - \alpha)}{\text{Cos} \ (\phi + \beta - \alpha)} \qquad (3.1)$$

To determine the angle β at any point along a streamline in terms of its x and y co-ordinates, it is necessary to find an analytical expression for each streamline. The x-y co-ordinate axes chosen for the finite element analysis are parallel to and perpendicular at the tool face, whereas the co-ordinates of the points on streamlines were measured with respect to the x'', y'' axes as shown in Fig. 3.2(d). The measured co-ordinates were transformed into x-y co-ordinates. For any point P on the streamlines in the primary zone having co-ordinates x_p'', y_p'' with respect to origin S (Fig. 3.2 d), the corresponding x-y co-ordinates x_p, y_p are given by the following equations

$$\begin{aligned} x_p &= (x_p'' + x_s') \sin\alpha + (y_p'' + y_s') \cos\alpha \\ y_p &= (y_p'' + y_s') \sin\alpha - (x_p'' + x_s') \cos\alpha \end{aligned} \qquad (3.2)$$

where

$$\begin{aligned} x_s' &= x_s \sin\alpha - y_s \cos\alpha \\ y_s' &= x_s \cos\alpha + y_s \sin\alpha \end{aligned} \qquad (3.3)$$

and x_s and y_s are the x, y co-ordinates of the tool cutting edge S and α is the rake angle.

It was found that the streamlines within the primary zone are very well approximated by a 3rd order polynomial i.e., by the general equation

$$y = c_1 + c_2 x + c_3 x^2 + c_4 x^3 \qquad (3.4)$$

Each streamline as those shown in Fig. 3.2(a) was treated separately. Nine evenly spaced points on a streamline were selected and the coefficients were found by fitting statistically a 3rd order polynomial. The polynomial so obtained fitted the streamlines very well as shown in Table 3.1.

By differentiating Eq(3.4), the total angle turned through by a streamline at any point on it may be found. Thus

$$\tan \beta = \frac{dy}{dx} = c_2 + 2c_3 x + 3c_4 x^2 \qquad (3.5)$$

Also,

$$\frac{d^2y}{dx^2} = 2c_3 + 6c_4 x \qquad (3.6)$$

In order to determine the maximum shear strain-rate $\dot{\gamma}$ at a point, it was assumed that SZ was a direction of maximum shear strain rate. Hence

$$\dot{\gamma} = \frac{\Delta V_s}{\Delta s} \qquad (3.7)$$

where ΔV_s is the change in the shear velocity V_s (i.e. in the direction SZ) and Δs is measured normal to SZ. From Fig. 3.2(b), ΔV_s can be expressed in terms of the chip velocity V_c, the shear angle ϕ, rake angle α and the angles β and $\Delta\beta$ which on substitution in Eq. (3.7) gives

$$\dot{\gamma} = \frac{d\beta}{ds} \cdot \frac{V_c \cos(\phi - \alpha)}{\cos^2(\phi + \beta - \alpha)} \qquad (3.8)$$

From Fig. 3.2(c),

$$\frac{ds}{dx} = \frac{\cos(\phi + \beta - \alpha)}{\cos \beta} \qquad (3.9)$$

Substitution of Eq. (3.9) in Eq. (3.8) gives

$$\dot{\gamma} = \frac{d\beta}{dx} \cdot \frac{V_c \cos\beta \cdot \cos(\phi - \alpha)}{\cos^3(\phi + \beta - \alpha)} \qquad (3.10)$$

Using the relation that $\tan \beta = dy/dx$, Eq. (3.10) can be written in the form

$$\dot{\gamma} = \frac{d^2y}{dx^2} \cdot \frac{V_c \cos(\phi - \alpha)}{\left[\cos(\phi - \alpha) - \sin(\phi - \alpha) \cdot \frac{dy}{dx}\right]^3} \qquad (3.11)$$

Table 3.1

Stream line co-ordinates.

y_m = Measured y co-ordinate

y_c = Calculated y co-ordinate

Flow Line No.	y-co-ordinate	Point 1	Point 2	Point 3	Point 4	Point 5	Point 6	Point 7	Point 8	Point 9
1	y_m	20.0	32.0	51.0	70.0	93.0	138.0	194.0	263.0	330.0
	y_c	17.68	34.85	50.89	66.42	91.45	138.3	198.1	263.4	327.8
2	y_m	138.0	146.0	152.0	162.0	182.0	223.0	278.0	338.0	401.0
	y_c	135.2	147.5	150.9	159.5	179.0	221.7	279.5	339.0	396.5
3	y_m	253.0	260.0	269.0	282.0	293.0	329.0	372.0	426.0	483.0
	y_c	249.5	264.3	271.2	278.3	290.8	329.5	374.7	428.4	479.1
4	y_m	365.0	368.0	379.0	388.0	404.0	438.0	472.0	527.0	574.0
	y_c	363.0	372.6	378.9	387.0	399.4	438.4	474.5	531.7	569.2
5	y_m	499.0	509.0	525.0	538.0	551.0	582.0	611.0	653.0	693.0
	y_c	497.4	512.2	525.2	537.2	549.6	579.0	614.3	655.9	690.1
6	y_m	601.0	609.0	620.0	632.0	651.0	685.0	718.0	761.0	805.0
	y_c	599.8	610.8	622.3	631.7	646.4	682.7	723.1	764.2	801.0
7	y_m	739.0	743.0	757.0	764.0	781.0	808.0	840.0	874.0	914.0
	y_c	737.5	745.3	757.1	765.5	777.2	805.5	845.7	874.7	911.4
8	y_m	850.0	852.0	856.0	862.0	871.0	901.0	930.0	962.0	995.0
	y_c	849.0	853.9	856.1	860.4	871.0	898.4	935.3	961.6	993.1

where $\frac{dy}{dx}$ and $\frac{d^2y}{dx^2}$ are given by Eqs. (3.5) and (3.6) respectively.

In order to obtain an expression for the total shear strain at a point, Eq. (3.8) is rearranged, giving

$$\frac{d\gamma}{d\beta} = \frac{dt}{ds} \cdot \frac{V_c \cos(\phi - \alpha)}{\cos^2(\phi + \beta - \alpha)} \qquad (3.12)$$

From the velocity diagram in Fig. 3.2(b), dt/ds is constant for all points on a streamline and equal to $1/V_c \cdot \cos(\phi - \alpha)$ which on substitution in Eq. (3.12) gives

$$\left.\begin{aligned} \frac{d\gamma}{d\beta} &= \frac{1}{\cos^2(\phi + \beta - \alpha)} \\ \text{and} \qquad \gamma &= \int_{-(\pi/2 - \alpha)}^{\beta} \frac{1}{\cos^2(\phi + \beta - \alpha)} \cdot d\beta \\ &= \cot\phi + \tan(\phi + \beta - \alpha) \end{aligned}\right\} \qquad (3.13)$$

where γ is the cumulative shear strain up to the point on the streamline where β is the angle turned.

For the initial portions of the streamlines, it was assumed that the velocities decreased linearly from the work velocity U at the start of the primary zone to the velocity U' (as shown in Fig. 3.2(b)) at the points where the polynomials began. However, the difference between U and U' for most of the cases was negligibly small.

3.3 Velocity and Strain-rate Distributions in the Secondary Zone.

In order to determine the velocity and the strain-rate distributions in the secondary zone, a series of radial lines with an angular spacing between the lines of 0.0015514 radians (5 minutes 20 seconds) was scribed on the side face of the polished circular discs of 98 mm diameter and 6.35 mm thickness. For this purpose, the discs were held in a fixture mounted on an OMT rotary table fitted with a radial grating and photoelectric reader having a digital display system reading direct

to one second of arc. The digital rotary table was mounted on the table of an Elliott vertical milling machine and a sharp carbide tool was held in the collect chuck of the machine spindle. The experimental setup is shown in Plate IV. After scribing the lines, the sideface of the specimen was cross-lapped in order to remove burrs and then polished with # 300 and # 600 emery papers until all the scratches were removed. The rest of the experimental procedure is similar to that described in Section 3.2.1. Some of the photographs of the streamlines showing the chip formation due to the secondary flow are shown in Plate V. A typical enlarged tracing of the deformed streamlines due to secondary chip formation is shown in Fig. 3.3.

As seen in Fig. 3.3, the chip material is dragged back over the sticking part of the tool-chip contact length. It was found that the extent of chip-dragging and the width of the secondary zone are somewhat less at speeds below 46 m/min. It was, therefore, concluded that for speeds below 46 m/min., the secondary zone could be considered as a plane frictional heat source with little error. For higher speeds, the dragging back of the material was much more evident and it was possible to measure the width of the secondary zone with a reasonable degree of accuracy. The grid lines were severely distorted near the tool face and accurate measurements of the velocity and strain-rate distributions are very difficult necessitating certain assumptions to be made.

For cutting speeds less than 46 m/min., the velocity of the material along the rake face was assumed to be constant and equal to the bulk chip velocity V_c. For higher speeds, it was assumed that the velocity of the material at the rake face started at $V_c/3$ at the tool edge and accelerated uniformly to V_c within the sticking part of the tool-chip contact lenght (36). In a direction perpendicular to the rake face, it was assumed that the velocity increased linearly from the value at the rake face to the bulk chip velocity at the streamline nearest to

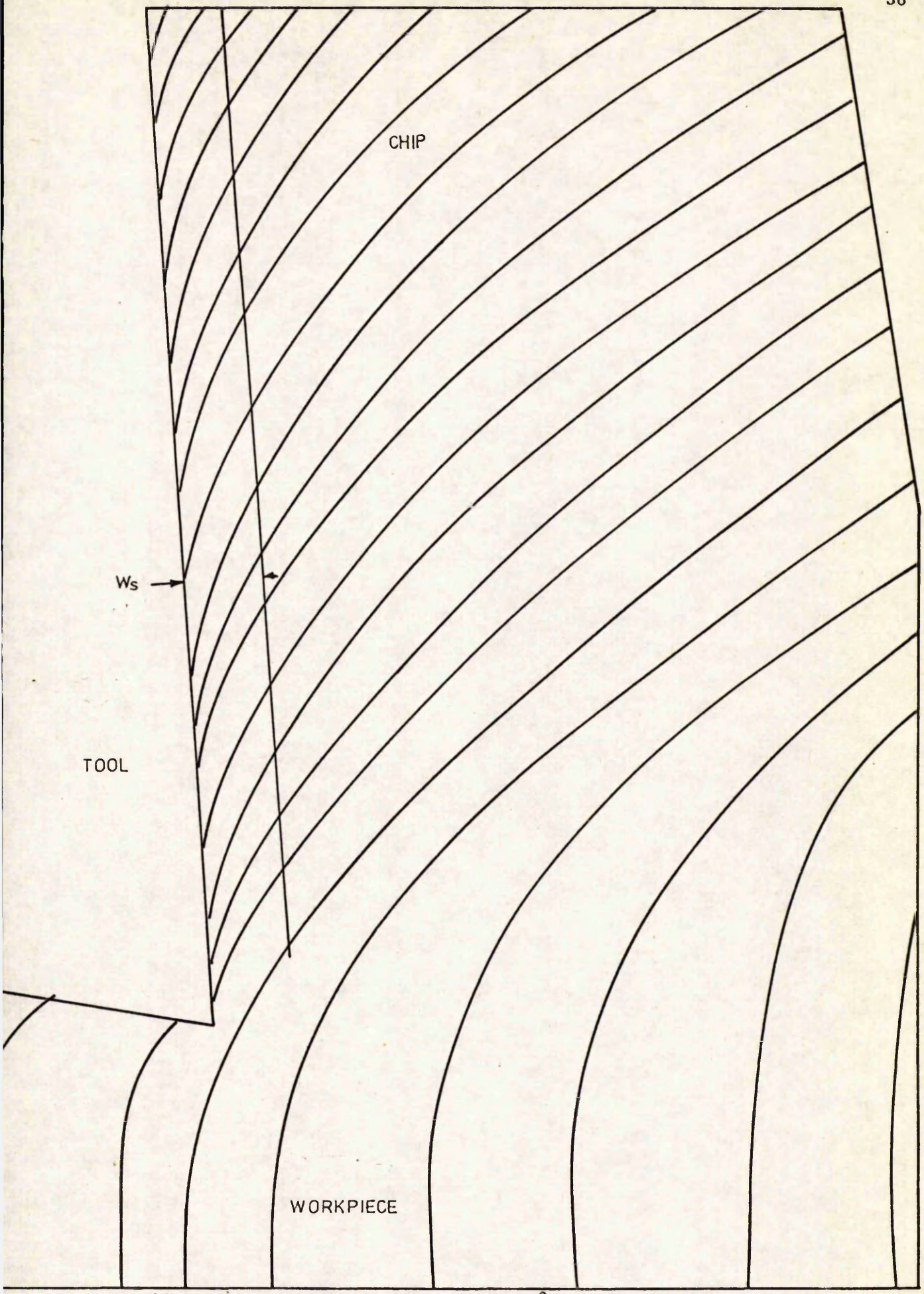

U = 131.5 m/min., t_1 = 0.3556 mm, α = 20° TOOL - CARBIDE

FIG. 3.3 Flow field tracing of secondary zone

the rake face. This assumption was necessary because of the mesh used for the finite element analysis.

For cutting speeds less than 46 m/min., the strain-rate was assumed to be zero throughout the secondary zone. For higher speeds, the strain-rate distribution was approximated as done by Tay et al (36). It was assumed that the shear strain-rate at the tool-chip interface (sticking part only) was constant and equal to V_c/w_s where V_c is the chip velocity and w_s is the maximum width of the secondary zone. The strain-rate within the secondary zone in a direction perpendicular to the rake face was assumed to decrease linearly from the value at the interface to zero at the boundary between the secondary zone and the rest of the chip. It is to be accepted that the above assumptions are quite approximate but seem to be reasonable in the view of the small size of the secondary zone and high intensity of turbulent deformation. Furthermore, the grid lines reaching the secondary zone are already severely distorted in the primary zone and any accurate analysis of the deformed lines is very difficult.

3.4 Flow Stress in the Primary Zone.

The flow stress of a metal is influenced by the temperature of deformation, degree of deformation or strain and the rate of deformation or strain-rate. The degree of dependency of the flow stress upon these variables varies considerably for different materials. Available data in the literature on the stress versus the strain, strain-rate and temperature under conditions as present in the shear zone (83) are limited.

Previous workers have attempted to derive a single equation expressing the stress in terms of strain, strain-rate and temperature. Lubahn (80) obtained such an equation containing six constants from three empirical relationships. He assumed the true stress-strain curve to be

a simple power law for large strains. However, this assumption was found to be in poor agreement with the results of Dorn et al (81). Alder and Phillips (82) observed that, for lower strain rates, the effect of strain rate on the stress could be expressed by a semi-logarithmic formula. This finding is supported by the results of Campbell and Ferguson (84) for the strain rate values lower than 5×10^{3} sec^{-1} (zone II) shown in Fig. 3.4.

Stevenson and Oxley (6, 79) assumed the stress-strain relationship of the form $\sigma = \sigma_1 \epsilon^n$ and obtained experimental data for the variation of σ_1 and n over a range of strain-rates and temperatures for a low carbon, free machining steel. However, these results give poorer approximation as the range of strain is increased (36). There is no accurate available data at the present time and the published literature contains many conflicting conclusions (87). An excellent review of the literature on the available flow stress data has been given by Altan and Boulger(86).

The experimental data for mild steel reported by Campbell and Ferguson (84) and Manjoine (85) were analysed further in order to derive an equation for the flow stress in terms of strain, strain-rate and temperature. Zone II of Campbell and Ferguson (Fig. 3.4) covers most of the temperature and strain-rate conditions present in the primary deformation zone. From Fig. 3.4, for a given strain, the following empirical equation could be derived. For the shear strain rate $\dot{\gamma} < 5 \times 10^{3}$ sec^{-1}

$$\tau = A + m \log \dot{\gamma} \qquad (3.14)$$

where, τ is the shear flow stress in MPa

$$A = 158.5777 - 0.666956T + 1.88557 \times 10^{-3} T^2,$$

$$m = 28.10716 - 5.93245 \times 10^{-2} T + 6.72203 \times 10^{-5} T^2, \qquad (3.15)$$

and T is in °C.

It was found that Manjoine's results (Fig. 3.5) also show similar trend as exhibited by Eq. (3.14).

For conversion from uniaxial stress and strain to the shear stress and strain, Von Mises Criterion was used, giving

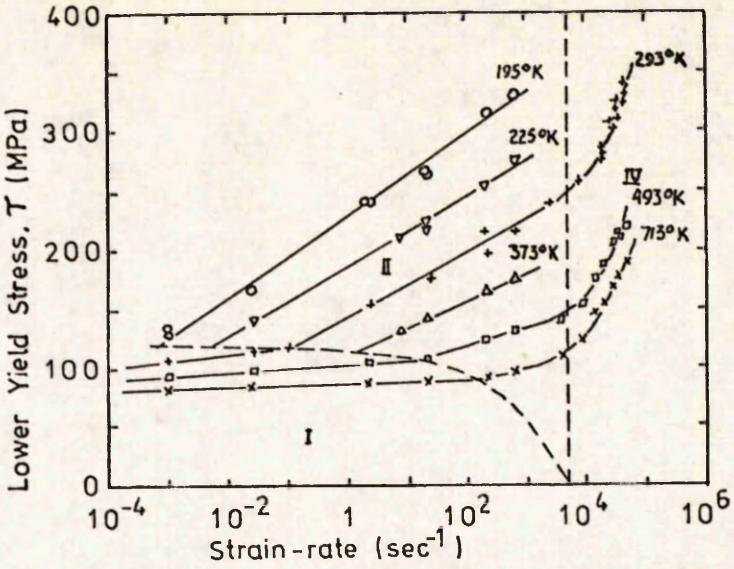

FIG. 3.4 (AFTER CAMPBELL AND FERGUSON(84))

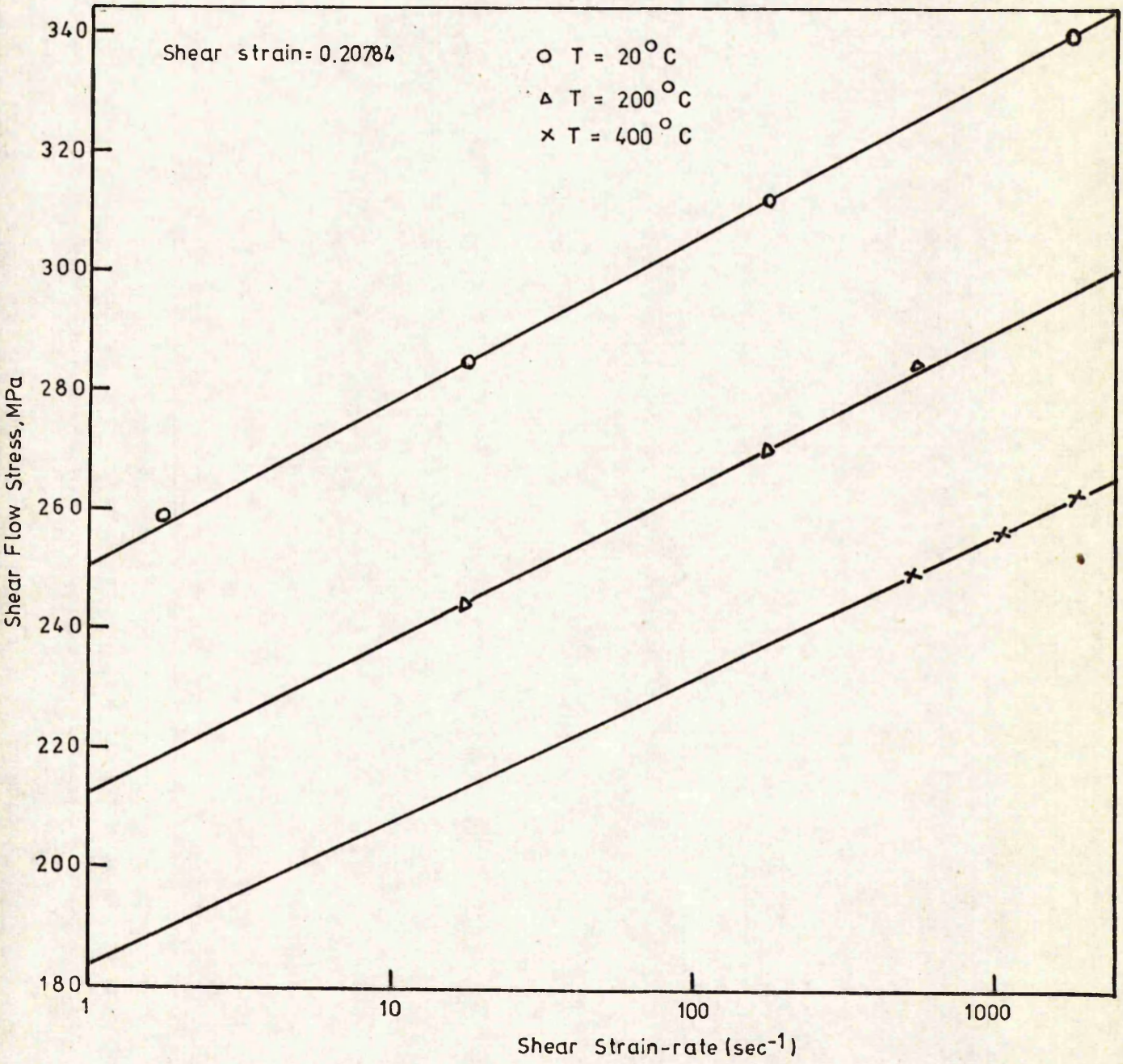

FIG. 3.5 (AFTER MANJOINE(85))

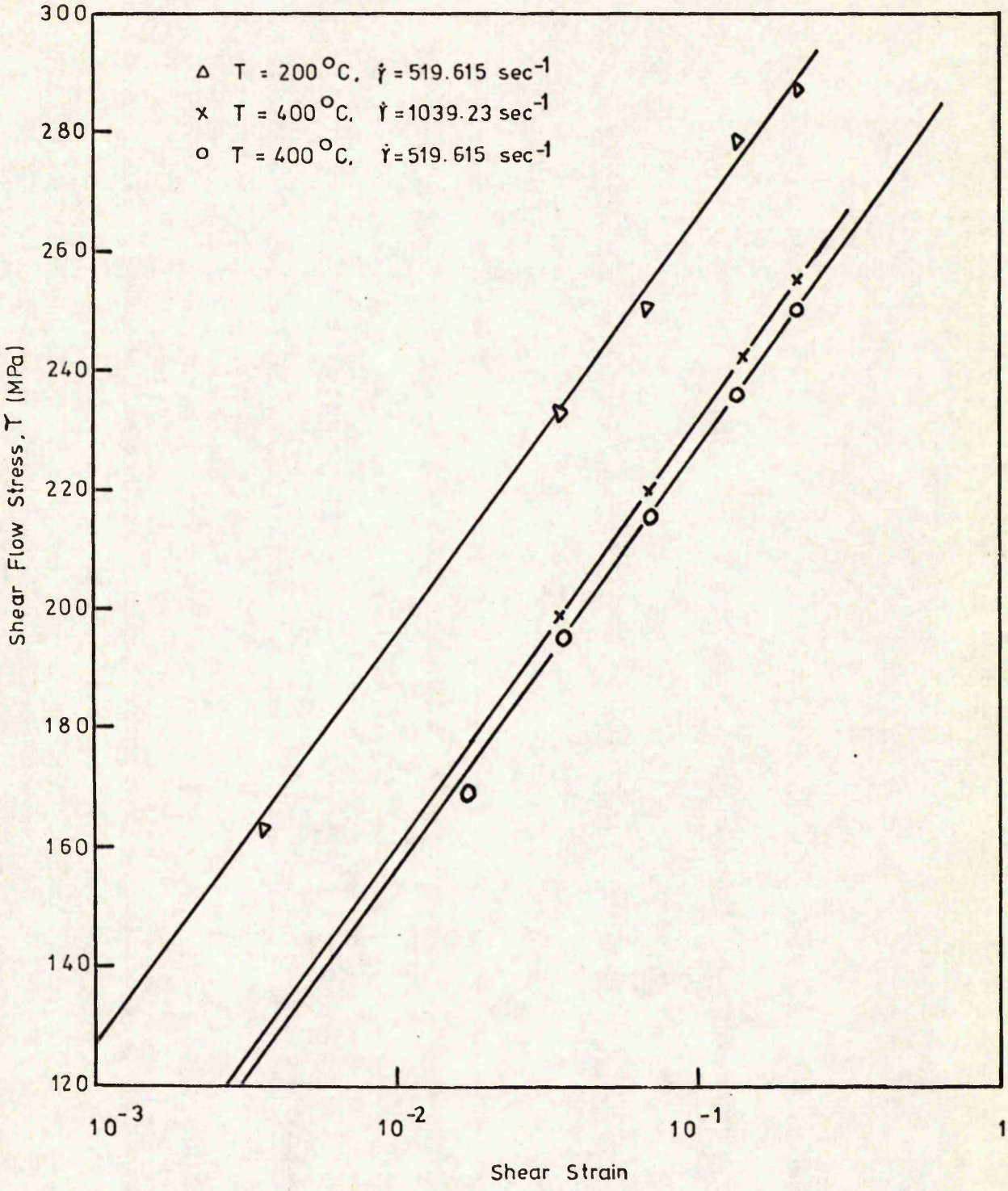

FIG. 3.6 (AFTER MANJOINE(85))

$$\left.\begin{aligned} \tau &= \sigma/\sqrt{3} \\ \gamma &= \sqrt{3}\,\epsilon \\ \dot{\gamma} &= \sqrt{3}\,\dot{\epsilon} \end{aligned}\right\} \qquad (3.16)$$

In order to find out the effect of shear strain on shear flow stress, Manjoine's results were plotted as shown in Fig. 3.6 showing a linear variation of flow stress with strain on a semi-log scale. Hence, for a given strain-rate, shear flow stress is related to the shear strain by

$$\tau = B + n \log \gamma \qquad (3.17)$$

where B and n are the functions of temperature provided the strain-rate remains constant. The experimental data reported by Campbell and Ferguson are for one strain ($\gamma = 0.01$) only. Manjoine's tests cover the strains up to the value of 0.20 only. Beyond this value, it was assumed that the same trend continues. This assumption is necessary because of the unavailability of suitable data for higher strains.

It can be shown that the equations (3.14) and (3.17) can be combined to give

$$\tau = C + G \log \dot{\gamma} + D \log \gamma + H \log \gamma \log \dot{\gamma} \qquad (3.18)$$

where C, G, D and H are the functions of temperature. Based on Eq.(3.15) it was assumed that these constants were the 2nd order functions of temperature, i.e.,

$$\left.\begin{aligned} C &= K_1 + K_2 T + K_3 T^2 \\ G &= K_4 + K_5 T + K_6 T^2 \\ D &= K_7 + K_8 T + K_9 T^2 \\ \text{and} \quad H &= K_{10} + K_{11} T + K_{12} T^2 \end{aligned}\right\} \qquad (3.19)$$

where K_1 ..... K_{12} are the constants to be determined experimentally and are independent of strain, strain-rate and temperature.

Substituting Eq. (3.19) into Eq. (3.18) and introducing a material constant K_0 in order to account for the variations in material properties,

the following general equation was obtained

$$\tau = K_0 \left\{ K_1 + K_2 T + K_3 T^2 + (K_4 + K_5 T + K_6 T^2) \log \dot{\varepsilon} + (K_7 + K_8 T + K_9 T^2) \log \varepsilon + (K_{10} + K_{11} T + K_{12} T^2) \log \varepsilon \log \dot{\varepsilon} \right\} \quad (3.20)$$

The constants K_1, K_2 ..... K_{12} in Eq. (3.20) were obtained using Manjoine's (85) experimental data. Twelve independent test conditions were fed to the computer in order to solve 12 simultaneous equations for the constants K_1, K_2 ..... K_{12}. Obviously, for these test conditions, the material constant K_0 is equal to 1. The empirical expression thus obtained is

$$\begin{aligned} \tau = K_0 \{ & 411.52 - 0.66895\,T + 6.9129 \times 10^{-4}\, T^2 \\ & - (9.5009 - 0.11417\,T + 1.1771 \times 10^{-4}\, T^2) \log \dot{\varepsilon} \\ & + (228.59 - 0.61197\,T + 7.4836 \times 10^{-4}\, T^2) \log \varepsilon \\ & - (54.980 - 0.18285\,T + 1.7638 \times 10^{-4}\, T^2) \log \dot{\varepsilon} \log \varepsilon \} \end{aligned} \quad (3.21)$$

where τ is shear flow stress in MPa.

In order to test the validity of equation (3.20), the equation was tested for several other test conditions (85). The test conditions, experimental and empirical stress values and the % variation are given in Table 3.2. It can be seen that the maximum variation between the experimental and empirical values of flow stress is less than 3%.

For the present investigations, the value of K_0 had to be determined. As a first approximation, the temperature distribution was obtained using a constant value of flow stress τ_{sz} given by

$$\tau_{sz} = R \cdot \cos \theta \cdot \sin \phi / w t_1 \quad (3.22)$$

where R is the resultant cutting force

ϕ is the shear angle

w is the width of cut

Table 3.2

Experimental flow stress based on Manjoine's results (85) and empirical flow stress values based on Eq. (3.21) with $K_o = 1.0$

S. No.	Temp °C	LOG OF (Strain-rate sec^{-1})	Strain	Expt. Stress MPa	Empirical Stress MPa	% Error
1	20.000	3.000	.20784	3.3400E+02	3.3400E+02	5.4461E-13
2	200.000	3.000	.20784	2.9050E+02	2.9050E+02	6.2616E-13
3	400.000	3.000	.20784	2.5650E+02	2.5650E+02	7.0916E-13
4	400.000	2.000	.20784	2.3230E+02	2.3230E+02	3.9152E-13
5	200.000	1.000	.20784	2.3850E+02	2.3850E+02	3.8134E-13
6	20.000	1.000	.20784	2.7840E+02	2.7840E+02	6.5337E-13
7	20.000	3.000	.13856	3.2300E+02	3.2300E+02	5.6315E-13
8	200.000	1.000	.06928	1.8570E+02	1.8570E+02	4.8977E-13
9	400.000	3.000	.06928	2.2150E+02	2.2150E+02	4.1061E-13
10	400.000	2.000	.06928	1.9250E+02	1.9250E+02	4.7246E-13
11	200.000	3.000	.06928	2.6200E+02	2.6200E+02	6.9427E-13
12	20.000	1.000	.13856	2.4930E+02	2.4930E+02	3.6482E-13
13	400.000	3.400	.20784	2.6630E+02	2.6618E+02	4.5062E-02
14	200.000	.400	.20784	2.2280E+02	2.2290E+02	-4.4883E-02
15	20.000	2.000	.20784	3.0625E+02	3.0620E+02	1.6327E-02
16	200.000	2.200	.20784	2.7000E+02	2.6970E+02	1.1111E-01
17	200.000	2.000	.06928	2.2370E+02	2.2385E+02	-6.7054E-02
18	200.000	2.400	.06928	2.3900E+02	2.3911E+02	-4.6025E-02
19	400.000	3.200	.06928	2.2730E+02	2.2730E+02	4.0013E-13
20	200.000	.600	.06928	1.7050E+02	1.7044E+02	3.5191E-02
21	20.000	.400	.13856	2.2700E+02	2.2719E+02	-8.3700E-02
22	200.000	1.000	.13856	2.2450E+02	2.1901E+02	2.4441E+00
23	200.000	2.000	.13856	2.5620E+02	2.4950E+02	2.6162E+00
24	400.000	2.600	.13856	2.3150E+02	2.3319E+02	-7.3172E-01
25	200.000	1.400	.13856	2.3720E+02	2.3121E+02	2.5267E+00

Table 3.3

Flow Stress Values

	Test No.	Speed m/min	Feed mm/rev	Rake angle $\alpha(^\circ)$	Shear angle $\phi(^\circ)$	Tool Material	τ_{sz} from measured forces	τ_{sz} from Eq(3.21)	% Variation
1	1	24.76	0.3556	41.0	48.5	HSS	463.41	484.75	4.60
2	3	24.78	0.2845	20.0	41.5	"	450.08	475.25	5.59
3	5	17.34	0.3556	41.0	47.4	"	446.10	480.17	7.64
4	6	24.68	0.3556	20.0	39.0	"	489.90	476.50	-2.73
5	9+	24.77	0.3556	20.0	37.0	"	465.02	480.25	3.27
6	11	45.96	0.3556	20.0	30.0	"	480.76	482.33	0.33
7	12+	45.77	0.3556	20.0	32.0	"	490.12	481.83	-1.69
8	13	24.77	0.3556	30.0	35.0	"	471.99	483.25	2.38
9	25++	17.34	0.3556	41.0	47.4	"	446.10	481.81	8.00
10	14	35.33	0.3556	20.0	36.0	Carbide	473.70	484.17	2.21
11	15	71.11	0.3556	20.0	33.0	"	485.48	488.17	0.55
12	17	35.24	0.2845	20.0	34.0	"	457.90	486.37	6.22
13	18	35.28	0.5690	20.0	38.5	"	454.50	477.44	5.04
14	19	35.15	0.3556	10.0	35.0	"	505.95	475.33	-6.05
15	21+	35.26	0.3556	20.0	35.0	"	470.60	480.25	2.05
16	23	130.73	0.3556	20.0	30.7	"	472.17	490.25	3.83
17	24+	131.38	0.3556	20.0	34.4	"	494.44	489.12	-1.07

+ Tests performed with coolant.

++ Tool with initial flank wear (0.376 mm)

t_1 is the undeformed chip thickness

and Θ is the angle between R and the plane SZ (Fig. 3.2 a).

Now, these temperatures were used to calculate the flow stress distribution in the primary zone taking K_0 equal to one in Eq. (3.21). The average value of flow stress τ_{av} was determined from the flow stress distribution. τ_{sz} and τ_{av} were obtained for three different tests and K_0 was taken as the average value of the quotient τ_{sz}/τ_{av}. It was found that for the workpiece material used for the present investigations, the material constant

$$K_0 = 1.410 \qquad (3.23)$$

In order to check the accuracy of Eqs. (3.21) and (3.23), the average effective stress τ_{sz} along the shear plane calculated from Eqs. (3.21) and (3.23) using the strains, strain-rates and temperatures obtained was compared with that calculated from the experimentally-measured forces and length of shear plane (Eq. (3.22)) as shown in Table 3.3 for all the tests. The maximum variation of τ_{sz} by the two methods is less that 8%.

3.5 Flow Stress in the Secondary Zone.

The shear and normal stress distributions along the tool-chip interface are assumed to be the same as those obtained by Zorev (88). Along the distance C_1 (Fig. 3.7) where sticking occurs the shear stress is constant and equal to τ_s, the maximum shear flow stress of the material in the secondary zone. Over the sliding length, the shear stress is given by

$$\tau = \mu_b \sigma_n = \mu_b \frac{\sigma_m}{C^n} \cdot x^n \qquad (3.24)$$

under the assumption that the distribution of the normal stress σ_n can be approximated by an exponential function of x, where μ_b is the coefficient of friction, σ_m the maximum normal stress, and n the exponent.

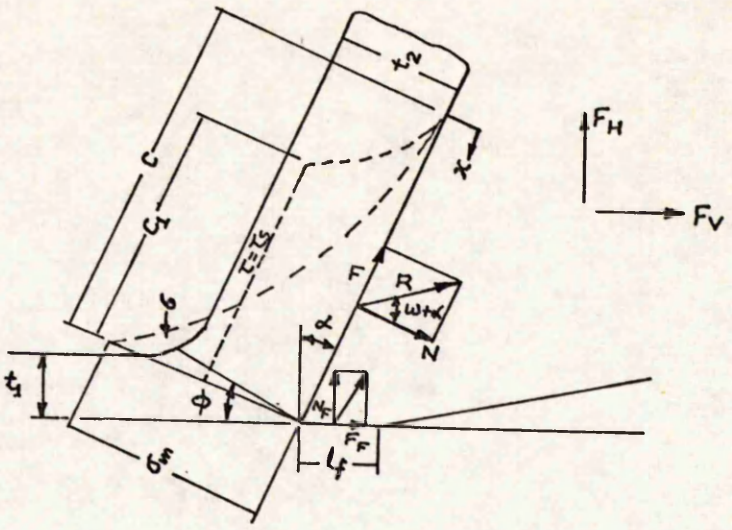

Fig. 3.7 Forces and stresses acting in orthogonal machining.

From Fig. 3.7, the coefficient of friction over the sliding range μ_b is given by

$$\mu_b = \frac{\tau_s}{\sigma_m} \left(\frac{c}{c - c_1} \right)^n \tag{3.25}$$

Substitution of Eq. (3.25) into Eq. (3.24) gives

$$\tau = \tau_s \cdot \frac{x^n}{(c-c_1)^n} \tag{3.26}$$

The maximum normal stress σ_m is related to the average normal stress q_N as

$$\sigma_m = (n + 1)\, q_N \tag{3.27}$$

By considering the moment equilibrium of the stress system shown in Fig. 3.7, the exponent n in Eq. (3.26) is found to be

$$n = 2 \left\{ \frac{c}{t_2 \left[\mu + \tan (\phi - \alpha) \right]} - 1 \right\} \tag{3.28}$$

where $\mu = F/N$ is the overall coefficient of friction, α is the rake angle, ϕ is the shear angle, F is the frictional force along tool-chip interface and N is the normal force.

The maximum shear stress τ_s can be determined by considering the equilibrium of the force system over the rake face in the x direction, i.e.

$$F = \tau_s . C_1 . w + \int_0^{C-C_1} \tau . dx . w \qquad (3.29)$$

where w is the width of cut and τ is given by Eq. (3.26) which on substitution in Eq. (3.29) gives

$$\tau_s = \frac{(n + 1) F}{(C + nC_1) w} \qquad (3.30)$$

It can be seen that for n = 1 and $C_1 = C/2$, Eq. (3.30) results in

$$\tau_s = \frac{4F}{3Cw} \qquad (3.31)$$

similar to the equation used by Tay et al (36). In general, the shear flow stress over the sticking and sliding lengths of the secondary zone is given by Eq. (3.30) and (3.26) respectively.

3.6 Material Properties of the Workpiece and Cutting Tool.

3.6.1 Workpiece Material.

Free machining steel was used as a workpiece material for all the tests. Its chemical composition and other properties (41) are given below.

Chemical Composition.

C	S	Mn	Si
0.18%	0.24%	1.23%	0.22%

Density, $\rho = 7.86 \times 10^3$ kg/m^3

Thermal Conductivity, $K = 62.802 - 0.041868T$ (W/m K)

where T is in °C.

Specific Heat, C_p (J/Kg K) $= 418.68 + 0.5756847T$ for $T < 360°C$

$= 625.93$ for $T \geq 360°C$

where T is in °C.

3.6.2 Tool Materials.

The tests were performed with high speed steel as well as cemented carbide tools.

Properties (43) of High Speed Steel used.

Chemical Composition.

C	Mn	Si	Cr	W	V	Co
0.84%	0.31%	0.20%	4.54%	21.81%	1.47%	5.30%

Density, $\rho = 8.17 \times 10^3$ Kg/m^3

Thermal Conductivity, $K = 40.612 - 0.0100483T$ W/m K

where T is in °C.

Specific heat, $C_p = 460.548$ J/Kg K

Properties of Cemented Carbide Used.

Chemical Composition.

Tungsten Carbide, WC	79.0%
Titanium Carbide, Tic	4.0%
Tantalum Carbide, Tac	8.0%
Cobalt, Co	9.0%

Density (45), $\rho = 12.6 \times 10^3$ Kg/m^3

Thermal Conductivity (45), K

Temp °C	50	100	150	200	300	400	500	600
W/m K	58.615	58.615	58.615	58.615	50.242	50.242	50.242	50.242

Specific Heat (44), $C_p = 251$ J/Kg K

The cemented carbide tip was clamped to a tool holder made of EN 27 steel.

Properties of EN 27 steel (42) used for tool holder.

Chemical Composition %

C	Si	Mn	S	P	Ni	Cr	Mo
0.34	0.27	0.55	0.003	0.024	3.53	0.78	0.39

Density, $\rho = 7.859 \times 10^3$ Kg/m^3

Specific Heat, $C_p = 460.548 + 0.3977458T$ (J/Kg K) where T is in °C.

Thermal Conductivity, K.

Temp °C	0	100	200	300	400	500	600	700	800
W/m K	33.076	33.913	35.169	35.588	35.588	33.494	30.564	28.345	26.796

3.7 Measured Input Data and Cutting Conditions.

The tests were desinged for various cutting conditions to find out the effect of cutting speed, feed, rake angle, coolant and initial flank wear on temperature distributions in orthogonal metal cutting. Besides, two different tool materials - high speed steel and cemented carbide - were used. The cutting conditions, which were constant for all the tests, were width of cut = 6.35 mm, clearance angle = 10° and room temperature T_{∞} = 20°C.

To obtain the necessary input data, several experiments were conducted employing the conditions identical to those used for obtaining the streamlines in the shear zone. In order to calculate the amount of heat generation, it is necessary to determine the cutting forces. Experiments were performed using a 'Kistler' three-component (piezo-electric) tool dynamometer for measuring the cutting force, F_V and feed force, F_H. The experimental setup is shown in Plate VI. A freshly ground tool was used for every test and after the test the tool was examined under a microscope. The tool-chip contact length and the sticking contact lenght were obtained from the wear scar on the tool. For the tests where it was not possible to measure the sticking contact length accurately, it was assumed that the sticking contact length was only about half the total contact length (40, 36).

In another experiment, designed to evaluate the force components acting on the flank face of the tool with known flank wear, the specimen was rotated in the reverse direction and the tool was pressed against it. The force components acting on the flank face for the given length of sliding contact length were measured. The measurements gave the force

component along the flank F_F = 20 N and the force component perpendicular to the flank, N_F = 42N for a given flank wear of 0.376 mm.

The cutting conditions and all other measured data are summarized in Table 3.4.

3.8 Experimental Measurement of Some Nodal Temperatures.

It was attempted to measure some nodal temperatures on the central axis of the tool along the tool rake face and tool flank face during orthogonal machining under the same test conditions. The tool was clamped to the tool-post with an overhang of 12.5 mm and thin mica-sheets were placed at the interfaces between the tool and toolpost for heat insulation. The high speed steel tool was reduced to 6.35 mm in width equal to that of the workpiece disc in order to simulate an ideal two-dimensional heat flow-condition. However, it was not possible with carbide tools because of the presence of tool-clamping screws. Insulated alumel-chromel thermocouple wires of 0.1219 mm diameter were adhered at different

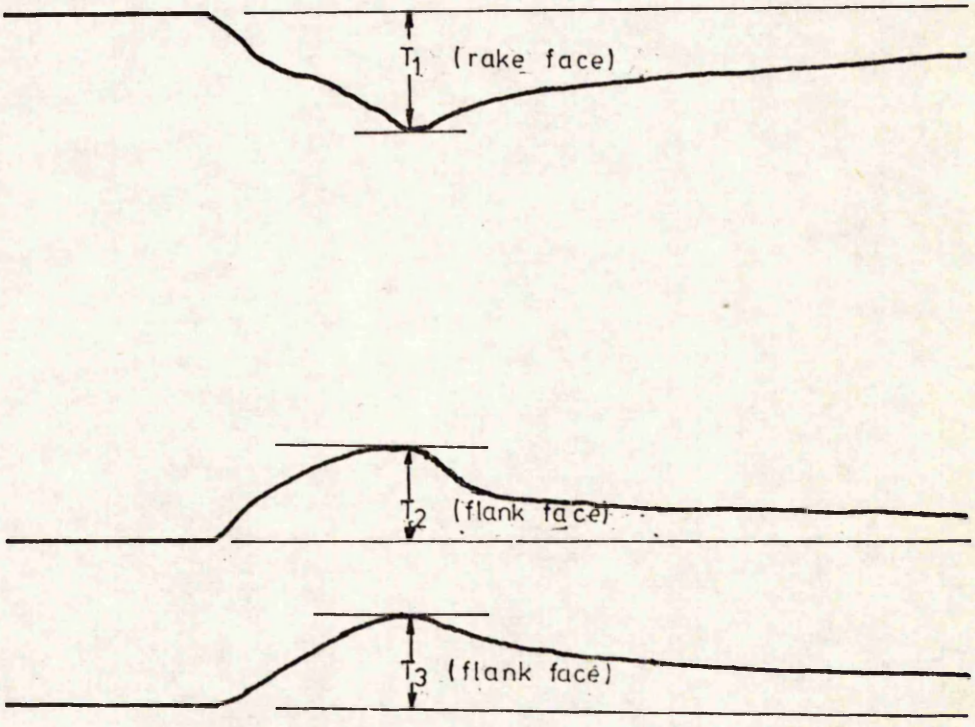

FIG. 3.8 A Typical Experimental Temperature Record

Table 3.4

Cutting Conditions and Measured Data.

Serial No.	Test Identification no.	Workpiece Revs/min. N rpm	Workpiece Diameter. D mm	Speed. U m/min	Feed. t_1 mm/rev	Rake angle. α (°)	Tool Material.	Shear angle. ϕ (°)	Chip Thickness ratio. t_1/t_2	Tool-chip Contact Length. C mm	Sticking part of Contact Length. C_1 mm	Vertical Component of Resultant force. F_V N	Horizontal Component of Resultant force. F_H N
1	1	80	98.50	24.76	0.3556	41.0	HSS	48.5	0.7750	0.9398	0.604	2425	280
2	3	80	98.60	24.78	0.2845	20.0	"	41.5	0.7143	1.524	0.8128	2700	1200
3	5	57	96.82	17.34	0.3556	41.0	"	47.4	0.7631	0.9144	0.5842	2300	256
4	6	80	98.20	24.68	0.3556	20.0	"	39.0	0.6634	1.9812	1.1176	3525	1560
5	9+	80	98.55	24.77	0.3556	20.0	"	37.0	0.6374	1.6000	0.7874	3300	1460
6	11	160	91.44	45.96	0.3556	20.0	"	30.0	0.5113	1.8288	1.1684	3500	1560
7	12+	160	91.06	45.77	0.3556	20.0	"	32.2	0.5517	1.8796	1.2192	3350	1420
8	13	80	98.55	24.77	0.3556	30.0	"	35.0	0.5743	1.2700	0.7366	2650	545
9	25++	57	96.80	17.34	0.3556	41.0	"	47.4	0.7630	0.9144	0.5842	2300	256
10	14	115	97.79	35.33	0.3556	20.0	Carbide	36.0	0.5903	0.6600	0.3300	2540	400
11	15	240	94.31	71.11	0.3556	20.0	"	33.0	0.5500	0.9144	0.4572	2900	770
12	17	115	97.54	35.24	0.2845	20.0	"	34.0	0.5703	0.6096	0.3048	2000	320
13	18	115	97.66	35.28	0.5690	20.0	"	38.5	0.6615	0.8128	0.4064	3975	760
14	19	115	97.28	35.15	0.3556	10.0	"	35.0	0.6250	1.1938	0.6096	3825	1990
15	21+	115	97.61	35.26	0.3556	20.0	"	35.0	0.5902	0.5588	0.2794	2525	376
16	23	480	86.69	130.73	0.3556	20.0	"	30.7	0.5152	0.9652	0.4826	3125	940
17	24+	480	87.12	131.38	0.3556	20.0	"	34.4	0.5890	0.9779	0.4826	3025	920

\+ Tests performed with coolant.

++ Tool with initial flank wear (0.376 mm)

locations along the tool rake face and flank face using a high temperature resistant scotch electrical tape and were connected to a 6-channel U-V recorder. The experimental setup is shown in Plate VII. Due to the chip flow obstruction on the tool face and the clearance required for the thermocouple wires along the flank, the nearest distances from the tool edge at which the temperatures could be measured were 3.92 mm away along the tool face and 5.0 mm down along the flank.

At higher speeds, the temperatures could not be measured due to the lack of adhering of the sticking tape at higher temperatures. A typical temperature record is shown in Fig. 3.8.

3.9 Determination of the Heat Transfer Coefficient of Coolant.

In order to determine the heat transfer coefficient of a liquid, it is necessary to have information about the variation of specific heat, viscosity, density and thermal conductivity of the liquid with temperature. Since such information about commercial coolants is lacking, it was decided to use water only as a coolant.

For normal cutting conditions, the coolant action in metal cutting gives rise to a low-quality and subcooled forced convection before the incipient boiling line where the general equations of forced convection are applicable provided the supply of coolant is sufficient and continuous. In order to apply the general equations of forced convection to calculate the heat transfer coefficient of a coolant in orthogonal machining, it is assumed that

(i) the flow is one-dimensional, i.e. the velocity is constant in any plane parallel or perpendicular to the surface under consideration,

(ii) the fluid is incompressible,

(iii) the pressure is constant throughout the flow field,

(iv) the flow is steady with respect to time

and (v) fluid flow is not affected by heat flow.

The tool, work and chip coolant areas are considered as seven

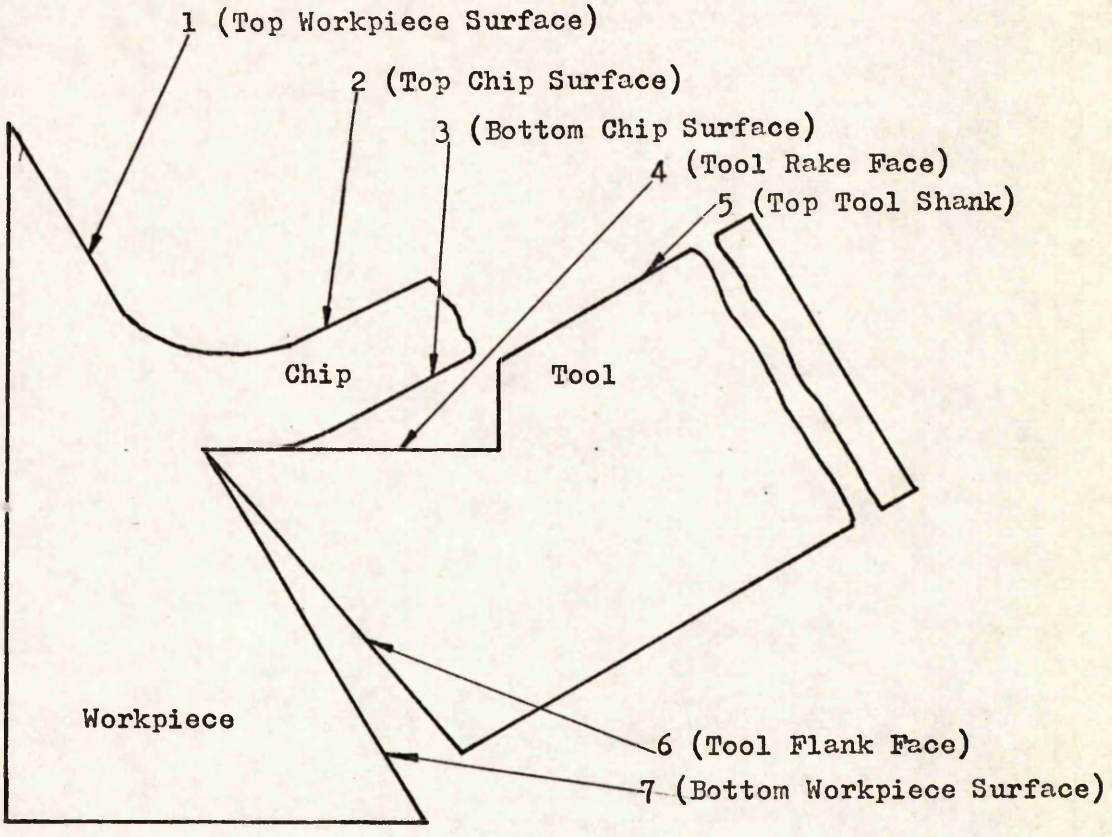

Fig. 3.9. Categorization of Coolant Surfaces for the Calculation of h.

different surfaces as shown in Fig. 3.9. The heat transfer coefficient h, for each surface is calculated separately and is, again, a function of local temperatures. Furthermore, each surface is assumed to be a flat one and so the following equations of forced convection (89, 90) could be used.

For laminar flow i.e., Renolds number $R_e < 5 \times 10^5$

$$N_u = 0.664 \; R_e^{0.5} \; P_r^{0.33} \quad \text{if } P_r > 0.1 \tag{3.32}$$

and $$N_u = 1.13 \; (R_e \; P_r)^{0.5} \quad \text{if } P_r < 0.1 \tag{3.33}$$

For turbulent flow i.e., $R_e > 5 \times 10^5$

$$N_u = 0.036 \cdot P_r^{0.33} \cdot (R_e^{0.8} - 23{,}200) \tag{3.34}$$

for $P_r > 0.5$

(for coolants, the value of P_r is always greater than 0.5)

where

$$\left.\begin{aligned} N_u \text{ (Nusselt number)} &= hL/K \\ P_r \text{ (Prandtl number)} &= C_p \mu /K \\ R_e \text{ (Reynolds number)} &= \rho u_\infty L/\mu \end{aligned}\right\} \qquad (3.35)$$

L = the significant length dimension of the system to specify the geometry of the object from which heat flows.

u_∞ = fluid velocity,

μ = viscosity of the fluid,

K = thermal conductivity of the fluid,

h = heat transfer coefficient,

C_p = specific heat of the fluid,

and ρ = density of the fluid.

All physical properties are taken at the mean film temp;

$$T_f = (T_s + T_\infty)/2$$

where, T_s is the surface temperature,

and T_∞ is the liquid bulk temperature.

Thus, for known fluid properties (91) and given temperatures of the surface and the fluid, h can be calculated using Eqs. (3.32) - (3.35). However, even 50% discrepancy in the value of h calculated by two different methods is not unusual in convective heat transfer(89). The average values of the heat transfer coefficient calculated for a typical case using water as a coolant in the present investigations are given below.

Type of surface (Fig. 3.9)	1	2	3	4	5	6	7
Average h W/m^2 K	284	377	880	880	160	440	300

3.10 Heat Generation due to Plastic Deformation in the Primary Zone.

It is well known that a very large fraction λ of the plastic deformation energy is transformed into thermal energy. When the plastic-strain energy is as large as that involved in cutting, all but 1 per cent or so of the strain energy appears as thermal energy, the small residual energy being associated with permanent lattice deformation (26). Thus to a good approximation it was assumed that the deformation energy is converted entirely into thermal energy, giving

$$\dot{Q} = \tau \dot{\imath} \tag{3.36}$$

where $\dot{Q}$ is the rate of heat generation per unit volume,

τ is the shear flow stress, and

$\dot{\imath}$ is the shear strain-rate.

The shear flow stress and shear strain-rate within the primary deformation zone were determined experimentally as described earlier.

3.11 Heat Generation in the Secondary Zone.

In the secondary zone, the heat is generated within the chip due to plastic deformation as well as over the contact length due to boundary friction. Similar to the primary deformation zone, the rate of heat generated per unit volume $\dot{Q}$ at a point due to deformation is given by

$$\dot{Q} = \tau_s \dot{\imath} \tag{3.37}$$

where τ_s is the maximum shear stress given by Eq. (3.30).

The heat generation rate per unit area q_x due to boundary friction at a point on the sticking length at a distance x from the tool edge was calculated as

$$q_x = \tau_s V_x \tag{3.38}$$

where V_x is the velocity at the point as described in Section 3.3.

Over the sliding contact length, the rate of heat generation per unit area due to the boundary friction at a point at a distance x from the tool edge is given by

$$q_x = \tau_x V_c \tag{3.39}$$

where V_c is the chip velocity and τ_x is the shear stress at the point given by

$$\tau_x = \frac{\tau_s \cdot (C - x)^n}{(C - C_1)^n} \tag{3.40}$$

where C is the tool chip contact length,

C_1 is the sticking length

and n is given by (Eq. 3.28).

3.12 Heat Generation over the Flank Face.

The heat is generated over the flank face of the tool due to boundary friction only if the tool has some flank wear. It was assumed that the distribution of the shear stress on the flank face of the tool is uniform, i.e.,

$$\tau_f = \frac{F_F}{\omega . l_f} \tag{3.41}$$

where F_F is the force component due to boundary friction parallel to the flank measured experimentally.

ω is the width of cut and

l_f is the length of flank wear land measured along the flank face.

The rate of heat generation per unit area over the length of flank wear land due to boundary friction was estimated as

$$q = \tau_f V_f \tag{3.42}$$

where V_f is the velocity along the flank face.

Chapter IV

COMPUTATIONAL METHODS AND COMPUTER PROGRAMS.

The program for implementing the algorithms described in Chapter two is carried out in five stages:

(i) Evaluation of the primary zone properties.

(ii) Mesh Generation.

(iii) Input data preparation.

(iv) Evaluation of element matrices and assembly and solution of system matrices.

(v) Graphical representation of the results.

The complete analysis requires the use of a number of computer programs SRATE, ELDAT, ELDATGEN (92), DATA, FETC, TPLOT and PRPLOT which have been developed for the analysis performed herein. Their functions are as follows:

SRATE: This program evaluates the properties of the primary zone, i.e., the strain, strain-rate and velocity distributions.

ELDATGEN(92): It generates the finite element mesh for the problem region.

ELDAT: It prepares the 'key diagram' (i.e., skeleton input data) for ELDATGEN.

DATA: It centralizes and checks for errors the input data required by the major program FETC.

FETC: It generates the individual element matrices, assembles them, injects the boundary conditions and solves the system matrices for the nodal temperatures employing an iterative procedure in order to account for the variation of material properties and flow stress with temperature.

TPLOT: It represents, graphically, the finite element mesh as a whole or in parts with or without node numbers and plots the temperature distributions and isothermals in the zones of

interest.

PRPLOT: It plots the strain, strain-rate, flow stress and temperature distributions in the primary zone.

The above programs are linked together by disc files. The output of one program is dumped on disc files and is used as input files for another program. The program flow path is shown in Fig. 4.1.

4.1 SRATE.

SRATE is developed to calculate velocity, strain and strain-rate distributions in the primary zone. The necessary input data can be divided in two parts:

(i) Cutting conditions, and

(ii) Stream-line co-ordinates.

(i) Cutting conditions: The values of feed t_1, rake angle α, work velocity U, chip thickness ratio CTR, number of flow lines and the co-ordinate magnification factor are read for each test. The chip thickness ratio CTR is obtained from the relationship

$$CTR = \frac{V_c}{U} \qquad (4.1)$$

where the chip velocity V_c was found by the change in width between stream-lines.

(ii) Streamline co-ordinates: The measured local co-ordinates of a number of points on each streamline, as described earlier, were stored on a disc. These are read from the disc for each streamline separately and stored in appropriate arrays.

A set calculation procedure is followed for each streamline. After transforming the co-ordinates into a global system, a third-order polynomial is fitted using the standard statistical subprogram 'MLR3' and the coefficients of the polynomial are obtained. At every point on the streamline, its angle with chip velocity β, $\frac{dy}{dx}$ and $\frac{d^2y}{dx^2}$ are calculated

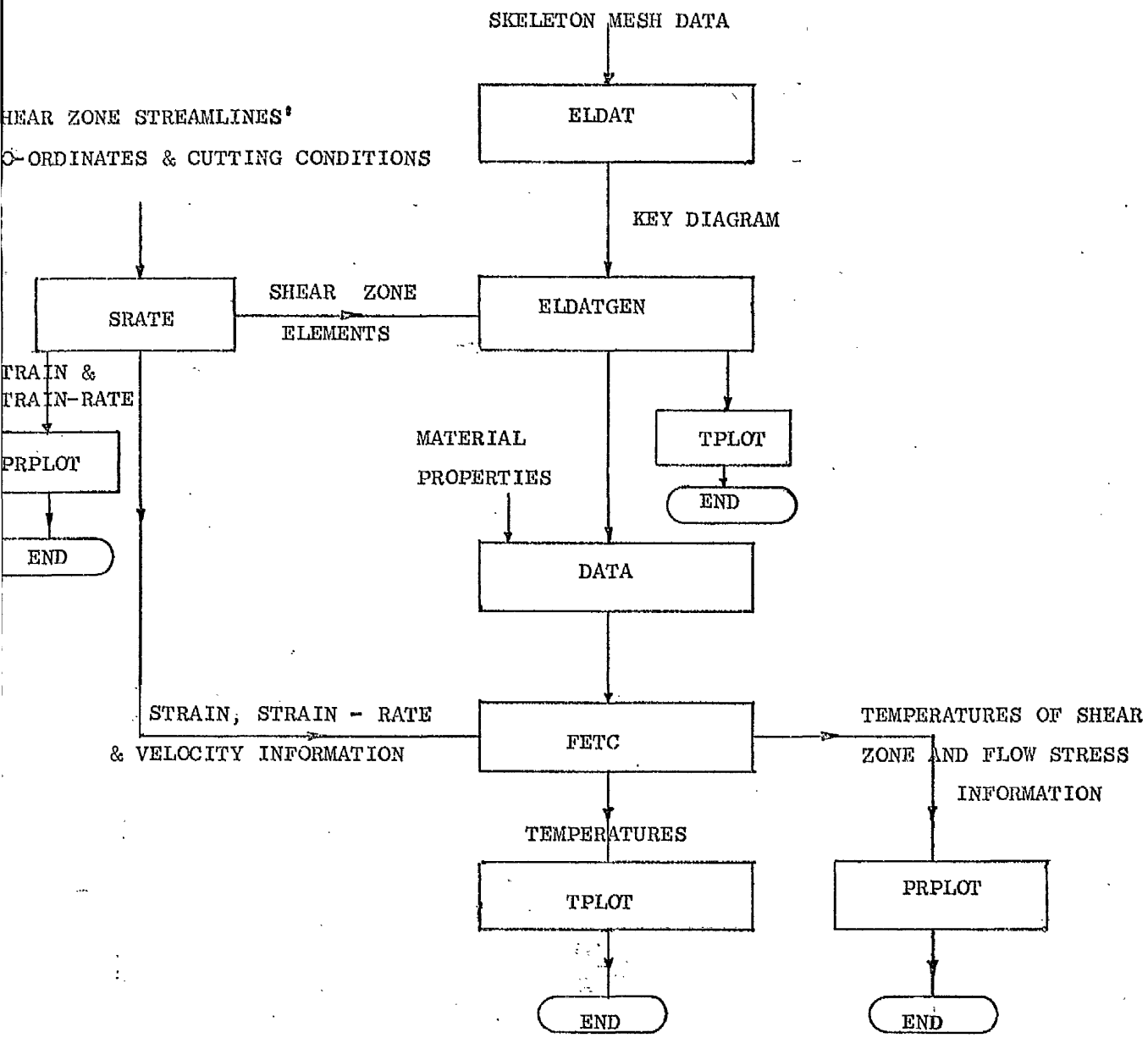

Fig. 4.1

Schematic Arrangement of Finite Element Programs.

in sequence and from these the values of velocity, strain-rate and strain are obtained. The operation is repeated for all the streamlines and the equations required for calculation are derived in Section 3.2. The sequencial procedure of the program is illustrated in the flow chart in Fig. 4.2.

The program output is diverted into three channels. The nodal coordinates of the shear zone elements and the cutting conditions are fed into ELDATGEN to be included as nodes in the mesh. The strain and strain-rate distributions are passed on to PRPLOT for plotting and analysis and this information coupled with the velocity distributions is passed on to FETC for temperature analysis.

4.2 ELDATGEN (92)

To perform an analysis using the Finite Element method, the problem region must be divided into a number of finite elements; these elements are considered to be interconnected at certain points (nodes) which are situated on the boundaries of the element. For each element in the mesh, the material properties, geometrical and nodal data have to be provided.

Each one of the nodes interconnecting the finite elements is assigned a number. The amount of core memory required for the storage of the system matrices is determined by the total number of nodes and the nodal bandwidth which may be defined as the maximum difference between any two node numbers of an element. The nodal bandwidth also influences the computing time required for the solution of the problem. Therefore, it is advantageous to number the nodes so that the nodal bandwidth is a minimum.

The preparation of this data is both time consuming and prone to error. To overcome these difficulties, a program called ELDATGEN has been developed by Abhary (92). For the sake of completeness, the existing program and the necessary modifications carried out are described, in brief, below.

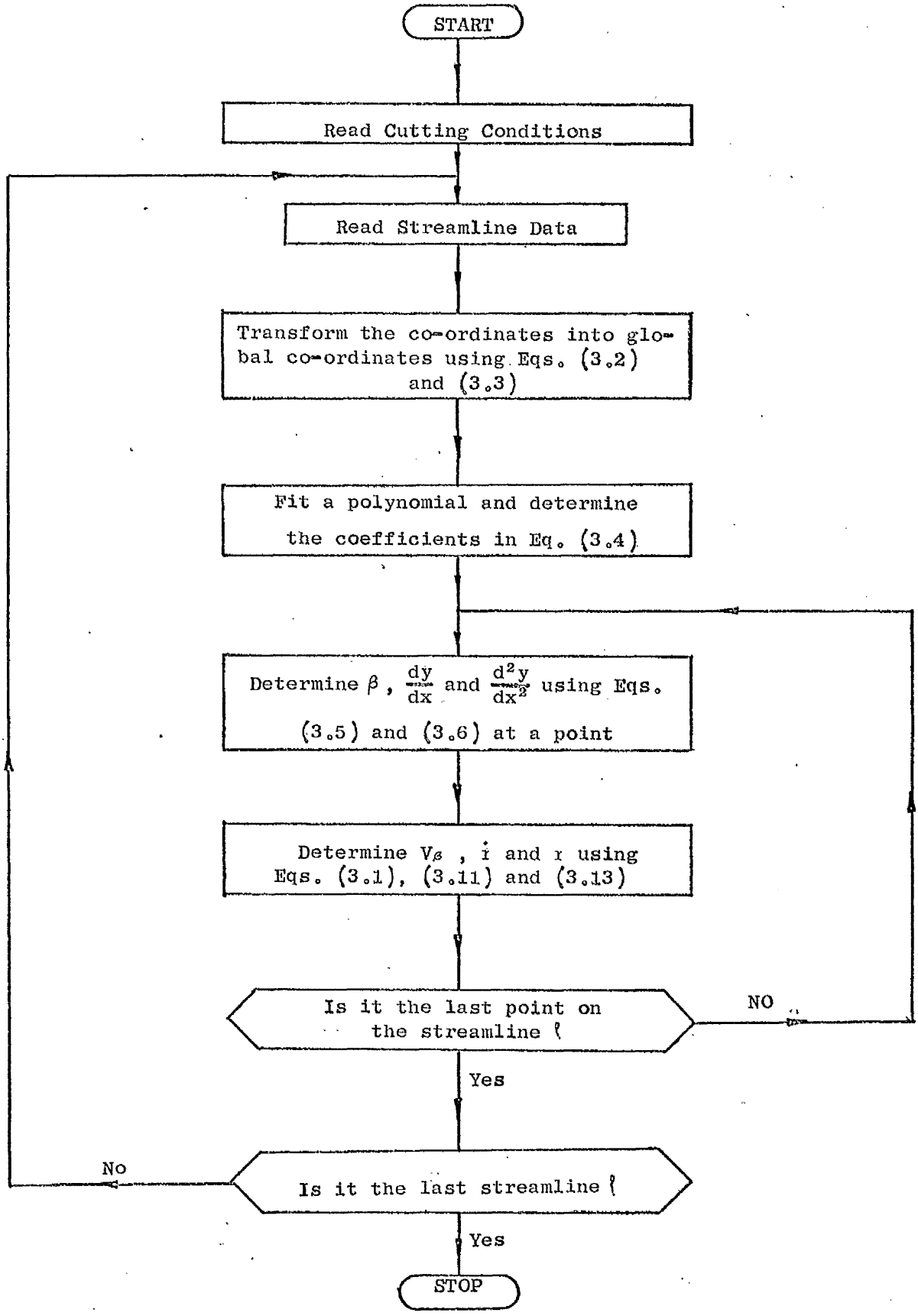

Fig. 4.2 Flow Chart for SRATE

The main function of ELDATGEN is to generate a mesh automatically from a skeleton input data to the required degree of fineness and also to number the nodes in an optimum way. The nodal data generated by it are passed on to FETC for evaluating the thermal matrix for each element; it is also used for graphical representation of the mesh.

The program is based on the chequerboard principle (92). The problem region is first divided into regions or 'zones' and a finite element mesh is generated within each zone. In the case of a two-dimensional problem, the region is divided into quadrilateral zones (if necessary, any one of the quadrilaterals can be degenerated into two triangles). Each zone in the x-y plane is represented in a chequerboard or key dlagram by a 'normalized' square, of two units side, defined in a new space $\xi - \eta$. (Assuming that a uniform grid is required, mesh points are created in equal increments in the ξ and η directions of the square). The $\xi - \eta$ co-ordinates of the points generated in the square can be easily calculated because the square is normalized; they are next transformed to the x-y space through a shape function using the relationships,

$$\begin{aligned} x &= [N] \quad \{x\}^e \\ y &= [N] \quad \{y\}^e \end{aligned} \tag{4.2}$$

where $\{x\}^e$, $\{y\}^e$ contain the x, y co-ordinates of boundary nodes and $[N]$ is a given shape function of ξ, η.

The type of shape function depends upon the complexity of the boundaries of the zone. If, for example, all the four boundaries of a zone were straight (Fig. 4.3), then the following shape function is used.

$$N_i = 1/4 \ (1 + \xi . \xi_i) \ (1 + \eta . \eta_i) \tag{4.3}$$

Normally, the x, y co-ordinates of the four corner nodes are sufficient to transform the normalized co-ordinates of a point (ξ, η space) to the co-ordinates in the x-y space. However, there are two circum-

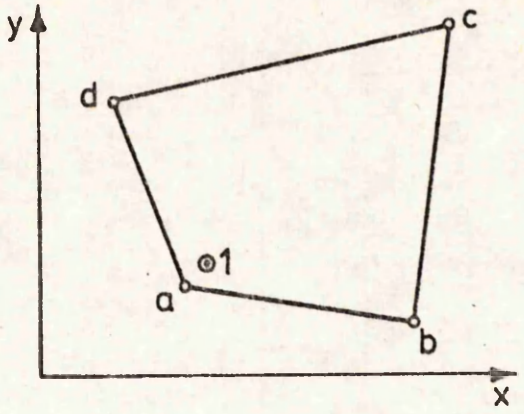

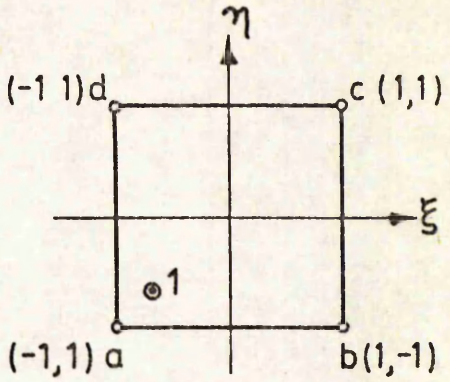

Fig. 4.3

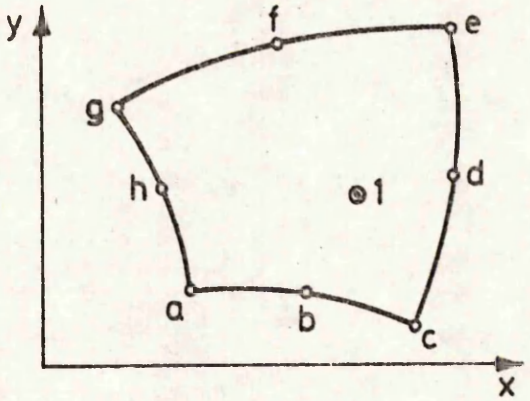

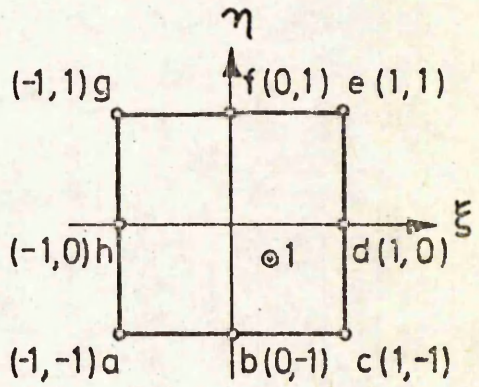

Fig. 4.4

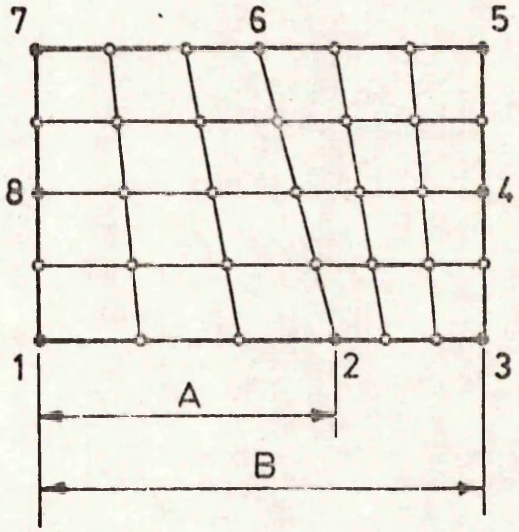

• Nodes used to define the zone.

∘ Nodes generated

Fig. 4.5

AFTER ABHARY(92)

stances that require the x-y co-ordinates of at least one more node. They are:

(i) Curved Boundary: If one of the boundaries of the zone is curved, the x-y co-ordinates of the node situated mid-way along the curved boundary are required for the transformation from the $\xi - \eta$ to the x-y space (node h, Fig. 4.4). The shape functions used are given by Eqs. (2.29) - (2.31).

(ii) Non-Uniform Mesh: If a non-uniform mesh is required in a particular zone, an additional node is introduced on one of the boundaries. This node is positioned to the right or left of the mid-position of the boundary. Its distance from the mid-position indicates the amount of grading or non-uniformity required in the zone. The boundary on which this additional node is placed must be a straight line. The x-y co-ordinates of this additional node must not be furnished; instead a weighting factor which expresses the distance between the additional mid-side node and the first corner node as a fraction of the boundary length is specified. For example, if a non-uniform mesh as shown in Fig. 4.5 is required, then a weighting factor equal to the ratio of the lengths A:B is assigned to node 2.

To specify the mesh fineness required, the normalized squares that correspond to the different zones are assembled to form a 'Key diagram' (which may be defined as a diagram consisting of one or more rows, with each row having the same number of squares). The position of a square in the key diagram should be consistent with the position of the corresponding zone in the structure. More often than not, when trying to arrange the normalized squares in the form of a key diagram, gaps occur which are filled by non-existent or 'void' zones.

An I, J system of axes is associated with the key diagram (Fig. 4.7), this system of axes should be consistent with the x-y system (Fig. 4.6(a)). The point (1, 1) in the I, J system is made to coincide with one of the

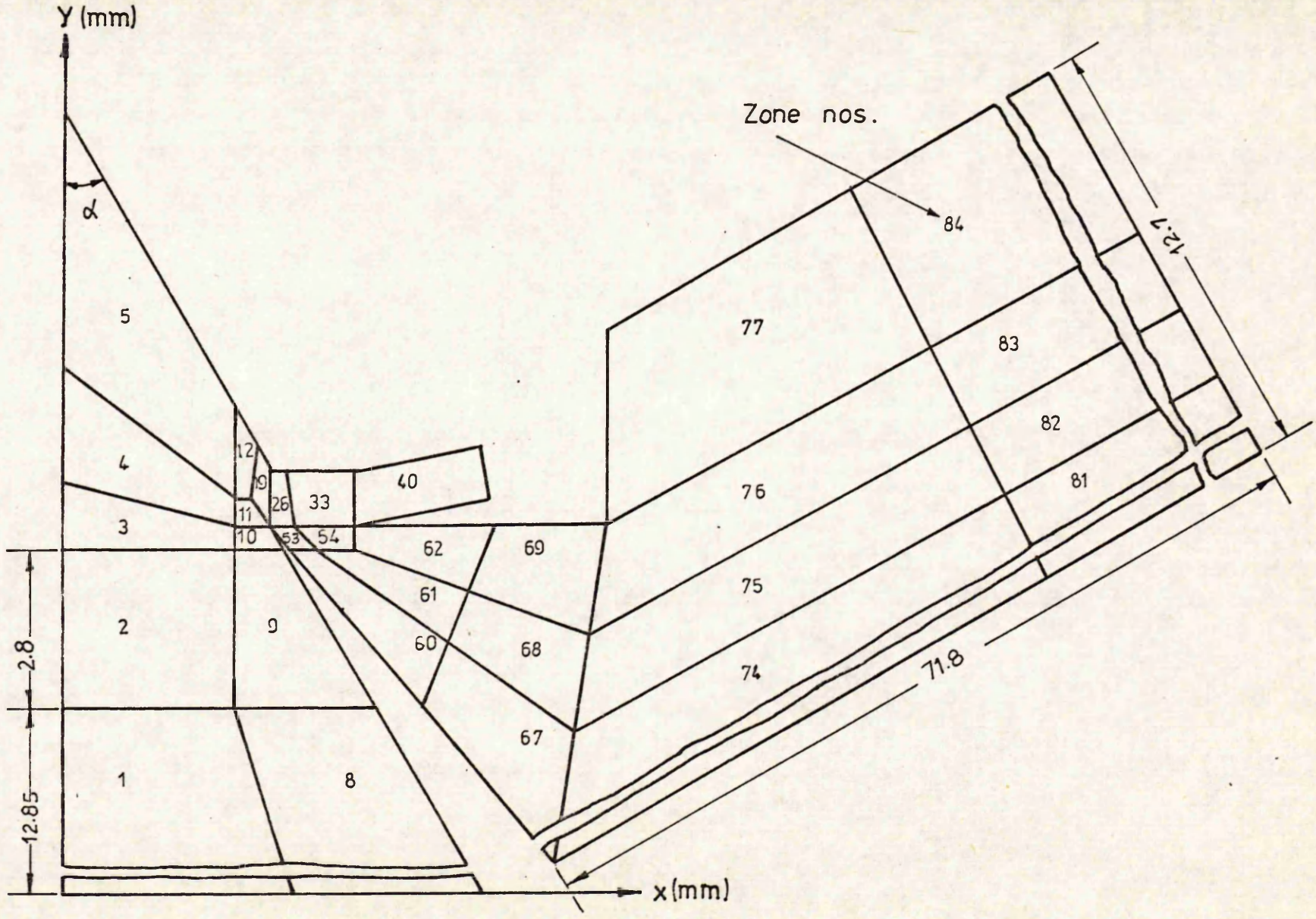

Fig. 4.6(a) Work-tool-chip composite system (hss tool)

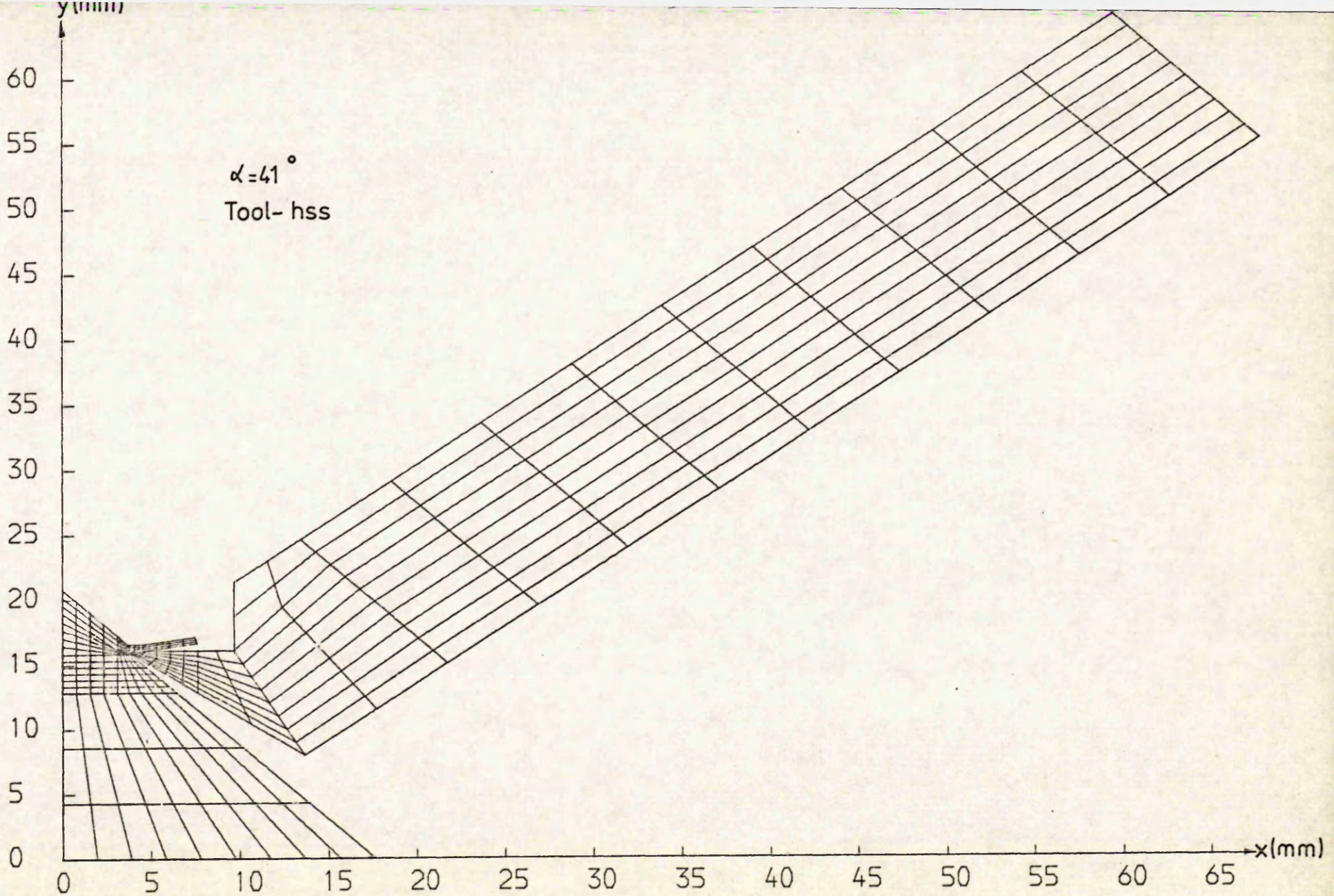

AUTOMATIC MESH GENERATION FOR THERMAL ANALYSIS IN ORTHOGONAL MACHINING

Fig. 4.6(b)

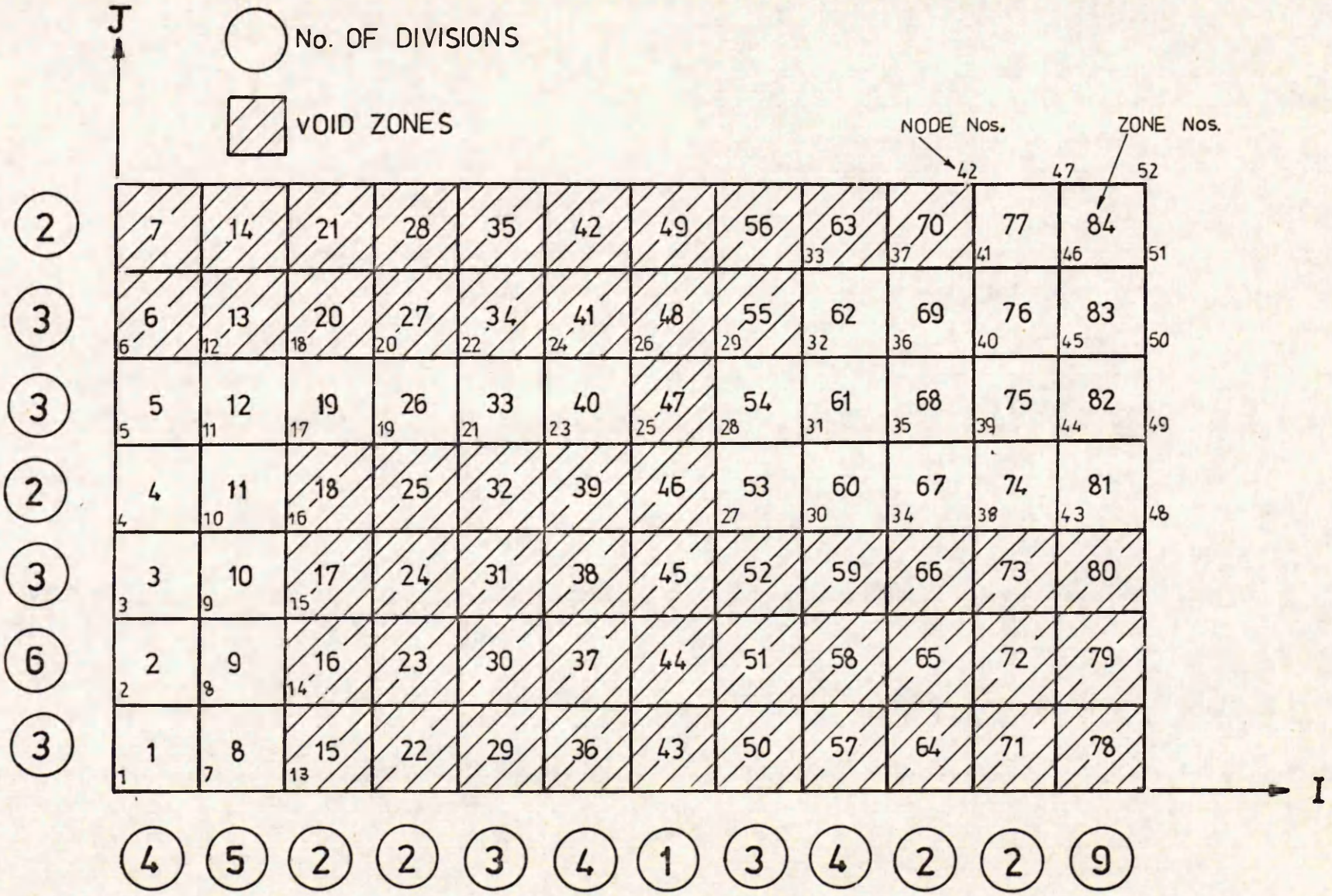

Fig. 4.7 Key diagram (hss tool)

four corners of the key diagram.

The mesh required for the problem region is indicated by taking each row and column in the key diagram and indicating the number of sub-divisions required in it. With the previous version of ELDATGEN, the type of two-dimensional elements which can be generated in a zone include triangular and quadrilateral linear elements only.

In order to generate the higher order elements required for the present investigations, some modifications have been incorporated. Again, Eq. (4.2) is used to map the points from the curvilinear co-ordinate (ξ , η) system to the x-y co-ordinate system. The zones are first divided into linear elements which are, then, converted into higher order elements by increasing and renumbering the nodes accordingly. It is assumed that the element boundaries are straight and the co-ordinates of mid-side nodes are calculated by interpolation. As a result, it has been possible to generate the quadratic and cubic quadrilateral elements automatically.

The input data to the program is supplied by ELDAT.

4.3 ELDAT.

ELDAT generates the input data and the key diagram for ELDATGEN. The factors which led to the development of ELDAT are that

1. the number of zones in the key diagram representing the tool-work-chip composite system is considerably large (more than 80) necessitating the manual calculation of the x-y co-ordinates of a number of key diagram nodes and

2. a separate but geometrically similar key diagram is required for each and every test due to a change in cutting conditions.

Fig.4.6(a) shows the problem region when a high speed steel cutting tool is used for machining. The corresponding key diagram consisting of 84 zones is shown in Fig. 4.7. Similar diagrams when a carbide tool is

used for machining are shown in Figs. 4.8 and 4.9 respectively. The key diagram for the carbide tool is divided into 92 zones. Obviously, the manual calculation of the input data for such a large number of zones for different tests is a cumbersome process and is liable to human error.

The program ELDAT takes care of the variations in cutting conditions and can generate the different key diagrams requiring very little data (say, 10 - 15 cards). The input data to be read for each test include the number of subdivisions required for each zone in the I and J directions, the tool material, feed, rake angle, tool-chip contact length, sticking contact length and distance of the step on tool face from tool edge measured along the tool axis. Using the simple geometrical relations as evident from Figs. 4.6 and 4.8, the program calculates the x-y co-ordinates of the nodes in the key diagram. The output is streamlined to meet the input data requirements of the parent program ELDATGEN.

4.4 DATA.

DATA serves as a front-end data checking device to the major program FETC. Its main advantage is that all the input data is centralized and, therefore, any errors in the input are checked or detected, thereby, reducing the chances of unsuccessful runs of FETC and wasted computer time. Furthermore, it calculates the bandwidth and the maximum and minimum node numbers of the generated mesh.

Input data to the program consist of the following items.

(1) Control Parameters: These parameters enable the computer to identify the problem in hand. They specify the type of problem -two dimensional or three dimensional - and the number of different materials present in the problem region.

(2) Material Properties: The values of thermal conductivity in x and y directions, specific heat and density in a number of sets, each corresponding to one type of material, are read and stored in the arrays -

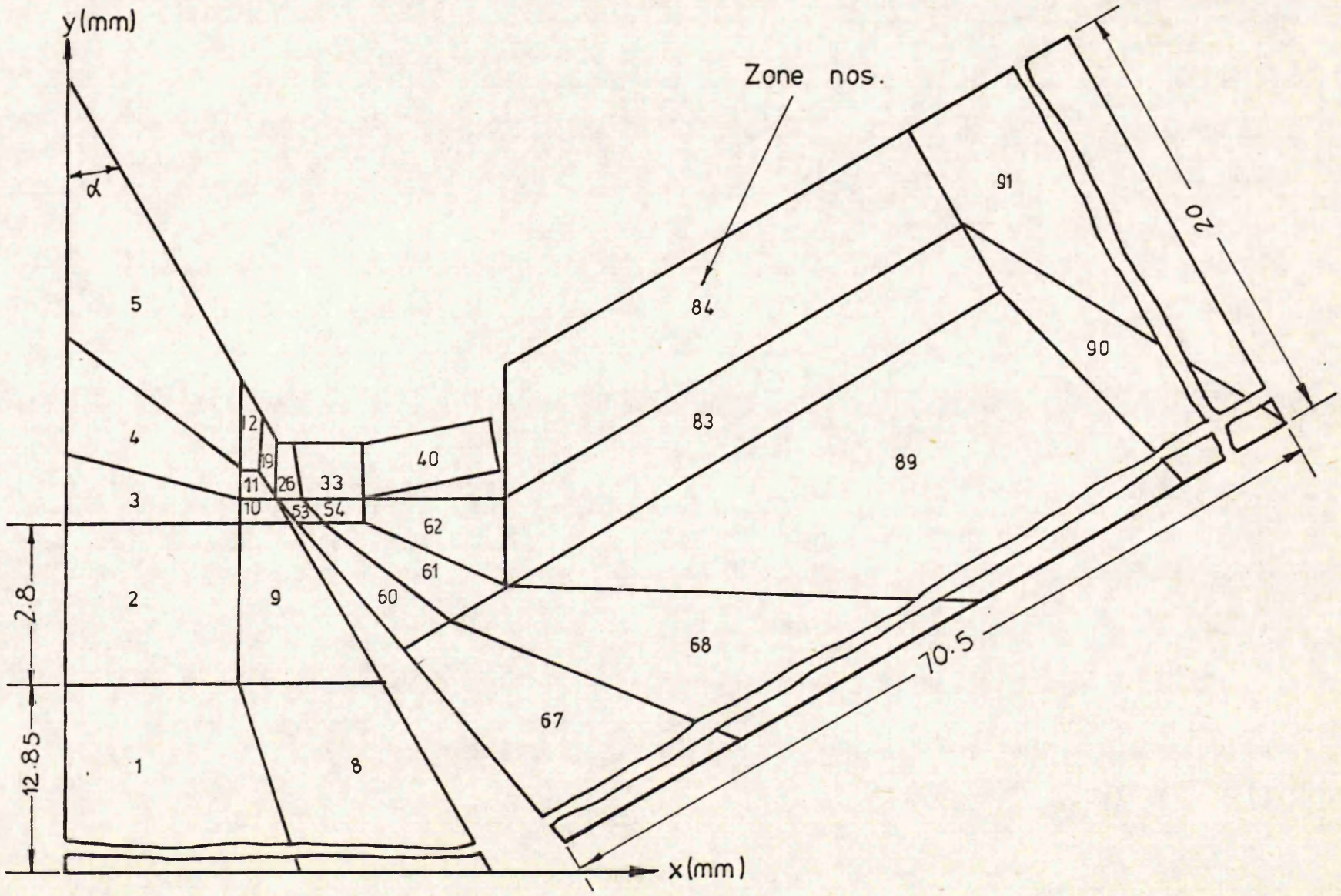

Fig. 4.8(a) Work-tool-chip composite system (carbide tool)

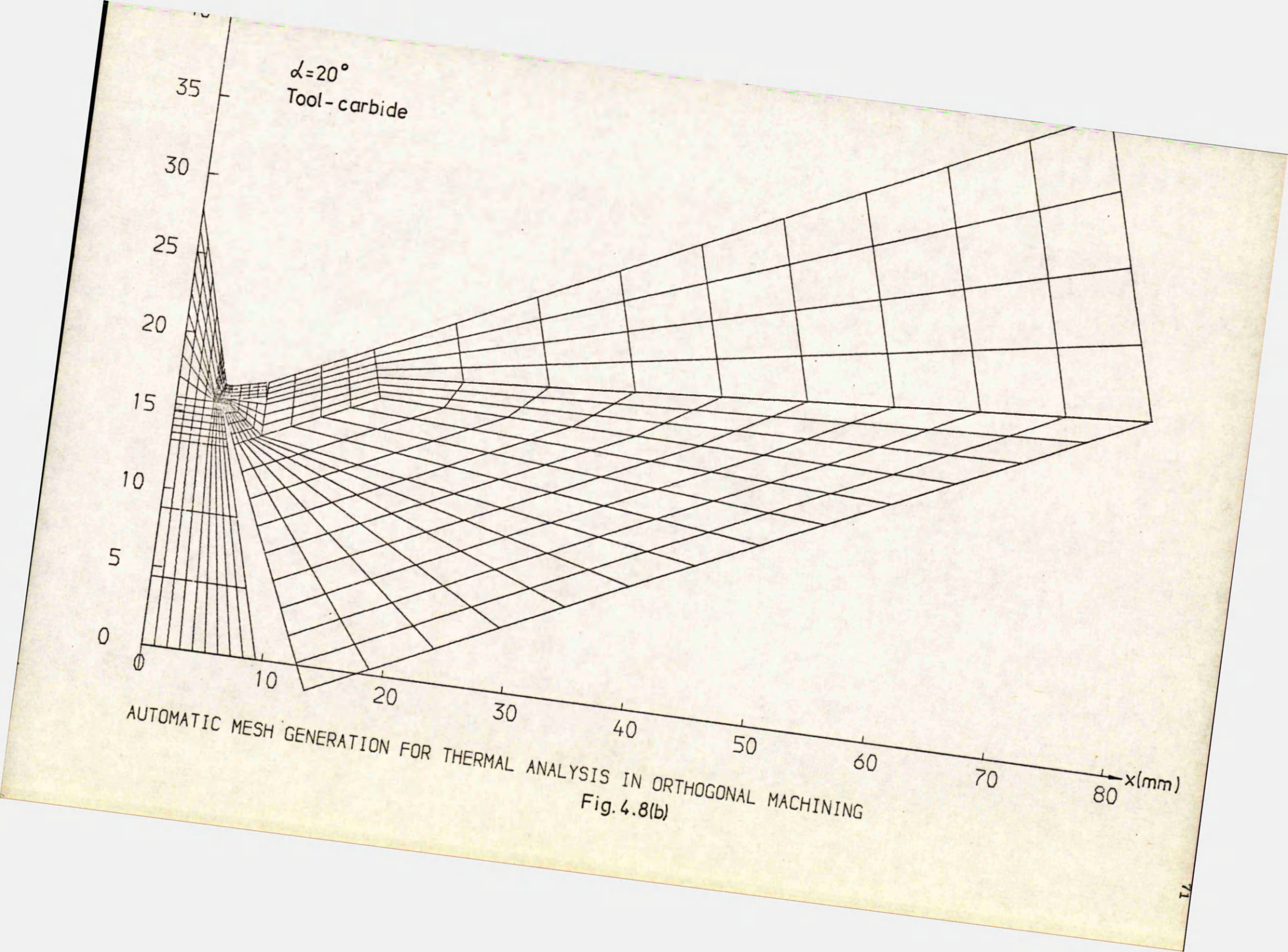

AUTOMATIC MESH GENERATION FOR THERMAL ANALYSIS IN ORTHOGONAL MACHINING

Fig. 4.8(b)

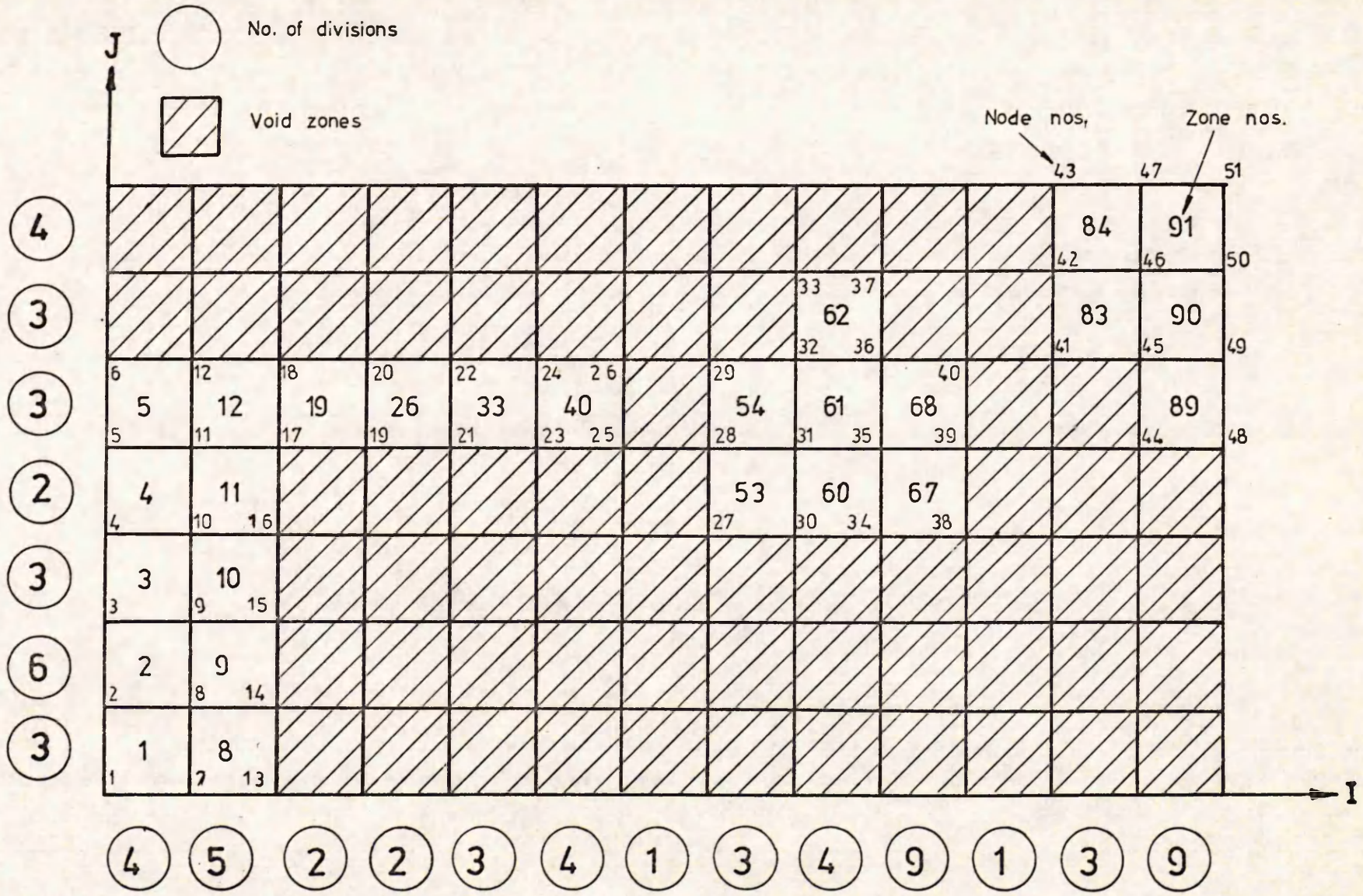

Fig. 4.9 Key diagram (carbide tool)

CKX, CKY, ACP and AROE respectively. The location index for each set of values in the arrays serves to be the material type number for the set.

(3) Boundary Conditions: An integer is read in to specify if any coolant is used during machining. If a coolant is used, further data regarding the element numbers affected by the coolant and the surface number (Fig. 3.9) to which the element belongs, relative length of the surface, surface fluid velocity and the location number of the first boundary node on each surface are read in and stored in the arrays - NBC, NSE, REL, VFLD and ICON respectively. In addition, a list of fixed temperature nodes and the number of elements shared by each of them is also read in.

(4) Elements with heat sources: They include the elements of the primary and secondary deformation zones as well as the elements on the flank face which are subjected to boundary friction in the case of a worn tool.

(5) Cutting forces: These include the force components F_V and F_H.

(6) Element data: These data include integer numbers indicating the type of element used and material type, thickness of the element, number of nodes in the element and their identifying numbers followed by nodal co-ordinates.

The flow chart for the program is shown in Fig. 4.10.

4.5 FETC.

FETC performs the core operations in the finite element analysis. It sets up the iterative procedure to allow for the variations of material properties with temperature and evaluates the element matrices, assembles them and solves the assembled matrices for each iteration until the solution is converged. The general procedure of the program is illustrated in the flow chart in Fig. 4.11.

The program has been used for the present investigations, to solve

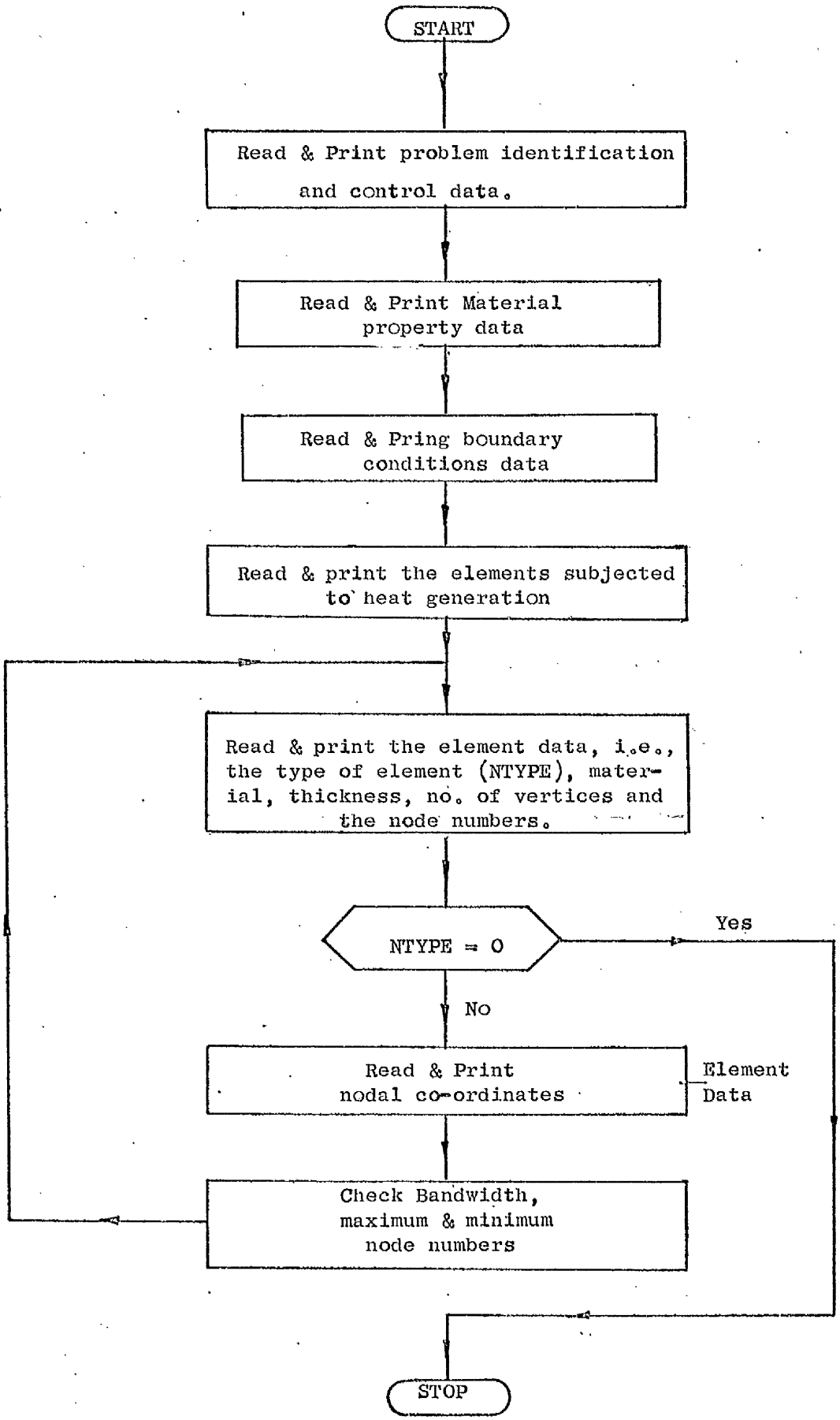

Fig. 4.10 FLOW-CHART FOR DATA.

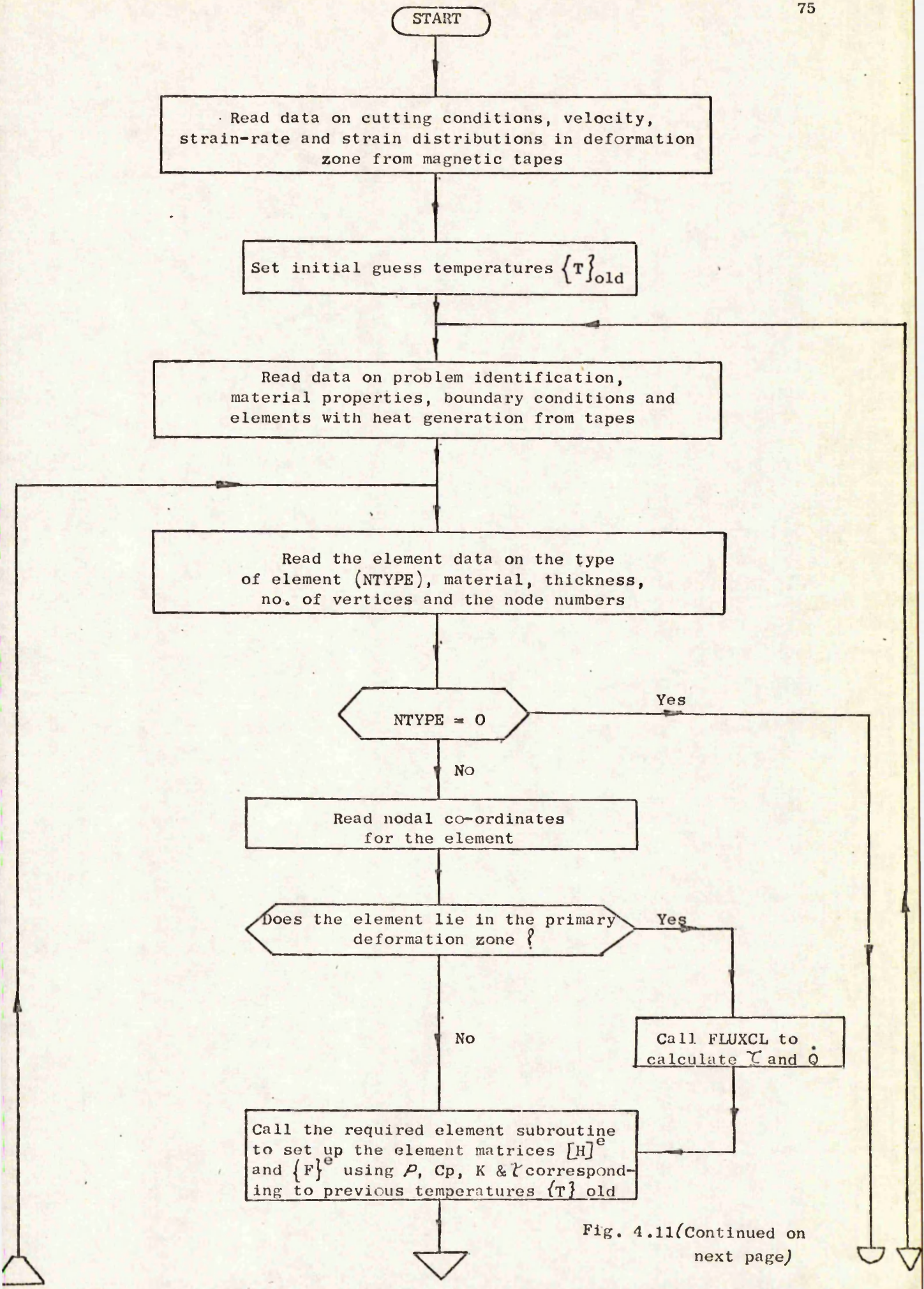

Fig. 4.11 (Continued on next page)

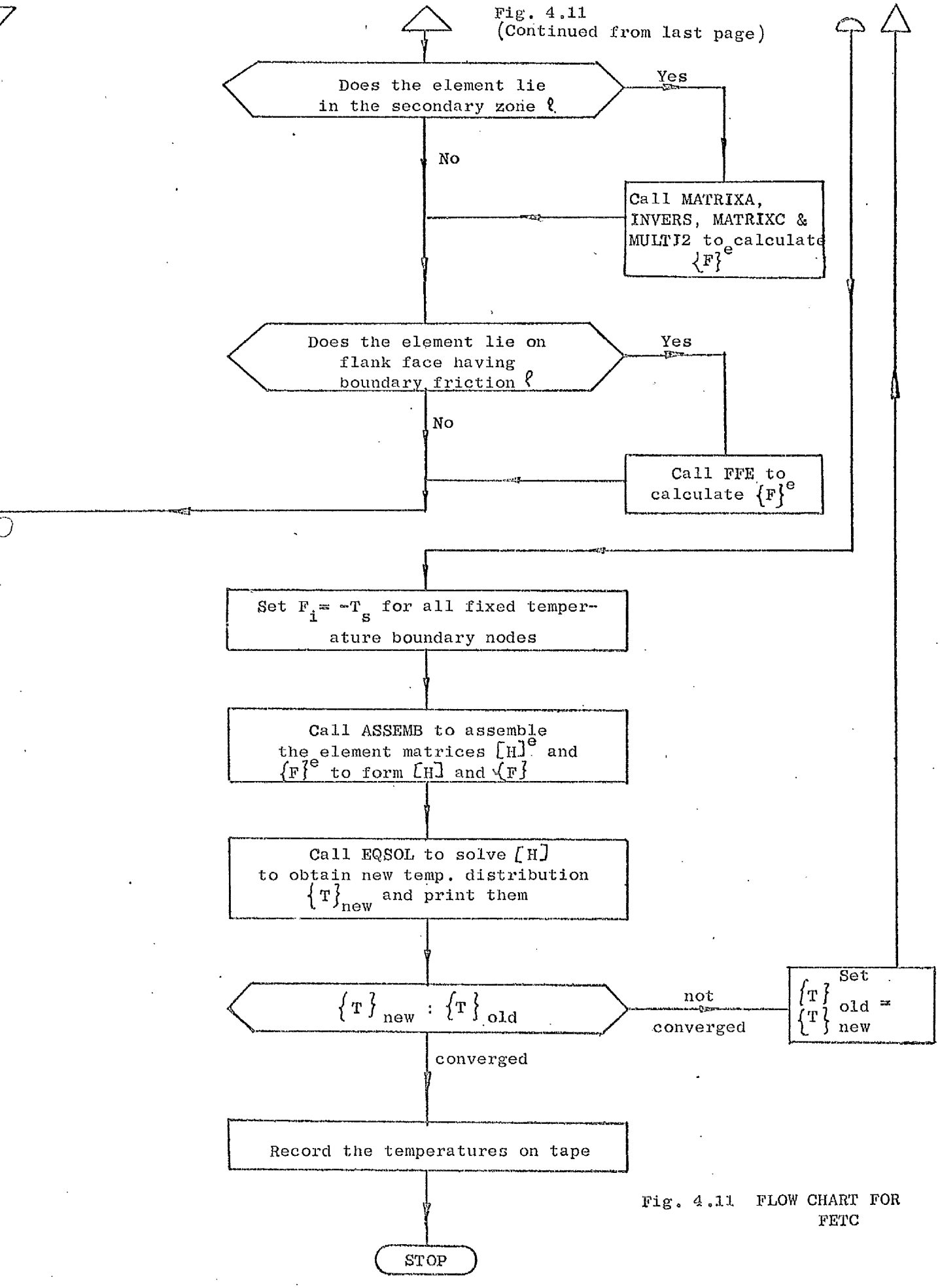

Fig. 4.11 FLOW CHART FOR FETC

the two dimensional temperature field problem, but it has the provision to solve the three dimensional problems, as well. The element data generated by ELDATGEN are routed through the program DATA to FETC. These data are not stored in FETC all at a time, but they are read from the tape one by one as they are required in order to optimise the use of storage. For the same reason, the element matrices after computation are stored sequentially on a disc file ready for the subsequent assembling operation. The assembled matrices are again dumped on disc files to be the data input files for solution which is performed by the subroutine EQSOL.

Auxiliary backing store is used extensively so that the whole working core of the computer can be devoted to storing the program and computational manoeuvre. This enables very large problems to be accommodated The program occupies the full working core (about 25 K in level 1 store and 100 K in level 2 store) available to users on the combined CDC 7600 - ICL 1906 A computer. Data transfer between auxiliary store and working core will be reduced and this will eventually lead to a saving in system time if more working core is allowed for computational manoeuvre, especially in the process of assembly.

The program has been written in such a way that new elements can be easily incorporated without much reorganisation and readjustment of the program. Most of the important arrays are dynamically dimensioned in all the subroutines. Any change of array size to adapt new situations can be affected simply by replacing the dimension statements or altering the values which determine the size or arrays in the subroutines. Furthermore, some space is made available at strategic points for the additions of new element routines. The four major aspects of the program are

(1) Iterative procedure.

(2) Evaluation of element matrices and heat loads and injection of boundary conditions.

(3) Assembly of system matrices and

(4) Solution of the assembled matrices.

4.5.1 Iterative Procedure.

The thermal conductivity, specific heat and density of the materials, the shear flow stress of the workpiece material and the heat transfer coefficient are not constant and, certainly, depend upon the temperature. It is necessary to take into account the temperature dependency of these variables. For this purpose, an iterative procedure is employed in which values for the properties in each iteration are based on the temperature obtained in the previous iteration. Of course, for the first iteration, the temperatures are arbitrarily set equal to zero. The old temperatures are stored in arrays B4 and A4 in the main program and the subroutine EQSOL respectively.

For each iteration, new $[H]$ and $\{F\}$ matrices of Eq. (2.10) are set up and a new set of temperature vector $\{T\}$ is solved. The new set of nodal temperatures is compared with the old set and the iteration procedure is continued until the difference between the two vectors is less than 1 percent. The temperature converged to within a relative error of less than 1 percent throughout the problem region in no more than five iterations for most of the tests. The new temperature vector is stored in arrays B3 and A3 in the main program and the subroutine EQSOL respectively. The iterative procedure is illustrated in the flow chart of Fig. 4.11.

4.5.2 Evaluation of Element Matrices and Heat Loads and Injection of Boundary Conditions.

Evaluation of element characteristics is the basic step in the finite element analysis. For convenience, the element equation (2.12) and the other related equations (2.13) and (2.16) are reproduced here, i.e.,

$$[H]^e \{T\}^e + \{F\}^e = 0 \qquad (4.4)$$

where $\left[H\right]^e = \int_v \left[G\right]^e \, dv$ (4.5)

and $\left[G\right]^e$ is the element thermal matrix given by

$$\left[G\right]^e = K \frac{\partial [N]^T}{\partial x} \cdot \frac{\partial [N]}{\partial x} + K \frac{\partial [N]^T}{\partial y} \cdot \frac{\partial [N]}{\partial y} + \rho C_p u \cdot [N]^T \frac{\partial [N]}{\partial x} + \rho C_p v \cdot [N]^T \frac{\partial [N]}{\partial y} \quad (4.6)$$

For evaluating the element matrix $[H]^e$ in Eq. (4.5), a general procedure is adopted for all the elements. The integration required in the above equation is carried out numerically. The derivatives of the shape functions with respect to the normalized co-ordinates and the Jacobian matrix are first calculated. Using Eq. (2.41), the local derivatives are transformed into the global derivatives as required in Eq. (4.6) for every integrating point. The operation necessitates the use of a number of subroutines which are described below.

4.5.2.1 Subroutine JACOBI.

This is a standard subroutine which takes the arrays of the co-ordinates and the local derivatives of the shape functions $\left[DSF\right]$ from the element subroutines and evaluates the Jacobian matrix $\left[J\right]$ and its determinant. The Jacobian is inverted and multiplied by the matrix $\left[DSF\right]$ to generate the matrix $\left[DSFT\right]$ containing the values of the transformed derivatives of the shape functions.

4.5.2.2 Subroutines BDB1 and BDB.

Evaluation of the expression given by Eq. (4.6) for every integrating point and the cumulative summation up to the point are carried out in subroutine BDB1 for a two dimensional analysis. Similar operation for a three dimensional case is performed in the subroutine BDB. Both the routines are general in nature and can be used for all elements, irrespective of the number of nodes.

It is worth mentioning that the program can be adapted to solve any other two or three dimensional field problem by just replacing the subroutines BDB and BDB1. No other change seems to be necessary provided the boundary conditions are similar in nature.

4.5.2.3 Element Subroutines.

The element subroutines follow a general modular pattern as shown in Fig. 4.12. For the reasons given below, it was considered necessary to inject the boundary conditions and calculate the heat loads due to the deformation energy while evaluating the element matrix.

(a) The coolant boundary condition as expressed by Eq. (2.2(c)) contributes to the element thermal matrix as well as to the element heat load vector. It is evident from Eq. (2.8) as its second term $\int_{S_h} N_i h \left[N\right] \left\{T\right\}^e ds$ is to be added to $\left[H\right]^e$ and the third term $\int_{S_h} N_i \; h \; T_\infty \; ds$ is to be included in the element heat load vector $\left\{F\right\}^e$ before these quantities can be calculated.

(b) The fixed temperature nodes (Eq. 2.2(a)) can be treated at the element level easily by setting

$$H^e_{ij} = \begin{cases} 1/ELE(I) & \text{if } i = j \\ 0 & \text{if } i \neq j \end{cases} \qquad (4.7)$$

where ELE(I) indicates the total number of elements to which the node is common.

(c) Calculation of the heat loads due to the deformation energy (first term of Eq. 2.11(b)) requiring numerical integration can be easily accommodated in element subroutines avoiding the repetition of the integration procedure and thus saving computational time.

In the main program FETC, element type number (NTYPE) with the problem type number (NPRO) directs the calculation of the element matrix to be done in the appropriate element subroutine. Presently, there are seven such element subroutines as given below.

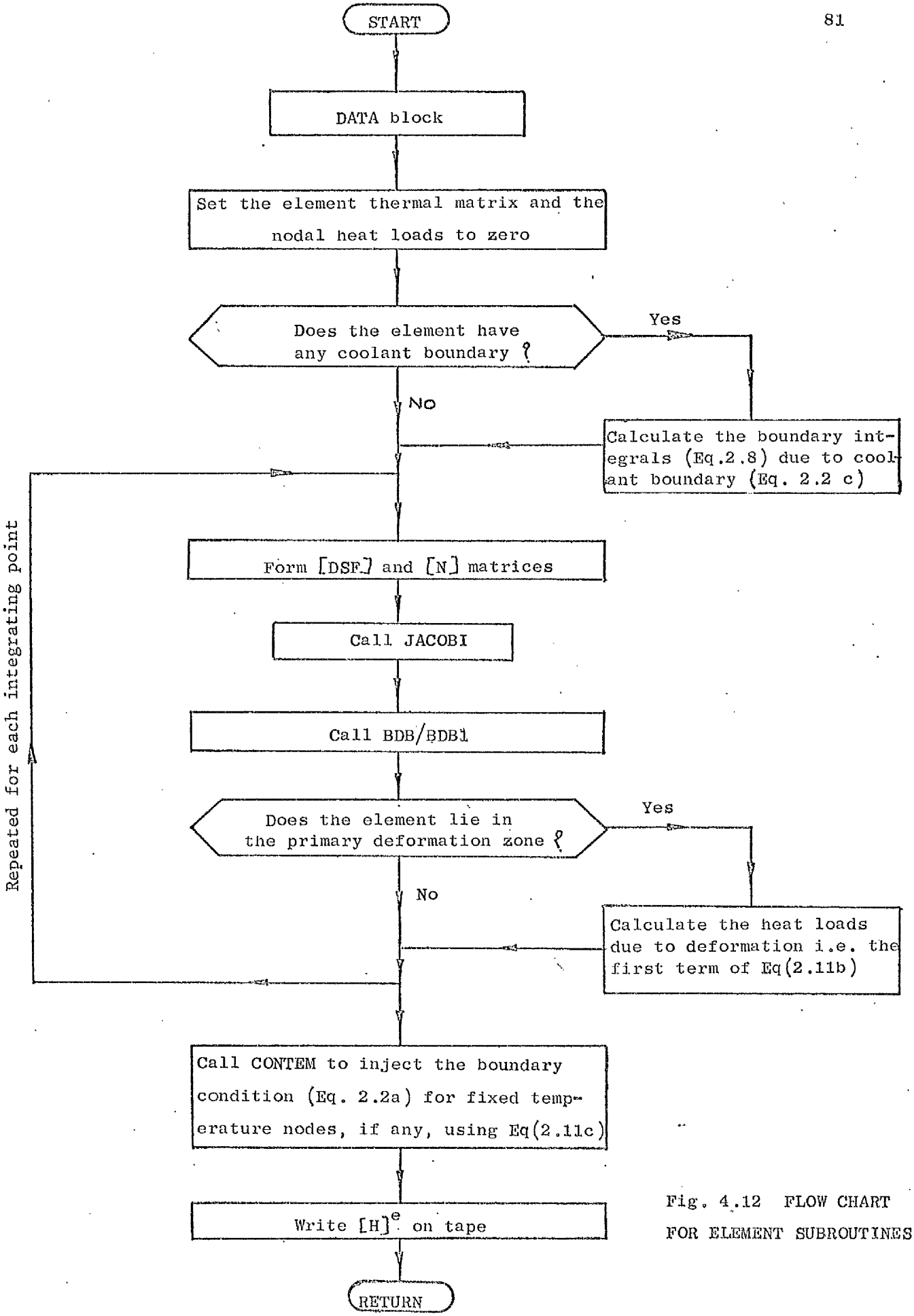

Fig. 4.12 FLOW CHART FOR ELEMENT SUBROUTINES

	NTYPE
1 - TRI3 (3 node triangular element)	3
2 - QUAD4 (4 node quadrilateral element)	4
3 - TRIA6 (6 node triangular element)	5
4 - TRIA9 (9 node triangular element)	6
5 - QUAD8 (8 node quadrilateral element)	7
6 - QUA12 (12 node quadrilateral element)	8
7 - HEXE8 (8 node hexahedron element)	9

The general procedure of obtaining element matrices is the same in all the subroutines. Brief description of each of the subroutines is given below.

(1) Subroutine TRI3 .

This subroutine is for a 3-node linear triangular element shown in Fig. 2.3(a). The shape functions are expressed in terms of the area co-ordinates L_1, L_2 and L_3 (Fig. 2.3(b)) and are given by Eq. (2.24).

The subroutine follows the general molular pattern and the integration has been carried out at one point, the centroid of the triangle.

(2) Subroutine QUAD4 .

This subroutine is for a linear 4-node quadrilateral element shown in Fig. (2.2(a)). The shape functions define the element geometry as well as the temperature pattern i.e.,

$$\begin{aligned} x &= [N] \{x\}^e \\ y &= [N] \{y\}^e \\ \text{and} \quad T &= [N] \{T\}^e \end{aligned} \tag{4.8}$$

where the shape functions $[N]$ are given by Eq. (4.3).

Gaussian quadrature formula (93) is well adapted to integrate the element matrix numerically in the domain of the $\xi - \eta$ system. For integration, 4 x 4 Gaussian integrating points have been used.

(3) Subroutine TRIA6 .

The quadratic 6-node triangular element was first derived by

Veubeke (94) and used for a two dimensional stress problem by Argyris (95). For this element (Fig. 2.3(c)), again, the area co-ordinates are used and the shape functions are expressed by Eqs. (2.27) and (2.28).

The subroutine follows the same general modular pattern as for other elements except that the integration has been carried out at the points given by Hammer et al (96).

(4) Subroutine TRIA9 .

For this subroutine, a complete cubic polynomial consisting of 10 terms has been used. This requires an additional mid-face node (Fig. 2.3(e)) to be included (39). The mid-face node is later eliminated. The equivalent shape functions are given earlier by Eqs. (2.34) - (2.36).

The integration is performed using a (5 x 5) points Gaussian method over the triangular area (39).

(5) Subroutine QUAD8 .

This subroutine serves the quadratic 8-node quadrilateral element (Fig. 2.2(c)) and is similar to QUAD4 except that the shape functions are different given by Eqs. (2.29 - 2.31).

The integration is performed over 4 x 4 Gaussian integrating points.

(6) Subroutine QUA12 .

This element subroutine is for the cubic 12-node quadrilateral element shown in Fig. 2.2(e). The shape functions used are given by Eqs. (2.37) - (2.39).

Again, a 4 x 4 points Gaussian integrating procedure is used in this subroutine.

(7) Subroutine HEXE8 .

This subroutine is for a linear 8-node hexahedron (three dimensional) element shown in Fig. 4.13.

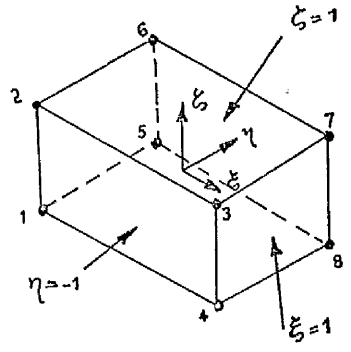

Fig. 4.13.

The normalized co-ordinates (ξ , η , ς) are used and the shape function for a node can be expressed as follows:

$$N_i = 1/8\ (1 + \varsigma\,\xi_i)\ (1 + \eta\,\eta_i)\ (1 + \varsigma\,\varsigma_i) \qquad (4.9)$$

The 14-points integration rule developed by Irons (97) has been used for numerical integration because it takes about half the computational time of that required with the 3 x 3 x 3 Gaussian integration (98).

4.5.2.4 Boundary Subroutines.

While evaluating the element matrix, a number of subroutines are called to inject the boundary conditions. It may be mentioned here that the boundary condition such as given by Eq. (2.2(b)) did not occur in the problems considered herein. Thus, the element contribution of the first term of Eq. (2.8) i.e., $\int_{Sqe} N_i . q . ds$ vanishes.

The contributions of the other two terms $\int_{She} N_i . h . N_j . ds$ and $\int_{She} N_i . h . T_\infty . ds$ arise on coolant boundary governed by Eq. (2.2(c))

and are evaluated by the subroutines HQ12 and HQ8 which, in turn, call the subroutines DCOSIN, CALHTC and HTCT. The boundary condition of Eq. (2.2(a)) is injected by the subroutine CONTEM. A brief description of each of these subroutines is given below.

(1) Subroutines HQ12 and HQ8.

Similar to the element subroutines, these subroutines have been written in modular form for the 12-node quadrilateral and 8-node quadrilateral elements respectively. The boundary integrals for the coolant boundary are evaluated using the Gauss quadrature integration (linear) technique. The linear integration is carried over 4 points and the flow chart is shown in Fig. 4.14.

For the coolant boundary elements, the additional contributions to the element matrix $\left[H\right]^{+}_{She}$ and to the element heat loads $\left\{F\right\}^{+}_{She}$ can be written down as

$$\left[H\right]^{+}_{She} = \int_{She} h \cdot \delta_i N_i N_j \, ds \tag{4.10}$$

$$\text{and } \left\{F\right\}^{+}_{She} = -\int_{She} h \cdot \delta_i N_i T_\infty \, ds \tag{4.11}$$

$$\text{where } \delta_i = \begin{cases} 1 & \text{for the nodes on boundary} \\ 0 & \text{for all other nodes of the element.} \end{cases} \tag{4.12}$$

Considering the relationships between the curvilinear co-ordinates (ξ, η) and the cartesian co-ordinates (x, y), dx can be expressed as

$$dx = \frac{\partial x}{\partial \xi} \cdot d\xi + \frac{\partial x}{\partial \eta} \cdot d\eta \tag{4.13}$$

where, for the linear boundaries,

$$dx = ly \, ds \tag{4.14}$$

and ly is the direction cosine of the outward normal and the y-direction.

Substitution of Eqs. (4.13) and (4.14) into Eqs. (4.10) and (4.11) and further simplification gives

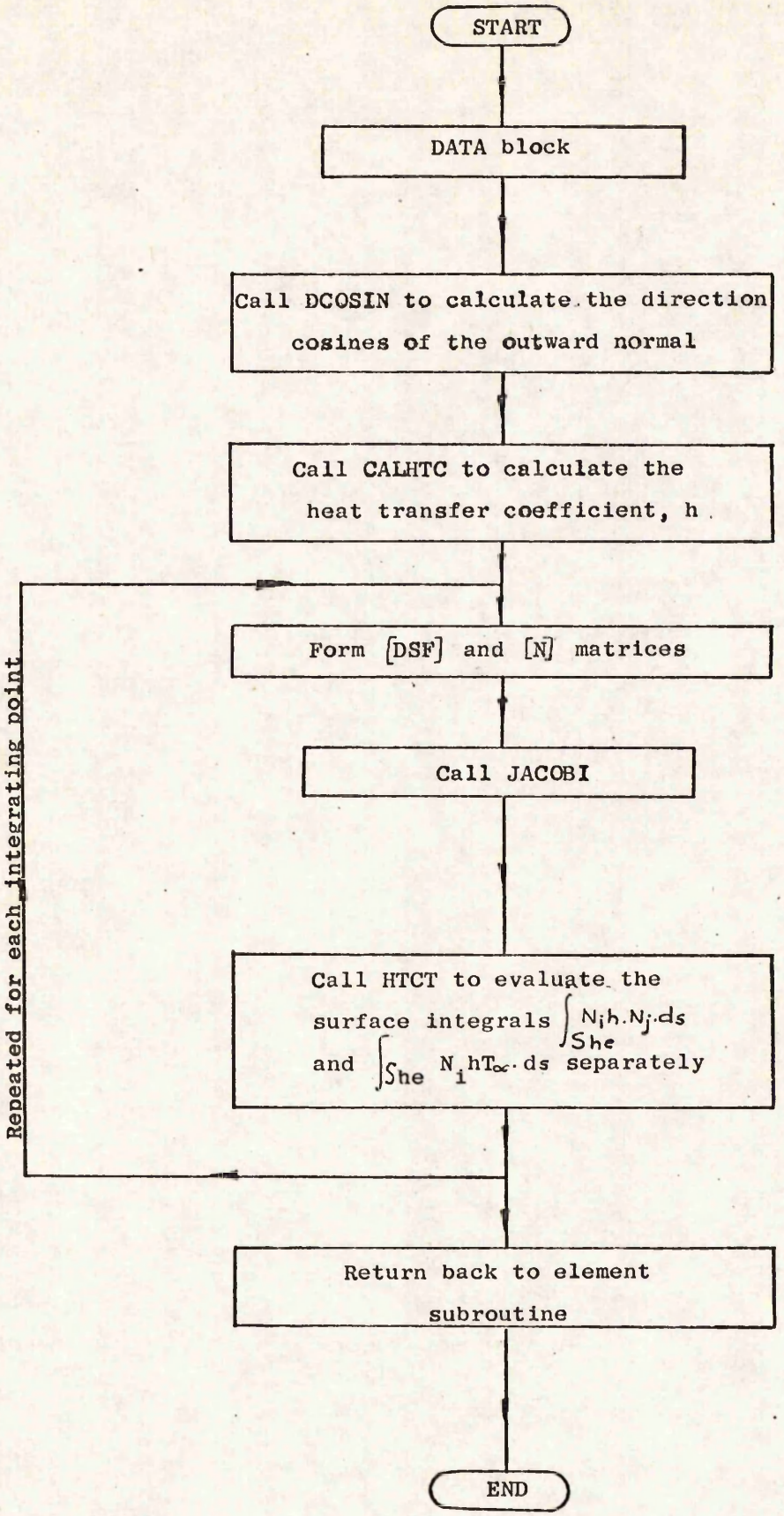

Fig. 4.14 FLOW CHART FOR THE SUBROUTINES HQ12/HQ8

$$\left[H\right]^{+}_{S_{he}} = \int_{\xi_1}^{\xi_2} \frac{h}{ly}\, \delta_i \cdot N_i \cdot N_j \, \frac{\partial [N]}{\partial \xi} \left\{x\right\}^e \, d\xi + \int_{\eta_1}^{\eta_2} \frac{h}{ly}\, \delta_i \, N_i \, N_j \, \frac{\partial [N]}{\partial \eta} \left\{x\right\}^e \, d\eta \qquad (4.15)$$

$$\text{and} \quad \left\{F\right\}^{+}_{S_{he}} = -\int_{\xi_1}^{\xi_2} \frac{h\, T_\infty}{ly}\, \delta_i \, N_i \, \frac{\partial [N]}{\partial \xi} \left\{x\right\}^e \, d\xi - \int_{\eta_1}^{\eta_2} \frac{h\, T_\infty}{ly}\, \delta_i \, N_i \, \frac{\partial [N]}{\partial \eta} \left\{x\right\}^e \, d\eta \qquad (4.16)$$

For the boundaries where ly tends to zero, similar expressions incorporating lx are used for evaluating $\left[H\right]^{+}_{S_{he}}$ and $\left\{F\right\}^{+}_{S_{he}}$. The computational procedure used in the subroutines HQ12 and HQ8 is based on Eqs. (4.15) and (4.16).

(2) Subroutine DCOSIN.

This subroutine calculates the direction cosines lx and ly of the outward normal with x and y axes respectively as required for Eqs. (4.15) and (4.16).

(3) Subroutine CALHTC.

This subroutine calculates the heat transfer coefficient h for the boundary elements subjected to water cooling. The properties of water i.e., density, specific heat, absolute viscosity, thermal conductivity and the Prandtl number (90, 91) at various temperatures are stored in DATA block WP. Using Eq. (3.35), the Reynolds number is calculated for which the physical properties are taken at the mean film temperature T_f given by

$$T_f = (T_s + T_\infty)/2 \qquad (4.17)$$

The surface temperature T_s is taken to be equal to the temperature obtained in the previous iteration.

If the value of Reynolds number is less than 5×10^5, Eqs. (3.32) and (3.33) are used to calculate the value of h, otherwise Eq. (3.34)

is used.

(4) Subroutine HTCT.

Similar to the subroutine BDB1, this subroutine is general in nature and can be used for all elements, irrespective of the number of nodes associated with the element. In this subroutine, the contributions from the boundary integral (Eqs. (4.15) and (4.16)) to the element matrix and element heat vector are calculated at each integrating point.

(5) Subroutine CONTEM.

This subroutine injects the boundary condition of the type given by

$$T = T_s \text{ on part of boundary } S_T \tag{4.18}$$

For such boundary nodes, the element matrix is modified as follows:

$$H^e_{ij} = \begin{cases} 1/\text{ELE}(I) & \text{if } i = j \\ 0 & \text{if } i \neq j \end{cases} \tag{4.19}$$

where ELE(I) indicates the total number of elements sharing the node under consideration. Similar operations for the nodal heat loads are done by setting $F_i = -T_s$ in the main program FETC (Fig. 4.11).

4.5.2.5 Subroutines for the Primary Zone Heat Loads.

The evaluation of the heat load vector for the elements lying in the primary zone is done by subroutines FLUXCL and DEFE as described below. Both the subroutines are versatile and can be used for all the elements.

(1) Subroutine FLUXCL.

This subroutine first calculates the shear flow stress using Eq. (3.21) based on the temperature obtained in the previous iteration. The rate of heat generation per unit volume $\dot{Q}$ due to plastic deformation is then calculated using Eq. (3.36).

(2) Subroutine DEFE.

This subroutine evaluates the term $-\iint_e N_i \dot{Q}\, dx.dy$ i.e., F_i^e due to the primary deformation. The evaluation is done by numerical integration.

4.5.2.6 Subroutines for the Secondary Zone Heat Loads.

The heat loads due to the plastic deformation in the secondary zone are calculated using the subroutines FLUXCL and DEFE as described above. The heat loads due to the boundary friction over the tool-chip contact length are given by

$$F_i^e = -\iint_e N_i \dot{Q}\, dx.dy \qquad (4.20)$$

In matrix form,

$$\left\{F\right\}^e = -\iint \left[N\right]^T \dot{Q}\, dx.dy \qquad (4.21)$$

The heat generation rate per unit area qx due to the boundary friction at a point on the contact length at a distance x from the tool edge is given by

$$qx = \dot{Q}\, dy = \tau_x V_x \qquad (4.22)$$

Substitution of Eq. (4.22) into Eq. (4.21) gives

$$\left\{F\right\}^e = -\int_0^l \left[N\right]^T \tau_x V_x\, dx \qquad (4.23)$$

where l is the length of the edge of the element subjected to the boundary friction.

In order to calculate the equivalent nodal heat loads $\left\{F\right\}^e$, consider a cubic 12-node quadrilateral element one edge of which is subjected to the heat flux qx (Fig. 4.15).

The temperature (99) over the length l can be set as

$$T = \alpha_1 + \alpha_2 x + \alpha_3 x^2 + \alpha_4 x^3$$

(since y is constant)

$$\text{or} \quad T = \left[P\right] \left\{\alpha\right\} \qquad (4.24)$$

$$\text{where} \quad \left[P\right] = \begin{bmatrix} 1 & x & x^2 & x^3 \end{bmatrix} \qquad (4.25)$$

$$\text{and} \quad \left\{\alpha\right\}^T = \begin{bmatrix} \alpha_1 & \alpha_2 & \alpha_3 & \alpha_4 \end{bmatrix} \qquad (4.26)$$

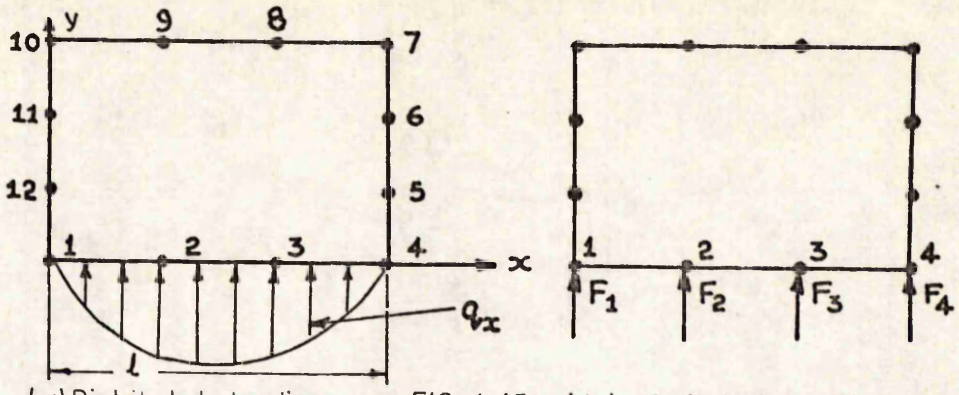

(a) Distributed loading FIG. 4.15 (b) Equivalent nodal loads

Substituting the nodal co-ordinates in Eq. (4.24),

$$\left\{ T \right\} = \left[A \right] \left\{ \alpha \right\} \tag{4.27}$$

where,

$$\left\{ T \right\} = \begin{Bmatrix} T_1 \\ T_2 \\ T_3 \\ T_4 \end{Bmatrix} , \quad \left\{ \alpha \right\} = \begin{Bmatrix} \alpha_1 \\ \alpha_2 \\ \alpha_3 \\ \alpha_4 \end{Bmatrix}$$

and,

$$\left[A \right] = \begin{bmatrix} 1 & x_1 & x_1^2 & x_1^3 \\ 1 & x_2 & x_2^2 & x_2^3 \\ 1 & x_3 & x_3^2 & x_3^3 \\ 1 & x_4 & x_4^2 & x_4^3 \end{bmatrix} \tag{4.28}$$

In terms of the shape functions, the temperature over the length l can be expressed as

$$T = \left[N \right] \left\{ T \right\} \tag{4.29}$$

where,

$$\left[N \right] = \begin{bmatrix} N_1 & N_2 & N_3 & N_4 \end{bmatrix} \tag{4.30}$$

Combining Eqs. (4.24), (4.27) and (4.29) and eliminating $\left\{\alpha\right\}$, $\left\{T\right\}$ and T,

$$\left[N \right] = \left[P \right] \left[A \right]^{-1}$$

$$\text{or } \left[N \right]^T = \left[A \right]^{-T} \left[P \right]^T \tag{4.31}$$

Substituting for $\left[N\right]^T$ from Eq. (4.31) into Eq. (4.23),

$$\left\{F\right\}^e = -\left[A\right]^{-T} \int_{x_1}^{x_4} \left[P\right]^T . \tau_x \, Vx \, . \, dx \qquad (4.32)$$

$$\text{or } \left\{F\right\}^e = -\left[A\right]^{-T} \left\{C_\gamma\right\} \qquad (4.33)$$

$$\text{where, } \left\{C_\gamma\right\} = \int_{x_1}^{x_4} \left[P\right]^T . \tau_x . V_x . dx \qquad (4.34)$$

For the sticking length,

$$qx = \tau_x \, V_x = \tau_s . V_x \qquad (4.35)$$

and for the sliding length,

$$qx = \tau_s \, V_c \, \frac{(C-x)^n}{(C-c_1)^n} \qquad (4.36)$$

as described in section 3.11.

The four subroutines MATRIXA , INVERS, MATRIXC and MULTI2 are required for calculating the equivalent nodal heat loads using Eqs. (4.32) - (4.34).

(1) Subroutine MATRIXA .

This subroutine generates the matrix $\left[A\right]$ given by Eq. (4.28) for all the elements. The value of an integer M indicates the element being considered.

(2) Subroutine INVERS.

This is a standard subroutine which can be used for inverting a matrix. In the calculation of heat loads, it is used for the inversion of the matrix [A].

(3) Subroutine MATRIXC .

This subroutine first calculates the stress exponent n using Eq. (3.28) and the maximum shear stress τ_s (Eq. (3.30)). The end - co-ordinates of the edge of the element are compared with those of the sticking length to find out whether the edge lies inside or outside the sticking length. For the elements subjected to sticking boundary friction,

the matrix $\left\{C_f\right\}$ is evaluated using Eqs. (4.34) and (4.35). For the elements under sliding boundary friction, Eqs. (4.34) and (4.36) are used to evaluate the matrix $\left\{C_f\right\}$.

(4) Subroutine MULTI2.

In order to calculate the heat loads finally (Eq. (4.33)), the inverted matrix $\left[A\right]^{-1}$ is transposed and multiplied by the column matrix $\left\{C_f\right\}$. The subroutine is general in nature and can be used for matrix multiplication.

4.5.2.7 Subroutine for the Flank Friction Heat Loads.

Some tests were conducted using tools with known initial flank wear. The wear on the flank face produces heat due to the friction between the tool and workpiece. The equivalent nodal heat loads over the flank wear land are given by

$$\left\{F\right\}^e = -\int_0^l \left[N\right]^T \tau_f V_f \, dl \qquad (4.37)$$

where V_f is the velocity along the flank face,

τ_f is the constant shear stress given by Eq. (3.41)

and l is the length of the edge of the element subjected to flank friction. Simplifying Eq. (4.37), it can be shown (99) that the equivalent nodal heat loads due to the distributed flux of constant magnitude $\tau_f V_f$ are given by

$$\left\{F\right\}^e = \begin{bmatrix} Q/2 \\ \\ Q/2 \end{bmatrix} \quad \text{for linear elements (Fig. 4.16(a))} \qquad (4.38)$$

$$\left\{F\right\}^e = \begin{bmatrix} Q/6 \\ 2Q/3 \\ Q/6 \end{bmatrix} \quad \text{for quadratic elements (Fig. 4.16(b))} \qquad (4.39)$$

and $$\left\{F\right\}^e = \begin{bmatrix} Q/8 & 3Q/8 & 3Q/8 & Q/8 \end{bmatrix}^T \quad \text{for cubic elements (Fig. 4.16(c))} \qquad (4.40)$$

where, $Q = \tau_f V_f . l$ (4.41)

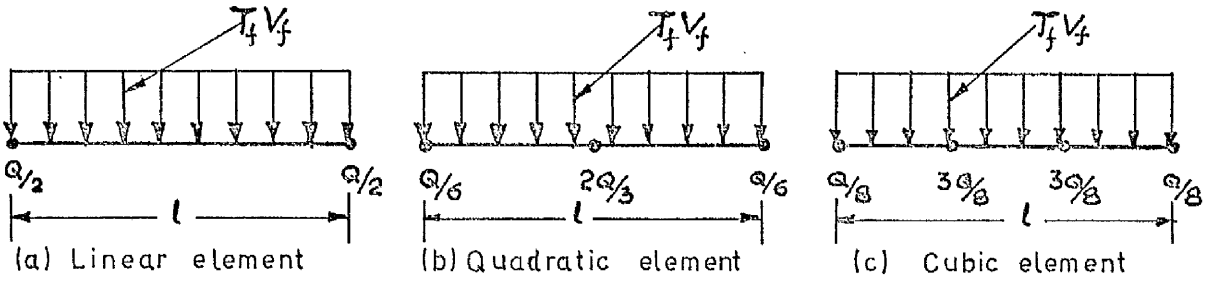

Fig. 4.16

The mathematical operations involved are performed by the subroutine FFE as described, in brief, below.

(1) Subroutine FFE.

This subroutine first calculates the total heat Q generated over the edge of the element using Eq. (4.41). It, then, evaluates the equivalent nodal heat loads using Eqs. (4.38) - (4.40) depending upon the type of the element.

4.5.3 Assembly of System Matrices.

The element matrices and the nodal heat loads are assembled to form the system matrices $[H]$ and $\{F\}$ by the subroutine ASSEMB. Element node numbers and the element matrices for each element are recorded on a disc file. The subroutine reads them from the disc file and carries out the assembling operation. It also places the nodal heat loads in appropriate rows. The nodal heat loads are stored in array BEP with the associated node numbers in the array IBEP. Before the start of the assembling operation, the matrices $[H]$ and $\{F\}$ are nulled. The basic operations of the subroutine are illustrated in Fig. 4.17.

For most problems, the system matrix $[H]$ has to be assembled in stages or parts (Fig. 4.18). The total number of storage locations available for the assembling operation, represented by the size of an array called B2, is specified by an integer parameter MAXSIZ. The

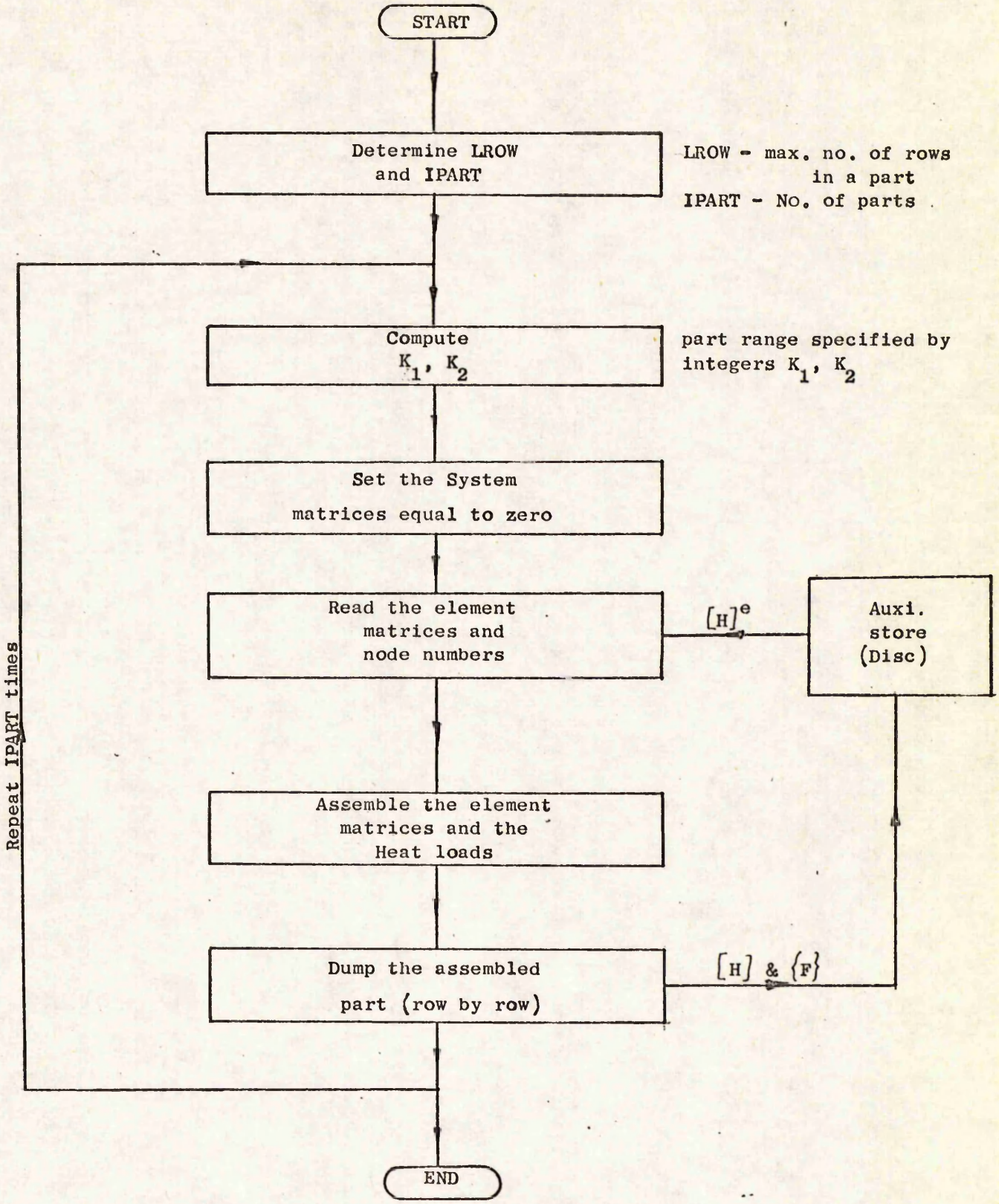

Fig. 4.17 FLOW CHART FOR SUBROUTINE ASSEMB

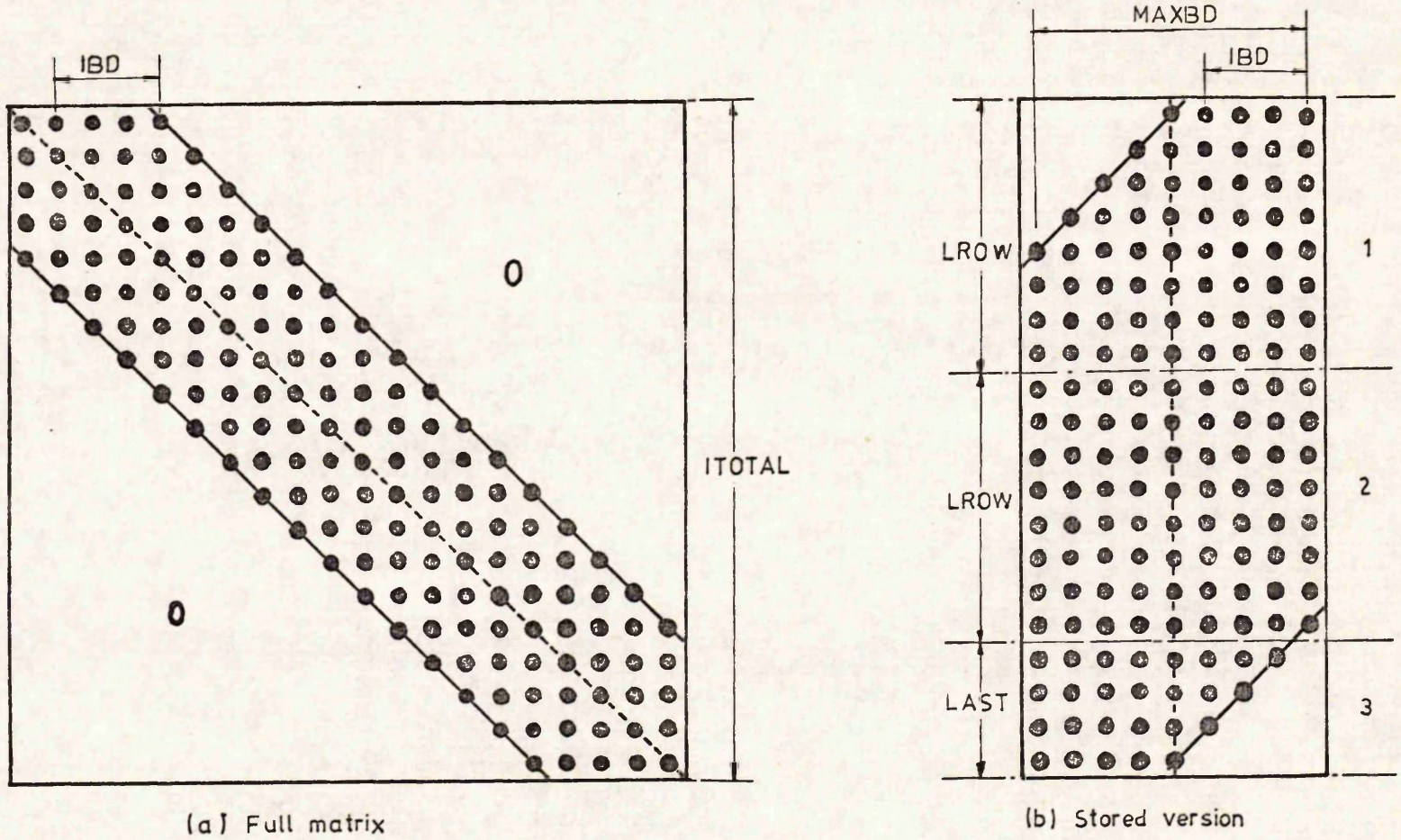

(a) Full matrix

(b) Stored version

MAXBD = 2*IBD+1

LROW = MAXSIZ/MAXBD

MAXSIZ = Maximum core available for assembling operation

FIG. 4.18 ASSEMBLED MATRIX [H]

Assembled in 3 parts

number of columns (MAXBD) and the number of rows (LROW) that can be assembled in each part are calculated as follows:

MAXBD = 2 * BANDWIDTH + 1

ITOTAL = total number of degrees of freedom.

LROW = MAXSIZ/MAXBD

and IPART = ITOTAL/LROW

For each part, row indices of the first row (K1) and the last row (K2) are calculated. They specify the range or limit of the part.

When the node numbers of an element are read from the disc file, the row indices in the element with respect to their locations in the assembled matrices are checked against the range specified by K1 and K2. Those falling inside the range are assembled and those outside the range are skipped. This is done for all the elements and the disc storing them is scanned once for each part assembly. The whole procedure is repeated for all the parts. It may be mentioned here that a bigger working core for the assembly operation reduces the amount of data transfer from the disc file storing element data and element matrices, because IPART will be smaller. Hence, MAXSIZ should be as large as possible.

The fully assembled parts of the matrix [H] are, then, recorded row by row onto a disc file ready for the subroutine EQSOL.

It is evident from the above description that there is practically no limit as to the size of the problem that can be analysed with this program as far as the assembly operation is concerned, provided the array B2 has sufficient storage locations to take atleast two rows.

4.5.4 Solution of Assembled Matrices.

The key factor in any finite element analysis is the subroutine for the solution of simultaneous equations. An efficient solution procedure can reduce the computational time as well as the core store requirement.

The assembled matrices, in the present program, are solved using

the Gaussian elimination procedure in subroutine EQSOL. The subroutine takes advantage of the fact that the matrix $[H]$ is banded. Auxiliary storage is used to cater for large problems. The main aspects of this subroutine are forward elimination, back substitution and the rearranging procedure.

Forward Elimination: Using Eq. (2.10), a set of N equations may be represented in partitioned form as

$$\begin{bmatrix} H_{11} & H_{12} & 0 \\ H_{21} & H_{22} & H_{23} \\ 0 & H_{32} & H_{33} \end{bmatrix} \begin{Bmatrix} T_1 \\ T_2 \\ T_3 \end{Bmatrix} + \begin{Bmatrix} F_1 \\ F_2 \\ F_3 \end{Bmatrix} = 0 \qquad (4.42)$$

where T is a vector of unknown temperatures, F is a vector of known heat loads and the matrix sizes are as follows:

$H_{11}(1 \times 1)$, $H_{12}(1 \times m)$, $H_{21}(m \times 1)$, $H_{22}(m \times m)$, $H_{23}(m \times (N - 1 - m))$, $H_{32}((N - 1 - m) \times m)$, $H_{33}((N - 1 - m) \times (N - 1 - m))$.

where m is the semi-bandwidth.

It may be mentioned here that $[H]$ is unsymmetric. The banded nature of the matrix $[H]$ is demonstrated by the zero submatrix which replaces the zero values beyond H_{12}. In the forward elimination (39), the $[H]$ matrix is reduced to an N - 1 matrix equation of the form

$$H^{*} T + F^{*} = \qquad (4.43)$$

where $$H^{*} = H_{22} - H_{21} H_{11}^{-1} H_{12} \qquad (4.44)$$

and $$F^{*} = F_2 - H_{21} H_{11}^{-1} F_1 \qquad (4.45)$$

Here, when H_{11} is eliminated only H_{22} is modified as the zero submatrix causes no change in H_{23}, H_{32} and H_{33}. This procedure is repeated by partitioning H^{*} in the same way until the matrix H^{*} is reduced to a 1 x 1 matrix. As a result, all the co-efficients in the lower triangle of the matrix $[H]$ are reduced to zero. For the large problems, this

operation is performed in stages as described earlier in Chapter II. The procedure is illustrated in the flow chart in Fig. 4.19.

Back Substitution: In the back substitution, the equations of the type

$$T_1 = -H_{11}^{-1} F_1 - H_{11}^{-1} H_{12} T_2 \qquad (4.46)$$

are used to solve for the temperatures except for the last unknown temperature T_n for which the direct value is given by H^* (being reduced to a 1x1 matrix). That is, the non-diagonal co-efficients of the upper triangle of $[H]$ are reduced to zero and the diagonal co-efficients are made equal to 1. The procedure is identical to the one described for the forward elimination, but now the stages (or parts) for the large problems are loaded in reverse order. Once both forward elimination and back substitution are performed in a certain stage, only the temperature values corresponding to that stage are stored. These values are recalled in a similar fashion as it was done in forward elimination.

Rearranging Procedure: Even though the co-efficients corresponding to the heat load vectors inside each stage are stored in the right position, the stages are finished in reverse order. The rearranging procedure places the values of the temperatures in their correct order.

4.6 TPLOT.

One of the disadvantages of the finite element analysis is the voluminous output produced by the analysis and the time needed to interpret the printed output. The use of the graph plotter as a means of displaying the results solves this difficulty to a large extent. The labelled nodal temperatures and the temperature contours are the most convenient types of display. They may be drawn over the whole area of the system or over some particular area of interest.

A second use of the plotting program is to draw the finite element mesh of the whole region or a part of it and to label the node numbers.

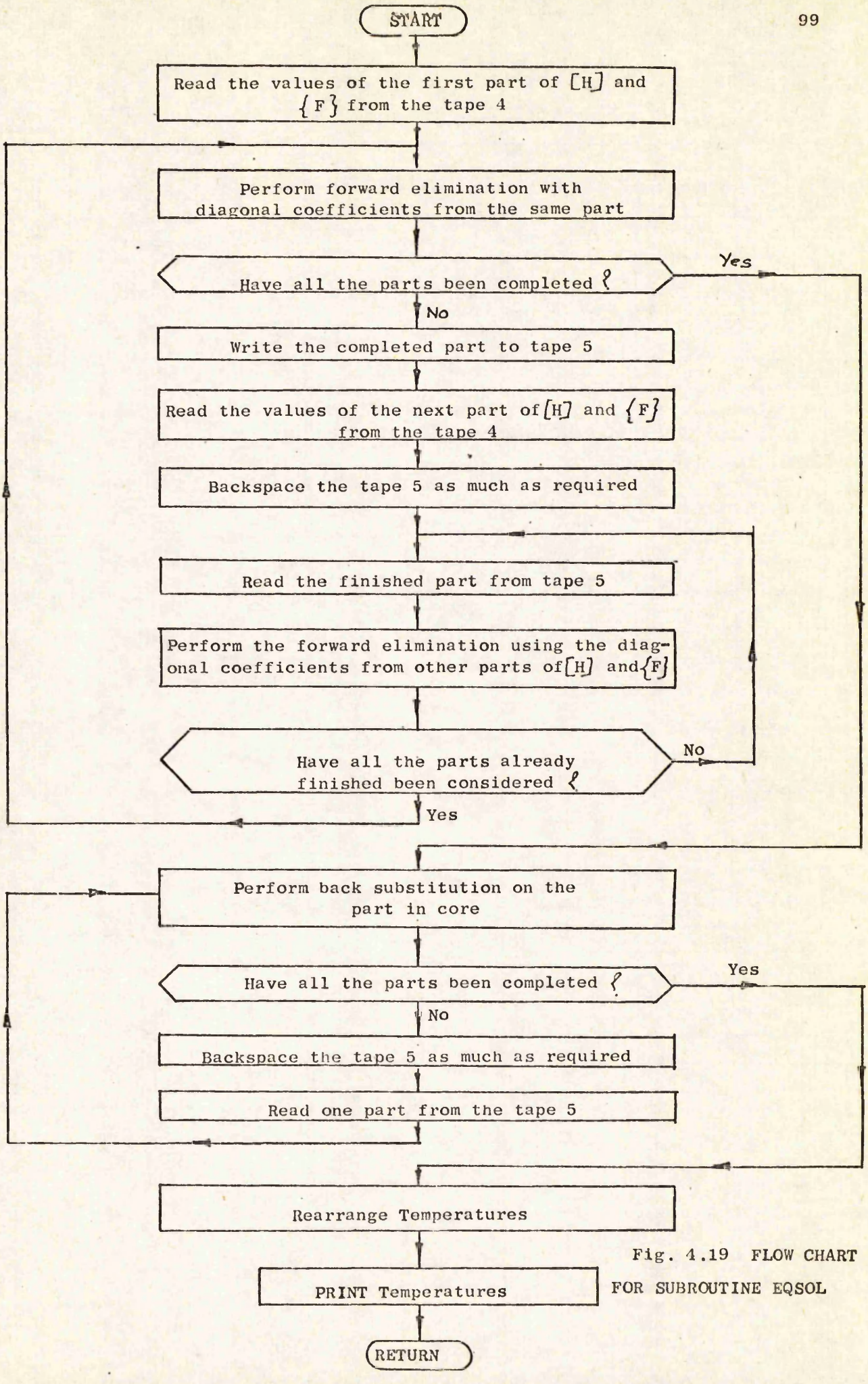

Fig. 4.19 FLOW CHART FOR SUBROUTINE EQSOL

This helps to a large extent in the preparation and verification of the input data for the main program.

The program TPLOT takes each element in the mesh, decomposes it into the lines which go to form that element, plots the line vectors and labels them either with node numbers or with nodal temperatures. If required, the isothermals can also be plotted over a particular area of interest. The view depends upon the angles of projection specified in the input data. The other data required by the program consist of the geometrical data (global co-ordinates), nodal temperatures and the information about the number of zones and the type of element in a zone. Most of the data is generated by the programs ELDATGEN and FETC.

Fig. 4.20 shows a flow chart for the program. The three subroutines required by the program are NODENO, PLOTCO and DRAW as described, in brief, below.

4.6.1 Subroutine NODENO (109)

In this subroutine each element in the zone is decomposed into and replaced by the lines which go to form it. For instance, a rectangular element is replaced by four lines and a triangle by three lines.

The two node numbers associated with each line are stored in arrays N_1 and N_2. The smaller of the two numbers is stored in vector N_1 and the larger in N_2. To avoid duplication, these two node numbers are compared with node numbers already in the two vectors and they are stored only if this line has not occurred before.

To label the line vectors with node numbers or with temperatures, the convention adopted here is to consider only the node numbers or the temperatures associated with vector N_2. In order to avoid certain nodal points to be overlooked, the vectors N_1 and N_2 are rearranged such that all the nodal points appear in vector N_2.

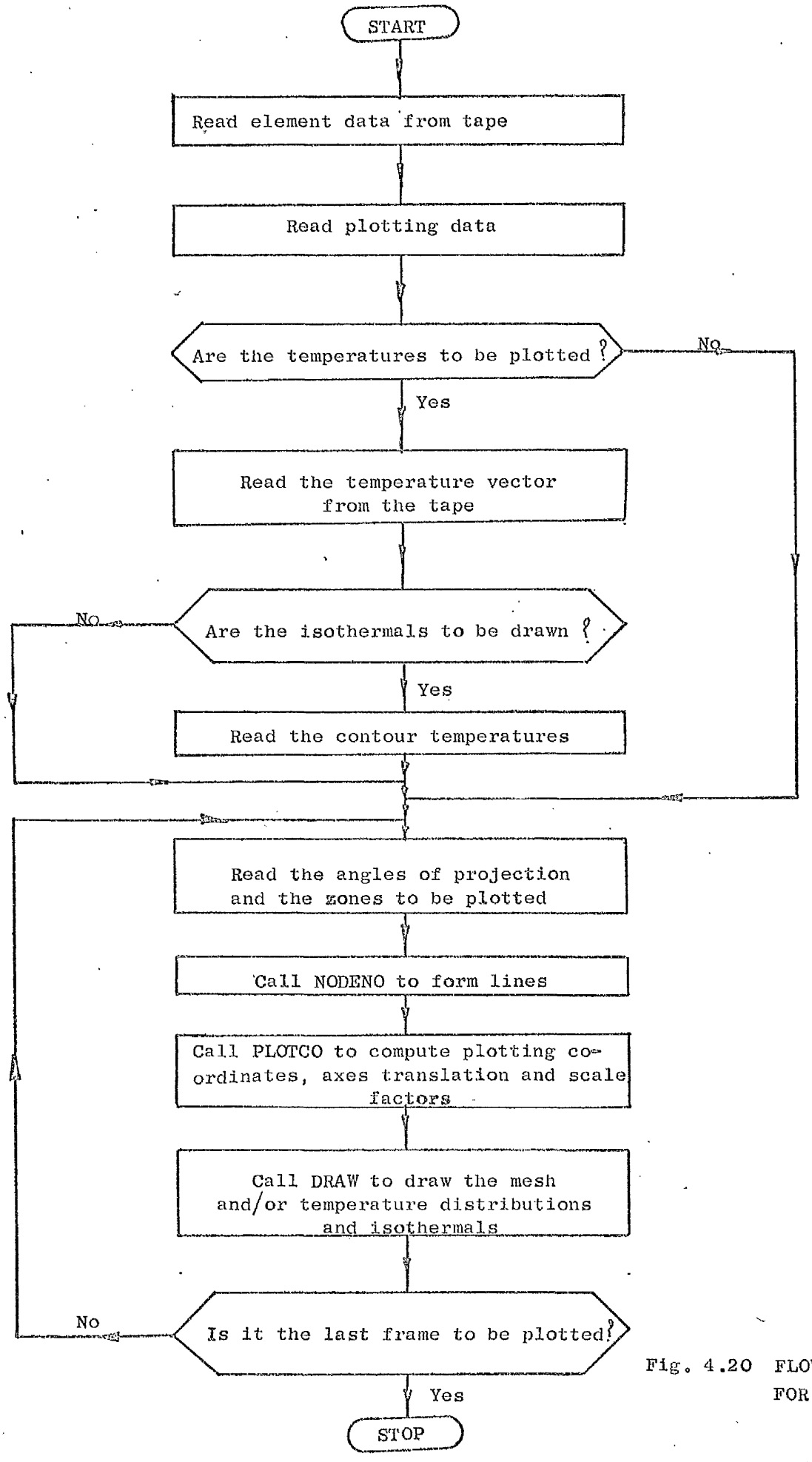

Fig. 4.20 FLOW CHART FOR TPLOT

4.6.2 Subroutine PLOTCO.

This subroutine decides about the plotting space, the dimensions of the mathematical space which is to be mapped over the plotting area, scale factors and the positioning and annotation of the axes. The variables A and C determine the maximum values of the plotting co-ordinates in the x and y directions respectively, whereas B and D find the minimum values. The dimensions of the mathematical space and the scale factors are fixed by A, B, C and D.

4.6.3 Subroutine DRAW.

This subroutine draws the finite element mesh, labels the node numbers or the temperatures and generates the isothermals. The integers NN and ID control the operations to be performed. If NN is equal to zero, the node numbers are not displayed. If ID is equal to 1 or 3, the temperatures are displayed. The isothermals are plotted if ID is greater than 1. To simplify programming, extensive use is made of a number of subroutines from the GHOST graphical output system (110).

4.7 PRPLOT.

The program PRPLOT plots the strain, strain-rate, flow stress and temperature distributions in the primary deformation zone. The values of all these variables and their locations are read from tapes. No other input data is necessary. The dimensions of the mathematical space to be mapped over the plotter space are fixed by calculating the maximum and minimum values of x and y co-ordinates.

The distributions of each variable are plotted on separate frames one by one by calling a subroutine BOUND four times. The subroutine BOUND draws and annotates the axes, defines the shear zone boundary, marks the locations and labels the variable values at all the points in the primary deformation zone. This subroutine is quite general in nature and

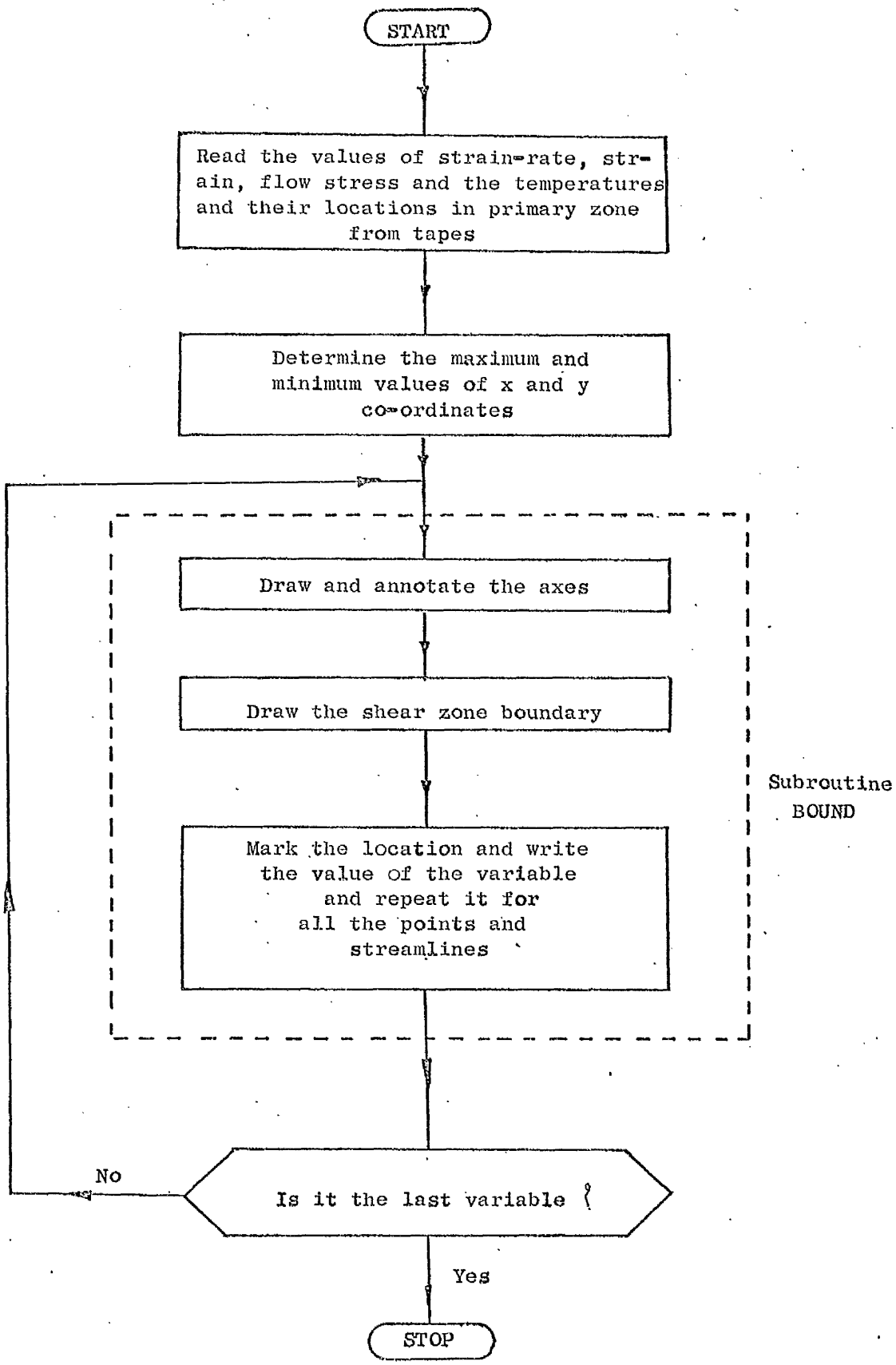

Fig. 4.21 FLOW CHART FOR PRPLOT

can be used for similar plotting jobs.

The different stages in plotting the distributions of the shear zone variables are illustrated in Fig. 4.21.

CHAPTER V

RESULTS AND DISCUSSION

5.1 Strain and Strain-rate Distribution in the Primary Zone.

The distribution of strain and strain-rate in the primary zone was obtained based on experimentally determined streamlines. The experimental technique and the method of analysis used were described in Chapter III. The distribution of the strain and strain-rate is shown in Figs. 5.1(a) - 5.17(a) and Figs. 5.1(b) - 5.17(b) respectively. It can be seen that the thickness of the deformation zone for most of the test cases is more or less uniform. The cutting conditions, the thickness of the deformation zone, the average shear strain along the shear plane determined experimentally as well as calculated based on shear plane theory are tabulated in Table 5.1.

The thickness of the shear zone d_{cn} was measured in the direction parallel to the chip at the centre of the shear zone. The values of d_{cn} are very small and vary from 0.141 mm to 0.291 mm for the given range of variables experimented with. The experimental value of d_{cn} (0.2286 mm) determined by Goriani and Kobayashi (75) for a typical cutting condition (U = 7.6 m/min., α = 35°, t_1 = 0.381 mm) and the results of Kececioglu (78) lie well within the values determined in the present work. It is seen from Table 5.1 that the shear-zone thickness decreases as the rake angle α and the cutting speed U increase. This can be explained by the fact that the increase in α results in a sharp tool edge providing a greater concentration of stress in a narrower area (78) and the higher cutting speeds do not provide as much time for dislocations to migrate and activate more shear planes. On the other hand, d_{cn} decreases with a decrease in the feed t_1 and with the use of a coolant. It is obvious that with the use of a coolant, the

TABLE 5.1

Shear Zone Strain Analysis.

Merchant

Serial No.	Test Identification No.	Speed,	Feed,	Rake Angle	Tool Material	Average Shear-zone Thickness	Average Shear Plane Strain	Shear strain from Eq.5.1a
		U	t_1	α		d_{cn}	γ_{sz}	γ_c
		m/min	mm/rev			mm		
1	1	24.76	0.3556	41.0	HSS	0.141	0.570	1.016
2	3	24.78	0.2845	20.0	"	0.276	0.770	1.524
3	5	17.34	0.3556	41.0	"	0.248	0.573	1.032
4	6	24.68	0.3556	20.0	"	0.282	0.870	1.579
5	9+	24.77	0.3556	20.0	"	0.218	1.048	1.633
6	11	45.96	0.3556	20.0	"	0.240	1.028	1.908
7	12+	45.77	0.3556	20.0	"	0.229	1.060	1.804
8	13	24.77	0.3556	30.0	"	0.236	0.852	1.516
9	25++	17.34	0.3556	41.0	"	0.248	0.573	1.032
10	14	35.33	0.3556	20.0	Carbide	0.271	1.057	1.663
11	15	71.11	0.3556	20.0	"	0.248	1.159	1.771
12	17	35.24	0.2845	20.0	"	0.201	1.159	1.732
13	18	35.28	0.5690	20.0	"	0.291	0.795	1.592
14	19	35.15	0.3556	10.0	"	0.283	1.206	1.894
15	21+	35.26	0.3556	20.0	"	0.266	1.028	1.696
16	23	130.73	0.3556	20.0	"	0.238	1.236	1.873
17	24+	131.38	0.3556	20.0	"	0.203	0.887	1.717

+ TESTS PERFORMED WITH COOLANT.

++ TOOL WITH INITIAL FLANK WEAR (0.376 mm)

decreased shear force tends to confine to a narrower area and with a decrease in t_1, fewer shear planes are activated and the volume of workpiece material available between the lower and upper boundaries of the shear zone is smaller. These observations are in good agreement with those made by Kececioglu (78).

The average shear strain γ in the chip for a typical cutting condition ($U = 24.8$ m/min., $\alpha = 41°$, $t_1 = 0.3556$ mm/rev., Test No. 1) varies from 0.57 to 1.0 with the maximum value along the tool face as shown in Fig. 5.1(a). Similar trends were observed with the other tests. For the sake of comparison, the shear strain values have also been calculated by the conventional method of analysis based on the shear plane type deformation according to the expression

$$\gamma_c = \cot\phi + \tan(\phi - \alpha) \qquad (5.1(a))$$

These values are also tabulated in Table 5.1. The calculated shear strain values γ_c based on Eq. (5.1(a)) are much higher than the experimental values of the average shear plane strain γ_{sz}. For example (for Test no. 1) the calculated shear strain is 1.016 as compared to the experimental value of 0.570 at the shear plane, but γ_c agrees with the average experimental shear strain value of 1.000 at the chip-end of the shear zone (Fig. 5.1(a)). Thus, the calculation of the shear strain based on shear plane theory does not represent the strain at the centre of the shear zone, but it seems to estimate approximately the average strain at the chip-end of the shear zone.

It is seen from Table 5.1 that the average shear strain γ_{sz} along the shear plane decreases with an increase in rake angle α. This can be attributed to smaller deformation which usually occurs with increased α. Similar observations were made by Ostafiev and Kobayashi(100). The increase in cutting speed results in a small increase in shear strain γ_{sz}, whereas γ_{sz} does not appear to vary consistently with the variation

of the feed t_1.

The average shear strain-rates $\dot{\gamma}_{sz}$ along the shear plane for various cutting conditions are tabulated in Table 5.2. The average values were obtained at the central shear plane SZ passing through the cutting edge from the experimentally determined strain-rate distributions shown in Figs. 5.1(b) - 5.17(b).

It is observed that, as expected (5, 78, 100), $\dot{\gamma}_{sz}$ increases with an increase in the cutting speed. Similar to the results of Kececioglu (78) and Nakayama (5), the average shear strain-rate $\dot{\gamma}_{sz}$ also increases with the rake angle. However, $\dot{\gamma}_{sz}$ does not seem to exhibit a consistent trend with the variation of the feed t_1. It may be of interest to compare the $\dot{\gamma}_{sz}$ values with the average shear strain-rates $\dot{\gamma}_m$ calculated from the thickness of the deformation zone obtained, using the equation

$$\dot{\gamma}_m = \frac{\gamma . U \sin\phi}{d_{cn}} \qquad (5.1(b))$$

where, γ is the shear strain,

U is the cutting velocity,

ϕ is the shear angle,

and d_{cn} is the thickness of the shear zone.

The values of $\dot{\gamma}_m$ are given in Table 5.2 and it can be seen that the calculation of the mean shear strain-rate $\dot{\gamma}_m$ by Eq. (5.1(b)) underestimates the strain-rate considerably except at very low speeds. It appears that the determination of the shear zone thickness is critical and the interpretation of the average strain rate based on d_{cn} needs careful consideration.

5.2 Flow Stress Distribution in the Primary Zone.

The flow stress distribution in the primary zone obtained from Eq. (3.21) is shown in Figs. 5.1 (c) - 5.17 (c). It is seen from

TABLE 5.2

Shear Zone Strain-rate Analysis

Serial No.	Test Identification No.	Speed, U	Feed, t_1	Rake Angle α	Tool Material	Average Strain-rate along shear plane, $\dot{\gamma}_{sz}$	Shear strain-rate from Eq. (5.1b) $\dot{\gamma}_m$
		m/min	mm/rev			sec^{-1}	sec^{-1}
1	1	24.76	0.3556	41.0	HSS	2733.0	2227.6
2	3	24.78	0.2845	20.0	"	1909.7	1511.3
3	5	17.34	0.3556	41.0	"	808.7	887.0
4	6	24.68	0.3556	20.0	"	2323.2	1449.5
5	9+	24.77	0.3556	20.0	"	2232.2	1860.9
6	11	45.96	0.3556	20.0	"	6674.7	3044.8
7	12+	45.77	0.3556	20.0	"	6492.7	3203.0
8	13	24.77	0.3556	30.0	"	2461.0	1520.9
9	25++	17.34	0.3556	41.0	"	808.7	887.0
10	14	35.33	0.3556	20.0	Carbide	3272.0	2124.5
11	15	71.11	0.3556	20.0	"	10846.2	4608.8
12	17	35.24	0.2845	20.0	"	4913.0	2830.1
13	18	35.28	0.5690	20.0	"	3442.8	2002.5
14	19	35.15	0.3556	10.0	"	3180.6	2248.6
15	21+	35.26	0.3556	20.0	"	2905.1	2149.4
16	23	130.73	0.3556	20.0	"	13560.3	8754.0
17	24+	131.38	0.3556	20.0	"	18869.3	10463.1

\+ TESTS PERFORMED WITH COOLANT.

++ TOOL WITH INITIAL FLANK WEAR (0.376 mm)

Fig. 5.1(c) that for Test no. 1, the flow stress varies from 368 MPa at the workpiece-end of the shear zone to 500 MPa at its chip-end. However, the distribution is non-uniform because of the combined effect of the strain, strain-rate and temperature variations and the difference between the lowest and the highest values of the flow stress for most of the cases is not larger than 15%.

It has been shown by Ostafiev and Kobayashi (100) that the flow stress remained almost constant over a wide range of strains encountered in metal cutting with a decreasing trend for strains smaller than 0.5. Increasing temperature and strain-rate have been shown (102) to have opposite effects on the flow stress under dynamic conditions. Kececioglu's results (101) indicated that this was, in general, true in metal cutting also. However, it must not be construed that the opposing effects of temperature and strain-rate on flow stress necessarily cancel each other under metal-cutting conditions, no doubt, the variations in the flow stress under different conditions of cutting are not large. This fact is demonstrated by the values of average shear flow stress τ_{sz} along the shear plane tabulated in Table 5.3 where τ_{sz} varies from 475 MPa to 490 MPa for the large range of variables experimented with.

It can also be seen from Table 5.3 that, in general, τ_{sz} increases with increasing rake angle α and velocity U. This can be explained by the fact that the increase in cutting velocity is associated with a comparatively larger increase in strain-rate as compared to the correspondingly smaller increase in temperature. The increase in τ_{sz} with an increase in α is the result of a corresponding decrease in temperature as well as an increase in strain-rate. It may be mentioned here that these results agree well with the observations made by Kececioglu (78).

5.3 Accuracy and Time Analysis of Finite Elements for Temperature Distribution.

Since the resulting accuracy of the computed temperature distribution

TABLE 5.3

Shear Zone Flow Stress Analysis.

Serial No.	Test Identification No.	Speed, U	Feed t_1	Rake Angle α	Tool Material	Average Flow Stress along shear plane, τ_{sz}
		m/min	mm/rev			MPa
1	1	24.76	0.3556	41.0	HSS	484.75
2	3	24.78	0.2845	20.0	"	475.25
3	5	17.34	0.3556	41.0	"	480.17
4	6	24.68	0.3556	20.0	"	476.50
5	9+	24.77	0.3556	20.0	"	480.25
6	11	45.96	0.3556	20.0	"	482.33
7	12+	45.77	0.3556	20.0	"	481.83
8	13	24.77	0.3556	30.0	"	483.25
9	25++	17.34	0.3556	41.0	"	481.91
10	14	35.33	0.3556	20.0	Carbide	484.17
11	15	71.11	0.3556	20.0	"	488.17
12	17	35.24	0.2845	20.0	"	486.37
13	18	35.28	0.5690	20.0	"	477.44
14	19	35.15	0.3556	10.0	"	475.33
15	21+	35.26	0.3556	20.0	"	480.25
16	23	130.73	0.3556	20.0	"	490.25
17	24+	131.38	0.3556	20.0	"	489.12

\+ TESTS PERFORMED WITH COOLANT.

++ TOOL WITH INITIAL FLANK WEAR (0.376 mm)

depends largely upon the choice of temperature functions and the refinement of the mesh, the finite element analysis for one typical test conditions was carried out using linear, quadratic and cubic quadrilateral elements as well as a linear triangular element. These four elements used will hereafterwards be referred to by the abbreviations shown below.

TRI3 - 3-node triangular element.

QUAD4 - 4-node quadrilateral element.

QUAD8 - 8-node quadrilateral element.

QUAD12 - 12-node quadrilateral element.

A low carbon steel of chemical composition (C - 0.12%, Mn = 0.675%, Ni = 0.05%, Si = 0.09%) was used as the workpiece material for the test. Machining was carried out with a high speed steel tool of rake angle α = 41° and clearance angle = 10° at a cutting speed U = 17.5 m/min., feed t_1 = 0.381 mm/rev. and the width of cut = 6.35 mm. The other measured data were:

Cutting force, F_V = 2000 N, Feed force, F_H = 251.0 N,

Flank frictional force F_F = 20.0 N, Flank Normal force, F_N = 42 N

Chip thickness ratio = 0.674, Initial flank wear = 0.376 mm,

Tool-chip contact length = 0.92 mm, sliding length = 0.60 mm.

Experimental temperature at a distance of 3.92 mm from tool edge along rake face, T_p = 198.7°C.

The problem region composed of the work-tool-chip composite system is shown in Fig. 5.18 and the corresponding key diagram is shown in Fig. 5.19. The mesh was refined successively by increasing the number of divisions N_h along the tool-chip contact length from 2 to 3 and then to 4. The divisions of other zones were also increased proportionately. The finest meshes thus generated using quadrilateral and triangular elements are shown in Figs. 5.20 and 5.21 respectively. The computed

temperature distributions in some of the important zones and the isothermals in the workpiece, tool and chip using QUAD12, QUAD8, QUAD4 and TRI3 elements with the finest mesh are shown in Figs. 5.22 - 5.27. The computed temperature T_p at a point P, 3.92 mm away from the tool-edge along the rake face and the maximum temperature T_{max} on the rake face for the various types of elements using three different types of meshes are tabulated in Table 5.4. The percentage error with respect to the experimental value in each case is also shown in the table. In addition to this, convergent curves have been plotted for the temperatures T_p and T_{max} in Figs. 5.28 and 5.29 respectively.

Examining the results obtained with the TRI3 element, it is seen that the temperature T_p varies initially with the number of divisions along the tool-chip contact length, but quickly converges to a constant value. With four divisions, this value is 94.4 percent of the experimental temperature. With the QUAD4 element, however, the curve starts from a much lower value, the temperature increases monotonically as the number of divisions N_h are increased and reaches up to 95% of the experimental value. With four divisions, the computed values of T_{max} and T_p are more accurate with the QUAD4 element as compared to the TRI3 element. With two or three divsions, however, the convergent curves for QUAD4 and TRI3 exhibit contrasting trends for the temperatures T_{max} and T_p. This may be attributed to the inherent peculiarities of the FEM. Considering the situation where the heat load Q is constant over an element of area A, the FEM will assign QA/3 to each node of the triangle. Consequently, if a node is common to n triangles, the heat contribution to it will be nQA/3, while a node which is included in only one triangle will receive only QA/3. Thus, if the geometric pattern of triangular elements is not symmetrical, the temperature distribution will not be symmetrical and small errors will exist which will increase with a coarser mesh. Similarly, a linear quadrilateral element assigns

TABLE 5.4

TEMPERATURE CONVERGENCE WITH DIFFERENT ELEMENTS.

Element Type	No. of Divisions along the tool-chip contact length.	Maximum temp. on rake face (computed) °C	Temperature at a point 3.92 mm distant from tool edge along rake face °C.	
			Computed value	% error (experimental temp. = 198.7°C)
4-node quadrilateral	2	213.0	160.0	19.47
	3	275.71	183.47	7.66
	4	283.46	188.72	5.02
8-node quadrilateral	2	265.98	190.61	4.07
	3	283.86	193.88	2.42
	4	291.64	195.79	1.46
12-node quadrilateral	2	273.61	190.91	3.92
	3	288.32	195.31	1.71
	4	293.57	197.58	0.56
3-node triangle	2	201.0	173.0	12.90
	3	249.74	186.92	5.92
	4	274.14	187.59	5.59

QA/4 to each node and the resulting nodal heat distributions are likely to be different in nature than those with triangular elements even with a geometrically similar mesh and some discrepancy with a coarse pattern is not ruled out.

With QUAD8 and QUAD12 elements, the results are fairly accurate even with a coarse mesh. With the finest mesh used, the computed temperature T_p converges to 99.4% of the experimental value with QUAD12 element and to 98.5% with QUAD8 element. (It may be mentioned here that, as described in Sections 3.8 and 5.6, the experimental measurement of temperatures is associated with inherent sources of error(1) and no estimate of accuracy can be made). Thus, the QUAD12 element, as anticipated, represents the most accurate element considered. Even the accuracy obtained with QUAD8 element appears to be quite acceptable for engineering applications.

Apart from the accuracy obtained with an element, one must consider the computing time required for element formulation, assembly and solution of the equations. Evaluation of the matrices for the higher-order elements takes considerably much larger time because of the increased number of integrating points. The time for assembly is small and can be neglected. The time for solution of the equations depends upon the number of nodes in the mesh and the bandwidth of the assembled matrices and is indicated by EQSOL. The total time required for computation is indicated by FETC. The times (CDC 7600 CPU seconds) required for FETC and EQSOL are shown in Table 5.5. The values of the bandwidth, the total number of elements and the total number of nodes are also given in the table. The computing times versus N_h (number of divisions along the tool-chip contact length) curves are plotted in Figs. 5.30 and 5.31. Figs. 5.32 and 5.33 show the computing times required by EQSOL and FETC for varying degrees of freedom. It can be observed that in the earlier part of the curves, for a given number of degrees of

TABLE 5.5

COMPUTING TIME ANALYSIS

Element Type	No. of Divisions along tool-chip contact length.	Total No. of elements	Total No of nodes	Bandwidth	Total Time taken for 'FETC' CPU secs.	Time taken for solving equations CPU secs.
4-node Quadri-lateral	2	67	92	10	1.26	0.150
	3	143	179	16	2.832	0.466
	4	266	313	22	5.762	1.340
8-node Quadri-lateral	2	67	250	28	4.309	1.585
	3	143	500	43	12.927	6.433
	4	266	891	64	41.206	27.000
12-node Quadri-lateral	2	67	408	45	11.913	6.348
	3	143	821	67	43.223	28.961
	4	266	1469	106	140.786	100.689
3-node Tri-angle	2	134	92	8	0.984	0.149
	3	286	179	11	1.737	0.309
	4	532	313	15	3.540	0.820

freedom, there is not much difference in the computing time required by different elements for the solution of the simultaneous equations as well as for the execution of the whole program FETC. But as the number of degrees of freedom increases, the curves begin to move apart. QUAD12 requires the maximum amount of time and TRI3 the least. In the case of QUAD12 and QUAD8 elements, the increase in computing time can be attributed to the increased bandwidth.

It can be seen from Figs. 5.30 and 5.31 that, for the same number of divisions along the tool-chip contact length, large computational times are required for the higher-order elements than with the simple linear models. This is because when utilizing the quadratic and cubic elements, the bandwidth as well as the total number of degrees of freedom are considerably increased. For instance, for the same mesh pattern with $N_h = 4$, the QUAD12 element model requires three and a half times more computing time than that for QUAD8 and 25 - 40 times more than that of the linear models. Since the computational time required by QUAD12 element model is intrinsically large and the linear element models necessitate a large number of nodal points in order to reach a reasonable accuracy, the QUAD8 element appears to be an efficient choice. Hence, for all subsequent analysis, the QUAD8 element model has been used.

In order to account for the variation of the thermal properties of the materials with temperature, an iterative procedure was employed in which values for the properties in each iteration were based on the temperature obtained in the previous iteration. For each iteration, new system matrices were calculated and a new set of nodal temperatures obtained. The temperature converged to within a relative error of less than 1 percent throughout the problem region in no more than four iterations. It may be of interest to look at the rate of convergence of

the temperatures with each iteration. Typical values of T_p and T_{max} at each iteration for the above models are given in Table 5.6. Figs. 5.34 and 5.35 show the convergence curves of T_p and T_{max} respectively against the number of iterations. An identical trend is exhibited by all element models. It is observed that the computed temperatures after the first iteration are considerably larger than those computed subsequently because of the lower starting nodal temperatures which were initially set equal to 0°C. With the second iteration, the increase in the specific heat of the materials with increased temperature brings the nodal temperatures close to but slightly lower than the final temperatures. After the third iteration, there is hardly any change in temperature (less than 1%) and for all practical purposes the temperature can be assumed to have converged.

5.4 The Temperature Distribution.

The temperature distribution and the isothermals obtained for the seventeen test conditions considered are shown in Figs. 5.36 - 5.52. The shear zone temperatures are shown separately on an enlarged area in Figs. 5.1(d) - 5.17(d).

5.4.1 Shear Zone Temperatures.

It can be seen from Figs. 5.1(d) - 5.17(d) that, in general, the temperatures increase progressively from the workpiece-end boundary towards the chip-end boundary of the shear zone. Although the temperature around the middle of the shear zone is approximately constant, the temperatures at the tool edge and along the tool-chip contact length are quite high. This indicates that the assumption of a constant shear plane temperature by Rapier (32) is very approximate.

From the temperature distribution shown in Figs. 5.1(d) - 5.17(d), the average shear plane temperatures T_s were obtained and are shown in

TABLE 5.6

TEMPERATURE CONVERGENCE WITH THE NUMBER OF ITERATIONS.

	T_p °C				T_{max} °C			
No. of iterations / Elements	1	2	3	4	1	2	3	4
QUAD8 891 Nodes	202.61	195.30	195.83	195.79	298.95	291.04	291.69	291.64
QUAD8 500 Nodes	200.87	193.46	193.91	193.88	290.66	283.35	283.91	283.86
QUAD8 250 Nodes	197.44	190.31	190.64	190.61	275.08	265.34	266.02	265.98
QUAD12 1469 Nodes	204.47	197.08	197.62	197.58	301.18	292.95	293.62	293.57
QUAD12 821 Nodes	202.60	194.86	195.35	195.31	296.49	287.71	288.37	288.32
QUAD12 408 Nodes	198.94	190.47	190.94	190.91	283.76	272.90	273.66	273.61
QUAD4 313 Nodes	194.44	188.24	188.75	188.72	287.22	282.91	283.50	283.46
QUAD4 179 Nodes	189.11	183.06	183.50	183.47	281.58	275.10	275.76	275.71
TRI3 313 Nodes	193.59	187.03	187.63	187.59	278.64	273.54	274.19	249.74
TRI3 179 Nodes	193.28	186.39	186.97	186.92	255.45	249.16	249.79	249.74

Table 5.7. It is seen from Table 5.7 that the average shear plane temperature increases with an increase in cutting velocity U, and it decreases with the increase in rake angle α. For instance, T_s is increased from 153.3°C to 169.5°C as U is increased from 24.7 m/min. to 46.0 m/min., whereas T_s is decreased to 97.7°C as α is increased from 20° to 41°. However, T_s does not appear to vary consistently with the feed t_1. Similar observations were made by Kececioglu (101) with mild steel using the calculation procedure of Loewen and Shaw (26) based on energy considerations.

In order to check the accuracy of the shear zone temperatures, the deformation energy E_s along the shear plane calculated from the product of the shear force F_s and the shear velocity V_s was compared with that obtained from the strain-rate and temperature-based flow stress considerations. The values as shown in Table 5.8 differ by less than 2%. For the calculations, the equations used are

$$\left.\begin{aligned} F_s &= R \cos\Theta \,, \\ V_s &= \frac{U \cos\alpha}{\cos(\phi - \alpha)} \\ \text{and} \qquad E_s &= F_s \cdot V_s \end{aligned}\right\} \qquad (5.2)$$

where R is the resultant cutting force, and Θ is the angle between R and the shear plane. It is worthwhile to mention here that a value of the heat generation rate at the tool edge was inferred such that a perfect heat balance between the total energy of the heat sources ΣQ and the total energy input ΣE was obtained. The value of ΣQ is equal to the summation of the total heat generated in the two deformation zones and the frictional heat dissipated at the interfaces, whereas ΣE is given by the product of the cutting force F_v and the cutting velocity U.

TABLE 5.7

SHEAR ZONE TEMPERATURE ANALYSIS

Serial No.	Test Identification No.	Speed, U	Feed, t_1	Rake Angle, α	Tool Material	Average Temperature along shear plane T_s
		m/min	mm/rev			°C
1	1	24.76	0.3556	41.0	HSS	97.7
2	3	24.78	0.2845	20.0	"	139.9
3	5	17.34	0.3556	41.0	"	89.2
4	6	24.68	0.3556	20.0	"	152.3
5	9+	24.77	0.3556	20.0	"	160.5
6	11	45.96	0.3556	20.0	"	169.5
7	12+	45.77	0.3556	20.0	"	169.5
8	13	24.77	0.3556	30.0	"	134.1
9	25++	17.34	0.3556	41.0	"	85.2
10	14	35.33	0.3556	20.0	Carbide	154.8
11	15	71.11	0.3556	20.0	"	160.5
12	17	35.24	0.2845	20.0	"	157.9
13	18	35.28	0.5690	20.0	"	147.6
14	19	35.15	0.3556	10.0	"	201.9
15	21+	35.26	0.3556	20.0	"	162.9
16	23	130.73	0.3556	20.0	"	167.6
17	24+	131.38	0.3556	20.0	"	149.0

+ TESTS PERFORMED WITH COOLANT.

++ TOOL WITH INITIAL FLANK WEAR (0.376 mm)

TABLE 5.8

SHEAR ENERGY ANALYSIS

Serial No.	Test Identification No.	Speed U	Feed, t_1	Rake Angle, α	Tool Material	Shear Energy from strain-rate Distributions	Shear Energy From Force Considerations	% Variation
		m/min	mm/rev			Watts	Watts	
1	1	24.76	0.3556	41.0	HSS	435.6	437.8	-0.507
2	3	24.78	0.2845	20.0	"	511.7	509.8	0.363
3	5	17.34	0.3556	41.0	"	291.6	289.7	0.663
4	6	24.68	0.3556	20.0	"	719.2	723.9	-0.648
5	9+	24.77	0.3556	20.0	"	704.2	712.6	-1.18
6	11	45.96	0.3556	20.0	"	1636.5	1645.3	-0.537
7	12+	45.77	0.3556	20.0	"	1510.1	1524.1	-0.920
8	13	24.77	0.3556	30.0	"	658.5	666.8	-1.24
9	25++	17.34	0.3556	41.0	"	285.8	289.7	-1.35
10	14	35.33	0.3556	20.0	Carbide	1061.4	1047.5	1.33
11	15	71.11	0.3556	20.0	"	2296.7	2297.3	-0.026
12	17	35.24	0.2845	20.0	"	843.4	841.3	0.258
13	18	35.28	0.5690	20.0	"	1528.9	1537.0	-0.528
14	19	35.15	0.3556	10.0	"	1279.1	1267.8	0.888
15	21+	35.26	0.3556	20.0	"	1060.4	1059.3	0.1057
16	23	130.73	0.3556	20.0	"	4610.4	4598.7	0.385
17	24+	131.38	0.3556	20.0	"	4172.9	4176.2	0.078

\+ TESTS PERFORMED WITH COOLANT.

++ TOOL WITH INITIAL FLANK WEAR (0.376 mm)

5.4.2 Tool-face Temperatures.

It is observed from Figs. 5.36 - 5.52 that a non-uniform temperature distribution exists on the rake face of the cutting tool and the maximum temperature always occurs at some distance from the cutting edge. The temperatures on the rake face are much higher than those on the flank face.

The experimental study of the development of the rake face wear of a cutting tool over a wide range of cutting conditions and different work-tool combinations indicates that cratering starts at some distance from the cutting edge and yields a particular depth profile (23, 103). The local temperature at the point of actual engagement being a principal factor for wear (104), the temperature distribution can be employed with advantage to explain the non-uniform crater wear observed over the tool rake face. From the isothermals in Figs. 5.36 - 5.52, it can be seen that the temperature on the rake face rises sharply up to the point of maximum temperature from the cutting edge and then the temperature drops moderately up to the point of chip separation. A further drop in temperature beyond the point of chip separation is slow and gradual.

5.4.2.1 Location of the Point of Maximum Tool-chip Interface Temperature.

The tool-chip interface temperature distributions are largely controlled by the pattern of heat generated due to the interface friction. It has long been recognized that the interface contact pressure in the region close to the tip of the tool acquires a value which produces adhesion between the chip and tool resulting in plastic flow in the chip. It has been shown (40, 105) that the plastic flow in the chip tends to make the pressure distribution uniform, while beyond this region the pressure decreases and vanishes towards the end of tool-chip contact. The region of constant pressure distribution is called 'the sticking zone'

and the remaining part 'the sliding zone' (40). For the present investigations, the shear stress in the sliding zone was assumed to be given by

$$\tau = \tau_s \cdot \left(\frac{x}{C - C_1} \right)^n \qquad (5.3)$$

$$\text{and} \quad n = 2 \left\{ \frac{C}{t_1 \left[\mu + \tan (\phi - \alpha) \right]} - 1 \right\} \qquad (5.4)$$

where, τ_s is the maximum shear stress of the workpiece,

C is the tool-chip contact length,

C_1 is the length of sticking zone,

x is measured from the point of chip separation towards the tool tip and $\leq (C - C_1)$

and μ is the overall co-efficient of friction given by the ratio of the frictional and normal forces acting on the rake face.

The values of C, C_1, n, μ, the maximum interface temperature T_{max} and the location of the maximum interface temperature expressed as a fraction of the contact length given by the ratio C'/C are tabulated in Table 5.9, where C' is the distance of the point of maximum temperature from the cutting edge.

From Table 5.9, the following observations can be made.

(i) The ratio C'/C increases with an increase in the feed t_1.

(ii) The ratio C'/C decreases with a decrease in cutting speed U and,

(iii) The increase in rake angle results in an increase of C'/C.

The first two observations can be explained in terms of the stress exponent n used in Eq. (5.3). It is evident that the point of location of the maximum temperature along the interface should lie somewhere in the sliding zone depending upon the variation of the heat generation

MAXIMUM TEMPERATURE ANALYSIS

Serial No.	Test Identification No.	Speed U	Feed t_1	Rake Angle, α	Tool Material	Tool-chip Contact length C	Sticking Length C_f	Maximum Temp. T_{max}	Location of T_{max} (as a fraction of C) C'/C	C.O.F. along tool-chip interface, μ	Stress Exponent, n
		m/min	mm/rev			mm	mm	°C			
1	1	24.76	0.3556	41.0	HSS	0.9398	0.604	532	0.691	1.095	1.268
2	3	24.78	0.2845	20.0	"	1.524	0.8128	490	0.556	0.960	3.700
3	5	17.34	0.3556	41.0	"	0.9144	0.5842	431	0.654	1.085	1.280
4	6	24.68	0.3556	20.0	"	1.9812	1.1176	585	0.566	0.961	3.670
5	9+	24.77	0.3556	20.0	"	1.600	0.7874	540	0.609	0.960	2.460
6	11	45.96	0.3556	20.0	"	1.829	1.1684	708	0.696	0.966	2.60
7	12+	45.77	0.3556	20.0	"	1.8796	1.2192	640	0.695	0.932	3.05
8	13	24.77	0.3556	30.0	"	1.270	0.7366	458	0.6365	1.020	1.69
9	25++	17.34	0.3556	41.0	"	0.9144	0.5842	370	0.724	1.085	1.280
10	14	35.33	0.3556	20.0	Carbide	0.660	0.330	512	0.559	0.553	0.681
11	15	71.11	0.3556	20.0	"	0.9144	0.4572	702	0.574	0.697	1.08
12	17	35.24	0.2845	20.0	"	0.6096	0.3048	448	0.542	0.550	1.06
13	18	35.28	0.5690	20.0	"	0.8128	0.4064	678	0.583	0.597	0.21
14	19	35.15	0.3556	10.0	"	1.1938	0.6096	740	0.540	0.767	1.425
15	21+	35.26	0.3556	20.0	"	0.5588	0.2794	496	0.572	0.542	0.300
16	23	130.73	0.3556	20.0	"	0.9652	0.4826	1072+++	0.726	0.753	0.984
17	24+	131.38	0.3556	20.0	"	0.9779	0.4826	1028	0.582	0.750	1.200

\+ TESTS PERFORMED WITH COOLANT.

++ TOOL WITH INITIAL FLANK WEAR (0.376 mm)

+++ BY EXTRAPOLATION.

(or to say the pressure variation) along the sliding length. It can be seen from Eq. (5.3) that an increase in n is associated with a steeper pressure variation in the sliding region and consequently a sharper heat gradient along the sliding length tending to shift T_{max} towards the tool tip. Thus, an increase in n results in an obvious decrease in the ratio C'/C. Furthermore, as seen from Eq. (5.4), n is increased by decreasing μ. It was found that the overall coefficient of friction μ over the tool-chip interface was increased with an increase in U and t_1. This may be attributed to the increased frictional resistance on the sliding region due to the enhanced molecular bonding at higher temperatures developed with higher values of U and t_1. To sum up, μ is increased with an increase in U and t_1 resulting in a decrease of n and hence, in an increase of C'/C.

With the high speed steel tools, the ratio C'/C has been found to increase considerably with an increase in the rake angle α, whereas with carbide tools, the increase in C'/C is marginal. In general, for high values of α under otherwise similar cutting conditions, the shear angle is found to be large with a corresponding low value of shear strain. Thus the work-hardening of the chip material may be reduced. This contributes to the low plastic stress for the chip material, and, therefore, a possible elongation of the sticking zone as a result of easier plastic flow. Experimental values of the sticking length and the tool-chip contact length with HSS tools were in line with this reasoning. Thus, the point of location of maximum temperature being dependent upon the sticking length as well, tends to shift towards the point of chip separation as α is increased. The values of C'/C given in Table 5.9 agree well with the experimental values reported by Qureshi and Koenigsberger (16) and Vieregge (31).

5.4.2.2 Effect of the Process Variables on Tool Temperatures.

In order to analyse the effect of cutting process parameters such as cutting speed, feed, rake angle, tool flank wear, use of coolant and tool materials on temperature distributions, the temperatures along the tool face and tool flank are plotted separately in Figs. 5.53 - 5.64. From these curves, it can be seen that the point of chip-separation is also accompanied by a sudden and drastic change in temperature gradient. Similarly, the end point of the wear land, if any, along the tool flank is reflected by a sudden rise of temperature just after the point (Fig. 5.64(b)). The highest temperature along the tool flank, similar to the tool face, occurs at some distance away from the cutting edge. The temperature distribution curve along the tool flank is smoother than that along the tool face.

It is seen from Figs. 5.53 - 5.55 that, as expected, the maximum temperatures as well as the temperatures all over the rake face and flank face increase with an increase in cutting speed. For instance, T_{max} is increased from 512°C to 1072°C (Fig. 5.55(a)) as the cutting speed is increased from 35.3 m/min to 130.7 m/min. Similarly, an increase in feed t_1 raises the temperatures all over the tool surfaces (Figs. 5.56 - 5.57).

An interesting fact emerged while analysing the effect of rake angle on temperature distributions. With an increase in rake angle, the tool temperatures are first decreased; but after a certain point, with a further increase in α the temperatures are also increased (Figs. 5.58 - 5.59). For example, T_{max} is decreased from 585°C to 458°C and is, then, increased back to 532°C as α is first increased from 20° to 30° and is, then, further increased to 41°. This can be attributed to a smaller included angle (between the tool flank and tool face) associated with increased α which contributes to two opposing factors:

(i) The total energy input to the system and hence the amount of

heat generated within the system is decreased calling for an overall decrease in temperatures and

(ii) The tool-tip area available for heat conduction is decreased promoting the local temperatures to rise.

With an increase in α up to a certain point, the first factor possibly predominates over the second and as a result the temperatures are decreased, but beyond the balancing point the second factor appears to gain larger importance and the temperatures along tool face and tool flank start rising again.

Water was used as a coolant because of its known thermal properties at elevated temperatures for four tests at different speeds - 24.8 m/min. and 46.0 m/min with a HSS tool and 35.3 m/min and 130.7 m/min with carbide tools - for which cutting data were also obtained under dry conditions. The computed temperatures along the tool face and tool flank for these speeds with and without using the coolant are plotted in Figs. 5.60 - 5.63. It can be seen that the temperatures with a coolant, as anticipated, are lower than those without coolant and the difference between the two increases as the curves move away from the tool edge along the tool face or along the tool flank. The maximum temperatures T_{max}, with the use of a coolant, are decreased from 585°C to 540°C and from 708°C to 640°C at cutting speeds of 24.8 m/min. and 46.0 m/min. respectively. The decrease in temperature with the use of a coolant can be attributed to the following factors:

(i) Reduction in the interfacial shear-stress along the chip-tool contact length (73) as reflected by an approximate 4 - 6% decrease in the cutting forces (Table 3.4), and

(ii) Heat losses from the surfaces flooded with coolant.

In order to determine the effect of existing tool flank wear on temperature distribution, two tests with different tools under otherwise

similar cutting conditions were performed. In one test, a freshly ground tool with no flank wear was used, whereas, in the other one, wear land of 0.376 mm in size on the tool flank was introduced before the test was performed. The computed temperatures along the tool face and tool flank for the above tests are shown in Figs. 5.64(a) and 5.64(b). It may be observed that the temperatures on the tool flank and the tool face with the worn tool are lower than those with the freshly ground tool and the maximum temperature on the tool face in the earlier case is 370°C as compared to 431°C with a new tool. This observation is in agreement with the experimental results of Olberts (113) who observed a lower tool-chip interface temperature (decreased by up to 60°C) when the flank wear land was increased from zero to 0.254 mm.

Thus, it appears that the introduction of a limited amount of flank land on a tool helps in bringing the tool temperatures down, although the temperatures in the adjoining workpiece region are increased (Figs. 5.38 & 5.44). This decrease in tool temperatures is due to a large conduction of heat away from the tool flank by the rubbing workpiece shoulder, even though an extra amount of small frictional heat Q_f (in this case, Q_f = 5.85 watts which is only 0.88% of the total heat input) is generated at the tool-work interface.

It is worthwhile to mention here that, for the present investigations, the actual flank wear was simulated with an artificial or ground flank land. The degree of similarity between the ground land and actual wear is approximate. It is obvious that the better surface-finish characteristics of the ground land and the possibility of some misalignment between the workpiece shoulder and the ground flank are likely to reduce the frictional heat Q_f resulting in lower tool temperatures than what should have been. However, the errors thus intro-

duced are not considered to be significant.

The tests were conducted with HSS as well as carbide tools. Typical test results are shown in Table 5.10.

Table 5.10

Tool Materials	Speed * m/min	Cutting force F_v, N	Feed force F_H, N	Maximum Temp. T_{max} °C.
HSS	24.70	3525	1560	585
Carbide	35.33	2540	400	512

* All other cutting conditions were the same.

It is seen that even at slightly higher cutting speed, but under otherwise similar cutting conditions, the temperatures with a carbide tool are lower than those with a HSS tool. This is mainly due to the decreased cutting and feed forces (up to 28% lower cutting force) with a carbide tool. The decrease in forces with a carbide tool can be attributed to the lower interfacial friction between the carbides and this workpiece material as evidenced by the complete absence of a built-up edge and the presence of finer finish on the underside of the chip.

5.5 Comparison of Present Results with Previous Work.

In previous work, the proportion β of the primary zone heat conducted into the workpiece has been related with $R_T \tan\phi$ (20, 27, 36, 106) where the thermal number R_T is given by

$$R_T = \frac{\rho C_p U t_1}{K} \qquad (5.5)$$

where, t_1 = unformed chip thickness (feed)

ρ, C_p and K are the density, specific heat and thermal conductivity of the workpiece material.

U = cutting speed

ϕ = shear angle

In order to find out β, the primary zone heat Q_s was calculated from flow stress and strain-rate distributions (Table 5.8) and the heat carried away by the workpiece Q_w was obtained from the equation

$$Q_w = w\, d_w\, U \left\{ (\rho C_p)_{T_w} T_w - (\rho C_p)_{T_\infty} T_\infty \right\} \qquad (5.6)$$

where, w is the width of the cut,

T_w is taken equal to the mean temperature across a section perpendicular to the direction of motion from the freshly-cut work surface to the lower workpiece boundary of depth d_w,

and T_∞ is the room temperature.

The ratio β is, then, given by $\beta = \frac{Q_w}{Q_s}$ (5.7)

In order to compare the present computed results with the previous work, the calculated values of β (Table 5.11) are plotted in Fig. 5.65 together with experimental values obtained by Nakayama (106) and Boothroyd (20) and theoretical values by Weiner (27) and Tay et al (36). Here, it is seen that the present results agree well with the experimental values. Similar to Boothroyd's experimental results, for a given value of $R_T \tan\phi$, β is found to be increased with an increase in α. Weiner's plane heat source theory is seen to underestimate β.

To compare the computed maximum tool-chip interface temperature T_{max} with the theoretical results of Rapier (32) and the experimental values of Boothroyd (20), the dimensionless ratio T_m/T_f was calculated as follows.

T_m, the maximum rise of temperature in the chip, was found by subtracting the average shear plane temperature T_s (Table 5.7) from the maximum temperature T_{max} (Table 5.9). T_f, the average rise of temperature given to the chip by the frictional heat source was

TABLE 5.11

PROPORTION OF SHEAR ZONE HEAT CONDUCTED INTO THE WORKPIECE, β

Serial No.	Test Identification No.	Speed U	Feed t_1	Rake Angle α	Tool Material	T_w (Eq. 5.6)	d_w (Eq. 5.6)	Q_w (Eq. 5.6)	Shear zone Heat Q_s	$R_T \tan\phi$	β (Q_w/Q_s)
		m/min	mm/rev			°C	mm	watts	watts		
1	1	24.76	0.3556	41.0	HSS	40.2	0.4963	95.95	435.6	8.692	0.2200
2	3	24.78	0.2845	20.0	"	43.6	0.5720	129.41	511.7	5.450	0.2530
3	5	17.34	0.3556	41.0	"	38.6	0.5895	73.61	291.6	6.193	0.2524
4	6	24.68	0.3556	20.0	"	46.6	0.575	146.21	719.2	6.206	0.2033
5	9+	24.77	0.3556	20.0	"	46.9	0.575	148.43	704.2	5.796	0.2108
6	11	45.96	0.3556	20.0	"	47.9	0.452	224.68	1636.5	8.240	0.1373
7	12+	45.77	0.3556	20.0	"	43.8	0.450	189.69	1510.1	8.952	0.126
8	13	24.77	0.3556	30.0	"	41.3	0.624	127.28	658.5	5.386	0.1933
9	25++	17.34	0.3556	41.0	"	38.5	0.5895	73.09	285.8	6.193	0.256
10	14	35.33	0.3556	20.0	Carbide	52.3	0.4492	198.99	1061.4	7.972	0.1875
11	15	71.11	0.3556	20.0	"	42.5	0.3267	202.12	2296.7	14.340	0.0880
12	17	35.24	0.2845	20.0	"	49.8	0.451	183.50	843.4	5.905	0.2176
13	18	35.28	0.5690	20.0	"	48.9	0.452	178.64	1528.9	13.940	0.1170
14	19	35.15	0.3556	10.0	"	53.2	0.5486	249.05	1279.1	7.642	0.1947
15	21+	35.26	0.3556	20.0	"	50.5	0.4370	182.51	1060.4	7.668	0.1720
16	23	130.73	0.3556	20.0	"	46.3	0.3248	432.99	4616.4	24.100	0.0938
17	24+	131.38	0.3556	20.0	"	40.5	0.3276	341.09	4172.9	27.940	0.0820

\+ TESTS PERFORMED WITH COOLANT.

++ TOOL WITH INITIAL FLANK WEAR (0.376 mm)

calculated from

$$T_f = T_c - T_s \qquad (5.8)$$

where T_c = average temperature of chip across a section perpendicular to the direction of chip velocity V_c at the point of chip separation.

Rapier, based on plane frictional heat source theory, expressed the ratio T_m/T_f as a function of R_T/α_T given by

$$T_m/T_f = 1.13 \cdot \sqrt{R_T/\alpha_T} \qquad (5.9)$$

where, the thermal number $R_T = \dfrac{\rho C_p V_c t_2}{K}$,

$\alpha_T t_2$ = length of heat source (tool-chip contact length)

and t_2 = chip thickness.

The computed values of T_m/T_f (Table 5.12) are compared with Rapier's Eq. (5.9) and the experimental values of Boothroyd in Fig. 5.66. The theoretical values of Rapier are shown here to have overestimated the actual temperatures. Boothroyd's experimental results show a large scatter. It is found that Boothroyd's tests were performed at high values of chip thickness which essentially give low values of α_T (say, 0.5 to 1.0) resulting in correspondingly high values of R_T/α_T. For the present investigations, α_T ranges from 1.0 to 4.0 (Table 5.12) and for most of the tests performed with lower feeds, α_T is greater than 2.0. In addition, Boothroyd used hot machining conditions. It is seen that the present computed results are in agreement with some of Boothroyd's experimental values.

5.6 Comparison between the Measured and Computed Temperatures.

It is felt that the experimental techniques of temperature - measurement have not, in general, reached a stage of development to

TABLE 5.12

MAXIMUM AND MEAN RISE OF TEMPERATURE IN CHIP

Serial No.	Cutting Conditions: Test Identification No.	Speed U	Feed t_1	Rake Angle α	Tool Material	Quantities of Eq. (5.9): $T_m = T_{max} - T^s$	T_f	T_m / T_f	R_T	$\alpha_T = C_1/t_2$	R_T/α_T
		m/min	mm/rev	°		°C	°C				
1	1	24.76	0.3556	41.0	HSS	434.3	167.97	2.586	13.59	2.048	6.635
2	3	24.78	0.2845	20.0	"	350.1	203.35	1.722	10.88	3.827	2.840
3	5	17.34	0.3556	41.0	"	341.8	161.05	2.122	9.52	1.962	4.850
4	6	24.68	0.3556	20.0	"	432.7	205.78	2.103	13.55	3.696	3.660
5	9+	24.77	0.3556	20.0	"	379.5	173.83	2.183	13.60	2.868	4.740
6	11	45.96	0.3556	20.0	"	538.5	187.83	2.867	25.24	2.629	9.600
7	12+	45.77	0.3556	20.0	"	470.5	177.17	2.656	25.13	2.916	8.620
8	13	24.77	0.3556	30.0	"	323.9	148.40	2.183	13.60	2.053	6.620
9	25++	17.34	0.3556	41.0	"	284.8	134.55	2.117	9.52	1.962	4.850
10	14	35.33	0.3556	20.0	Carbide	357.2	111.78	3.195	11.30	1.096	10.310
11	15	71.11	0.3556	20.0	"	541.5	152.70	3.547	22.74	1.414	16.080
12	17	35.24	0.2845	20.0	"	290.1	103.23	2.810	9.02	1.222	7.377
13	18	35.28	0.5690	20.0	"	530.4	121.96	4.349	18.05	0.945	19.100
14	19	35.15	0.3556	10.0	"	538.1	169.62	3.174	11.24	2.098	5.356
15	21+	35.26	0.3556	20.0	"	333.1	103.72	3.211	11.28	0.927	12.160
16	23	130.73	0.3556	20.0	"	864.4	161.40	5.355	41.80	1.398	29.892
17	24+	131.38	0.3556	20.0	"	879.0	181.87	4.833	42.01	1.620	25.940

\+ TESTS PERFORMED WITH COOLANT.

++ TOOL WITH INITIAL FLANK WEAR (0.376 mm)

provide a check on the temperature distributions described above (1, 36). However, some nodal temperatures were measured experimentally using the technique of single point temperature measurement by attaching standard thermocouple wires. It may be mentioned here that even this method which is most commonly used, is associated with many problems. These include the interference to heat flow caused by the attached thermocouples, inaccuracies in proper and point location of the thermocouples, snapping off the thermocouples by the rubbing chip and the workpiece shoulder and response time of thermocouples. Besides, in order to ensure the steady state conditions at the locations far away from the sources of heat generation, it is necessary to continue the machining operation for a longer duration.

Keeping in view the above limitations, the experimental measurement of some nodal temperatures was confined to two tests only conducted at the lowest speeds using high speed steel tools of 6.35 mm width. The experimental method has been described earlier in Chapter III. The experimental and computed temperatures for three nodes in each case are listed in Table 5.13. Good agreement is obtained between the computed and experimental temperatures, of course, the experimental results are very limited.

5.7 Influence of Input Data on the Accuracy of Computed Temperatures.

For a prediction of the complete temperature distribution in the workpiece, tool and chip during orthogonal machining, the input data necessary, apart from the usual cutting conditions and material properties, are: the tool-chip contact length C, the sticking length C_1, tool force readings, the width of the secondary zone, chip-thickness and the distribution of velocity, strain and strain-rate in the primary zone. Evidently, these input data affect, to a large extent, the accuracy of computed temperatures.

For the present investigations, it was possible to obtain the values of tool-chip contact length C and the sticking length C_1 accurately from a scar on the high speed steel tools. With carbide tools, it was not possible to measure the value of C_1 accurately because of low interfacial friction and hence, the sticking length was assumed to be equal to half of the contact length (36, 40). None of the tests exhibited any significant presence of built-up edge formation which is likely to alter the values of C and C_1. It may be mentioned here that even a slight error in the values of C and C_1 may introduce some error in tool face temperatures. For example, for the same heat input, an increase in the value of contact length C will decrease the tool face temperatures.

The tool forces control the total energy input to the system in the computer analysis and, therefore, an accurate measurement of the cutting force and feed force is necessary. Good agreement was obtained between the total energy input calculated from the force considerations and the total heat input obtained by summing up the deformation heat in the two zones and the frictional heat. This provided the necessary check on the accuracy of heat input.

The width of the secondary zone, as described earlier, has been measured from flow lines. However, this measurement is approximate and is likely to introduce some, though not significant, errors in the computed temperatures. On the other hand, the chip thickness and the distribution of velocity, strain and strain-rate in the primary zone have been measured accurately.

TABLE 5.13

COMPARISON BETWEEN COMPUTED AND MEASURED TEMPERATURES.

Serial No.	Cutting Conditions					Temperatures on Tool Flank Face				Temperatures on Tool Rake Face			
	Test Identification No.	Speed, U	Feed, t_1	Rake Angle α	Tool Material	Distance from cutting edge	Expt. temp T_E	Computed Temp. T_c	% Variation w.r.t. T_E	Distance from cutting edge	Expt. Temp. T_E	Computed Temp. T_c	% Variation w.r.t. T_E
		m/min	mm/rev			mm	°C	°C		mm	°C	°C	
1	5	17.34	0.3556	41°	HSS	5.0	253.7	266.0	4.85	5.5	253.8	254.0	0.08
						7.2	233.0	242.0	5.15				
2	25+	17.34	0.3556	41°	HSS	5.0	213.0	217.0	1.87	5.5	205.0	209.0	1.45
						7.2	185.0	197.0	6.48				

+ TOOL WITH INITIAL FLANK WEAR (0.376 mm)

CHAPTER VI

CONCLUSIONS AND SUGGESTIONS FOR FURTHER WORK.

6.1 Conclusions.

From the results obtained it is established that the finite element method using the Galerkin approach can be applied successfully to predict the complete temperature distribution in the workpiece, tool and chip during orthogonal machining under a given set of cutting conditions. The type and the size of the elements used and the necessary velocity, strain-rate and flow stress distributions in the deformation zones affect, to a large extent, the overall accuracy of the predicted temperatures.

The results obtained from different elements show that an appreciable improvement in the accuracy can be obtained with the same number of degrees of freedom when higher-order elements are used. Hence, much fewer higher-order elements may be adequate to achieve a certain accuracy. However, with higher-order elements, the computer time necessary to perform the numerical integration can be excessive. Although QUAD12 has yielded the most accurate results, QUAD8 was chosen for the investigations reported herein because it takes relatively less computing time and is nearly as accurate as QUAD12.

The computer programs developed contain the facility to use any one or a combination of linear, quadratic and cubic triangular as well as quadrilateral elements and theoretically, it should be possible to solve numerically any physical problem involving heat or mass transfer or fluid motion by minor modifications into the programs. There are no limits on the size of the finite element system that can be analysed because of the provisions of using backing store as required. In order to reduce the computational time, facilities have been incorporated towards the

full utilisation of the core storage and advantageous consideration of the banded nature of the system matrices. (The computer processing time on CDC 7600 for one set of machining conditions using a mesh consisting of 317 QUAD8 elements with a total of 1062 nodes requiring five iterations is approximately 75 secs.). These aspects demonstrate that the programs are versatile, efficient and general. The main program FETC is also flexible because any new two or three dimensional element can be added quite easily.

The strain and strain-rate distributions in the primary zone obtained experimentally indicate that the maximum values of strain and strain-rate occur along the tool face. It is of interest to note that the shear strain calculated based on shear plane theory does not represent the strain at the central plane but gives an approximate average value of the strain at the chip-end of the shear zone. The average shear strain rates $\dot{\gamma}_m$ calculated from the thickness of the deformation zone d_{cn} underestimates the strain-rate and the interpretation of $\dot{\gamma}_m$ based on d_{cn} needs careful consideration. The average shear strain along the shear plane is shown to decrease with an increase in the rake angle and a decrease in cutting speed. The average shear strain-rate along the shear plane is found to increase with an increase in the cutting speed and an increase in the rake angle as well.

Flow stress in the primary zone considered as a function of strain, strain-rate and temperature does not vary largely because the rise in temperature at the points of large deformations is partly compensated for by a rise in strain-rate there. The average shear flow stress along the shear plane increases marginally when the rake angle α and the cutting speed U increase.

The assumptions made regarding the velocities and strain-rates in the secondary zone are the main sources of error. As more information

becomes available from accurate studies of deformation in this zone, the assumptions may be modified and the accuracy improved. It is believed, however, that the errors arising out of these approximations are not serious and the present results are already sufficiently accurate to be useful for related investigations.

The primary zone temperatures are found to increase progressively from the workpiece-end boundary towards the chip-end boundary with the maximum values along the tool-chip contact length. The average shear plane temperature increases with an increase in cutting speed and a decrease in rake angle. A non-uniform temperature distribution is obtained on the rake face of the cutting tool and the maximum temperature always occurs at some distance from the cutting edge. With an increase in cutting speed, feed and rake angle, the point of maximum temperature tends to move towards the region where the chip separates from the tool.

The overall temperatures increase with increase in speed and feed. With an increase in rake angle α , the tool temperatures are, first, decreased; but after a certain point, with further increase in α the temperatures are also increased. With the use of a coolant, a 5 - 10% decrease in maximum temperature has been obtained. It appears that introduction of a small amount of flank wear land on the tool helps in bringing the tool temperatures down, although the temperatures in the adjoining workpiece region are increased. Under similar cutting conditions, lower temperatures are obtained with a carbide tool than those with a HSS tool.

Good agreement is obtained between the present computed results and the previous work. In addition, satisfactory co-relation with the limited experimental values further substantiates the belief that the finite element procedure described here based on experimentally measured velocity and strain-rate distributions and material flow stress properties

provides a reasonably accurate estimate of temperature distributions.

6.2 Suggestions for Further Work.

In the present study, certain assumptions have been made regarding the velocities and strain-rates in the secondary zone which need to be revised for better accuracy. Hence, more precise information should be obtained from studies of deformation in this region and this should be included in the f.e.m. model for future work.

The computer programs can be used for investigating the relative effectiveness of the cutting fluids with respect to the tool temperatures provided the data on their thermal properties or the heat transfer coefficients can be obtained. The results on the influence of tool flank wear on tool-chip interface temperature are encouraging and should be investigated in greater detail. Actual flank wear, in a number of successively increasing steps, should be used for machining tests as well as for the measurement of frictional force along the work-tool interface.

The programs could also be used to predict temperatures in welding, extrusion and milling processes. To an advantage, the heat transfer phenomenon in welding (111) is governed by a quasi-steady state equation similar to the one used here. The equation governing the extrusion process (112) is also, more or less, similar but the boundary conditions are different and may require minor modification to the software developed. In the case of milling, where an accurate experimental measurement of tool temperatures is nearly a physical impossibility, extensive modification to the software may be necessary in order to cater for the time cycle and the variable chip thickness.

Further investigations may be also carried out to study the effect of tool thermal properties and even tool design on temperatures using

the analysis procedure given here. It is hoped that the temperature distributions presented herein will be extended to a study of surface integrity problems; and will be related to tool wear, deformation and a workpiece material's flow stress properties.

REFERENCES

1. Barrow, G., 'A Review of Experimental and Theoretical Techniques for Assessing Cutting Temperatures', Annals of the CIRP V22/2, 1973, pp. 203 - 211.

2. Yellowley, I. and Barrow, G., 'The Stress-temperature method of assessing Tool-life'. Proceedings of the 14th International MTDR Conference, 1974, pp. 733 - 740.

3. Opitz, H., Gappisch, M., Koenig, W., Pape, R. and Wicher, R., 'Einfluss Oxydischer Einschlusse auf die Bearbeitbarkeit von Stahl CK45 mit Hartmetall - Drehwerkzeugen', Archiv fur das Eisenhuttenwesen V. 33, 1962, p. 841.

4. Kardos, A., 'Relation of Cutting Temperature to Toollife in Turning of Aluminium Alloy', Acta Technica, V. 34, 1960, p.71.

5. Nakayama, K., 'Studies of the Mechanism of Metal Cutting', Bulletin of the Faculty of Engineering, Yokohama National University, V. 7, March, 1958, P. 1.

6. Stevenson, M.G. and Oxley, P.L.B., 'An experimental investigation of the influence of strain-rate and temperature on the flow stress properties of a low carbon steel using a machining test', Proceedings of the Institute of Mechanical Engineers, V. 185, 1970 - 71, pp 741 - 54.

7. Henkin, A. and Datsko, J., 'The Influence of Physical Properties on Machinability', Journal of Engineering for Industry, Trans. ASME, Series B, V. 85, 1963, pp. 321 - 327.

8. Lenz, E., 'Temperatures in Metal Cutting,' Proceedings of the

International Conference on Manufacturing Technology, University of Michigan, Sept. 1967, pp. 553 - 567.

9. Gottwein, K., 'Die Messung der Schneidentemperatur beim Abdrehen von Flusseisen,' Maschinenbau, V.4, 1925, p. 1129.

10. Shore, H., 'Thermoelectric Measurement of Cutting Tool Temperature,' Journal of the Washington Academy of Sciences, V. 5, 1925, p. 85.

11. Herbert, E.G., 'The Measurement of Cutting Temperatures,' Proceedings of the Institution of Mechanical Engineers, V. 1, 1926, p. 289.

12. Shaw, M.C., Cook, N.H., and Smith, P.A., 'Report on the Cooling Characteristics of Cutting Fluid,' ASTME Research Report No. 19, 1958.

13. Holland, M.B., and Eglund, J.E., 'Thermocouple - Technique Investigation of Temperature Distribution in the Workpiece during Metal Cutting,' ASTME Research Report No. 7, 1957.

14. Reichenbach, G. S.. 'Experimental Measurement of Metal Cutting Temperature Distributions,' Transactions of the ASME, V. 80, 1958, p. 525.

15. Kusters, K.J., 'Temperaturen im Schneidkeil Spanender Werkzeuge', Industrie - Anzeiger, V. 89, 1956, p. 1337.

16. Qureshi, A.H. and Koenigsberger, F., 'An Investigation into the Problem of Measuring the Temperature Distribution on the Rake Face of a Cutting Tool', Annals of the C.I.R.P., V.14, 1966, pp. 189 - 199.

17. Lenz., E., 'Die Temperaturen in der Kontaztzone Span-Werkzeug beim Drehvorgang,' Annals of CIRP, V. 13, 1966, p. 201.

18. Lenz, E., 'Die Temperaturverteilung in der Kontaktzone Span -Werkzeug

beim Drehen von Stahl mit Hartmetall-Werkzeugen', Annals of CIRP, V. 14, 1967, pp. 137 - 44.

19. Prins, O.D., 'The Influence of Wear on the Temperature Distribution at the Rake Face', Annals of CIRP, V. 19, 1971, pp. 579 - 84.

20. Boothroyd, G., 'Temperatures in Orthogonal Metal Cutting', Proceedings of the Institution of Mechanical Engineers, V. 177, 1963, pp. 789 - 802.

21. Trigger, K.J. and Chao, B.T., 'An Analytical Evaluation of Metal - Cutting Temperatures', Trans. ASME, V. 73, 1951, pp. 57-68.

22. Chao, B.T., and Trigger, K.J., 'Temperature Distribution at the Tool-Chip Interface in Metal Cutting', Trans. ASME , V. 77, 1955, pp. 1107 - 1119.

23. Chao, B.T., and Trigger, K.J., 'Temperature Distribution at Tool-Chip and Tool-Work Interface in Metal Cutting', Trans. ASME, 1956, Paper No. 56-A-87.

24. Hahn, R.S., 'On the Temperature Developed at the Shear Plane in the Metal-Cutting Process', Proceedings of the First U.S. National Congress of Applied Mechanics, 1951, pp. 661 - 666.

25. Leone, W.C., 'Distribution of Shear-zone Heat in Metal Cutting', Trans. ASME, V. 76, 1954, pp. 121 - 125.

26. Loewen, E.G. and Shaw, M.C., 'On the Analysis of Cutting - Tool Temperatures', Trans. ASME, V. 76, 1954, pp. 217 - 231.

27. Weiner, J.H., 'Shear-plane Temperature Distribution in Orthogonal Cutting', Trans. ASME, V.77, 1955, pp. 1331 - 1341.

28. Rall, D.L. and Giedt, W.H., 'Heat Transfer to, and Temperature Distribution in, a Metal - Cutting Tool', Trans. ASME, V. 78, 1956, pp. 1507 - 1515.

29. Scrutton, R.F., 'Thermal Analysis of Plastic Flow at the Chip-Tool Interface in Metal Cutting', Journal of Engineering for Industry, Trans. ASME, V.89, Series B, 1967.

30. Scrutton, R.F., 'Temperatures in the Shear Zone in Metal Cutting', Trans. ASME, 1967, Paper No. 67-WA/PROD -23.

31. Vieregge, G., 'Die Energieverteilung und die Temperatur bei der Zerspanung', Werkstatt und Betrieb, V. 86, 1953, p. 691.

32. Rapier, A.C., 'A Theoretical Investigation of the Temperature Distribution in Orthogonal Cutting Process', British Journal of Applied Physics, V. 4, 1954, pp. 400 - 405.

33. Dutt, R.P. and Brewer, R.C., 'On the Theoretical Determination of the Temperature Field in Orthogonal Machining', International Journal of Production Research, V. 4, No. 2, 1965, pp. 91 - 114.

34. Altan, T., Ostafiev, V. and Kobayashi, S., 'Numerical Calculation of the Temperature Distribution in Orthogonal Metal Cutting', Trans. ASME, 1967, Paper No. 67-PROD-17.

35. Mansour, N.M. et al., 'Temperature Field and Crater Wear in Metal Cutting using a Quasi-finite Element Approach', International Journal of Production Research, V. 11. No. 1, 1973, pp. 59 - 68.

36. Tay, A.O., Stevenson, M.G. and Davis, G.V., 'Using the Finite Element Method to Determine Temperature Distributions in Orthogonal Machining', Proceedings of the Institution of Mechanical Engineers, V. 188, 1974, pp. 627 - 638.

37. Shafto, G.R., Howes, T.D., and Andrew, C., 'Thermal Aspects of Creep Feed Grinding', Proceedings of the 16th International Machine Tool Design and Research Conference held at Manchester, 1975.

38. Yalamanchili, R.V.S. and Chu, S.C., 'Stability and Oscillation Characteristics of Finite Element, Finite Difference, and Weighted Residuals Methods for Transient Two-dimensional Heat Conduction in Solids', Trans. ASME, Journal of Heat Transfer, May, 1973, p.235.

39. Zienkiewicz, O.C., 'The Finite Element Method in Engineering Science', McGraw - Hill, London, 1971.

40. Zorev, N.N., 'Inter-relationship of Processes in Chip Formation Zone and Tool-chip Interface', Russian Engineering Journal, V. 43, n. 12, December 1963, p. 28.

41. British Iron and Steel Institute, 'Physical Constants of Some Commercial Steels at Elevated Temperatures', 1953, Butterworths Scientific Publications, London.

42. Woolman, J. and Mottram, R.A., 'The Mechanical and Physical Properties of the British Standard EN Steels', Vol. 2, BASRA, 1966.

43. Metals Handbook, 'Properties and Selection of Metals', ASME, Vol. 1, 1961.

44. Smithells, C.J. and Brandes, E.A., 'Metals Reference Book', Fifth Edition, Butterworth & Co. Ltd., London, 1976.

45. CARBOLOY Grades/Properties Handbook, 'Cemented Carbide', Metallurgical Products Dept., General Electric Company, Detroit, 1967.

46. Zienkiewicz, O.C. and Cheung, Y.K., 'Finite Elements in the Solution

of Field Problems', The Engineer, Vol. 220, pp. 507 - 510, 1965.

47. Visser, W., 'A Finite Element Method for the Determination of Non-stationary Temperature Distribution and Thermal Deformations', Proc. Conf. on Matrix Meth. Struct. Mech., Air Force Inst. of Techn., Wright-Patterson Air Force Base, Ohio, pp. 925 - 944, 1965.

48. Wilson, E.L. and Nickell, R.E., 'Application of the Finite Element Method to Heat Conduction Analysis', Nucl. Eng. Design, Vol. 4, pp. 276 - 286, 1966.

49. Zienkiewicz, O.C., Bahrani, A.K. and Arlett, P.L., 'Solution of three-dimensional problems by the finite element method', The Engineer, Vol. 224, pp. 547 - 550, 1967.

50. Zienkiewicz, O.C. and Parekh, C.J., 'Transient Field Problems: Two-dimensional and three-dimensional analysis by Iso-parametric finite elements', Int. J. Num. Meth. Eng., Vol. 2, pp. 61 - 71, 1970.

51. Zlamal, M., 'On some Finite Element Procedures for Solving Second-order Boundary Value Problems', Num. Math., Vol. 14, pp. 42 - 48, 1969.

52. Crandall, S., Engineering Analysis, McGraw-Hill, New York, 1956.

53. Szabo, P.A. and Lee, G.C., 'Derivation of the stiffness matrix for plates by Galerkin method', International J. Num. Meth. in Engng., Vol. 1, 1969.

54. Finlayson, B.A., The Method of Weighted Residuals and Variational Principles, Academic Press, London 1972.

55. Cowley, A. and Hinduja, S., 'The Finite Element Method for Machine

Tool Structural Analysis,' Annals of the CIRP, Vol. XVIV, pp. 171 - 181, 1971.

56. Hinduja, S., 'Analysis of Machine Tool Structures by the Finite Element Method', Ph.D thesis, UMIST, Oct, 1971.

57. Desai, C.S. and Abel, J.F., 'Introduction to the Finite Element Method', Van Nostrand Reinhold Co., New York, 1972.

58. Martin, H.C. and Carey, G.F., 'Introduction to Finite Element Analysis', McGraw-Hill, New York, 1973.

59. Tay, A.O. and Davis, G.D.V., 'Application of the Finite Element Method to Convection Heat Transfer between Parallel Planes'. Int. J. Heat Mass Transfer, V. 14, pp. 1057 - 1069, 1971.

60. Reid, J.K. and Turner, A.B., 'Fortran Subroutines for the Solution of Laplace's equation over a General Region in Two Dimensions', Report no. HL 70/4661, U.K.A.E.A. Research Group, Atomic Energy Research Establishment, Harwell, Sept. 1970.

61. Mote, C.D., JR., 'Unsymmetrical, Transient Heat Conduction, Rotating Disc Applications', ASME transactions, Journal of Engng. for Industry, pp. 181 - 190, Feb, 1970.

62. Pian, T.H.H. and Tong, P., 'Finite Element Methods in Continuum Mechanics', IN 'Advances in Applied Mechanics', Vol. 12, pp. 2 - 58, 1972.

63. Emery, A.F. and Carson, W.W., 'An evaluation of the use of the finite element method in the computation of temperature', transactions of ASME, J. of heat transfer, pp. 136 - 145, May, 1971.

64. Beckett, R.E. and Chu, S.C., 'Finite element method applied to heat conduction in solids with nonlinear boundary conditions', Trans. of ASME, J. of Heat transfer, pp. 126 - 129, Feb, 1973.

++65. Gallagher, R.H., 'Finite Element Lake Circulation and Thermal Analysis', pp. 361 - 369.

++66. Hsu, M.B. and Nickell, R.E., 'Coupled Convective and Conductive Heat Transfer by Finite Element Methods', pp. 427 - 450.

++67. Hood, P. and Taylor, C., 'Navier Stokes equations using Mixed Interpolation', pp. 121 - 132.

68. Emery, A.F., 'The use of singularity programming in finite-difference and finite-element computations of temperature', Trans. ASME, J. of Heat Transfer, pp. 344 - 351, August, 1973.

69. Ralston, A., 'A first course in Numerical Analysis', McGraw Hill, New York, 1965.

70. Irons, B.M., 'Engineering applications of numerical integration in the stiffness method', A.I.A.A. Jnl, Vol. 4, pp. 2035-2037, 1966.

71. Ergatoudis, J., Irons, B.M. and Zienkiewicz, O.C., 'Curved iso-parametric quadrilateral elements for finite element analysis', Int. J. Solids Structures, Vol. 4, pp. 31-42, 1968.

72. Childs, T.H.C., 'A new visio-plasticity technique and a study of curly chip formation', Int. J. Mech. Sci., 1971, Vol. 13, p. 373.

73. Childs, T.H.C., 'Rake face action of cutting lubricants: an analysis of, and experiments on, the machining of iron lubricated by Carbon

++ From the Book 'Finite Element Methods in Flow Problems' by Oden, J.T. et al, UAH Press, Alabama, 1974.

tetrachloride', Proc. Instn. Mech. Engrs., 1972, Vol. 186, pp. 717 - 727.

74. Stevenson, M.G. and Oxley, P.L.B., 'An experimental investigation of the influence of speed and scale on the strain-rate in a zone of intense plastic deformation', Proc. Instn. Mech. Engrs., 1969-70, Vol. 184, Pt. 1, No. 31, pp. 561 - 576.

75. Goriani, V.L. and Kobayashi, S., 'Strain and strain-rate distributions in orthogonal metal cutting', Annals of the CIRP, V.XV, 1967, pp. 425 - 431.

76. Ellis, J., Kirk, R. and Barrow. G., 'The development of a quick-stop device for metal cutting research', Int. J. Mach. Tool Des. Res., Vol. 9, pp. 321 - 339, 1969.

77. Palmer, W.B. and Oxley, P.L.B., 'Mechanics of orthogonal machining', Proc. Instn. Mech Engrs., 1959, V. 173 (24), p. 623.

78. Kececioglu, D., 'Shear strain-rate in metal cutting and its effect on shear flow stress', Trans. Am. Soc. Mech. Engrs., 1958, V. 80, p. 158.

79. Stevenson, M.G. and Oxley, P.L.B., 'High temperature stress-strain properties of a low carbon steel from hot machining tests', Proc. Instn. Mech. Engrs., 1973, Vol. 187, pp. 263 - 272.

80. Lubahn, J.D. and Schenectady, N.Y., 'Derivation of stress, strain, temperature, strain-rate relation for plastic deformation', Trans. of ASME, J. of Appl. Mech., September 1947, p. A-229.

81. Dorn, J.E., Pietrokowsky, P. and Tietz, T.E., Trans. Amer. Inst. Min. Met. Eng., 1950, V. 188, p. 933.

82. Alder, J.F. and Phillips, V.A., 'The effect of strain rate and temperature on the resistance of aluminium, copper, and steel to compression', Journal of the Institute of Metals, 1954 - 55, Vol. 83, p. 80.

83. Spaans, C., 'A treatise on the streamlines and the stress, strain, and strain-rate distributions, and on stability in the primary shear zone in metal cutting', Transactions of the ASME, May 1972, J. of Engg. for Industry, p. 690.

84. Campbell, J.D. and Ferguson, W.G., 'The temperature and strain-rate dependence of the shear strength of mild steel', Phil. Mag., 1970, V. 21, pp. 63 - 82.

85. Manjoine, M.J., 'Influence of rate of strain and temperature on yield stresses of mild steel', Trans. of ASME, Journal of Applied Mechanics, Dec. 1944, pp. A-211 - A-218.

86. Altan, T. and Boulger, F.W., 'Flow stress of metals and its application in metal forming analyses', Trans. ASME, Journal of Engineering for Industry, Nov. 1973, p. 1009.

87. Woodward, R.L. and Brown, R.H., 'Dynamic stress-strain properties of a steel and a brass at strain rates up to 10^4 per second', Proc., Instn. Mech. Engrs. Vol. 189, Applied Mechanics Group, p. 107.

88. Zorev, N.N., 'Metal cutting mechanics', 1966, Pergamon Press, Oxford.

89. Kreith, F., 'Principles of heat transfer', 1973, Intext Educational Publishers, New York.

90. Rohsenow, W. and Hartnett, J.P., 'Handbook of heat transfer', 1973

McGraw-Hill, New York.

91. Engineering Sciences Data, Heat Transfer Subsciences, 1970, Technical Editing and Production Ltd., London.

92. Abhary, K.G., 'Organisation of input data for finite element models', M.Sc Thesis, UMIST, 1973.

93. Scarborough, J.B., 'Numerical Mathematical Analysis', John Hokins Press, London.

94. Veubeke, F.D.B., 'Displacement and equilibrium models in the finite element method', Chapter 9 of stress analysis, ed. O.C. Zienkiewicz and G.S. Holister, J. Wiley & Son, 1965.

95. Argyris, J.H., 'Triangular elements with linearly varying strain for the matrix displacement method', J. Roy. Aero. Soc. Tech. Note, V. 69, pp. 711 - 13, Oct. 1965.

96. Hammer, P.C., Marlowe, O.P. and Stroud, A.H., 'Numerical integration over simplexes and cones', Math. Tables Aids Comp., V. 10, pp. 130 - 137, 1956.

97. Irons, B.M., 'Quadrature rules for brick based finite elements', University of Wales, Swansea.

98. Salamassi, R.N., 'The development of higher-order finite elements', M.Sc Dissertation, UMIST, 1975.

99. Hinduja, S., 'Distributed Loading', Internal, Note, UMIST, 1974.

100. Ostafiev, V.A. and Kobayashi, S., 'Stress, strain and strain rate in metal cutting', Proceedings of the 7th International MTDR Conference, Birmingham, Sept. 1966.

101. Kececioglu, D., 'Shear-zone temperature in metal cutting and its effects on shear-flow stress', Trans. ASME, V. 80, 1958, pp. 541-546.

102. Shaw, M.C. and Finnie, I., 'The shear stress in metal cutting' Trans. ASME, V. 77, 1955, pp. 115 - 125.

103. Kurimoto, T., 'An Investigation on the Action of Cutting Fluids', Ph.D. Thesis to be submitted in May, 1977, UMIST, Manchester, U.K.

104. Trent, E.N. 'Some factors affecting wear on cemented carbide tools', Proc. Inst. Mech. Engrs. London, V. 166, 1952, p. 64.

105. Sun, E.Y.C., 'An investigation into some aspects of the analytical tool-chip interface temperature distribution, tool wear and tool life in machining mild steel,' Ph.D thesis, UMIST, 1955.

106. Nakayama, K., 'Temperature rise of workpiece during metal cutting', Bull. Fac. Engng. Nat. Univ. Yokohama, 1965, V. 5, p.1.

107. Kark, S.K., 'Dynamic analysis of machine tool structures by the finite element method', Ph.D. Thesis, UMIST, Oct. 1974.

108. Ahmad, S., Irons, B.M. and Zienkiewicz, O.C., 'Curved thick shell and membrane elements with particular reference to axi-symmetrical problems', Proc. 2nd. Conf. on Matrix Methods in Structural Mechanics, Wright Patterson AFB, Ohio, November, 1968.

109. Kark, S.K., 'Computer Graphic presentation of machine tool structure', M.Sc. Dissertation, UMIST, 1971.

110. The University of Manchester Regional Computer Centre, 'Ghost Graphical Output System', 1976.

111. Rosenthal, D., "Mathematical theory of heat distribution during welding and cutting", The Welding Journal, May 1941, pp. 220-S - 234-S.

112. Altan, T. and Kobayashi, S., "A numerical method for estimating the temperature distributions in extrusion through conical dies", Proceedings of the ASME Production Engineering Conference, Cleveland, Ohio, May, 1967.

113. Olberts, D.R., "A study of the effects of tool flank wear on tool chip interface temperature", Transactions of the ASME, Journals of Engg. for Industry, May, 1959, pp. 152 - 158.

FIGURES FOR CHAPTER V

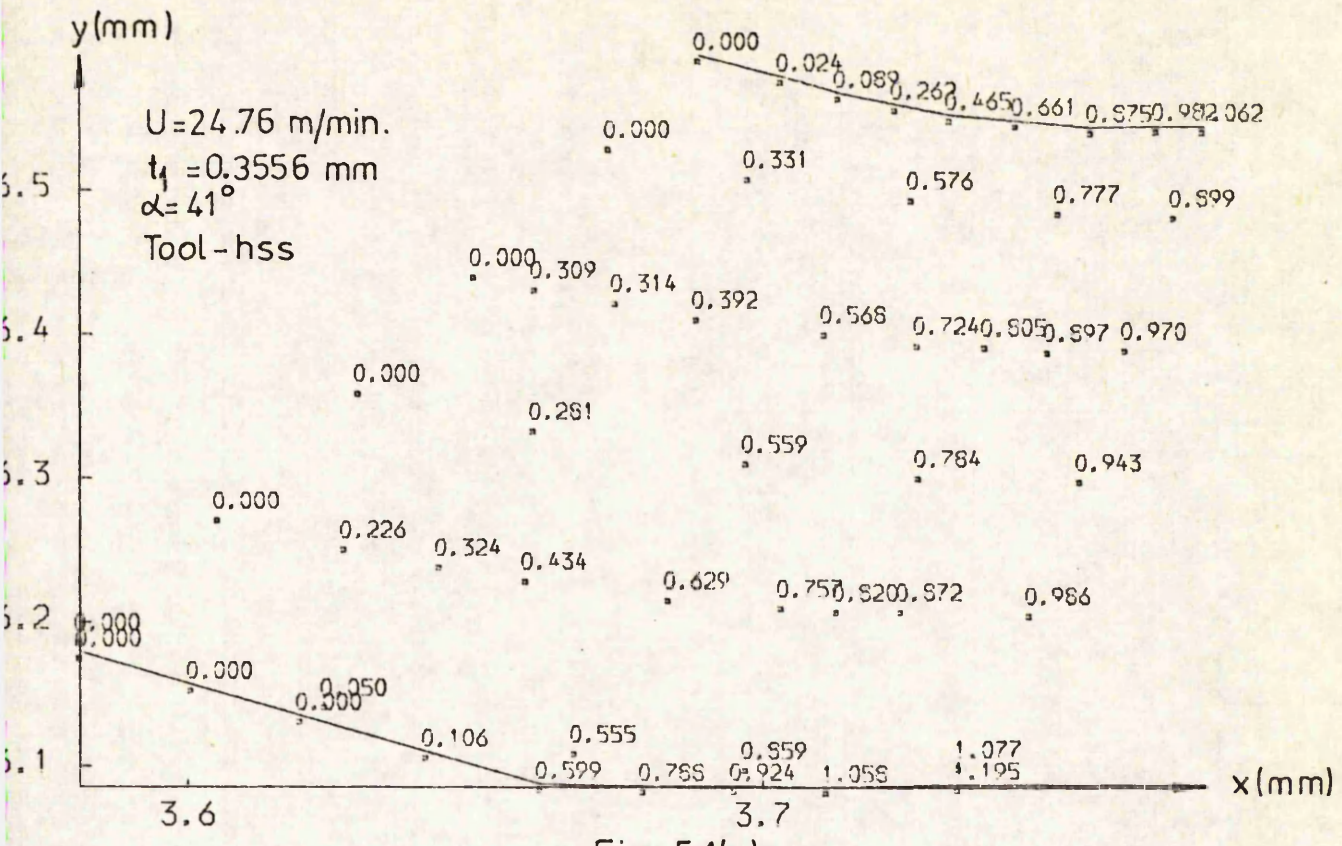

Fig. 5.1(a)

THE DISTRIBUTION OF TOTAL STRAIN
TEST NO. = 1

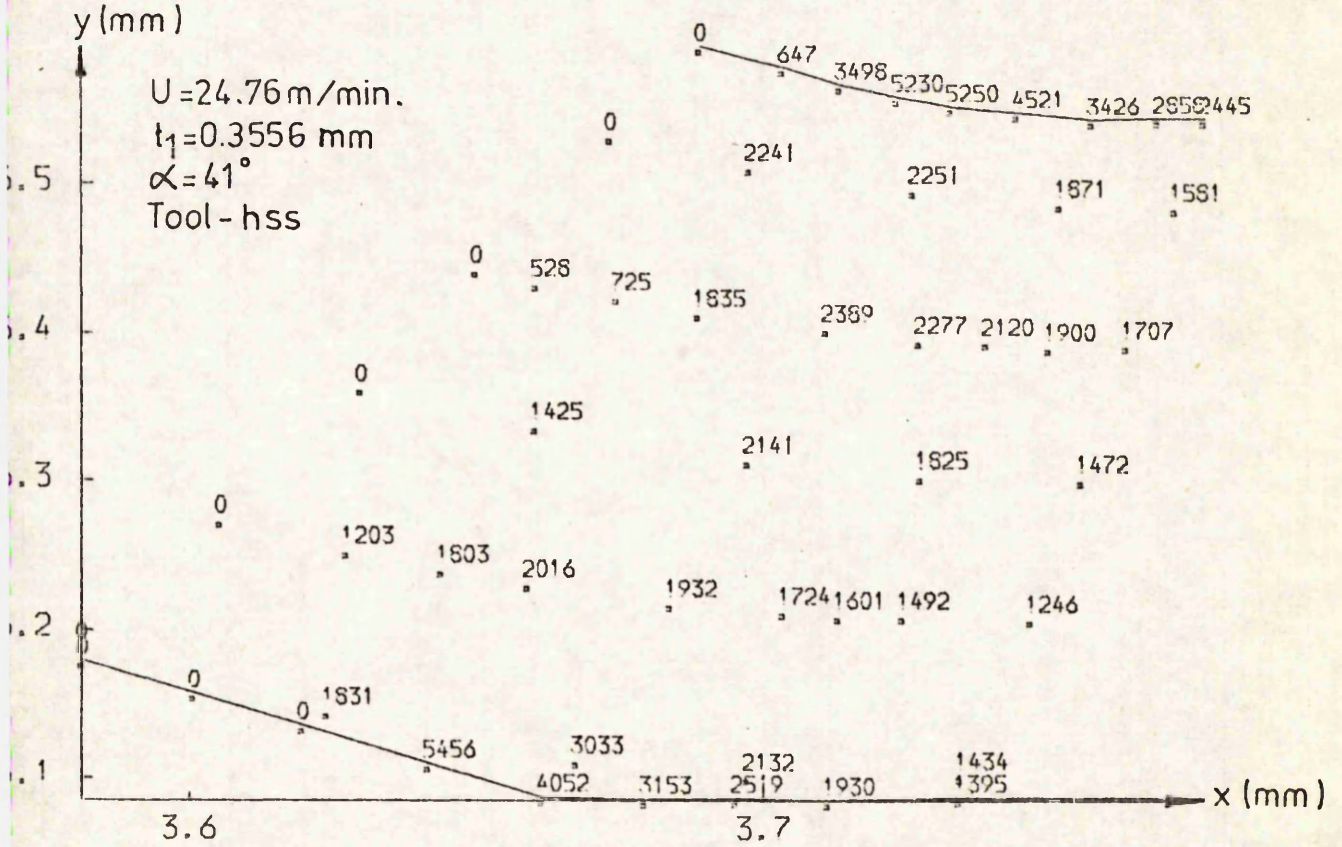

Fig. 5.1(b)

STRAIN-RATE DISTRIBUTION IN DEFORMATION ZONE, (1/SEC)
TEST NO. = 1

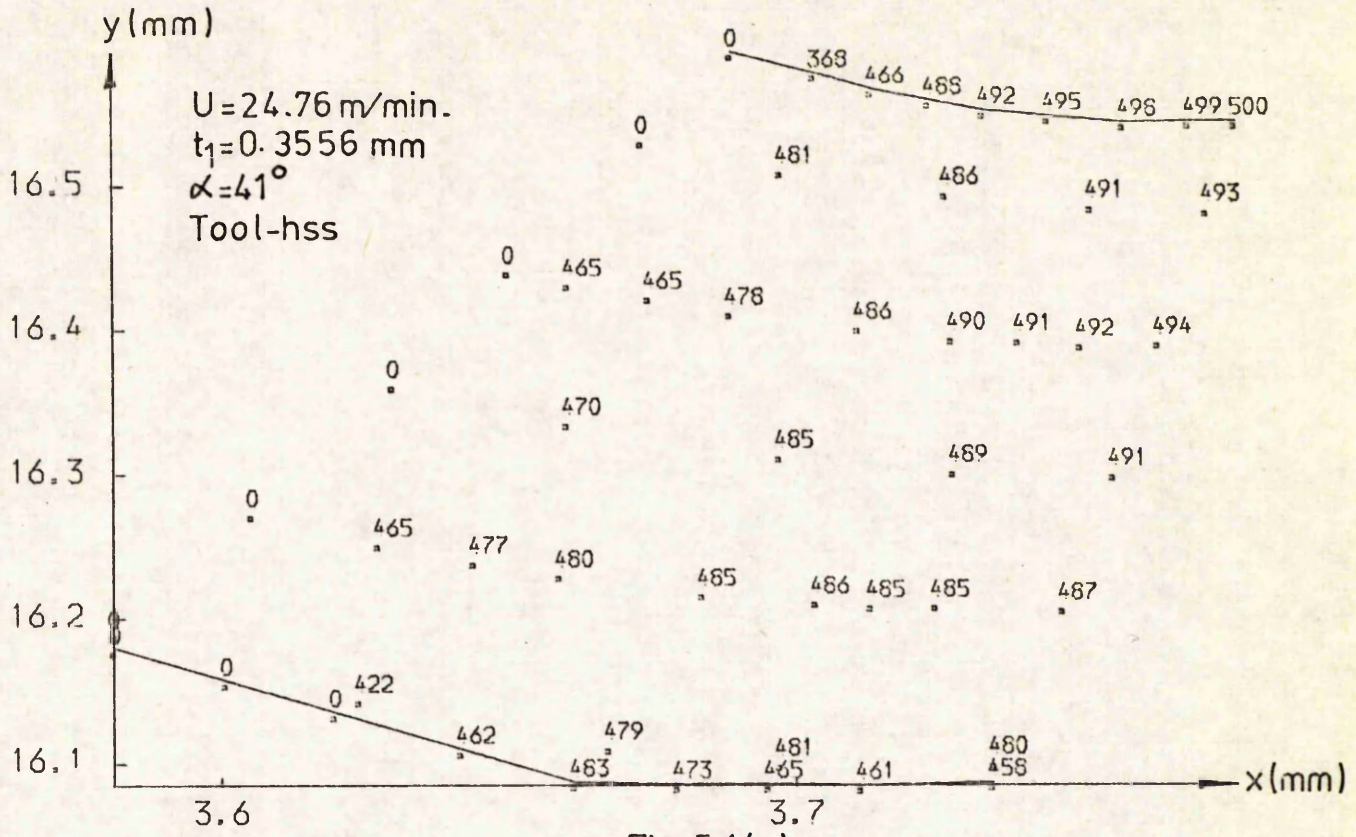

Fig. 5.1(c)

FLOW STRESS DISTRIBUTION (MEGA PASCALS)
TEST NO.= 1

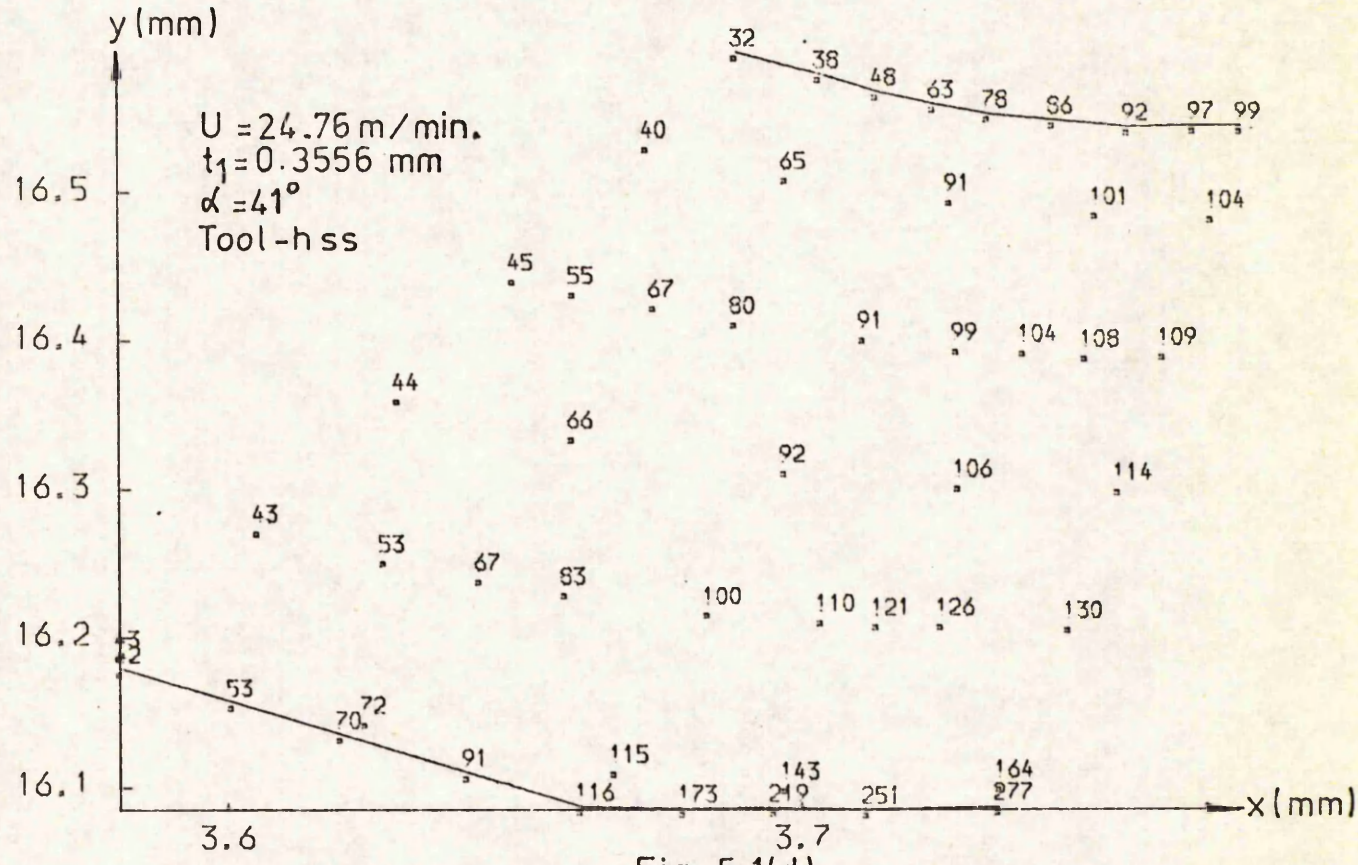

Fig. 5.1(d)

TEMPERATURE DISTRIBUTION IN DEFORMATION ZONE, (O C)
TEST NO.= 1

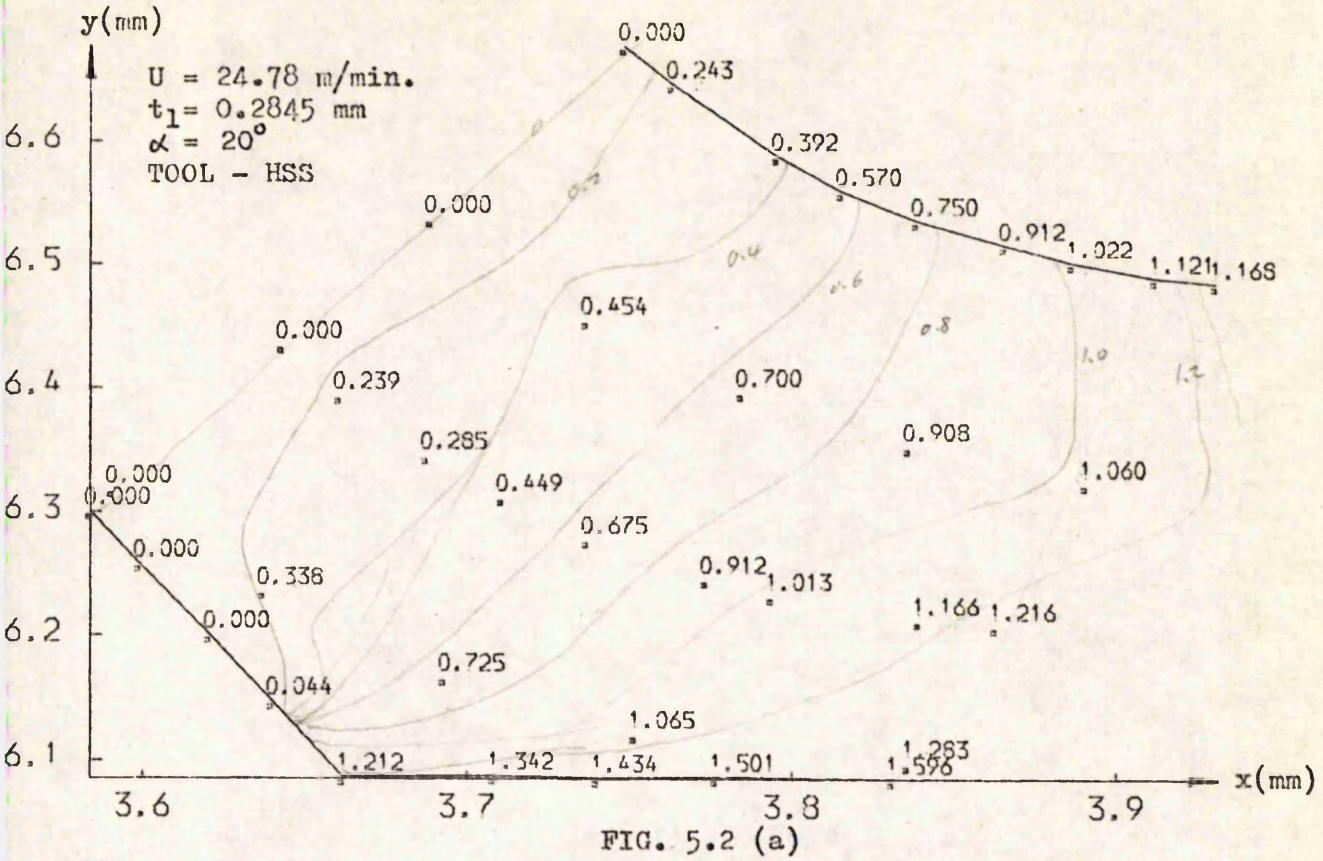

FIG. 5.2 (a)

THE DISTRIBUTION OF TOTAL STRAIN
TEST NO. = 3

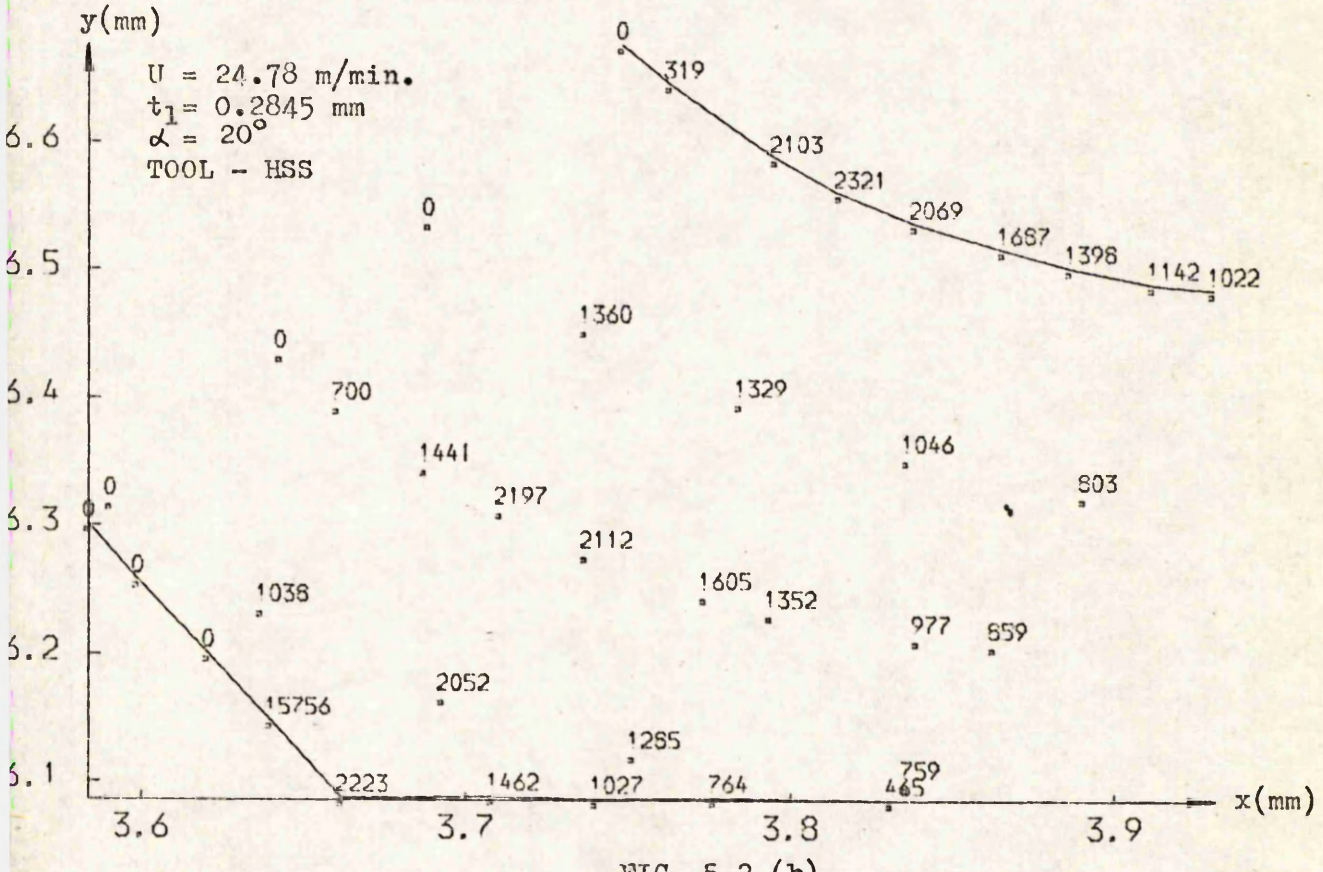

FIG. 5.2 (b)

STRAIN-RATE DISTRIBUTION IN DEFORMATION ZONE, (1/SEC)
TEST NO. = 3

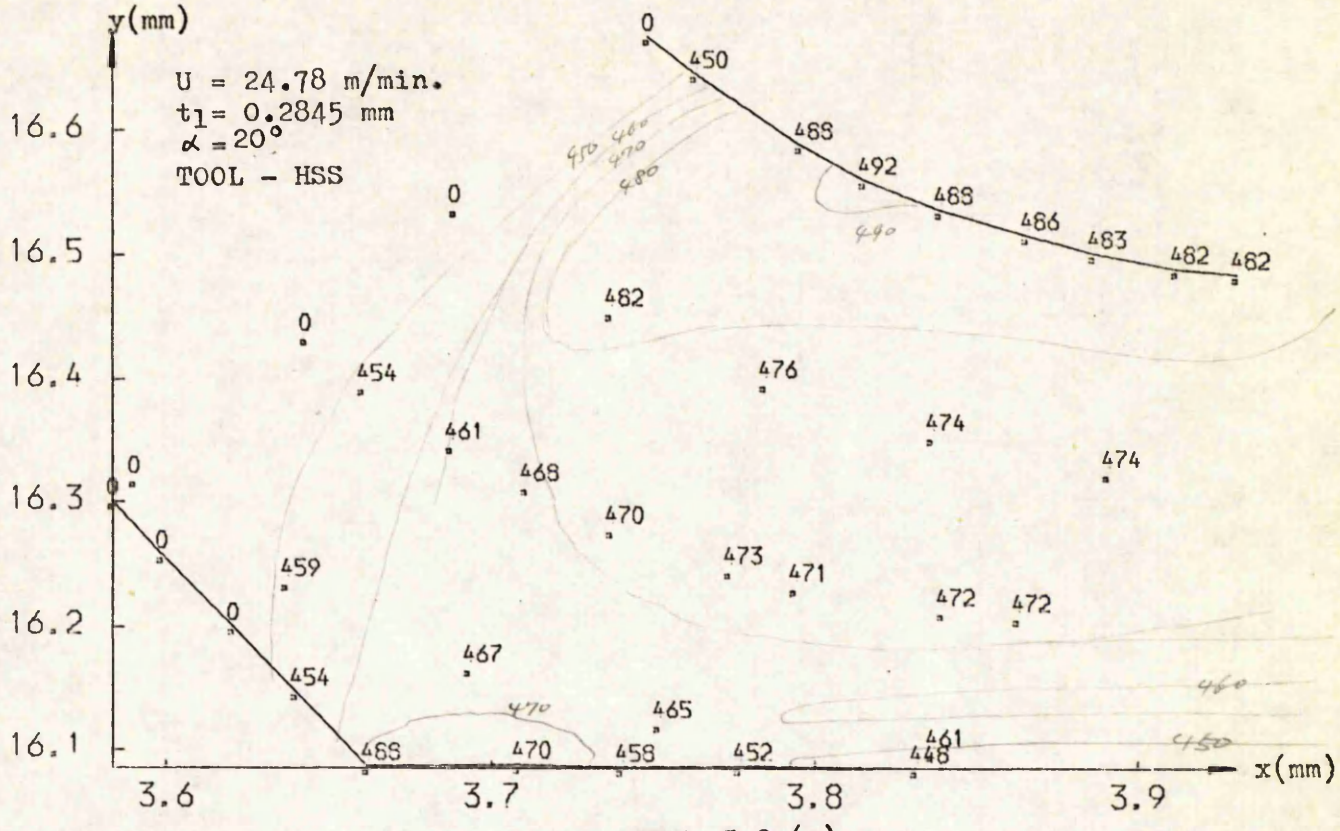

FIG. 5.2 (c)
FLOW STRESS DISTRIBUTION (MEGA PASCALS)
TEST NO. = 3

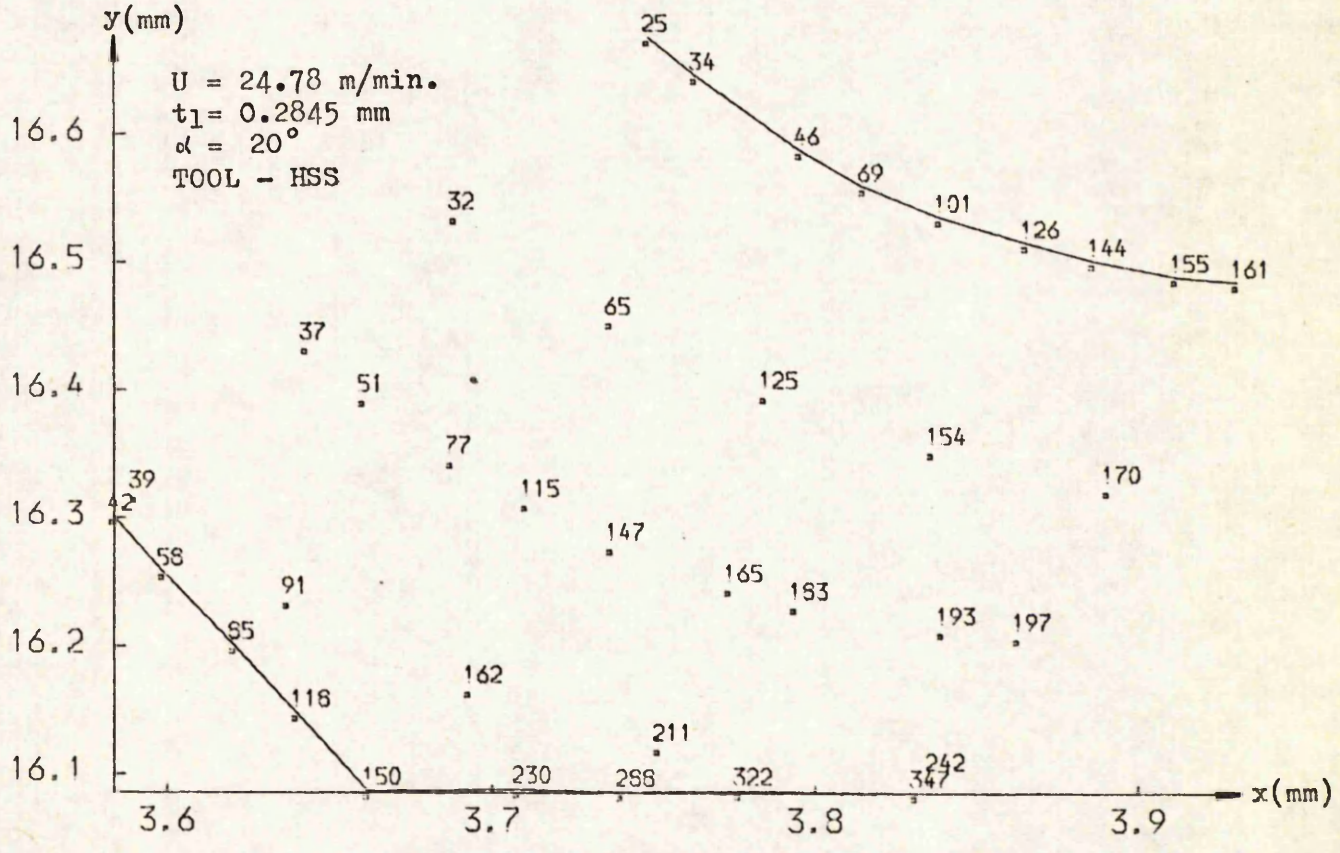

FIG. 5.2 (d)
TEMPERATURE DISTRIBUTION IN DEFORMATION ZONE, (O C)
TEST NO. = 3

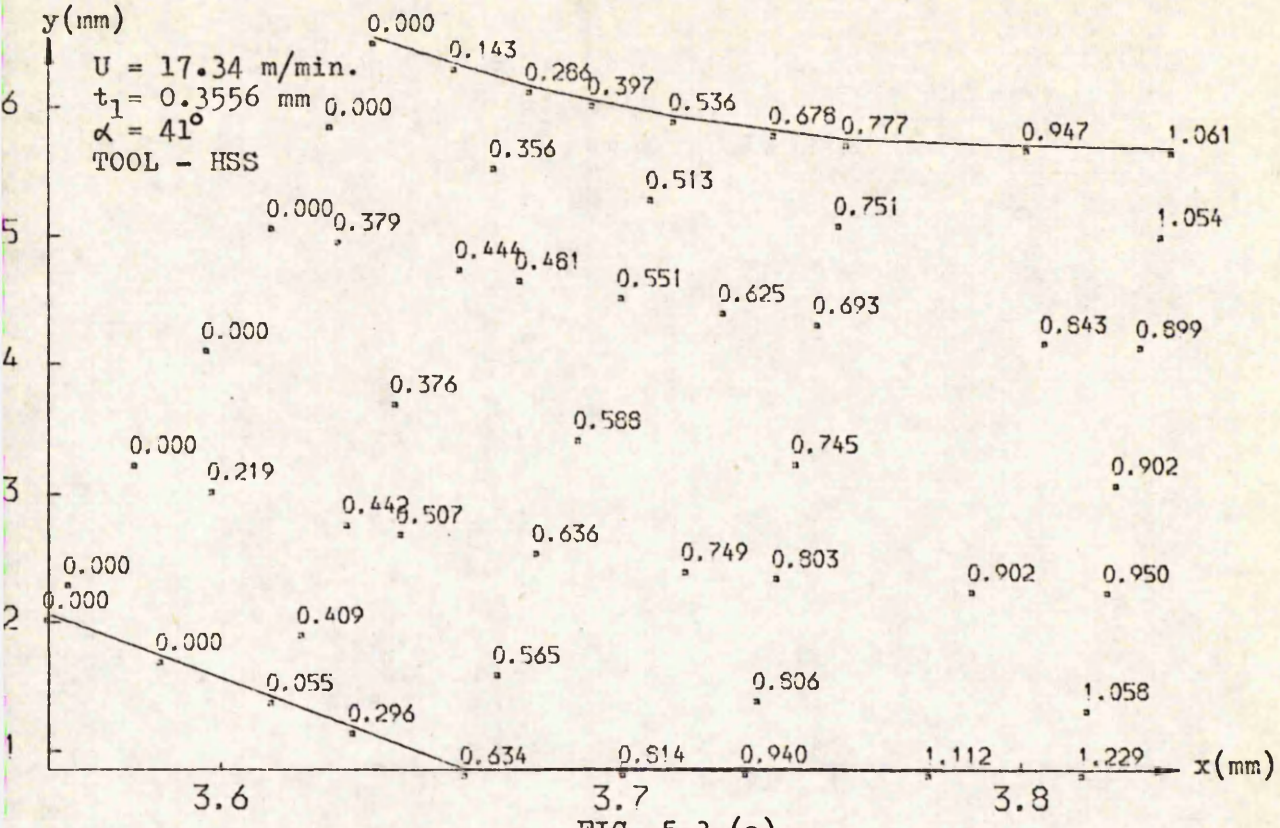

FIG. 5.3 (a)

THE DISTRIBUTION OF TOTAL STRAIN
TEST NO. = 5

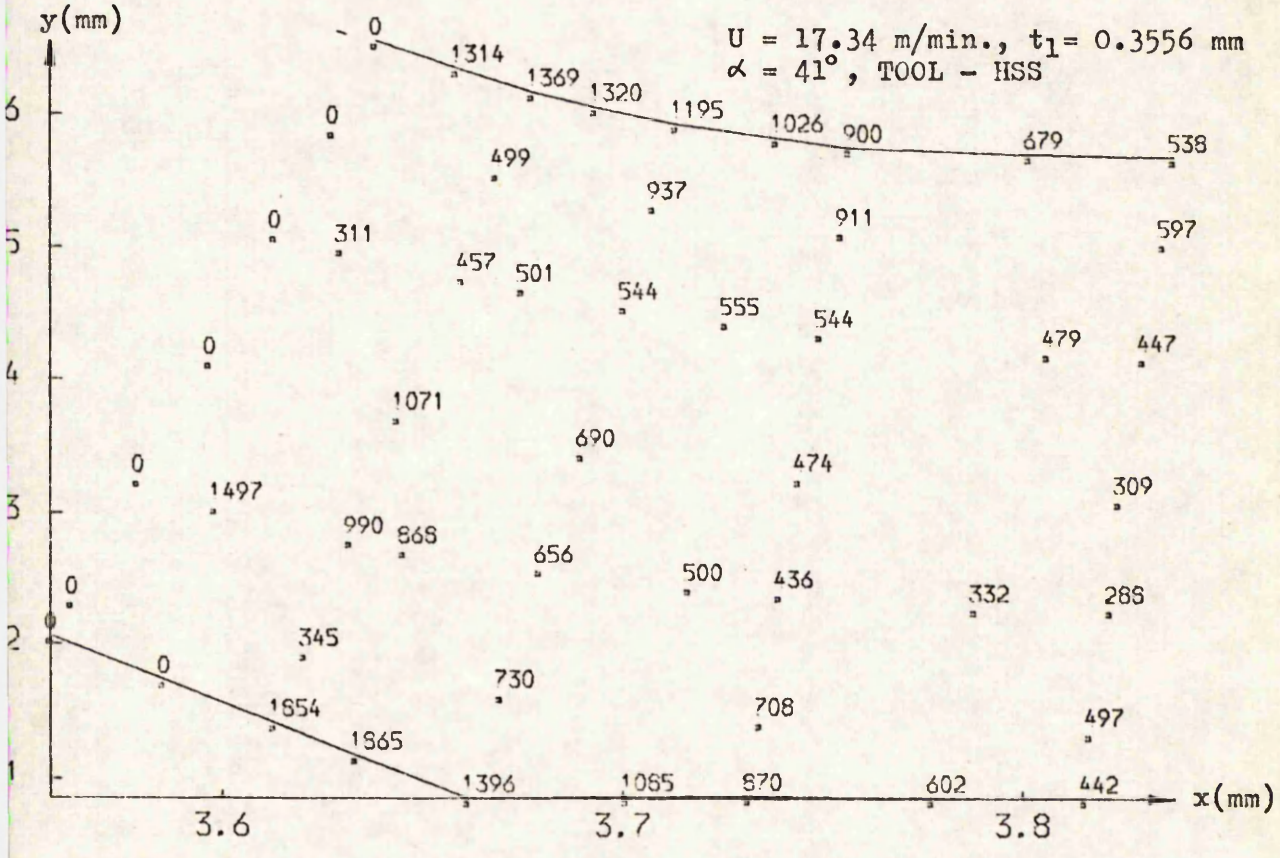

FIG. 5.3 (b)

STRAIN-RATE DISTRIBUTION IN DEFORMATION ZONE, (1/SEC)
TEST NO. = 5

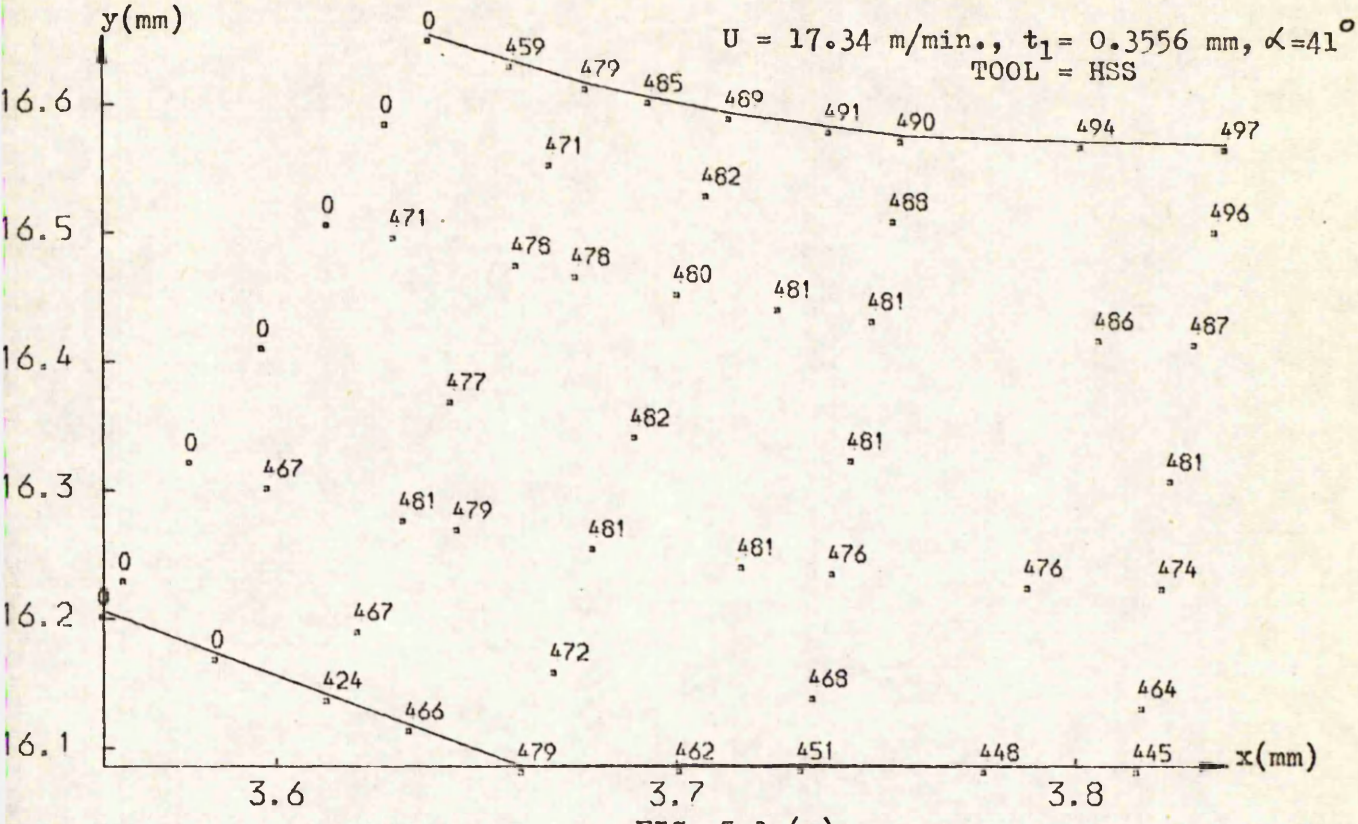

FIG. 5.3 (c)

FLOW STRESS DISTRIBUTION (MEGA PASCALS)
TEST NO. = 5

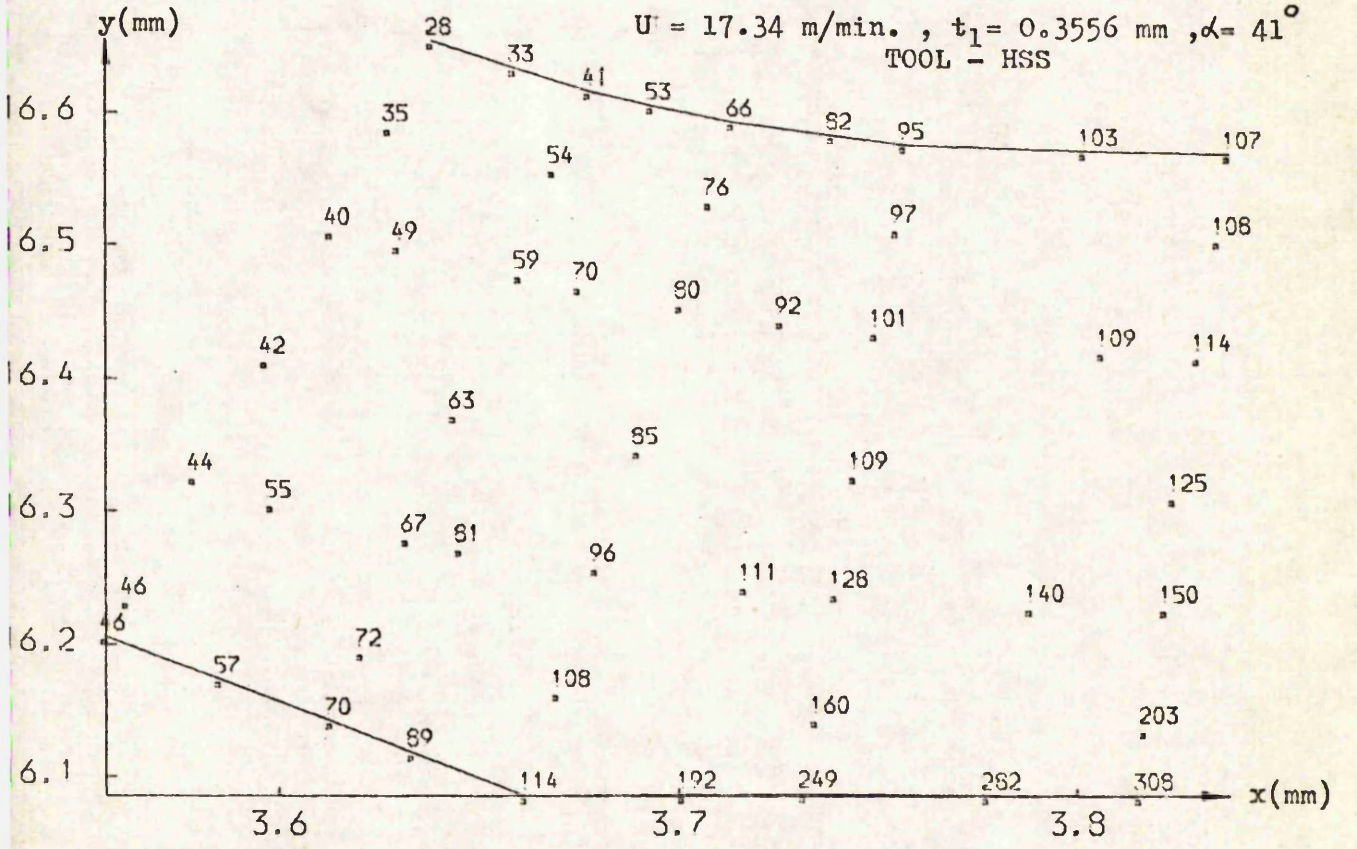

FIG. 5.3 (d)

TEMPERATURE DISTRIBUTION IN DEFORMATION ZONE, (O C)
TEST NO. = 5

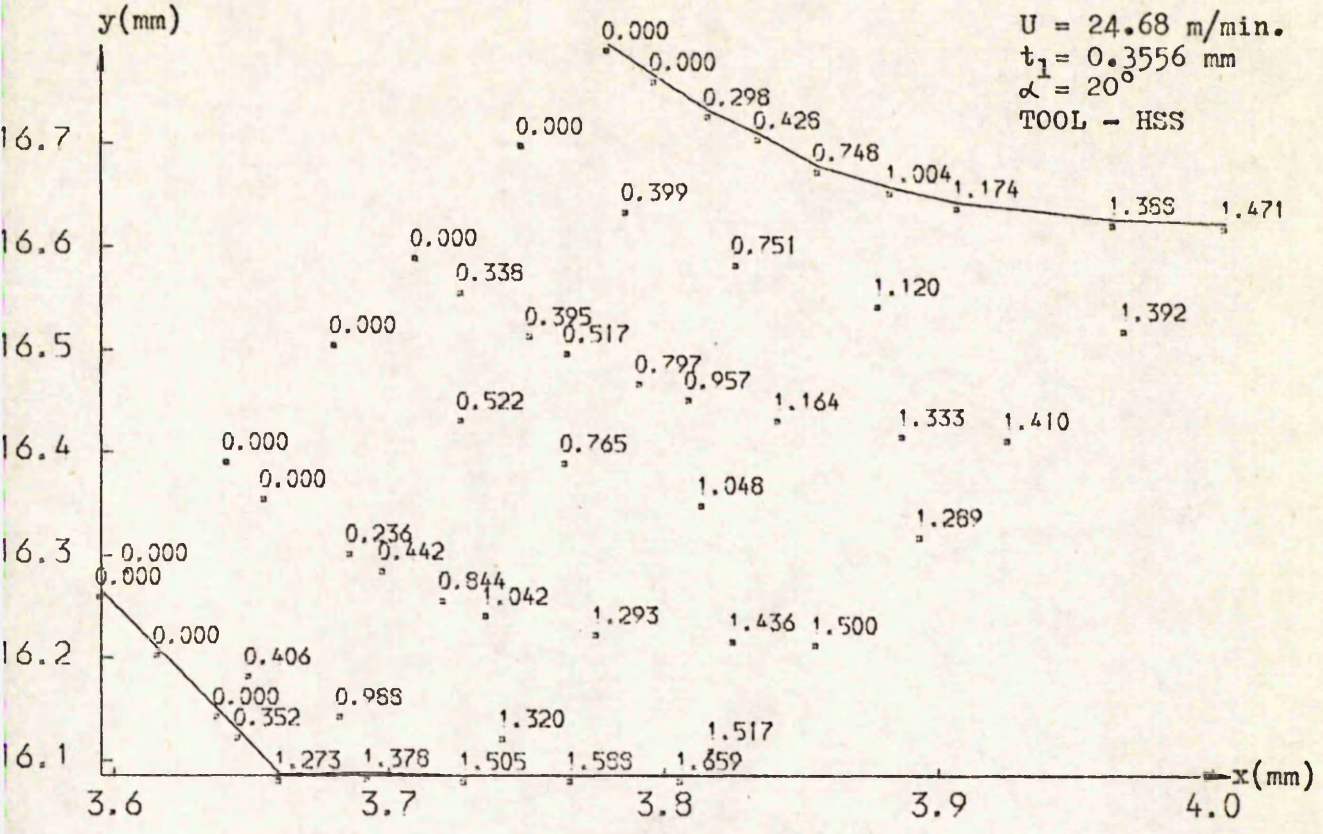

FIG. 5.4 (a)
THE DISTRIBUTION OF TOTAL STRAIN
TEST NO. = 6

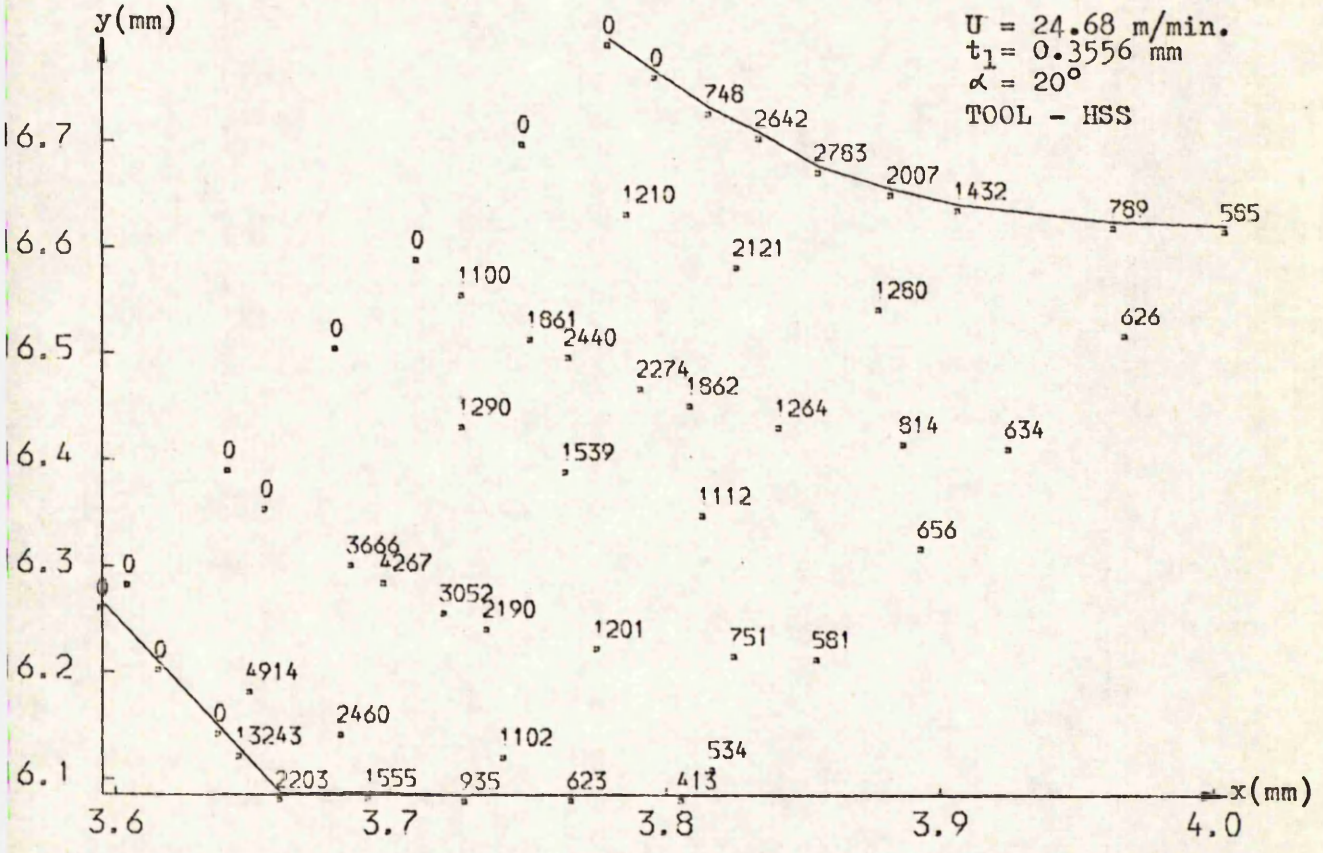

FIG. 5.4 (b)
STRAIN-RATE DISTRIBUTION IN DEFORMATION ZONE, (1/SEC)
TEST NO. = 6

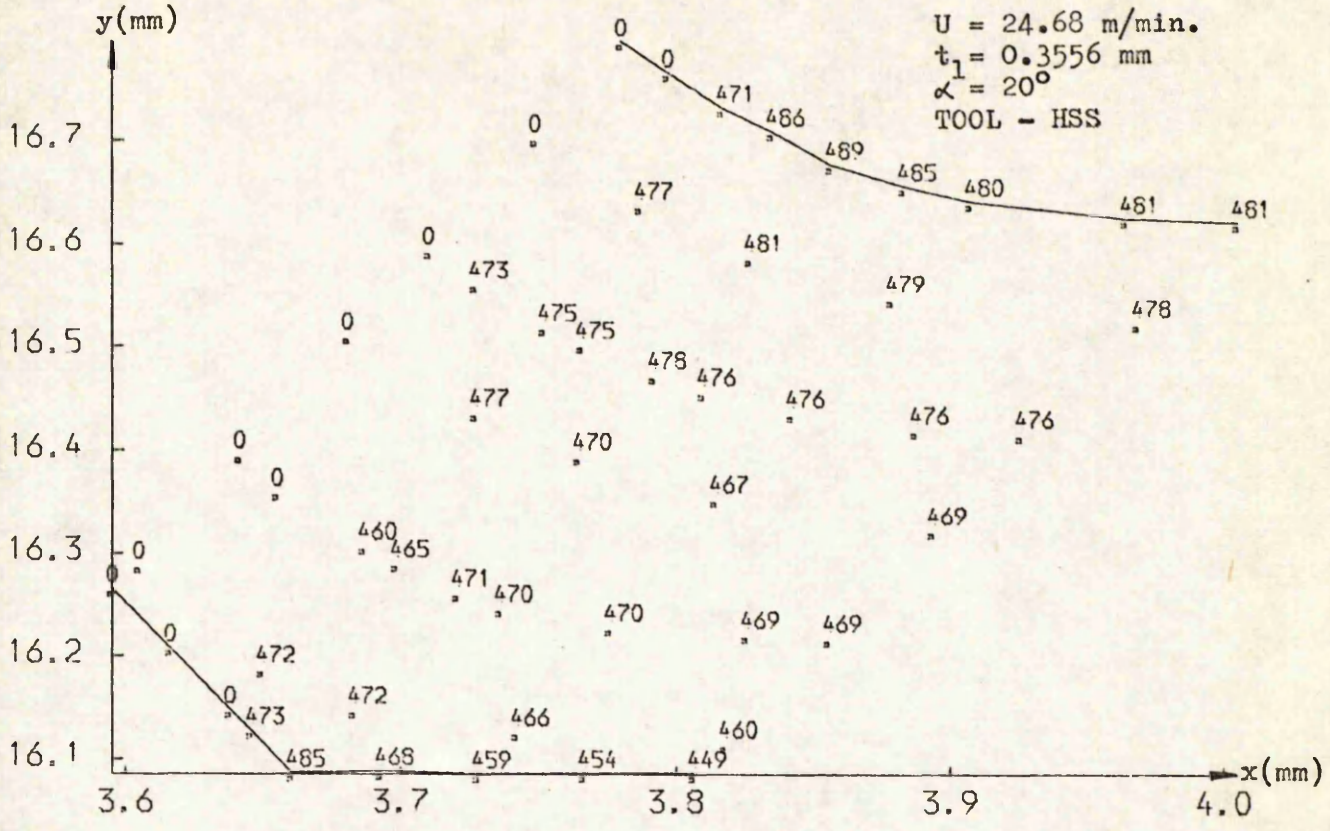

FIG. 5.4 (c)
FLOW STRESS DISTRIBUTION (MEGA PASCALS)
TEST NO. = 6

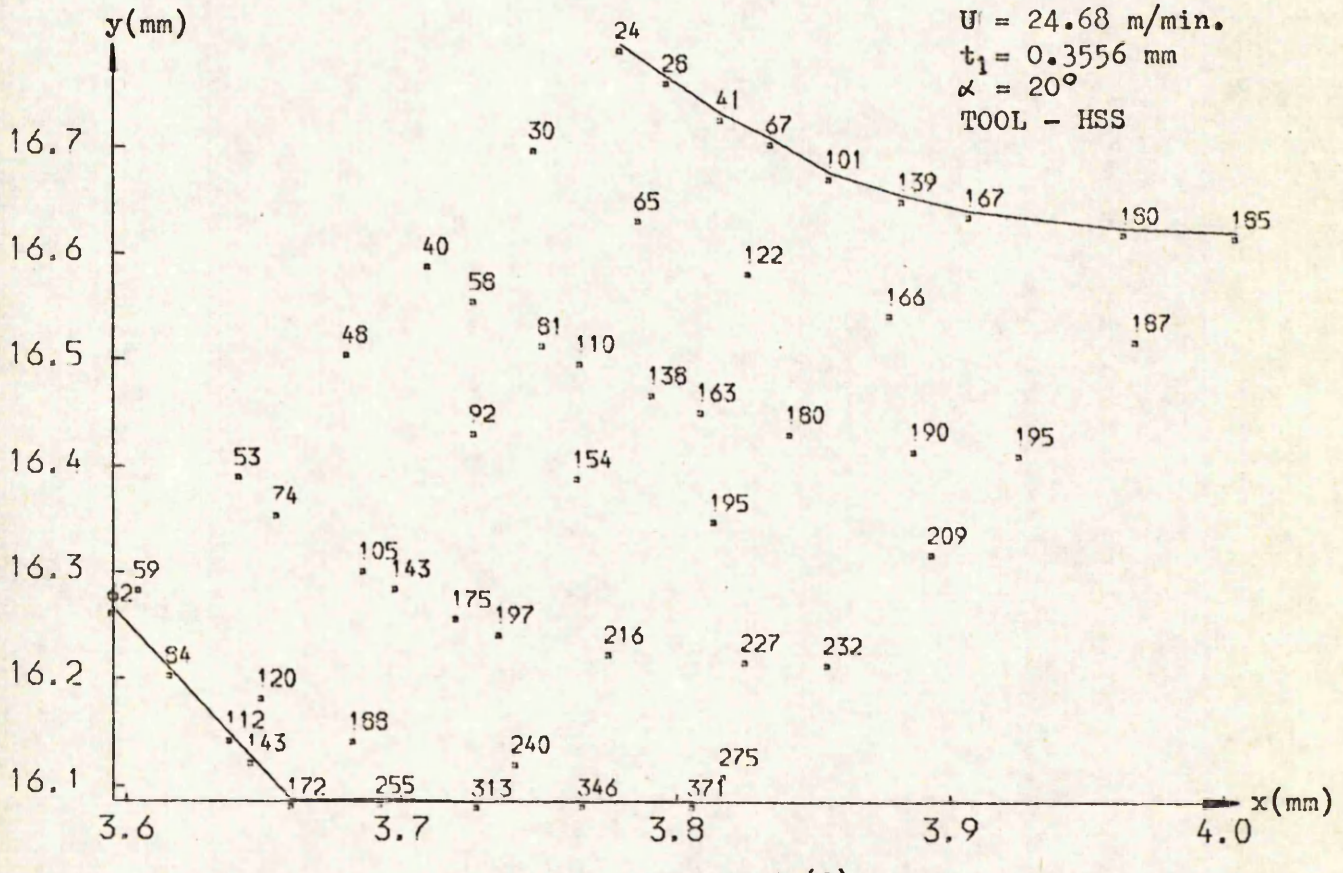

FIG. 5.4 (d)
TEMPERATURE DISTRIBUTION IN DEFORMATION ZONE, (O C)
TEST NO. = 6

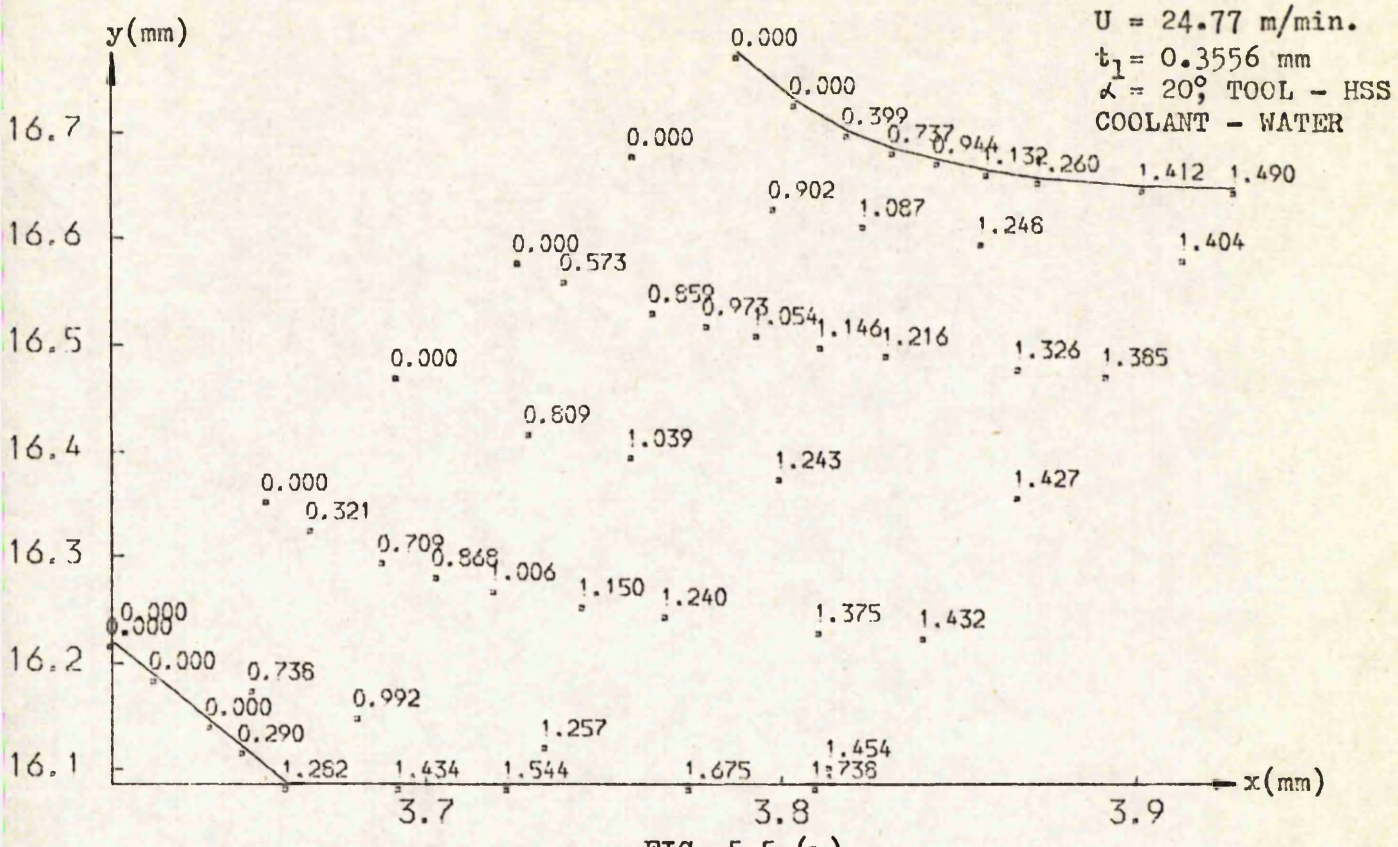

FIG. 5.5 (a)
THE DISTRIBUTION OF TOTAL STRAIN
TEST NO. = 9

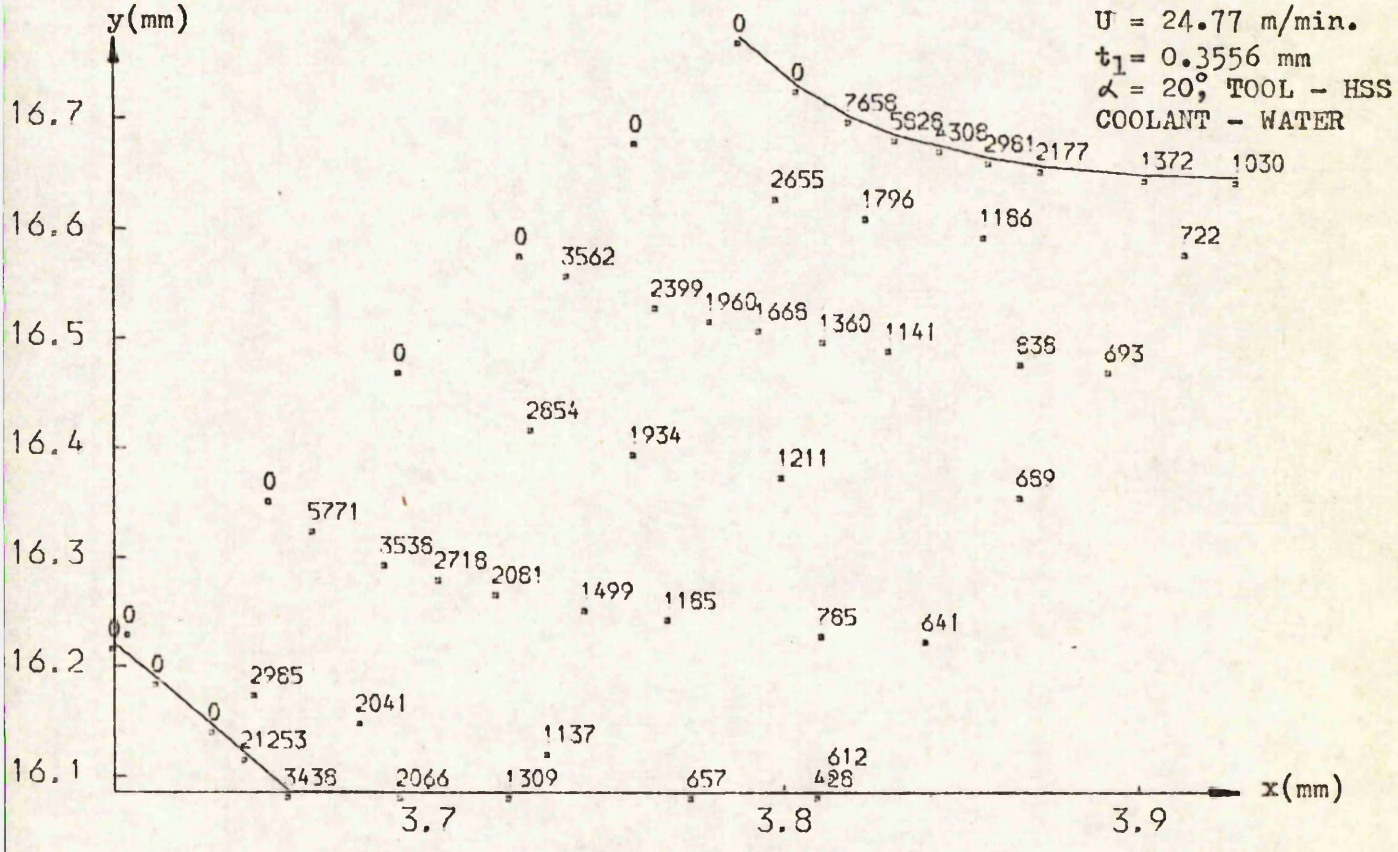

FIG. 5.5 (b)
STRAIN-RATE DISTRIBUTION IN DEFORMATION ZONE, (1/SEC)
TEST NO. = 9

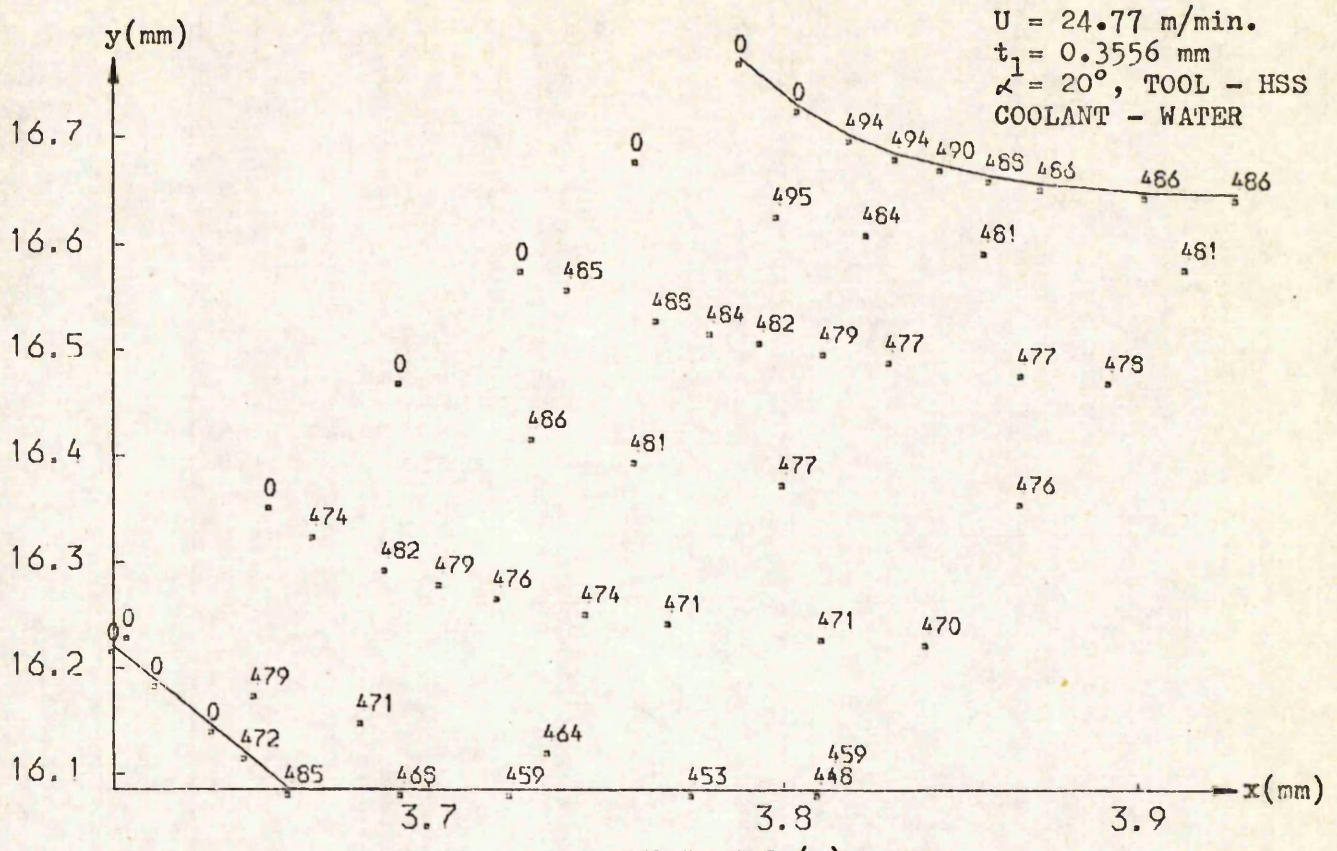

FIG. 5.5 (c)
FLOW STRESS DISTRIBUTION (MEGA PASCALS)
TEST NO.= 9

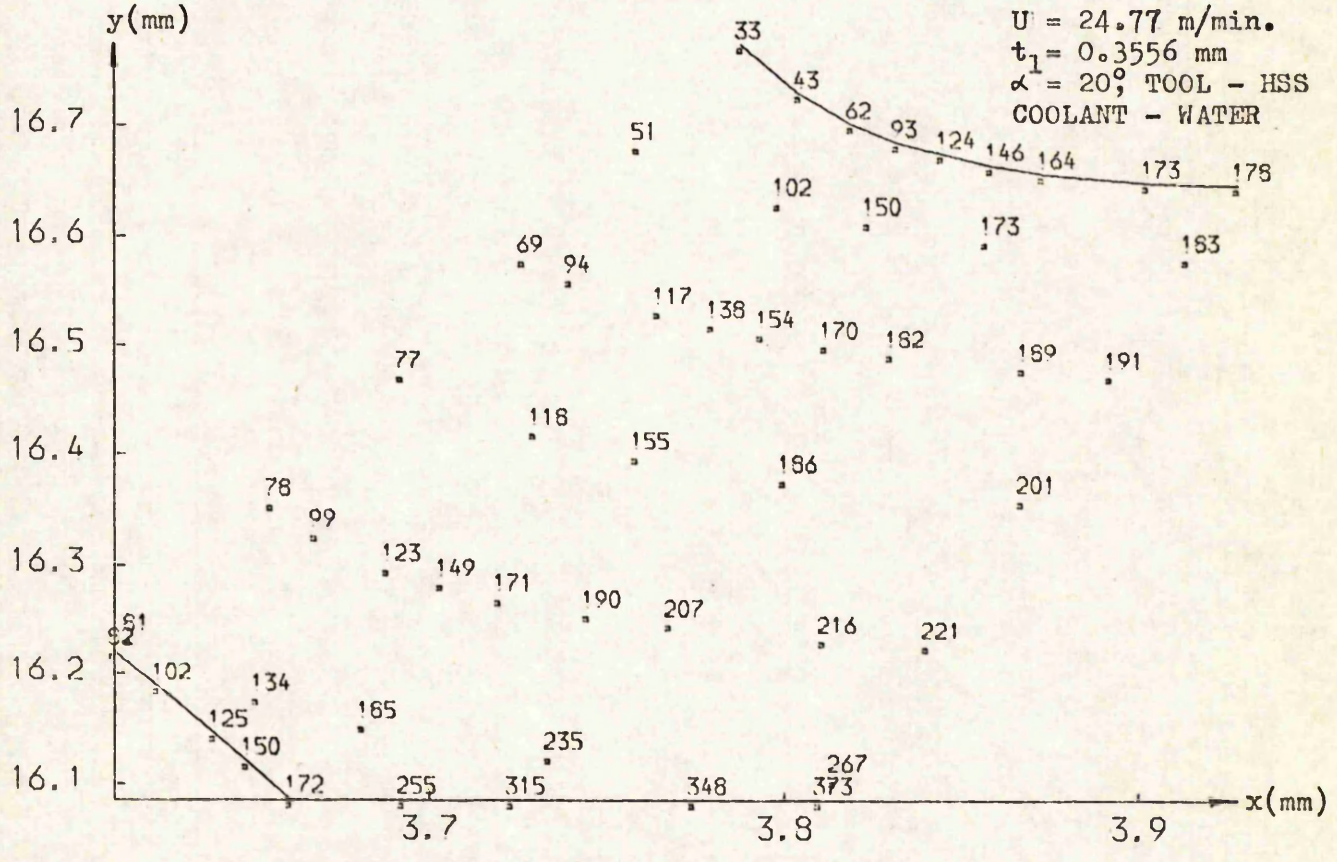

FIG. 5.5 (d)
TEMPERATURE DISTRIBUTION IN DEFORMATION ZONE, (O C)
TEST NO.= 9

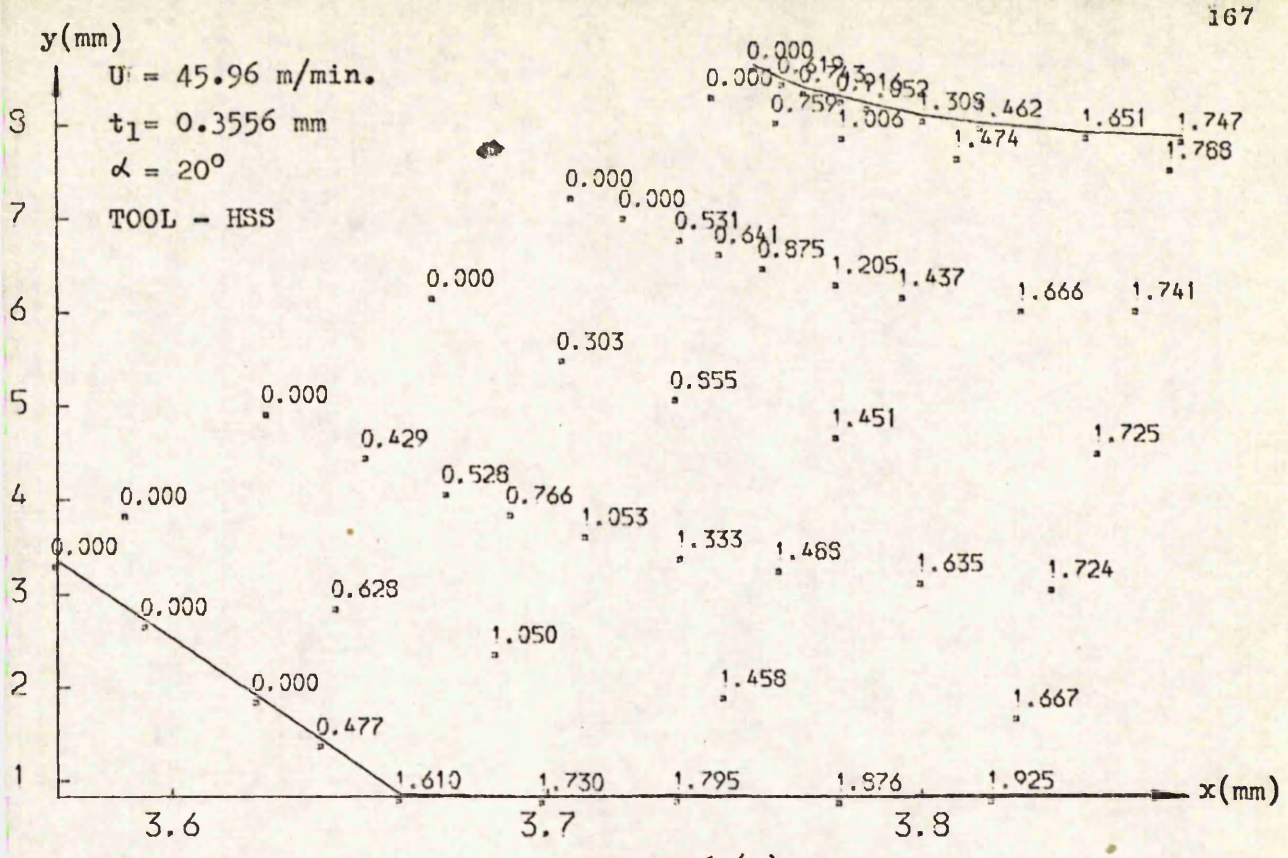

FIG. 5.6 (a)
THE DISTRIBUTION OF TOTAL STRAIN
TEST NO. = 11

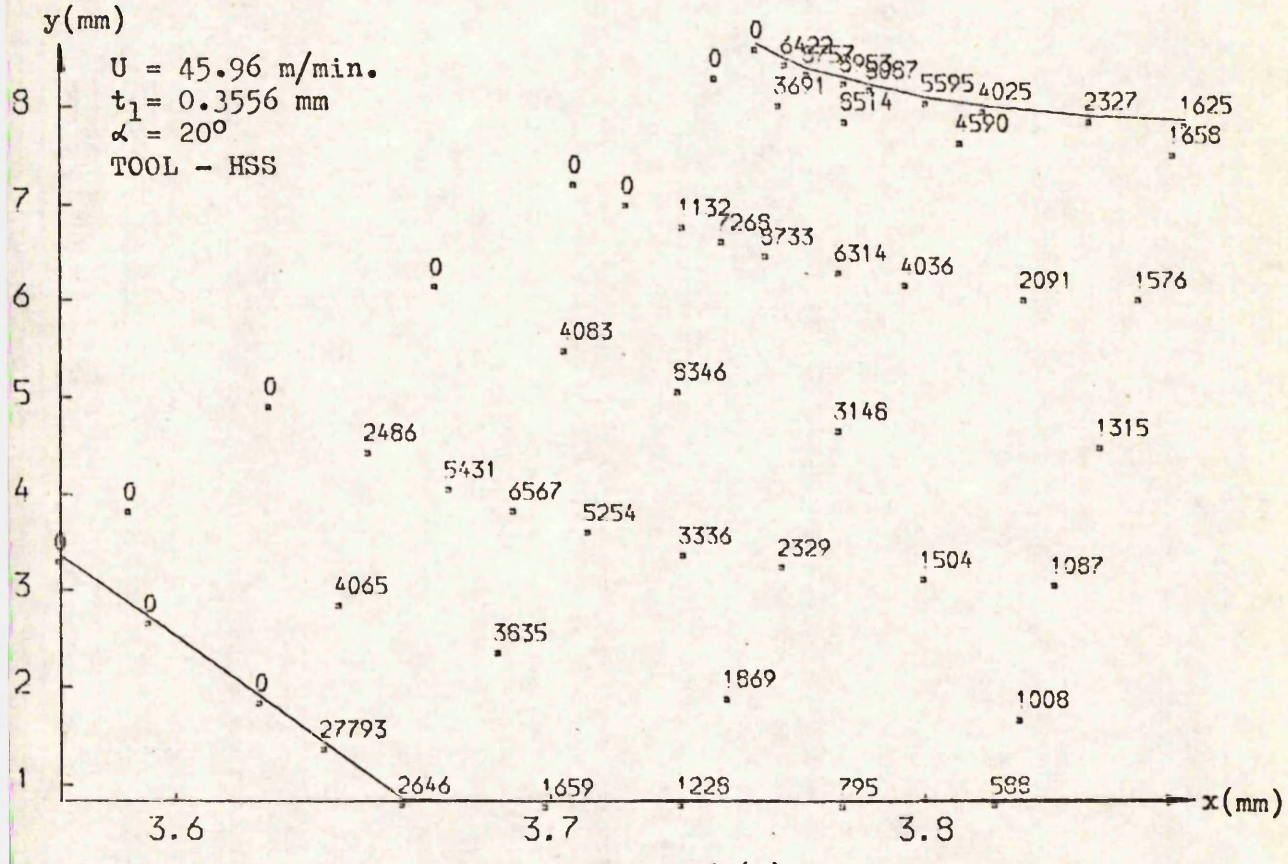

FIG. 5.6 (b)
STRAIN-RATE DISTRIBUTION IN DEFORMATION ZONE, (1/SEC)
TEST NO. = 11

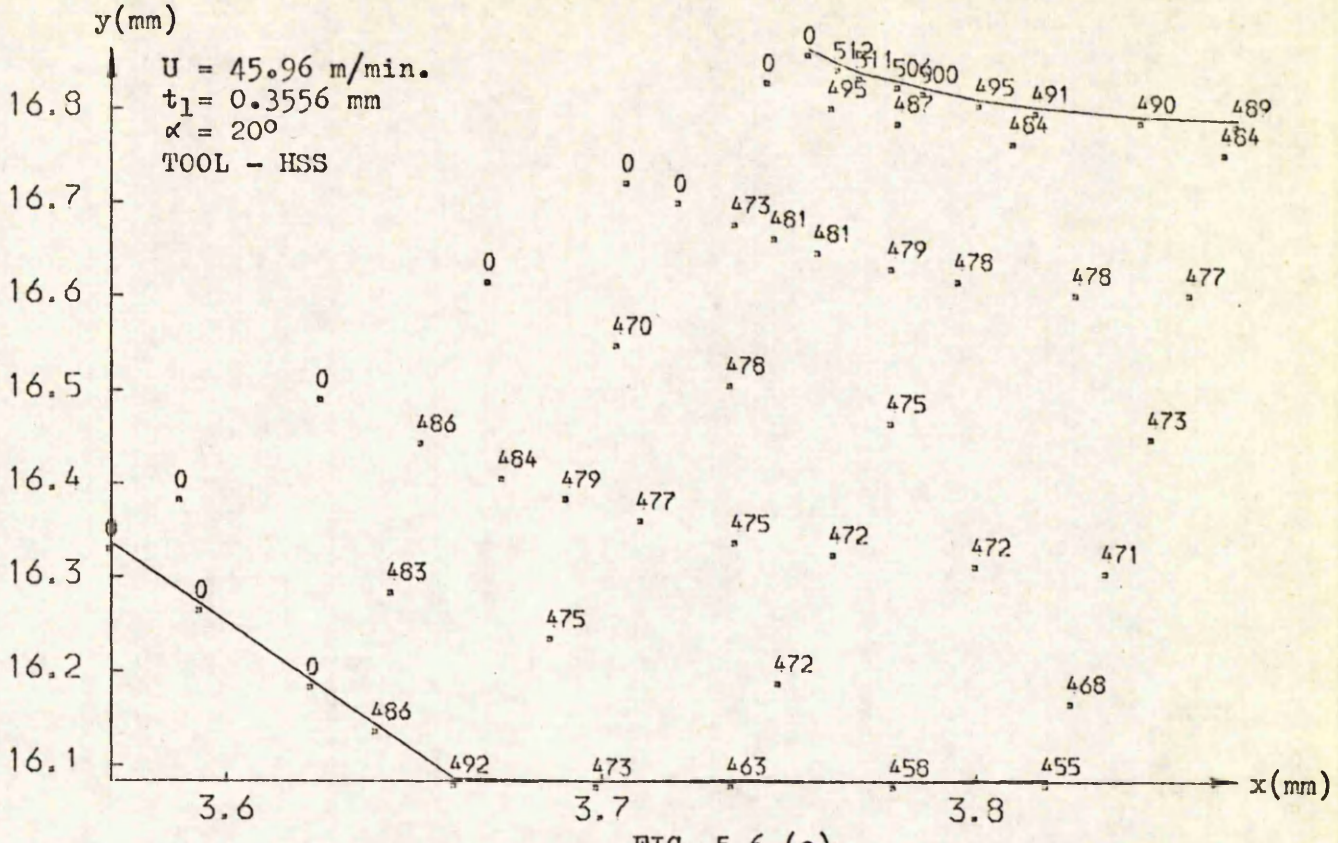

FIG. 5.6 (c)

FLOW STRESS DISTRIBUTION (MEGA PASCALS)
TEST NO. = 11

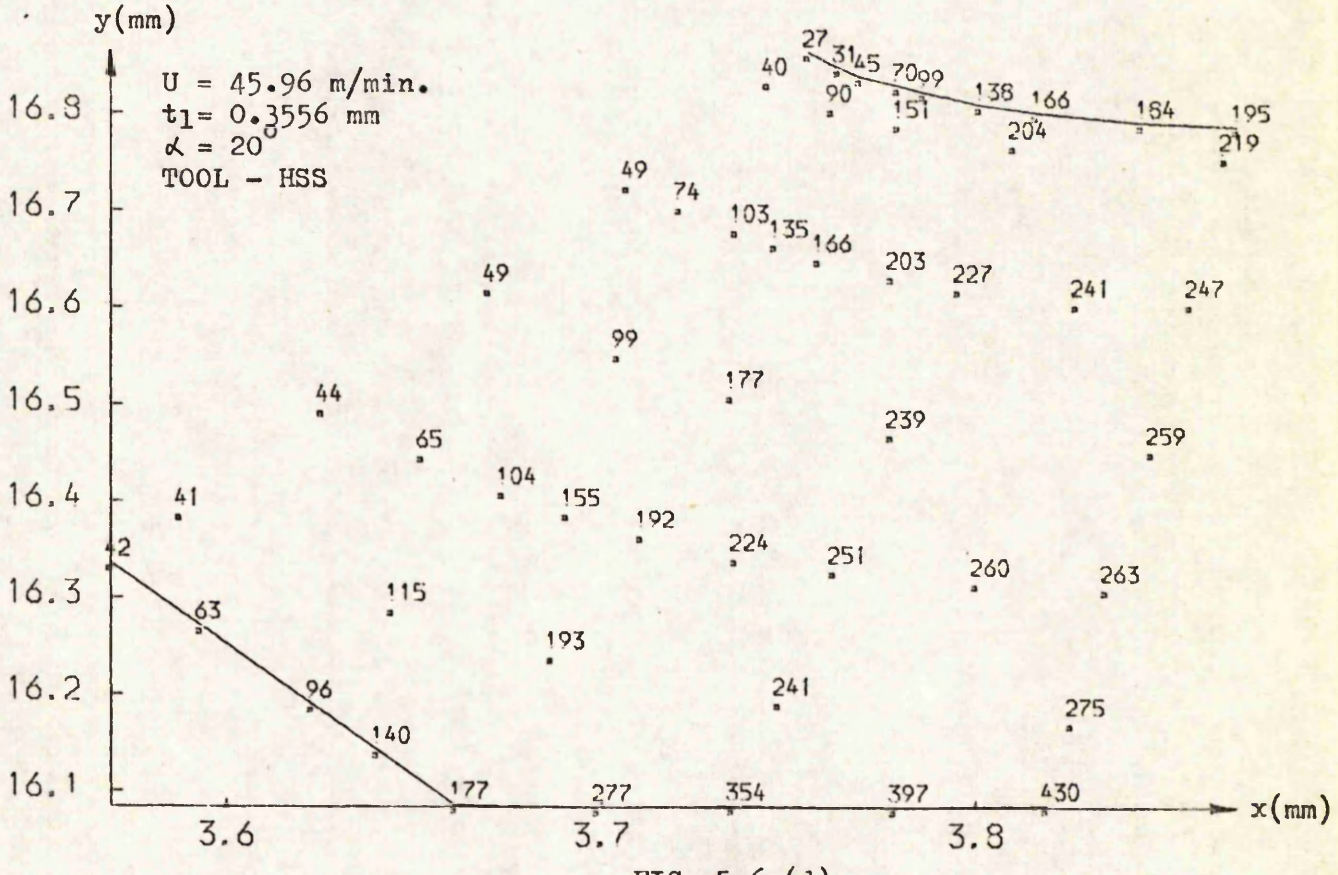

FIG. 5.6 (d)

TEMPERATURE DISTRIBUTION IN DEFORMATION ZONE, (O C)
TEST NO. = 11

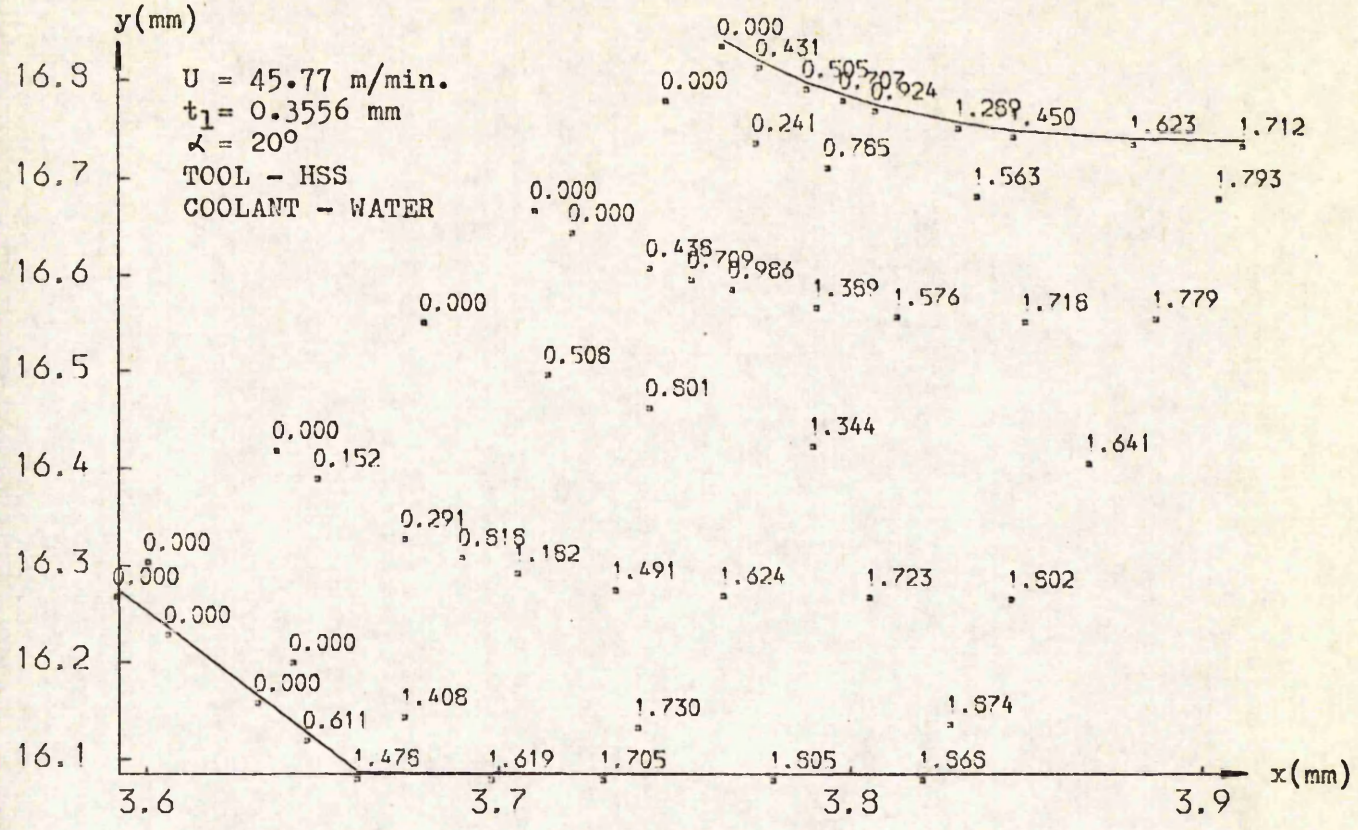

FIG. 5.7 (a)
THE DISTRIBUTION OF TOTAL STRAIN
TEST NO.= 12

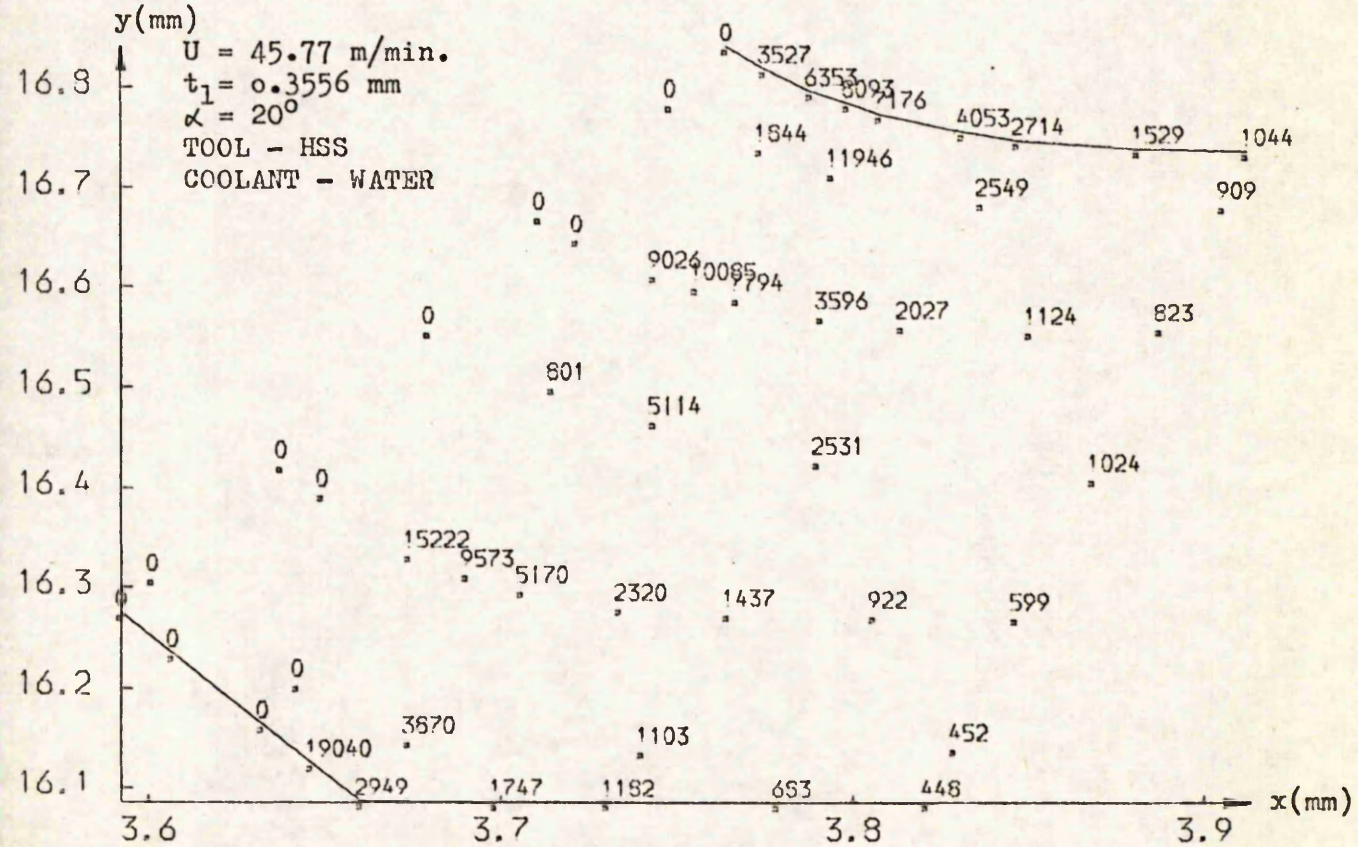

FIG. 5.7 (b)

STRAIN-RATE DISTRIBUTION IN DEFORMATION ZONE, (1/SEC)
TEST NO.= 12

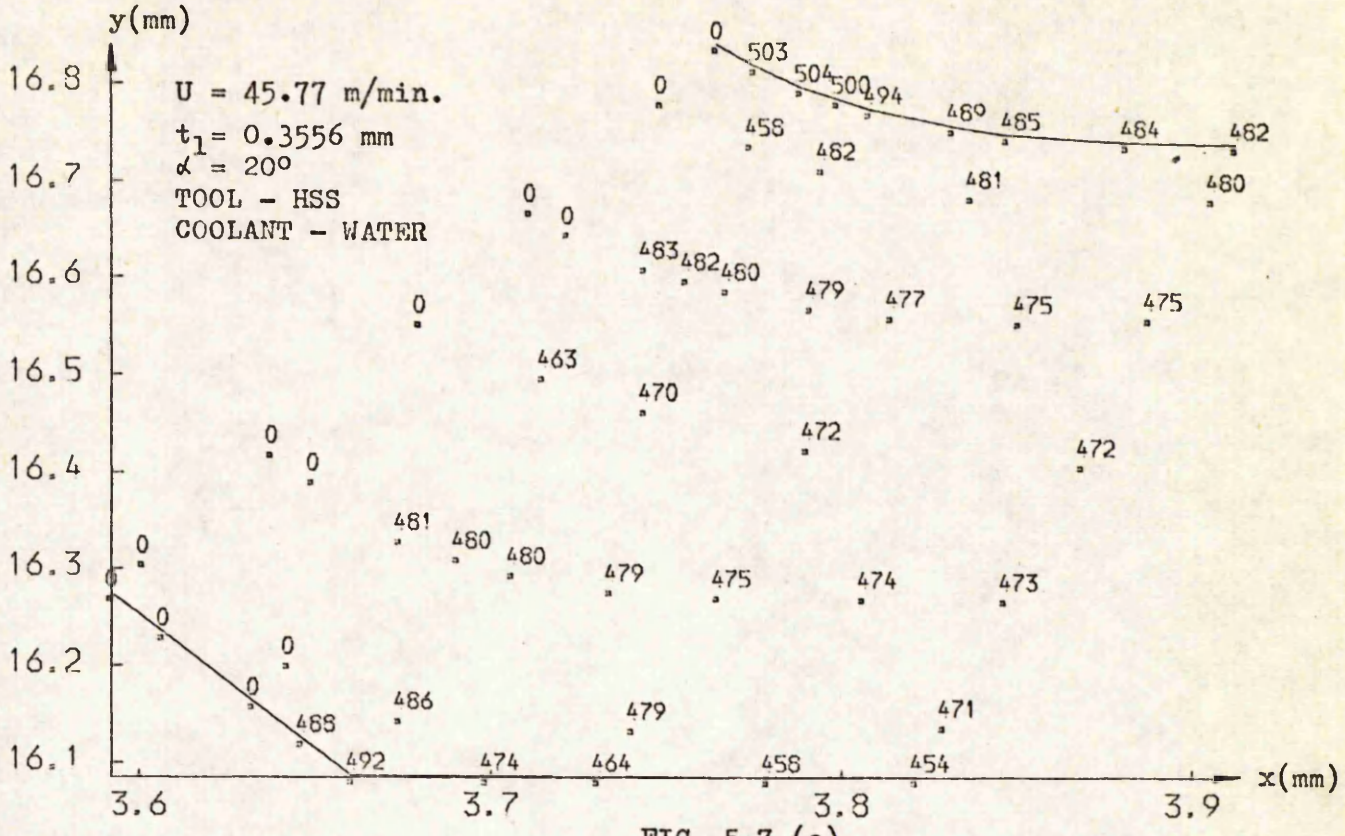

FIG. 5.7 (c)

FLOW STRESS DISTRIBUTION (MEGA PASCALS)
TEST NO.= 12

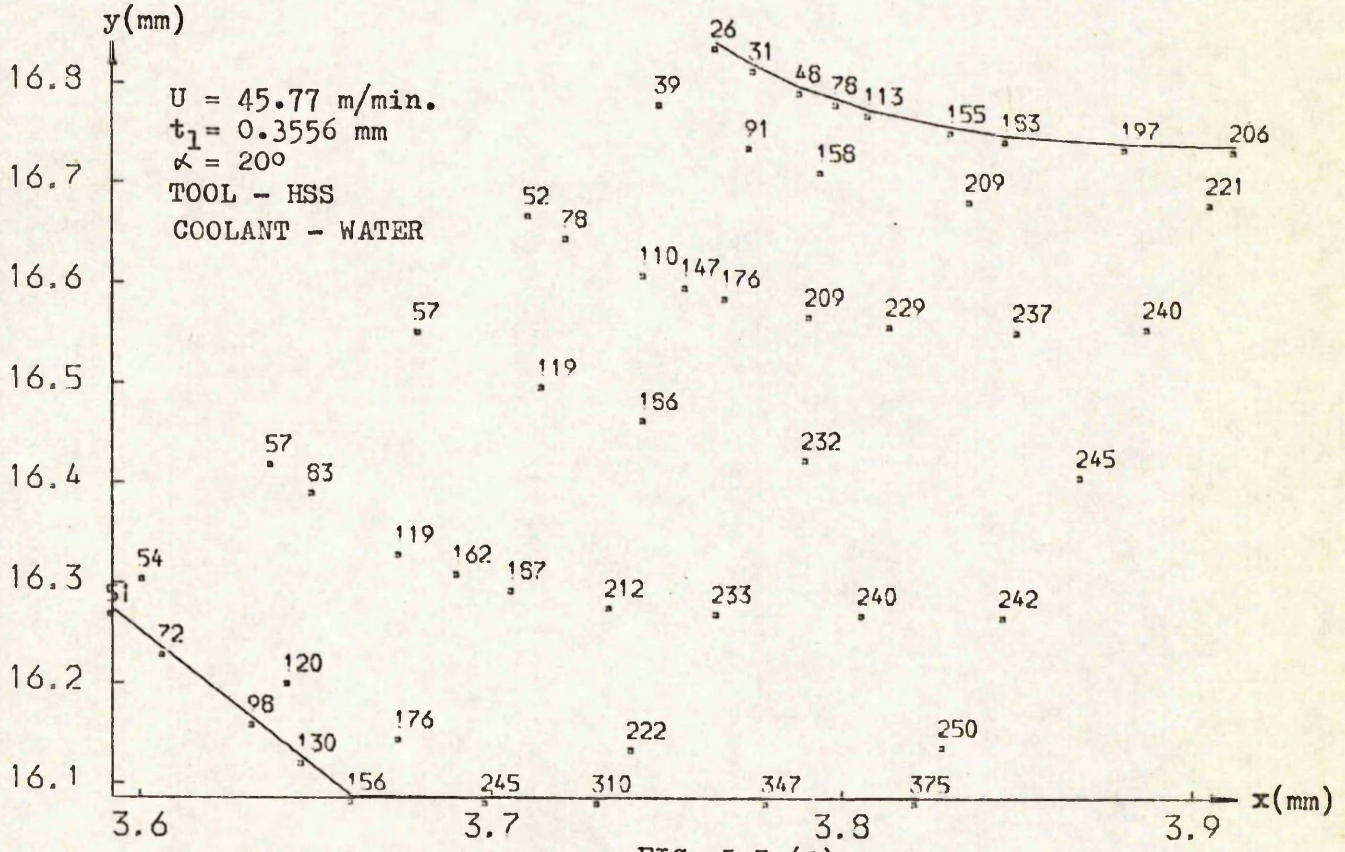

FIG. 5.7 (d)

TEMPERATURE DISTRIBUTION IN DEFORMATION ZONE, (O C)
TEST NO.= 12

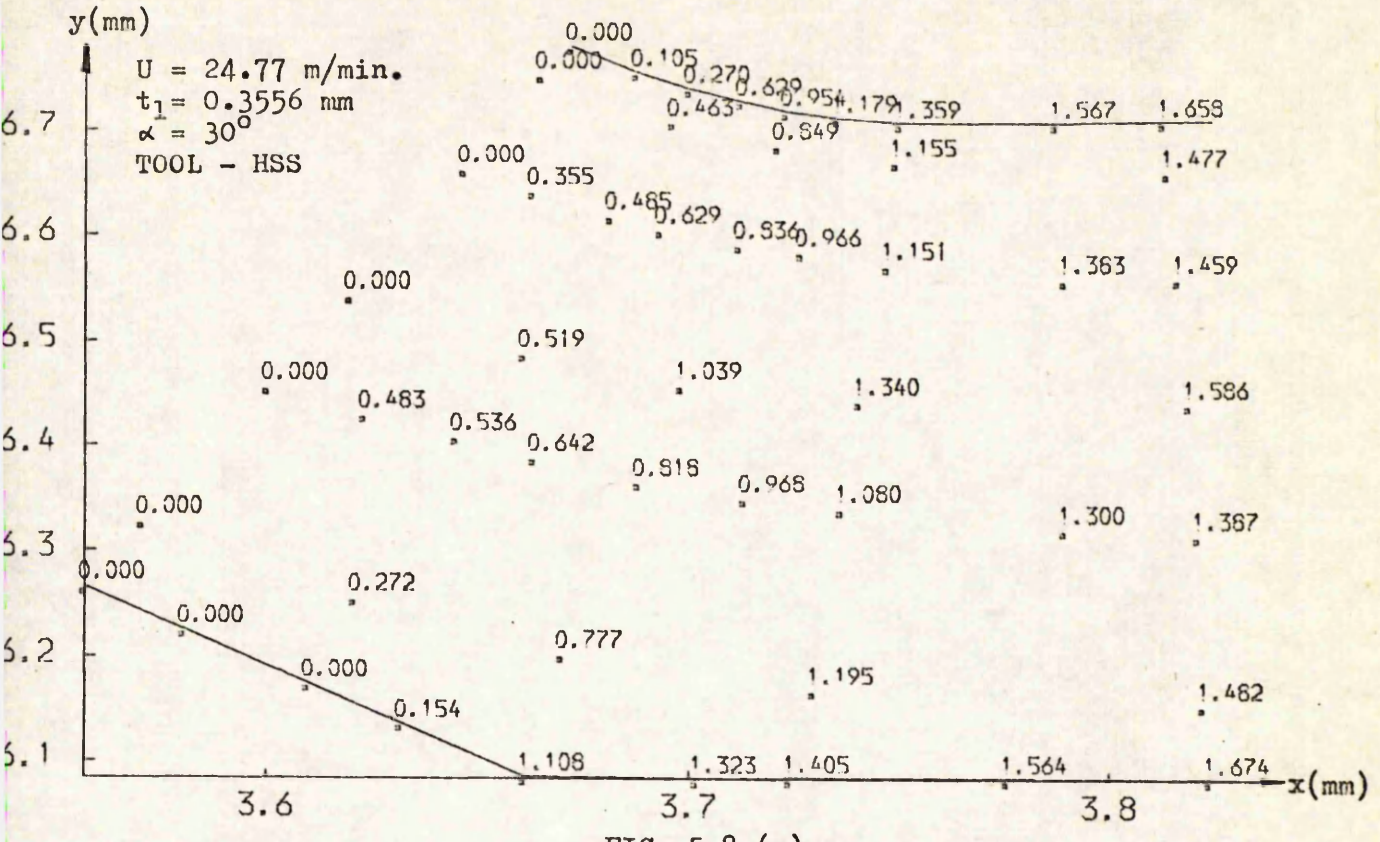

FIG. 5.8 (a)
THE DISTRIBUTION OF TOTAL STRAIN
TEST NO. = 13

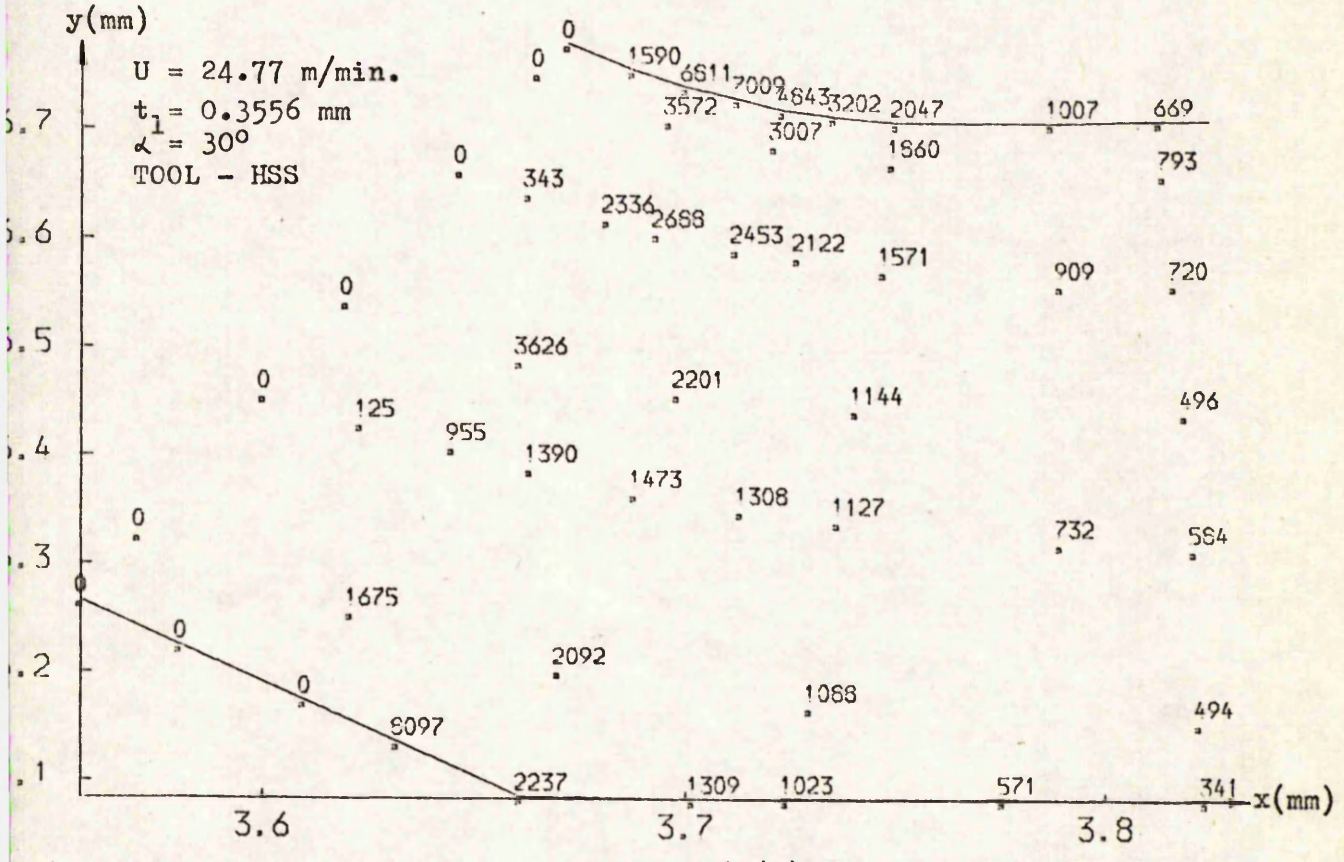

FIG. 5.8 (b)
STRAIN-RATE DISTRIBUTION IN DEFORMATION ZONE, (1/SEC)
TEST NO. = 13

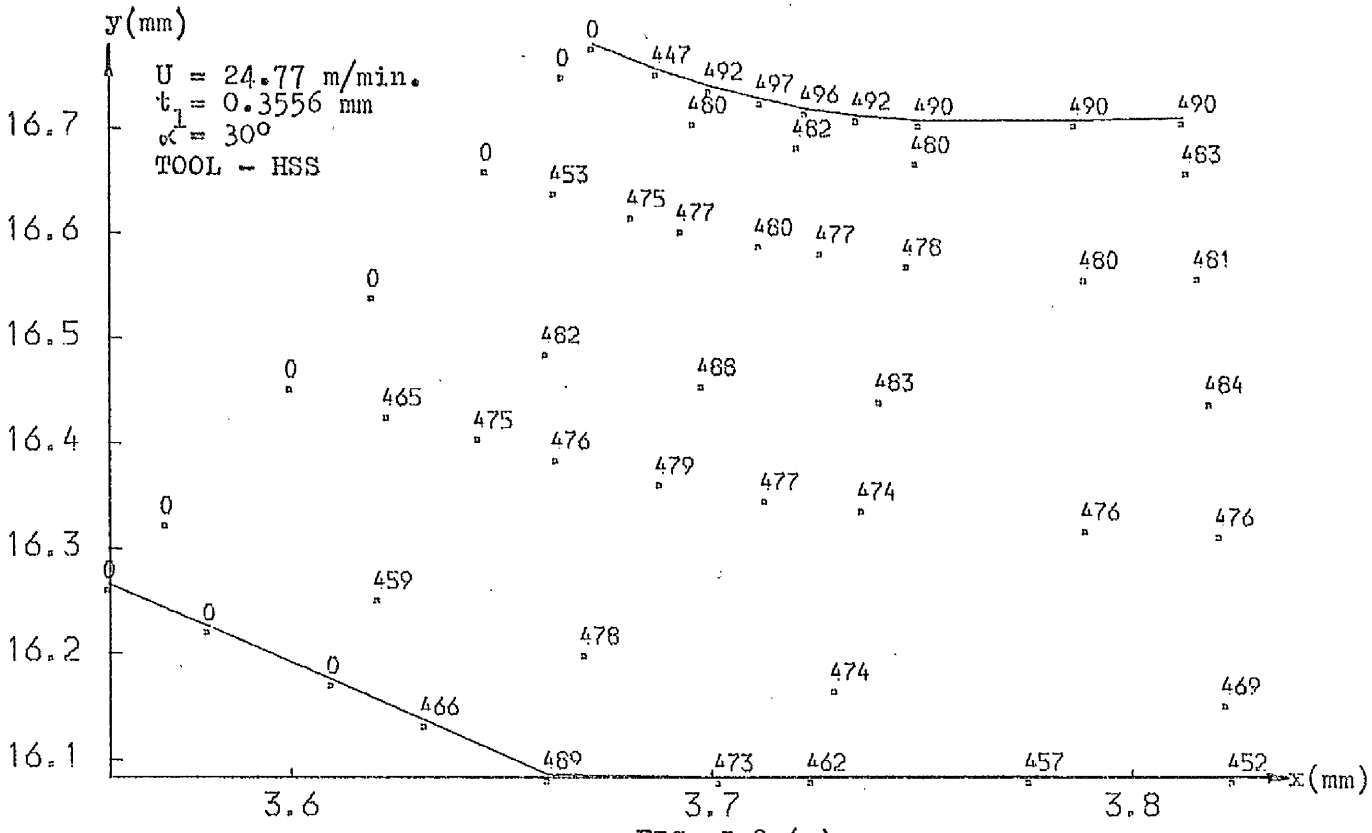

FIG. 5.8 (c)

FLOW STRESS DISTRIBUTION (MEGA PASCALS)
TEST NO.= 13

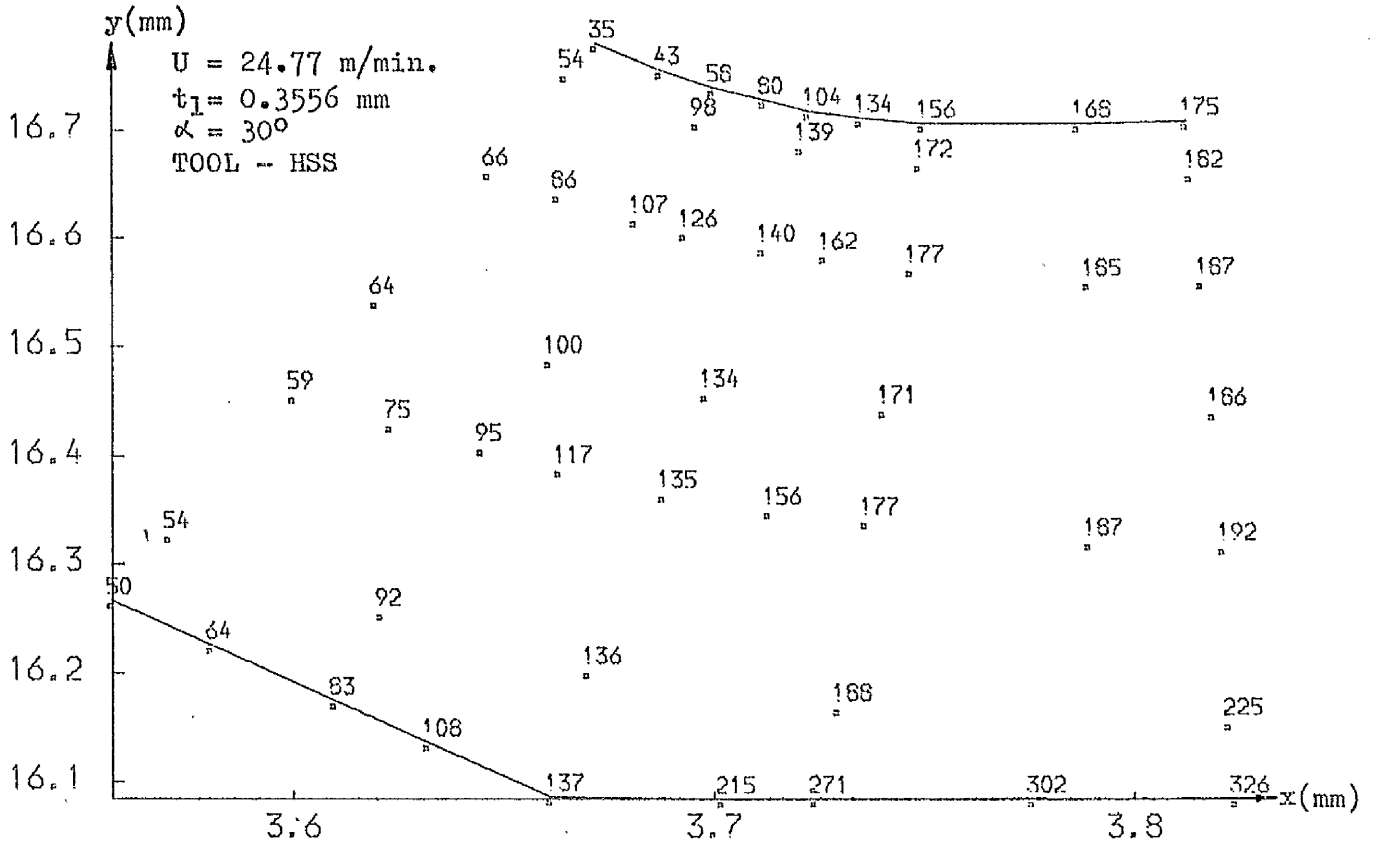

FIG. 5.8 (d)

TEMPERATURE DISTRIBUTION IN DEFORMATION ZONE, (O C)
TEST NO.= 13

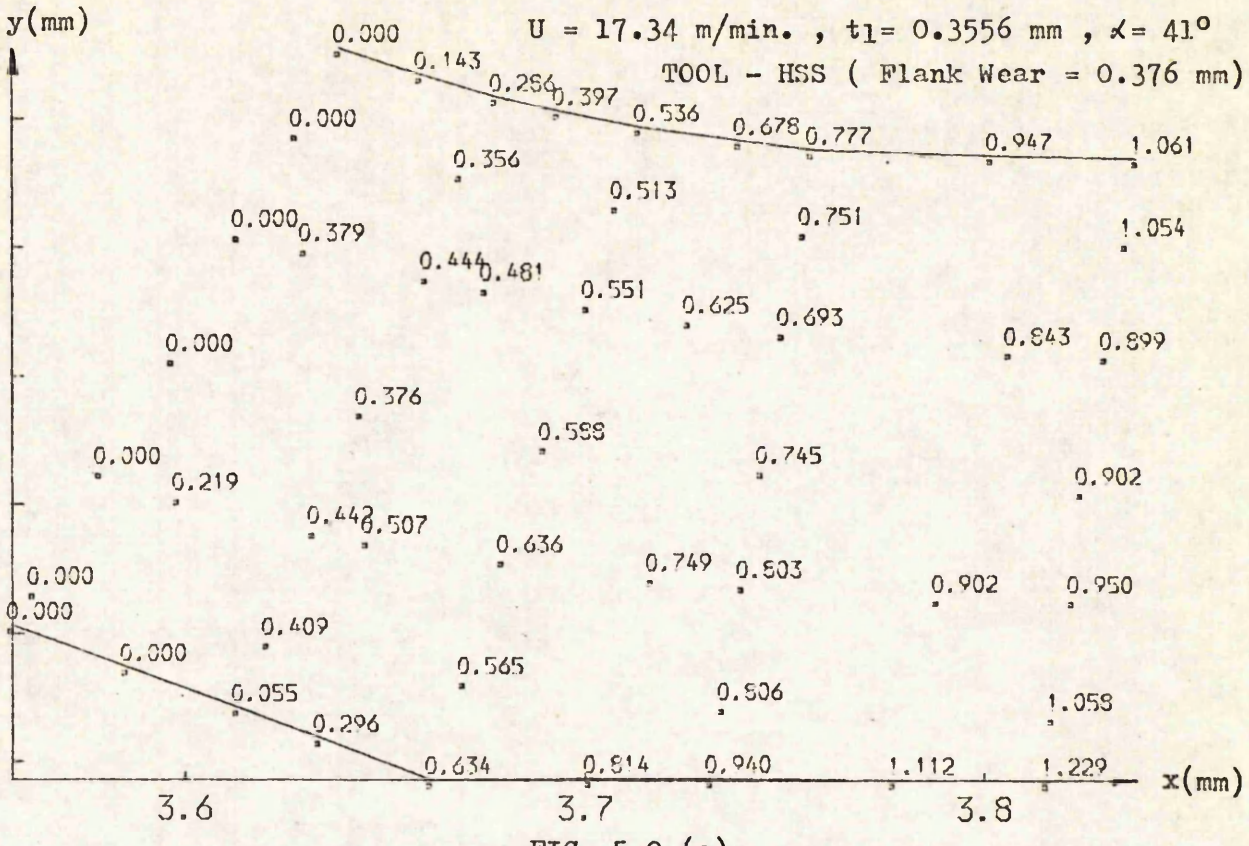

FIG. 5.9 (a)
THE DISTRIBUTION OF TOTAL STRAIN
TEST NO.= 25

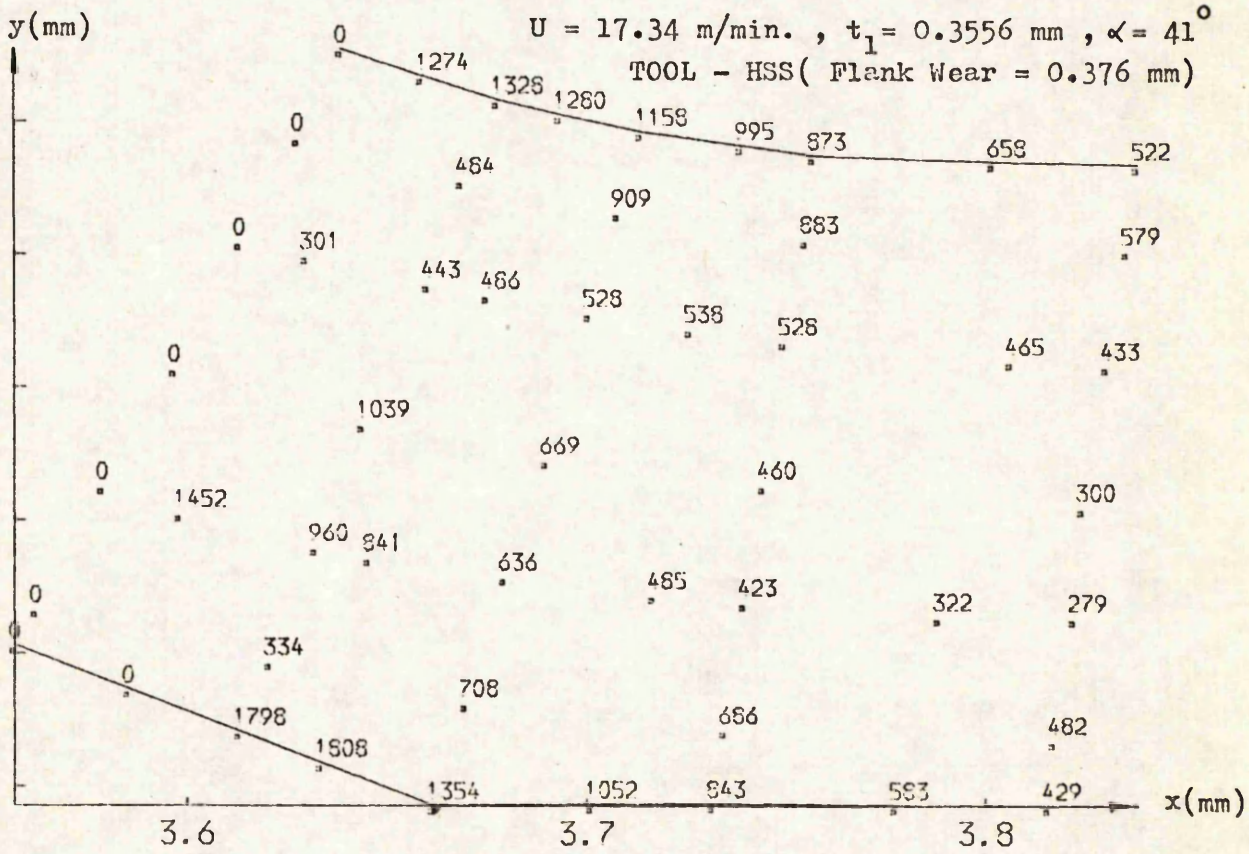

FIG. 5.9 (b)
STRAIN-RATE DISTRIBUTION IN DEFORMATION ZONE, (1/SEC)
TEST NO.= 25

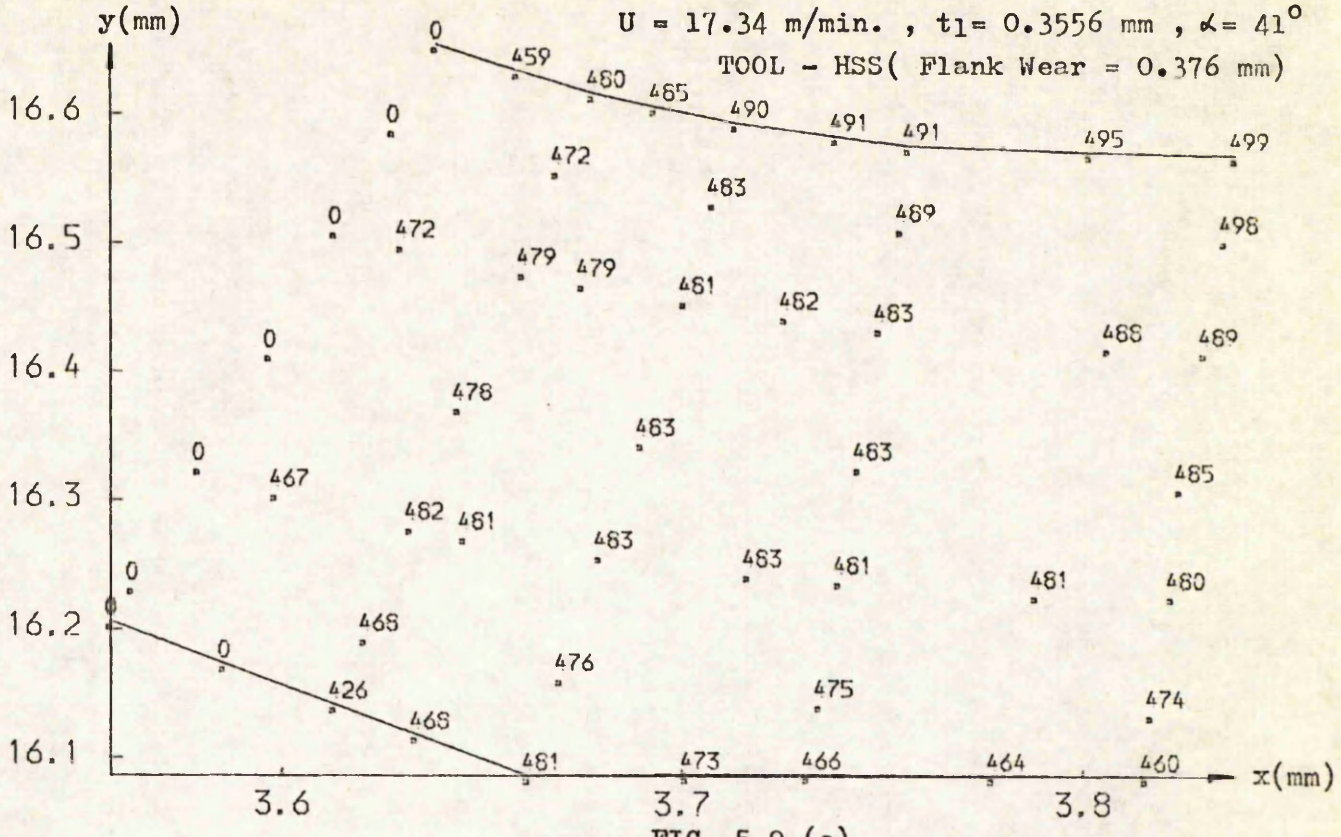

FIG. 5.9 (c)

FLOW STRESS DISTRIBUTION (MEGA PASCALS)
TEST NO.= 25

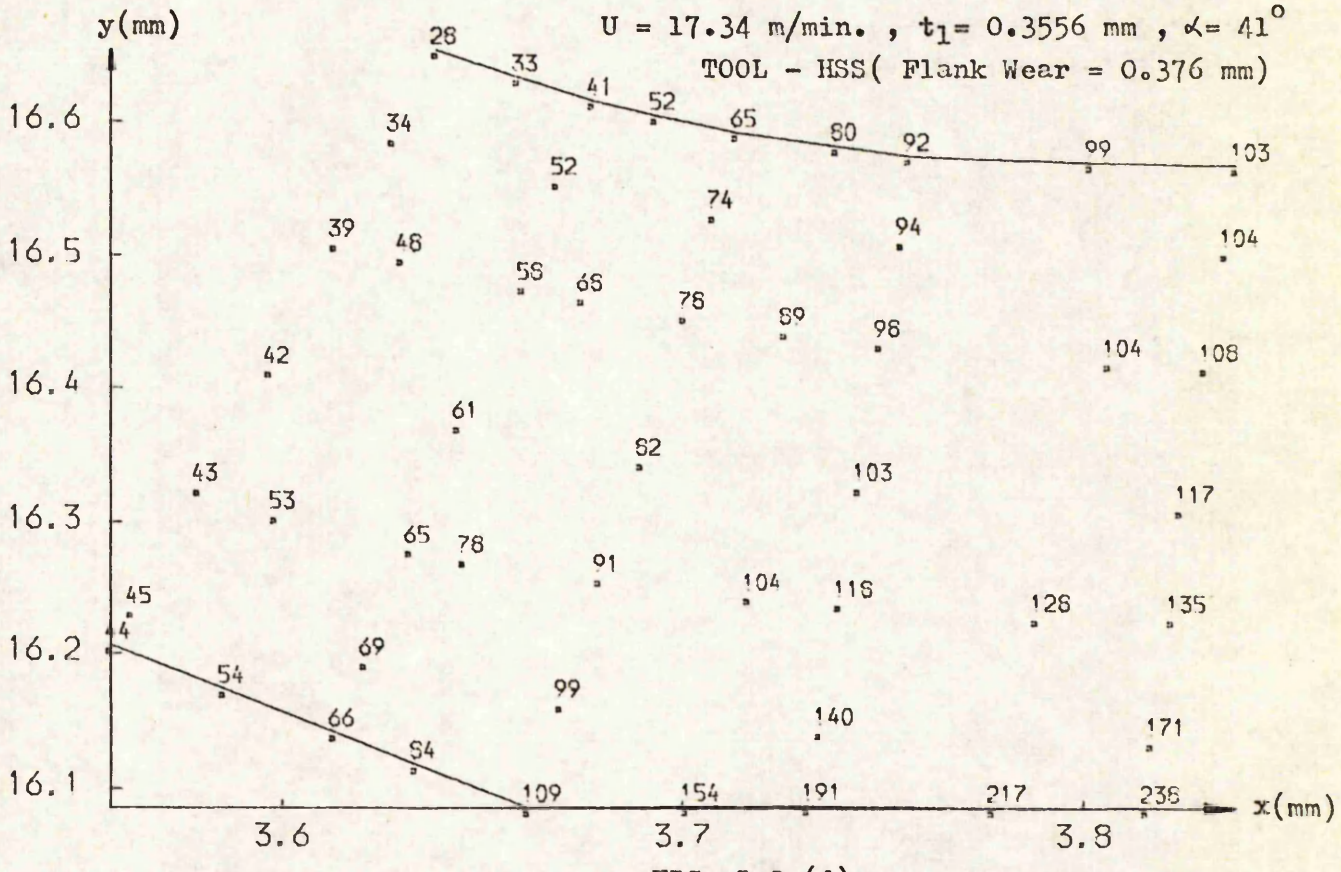

FIG. 5.9 (d)

TEMPERATURE DISTRIBUTION IN DEFORMATION ZONE, (O C)
TEST NO.= 25

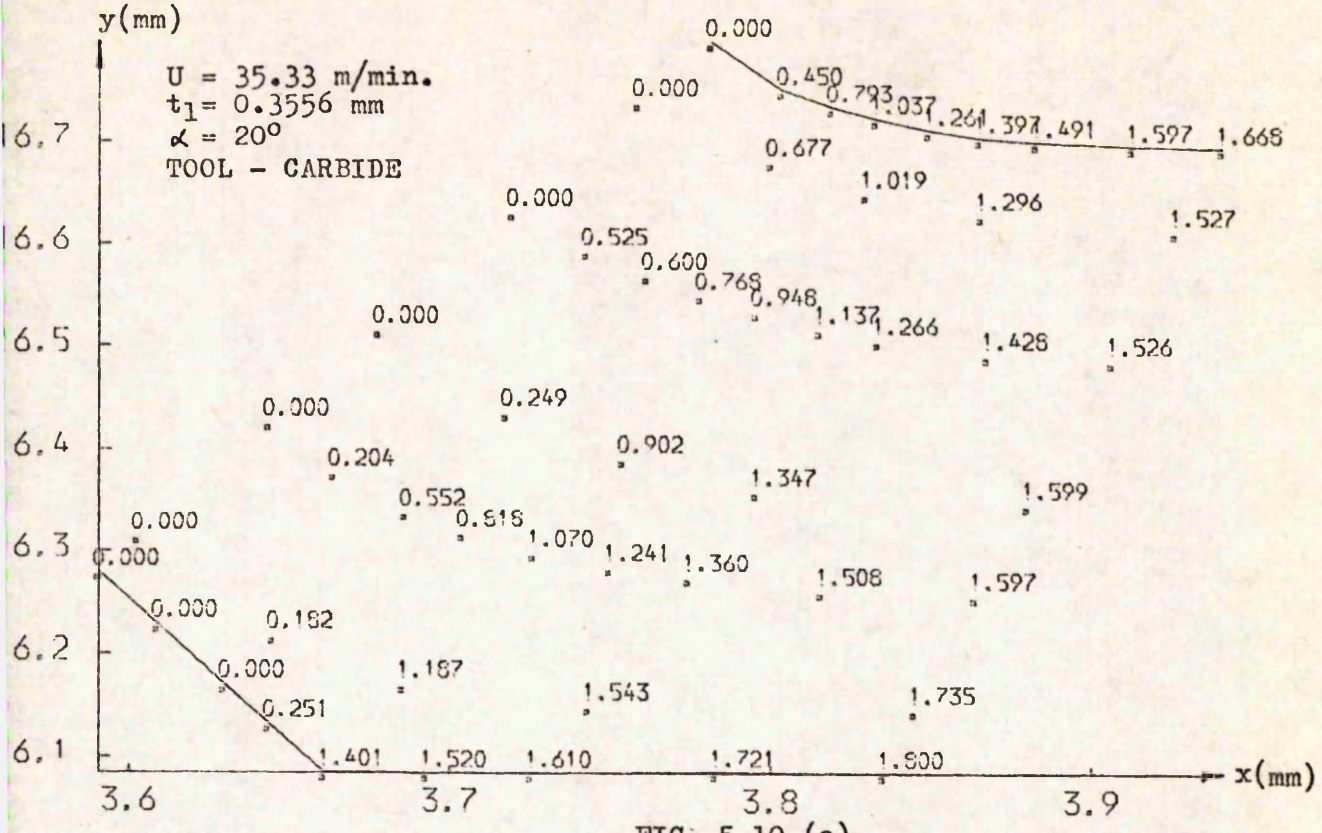

FIG. 5.10 (a)

THE DISTRIBUTION OF TOTAL STRAIN
TEST NO. = 14

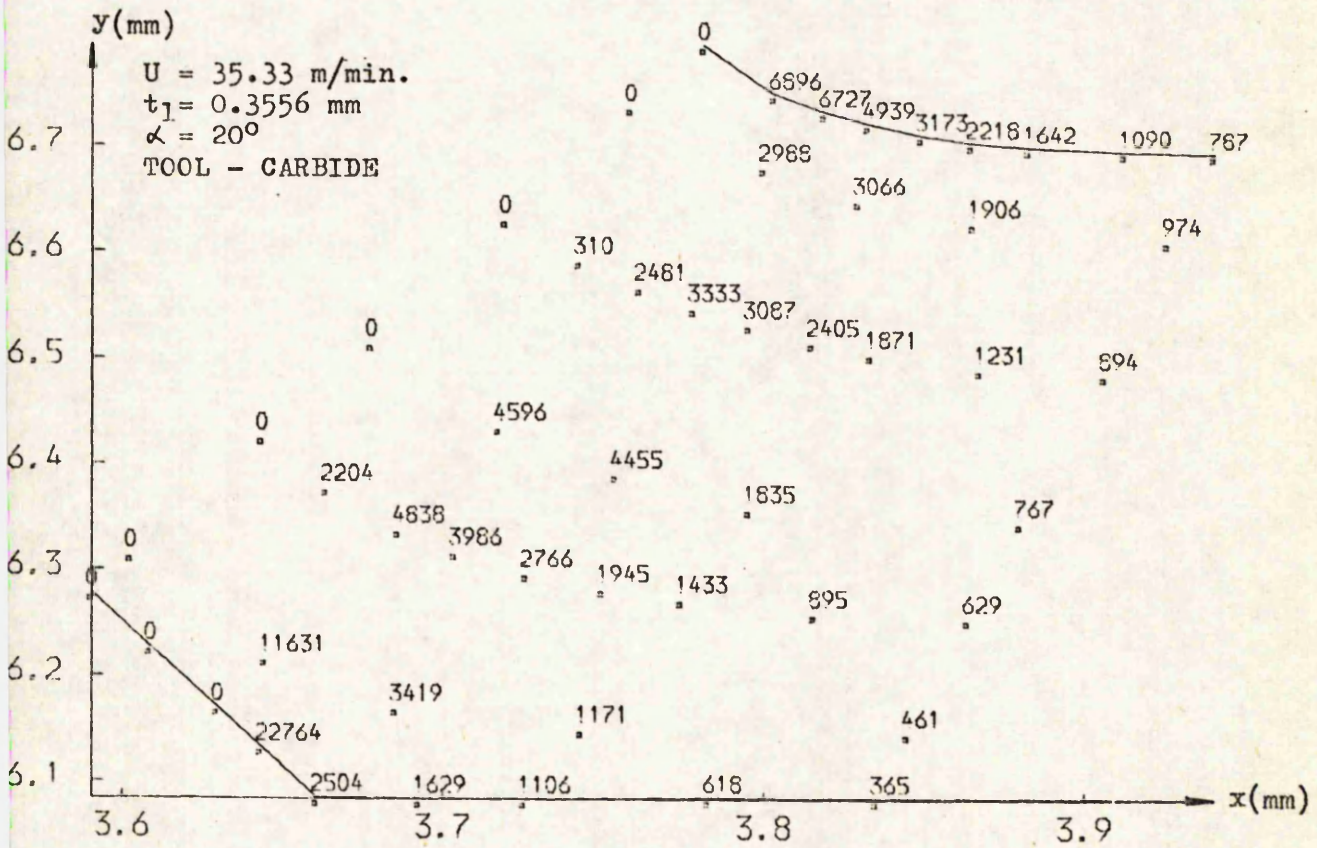

FIG. 5.10 (b)

STRAIN-RATE DISTRIBUTION IN DEFORMATION ZONE, (1/SEC)
TEST NO. = 14

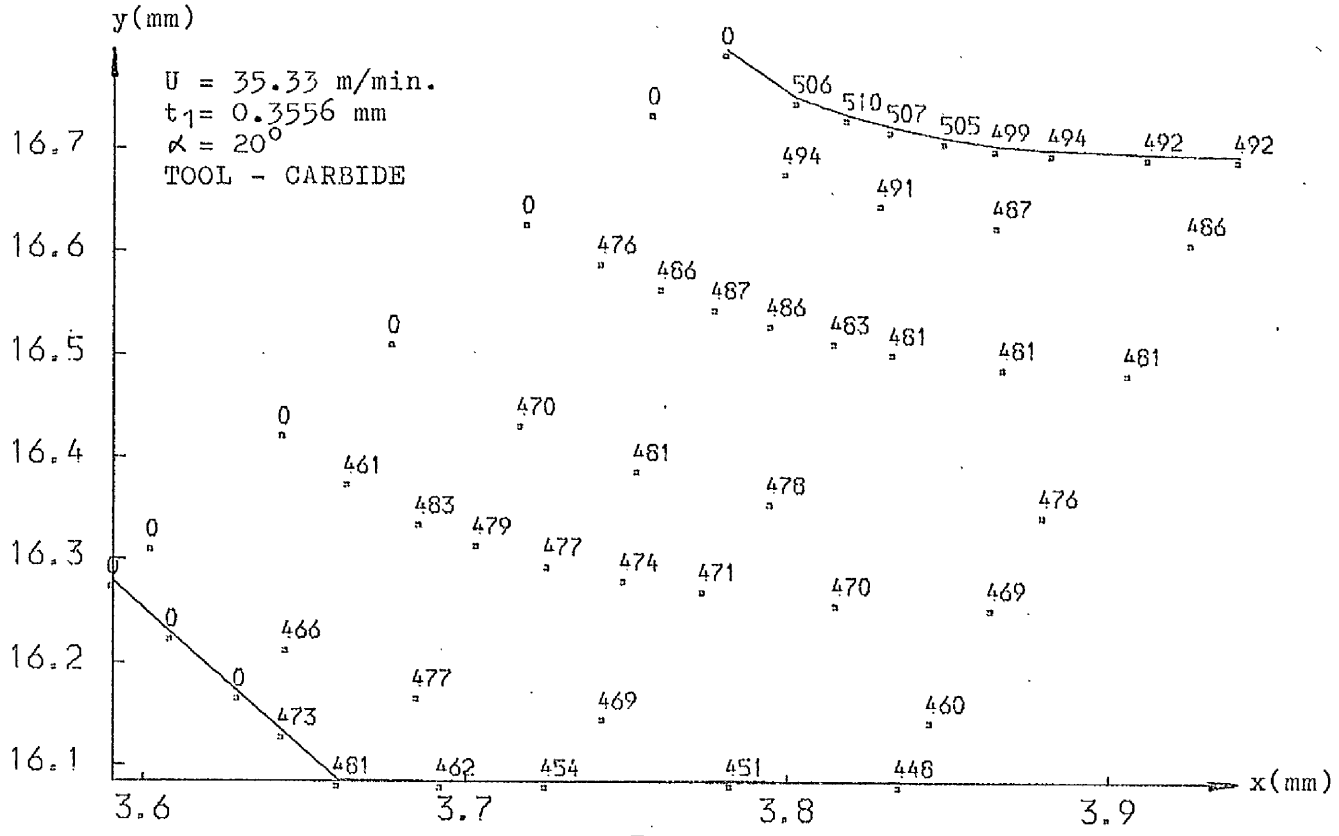

FIG. 5.10 (c)

FLOW STRESS DISTRIBUTION (MEGA PASCALS)
TEST NO.= 14

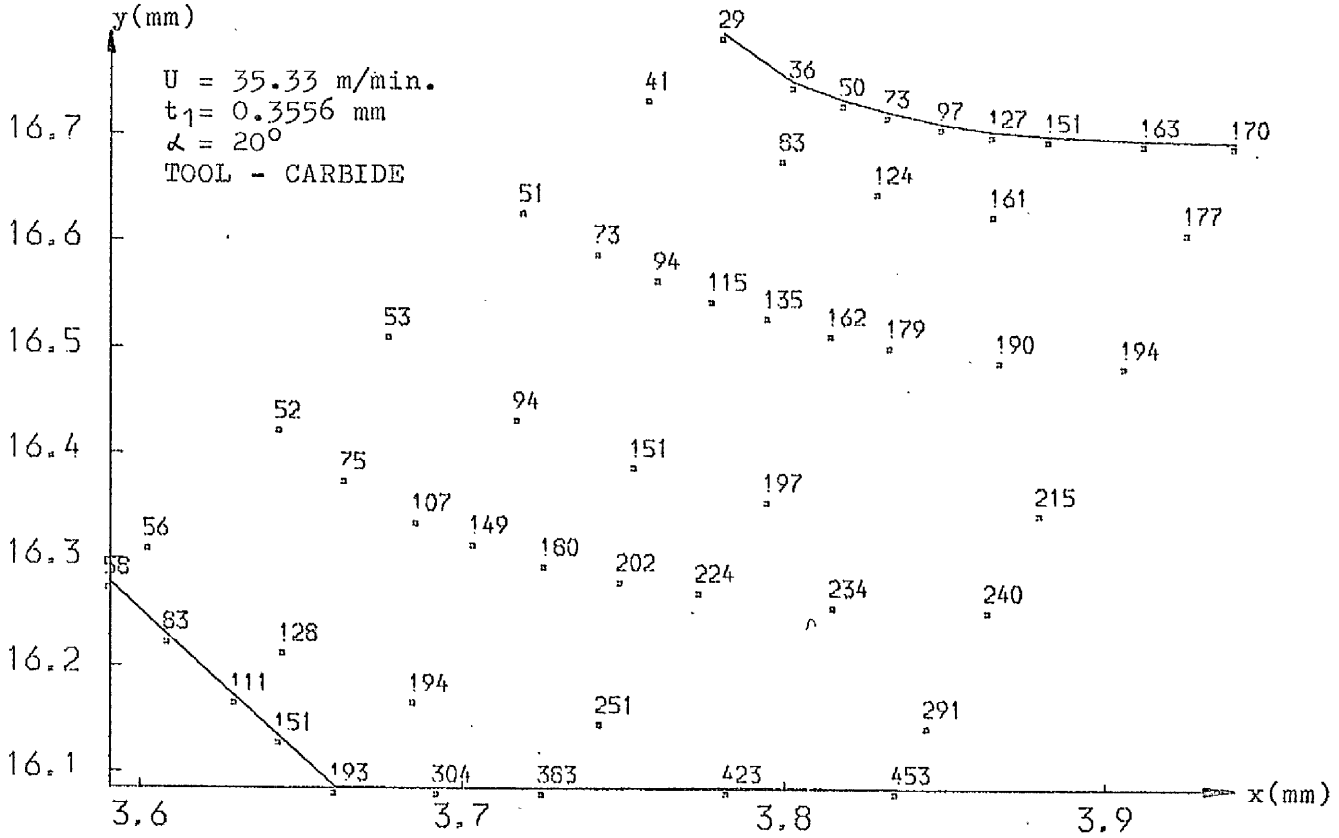

FIG. 5.10 (d)

TEMPERATURE DISTRIBUTION IN DEFORMATION ZONE, (O C)
TEST NO.= 14

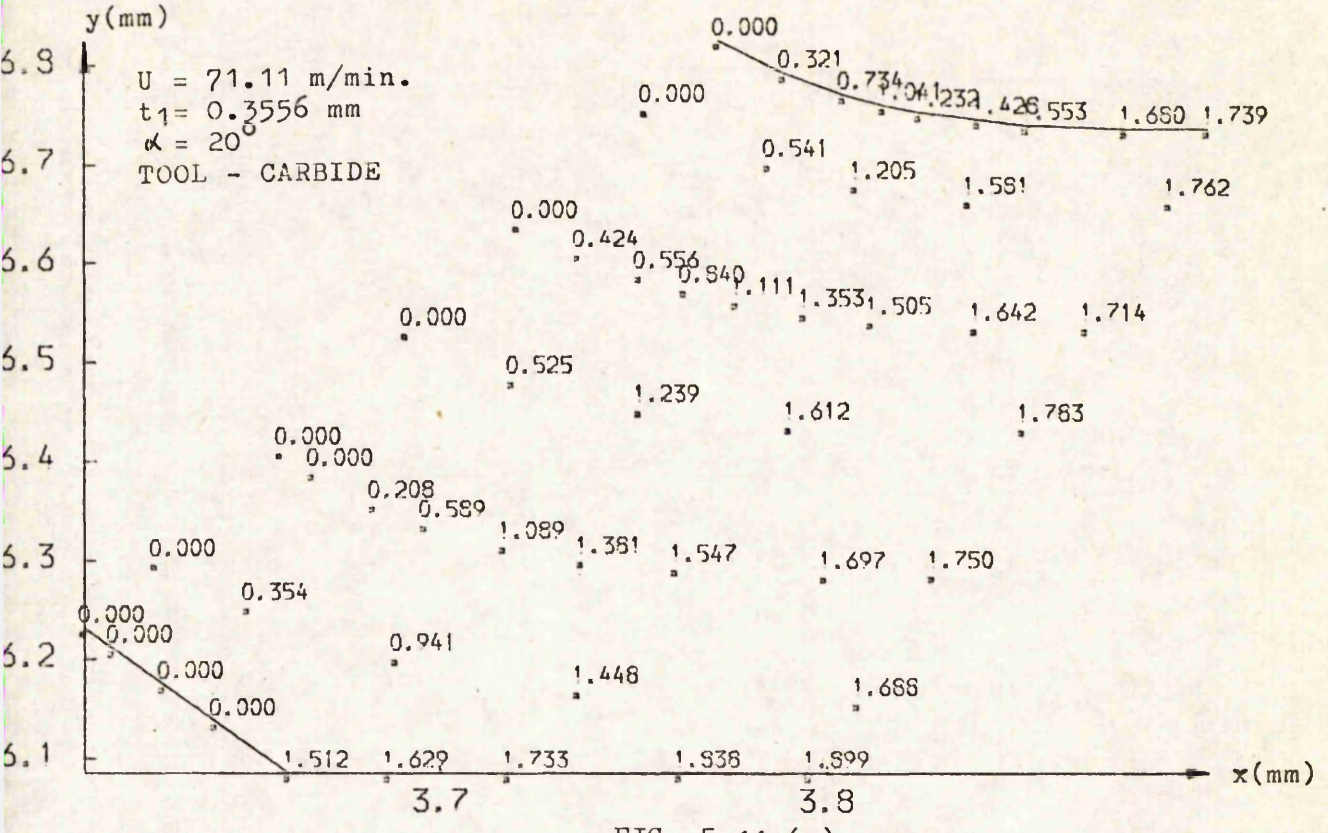

FIG. 5.11 (a)

THE DISTRIBUTION OF TOTAL STRAIN
TEST NO.= 15

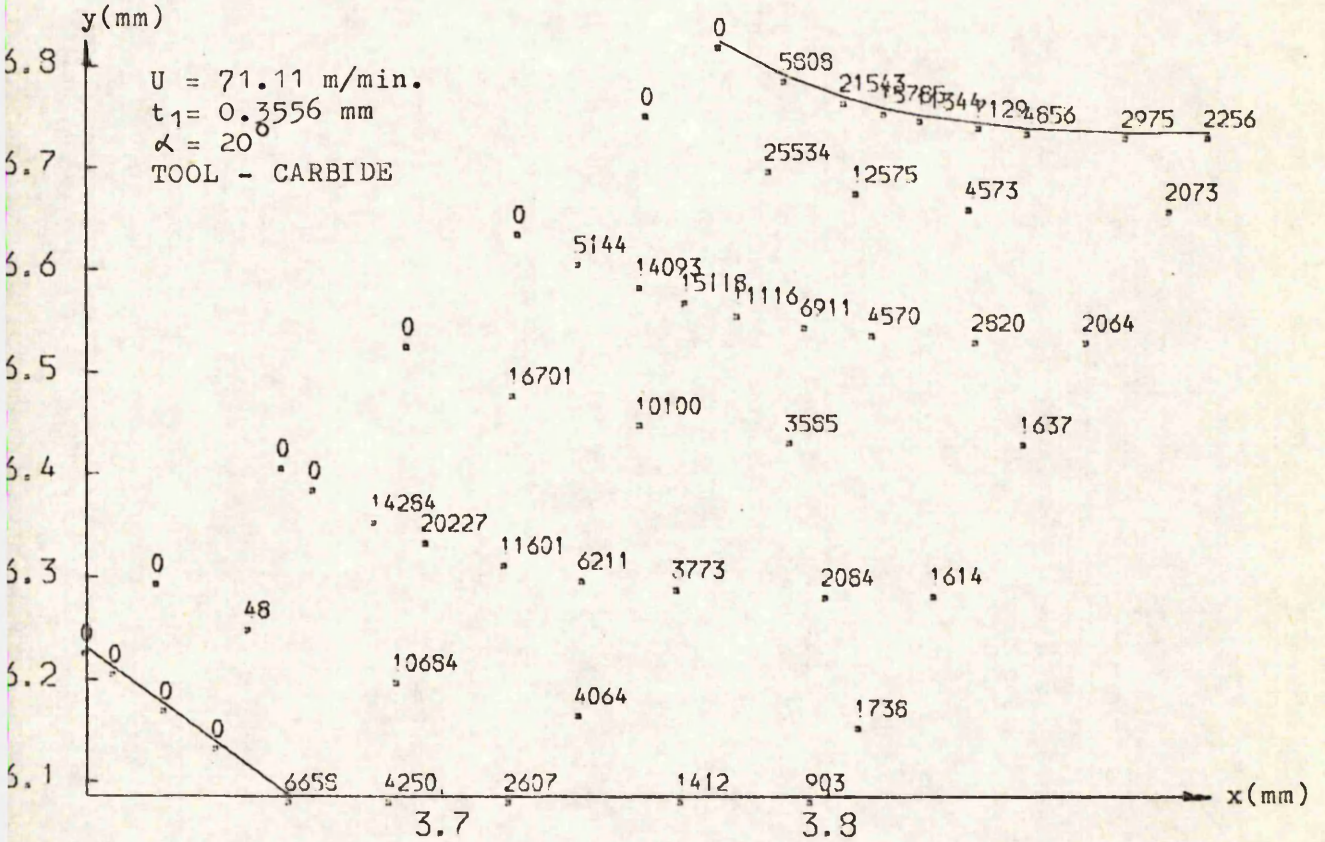

FIG. 5.11 (b)

STRAIN-RATE DISTRIBUTION IN DEFORMATION ZONE, (1/SEC)
TEST NO.= 15

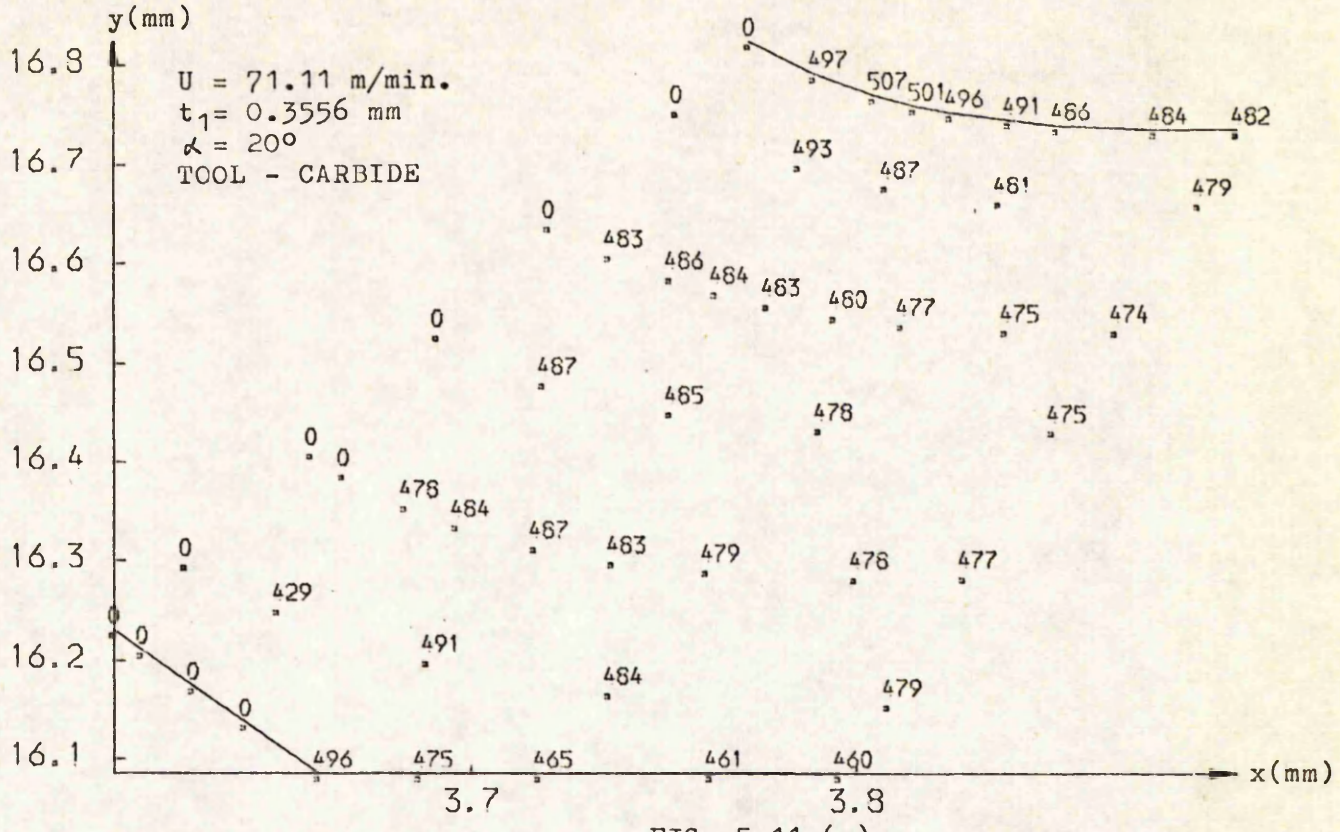

FIG. 5.11 (c)

FLOW STRESS DISTRIBUTION (MEGA PASCALS)
TEST NO.= 15

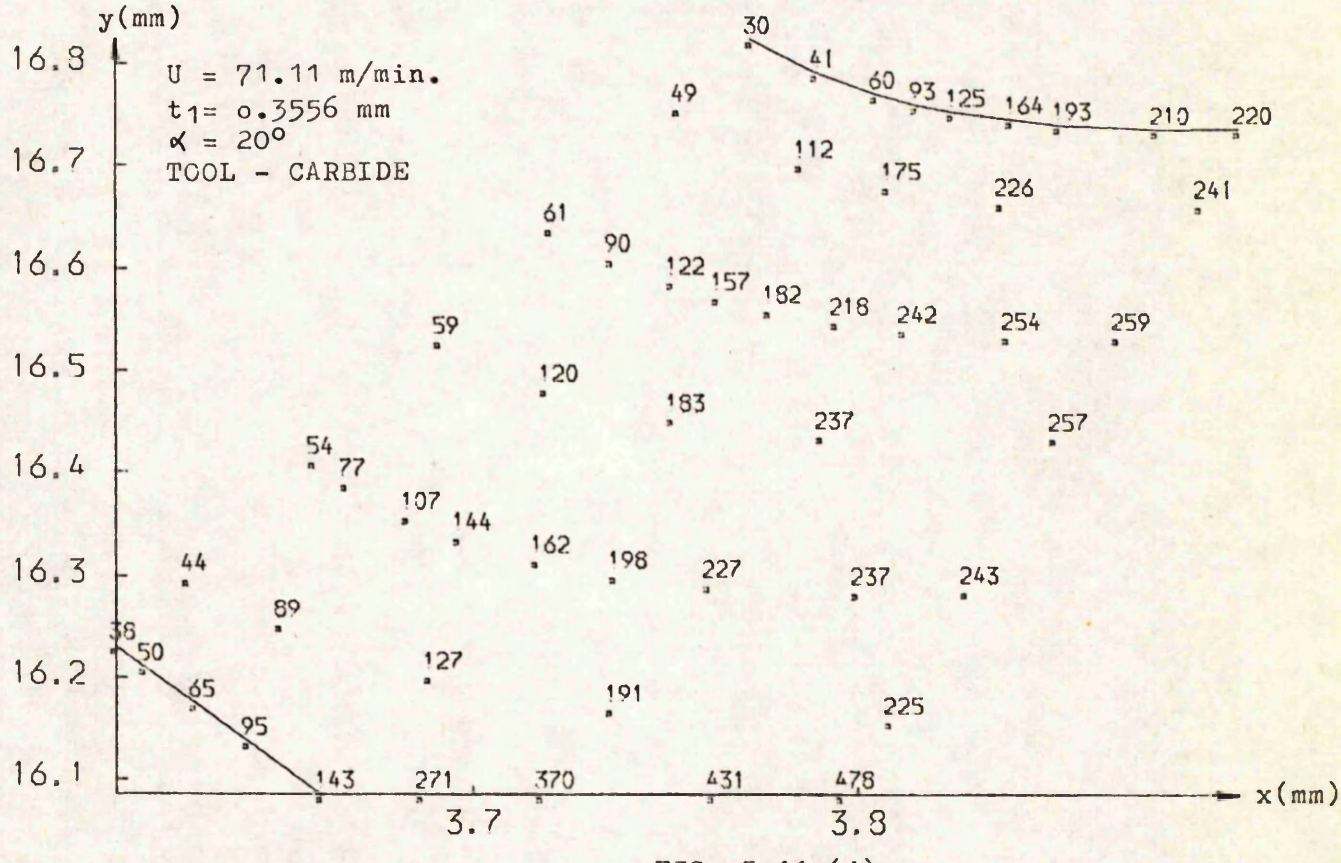

FIG. 5.11 (d)

TEMPERATURE DISTRIBUTION IN DEFORMATION ZONE, (O C)
TEST NO.= 15

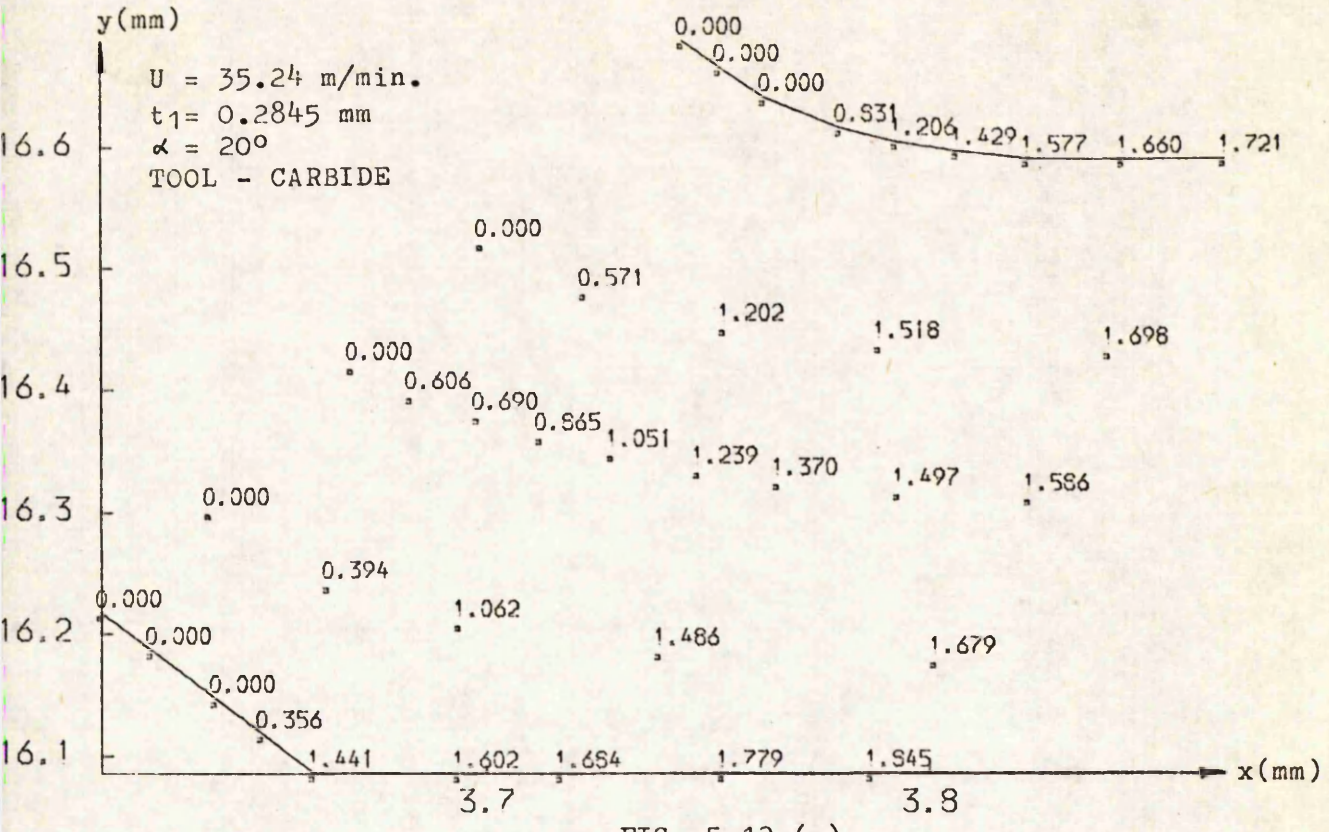

FIG. 5.12 (a)

THE DISTRIBUTION OF TOTAL STRAIN
TEST NO.= 17

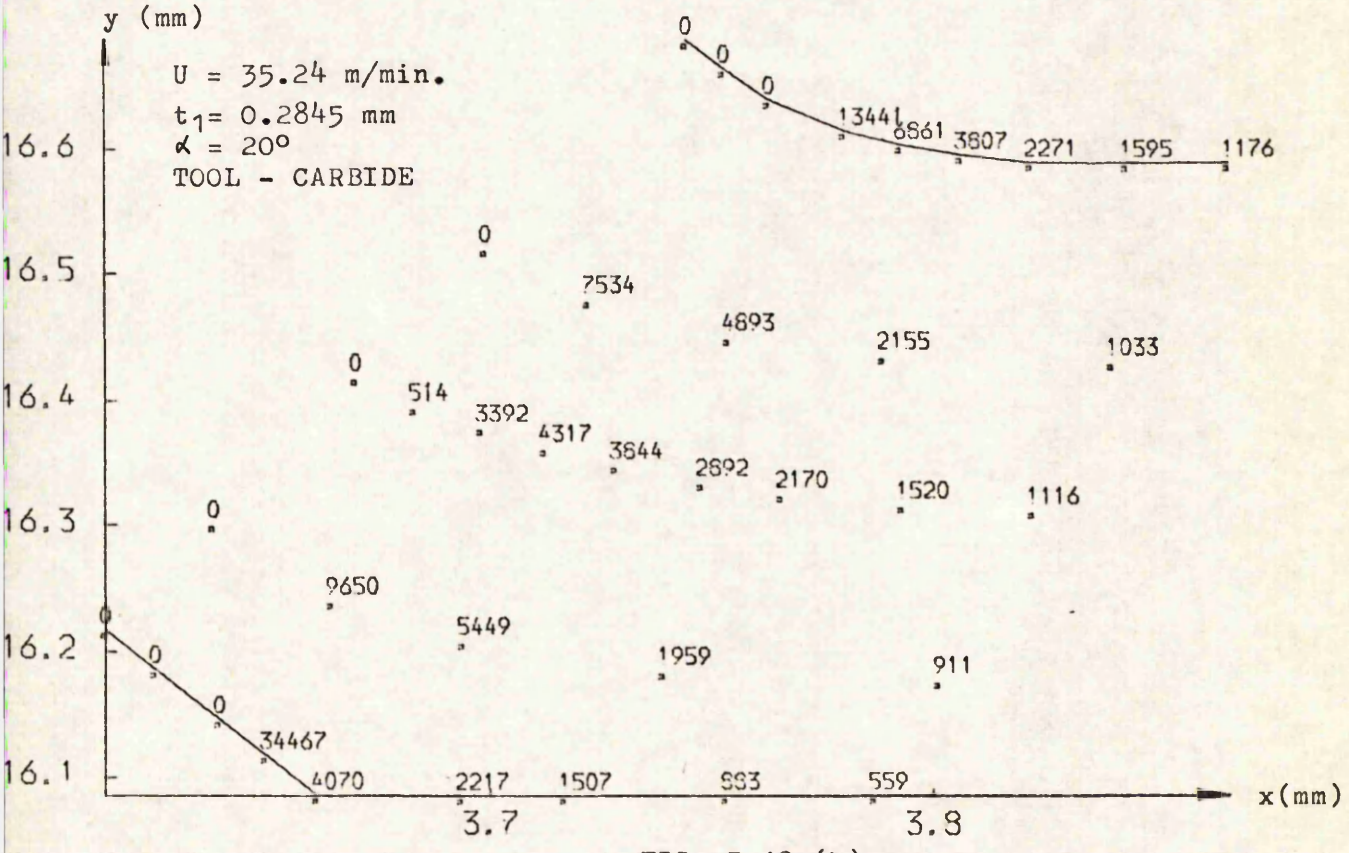

FIG. 5.12 (b)

STRAIN-RATE DISTRIBUTION IN DEFORMATION ZONE, (1/SEC)
TEST NO.= 17

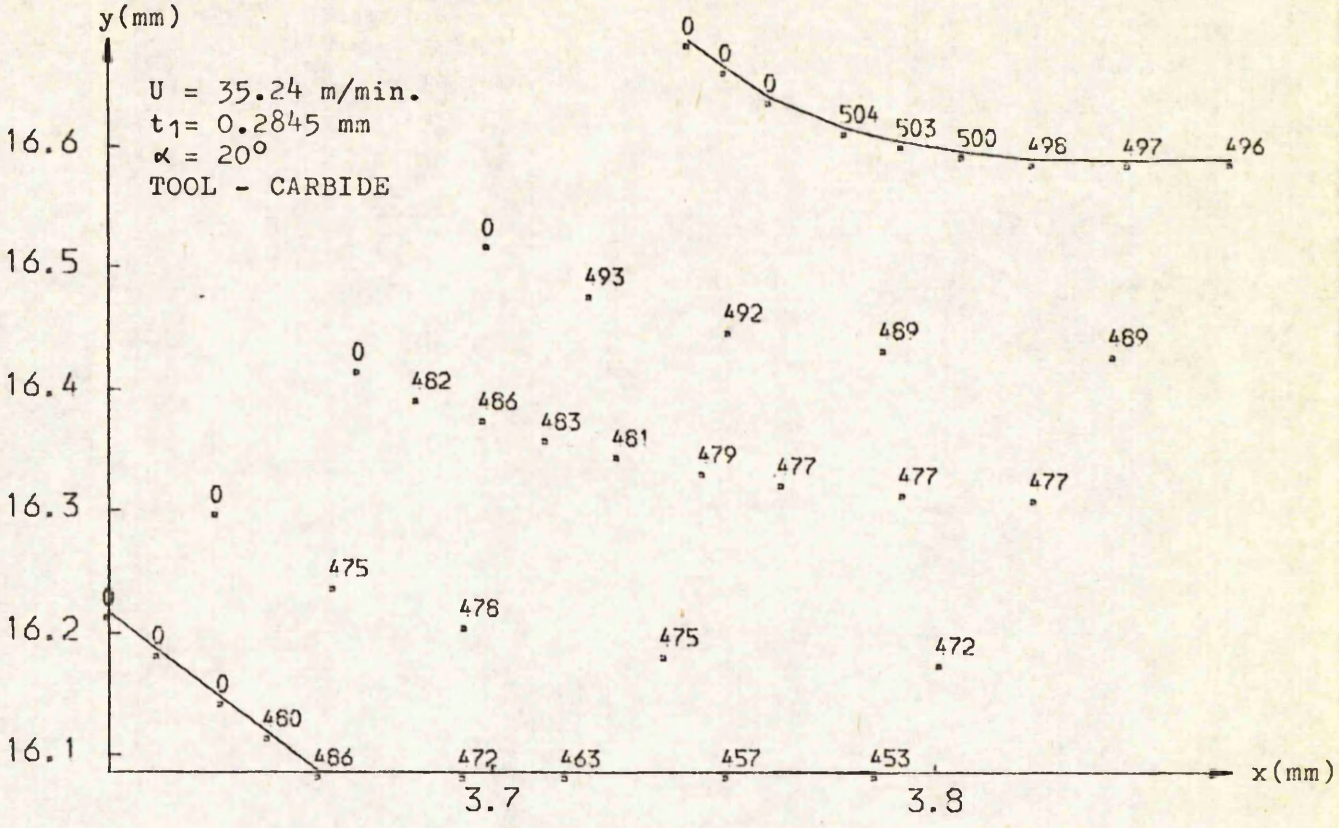

FIG. 5.12 (c)
FLOW STRESS DISTRIBUTION (MEGA PASCALS)
TEST NO.= 17

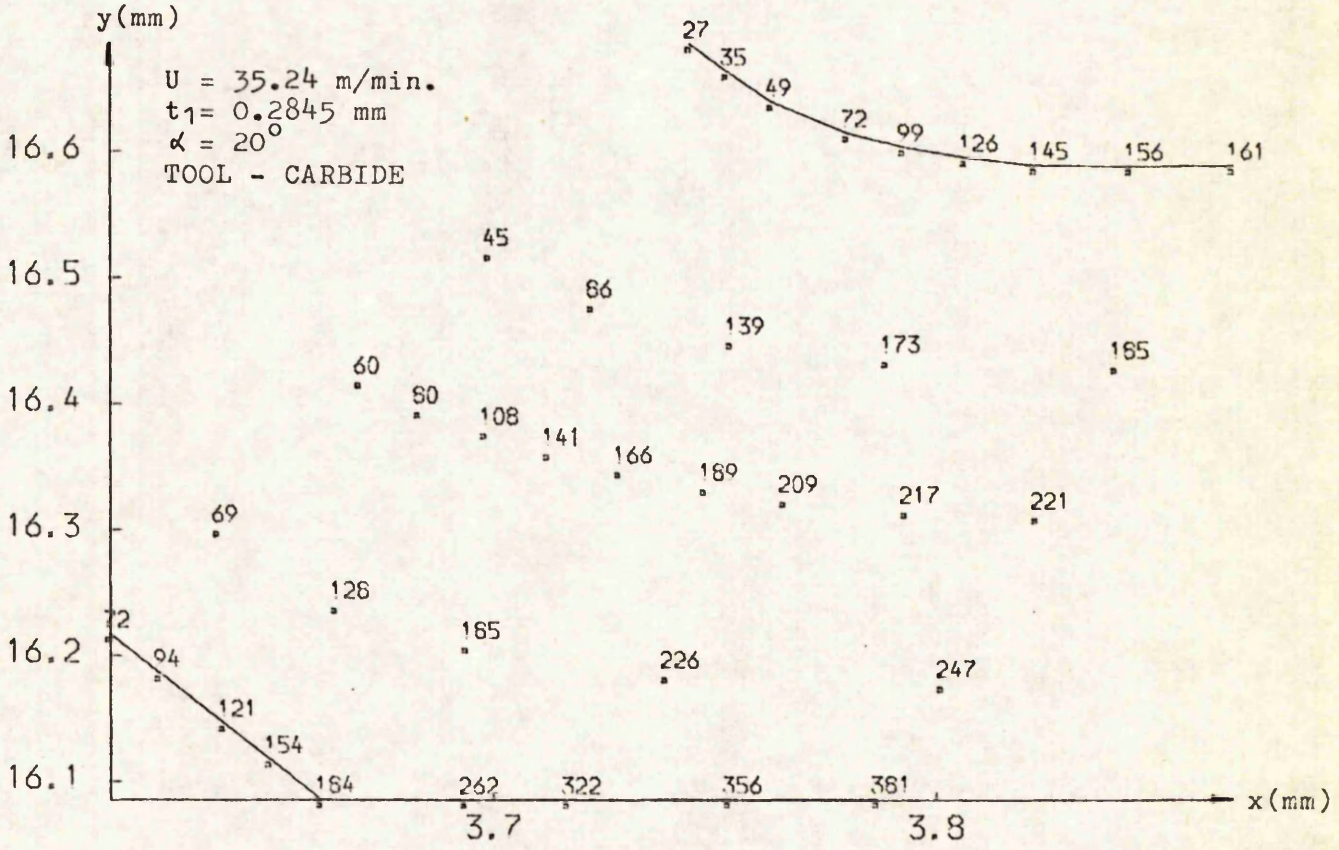

FIG. 5.12 (d)
TEMPERATURE DISTRIBUTION IN DEFORMATION ZONE, (0 C)
TEST NO.= 17

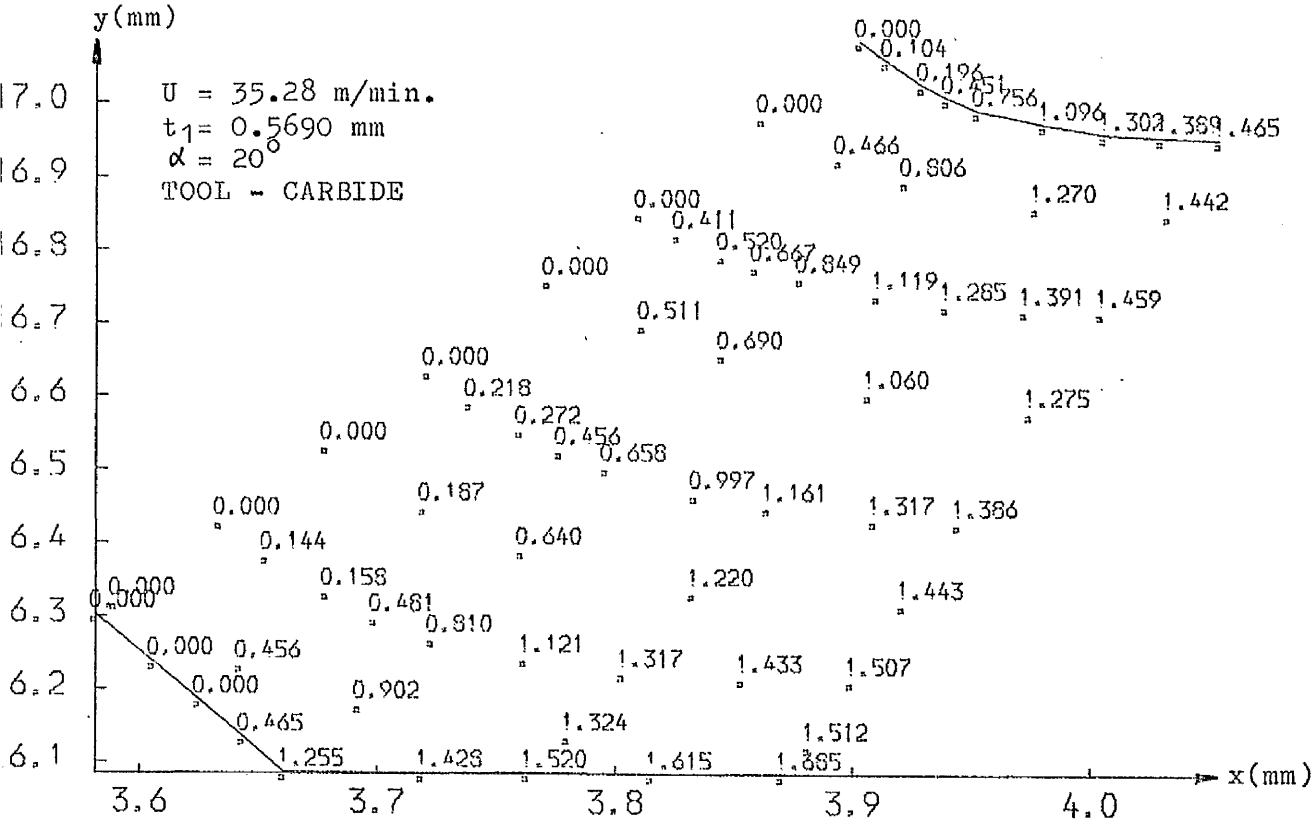

FIG. 5.13 (a)
THE DISTRIBUTION OF TOTAL STRAIN
TEST NO.= 18

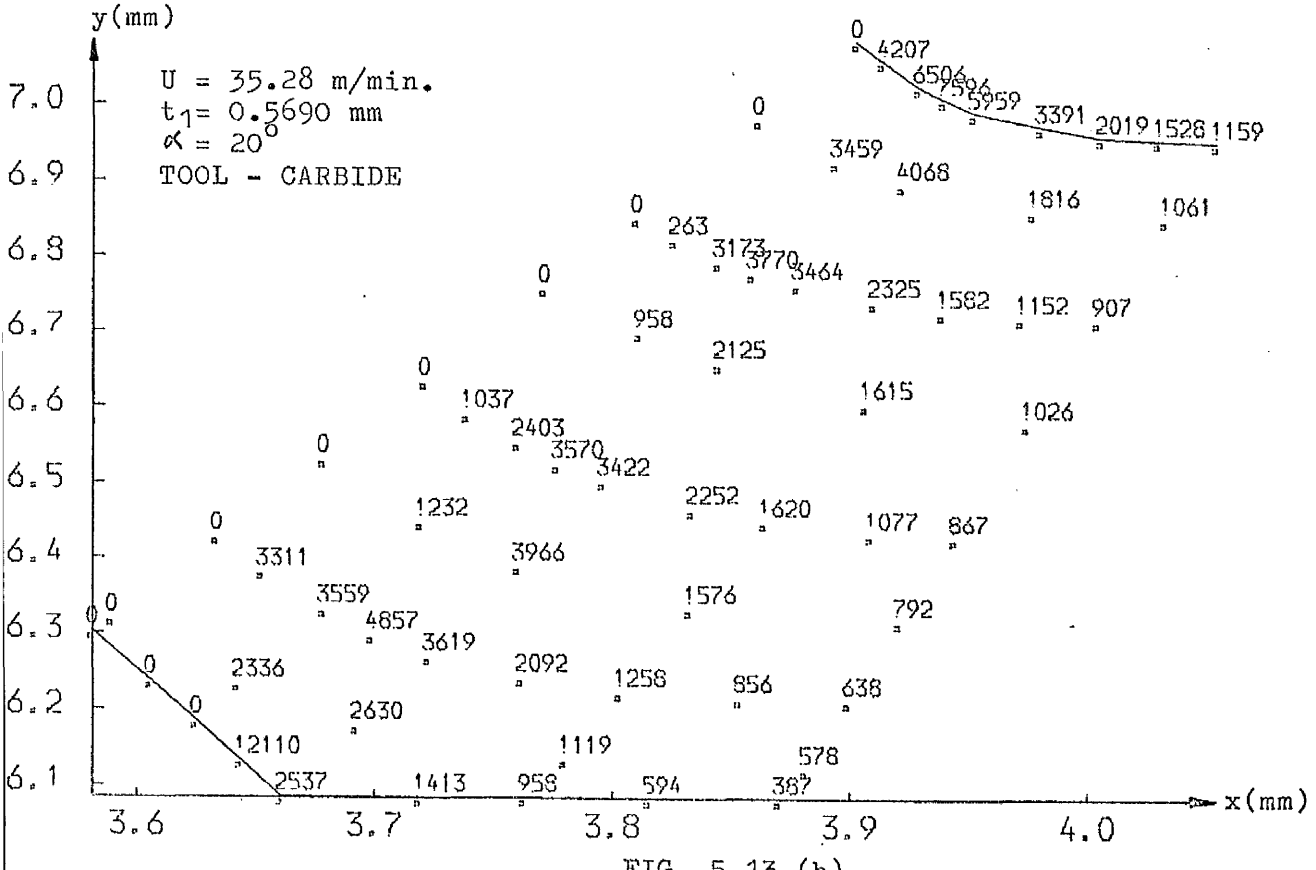

FIG. 5.13 (b)
STRAIN-RATE DISTRIBUTION IN DEFORMATION ZONE, (1/SEC)
TEST NO.= 18

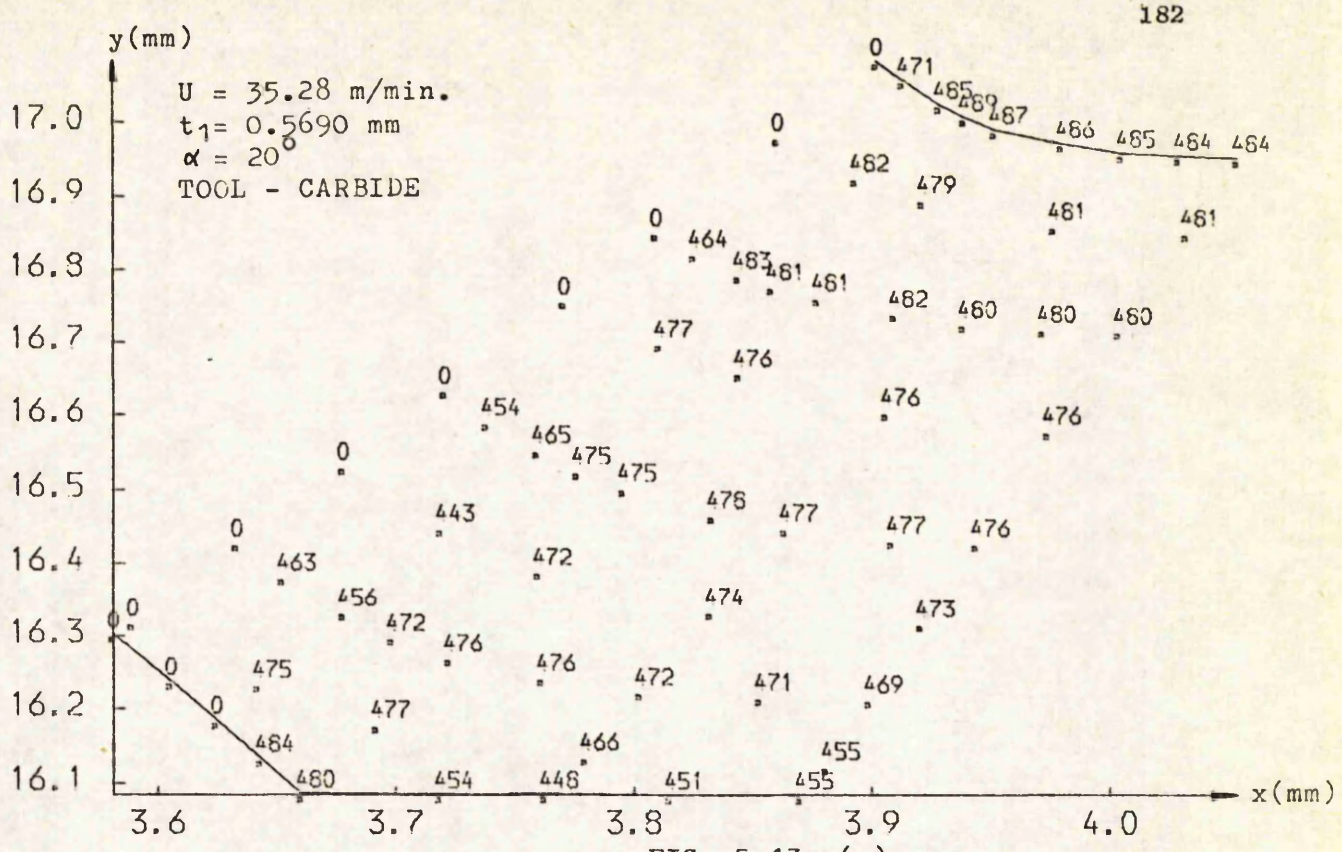

FIG. 5.13 (c)

FLOW STRESS DISTRIBUTION (MEGA PASCALS)
TEST NO.= 18

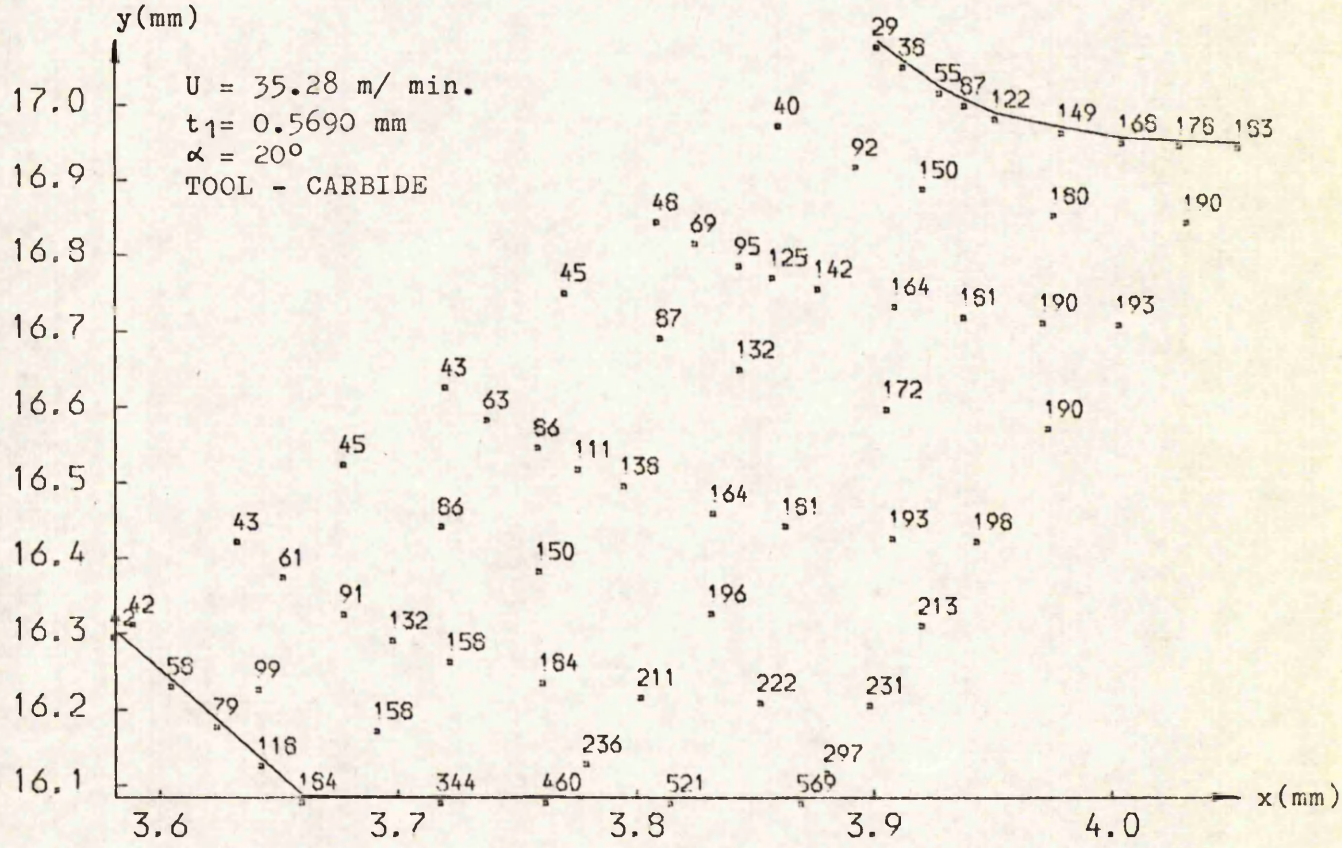

FIG. 5.13 (d)

TEMPERATURE DISTRIBUTION IN DEFORMATION ZONE, (O C)
TEST NO.= 18

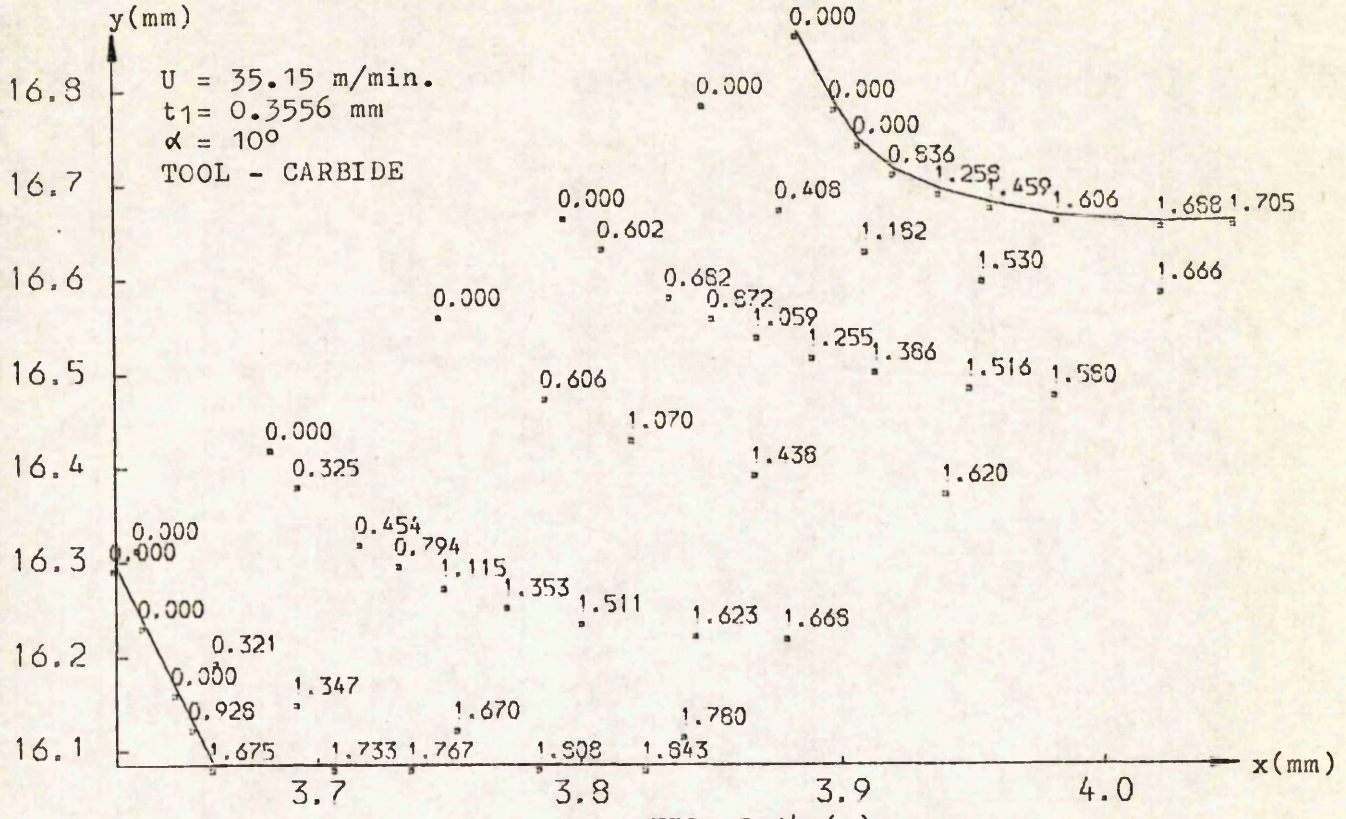

FIG. 5.14 (a)

THE DISTRIBUTION OF TOTAL STRAIN
TEST NO.= 19

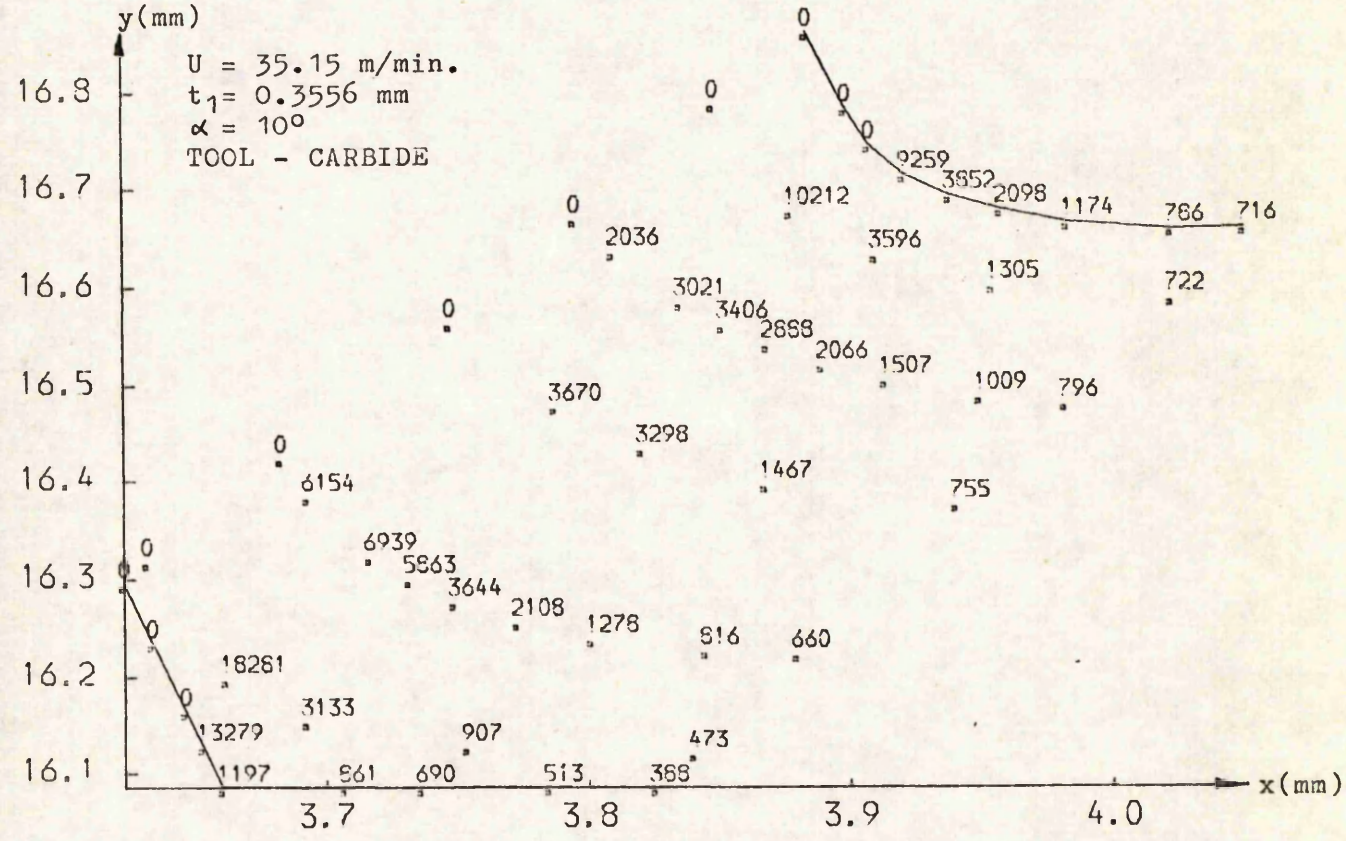

FIG. 5.14 (b)

STRAIN-RATE DISTRIBUTION IN DEFORMATION ZONE, (1/SEC)
TEST NO.= 19

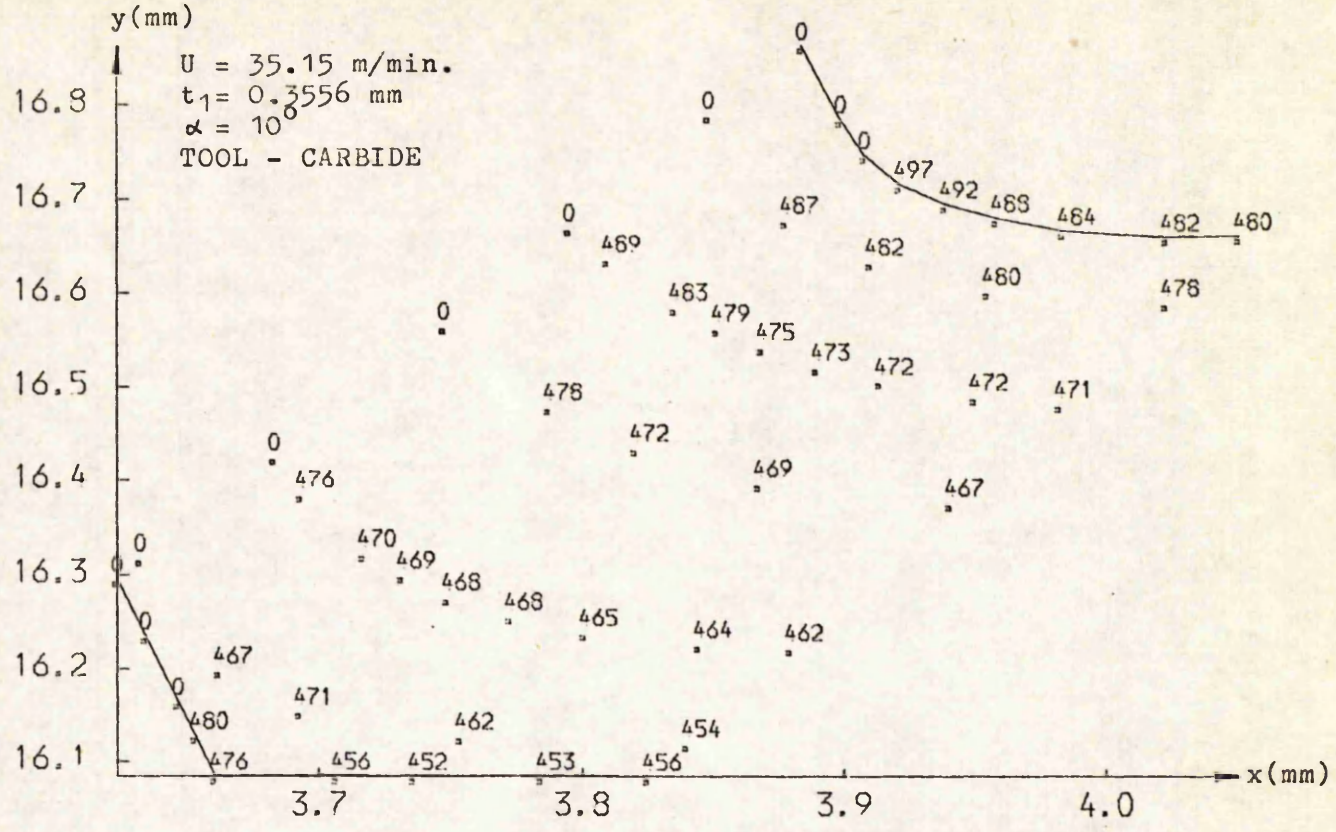

FIG. 5.14 (c)

FLOW STRESS DISTRIBUTION (MEGA PASCALS)
TEST NO.= 19

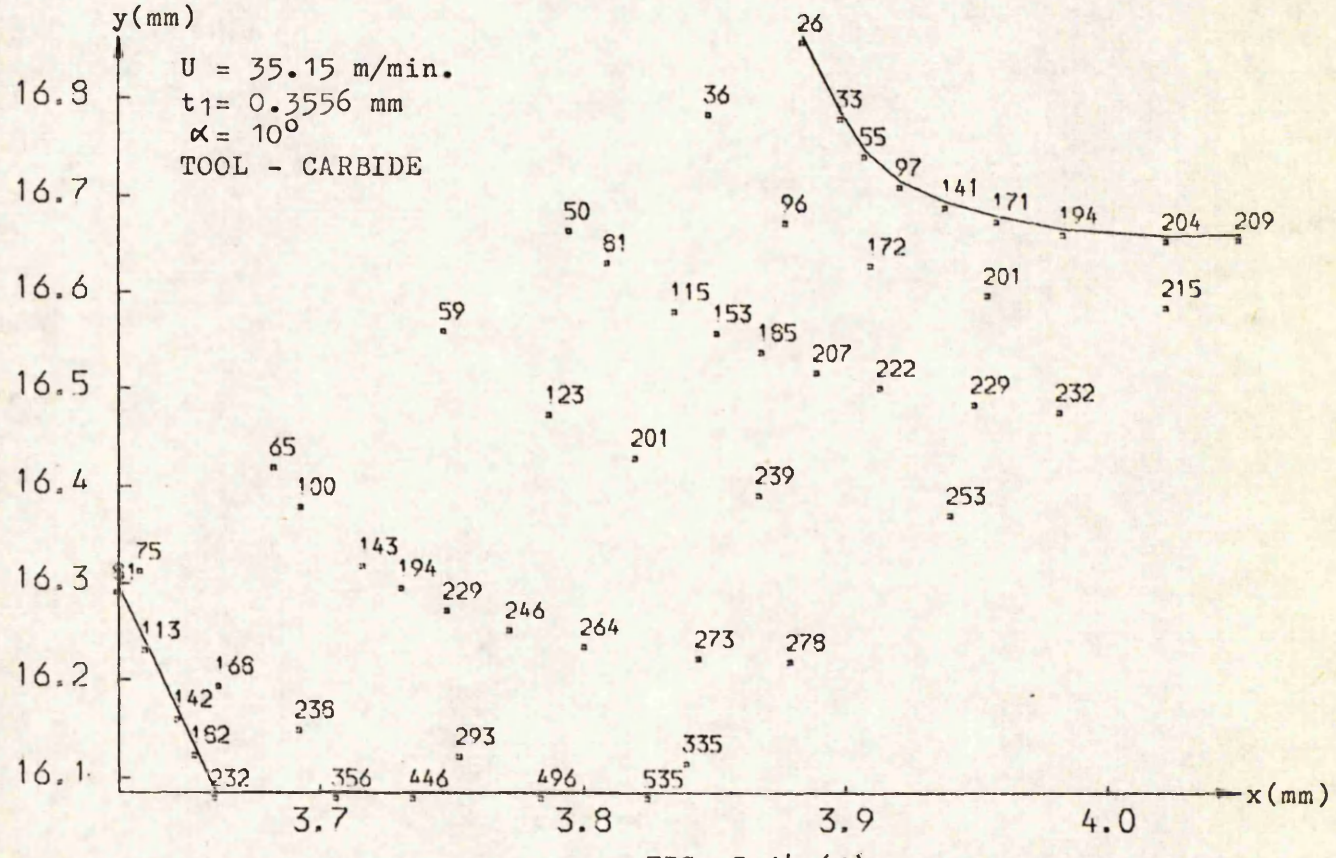

FIG. 5.14 (d)

TEMPERATURE DISTRIBUTION IN DEFORMATION ZONE, (O C)
TEST NO.= 19

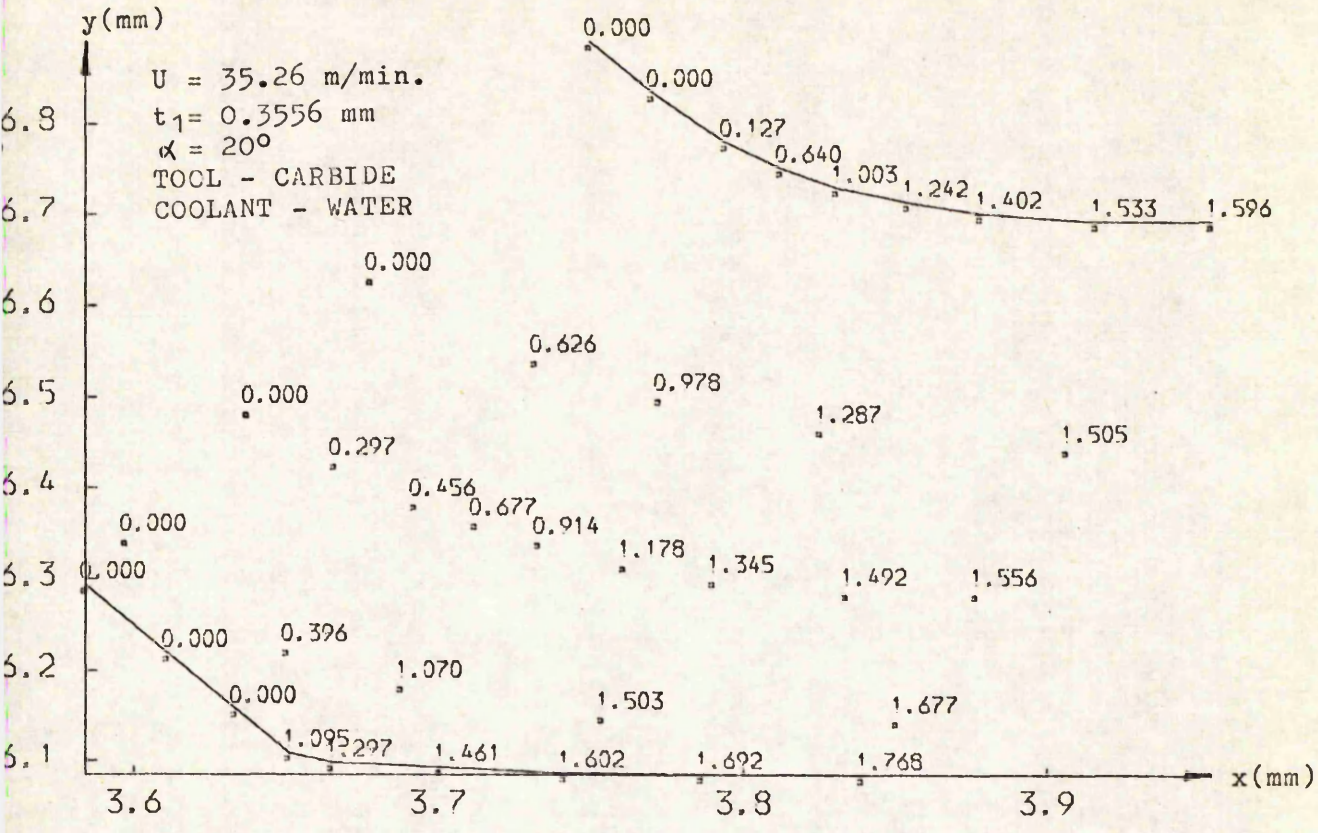

FIG. 5.15 (a)
THE DISTRIBUTION OF TOTAL STRAIN
TEST NO.= 21

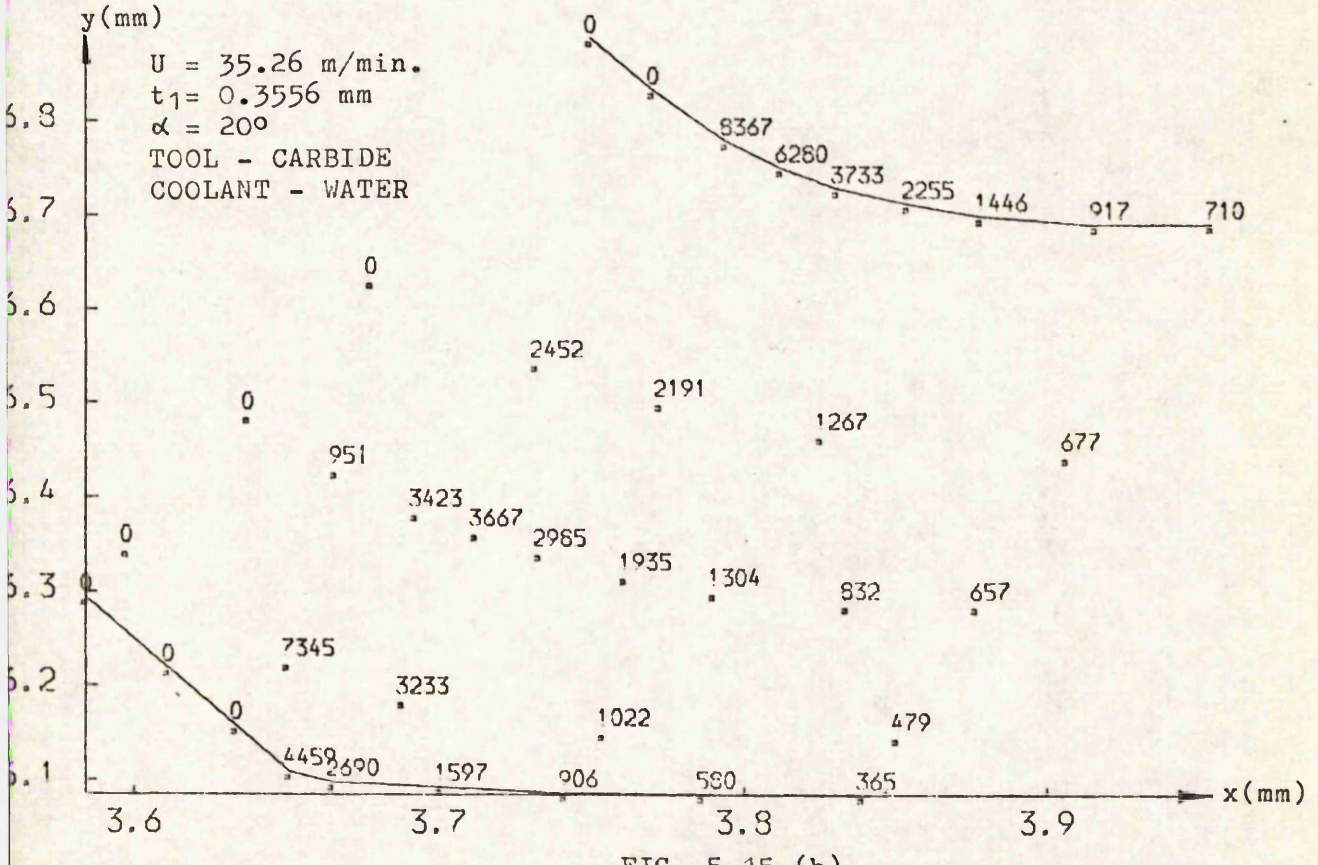

FIG. 5.15 (b)
STRAIN-RATE DISTRIBUTION IN DEFORMATION ZONE, (1/SEC)
TEST NO.= 21

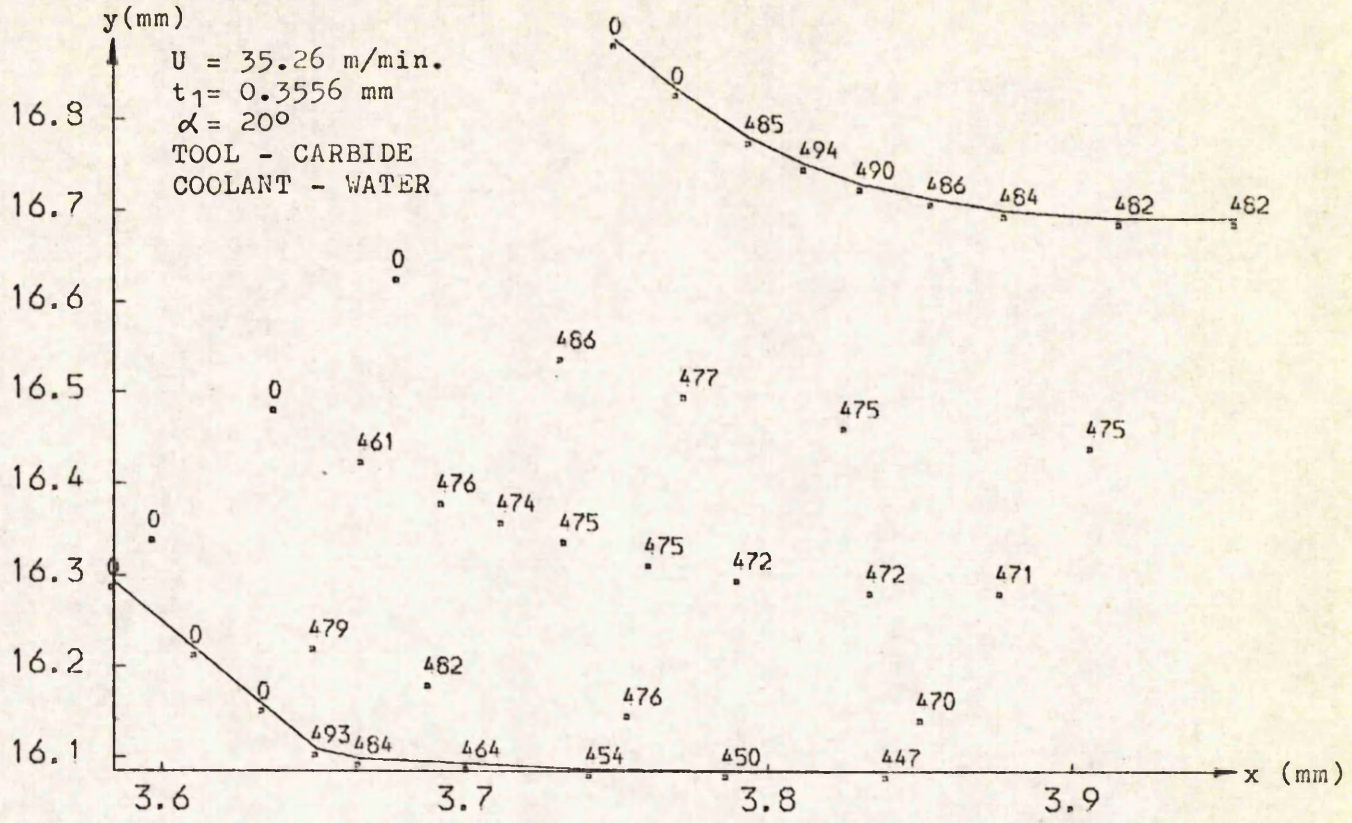

FIG. 5.15 (c)
FLOW STRESS DISTRIBUTION (MEGA PASCALS)
TEST NO. = 21

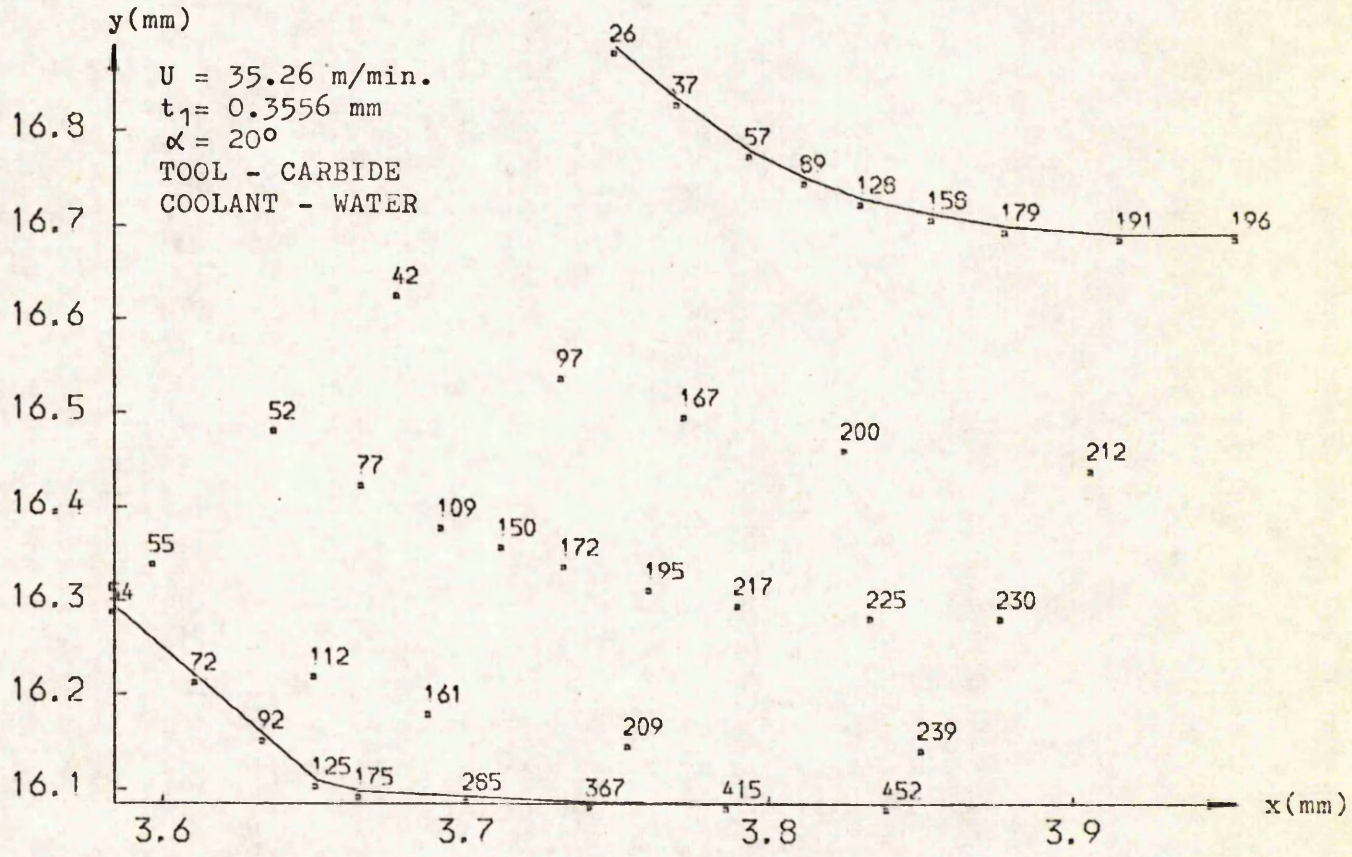

FIG. 5.15 (d)
TEMPERATURE DISTRIBUTION IN DEFORMATION ZONE, (O C)
TEST NO. = 21

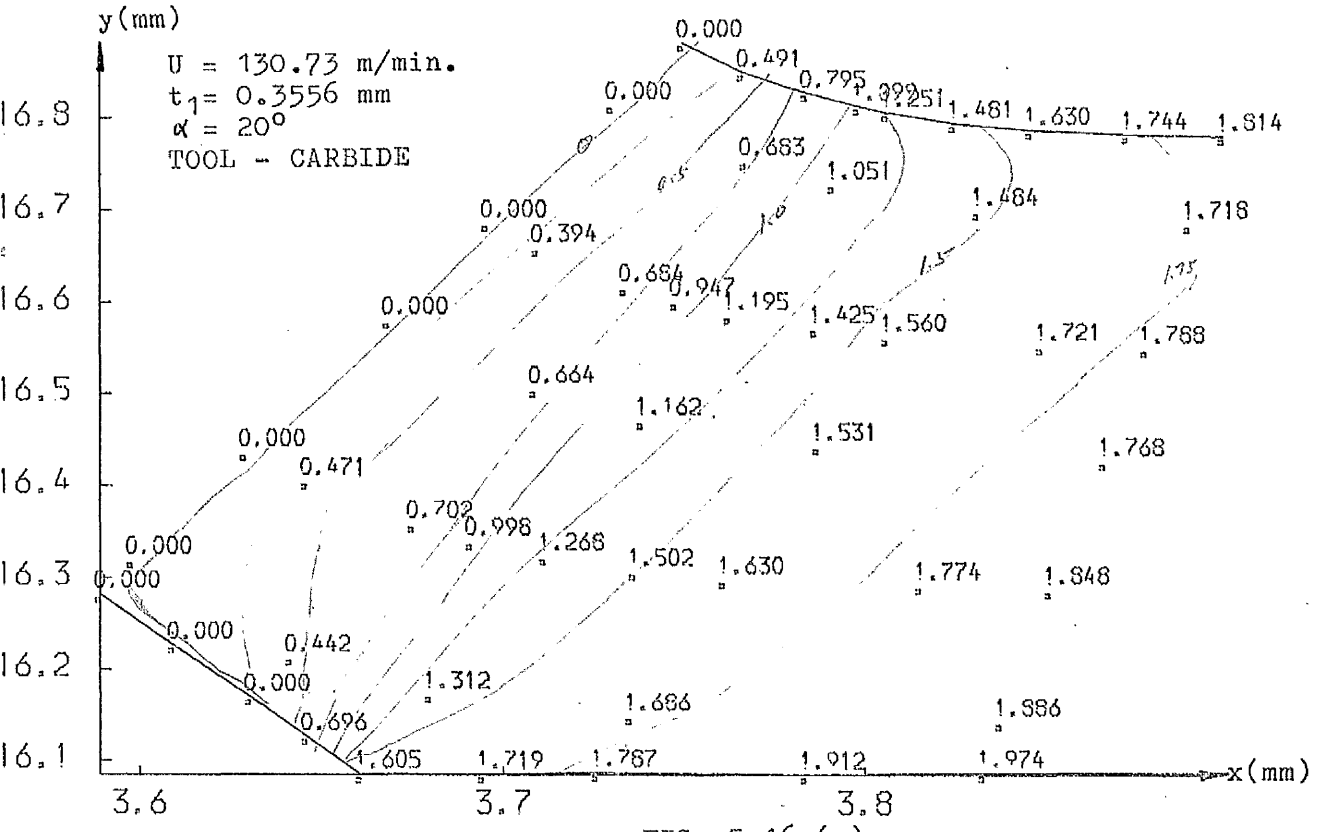

FIG. 5.16 (a)

THE DISTRIBUTION OF TOTAL STRAIN
TEST NO.= 23

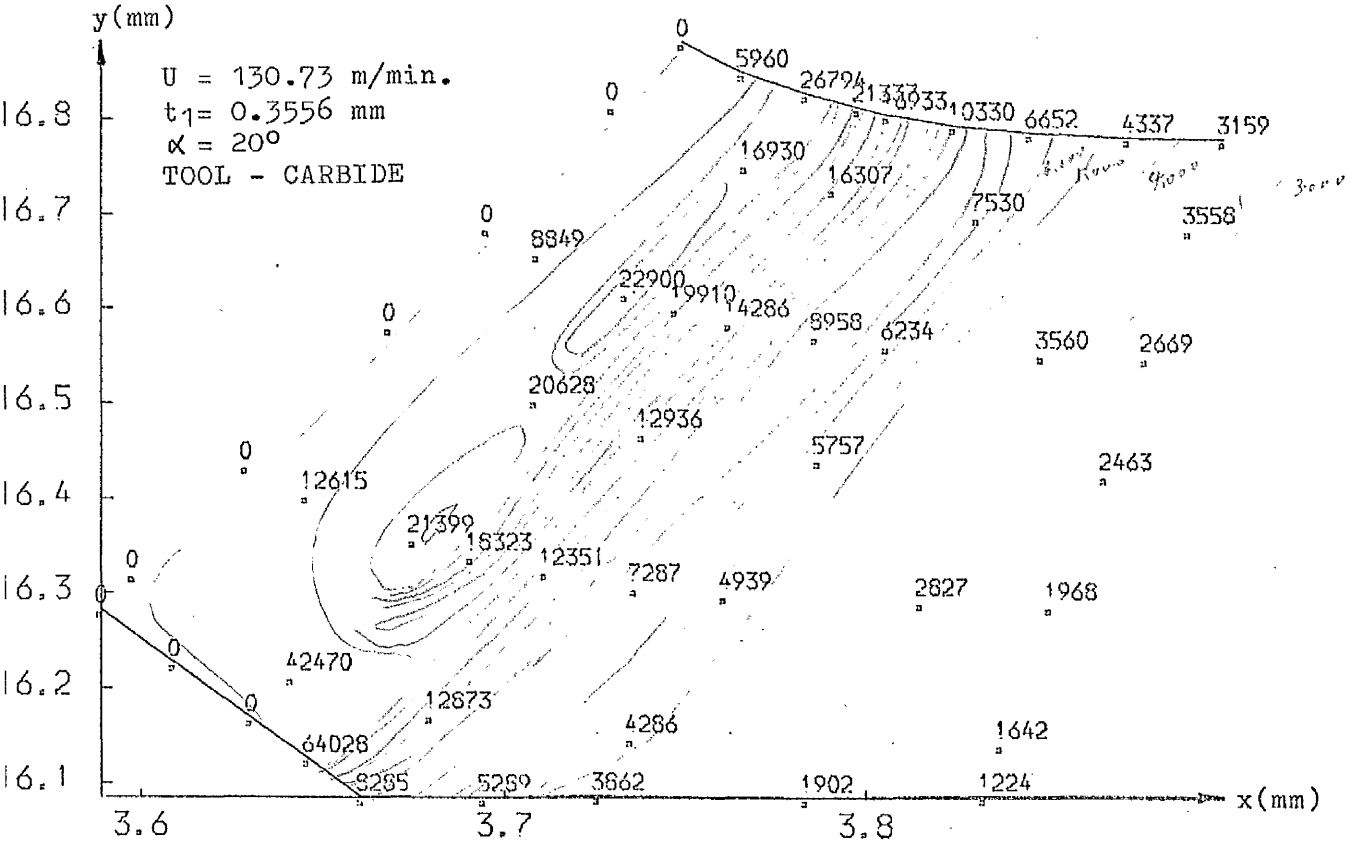

FIG. 5.16 (b)

STRAIN-RATE DISTRIBUTION IN DEFORMATION ZONE, (1/SEC)
TEST NO.= 23

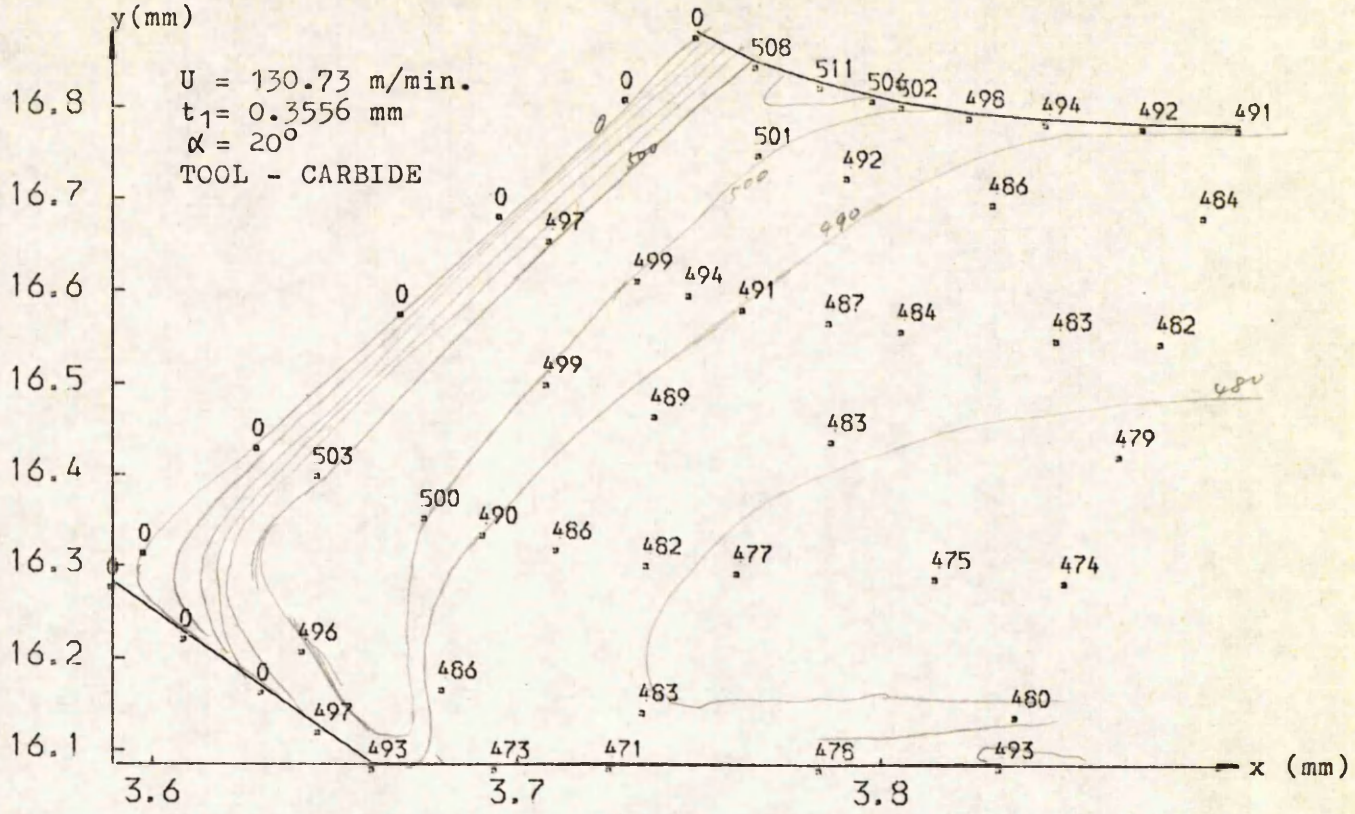

FIG. 5.16 (c)

FLOW STRESS DISTRIBUTION (MEGA PASCALS)
TEST NO.= 23

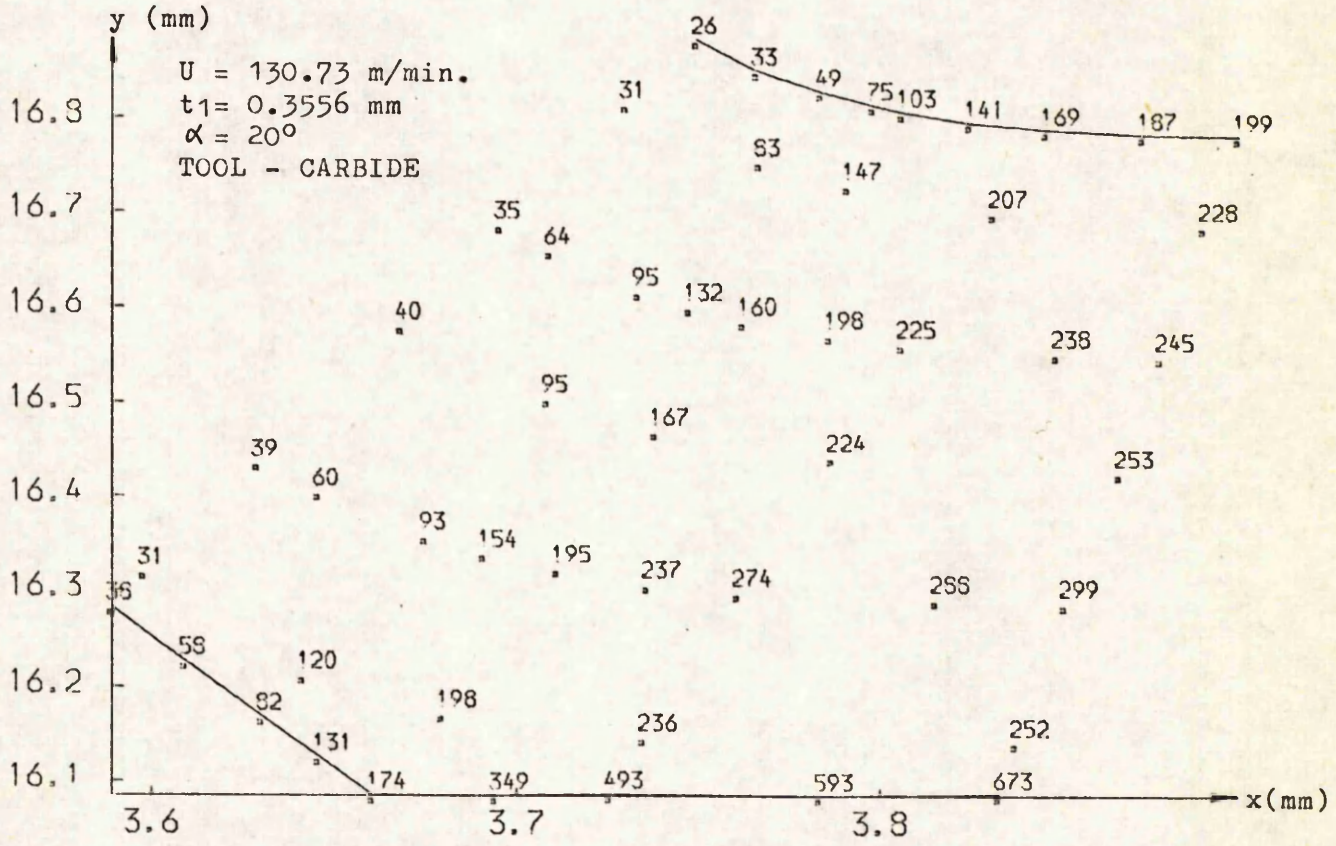

FIG. 5.16 (d)

TEMPERATURE DISTRIBUTION IN DEFORMATION ZONE, (O C)
TEST NO.= 23

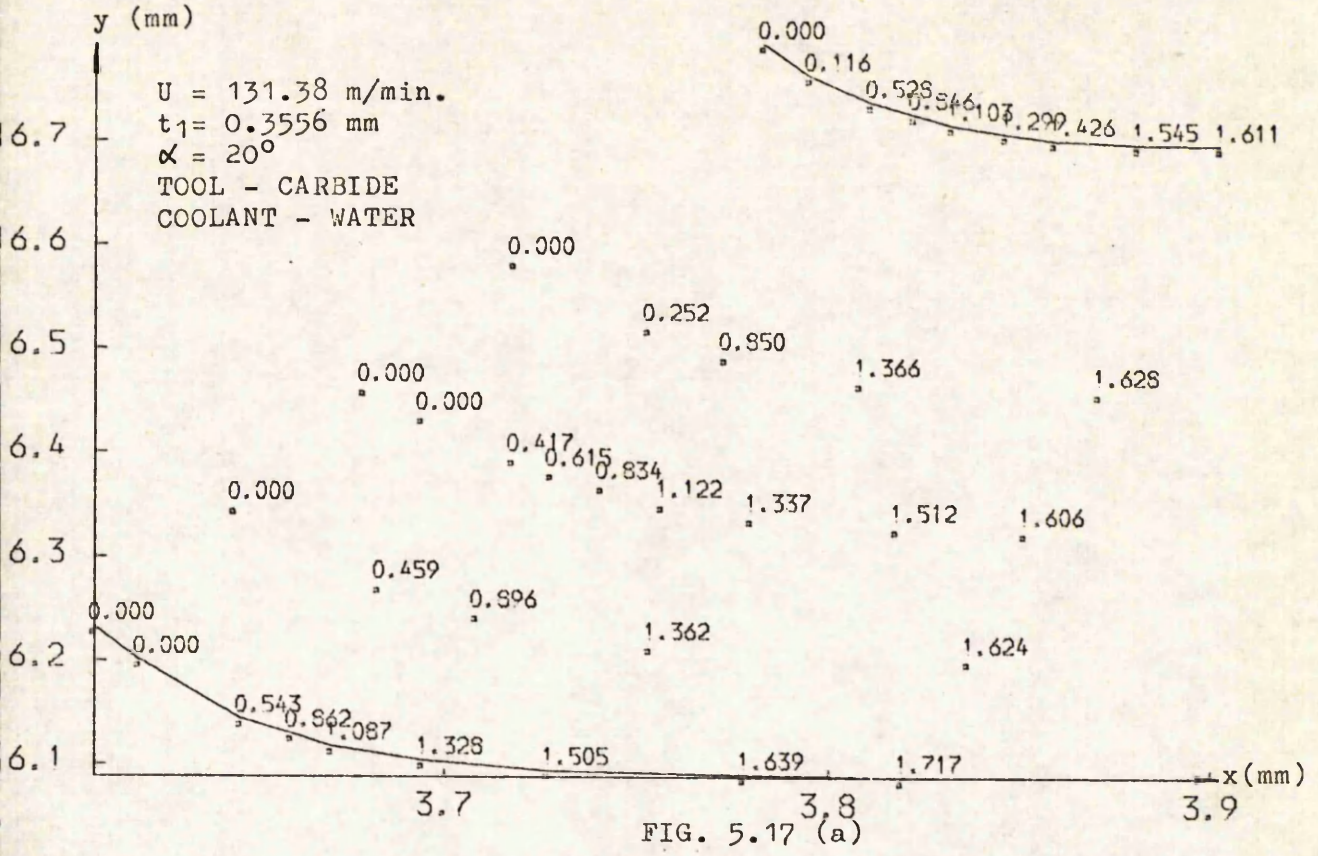

FIG. 5.17 (a)

THE DISTRIBUTION OF TOTAL STRAIN
TEST NO.= 24

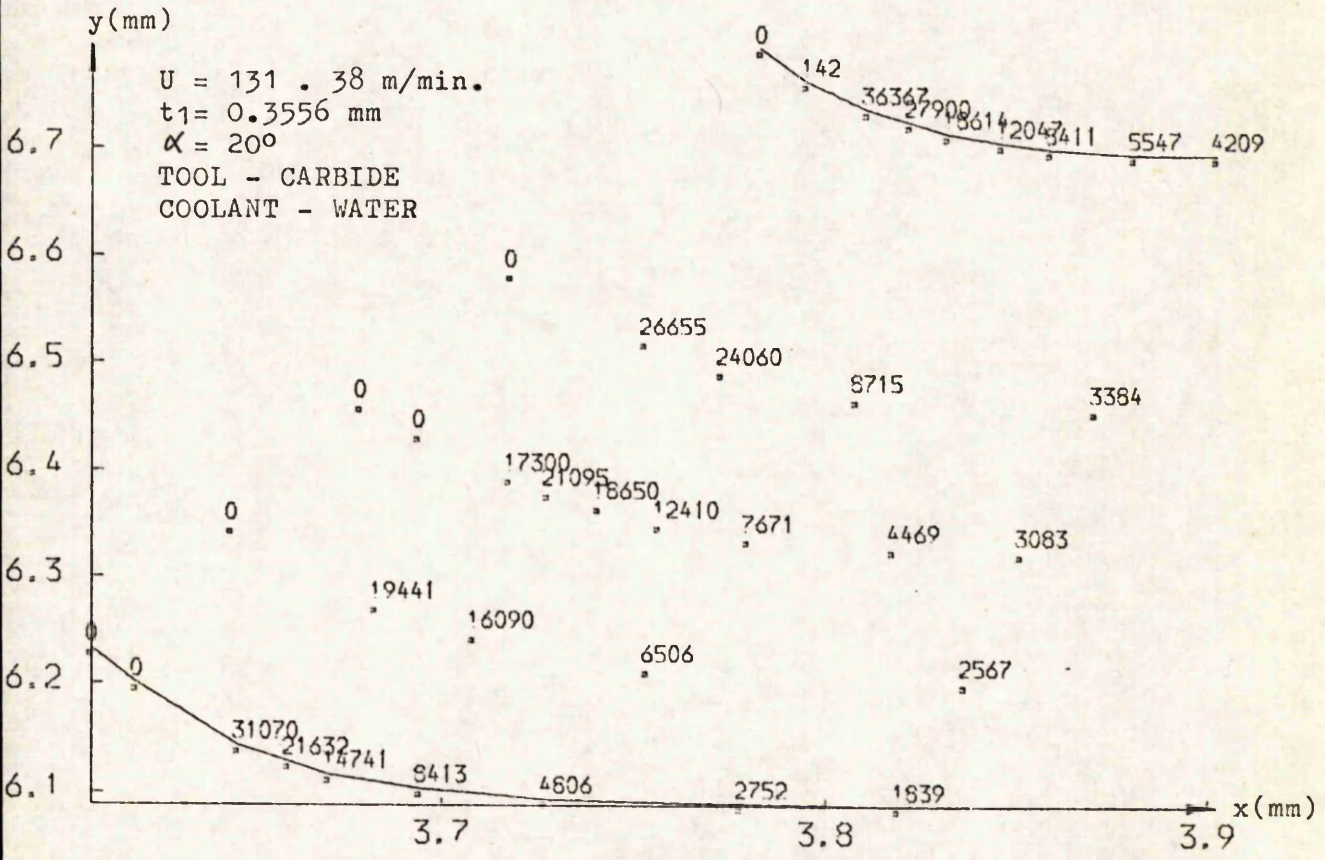

FIG. 5.17 (b)

STRAIN-RATE DISTRIBUTION IN DEFORMATION ZONE, (1/SEC)
TEST NO.= 24

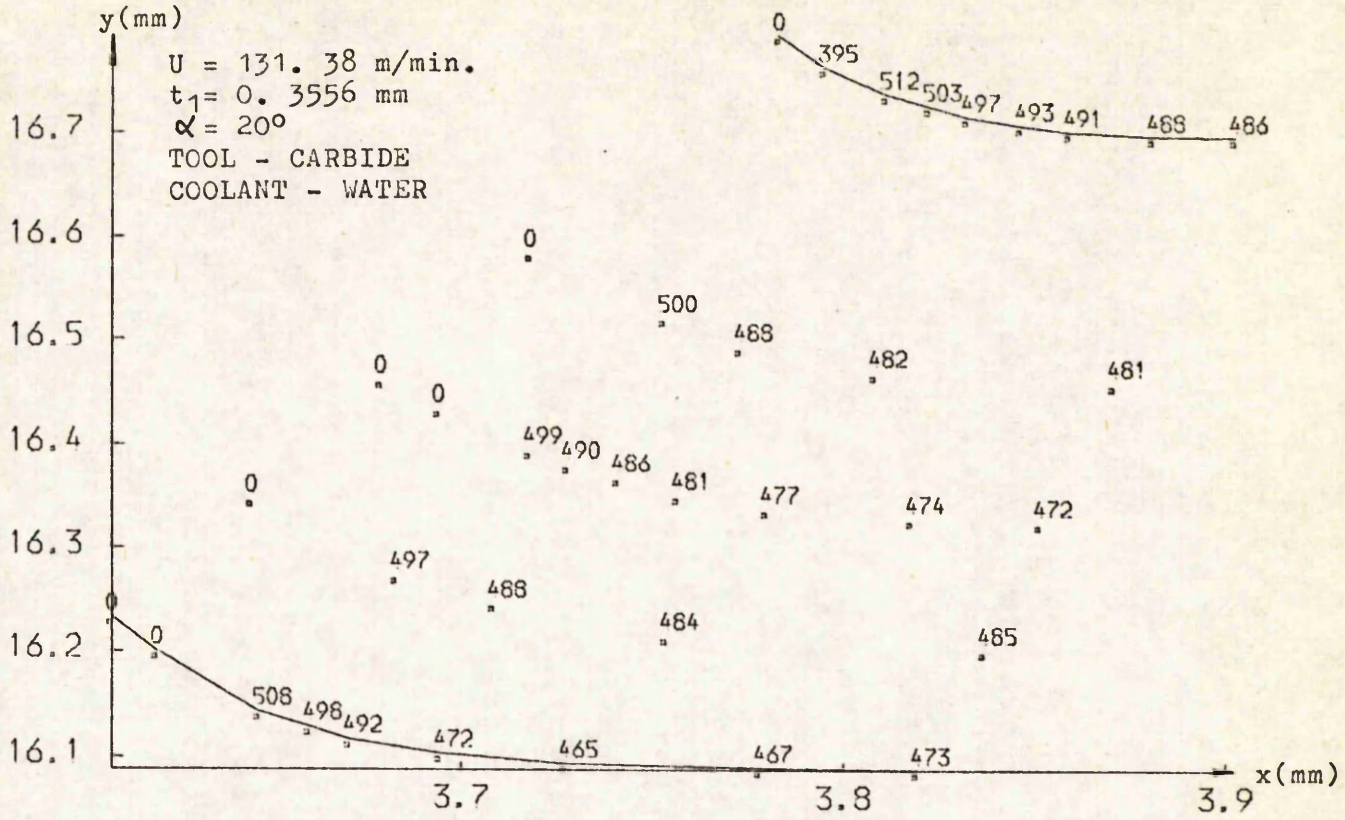

FIG. 5.17 (c)

FLOW STRESS DISTRIBUTION (MEGA PASCALS)
TEST NO.= 24

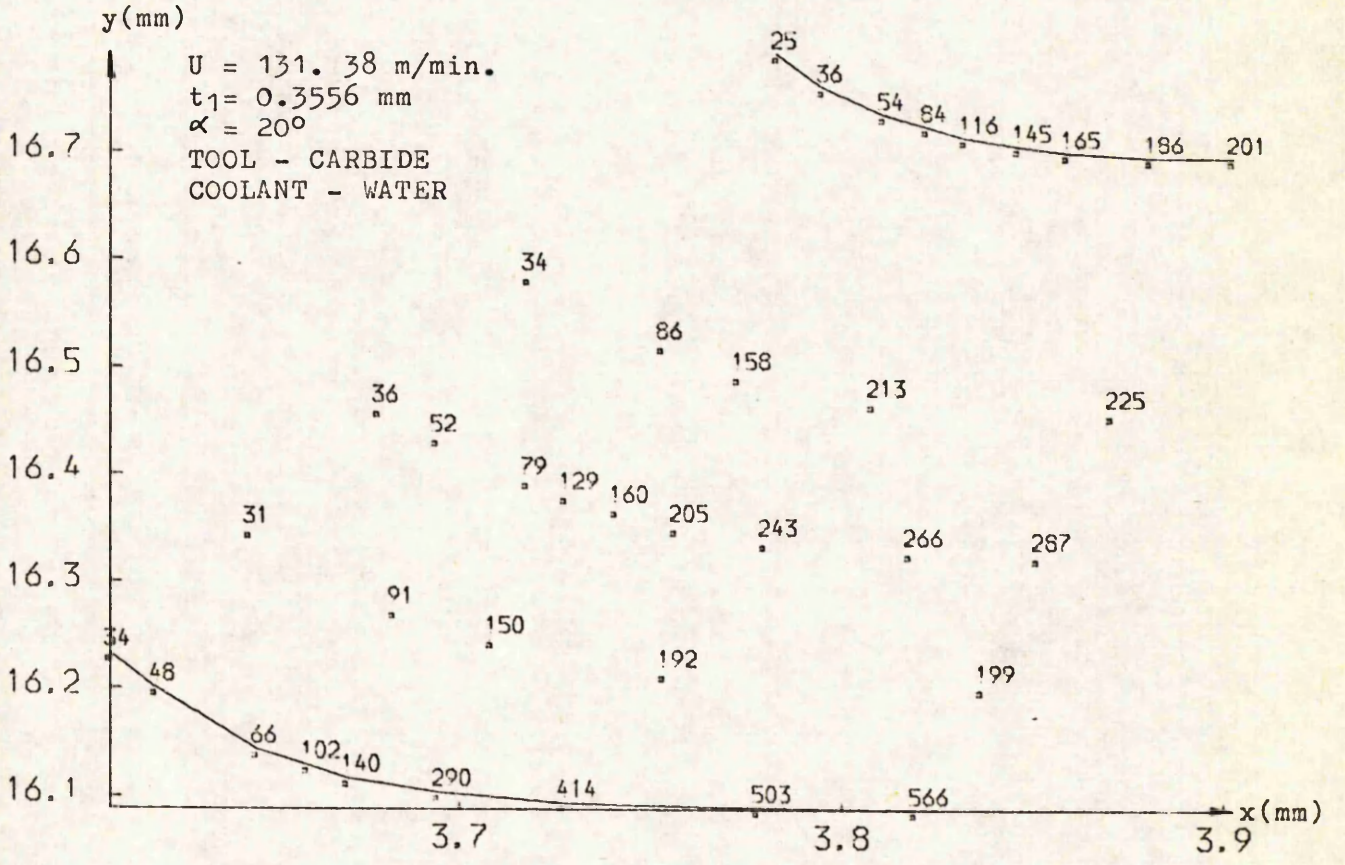

FIG. 5.17 (d)

TEMPERATURE DISTRIBUTION IN DEFORMATION ZONE, (O C)
TEST NO.= 24

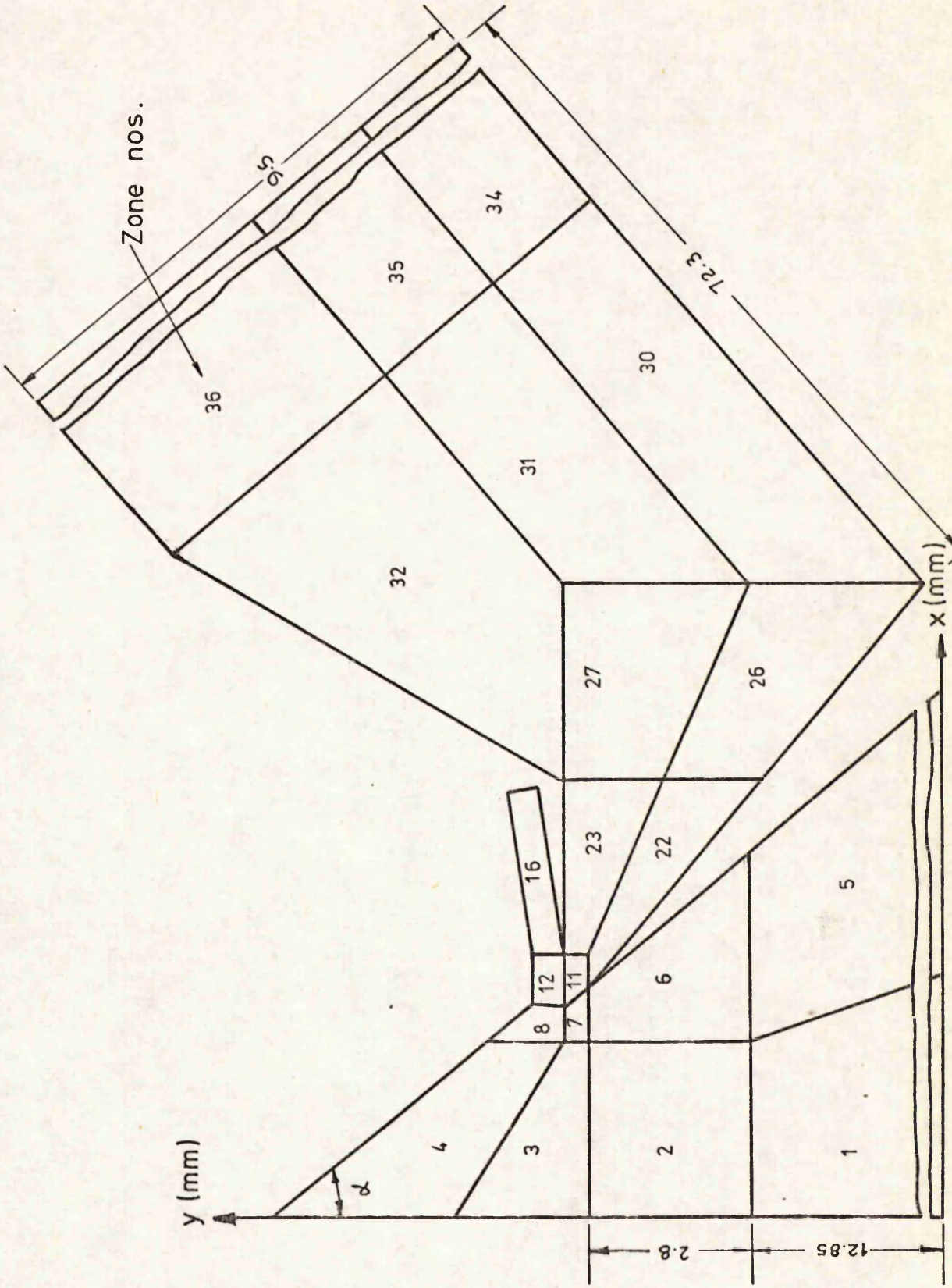

Fig. 5.18 Work-tool-chip composite system for convergence analysis

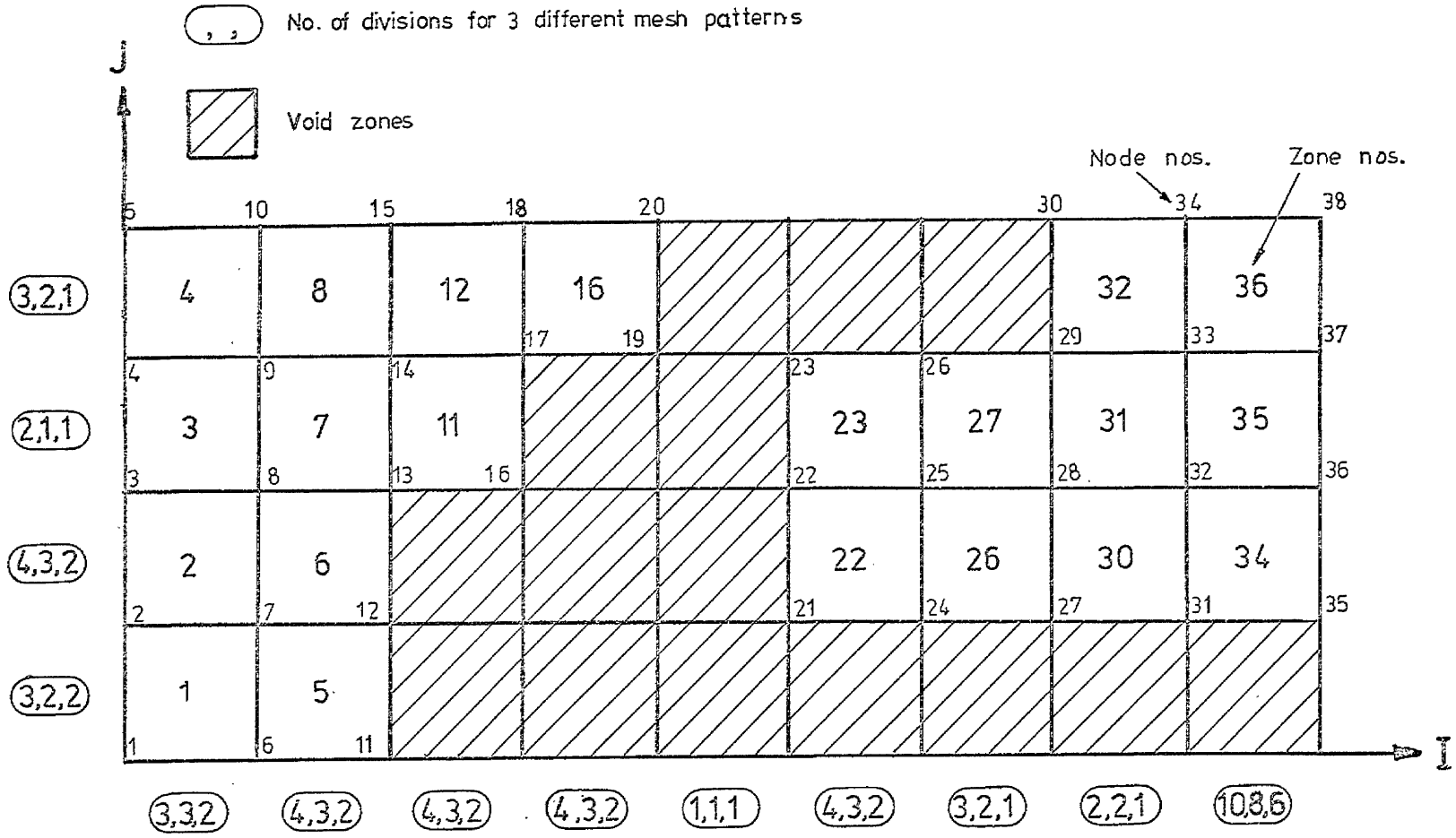

Fig. 5.19 Key diagram

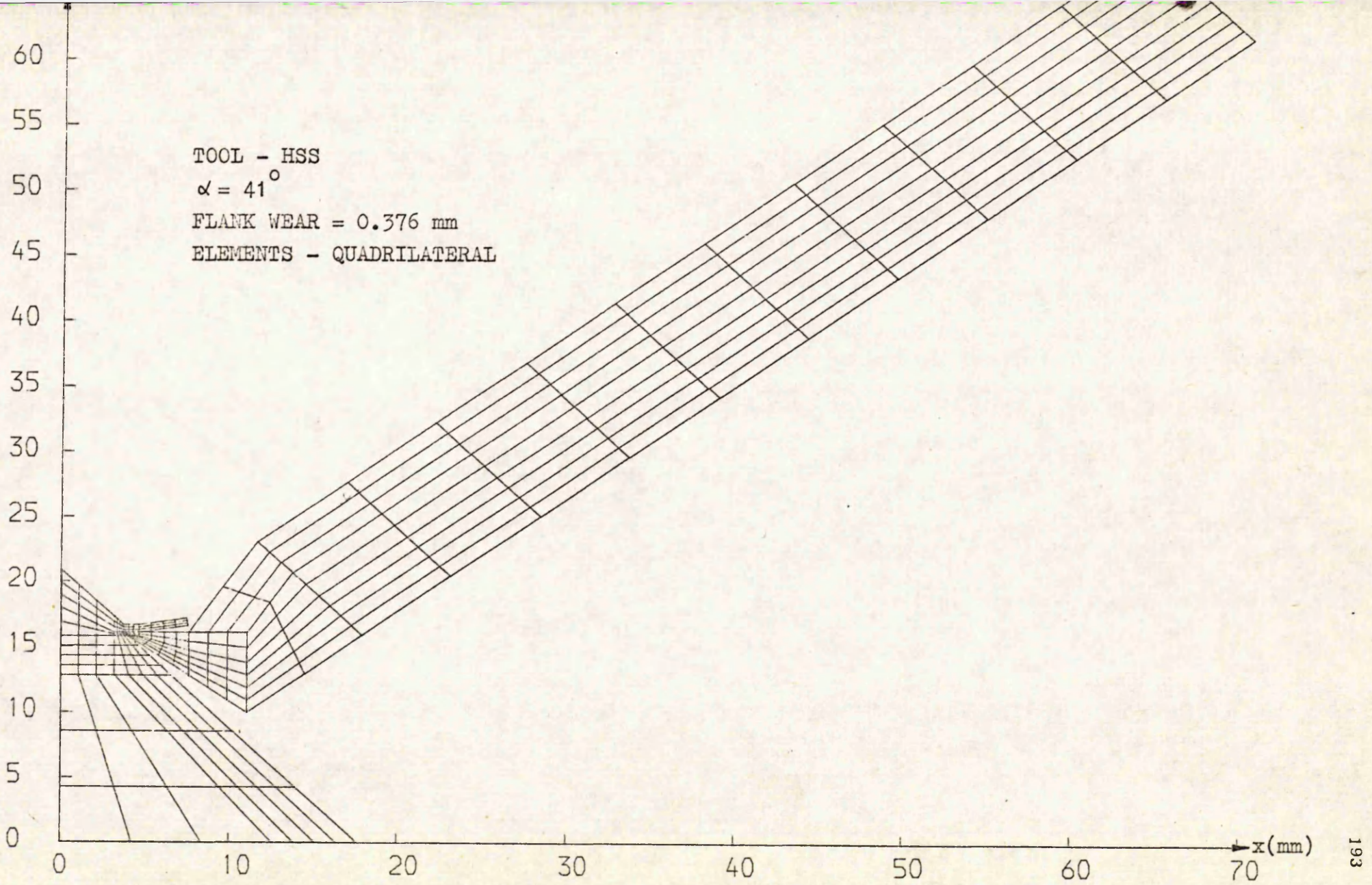

AUTOMATIC MESH GENERATION FOR THERMAL ANALYSIS IN ORTHOGONAL MACHINING

FIG. 5.20

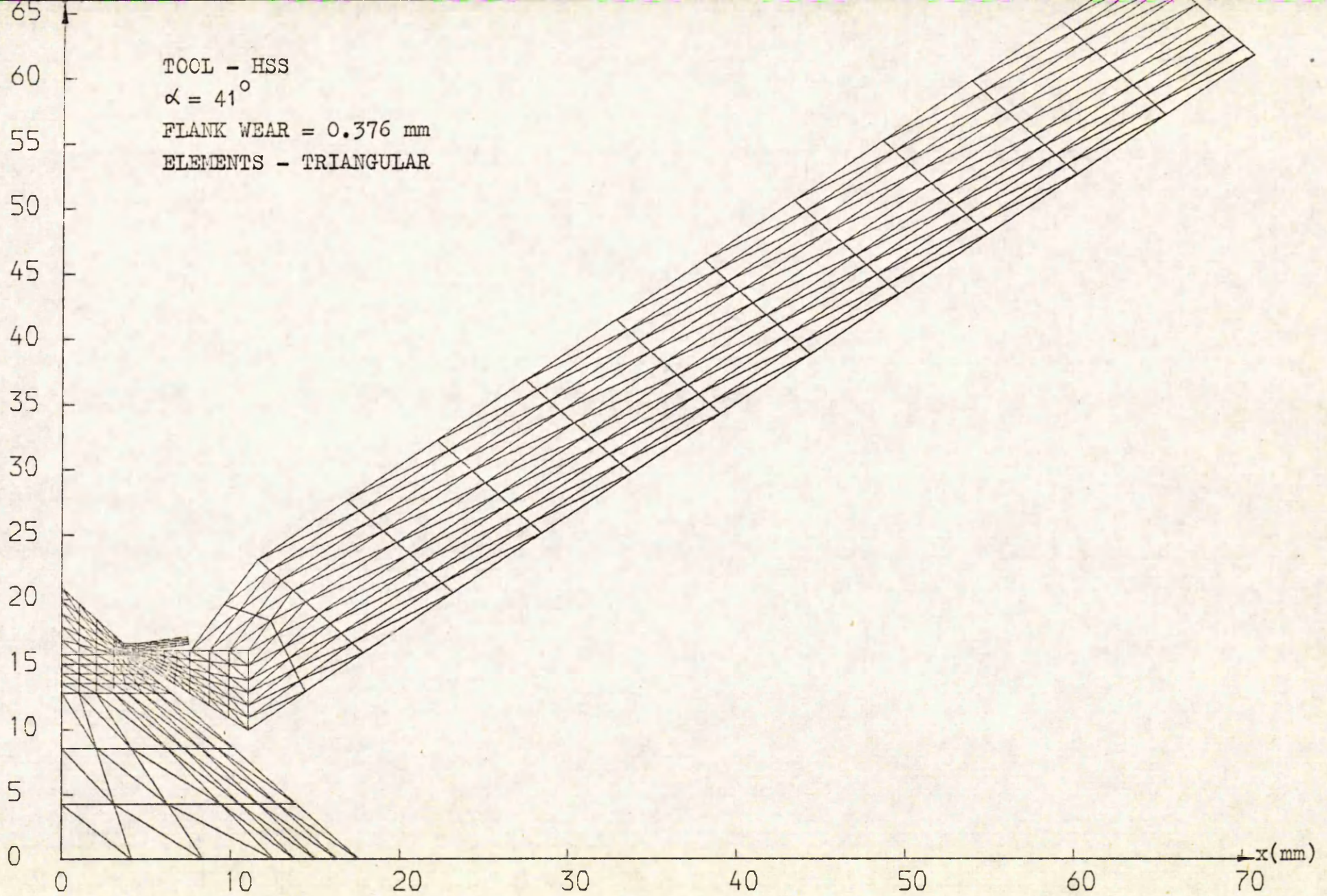

AUTOMATIC MESH GENERATION FOR THERMAL ANALYSIS IN ORTHOGONAL MACHINING , FIG. 5.21

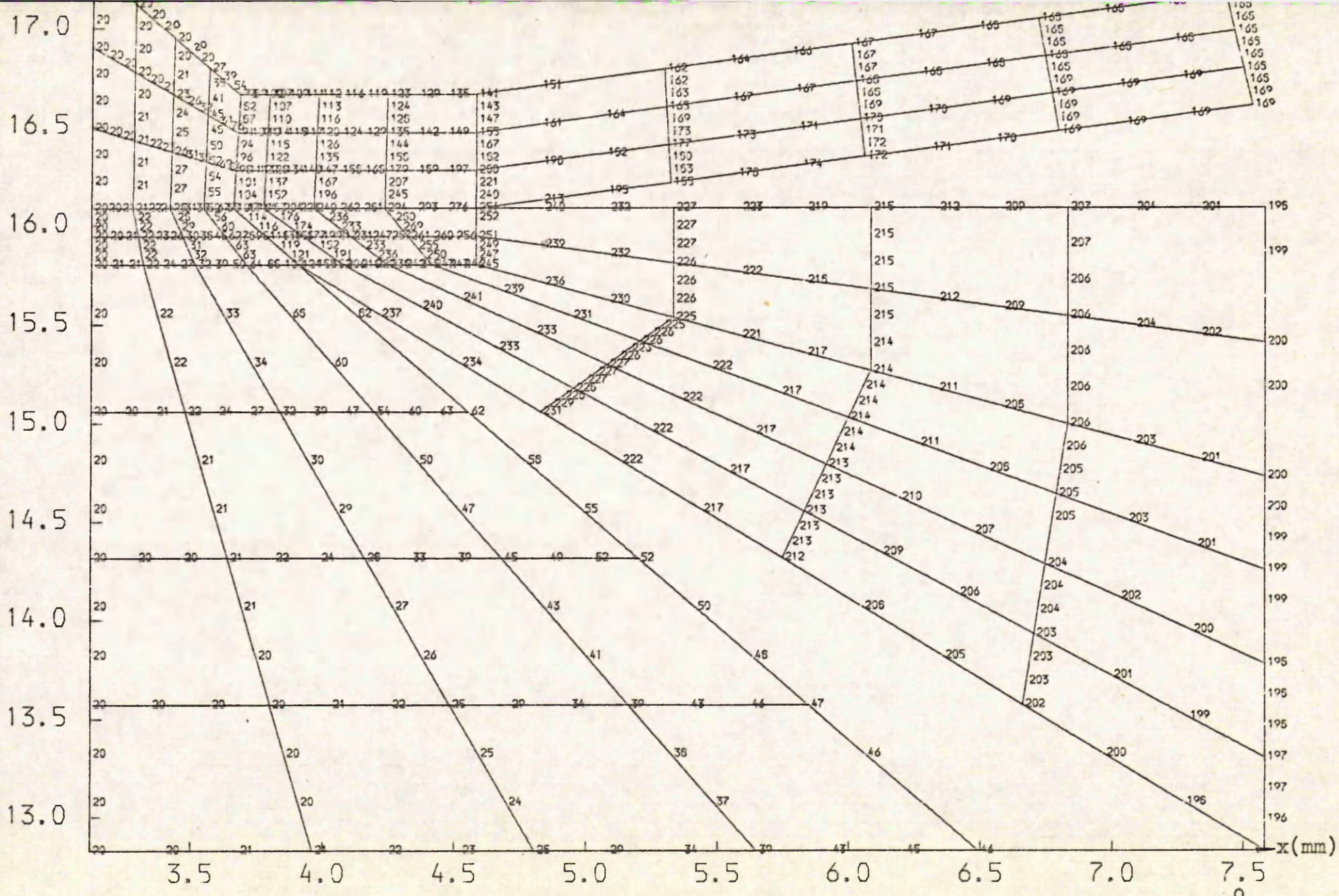

TEMPERATURE DISTRIBUTION IN WORKPIECE, TOOL AND CHIP PREDICTED BY FINITE ELEMENT ANALYSIS (°C)
THETA= 0.00, NODES= 1469, ZONES CHOSEN ARE 6, 7, 8, 11, 12, 16, 22, 23 , FIG. 5.22

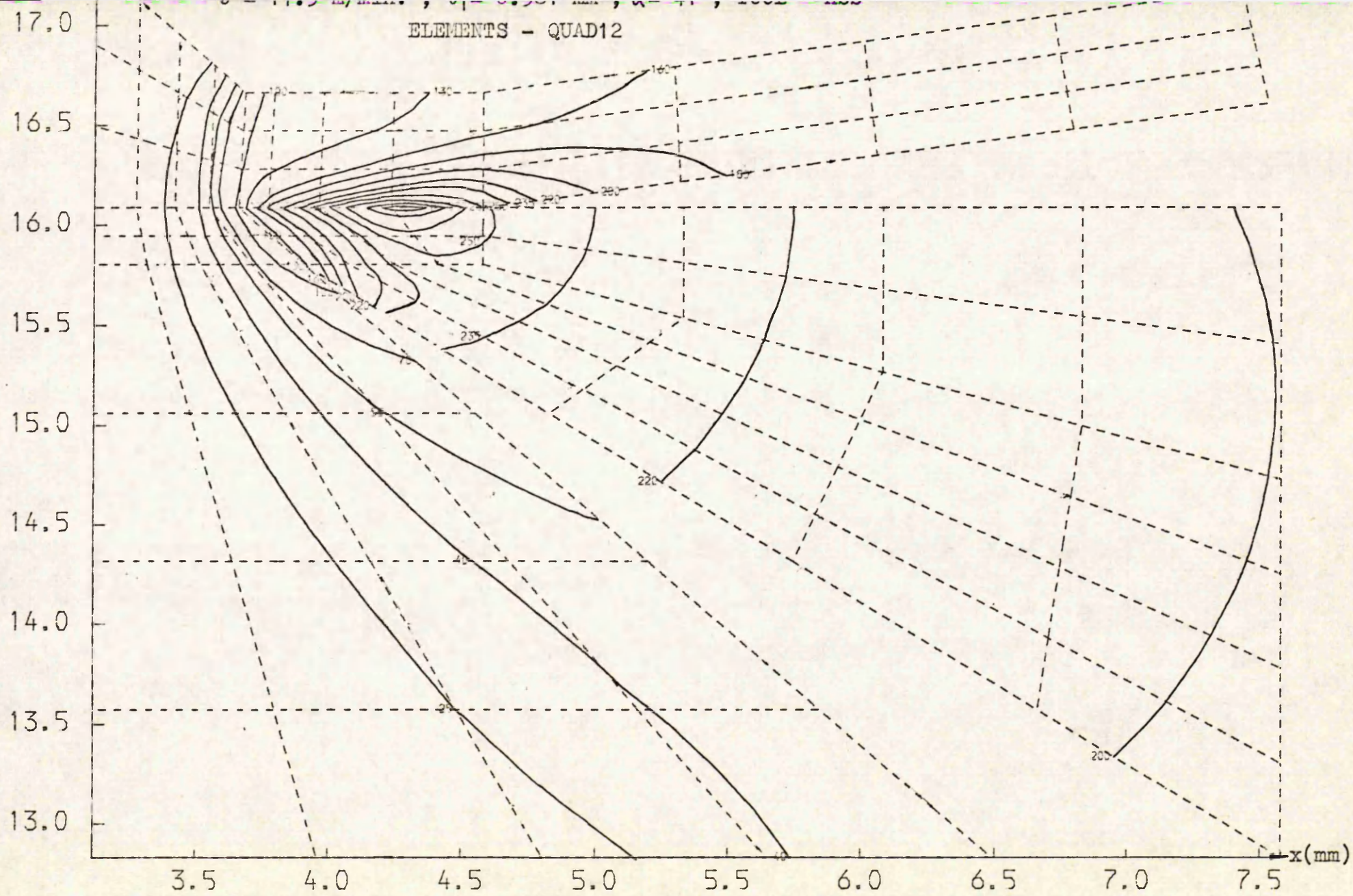

ISOTHERMALS IN WORKPIECE, TOOL AND CHIP PREDICTED BY FINITE ELEMENT ANALYSIS (^{o}C)
THETA= 0.00, NODES= 1469, ZONES CHOSEN ARE 6, 7, 8, 11, 12, 16, 22, 23 , FIG. 5.23

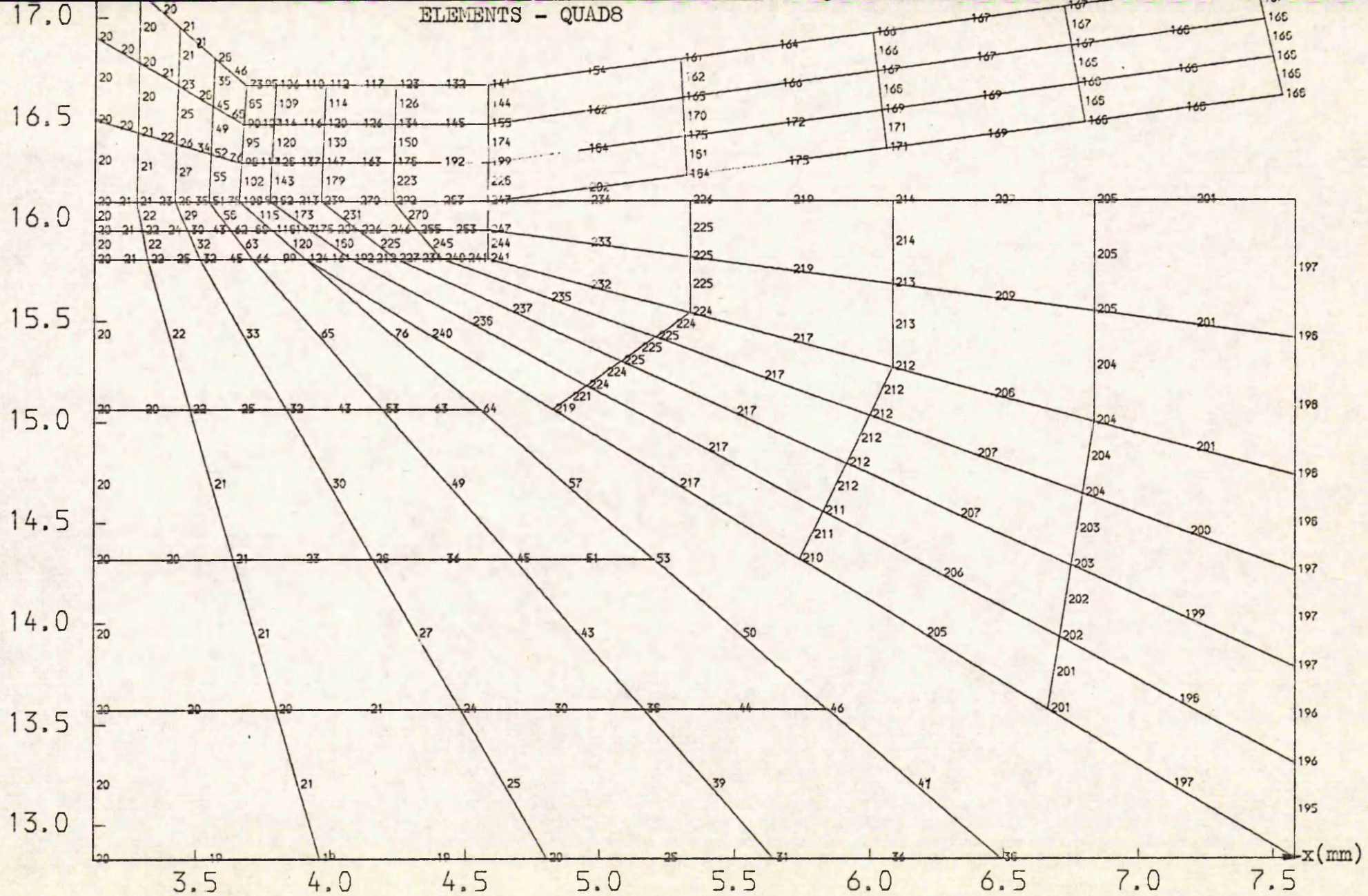

TEMPERATURE DISTRIBUTION IN WORKPIECE, TOOL AND CHIP PREDICTED BY FINITE ELEMENT ANALYSIS (°C)
THETA= 0.00, NODES= 891, ZONES CHOSEN ARE 6, 7, 8, 11, 12, 16, 22, 23, FIG. 5.24

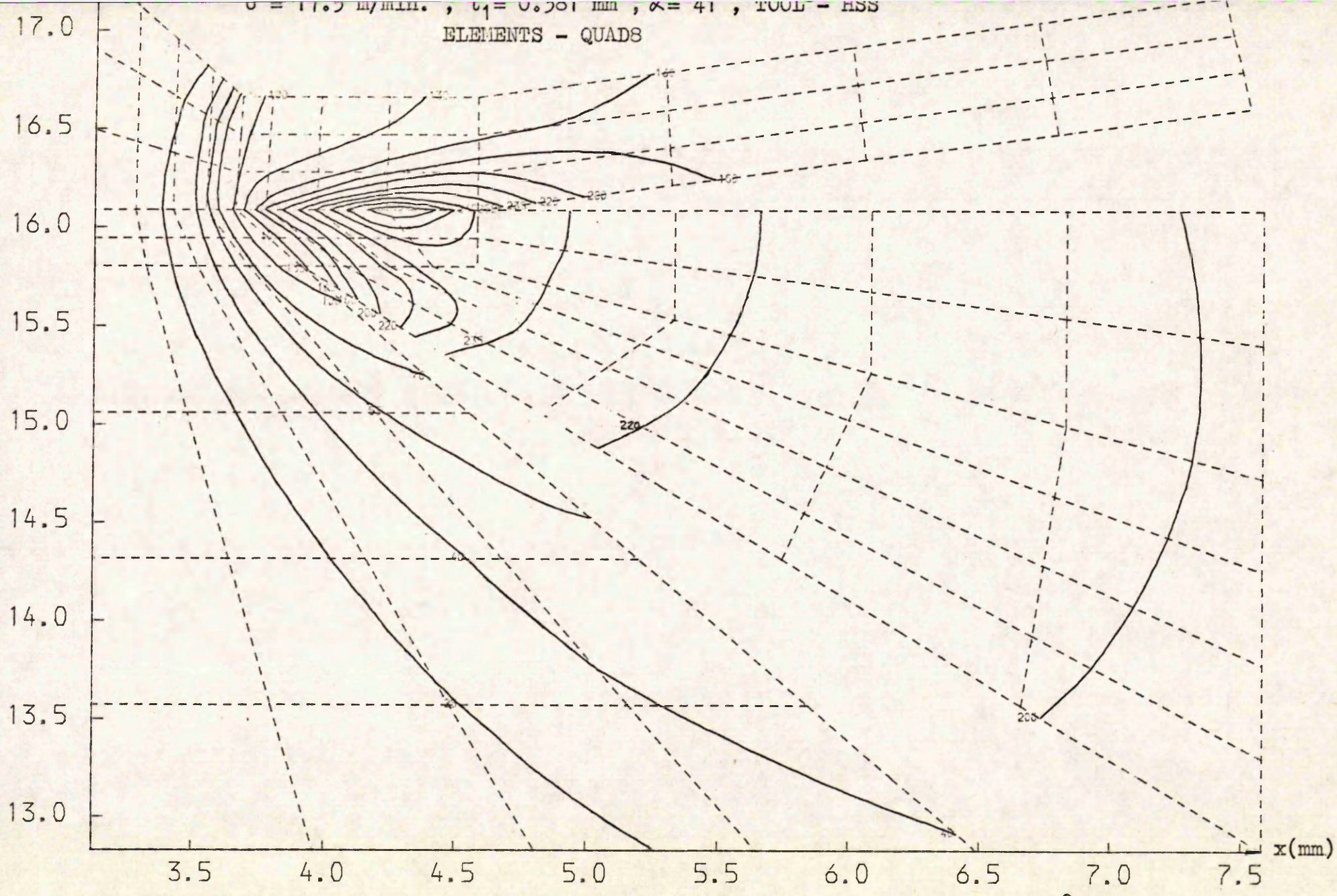

ISOTHERMALS IN WORKPIECE, TOOL AND CHIP PREDICTED BY FINITE ELEMENT ANALYSIS (°C) , FIG. 5.25
THETA= 0.00, NODES= 891, ZONES CHOSEN ARE 6, 7, 8, 11, 12, 16, 22, 23

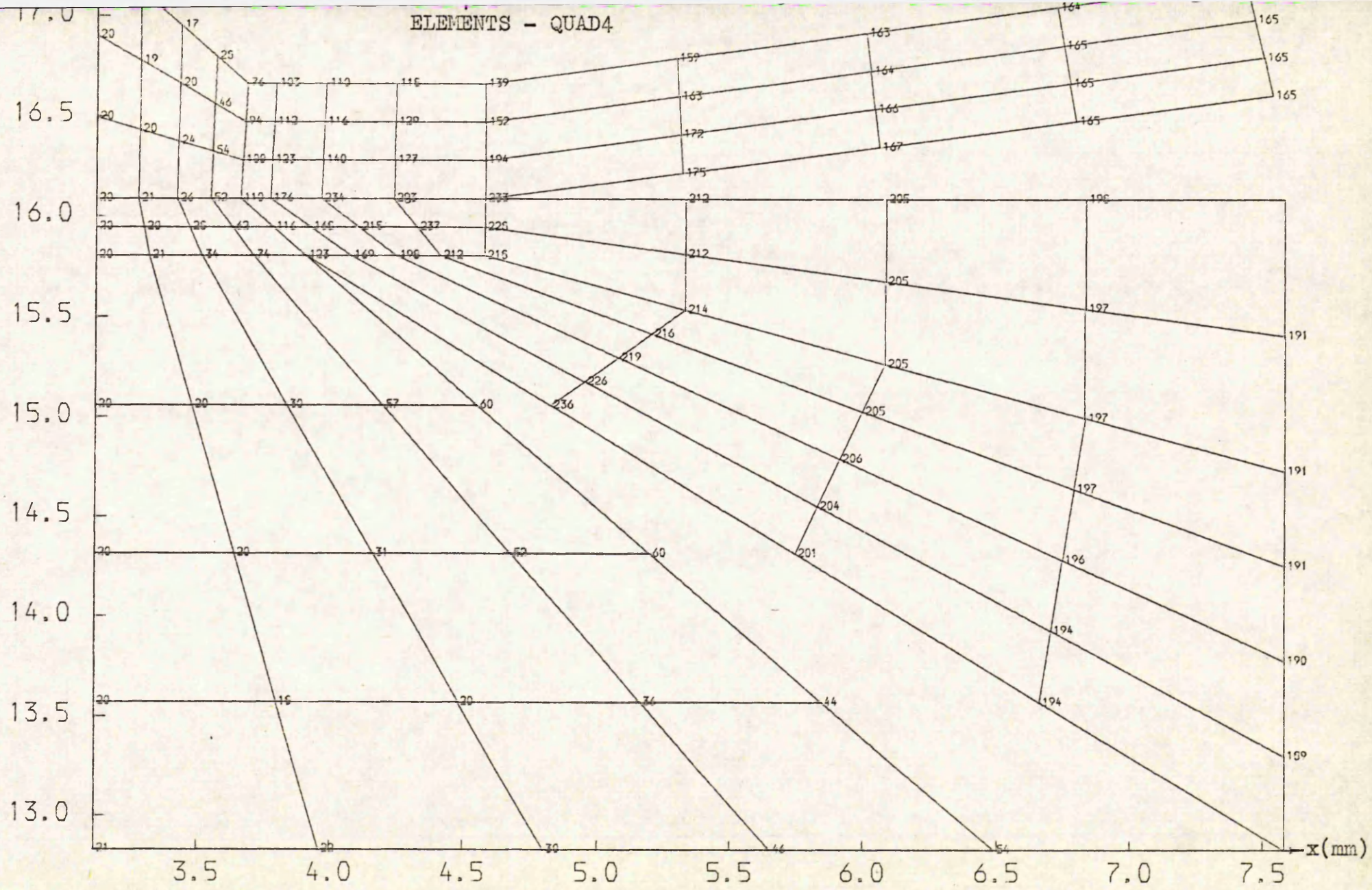

TEMPERATURE DISTRIBUTION IN WORKPIECE, TOOL AND CHIP PREDICTED BY FINITE ELEMENT ANALYSIS (°C)
THETA= 0.00, NODES= 313, ZONES CHOSEN ARE 6, 7, 8, 11, 12, 16, 22, 23, **FIG. 5.26**

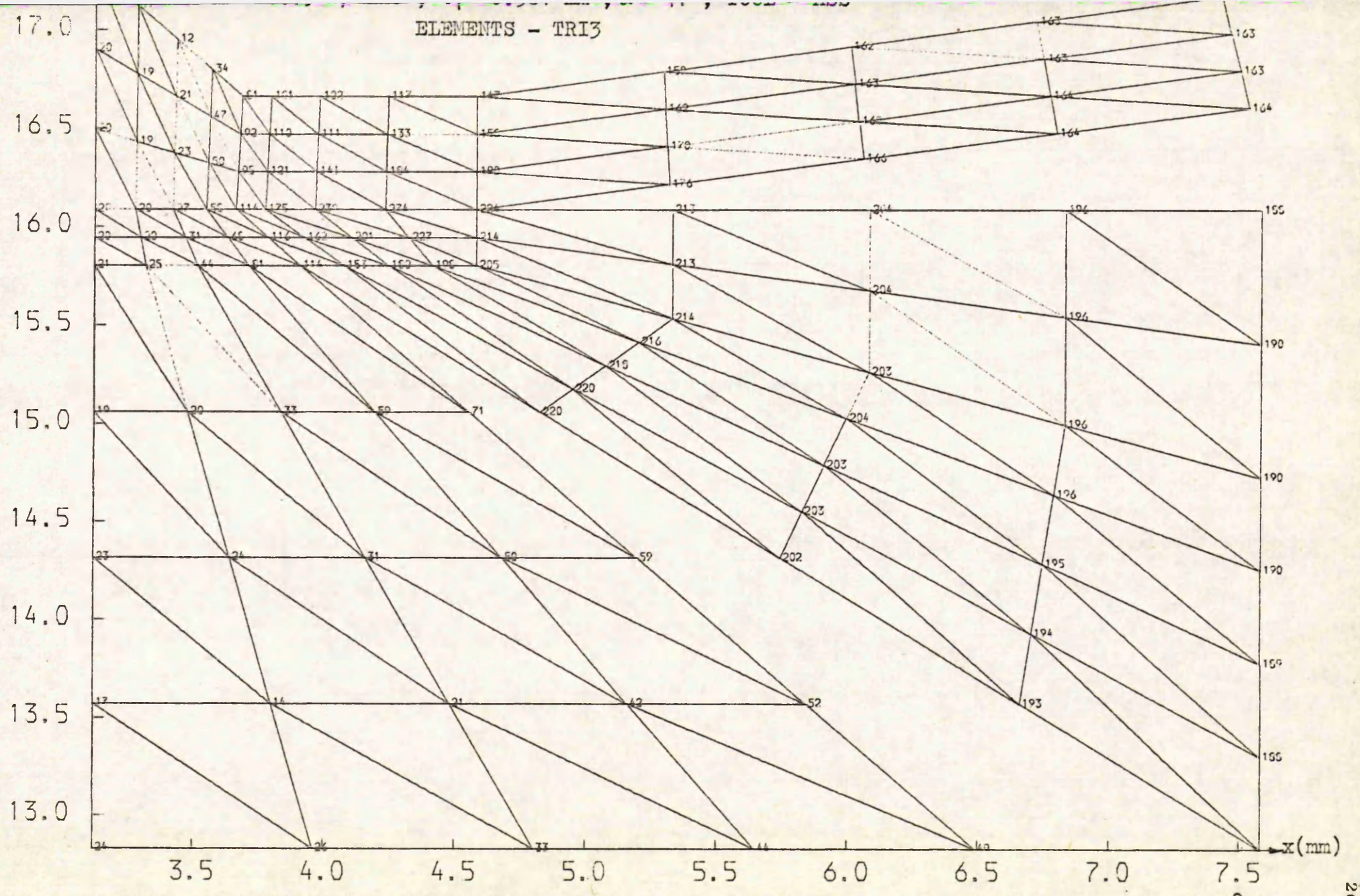

TEMPERATURE DISTRIBUTION IN WORKPIECE, TOOL AND CHIP PREDICTED BY FINITE ELEMENT ANALYSIS (°C)
THETA= 0.00, NODES= 313, ZONES CHOSEN ARE 6, 7, 8, 11, 12, 16, 22, 23, FIG. 5.27

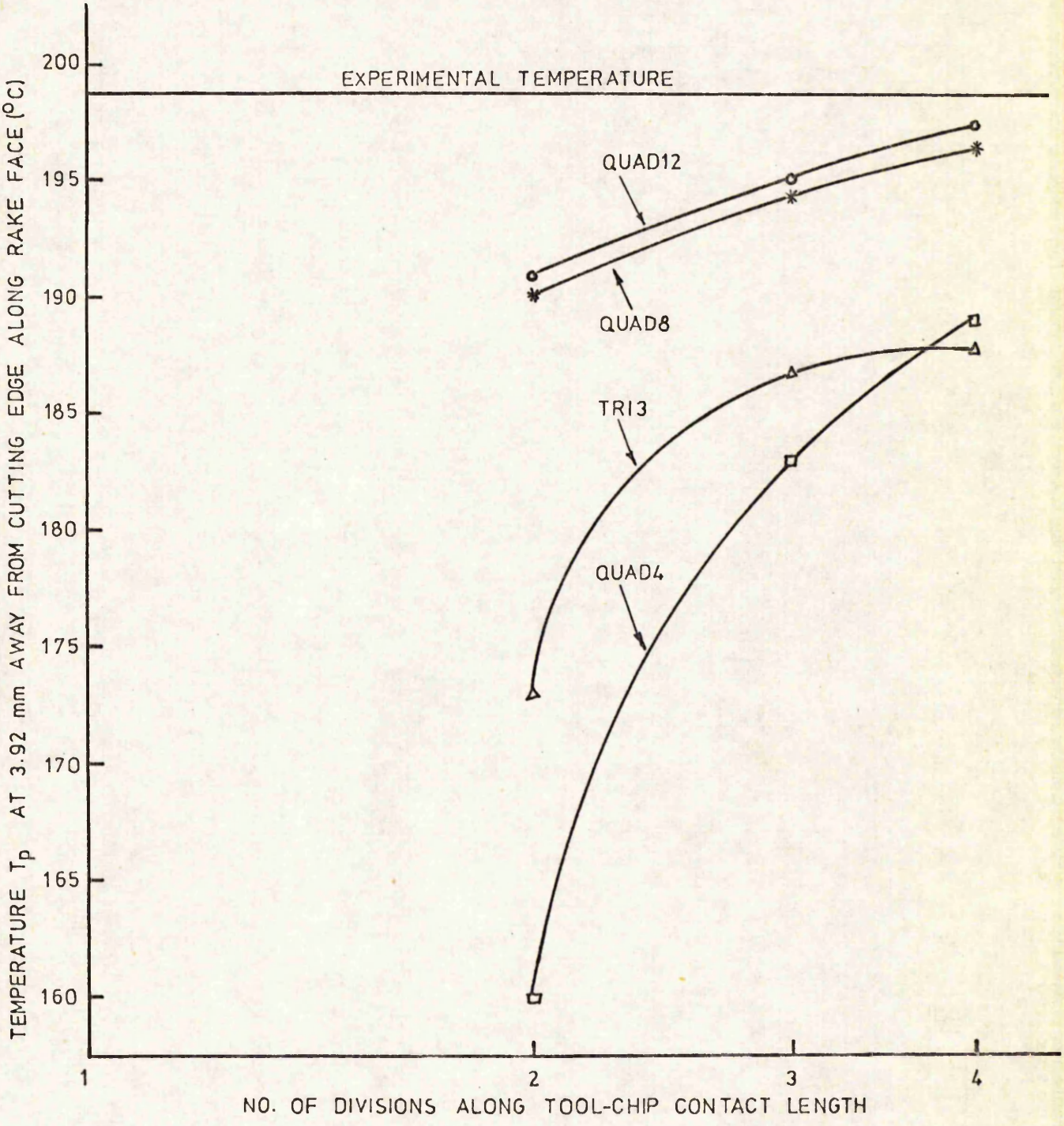
EXPERIMENTAL TEMPERATURE
QUAD12
QUAD8
TRI3
QUAD4
200
195
190
185
180
175
170
165
160
TEMPERATURE T_p AT 3.92 mm AWAY FROM CUTTING EDGE ALONG RAKE FACE (°C)
1
2
3
4
NO. OF DIVISIONS ALONG TOOL-CHIP CONTACT LENGTH

FIG. 5.28

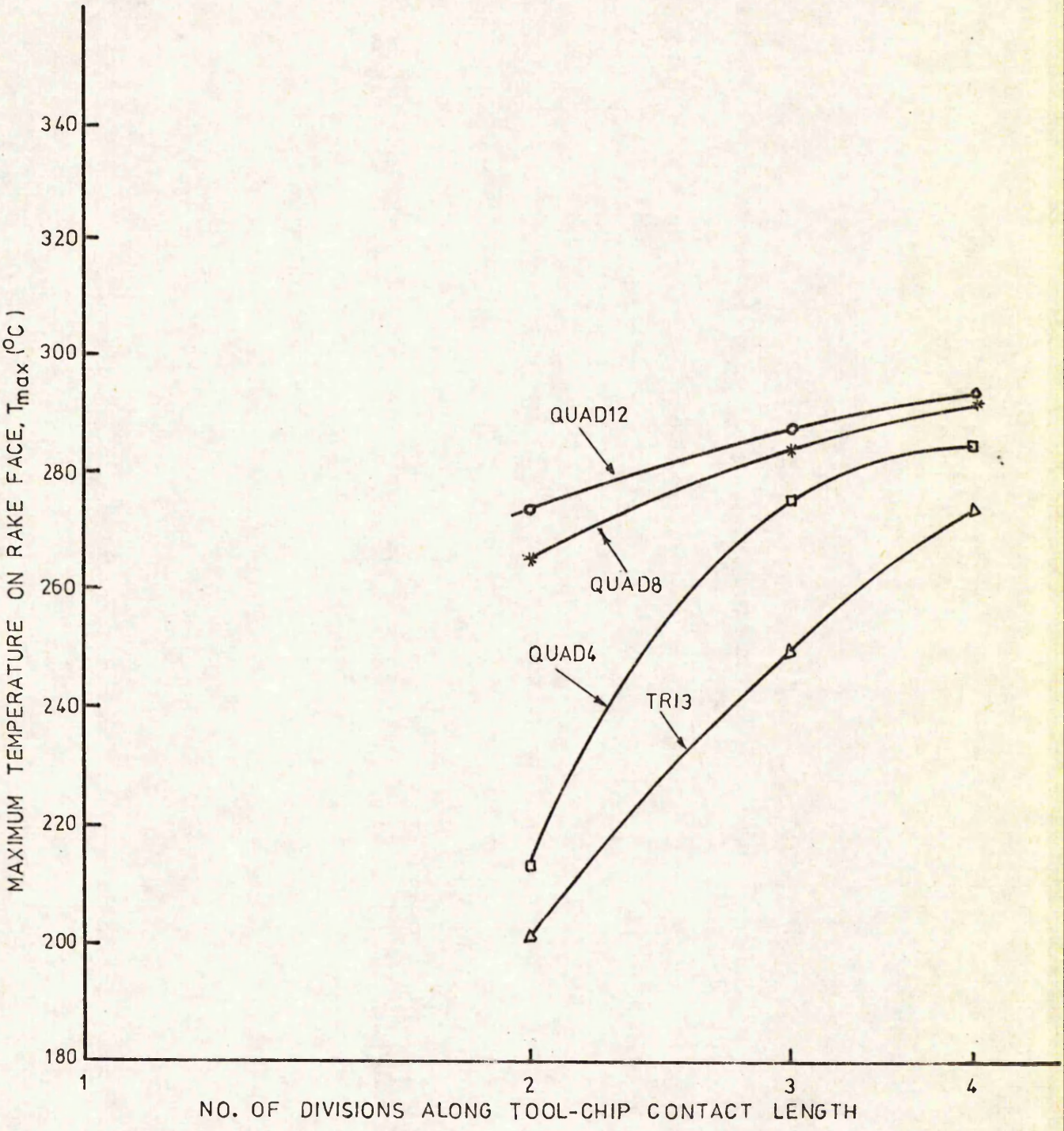
MAXIMUM TEMPERATURE ON RAKE FACE, T_{max} (°C)
340
320
300
280
260
240
220
200
180
1
2
3
4
NO. OF DIVISIONS ALONG TOOL-CHIP CONTACT LENGTH
QUAD12
QUAD8
QUAD4
TRI3

FIG. 5.29

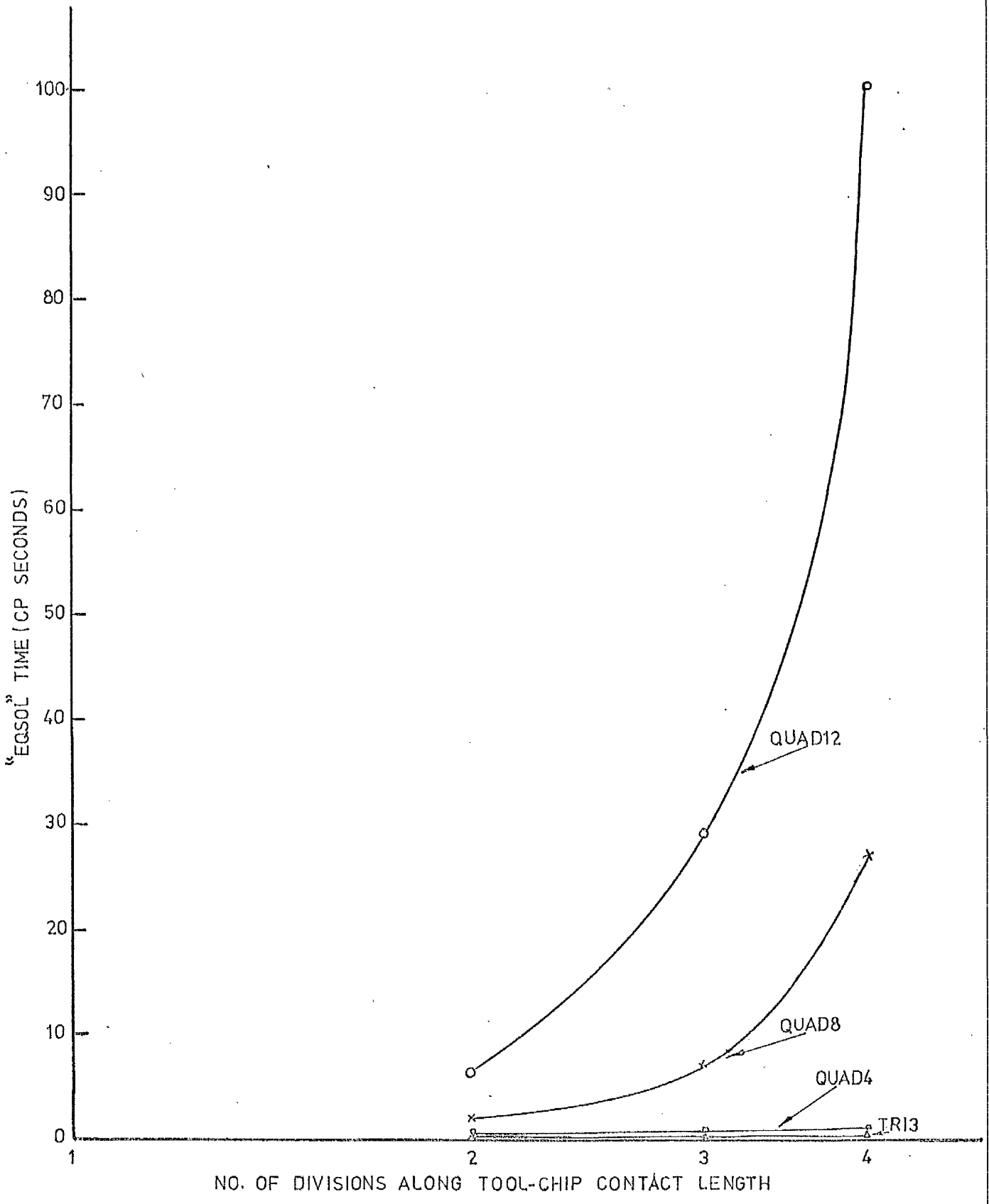
100
90
80
70
60
50
40
30
20
10
0
"EQSOL" TIME (CP SECONDS)
QUAD12
QUAD8
QUAD4
TRI3
1
2
3
4
NO. OF DIVISIONS ALONG TOOL-CHIP CONTACT LENGTH

FIG. 5.30

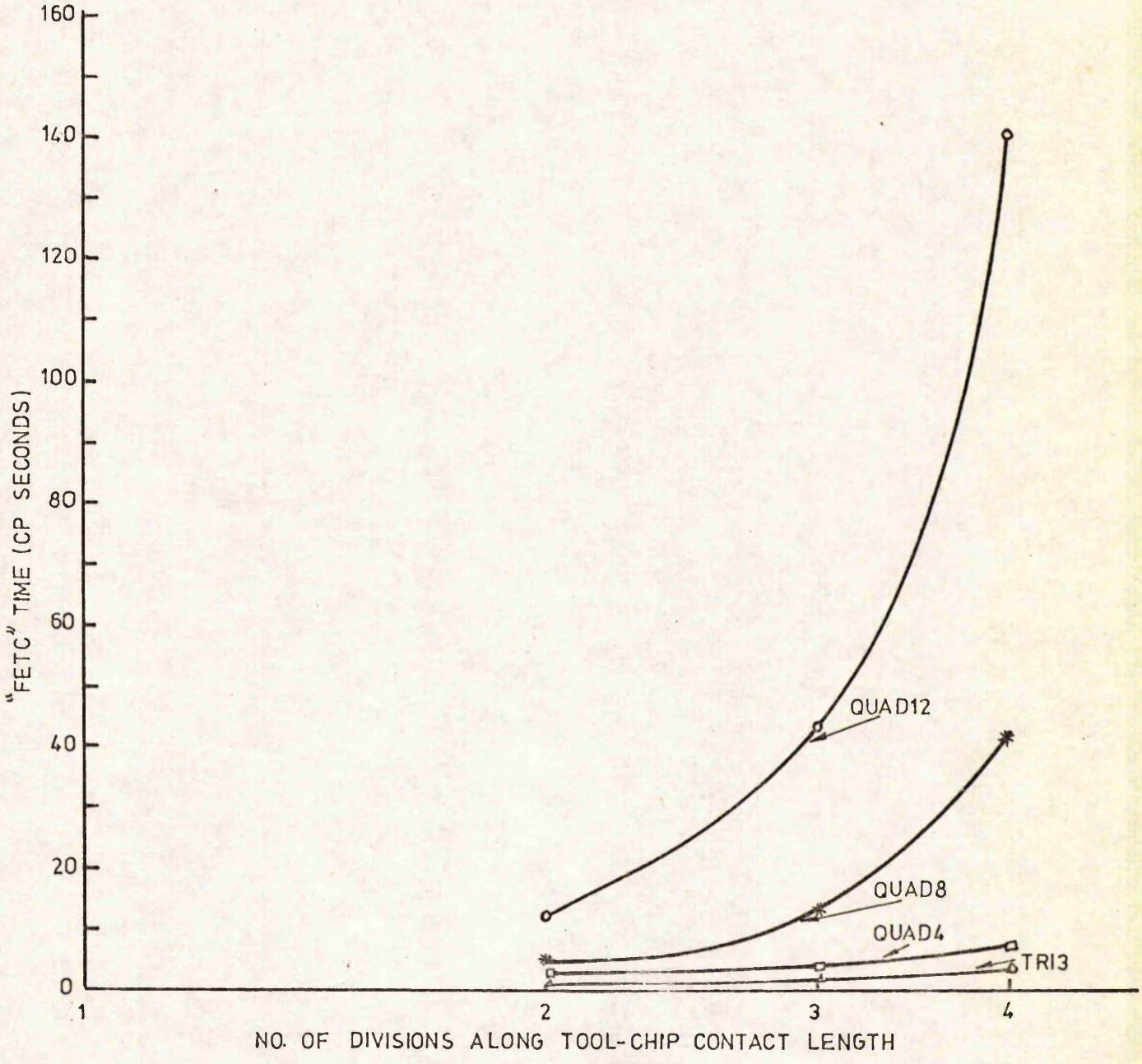
160
140
120
100
80
60
40
20
0
"FETC" TIME (CP SECONDS)
QUAD12
QUAD8
QUAD4
TRI3
1
2
3
4
NO. OF DIVISIONS ALONG TOOL-CHIP CONTACT LENGTH

FIG. 5.31

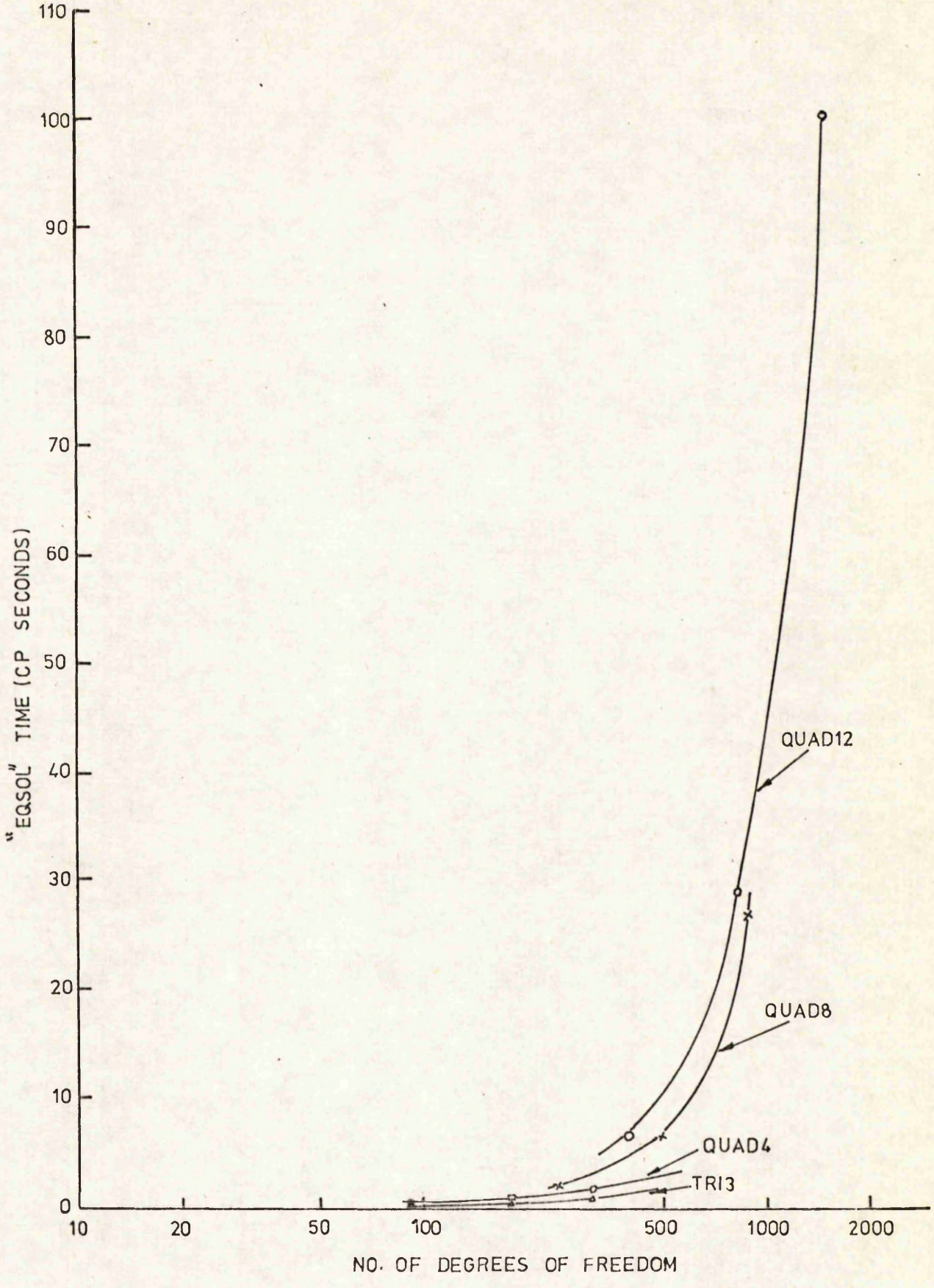
110
100
90
80
70
60
50
40
30
20
10
0
"EQSOL" TIME (CP SECONDS)
10
20
50
100
500
1000
2000
NO. OF DEGREES OF FREEDOM
QUAD12
QUAD8
QUAD4
TRI3

FIG. 5. 32

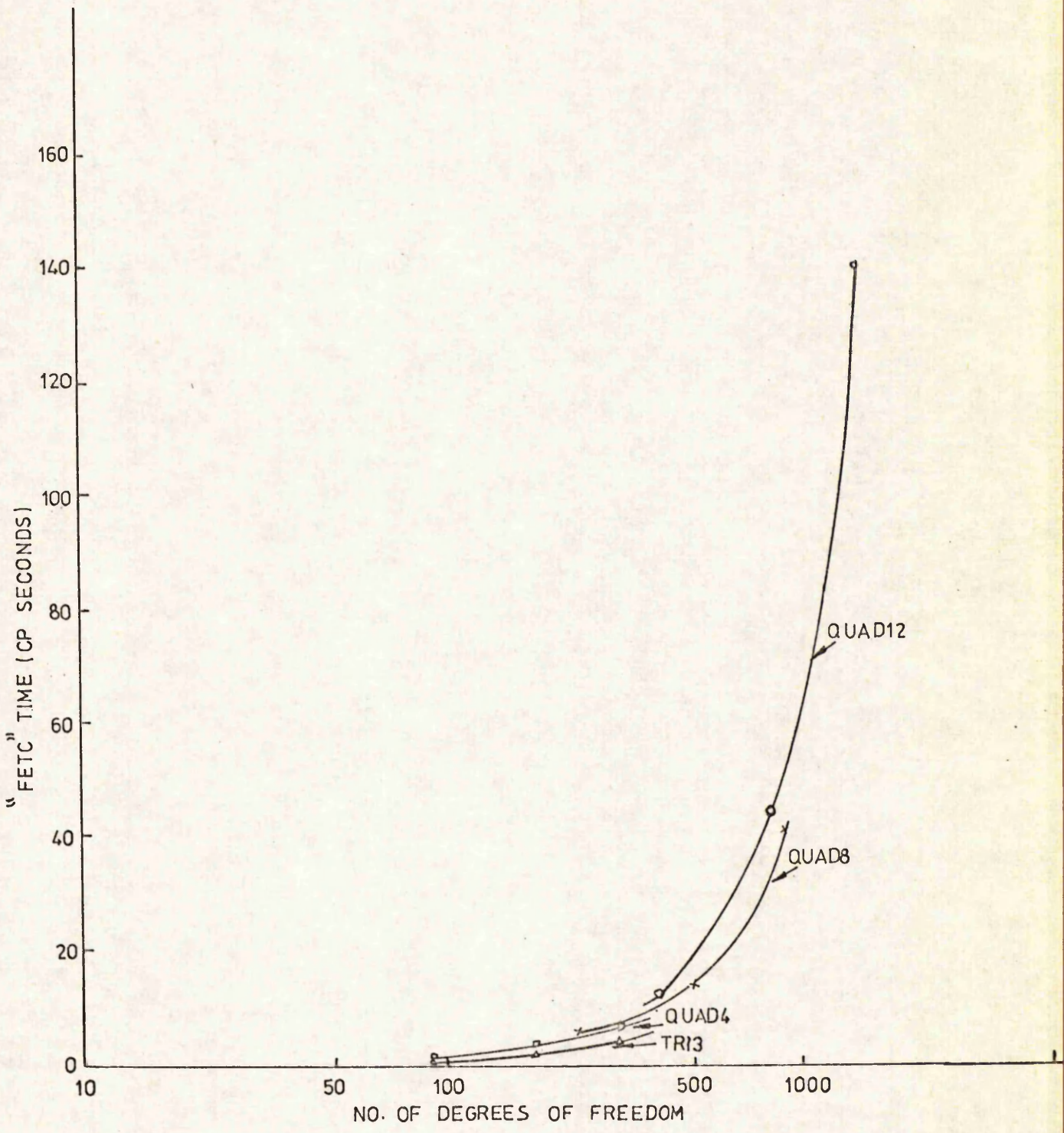
"FETC" TIME (CP SECONDS)
160
140
120
100
80
60
40
20
0
10
50
100
500
1000
NO. OF DEGREES OF FREEDOM
QUAD12
QUAD8
QUAD4
TRI3

FIG. 5.33

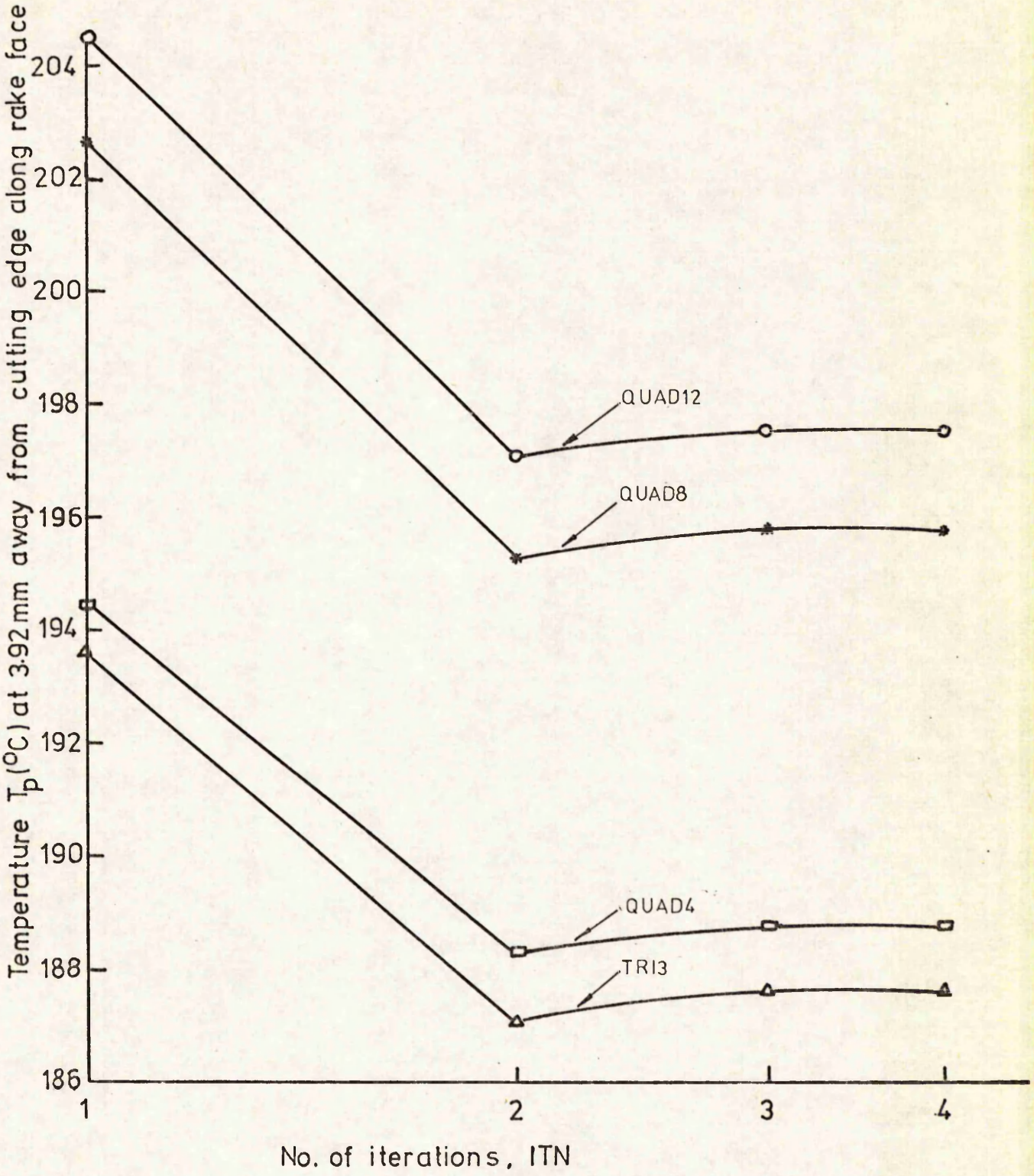
Temperature T_p(°C) at 3.92 mm away from cutting edge along rake face
204
202
200
198
196
194
192
190
188
186
1
2
3
4
No. of iterations, ITN
QUAD12
QUAD8
QUAD4
TRI3

FIG. 5.34

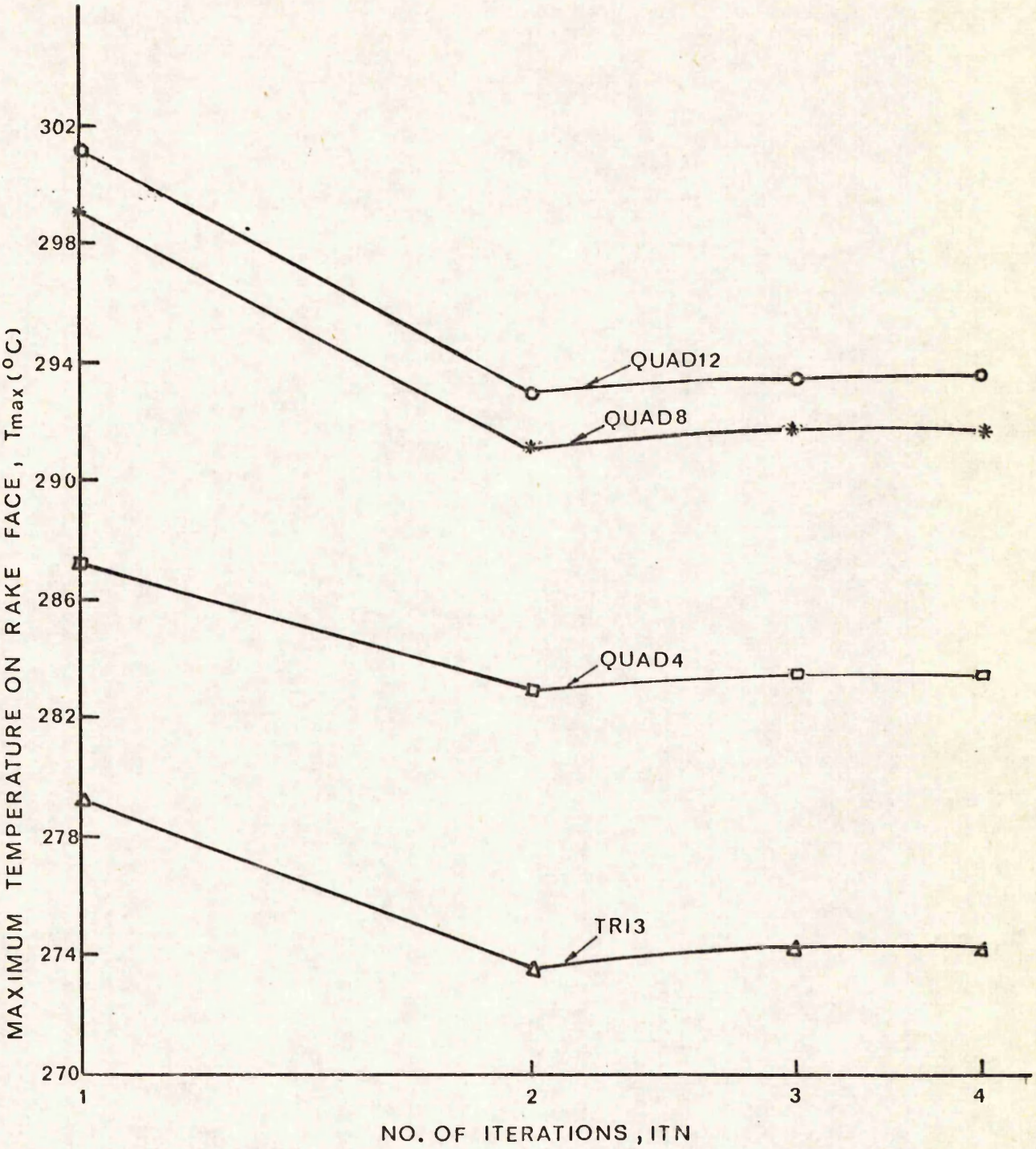
MAXIMUM TEMPERATURE ON RAKE FACE, T_{max} (°C)
302
298
294
290
286
282
278
274
270
QUAD12
QUAD8
QUAD4
TRI3
1
2
3
4
NO. OF ITERATIONS, ITN

FIG. 5.35

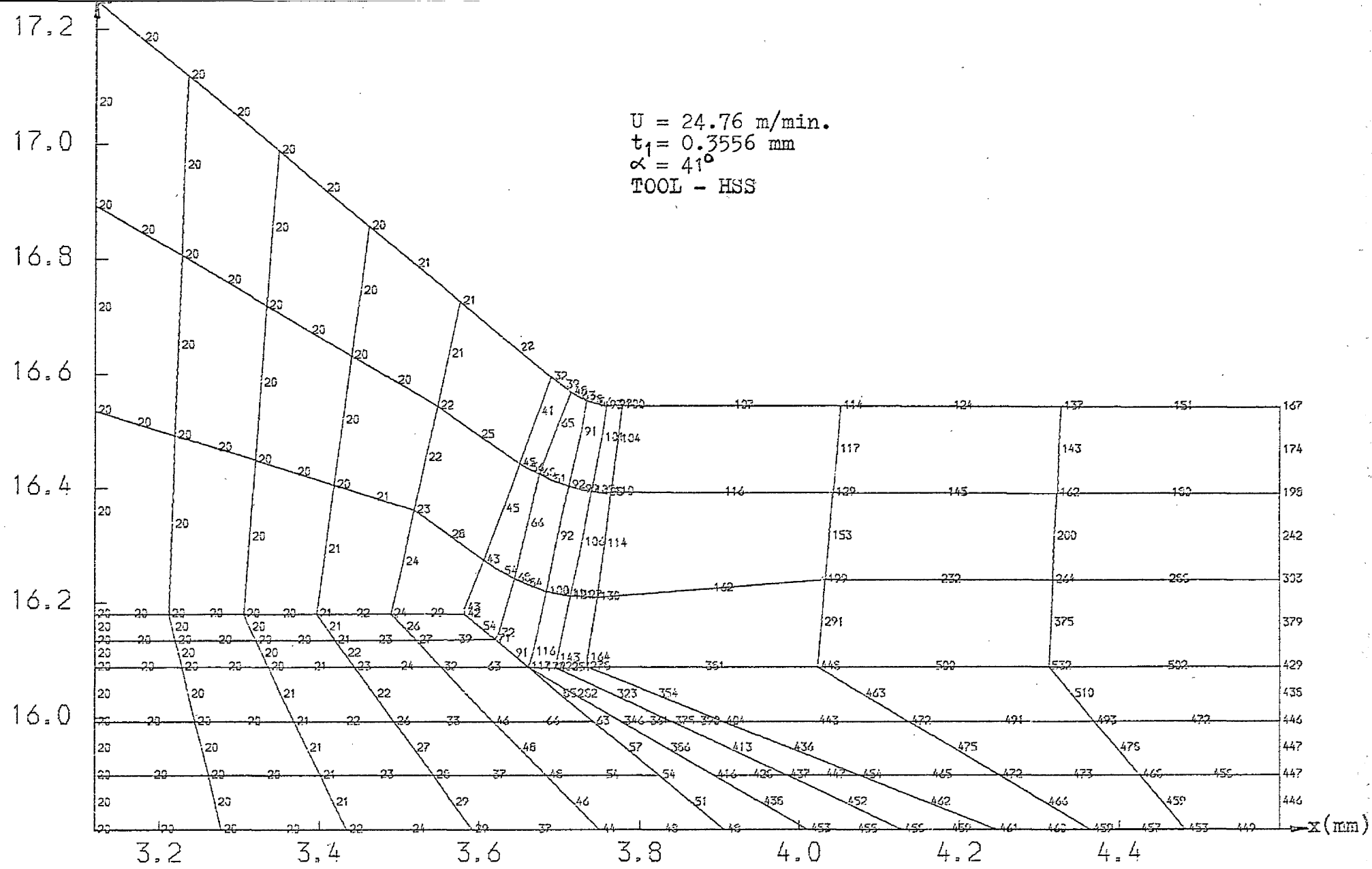

TEMPERATURE DISTRIBUTION IN WORKPIECE, TOOL AND CHIP PREDICTED BY FINITE ELEMENT ANALYSIS (°C)
TEST NO. = 1, NODES = 1192, ZONES CHOSEN ARE 10, 11, 12, 19, 26, 33, 53, 54

FIG. 5.36 (a)

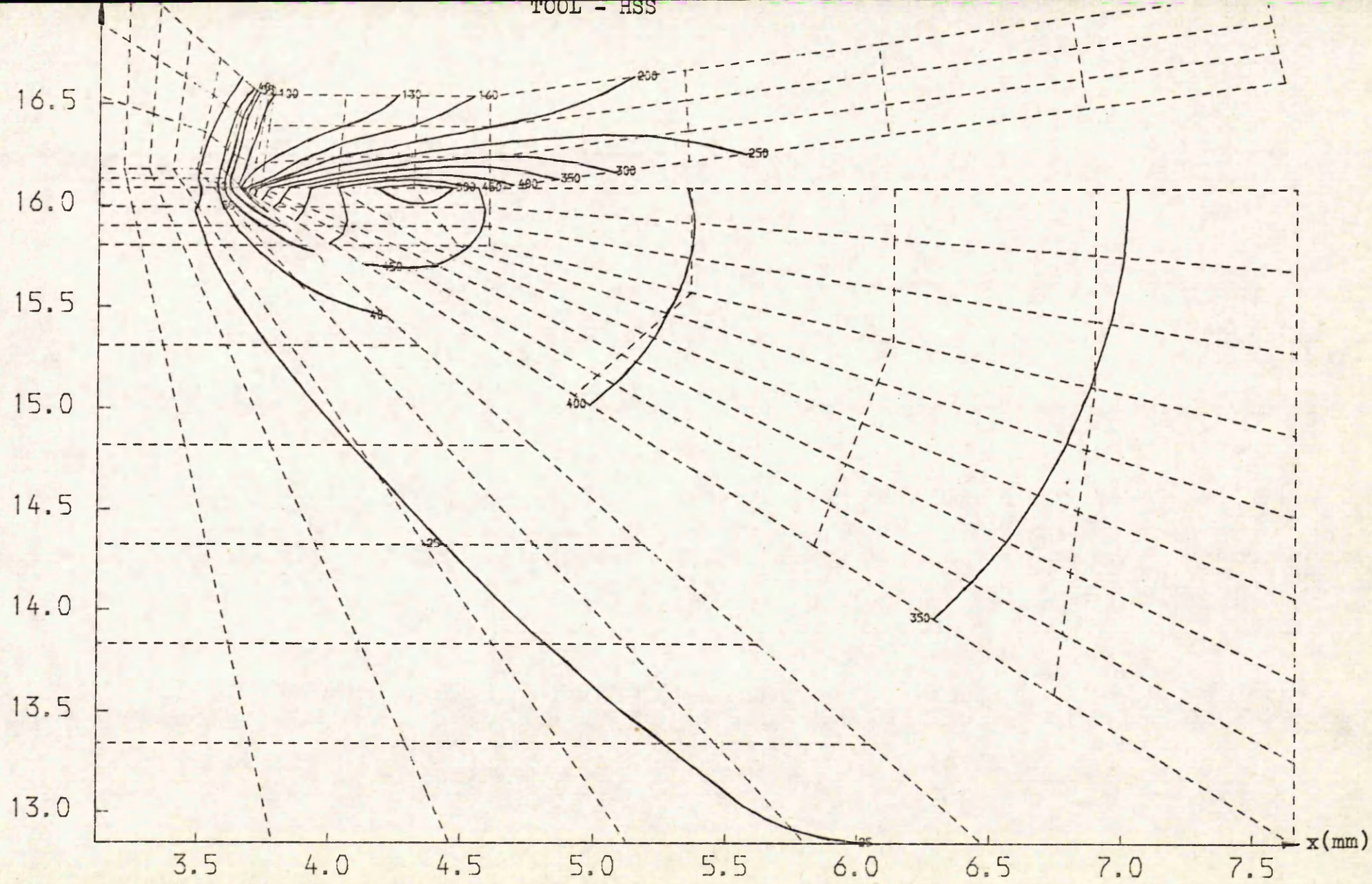

ISOTHERMALS IN WORKPIECE, TOOL AND CHIP PREDICTED BY FINITE ELEMENT ANALYSIS (°C)
TEST NO.= 1, NODES= 1192, ZONES CHOSEN ARE 9, 10, 11, 12, 19, 26, 33, 40, 53, 54, 60, 61, 62

FIG. 5.36 (b)

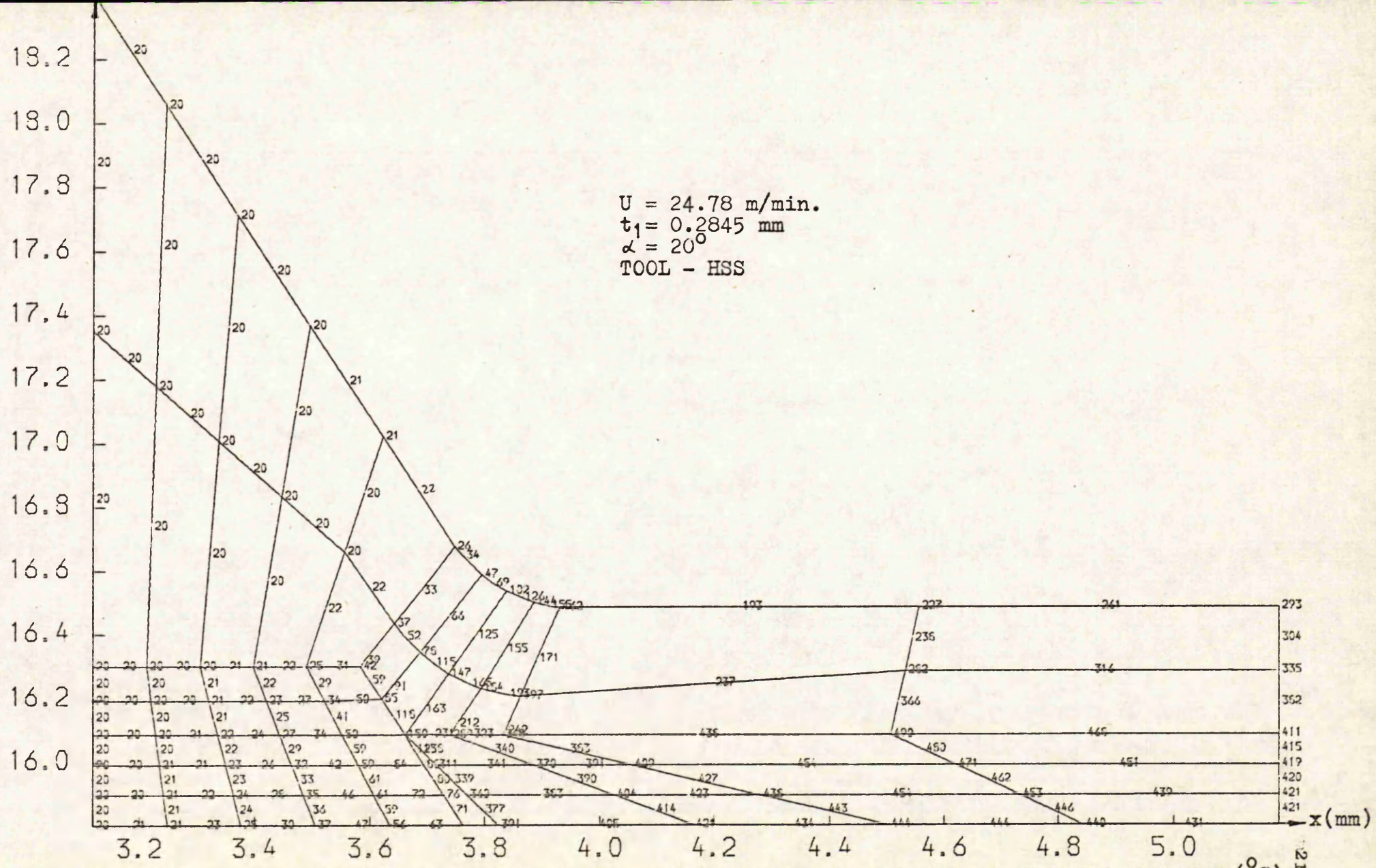

TEMPERATURE DISTRIBUTION IN WORKPIECE, TOOL AND CHIP PREDICTED BY FINITE ELEMENT ANALYSIS (°C)
TEST NO. = 3, NODES = 1062, ZONES CHOSEN ARE 10, 11, 12, 19, 26, 33, 53, 54

FIG.5.37 (a)

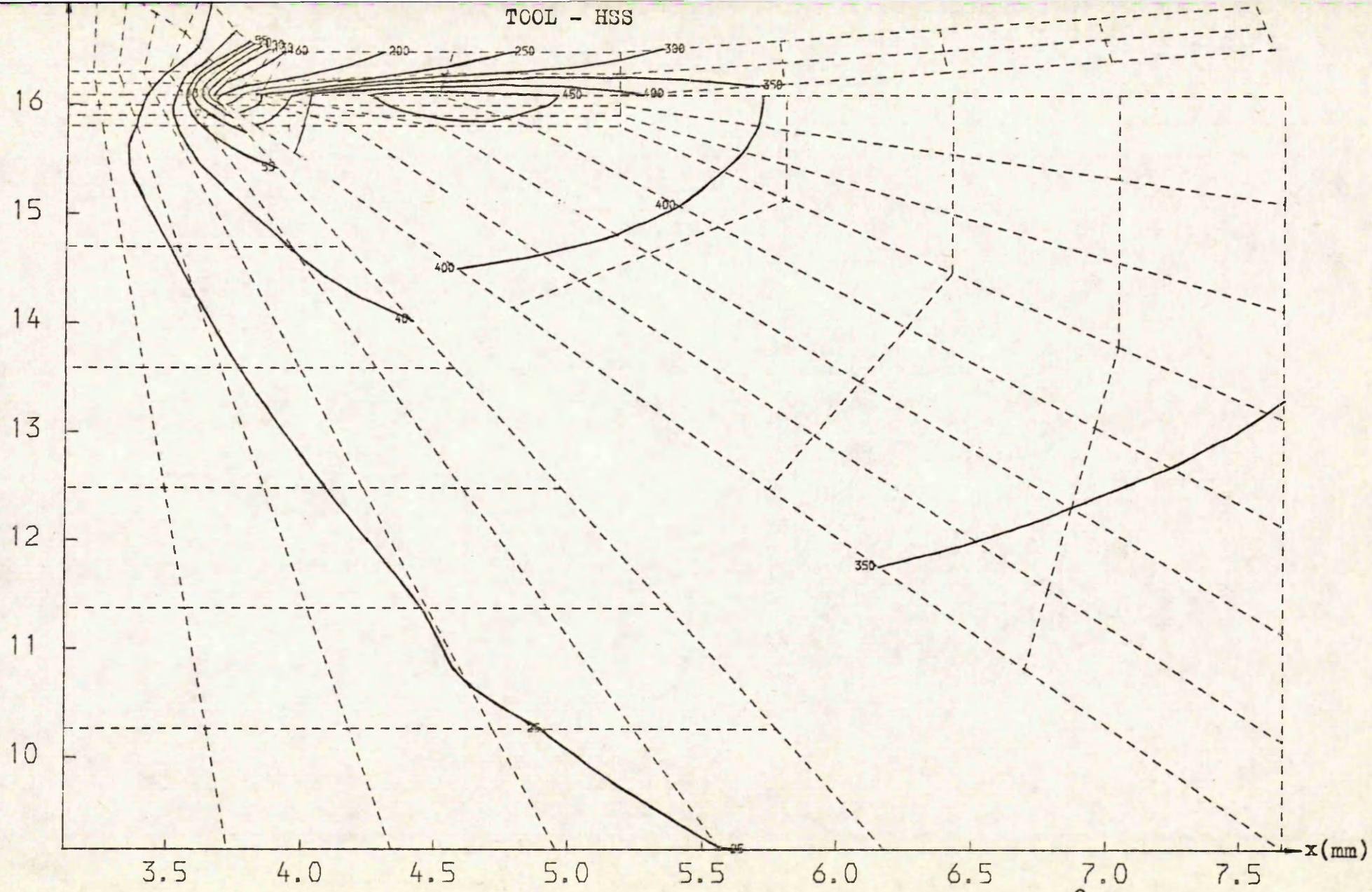

ISOTHERMALS IN WORKPIECE, TOOL AND CHIP PREDICTED BY FINITE ELEMENT ANALYSIS (^{o}C)
TEST NO.= 3, NODES= 1062, ZONES CHOSEN ARE 9, 10, 11, 12, 19, 26, 33, 40, 53, 54, 60, 61, 62

FIG. 5.37(b)

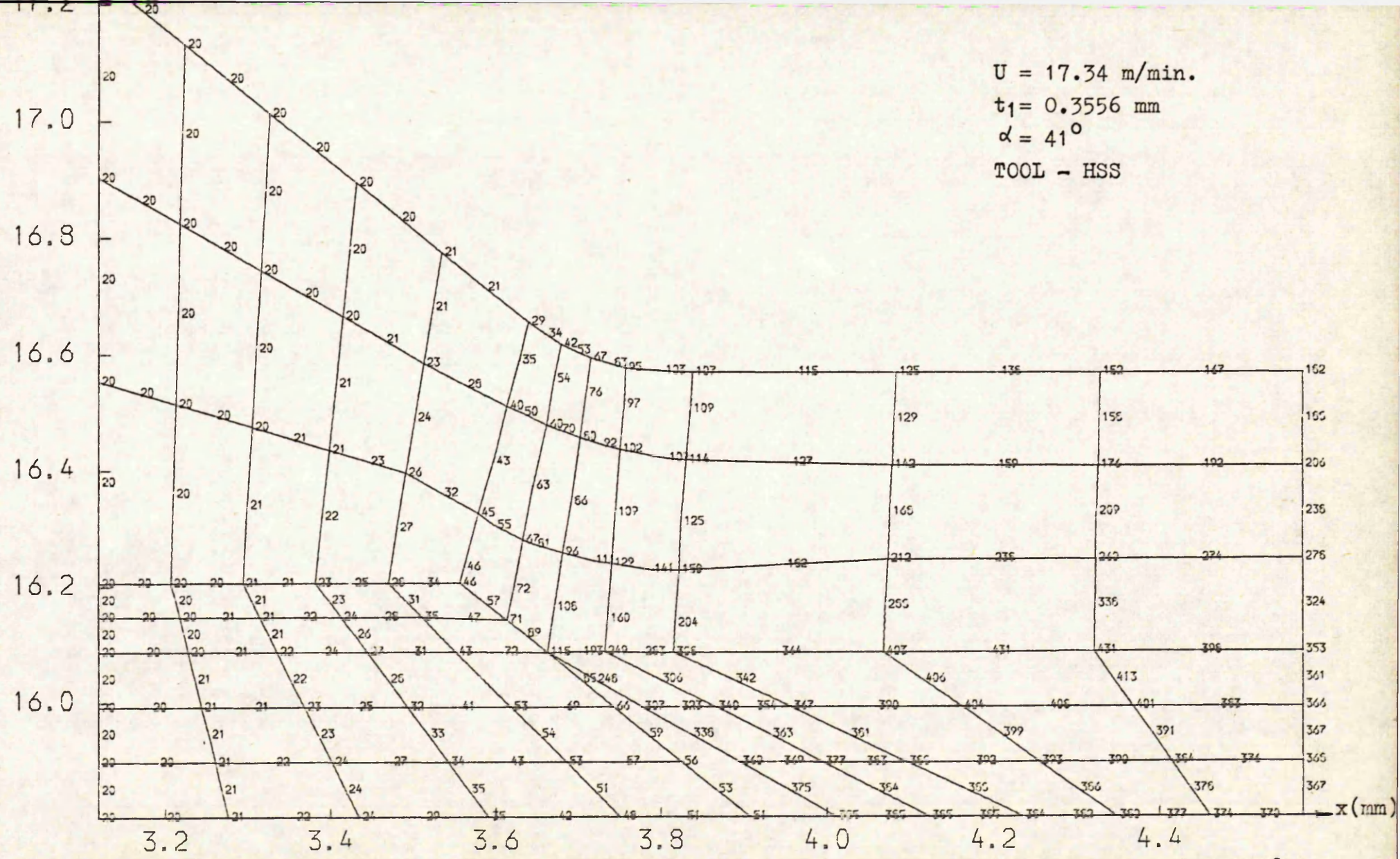

TEMPERATURE DISTRIBUTION IN WORKPIECE, TOOL AND CHIP PREDICTED BY FINITE ELEMENT ANALYSIS (°C)
TEST NO. = 5, NODES= 1192, ZONES CHOSEN ARE 10, 11, 12, 19, 26, 33, 53, 54

FIG. 5.38(a)

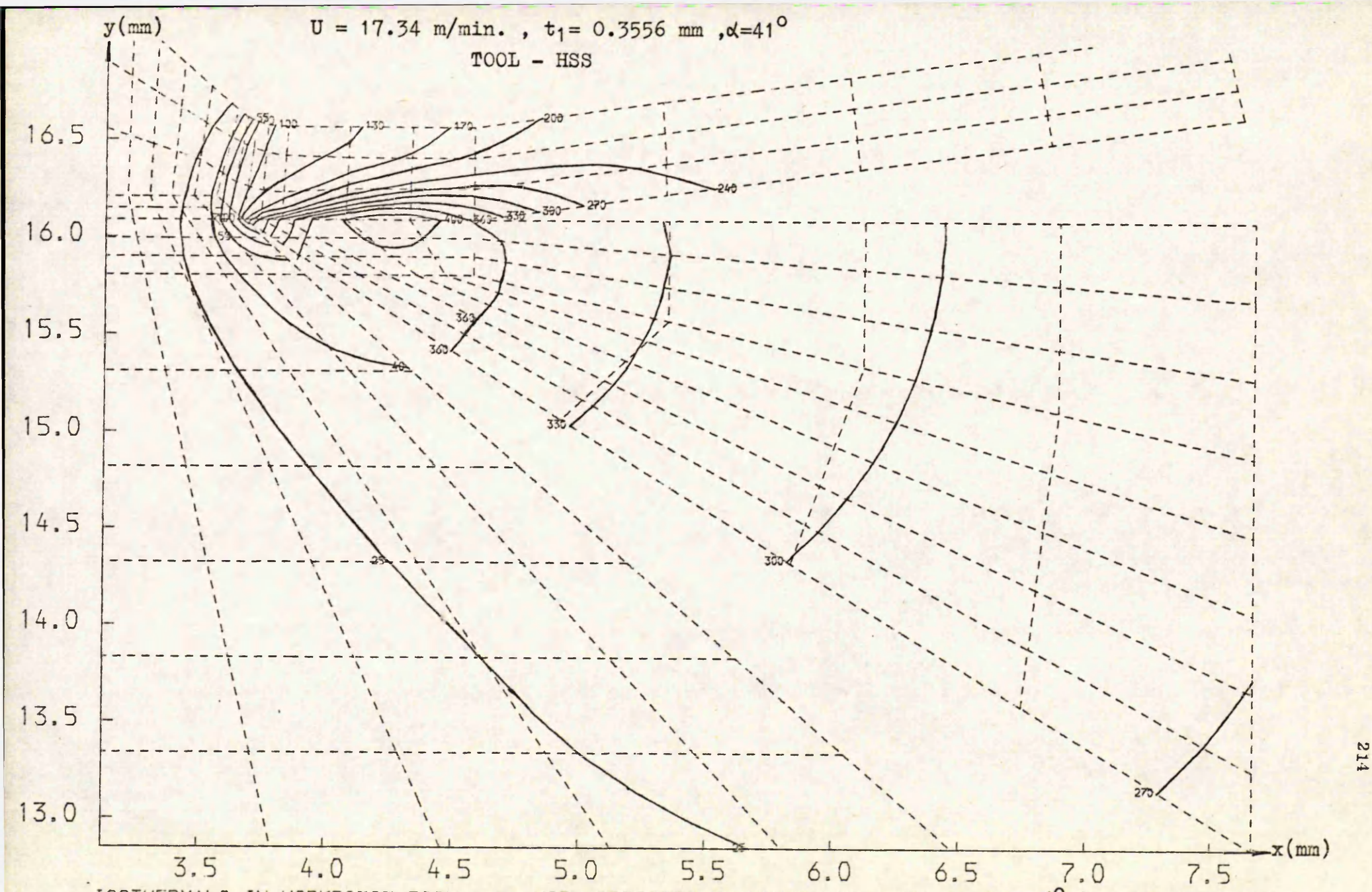

ISOTHERMALS IN WORKPIECE, TOOL AND CHIP PREDICTED BY FINITE ELEMENT ANALYSIS (°C). FIG. 5.38 (b)
TEST NO.= 5, NODES= 1192, ZONES CHOSEN ARE 9, 10, 11, 12, 19, 26, 33, 40, 53, 54, 60, 61, 62

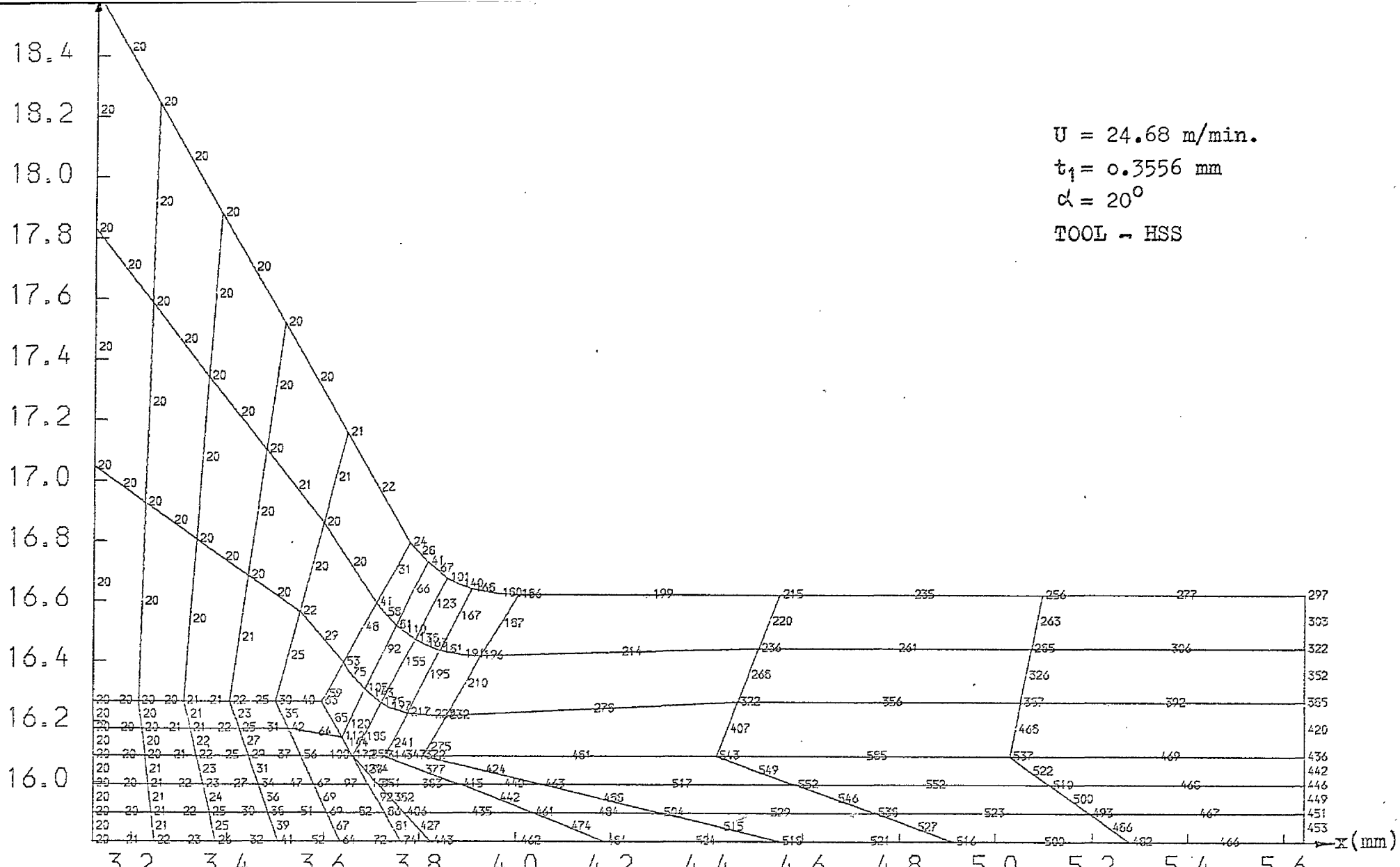

TEMPERATURE DISTRIBUTION IN WORKPIECE, TOOL AND CHIP PREDICTED BY FINITE ELEMENT ANALYSIS (°C)
TEST NO. = 6, NODES= 1192, ZONES CHOSEN ARE 10, 11, 12, 19, 26, 33, 53, 54

FIG. 5.39 (a)

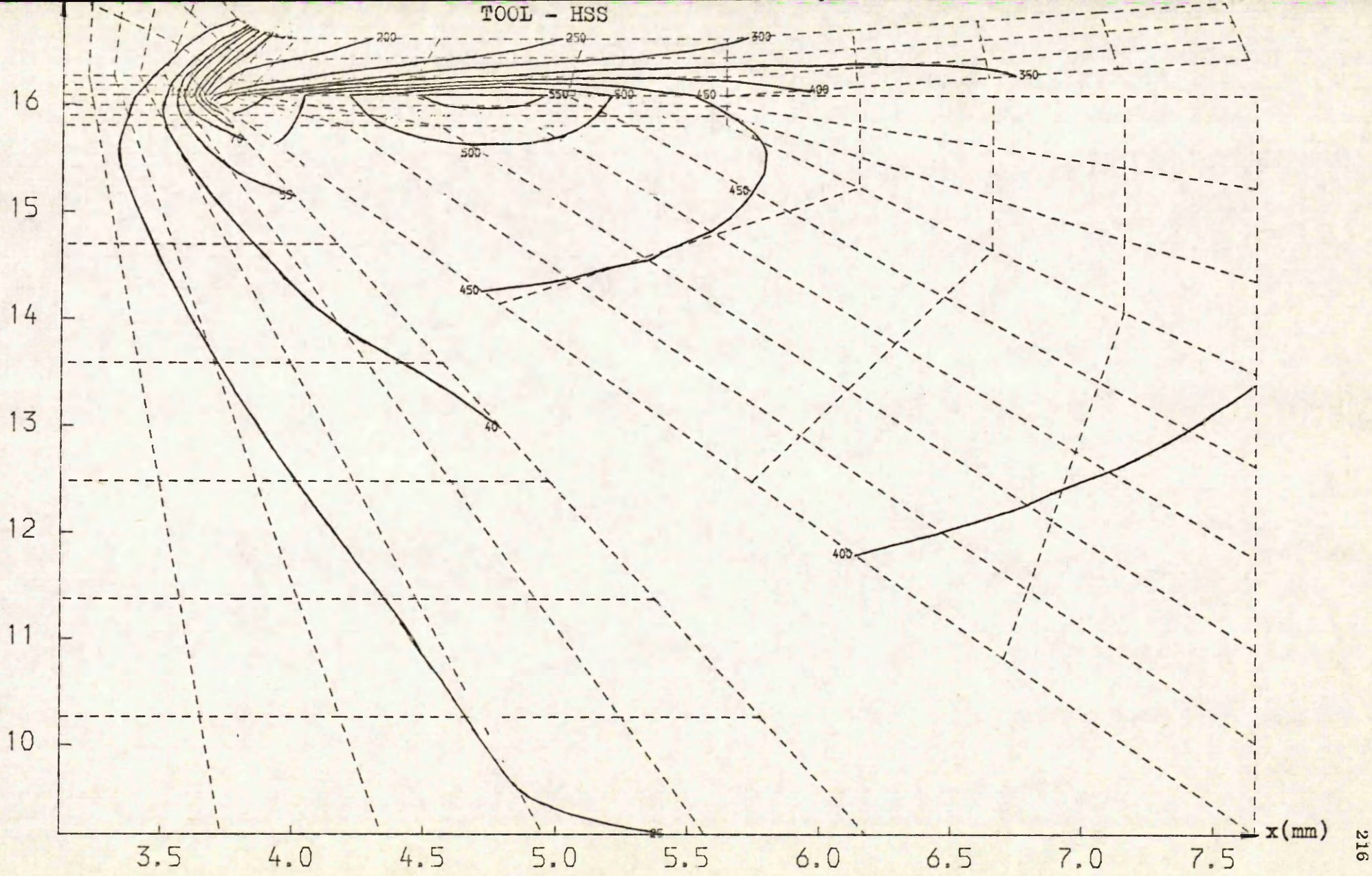

ISOTHERMALS IN WORKPIECE, TOOL AND CHIP PREDICTED BY FINITE ELEMENT ANALYSIS (°C)
TEST NO. = 6, NODES= 1192, ZONES CHOSEN ARE 9, 10, 11, 12, 19, 26, 33, 40, 53, 54, 60, 61, 62

FIG. 5.39 (b)

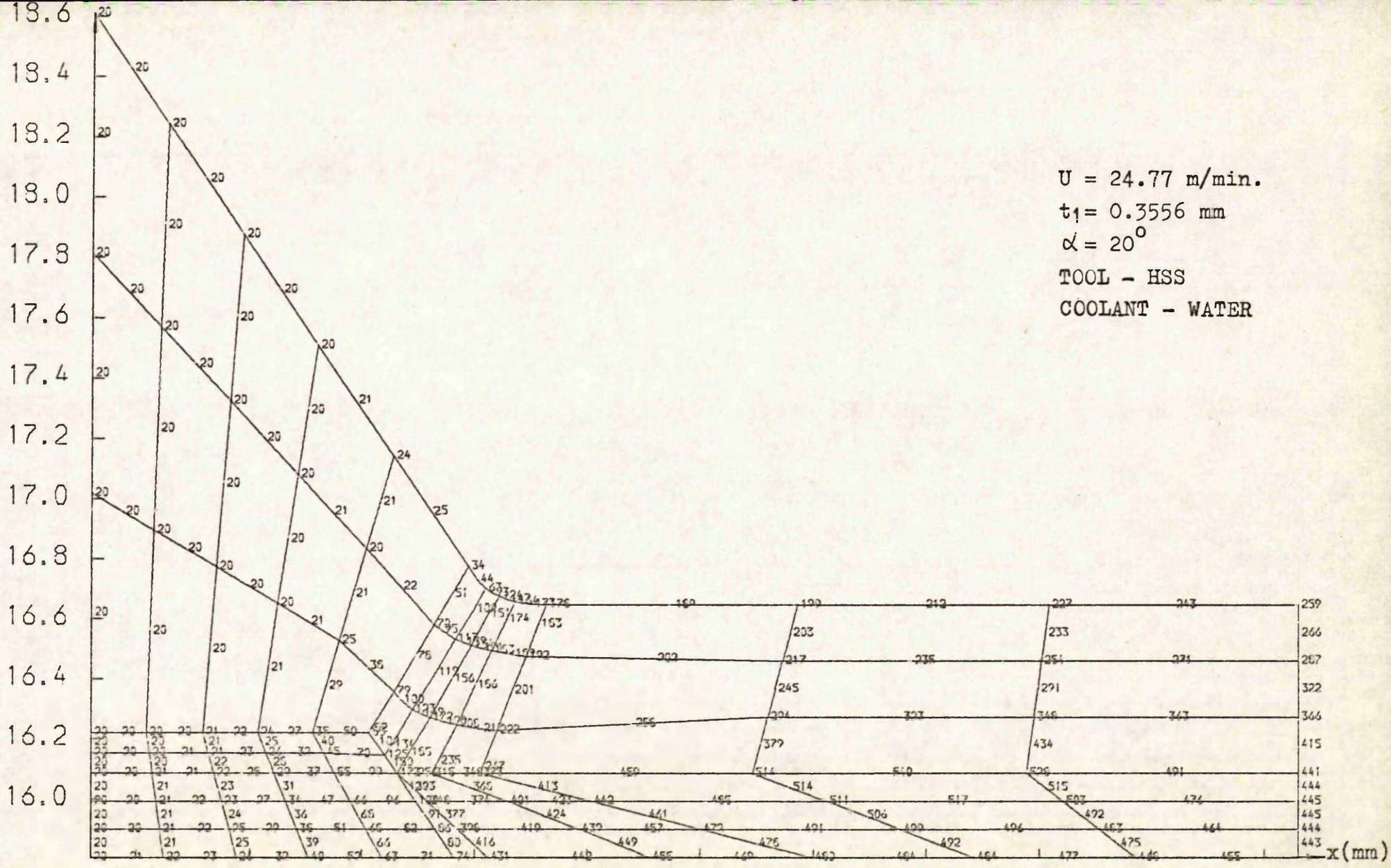

TEMPERATURE DISTRIBUTION IN WORKPIECE, TOOL AND CHIP PREDICTED BY FINITE ELEMENT ANALYSIS(^{o}C)
TEST NO.= 9, NODES= 1192, ZONES CHOSEN ARE 10, 11, 12, 19, 26, 33, 53, 54

FIG. 5.40 (a)

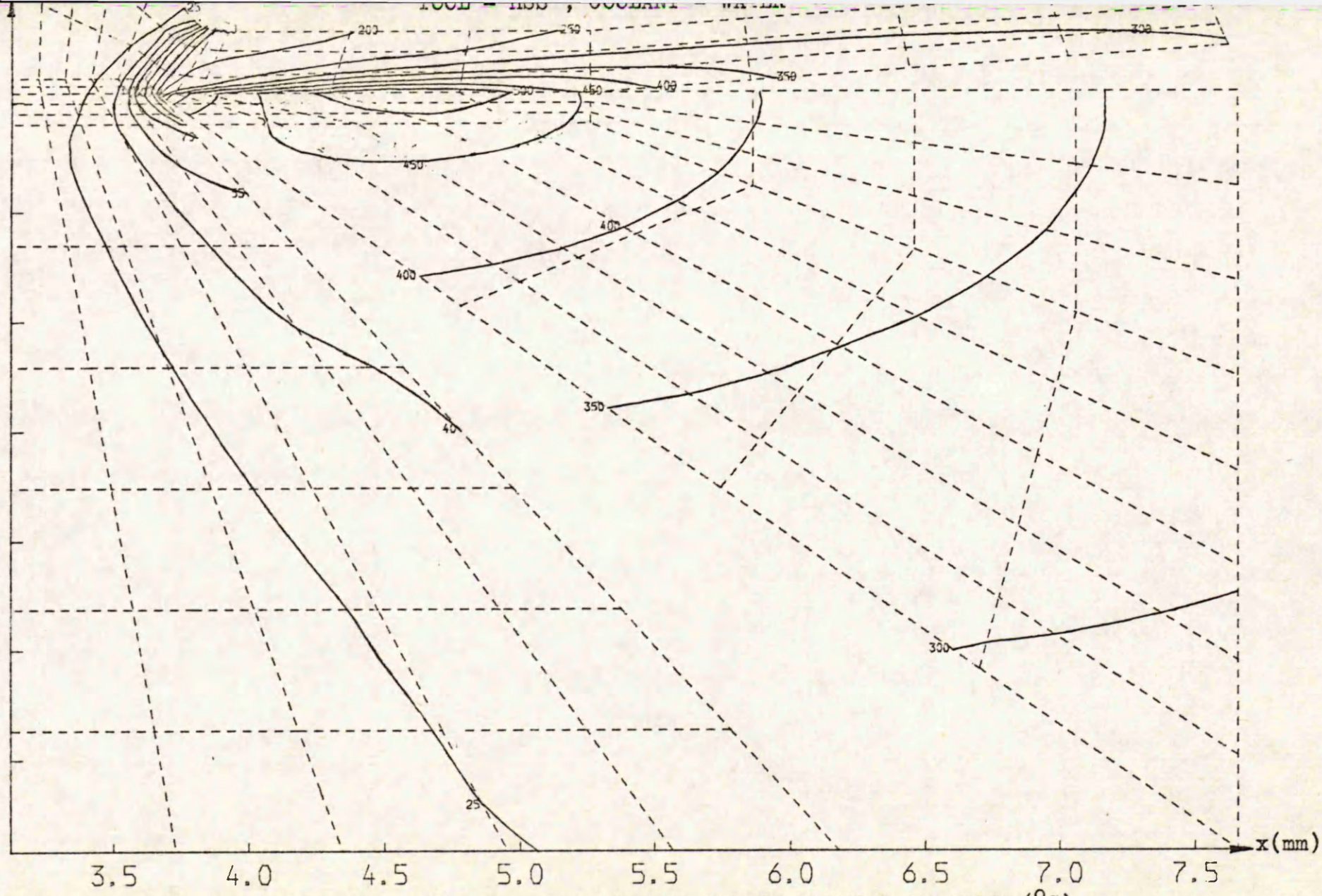

ISOTHERMALS IN WORKPIECE, TOOL AND CHIP PREDICTED BY FINITE ELEMENT ANALYSIS (°C)
TEST NO.= 9, NODES= 1192, ZONES CHOSEN ARE 9, 10, 11, 12, 19, 26, 33, 40, 53, 54, 60, 61, 62

FIG. 5.40 (b)

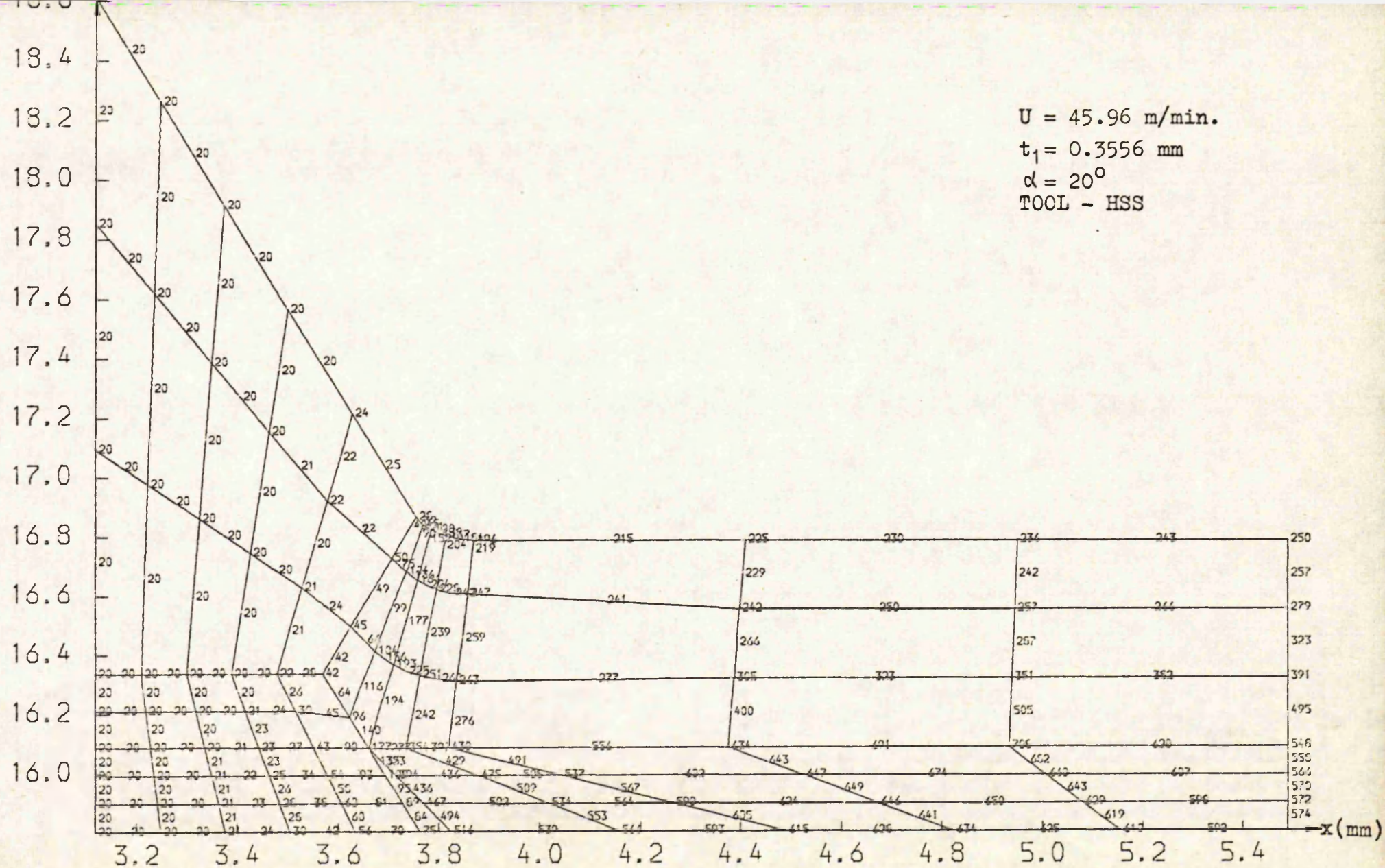

TEMPERATURE DISTRIBUTION IN WORKPIECE, TOOL AND CHIP PREDICTED BY FINITE ELEMENT ANALYSIS (°C)
TEST NO. = 11, NODES= 1192, ZONES CHOSEN ARE 10, 11, 12, 19, 26, 33, 53, 54

FIG. 5.41 (a)

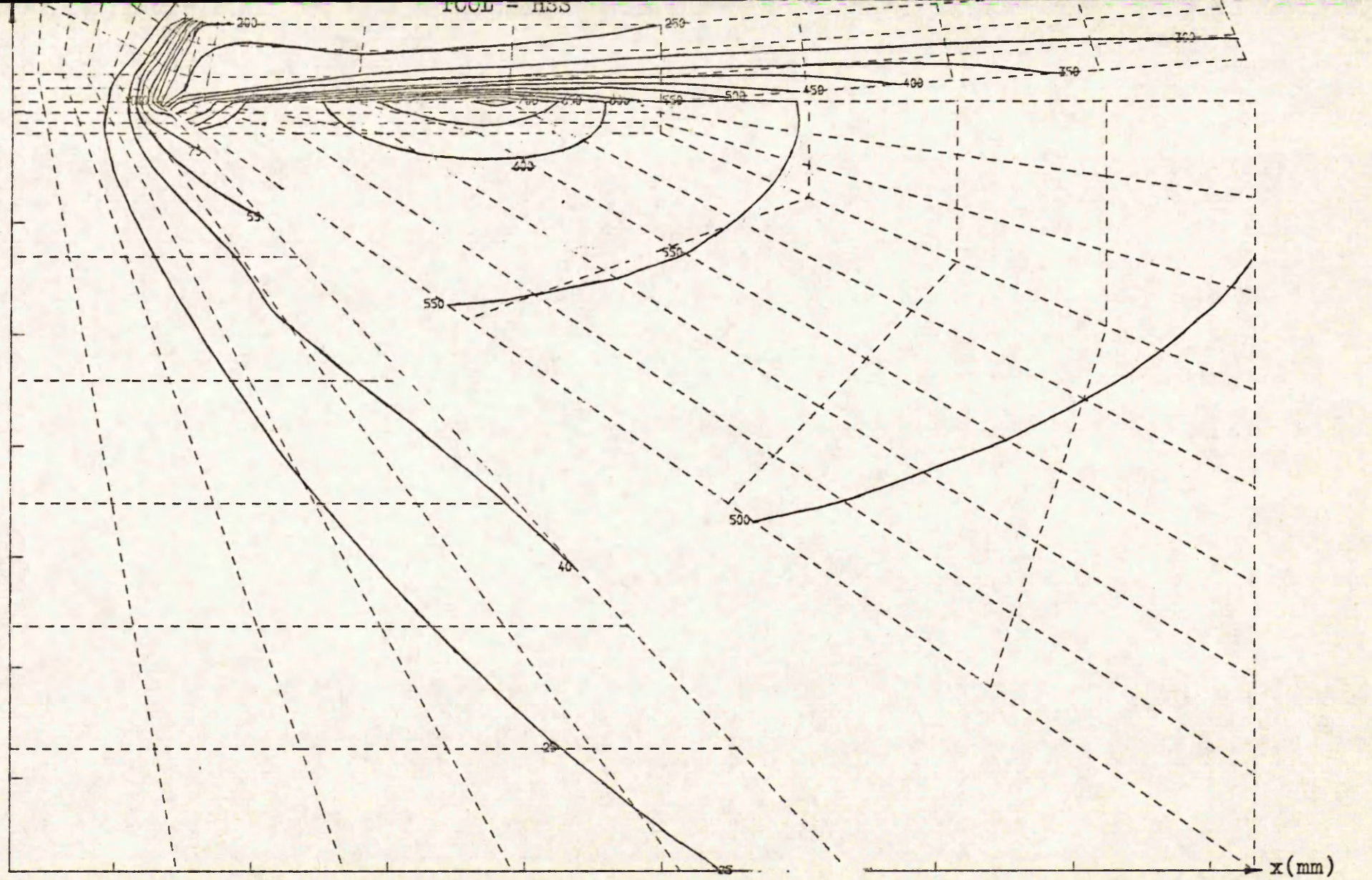

ISOTHERMALS IN WORKPIECE, TOOL AND CHIP PREDICTED BY FINITE ELEMENT ANALYSIS (°C)
TEST NO.= 11, NODES= 1192, ZONES CHOSEN ARE 9, 10, 11, 12, 19, 26, 33, 40, 53, 54, 60, 61, 62

FIG. 5.41 (b)

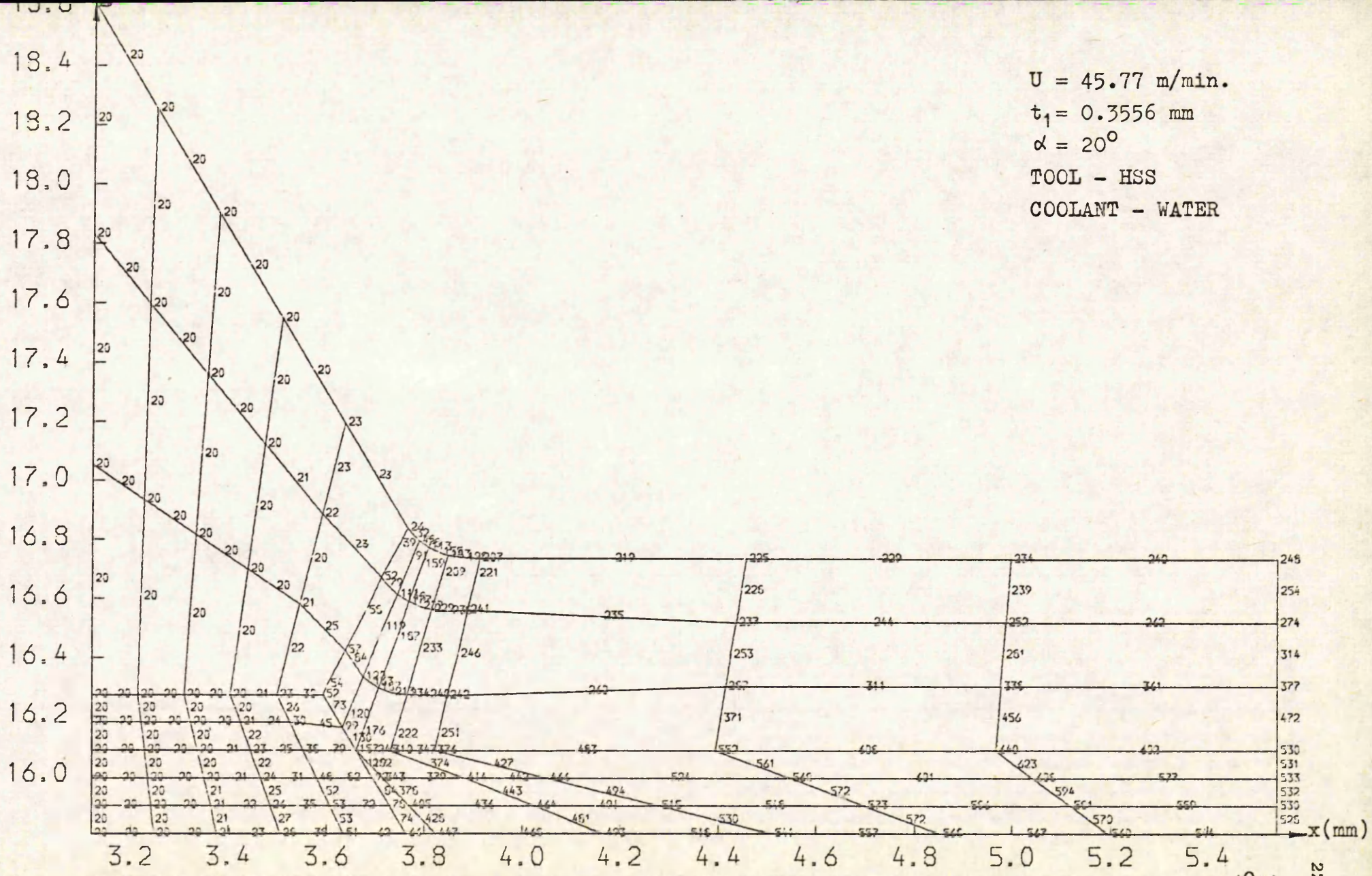

TEMPERATURE DISTRIBUTION IN WORKPIECE, TOOL AND CHIP PREDICTED BY FINITE ELEMENT ANALYSIS (°C)
TEST NO. = 12, NODES= 1192, ZONES CHOSEN ARE 10, 11, 12, 19, 26, 33, 53, 54

FIG. 5.42 (a)

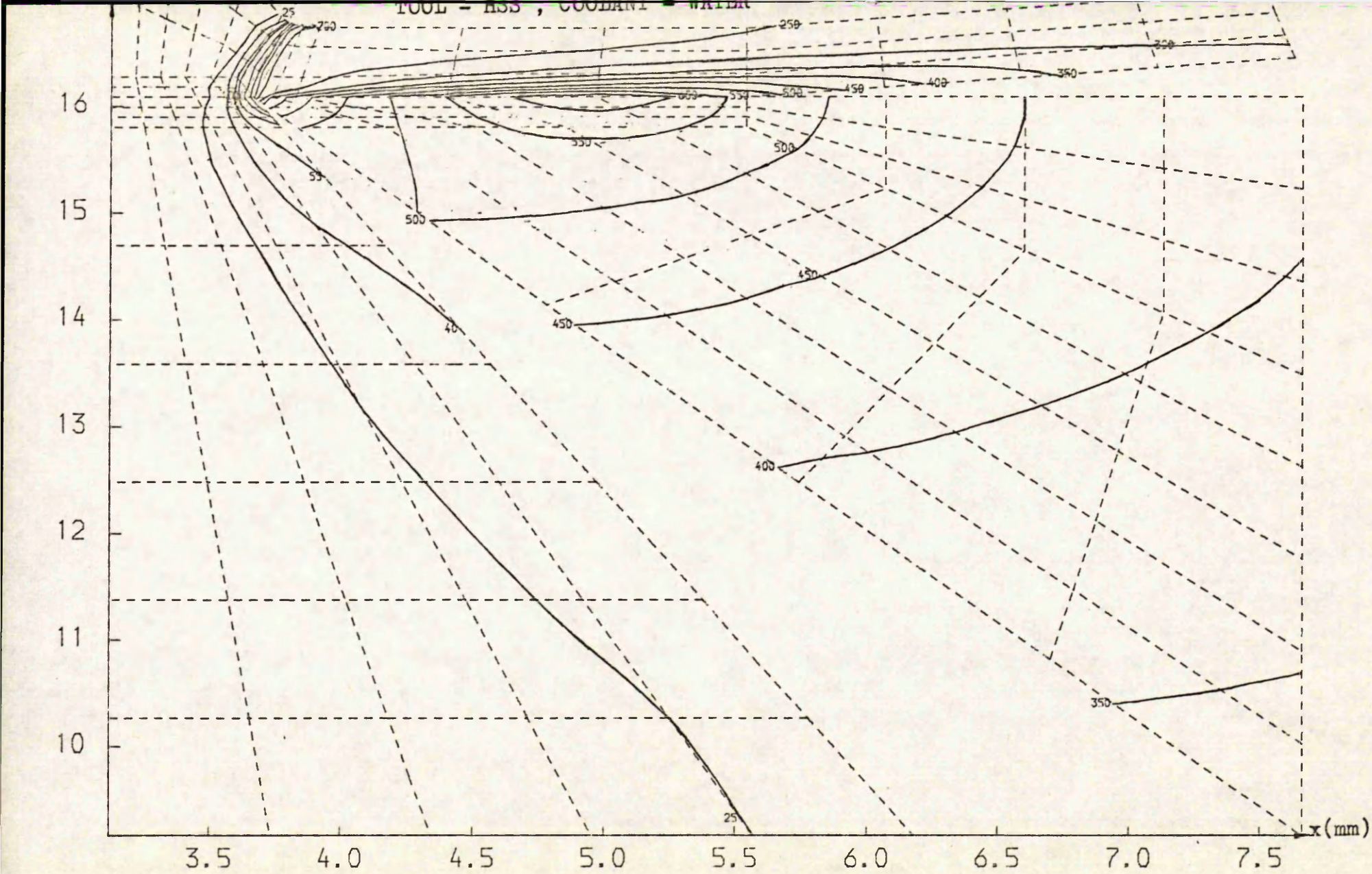

ISOTHERMALS IN WORKPIECE, TOOL AND CHIP PREDICTED BY FINITE ELEMENT ANALYSIS (°C)
TEST NO.= 12, NODES= 1192, ZONES CHOSEN ARE 9, 10, 11, 12, 19, 26, 33, 40, 53, 54, 60, 61, 62

FIG. 5.42 (b)

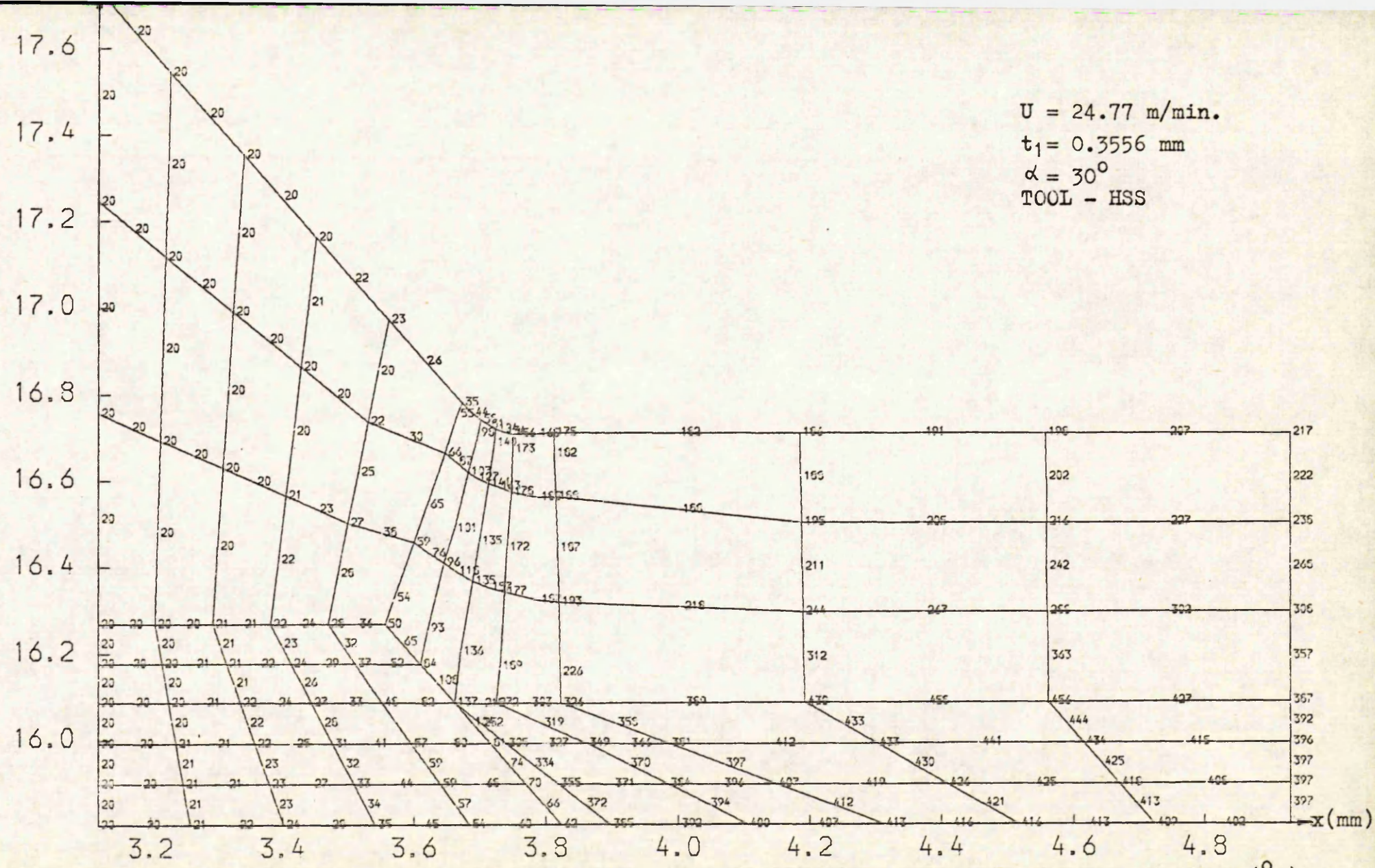

TEMPERATURE DISTRIBUTION IN WORKPIECE, TOOL AND CHIP PREDICTED BY FINITE ELEMENT ANALYSIS (°C)
TEST NO. = 13, NODES= 1192, ZONES CHOSEN ARE 10, 11, 12, 19, 26, 33, 53, 54

FIG. 5.43 (a)

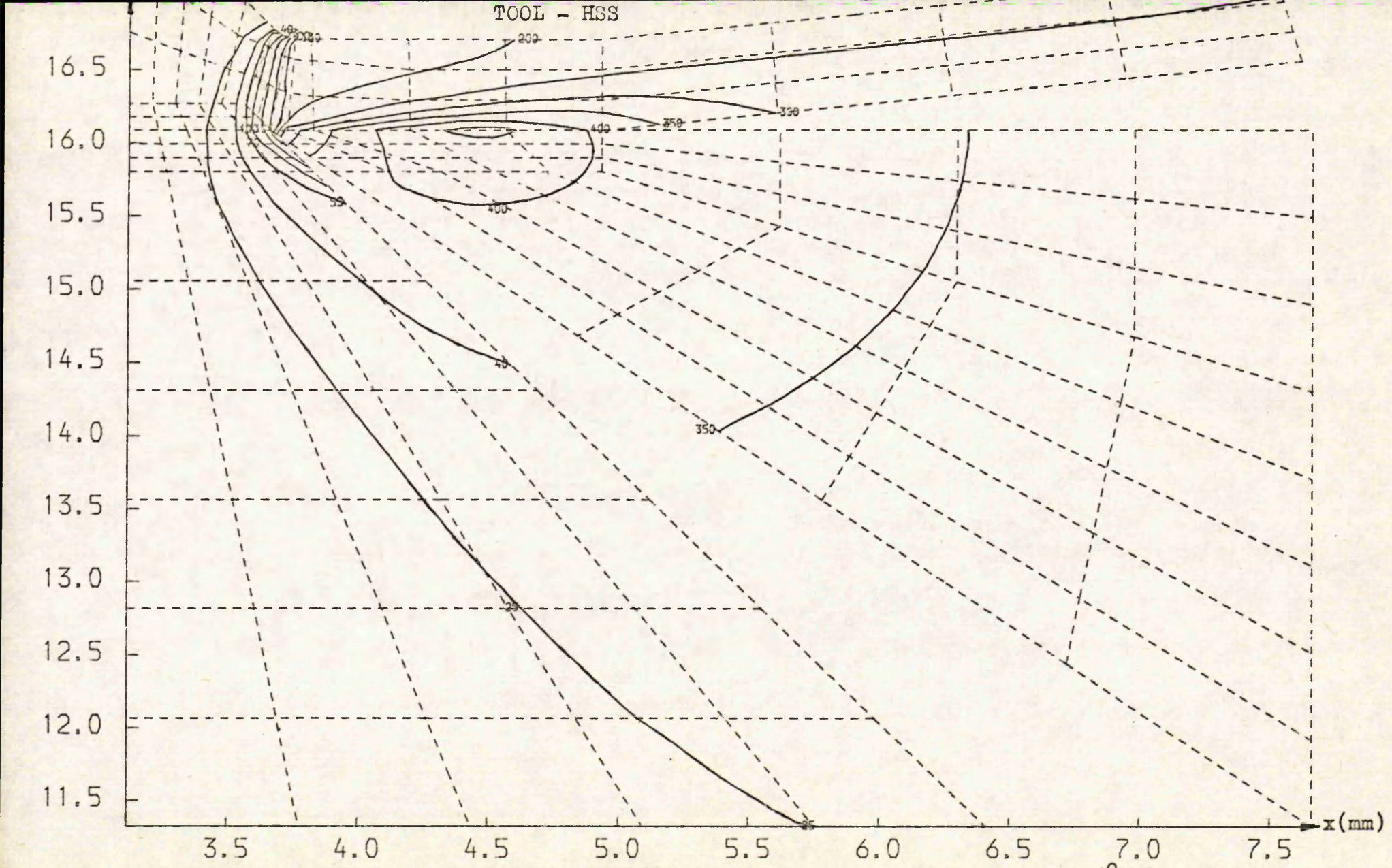

ISOTHERMALS IN WORKPIECE, TOOL AND CHIP PREDICTED BY FINITE ELEMENT ANALYSIS(^{o}C)
TEST NO.= 13, NODES= 1192, ZONES CHOSEN ARE 9, 10, 11, 12, 19, 26, 33, 40, 53, 54, 60, 61, 62

FIG. 5.43 (b)

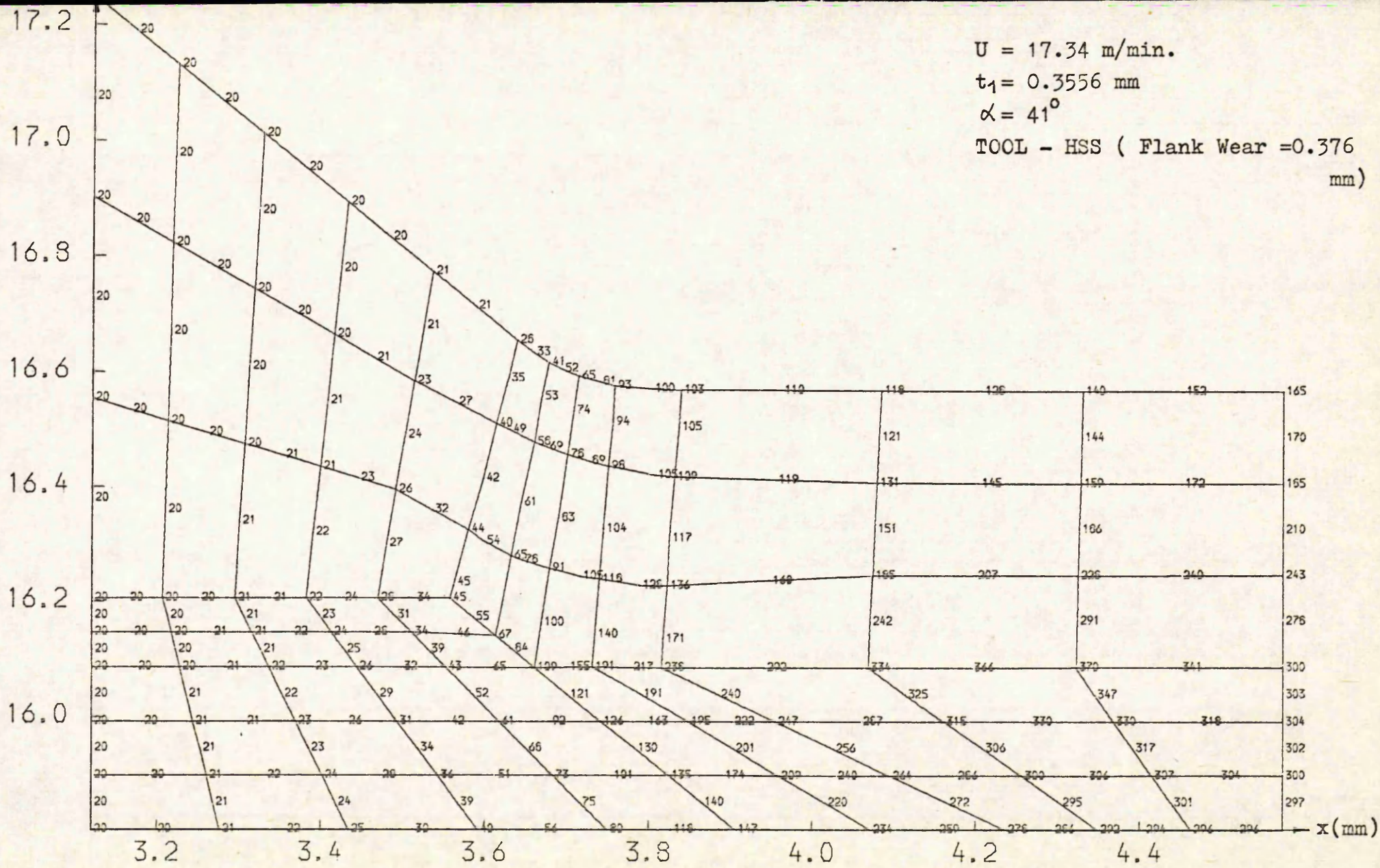

TEMPERATURE DISTRIBUTION IN WORKPIECE, TOOL AND CHIP PREDICTED BY FINITE ELEMENT ANALYSIS (°C)
TEST NO.=25, NODES= 1186, ZONES CHOSEN ARE 10, 11, 12, 19, 26, 33, 53, 54

FIG. 5.44 (a)

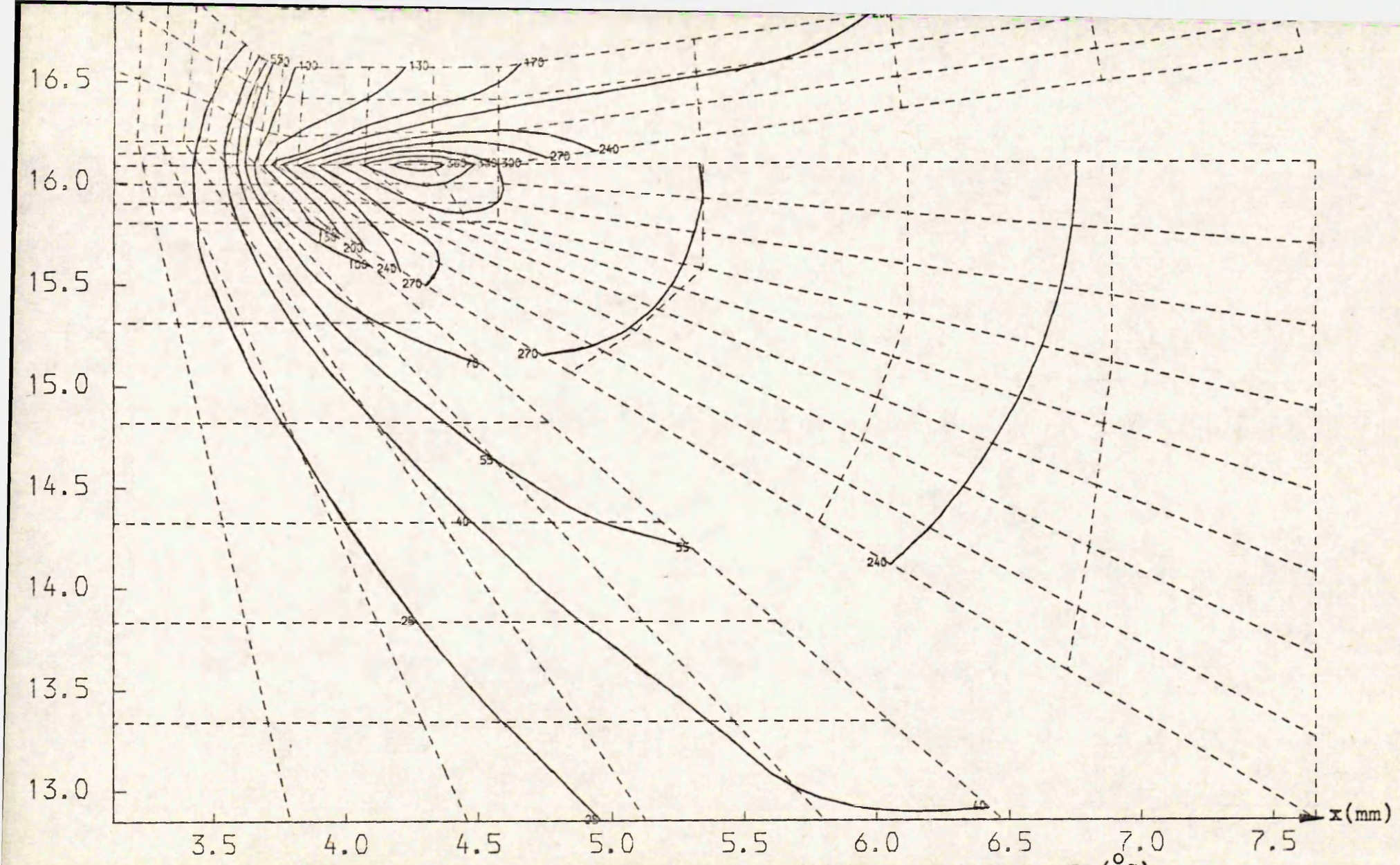

ISOTHERMALS IN WORKPIECE, TOOL AND CHIP PREDICTED BY FINITE ELEMENT ANALYSIS (^{o}C)
TEST NO.=25, NODES= 1186, ZONES CHOSEN ARE 9, 10, 11, 12, 19, 26, 33, 40, 53, 54, 60, 61, 62

FIG. 5.44 (b)

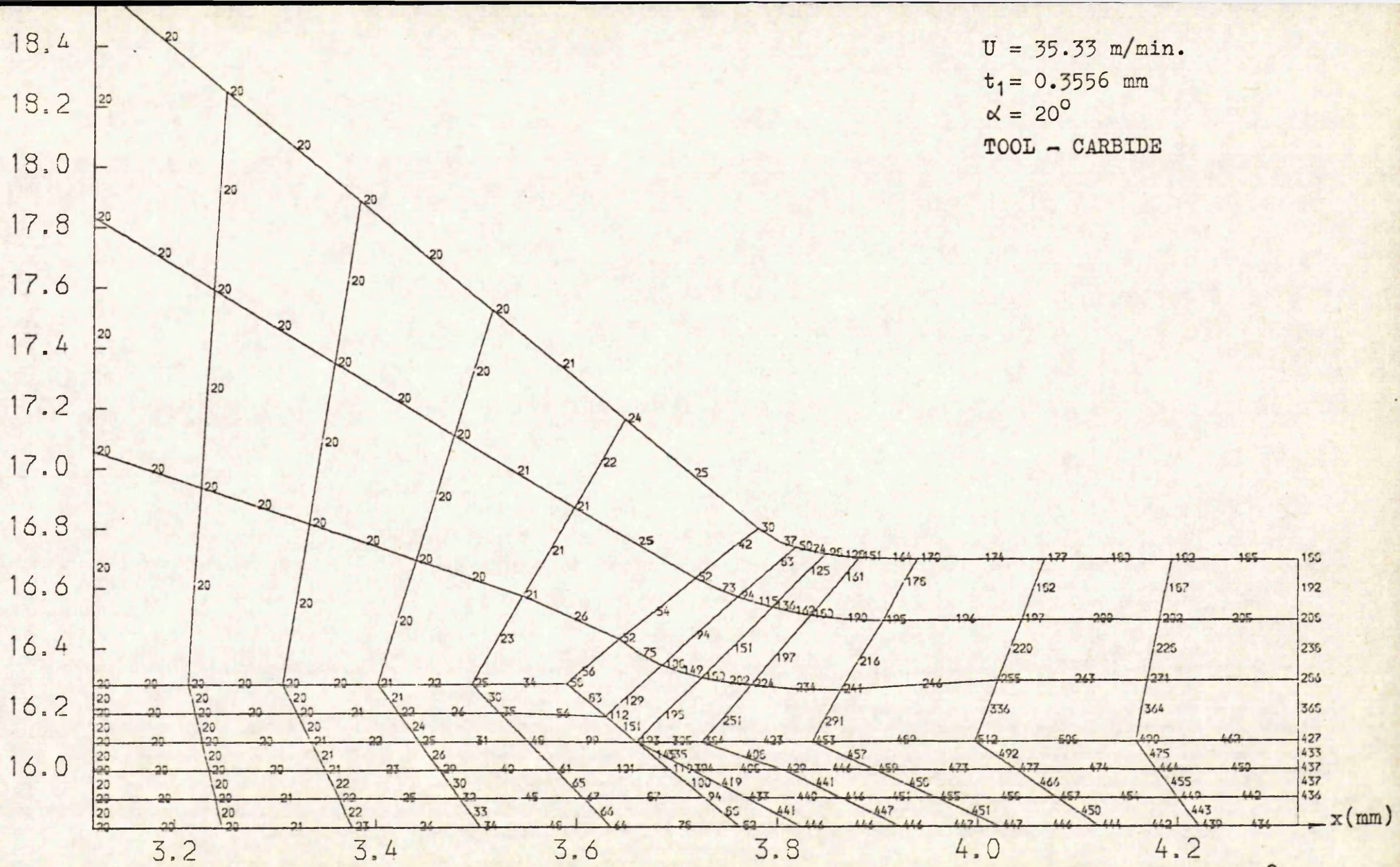

TEMPERATURE DISTRIBUTION IN WORKPIECE, TOOL AND CHIP PREDICTED BY FINITE ELEMENT ANALYSIS (°C)
TEST NO. = 14, NODES= 1284, ZONES CHOSEN ARE 10, 11, 12, 19, 26, 33, 53, 54

FIG. 5.45 (a)

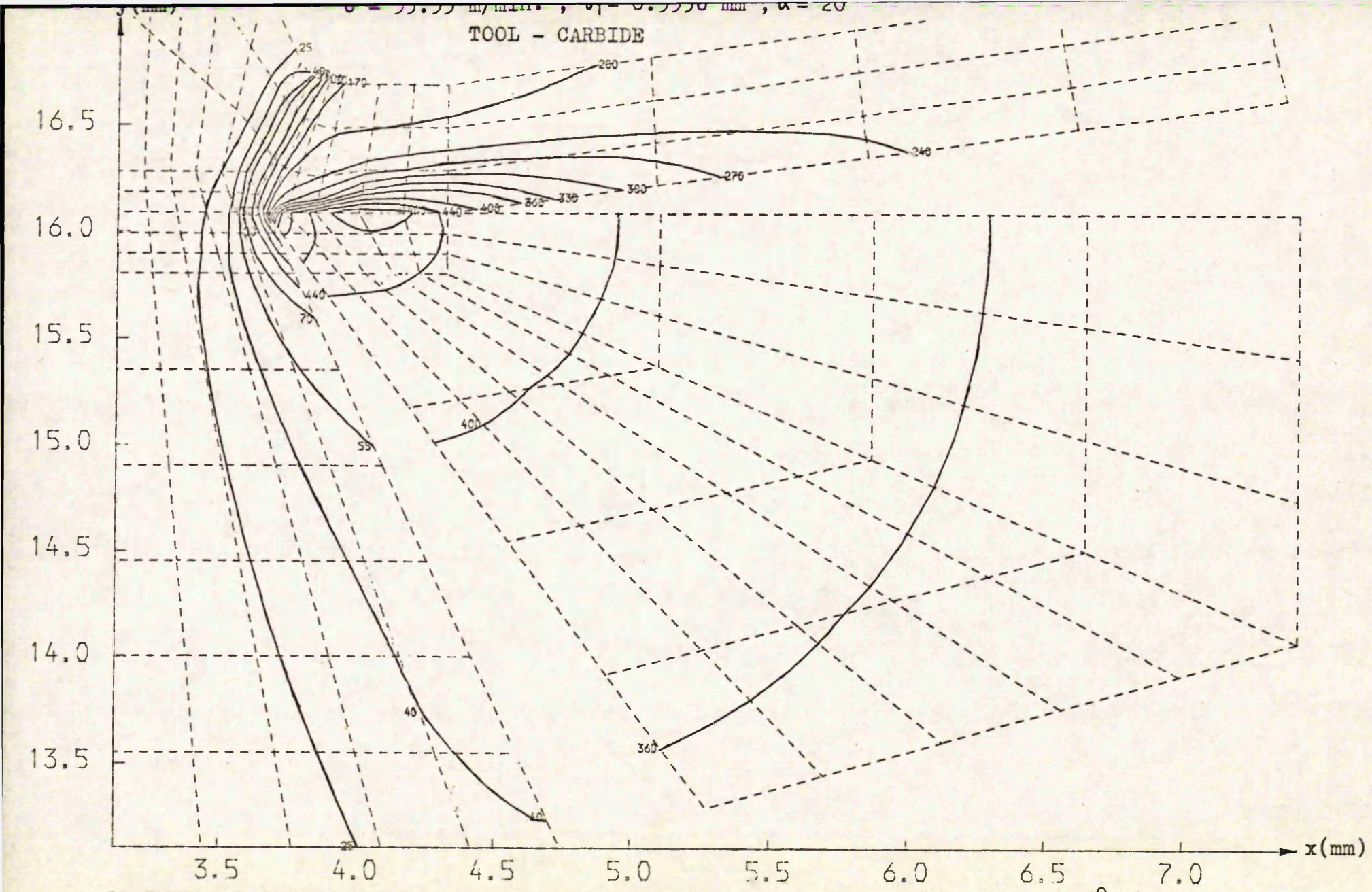

ISOTHERMALS IN WORKPIECE, TOOL AND CHIP PREDICTED BY FINITE ELEMENT ANALYSIS (°C)
TEST NO.= 14, NODES= 1284, ZONES CHOSEN ARE 9, 10, 11, 12, 19, 26, 33, 40, 53, 54, 60, 61, 62

FIG. 5.45 (b)

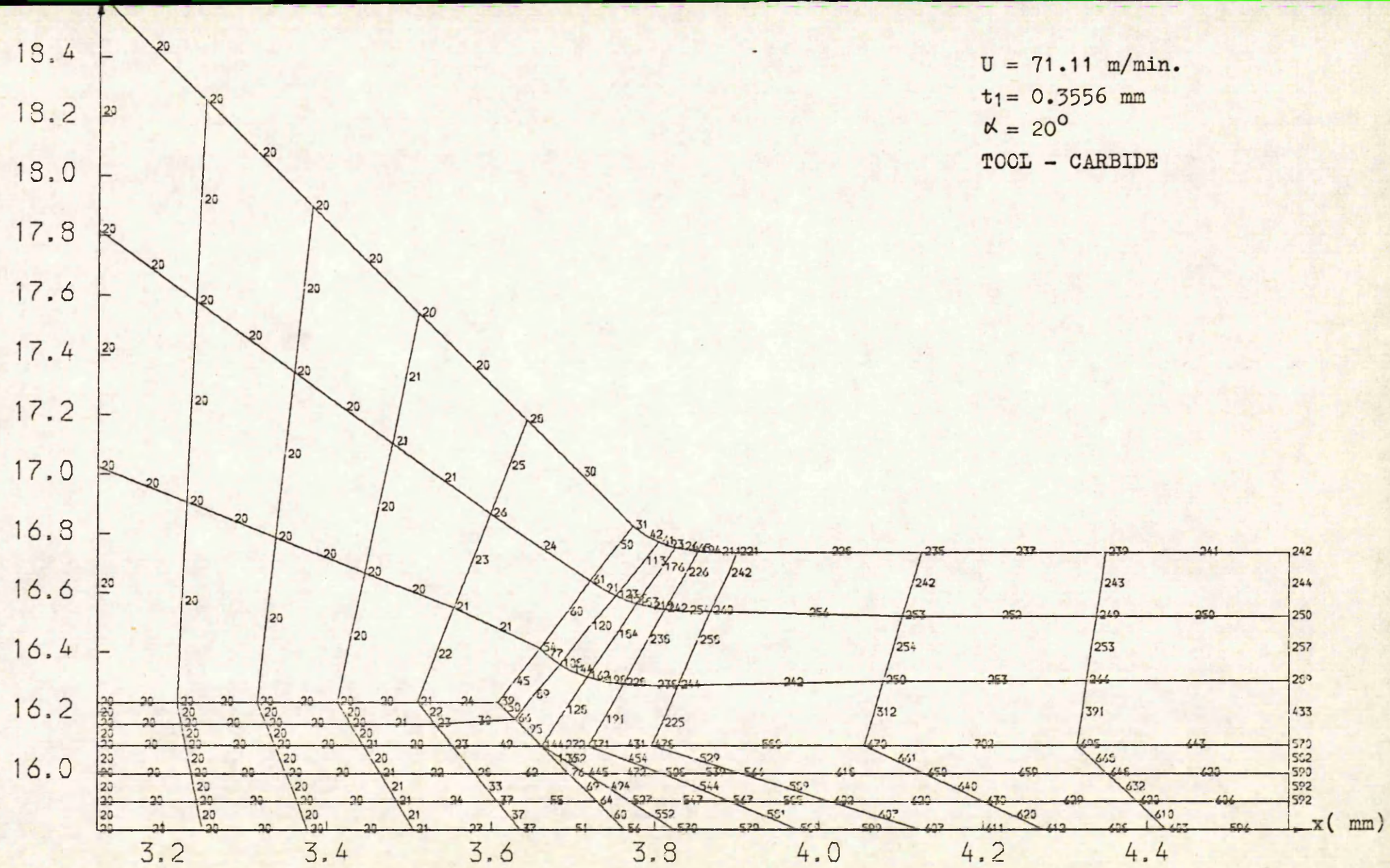

TEMPERATURE DISTRIBUTION IN WORKPIECE, TOOL AND CHIP PREDICTED BY FINITE ELEMENT ANALYSIS (°C)
TEST NO.= 15, NODES= 1284, ZONES CHOSEN ARE 10, 11, 12, 19, 26, 33, 53, 54

FIG. 5.46 (a)

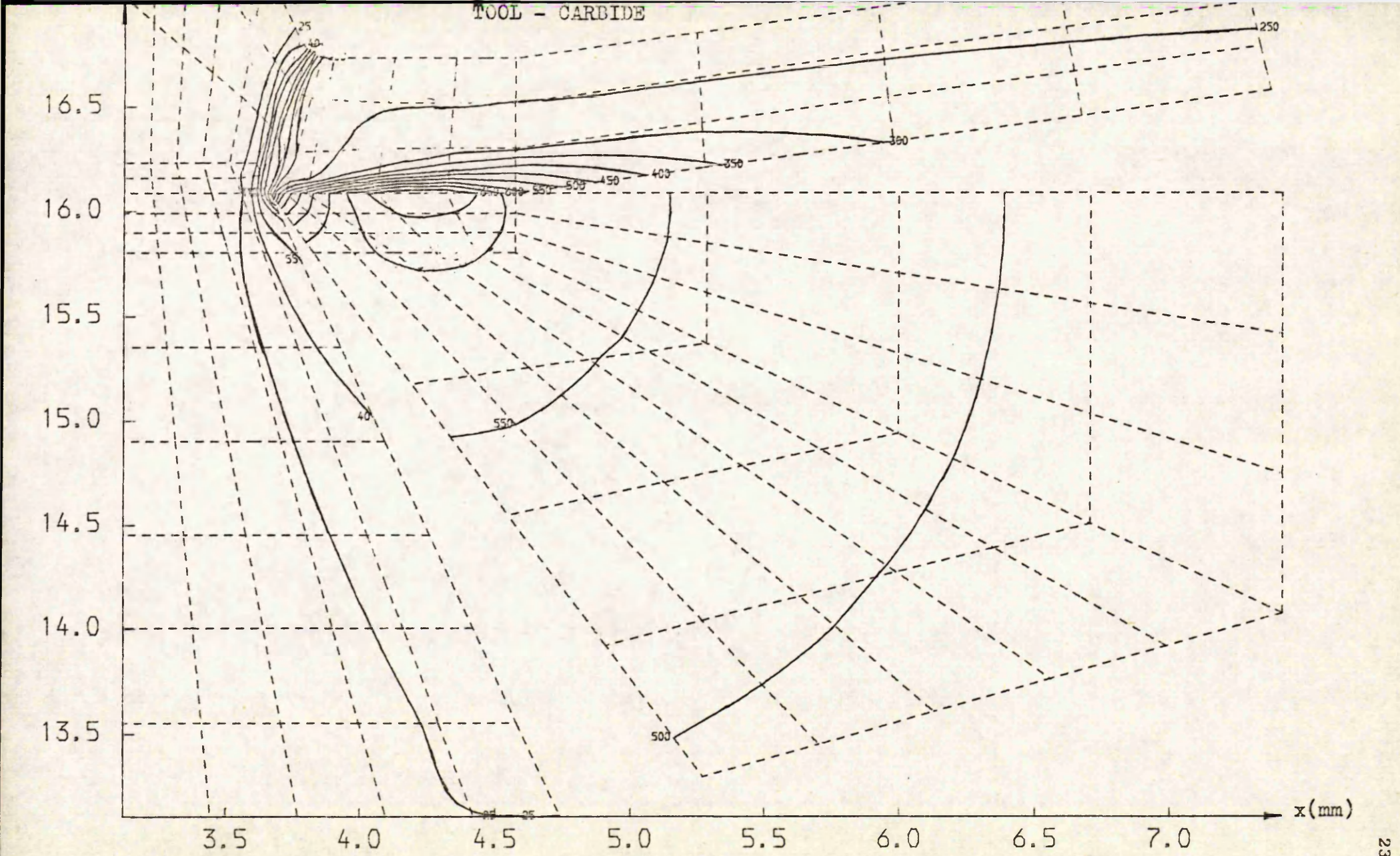

ISOTHERMALS IN WORKPIECE, TOOL AND CHIP PREDICTED BY FINITE ELEMENT ANALYSIS (°C)
TEST NO. = 15, NODES= 1284, ZONES CHOSEN ARE 9, 10, 11, 12, 19, 26, 33, 40, 53, 54, 60, 61, 62

FIG. 5.46 (b)

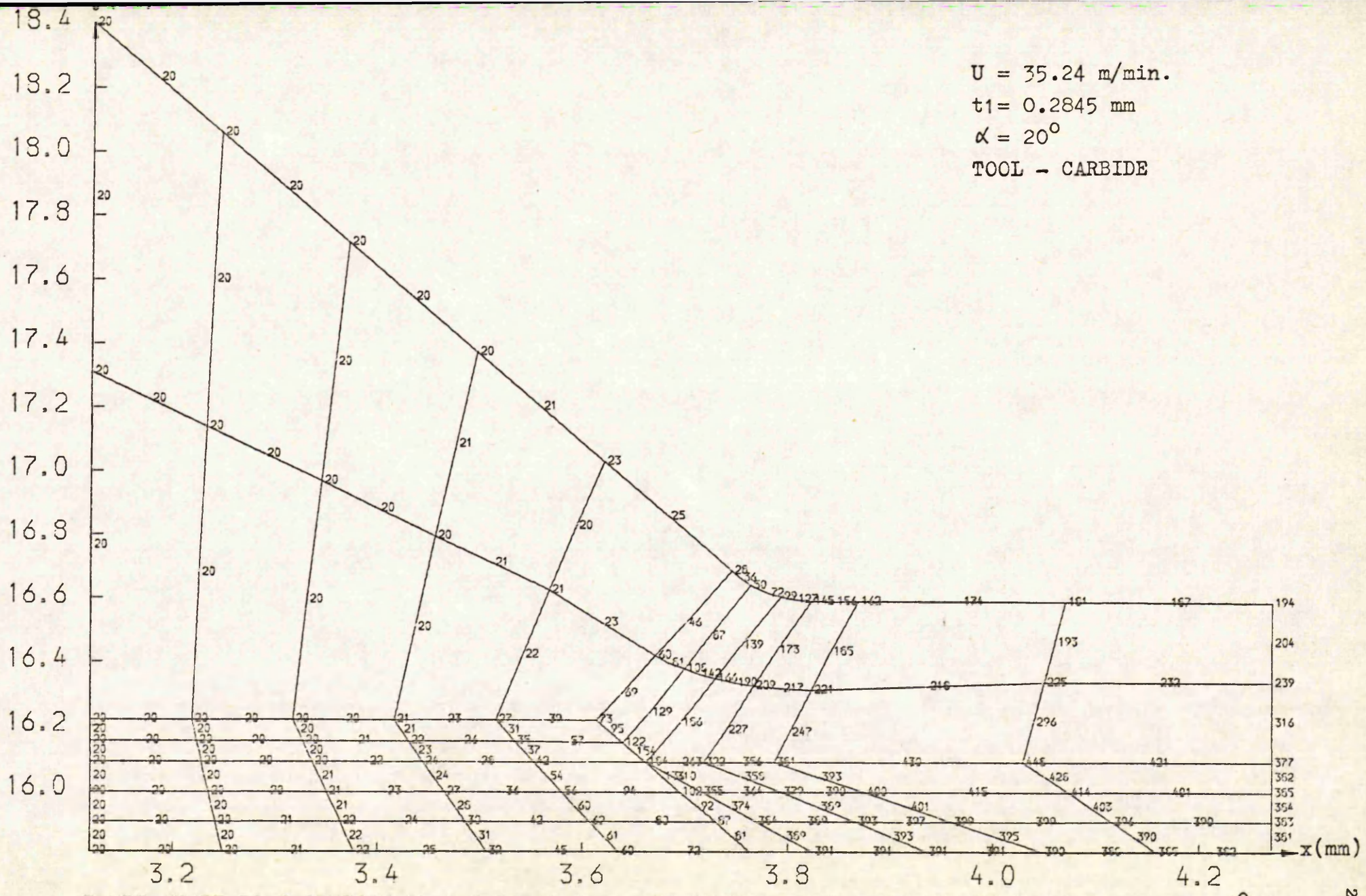

TEMPERATURE DISTRIBUTION IN WORKPIECE, TOOL AND CHIP PREDICTED BY FINITE ELEMENT ANALYSIS (°C)
TEST NO.= 17, NODES= 1116, ZONES CHOSEN ARE 10, 11, 12, 19, 26, 33, 53, 54

FIG. 5.47(a)

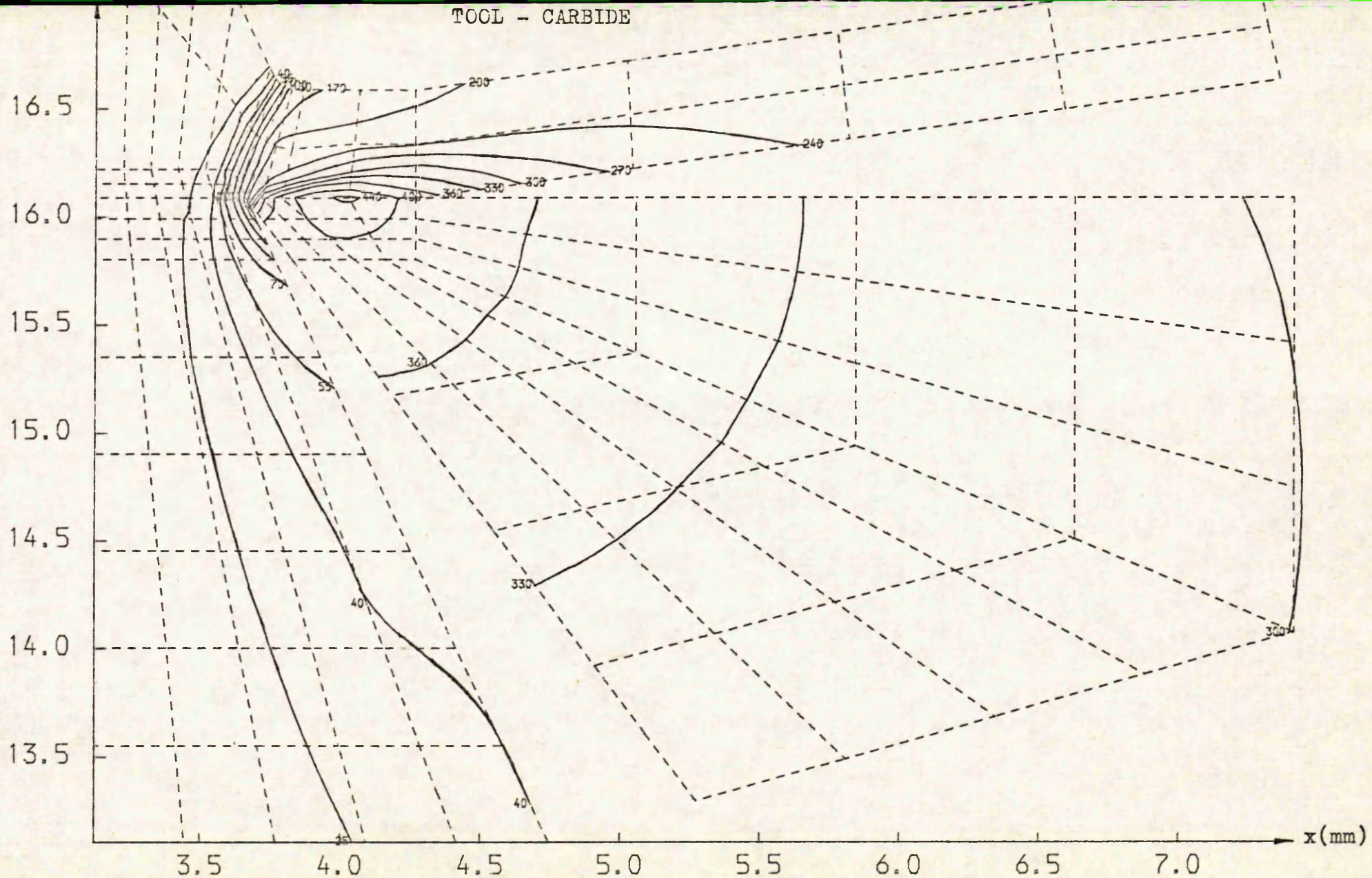

ISOTHERMALS IN WORKPIECE, TOOL AND CHIP PREDICTED BY FINITE ELEMENT ANALYSIS(°C)
TEST NO.= 17, NODES= 1116, ZONES CHOSEN ARE 9, 10, 11, 12, 19, 26, 33, 40, 53, 54, 60, 61, 62

FIG. 5.47 (b)

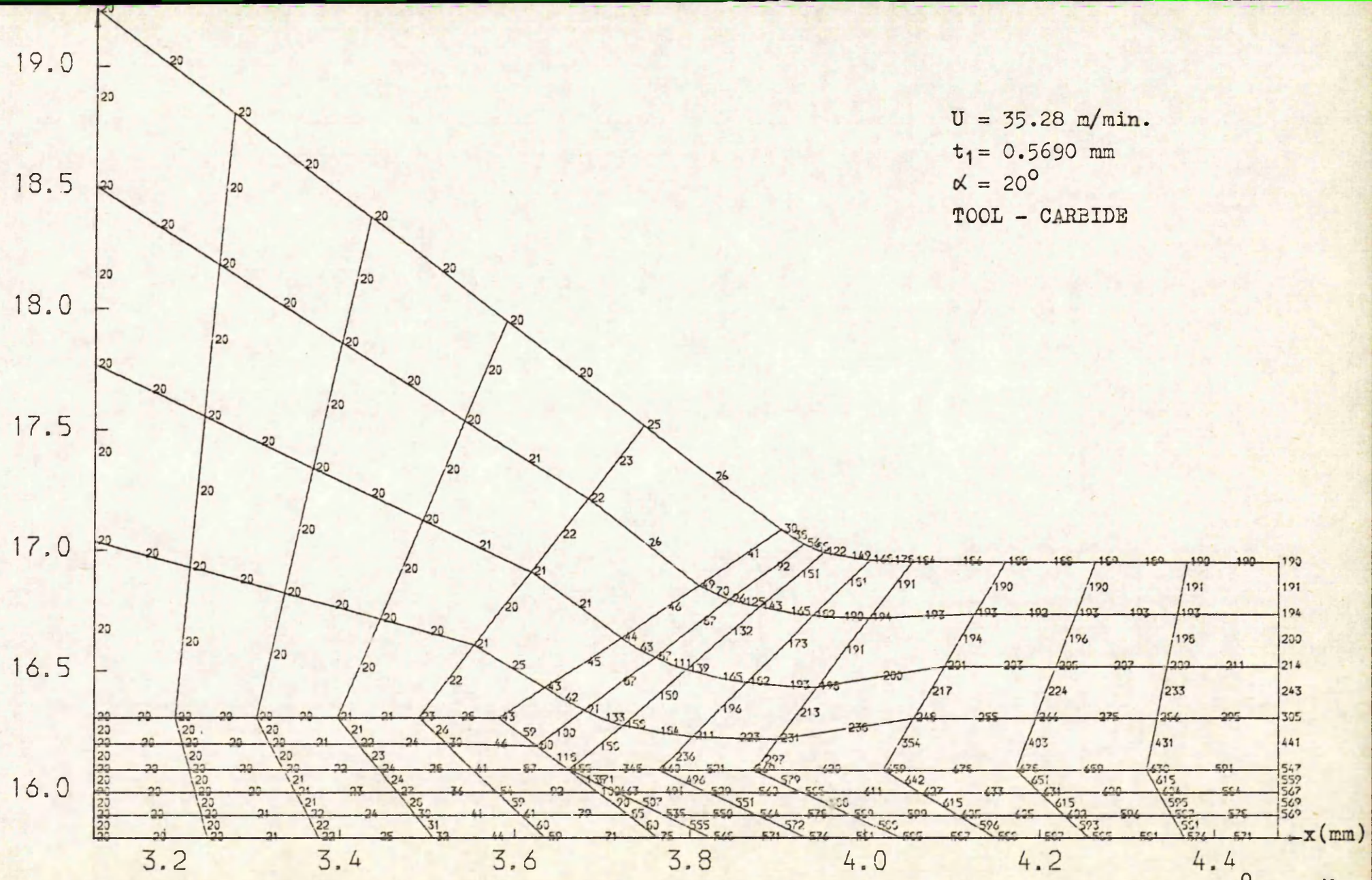

TEMPERATURE DISTRIBUTION IN WORKPIECE, TOOL AND CHIP PREDICTED BY FINITE ELEMENT ANALYSIS(°C)
TEST NO.= 18, NODES= 1458, ZONES CHOSEN ARE 10, 11, 12, 19, 26, 33, 53, 54

FIG. 5.48 (a)

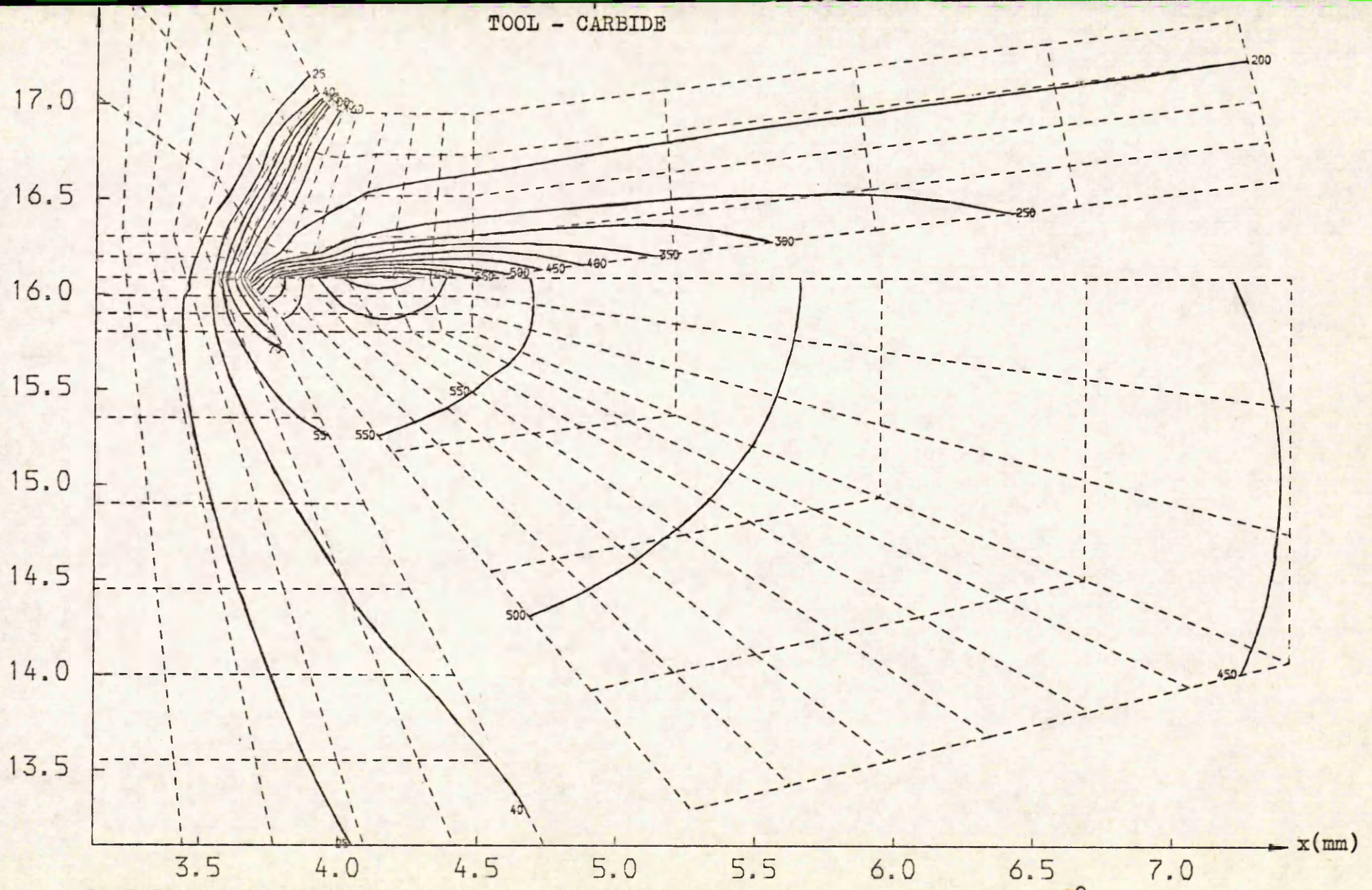

ISOTHERMALS IN WORKPIECE, TOOL AND CHIP PREDICTED BY FINITE ELEMENT ANALYSIS(°C)
TEST NO.= 18, NODES= 1458, ZONES CHOSEN ARE 9, 10, 11, 12, 19, 26, 33, 40, 53, 54, 60, 61, 62

FIG.5.48 (b)

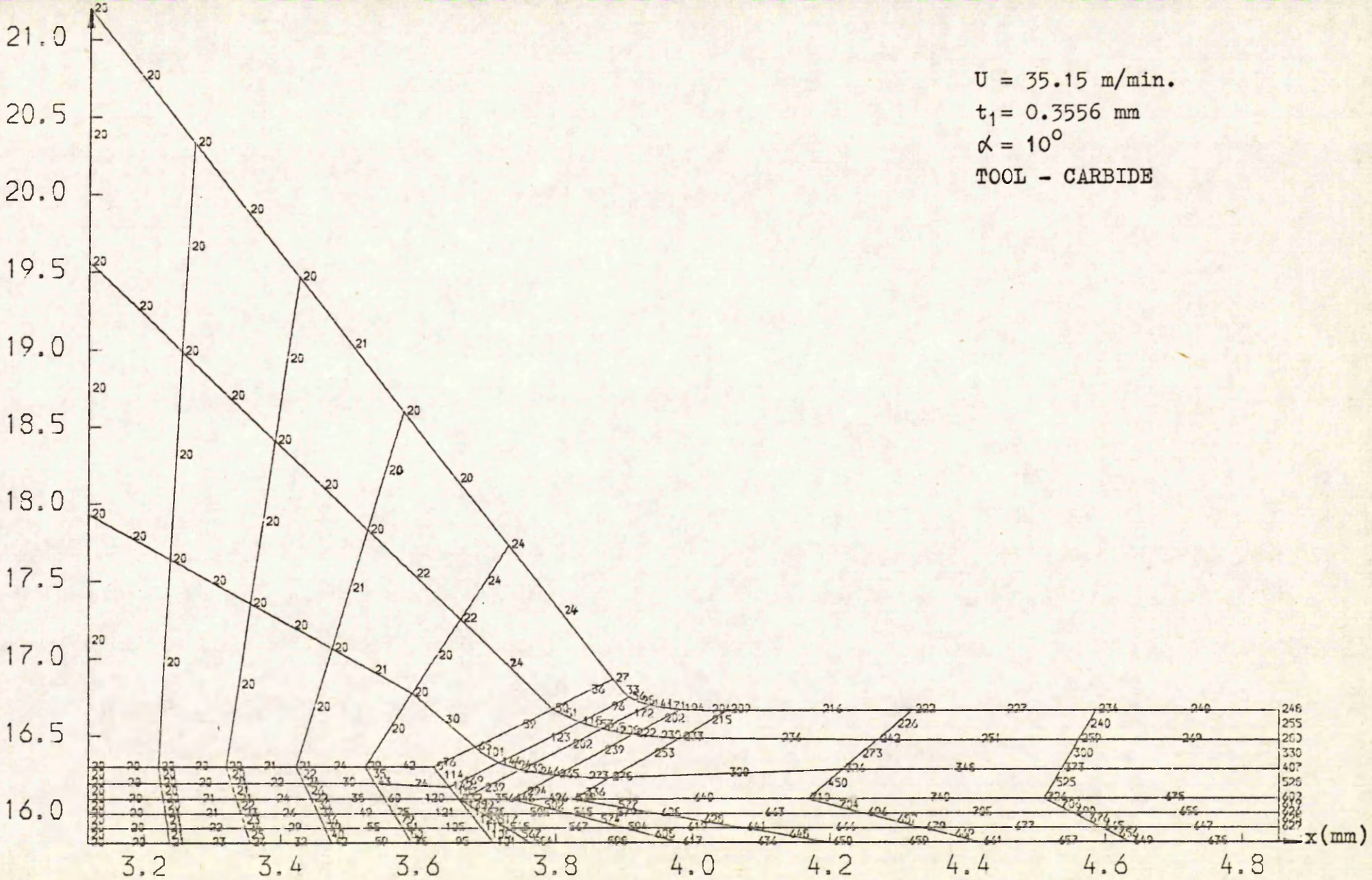

TEMPERATURE DISTRIBUTION IN WORKPIECE, TOOL AND CHIP PREDICTED BY FINITE ELEMENT ANALYSIS(°C)
TEST NO. = 19, NODES= 1284, ZONES CHOSEN ARE 10, 11, 12, 19, 26, 33, 53, 54

FIG. 5.49 (a)

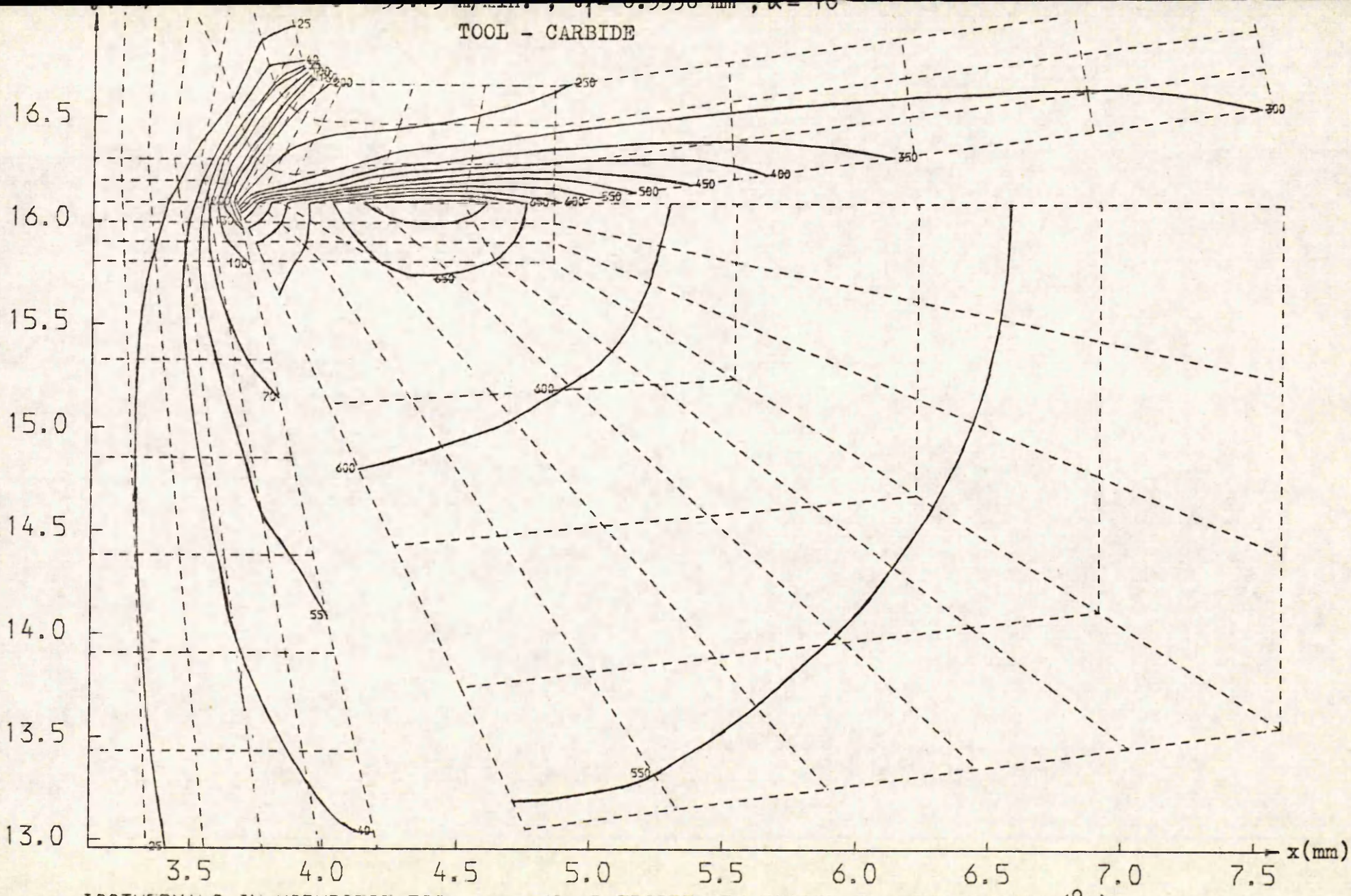

ISOTHERMALS IN WORKPIECE, TOOL AND CHIP PREDICTED BY FINITE ELEMENT ANALYSIS(^{o}C)
TEST NO.= 19, NODES= 1284, ZONES CHOSEN ARE 9, 10, 11, 12, 19, 26, 33, 40, 53, 54, 60, 61, 62

FIG. 5.49 (b)

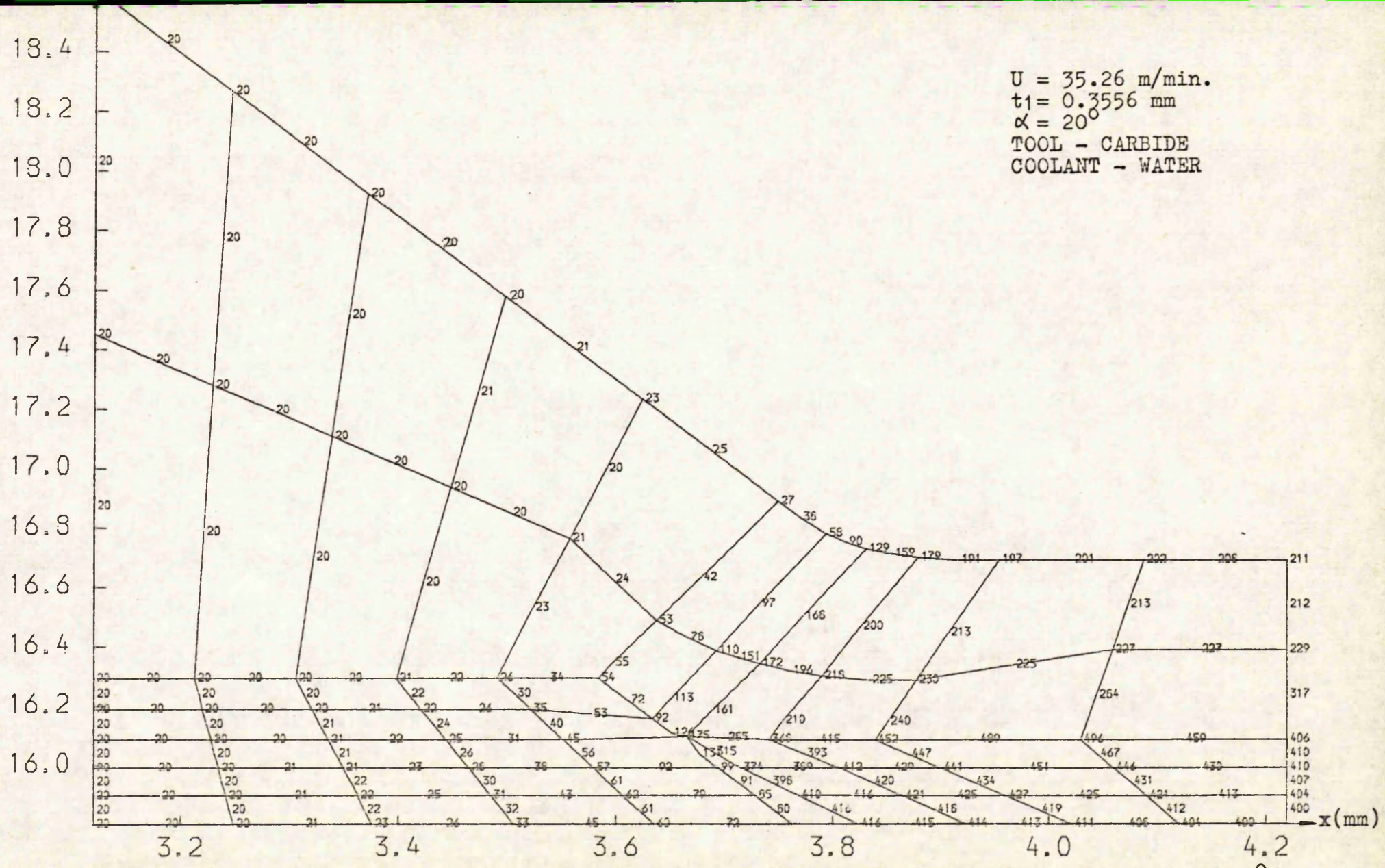

TEMPERATURE DISTRIBUTION IN WORKPIECE, TOOL AND CHIP PREDICTED BY FINITE ELEMENT ANALYSIS (°C)
TEST NO.= 21, NODES= 1116, ZONES CHOSEN ARE 10, 11, 12, 19, 26, 33, 53, 54

FIG. 5.50 (a)

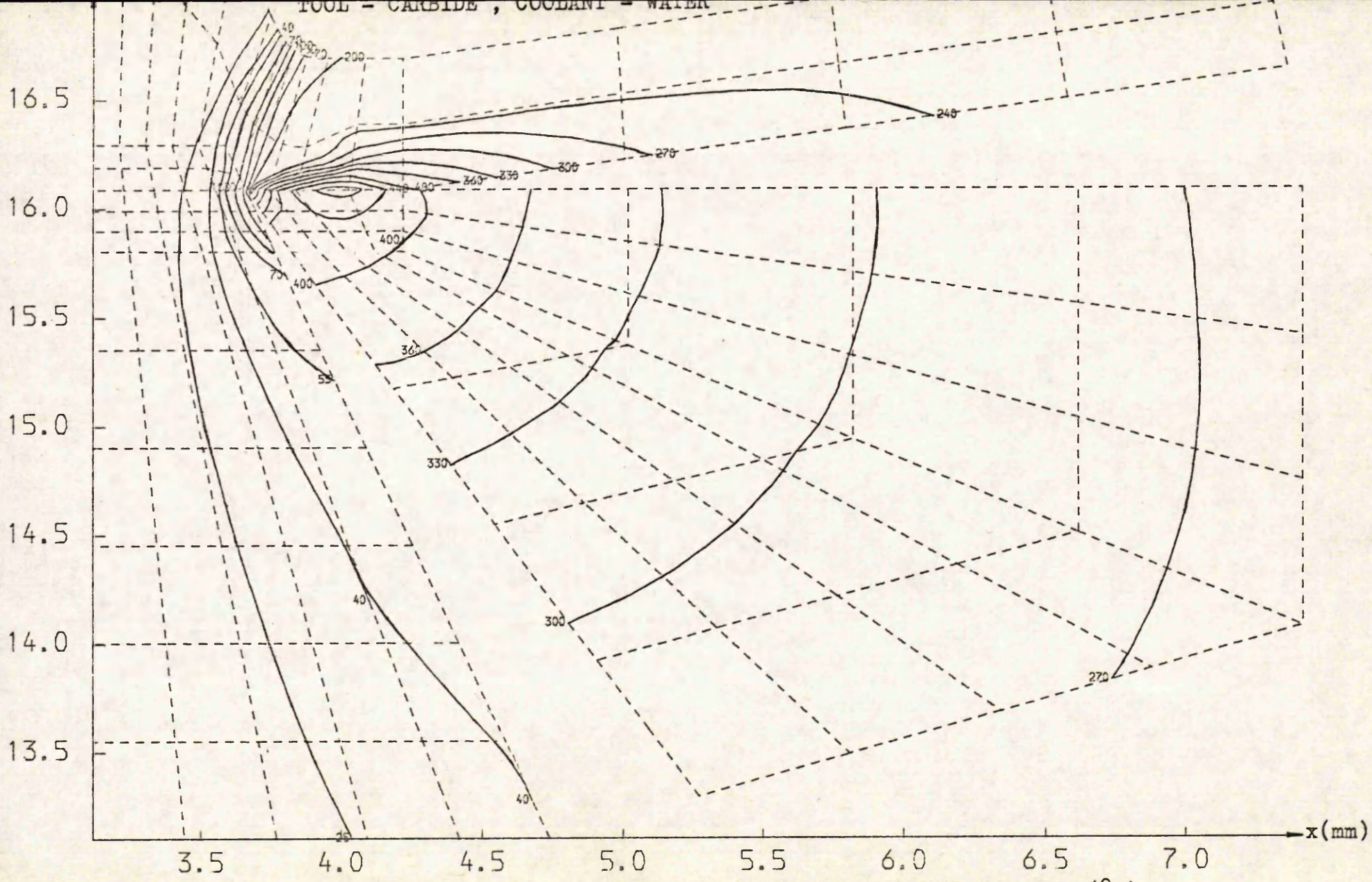

ISOTHERMALS IN WORKPIECE, TOOL AND CHIP PREDICTED BY FINITE ELEMENT ANALYSIS (°C)
TEST NO.= 21, NODES= 1116, ZONES CHOSEN ARE 9, 10, 11, 12, 19, 26, 33, 40, 53, 54, 60, 61, 62

FIG. 5.50 (b)

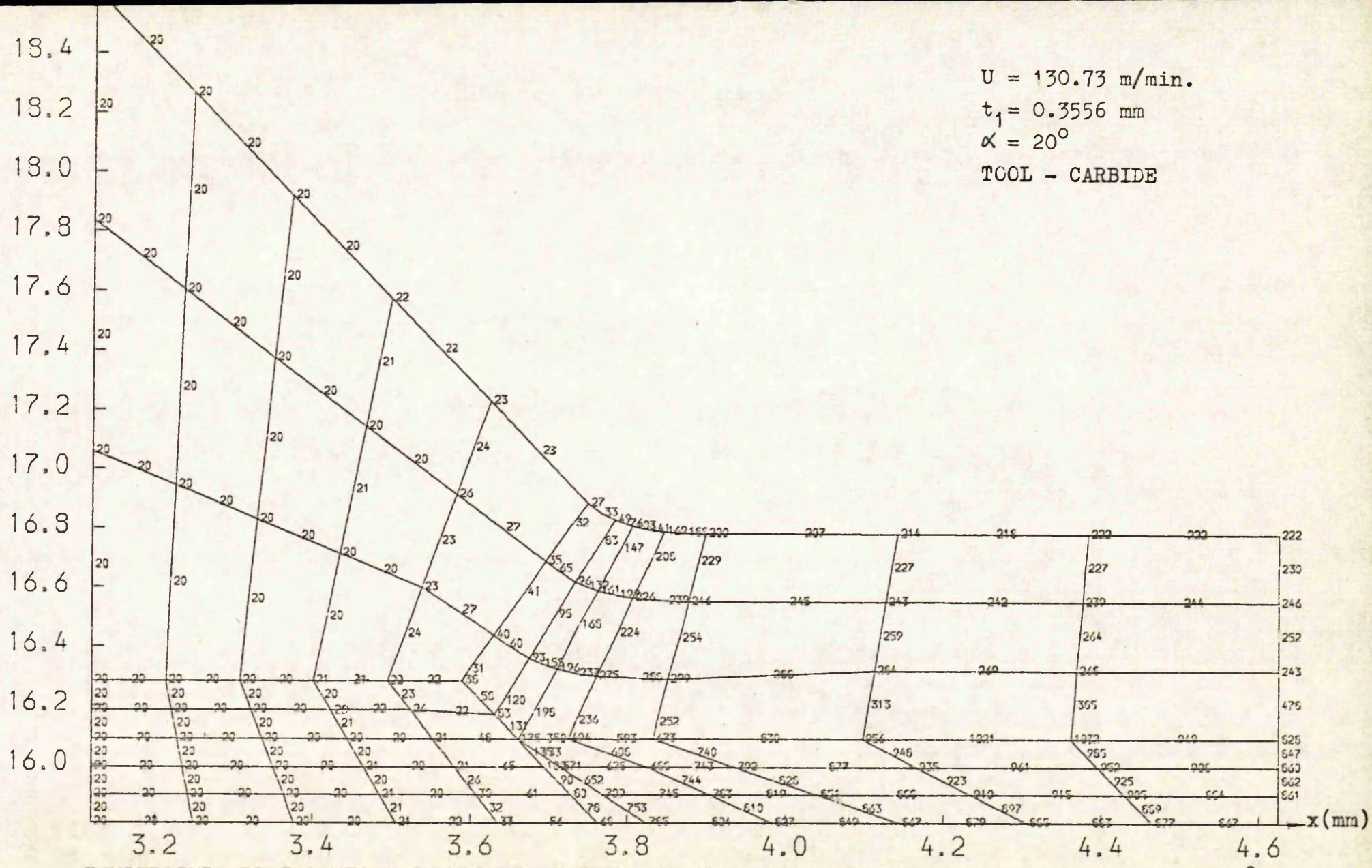

TEMPERATURE DISTRIBUTION IN WORKPIECE, TOOL AND CHIP PREDICTED BY FINITE ELEMENT ANALYSIS (°C)
TEST NO. = 23, NODES= 1284, ZONES CHOSEN ARE 10, 11, 12, 19, 26, 33, 53, 54

FIG. 5.51 (a)

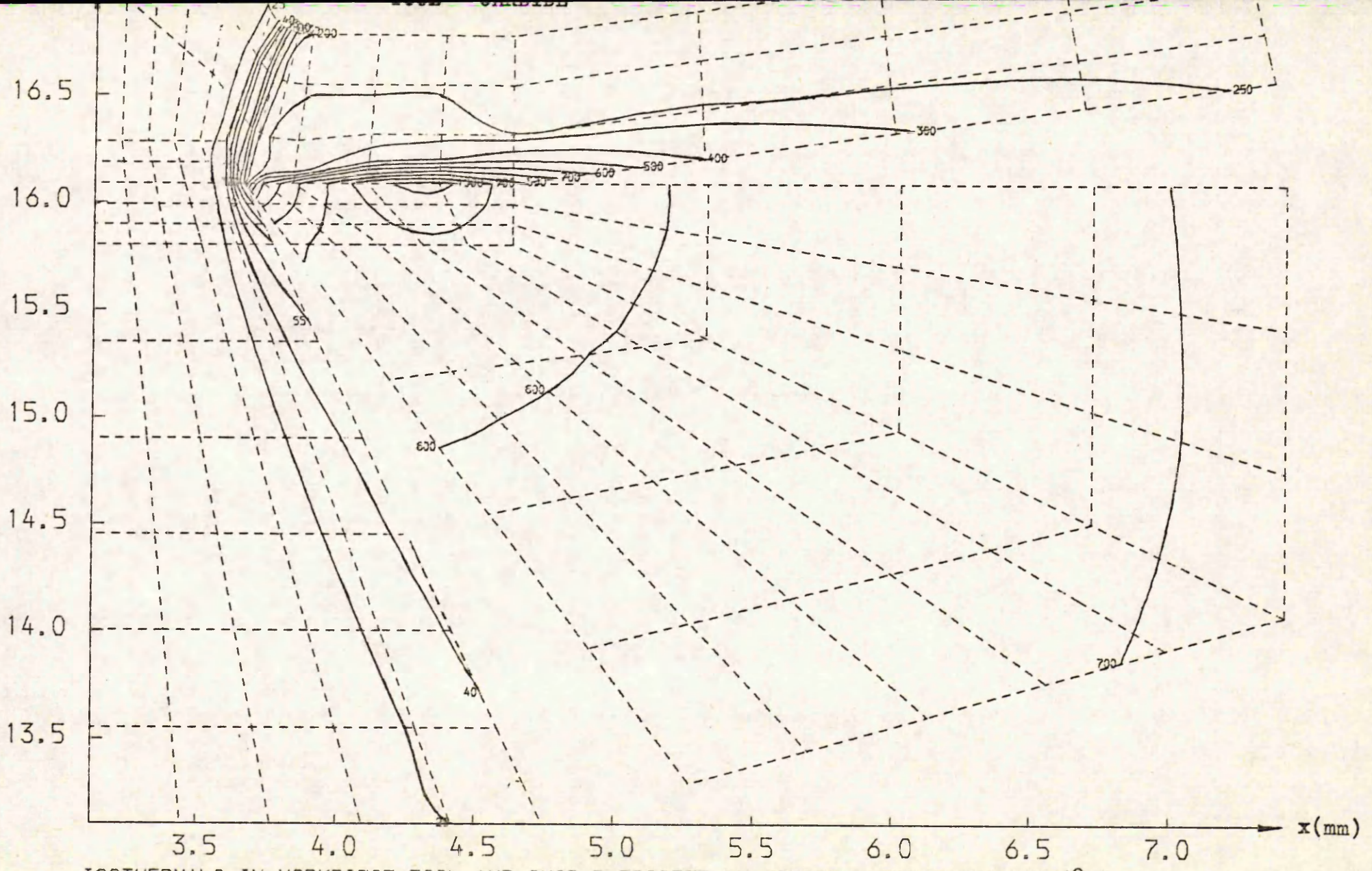

ISOTHERMALS IN WORKPIECE, TOOL AND CHIP PREDICTED BY FINITE ELEMENT ANALYSIS(°C)
TEST NO.= 23, NODES= 1284, ZONES CHOSEN ARE 9, 10, 11, 12, 19, 26, 33, 40, 53, 54, 60, 61, 62

FIG. 5.51 (b)

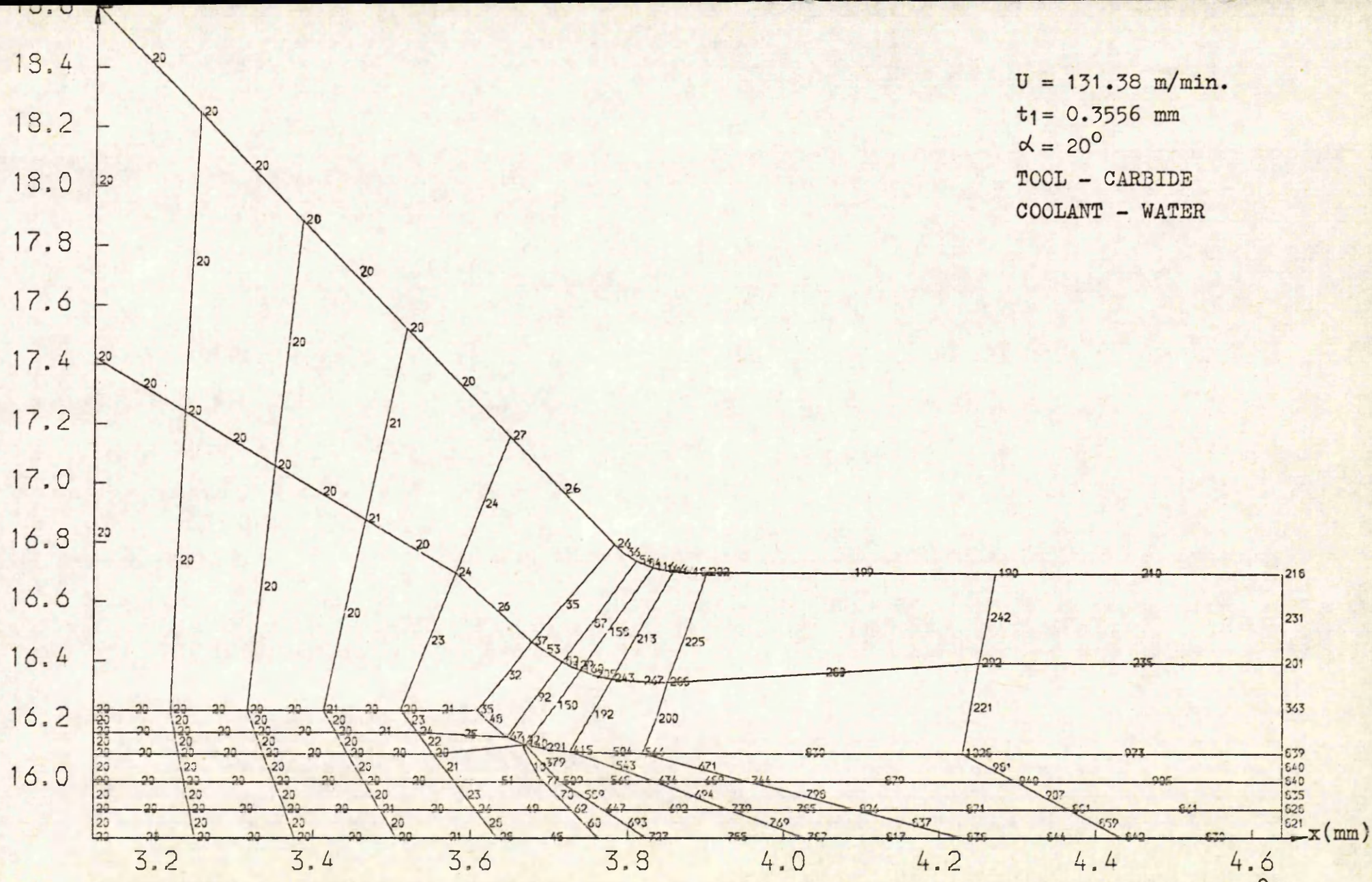

TEMPERATURE DISTRIBUTION IN WORKPIECE, TOOL AND CHIP PREDICTED BY FINITE ELEMENT ANALYSIS (°C)
TEST NO. = 24, NODES= 1116, ZONES CHOSEN ARE 10, 11, 12, 19, 26, 33, 53, 54

FIG. 5.52 (a)

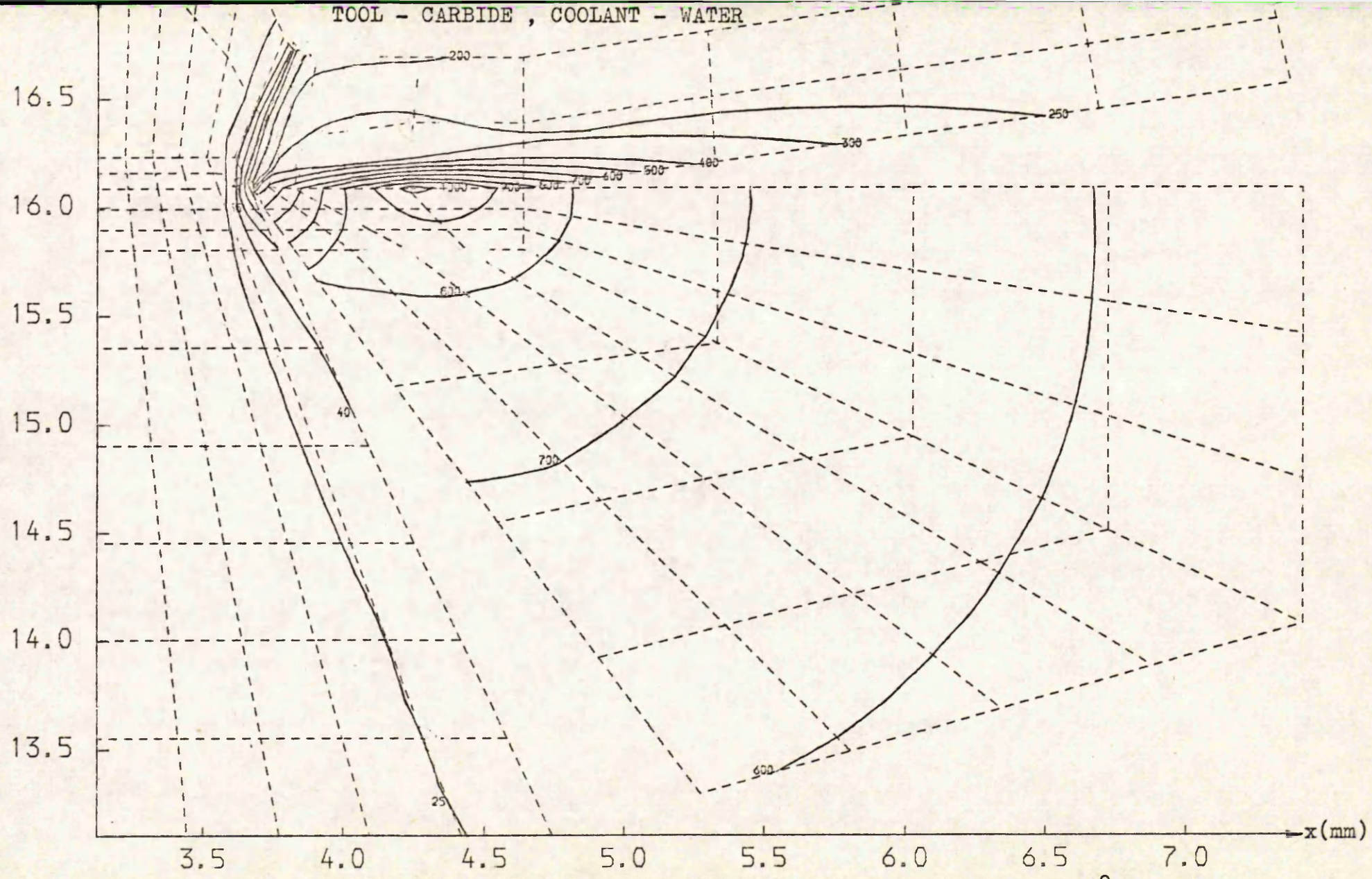

ISOTHERMALS IN WORKPIECE, TOOL AND CHIP PREDICTED BY FINITE ELEMENT ANALYSIS (°C)
TEST NO.= 24, NODES= 1116, ZONES CHOSEN ARE 9, 10, 11, 12, 19, 26, 33, 40, 53, 54, 60, 61, 62

FIG. 5.52 (b)

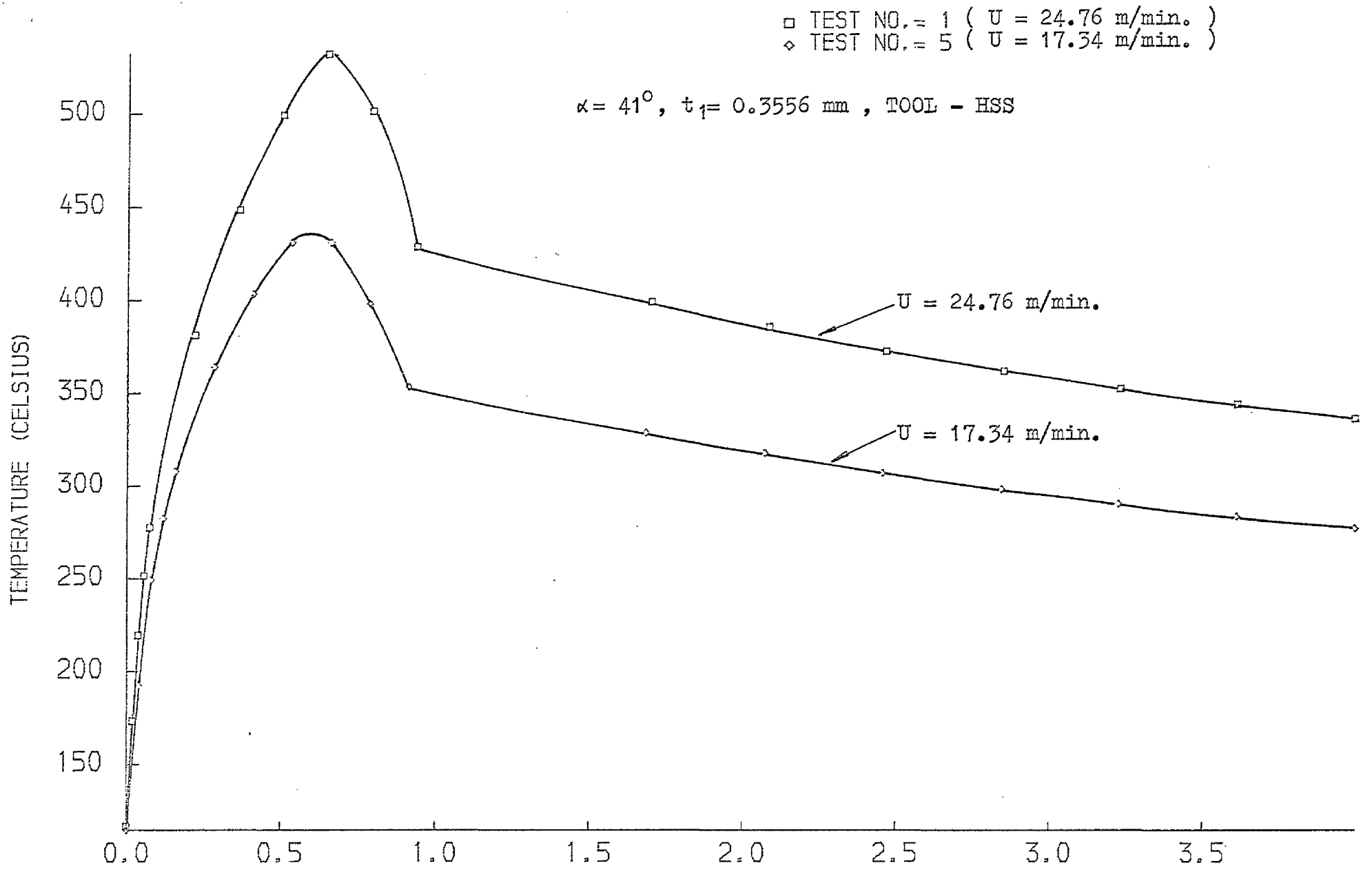

FIG. 5.53 (a) EFFECT OF CUTTING SPEED ON RAKE FACE TEMPERATURES

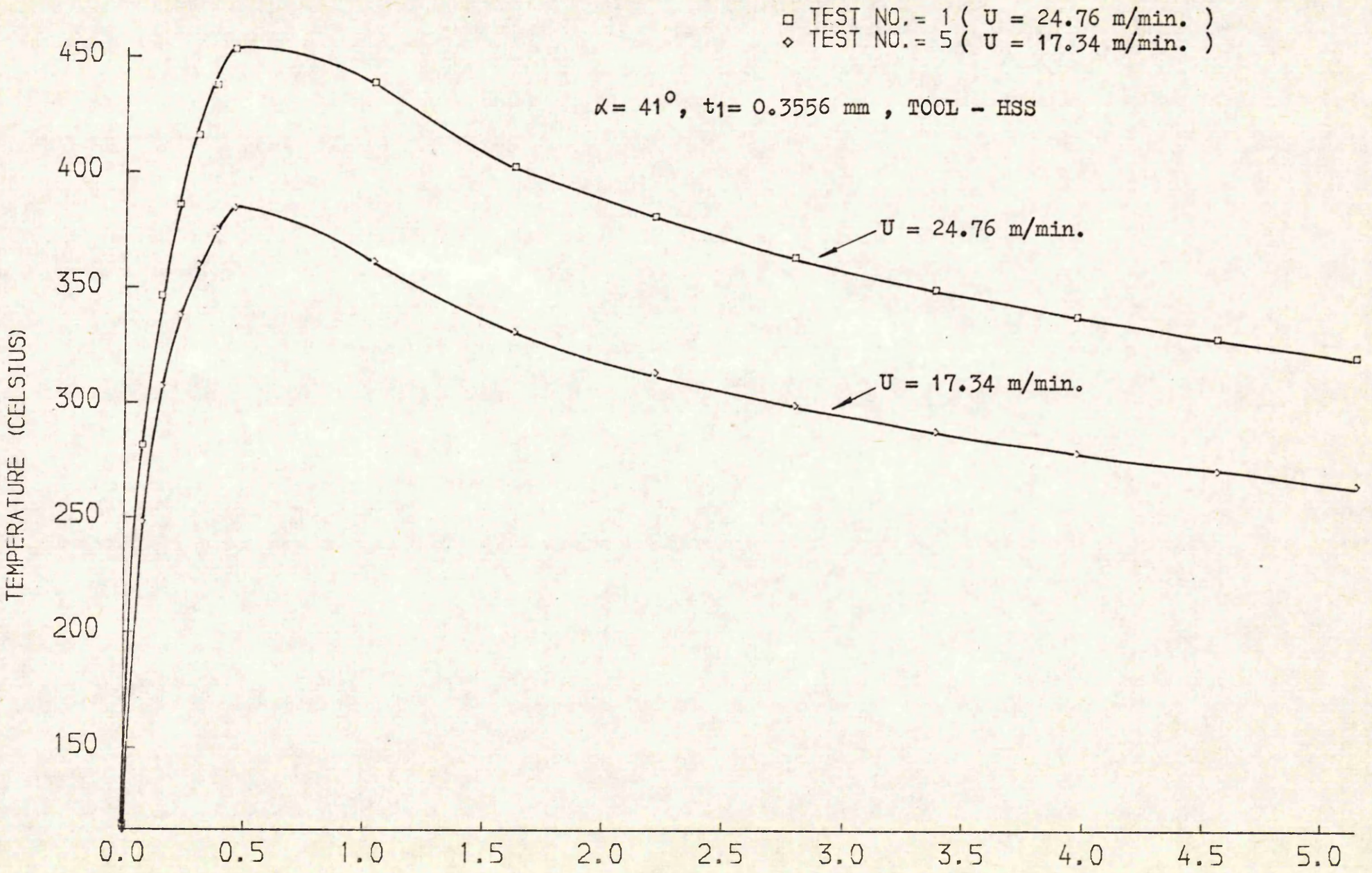

FIG. 5.53 (b) EFFECT OF CUTTING SPEED ON FLANK FACE TEMPERATURES

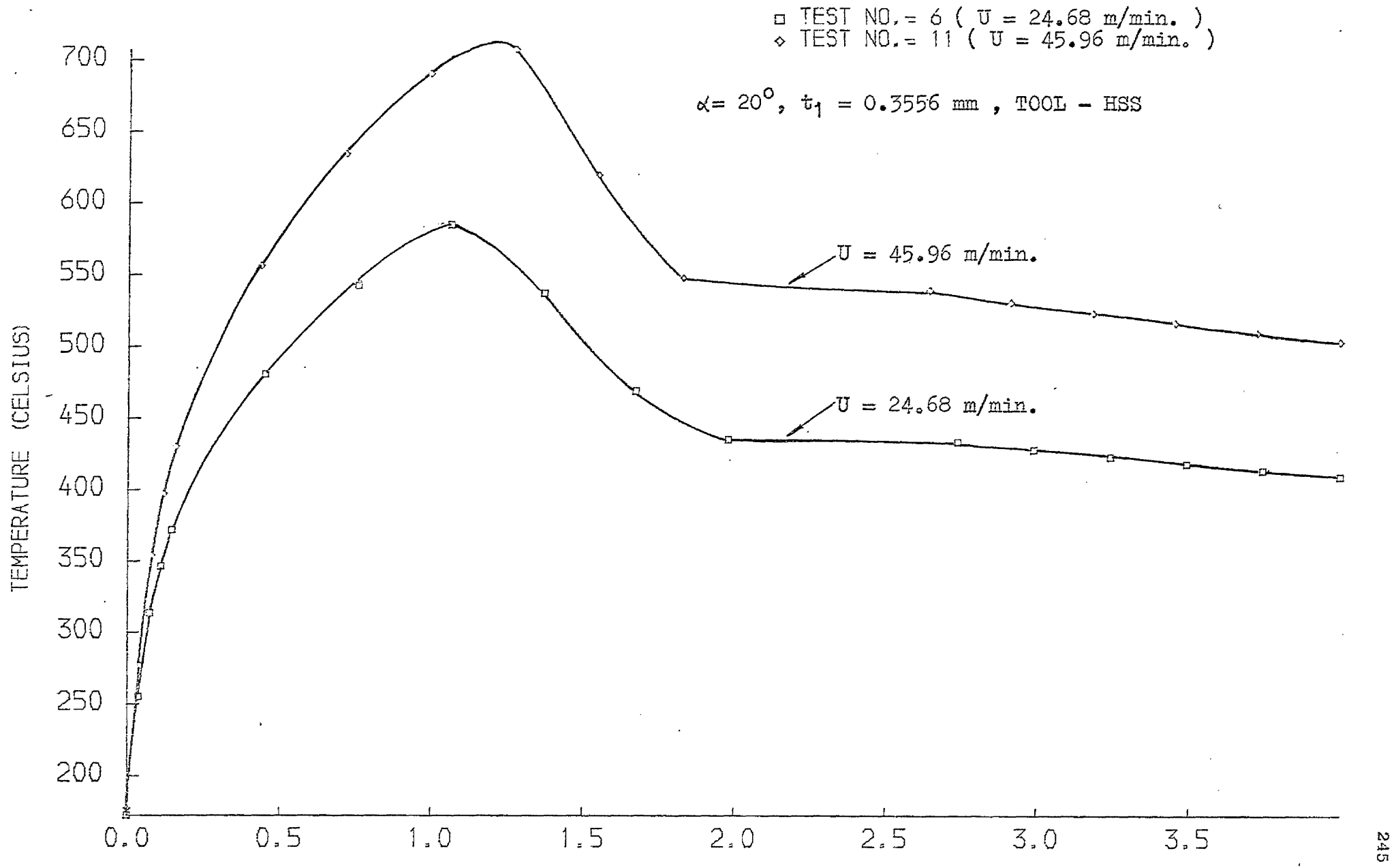

FIG. 5.54 (a) EFFECT OF CUTTING SPEED ON RAKE FACE TEMPERATURES

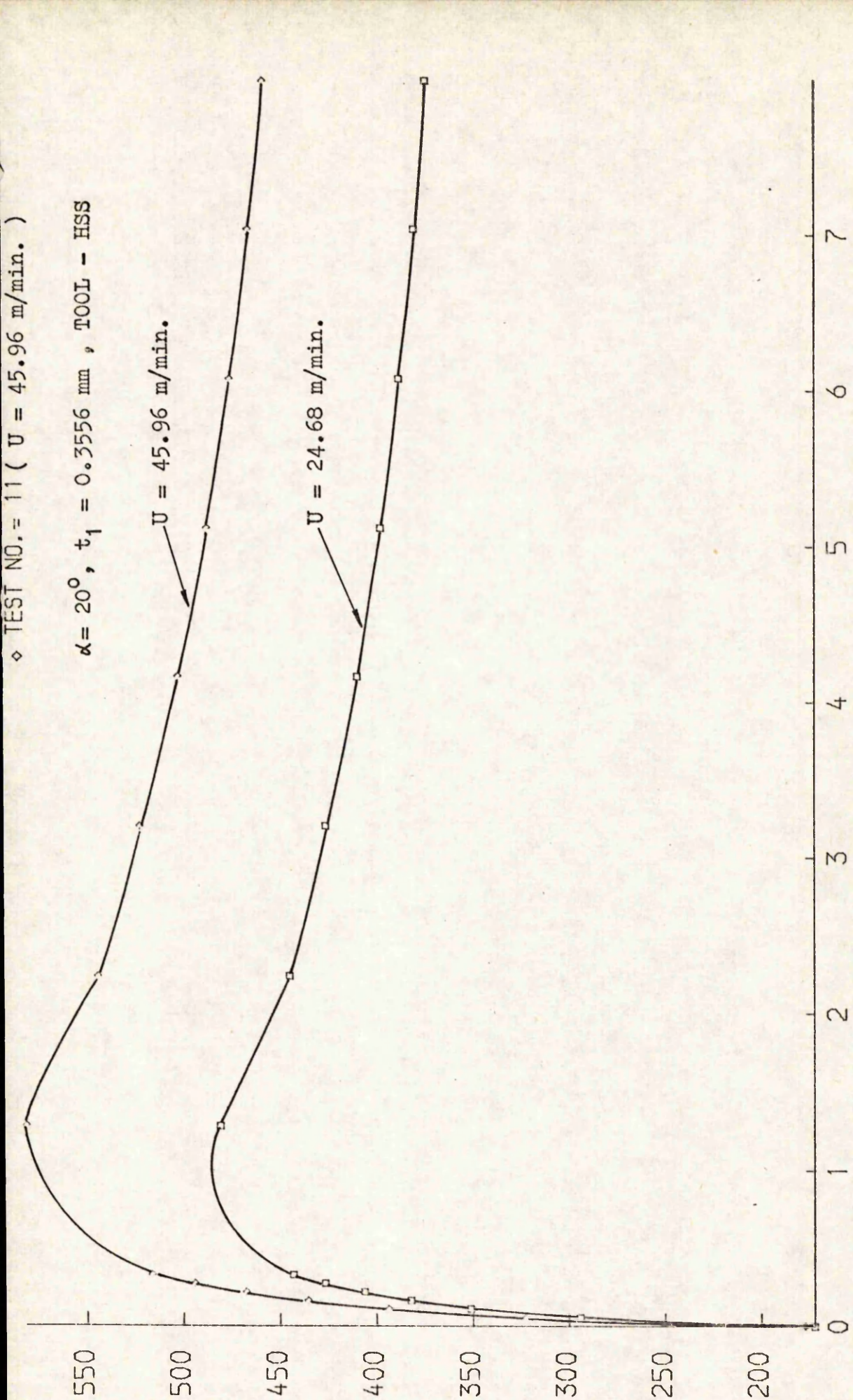

FIG. 5.54 (b) EFFECT OF CUTTING SPEED ON FLANK FACE TEMPERATURES

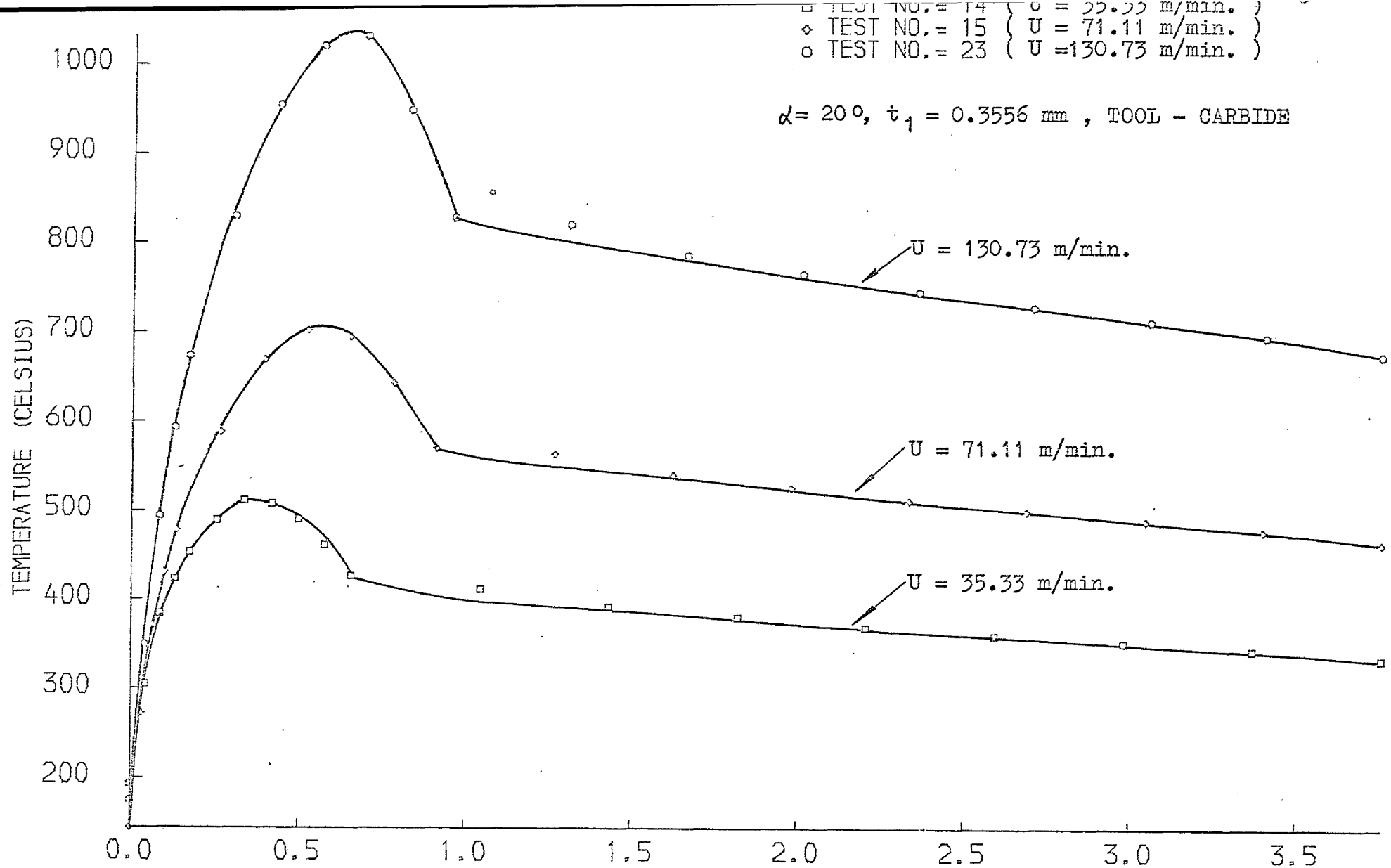

FIG. 5.55 (a) EFFECT OF CUTTING SPEED ON RAKE FACE TEMPERATURES

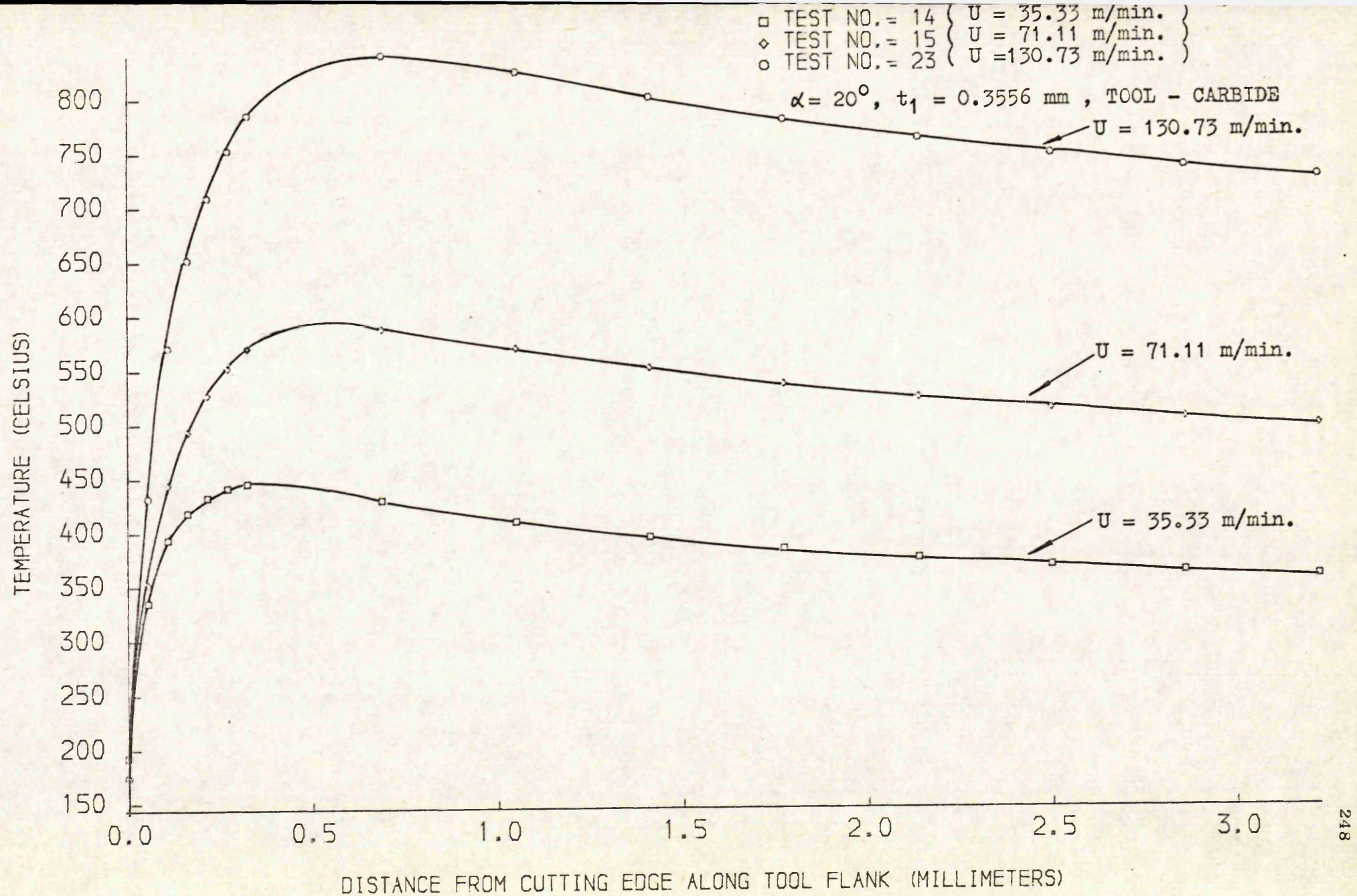

FIG. 5.55 (b) EFFECT OF CUTTING SPEED ON FLANK FACE TEMPERATURES

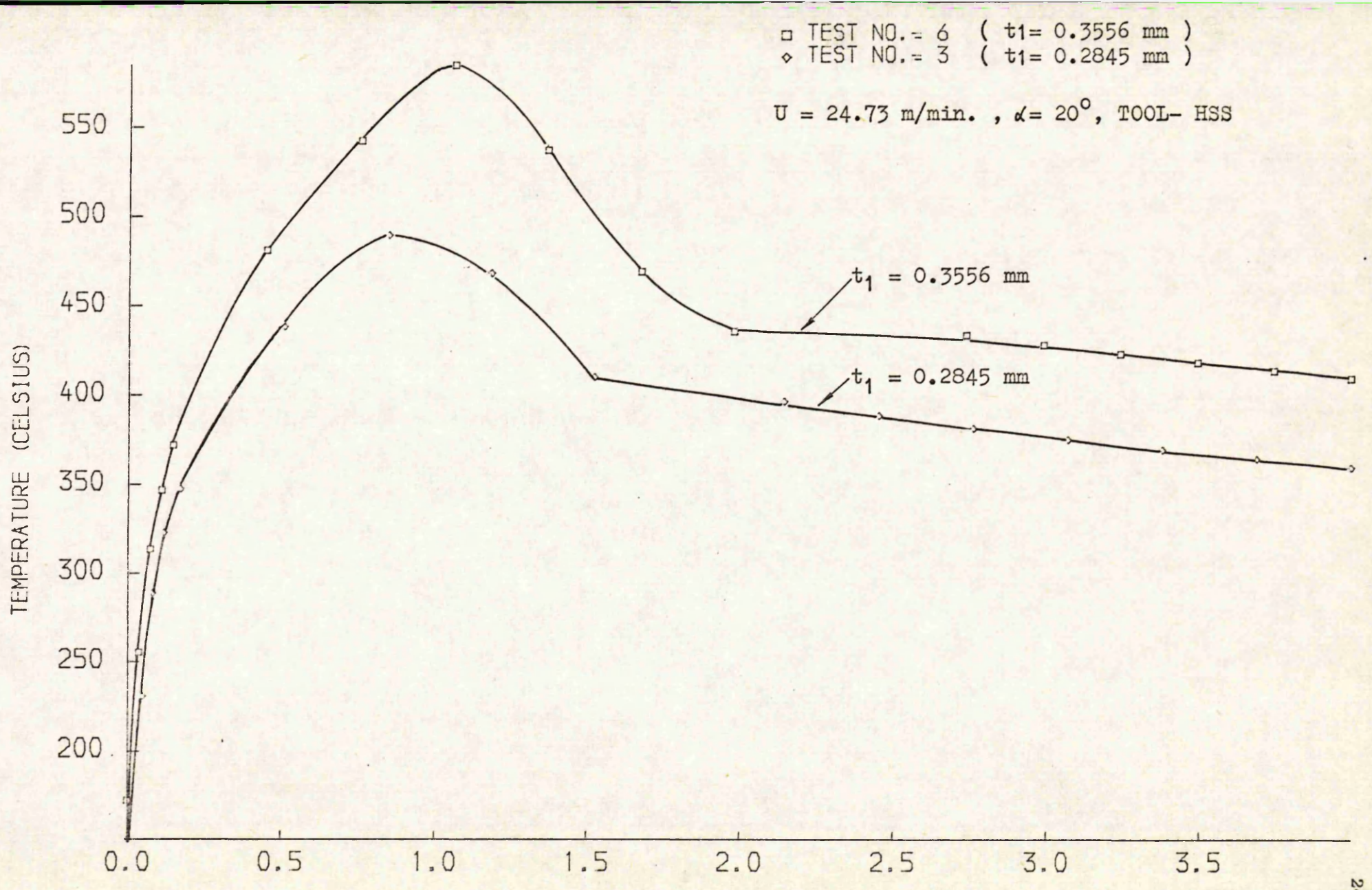

FIG. 5.56 (a) EFFECT OF FEED ON RAKE FACE TEMPERATURES

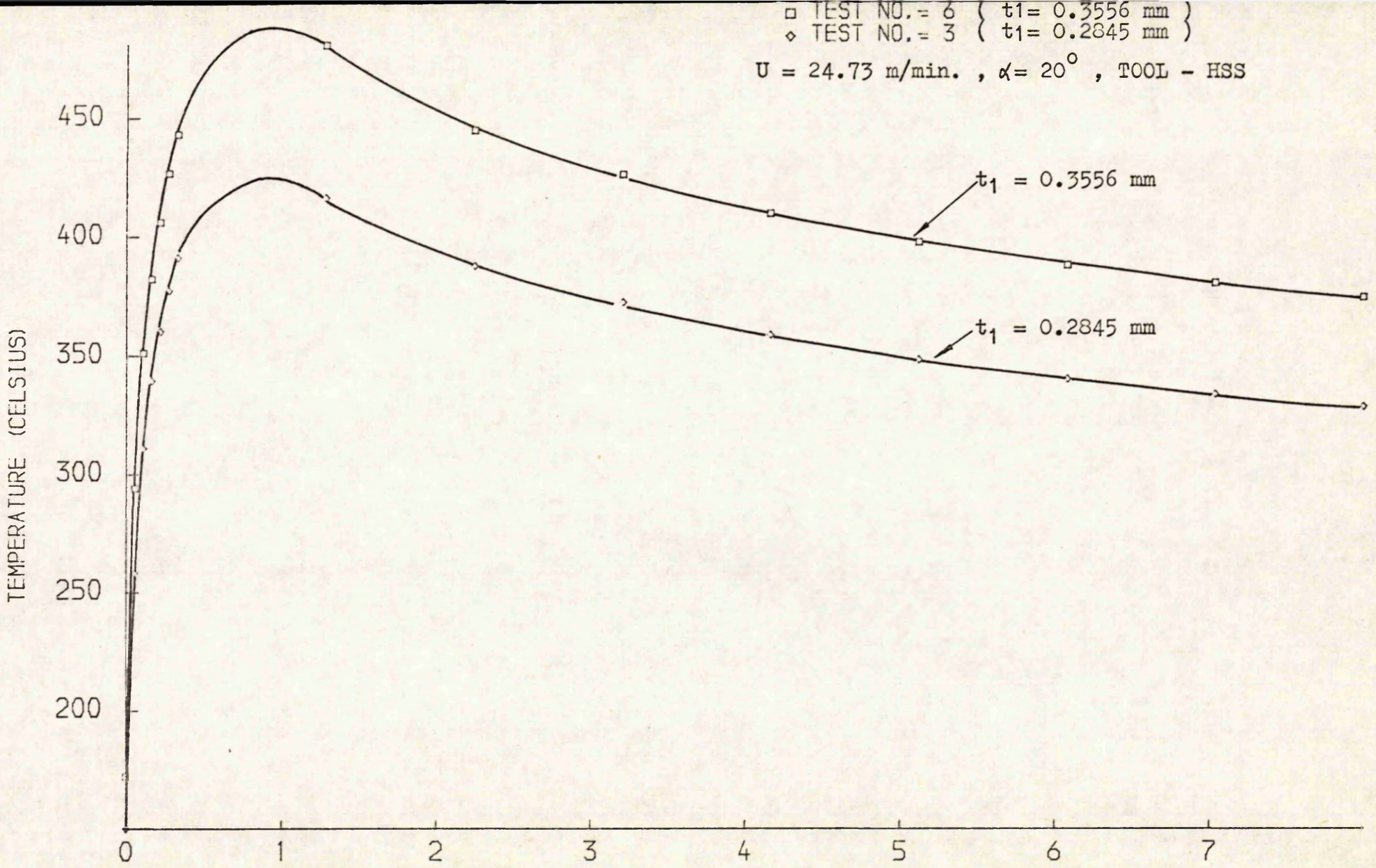

FIG. 5.56 (b) EFFECT OF FEED ON FLANK FACE TEMPERATURES

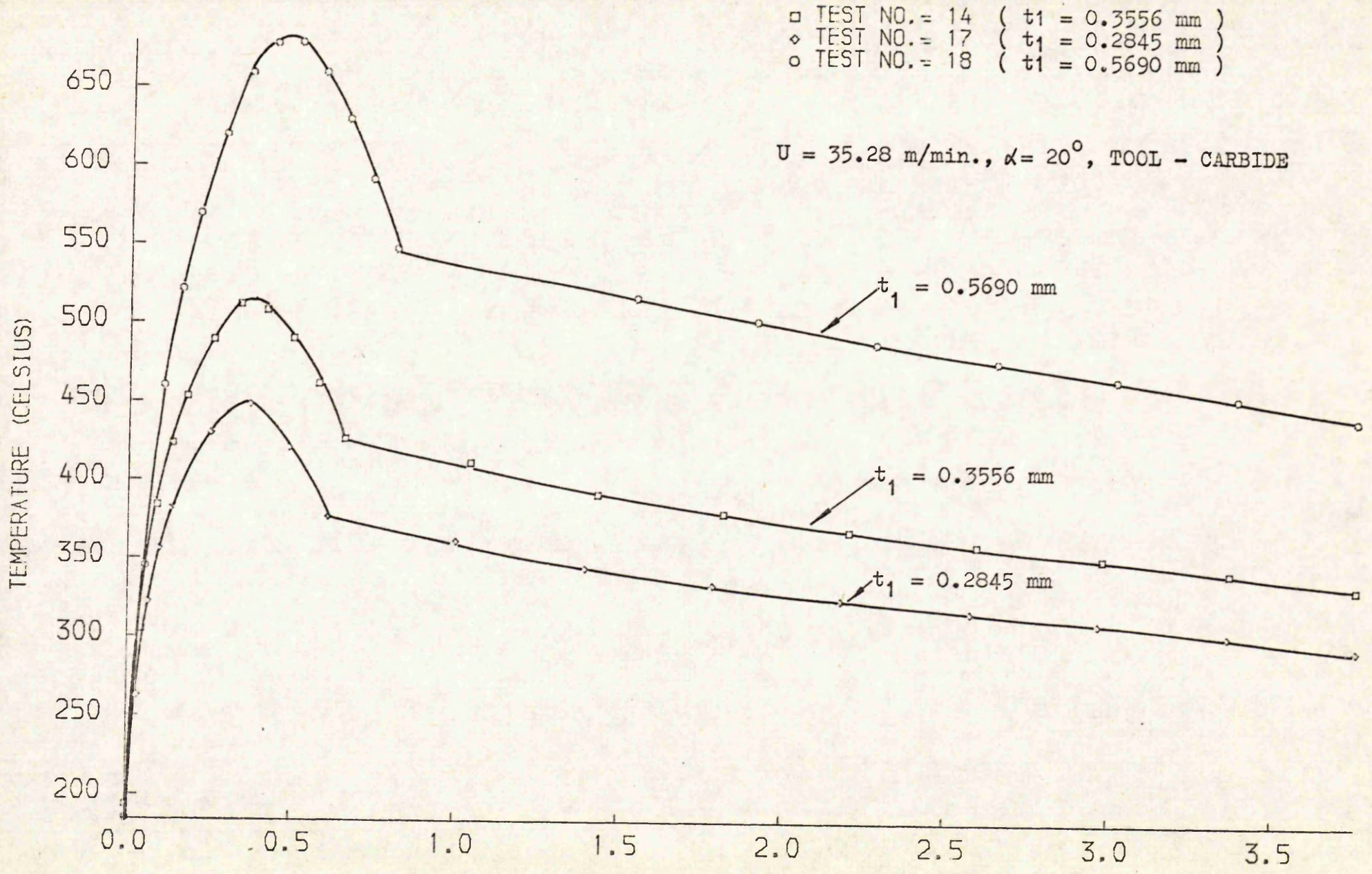

FIG. 5.57 (a) EFFECT OF FEED ON RAKE FACE TEMPERATURES

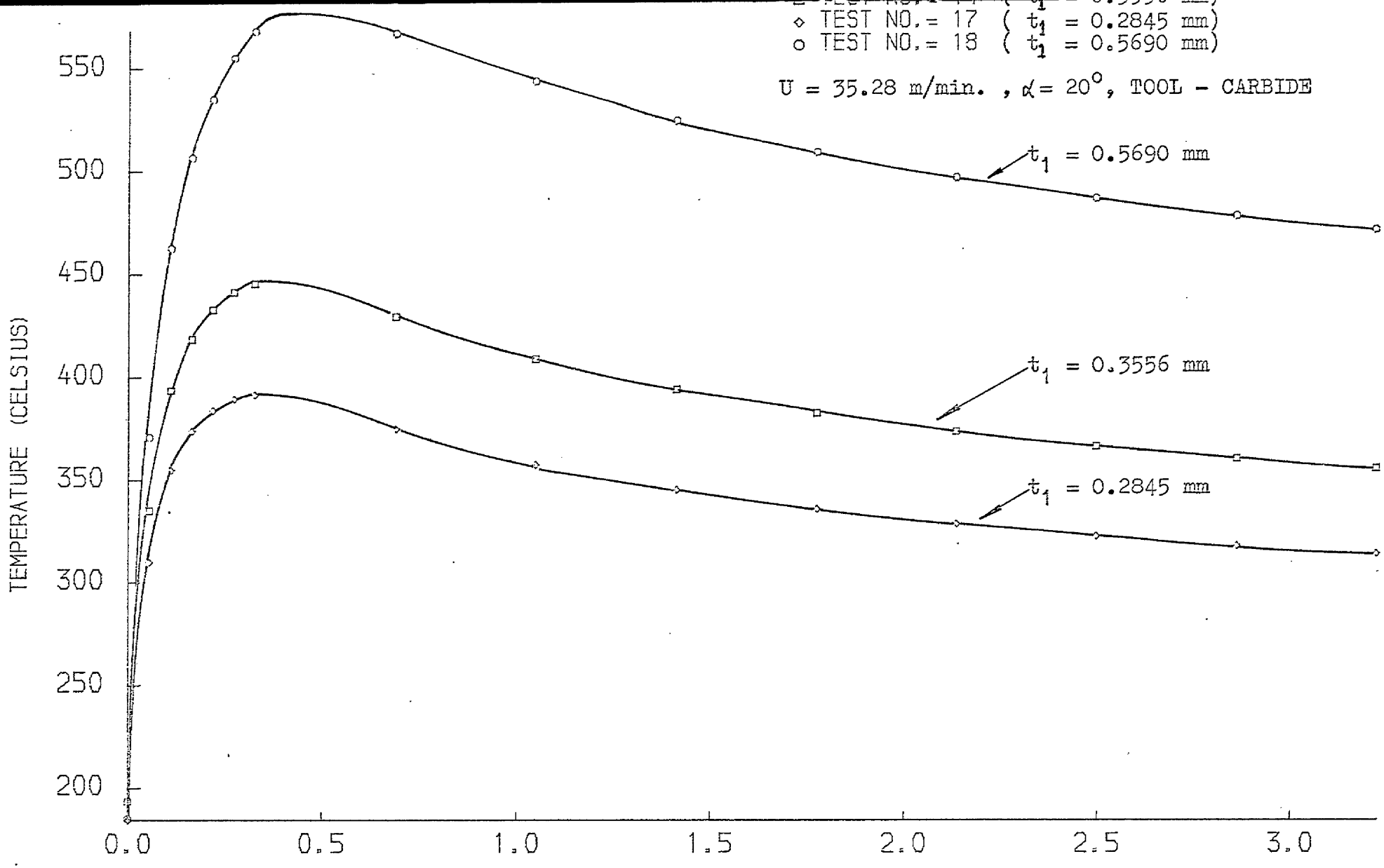

FIG. 5.57 (b) EFFECT OF FEED ON FLANK FACE TEMPERATURES

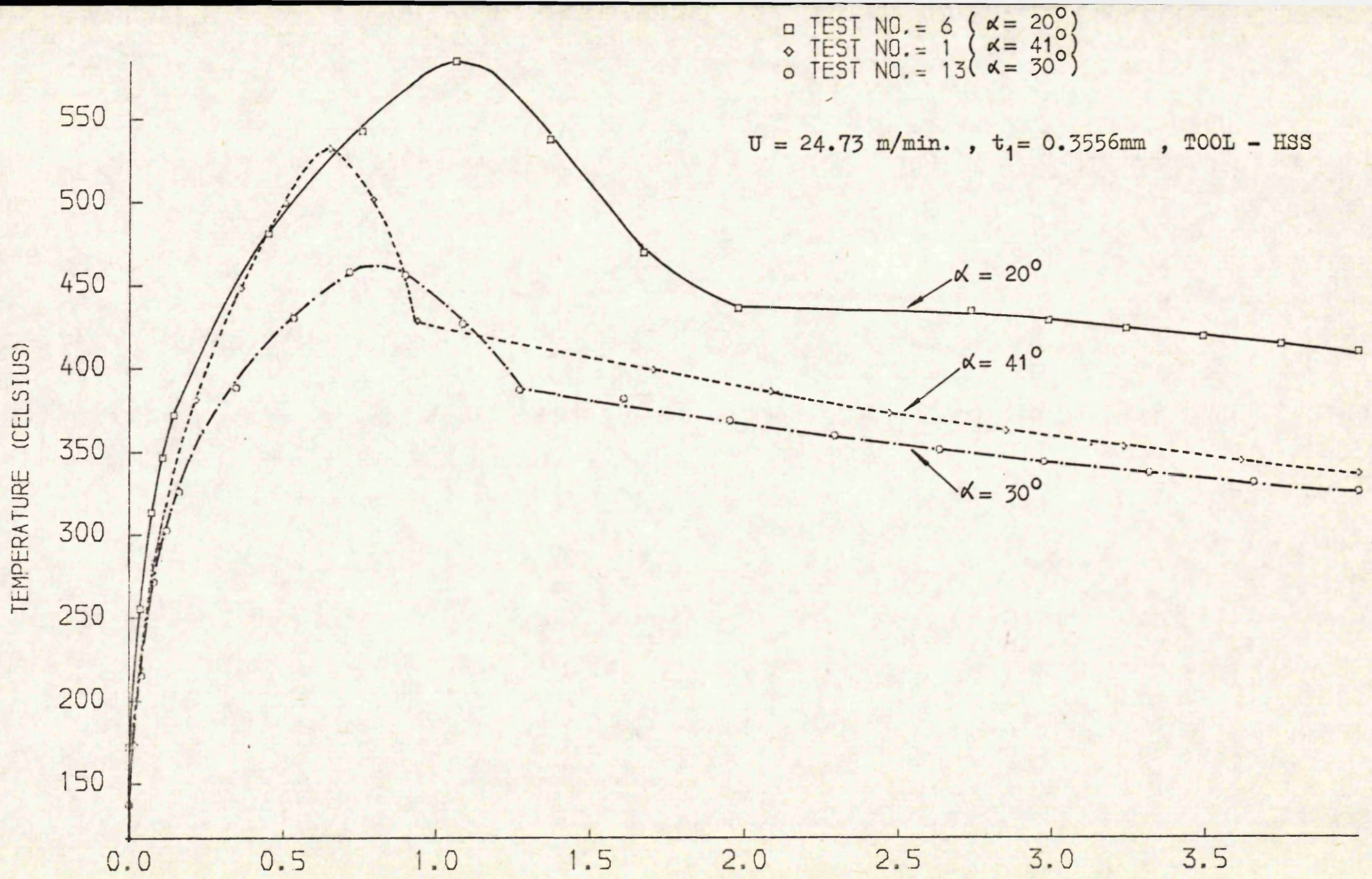

FIG. 5.58 (a) EFFECT OF RAKE ANGLE ON RAKE FACE TEMPERATURES

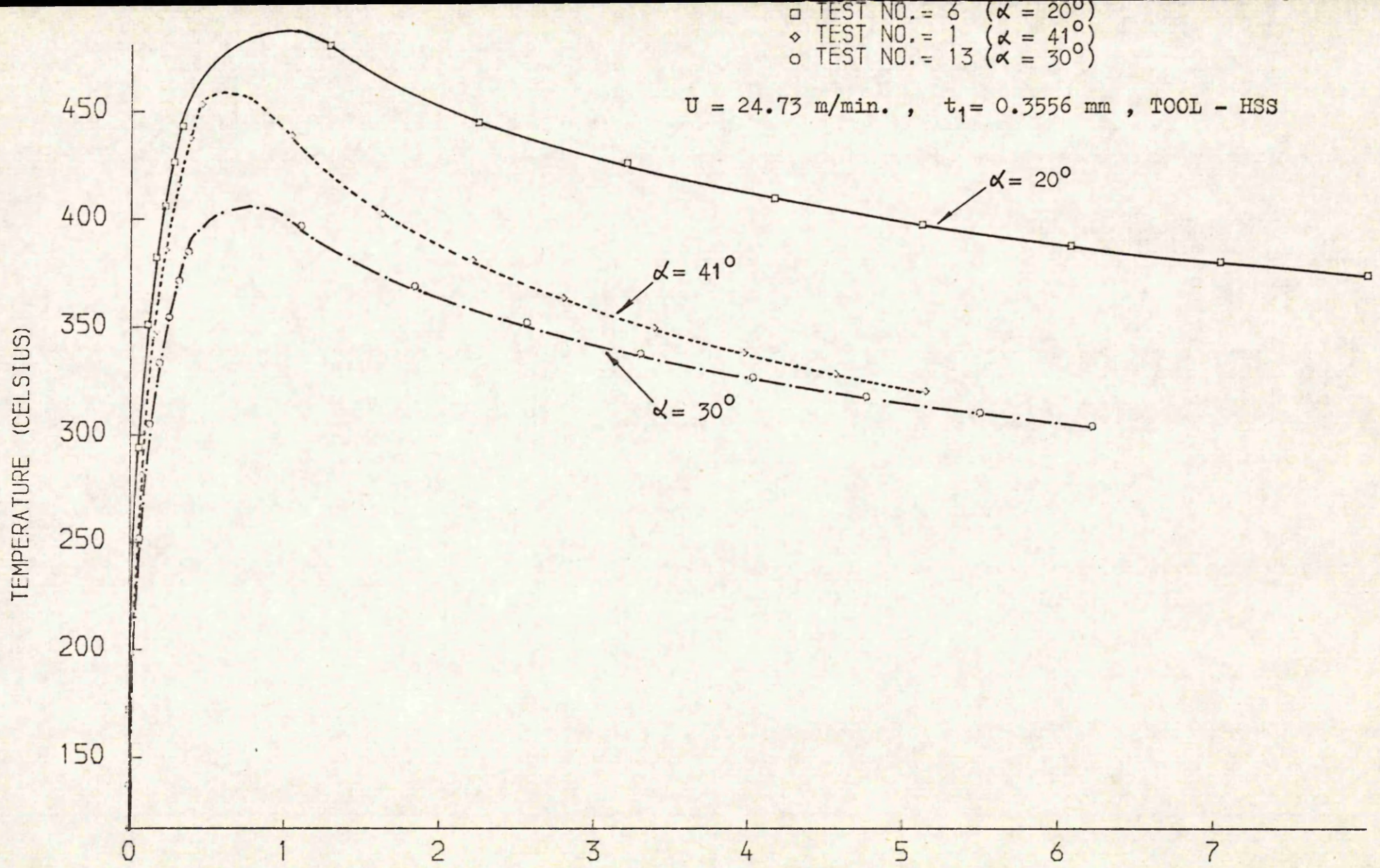

FIG. 5.58 (b) EFFECT OF RAKE ANGLE ON FLANK FACE TEMPERATURES

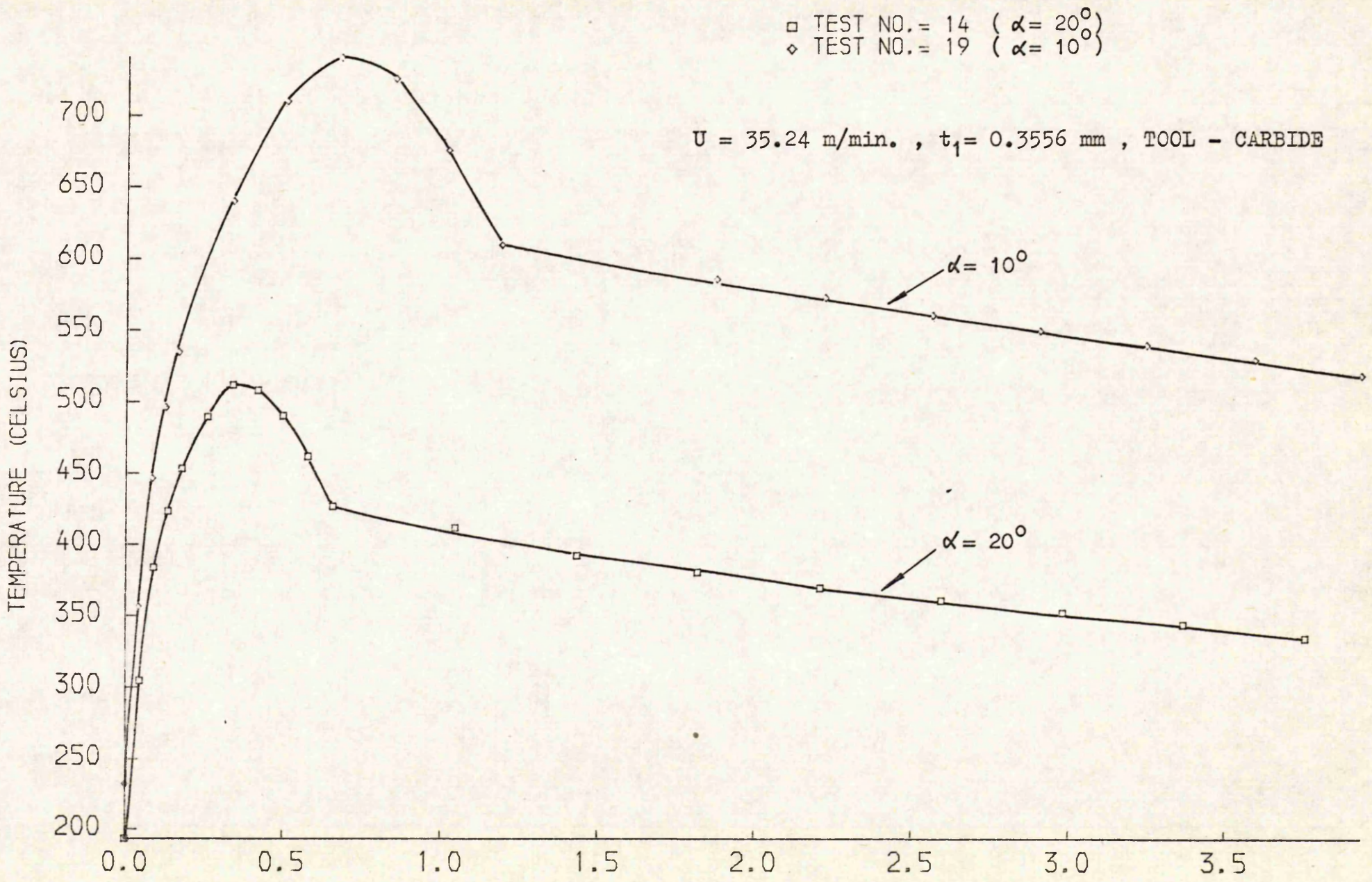

FIG.5.59 (a) EFFECT OF RAKE ANGLE ON RAKE FACE TEMPERATURES

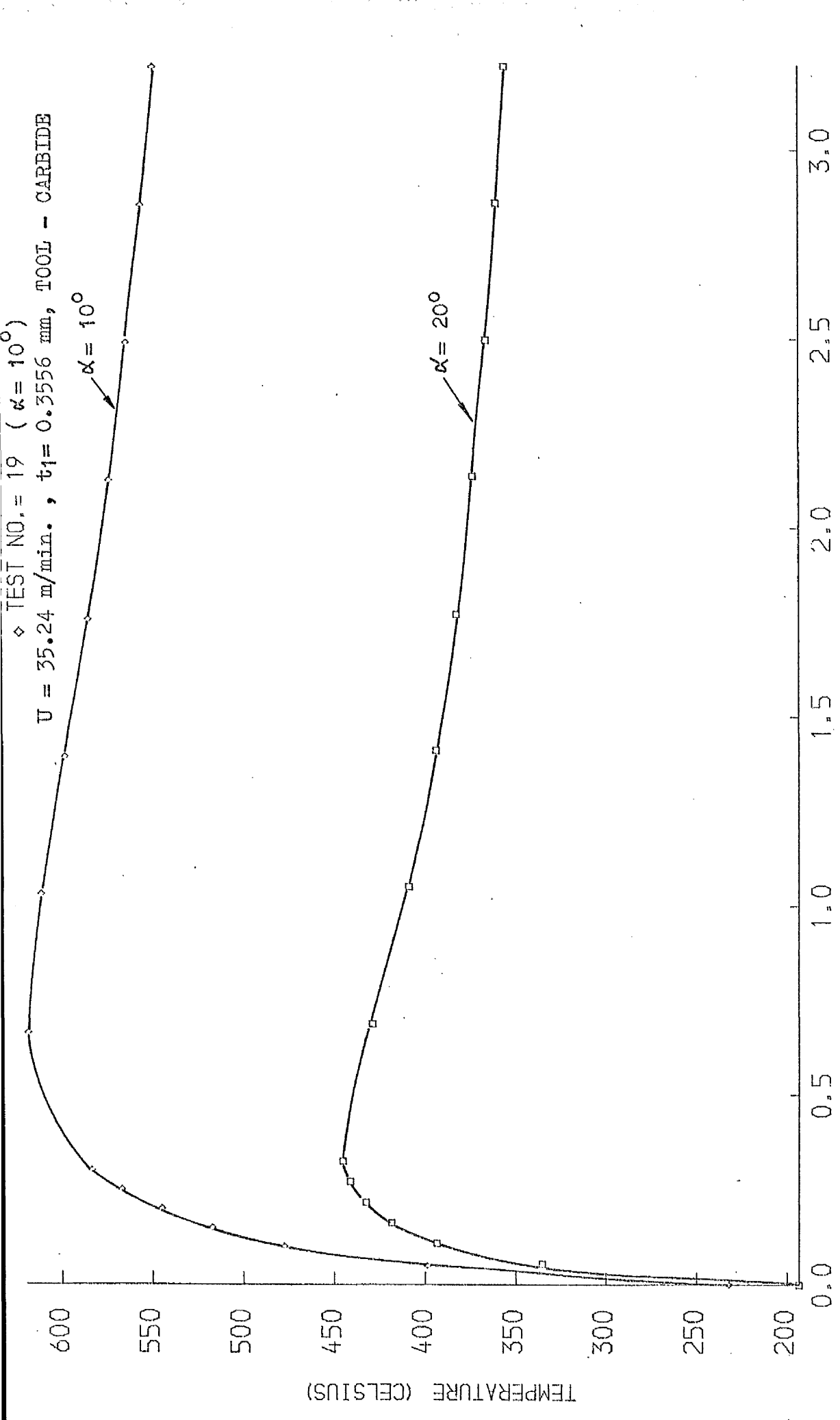

FIG.5.59 (b) EFFECT OF RAKE ANGLE ON FLANK FACE TEMPERATURES

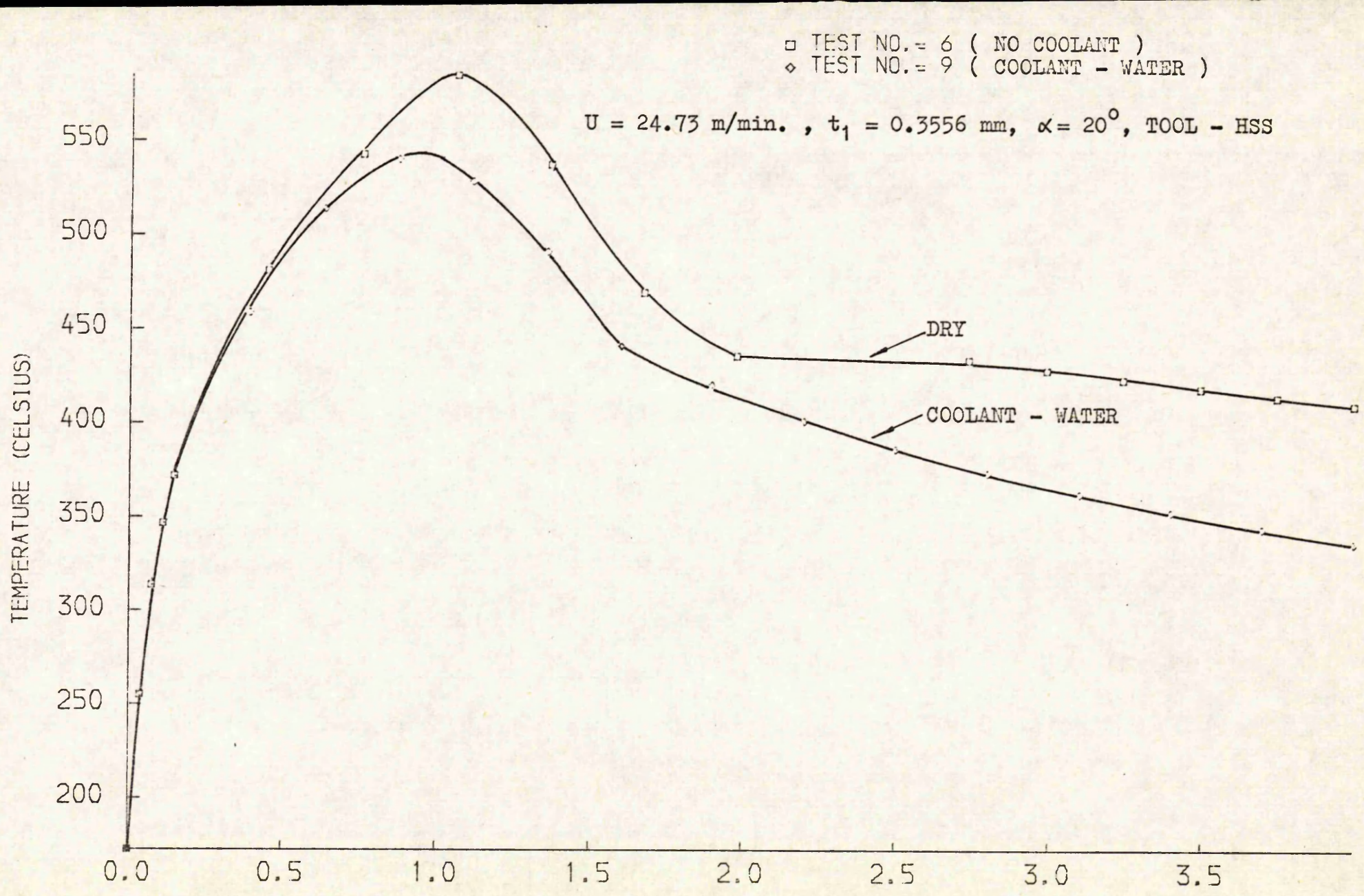

FIG. 5.60 (a) EFFECT OF COOLANT ON RAKE FACE TEMPERATURES

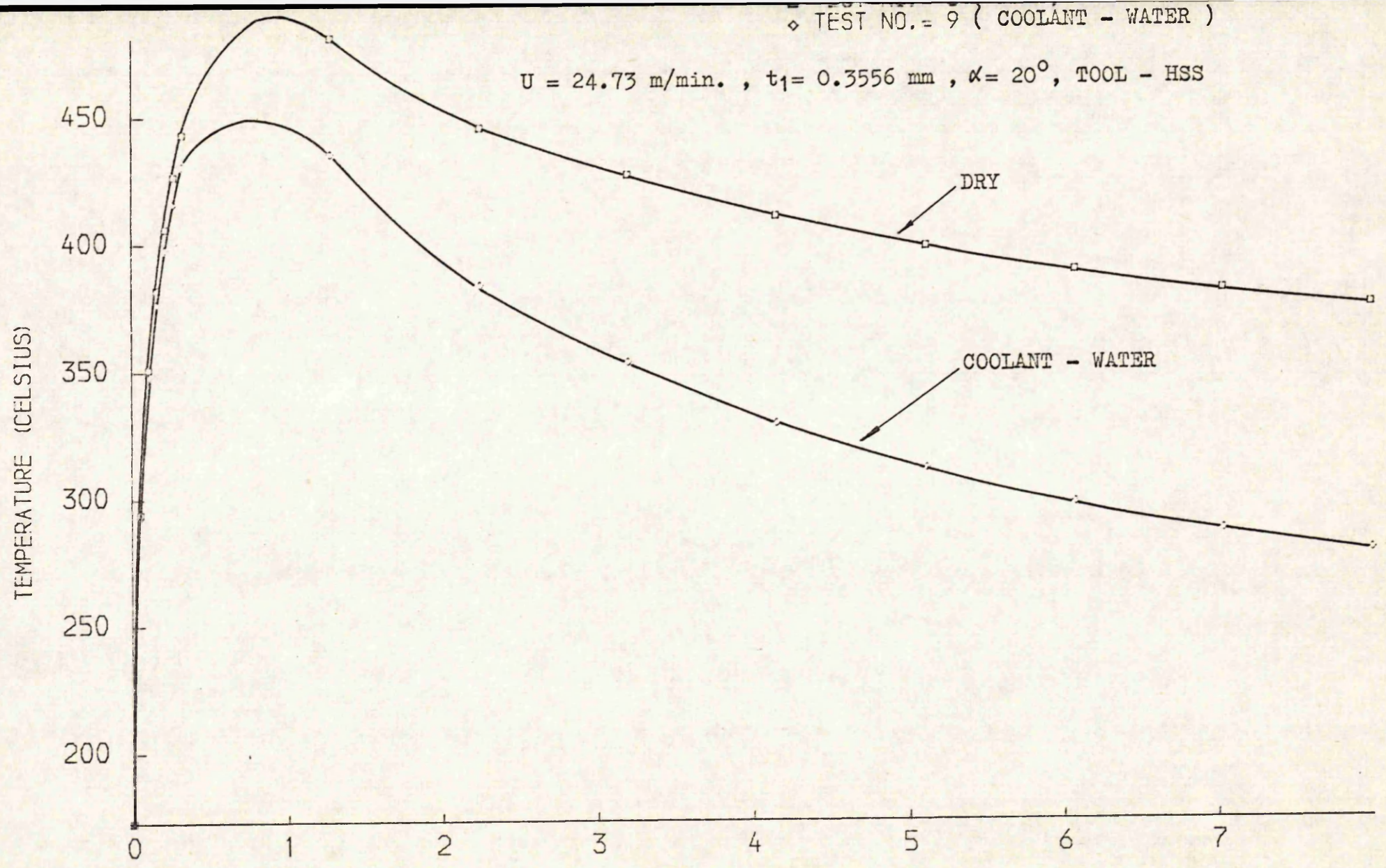

FIG. 5.60 (b) EFFECT OF COOLANT ON FLANK FACE TEMPERATURES

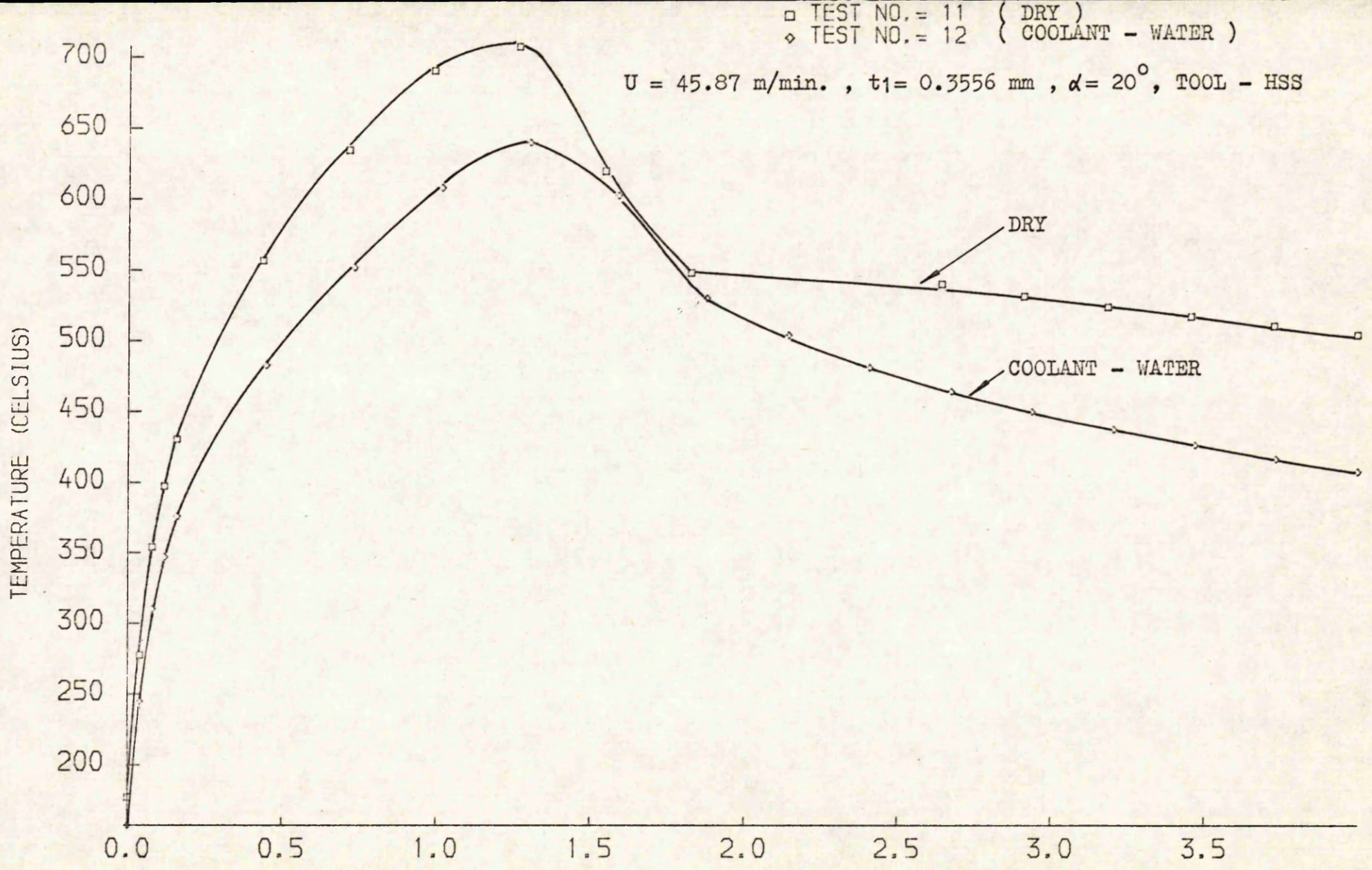

FIG. 5.61 (a) EFFECT OF COOLANT ON RAKE FACE TEMPERATURES

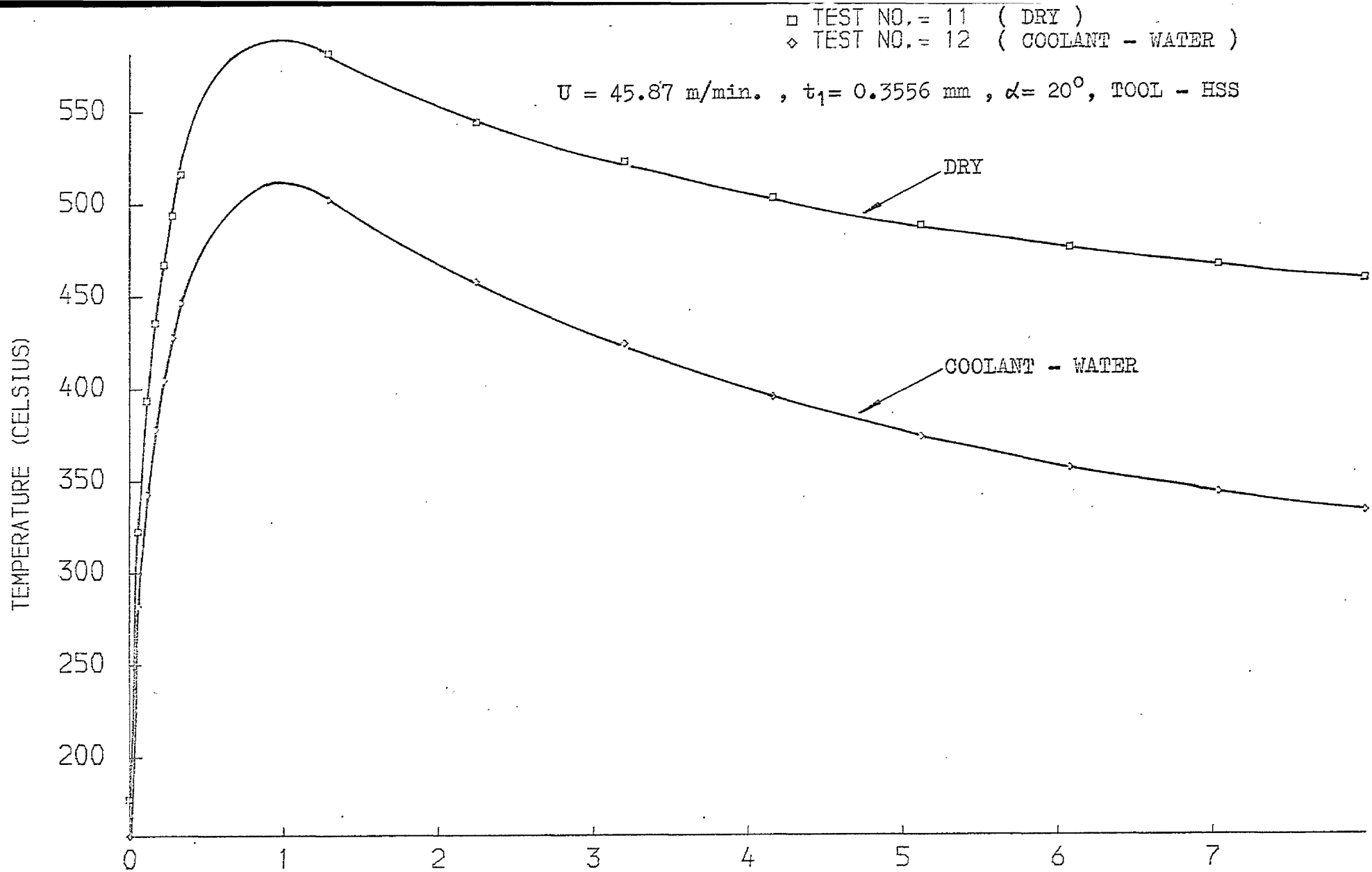

FIG. 5.61 (b) EFFECT OF COOLANT ON FLANK FACE TEMPERATURES

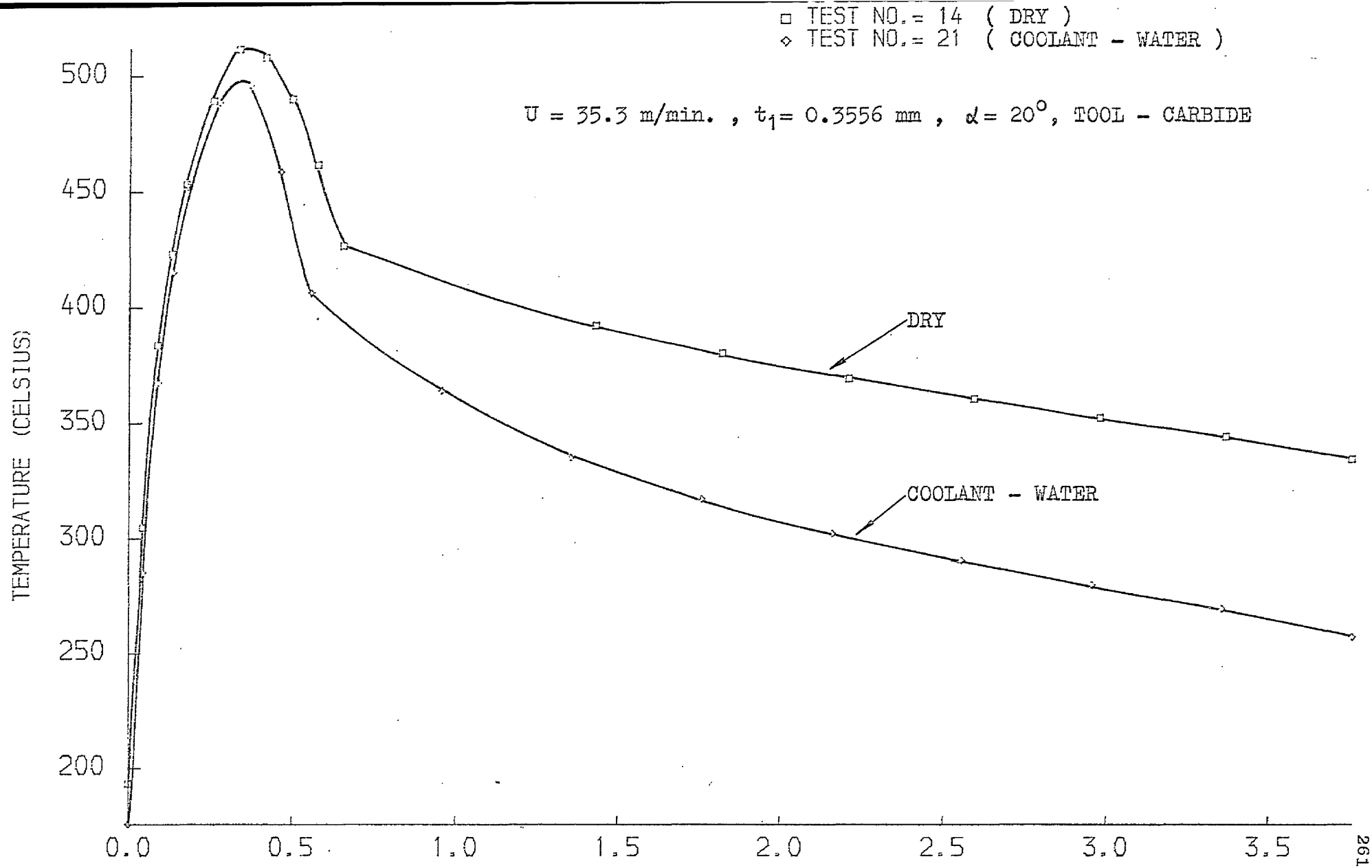

FIG. 5.62 (a) EFFECT OF COOLANT ON RAKE FACE TEMPERATURES

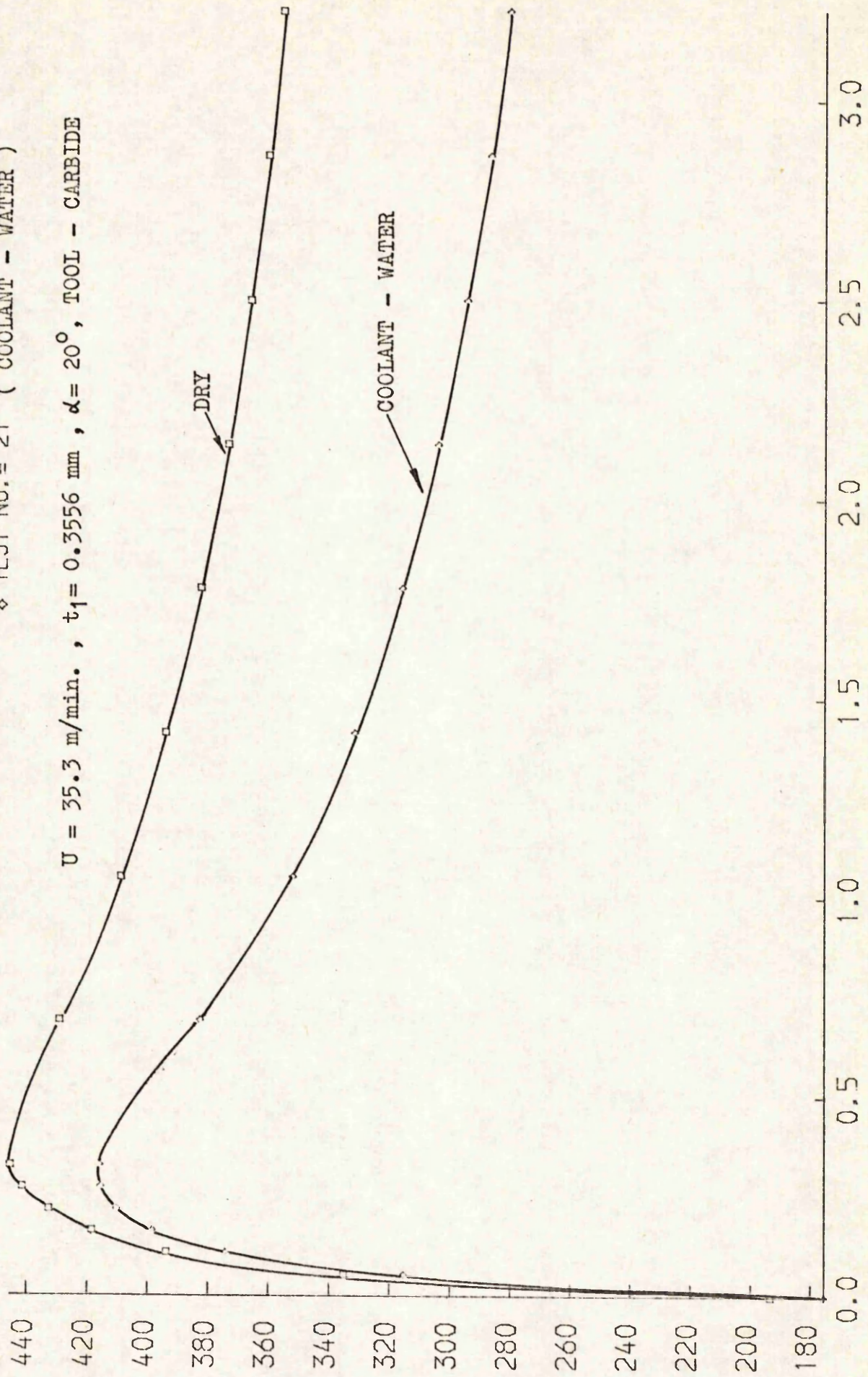

FIG. 5.62 (b) EFFECT OF COOLANT ON FLANK FACE TEMPERATURES

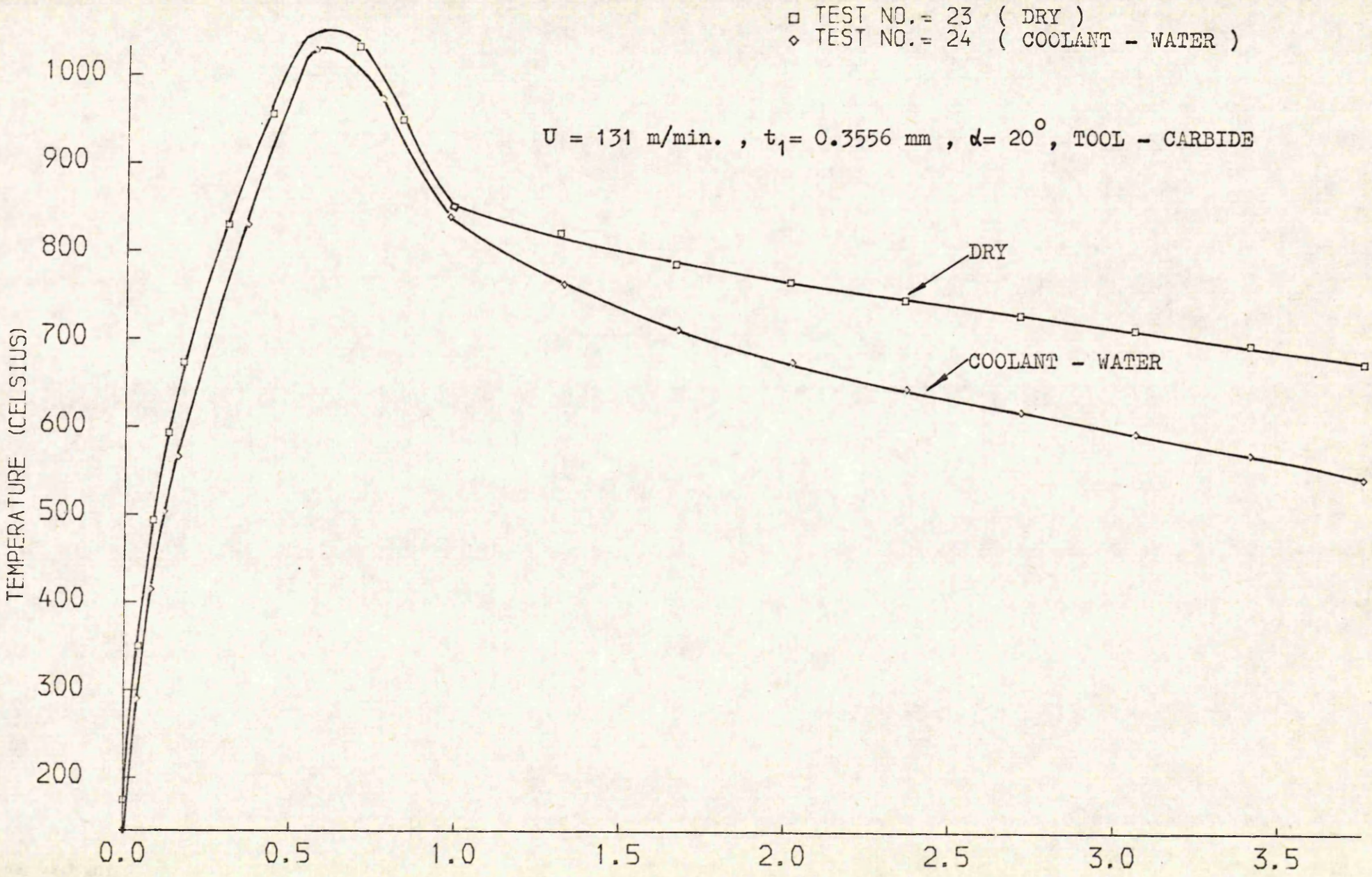

FIG. 5.63 (a) EFFECT OF COOLANT ON RAKE FACE TEMPERATURES

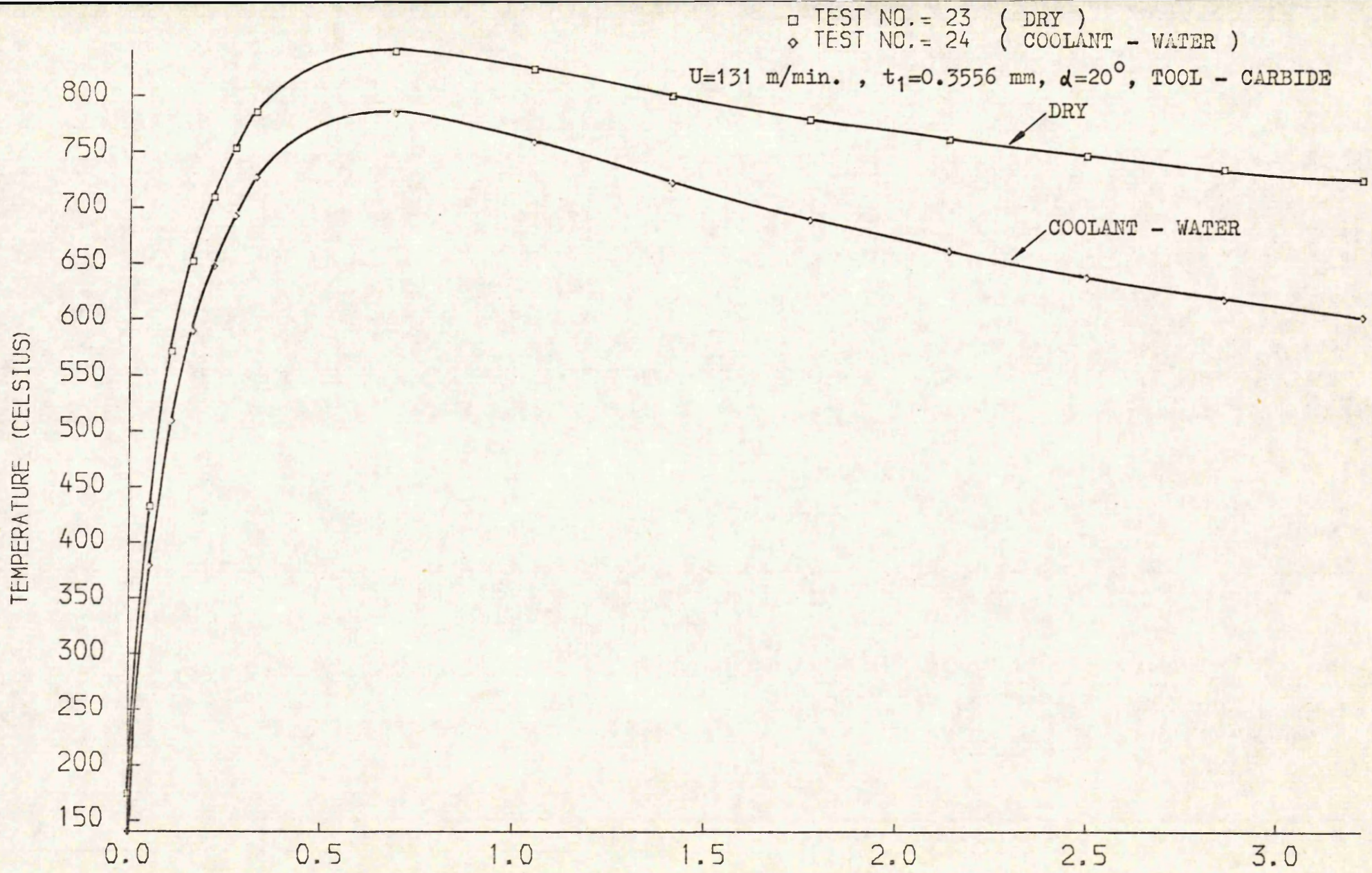

FIG. 5.63 (b) EFFECT OF COOLANT ON FLANK FACE TEMPERATURES

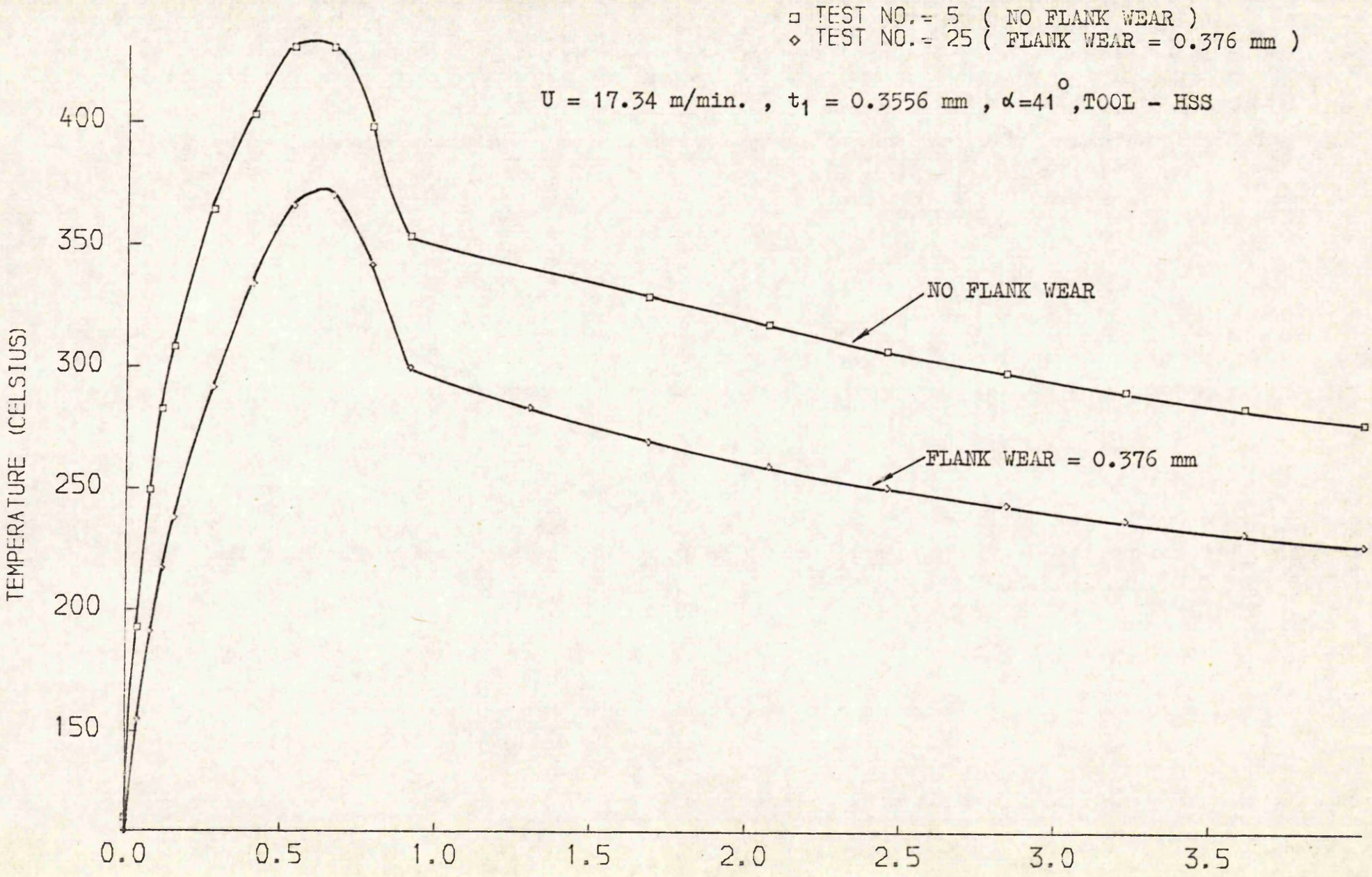

FIG. 5.64 (a) EFFECT OF TOOL FLANK WEAR ON RAKE FACE TEMPERATURES

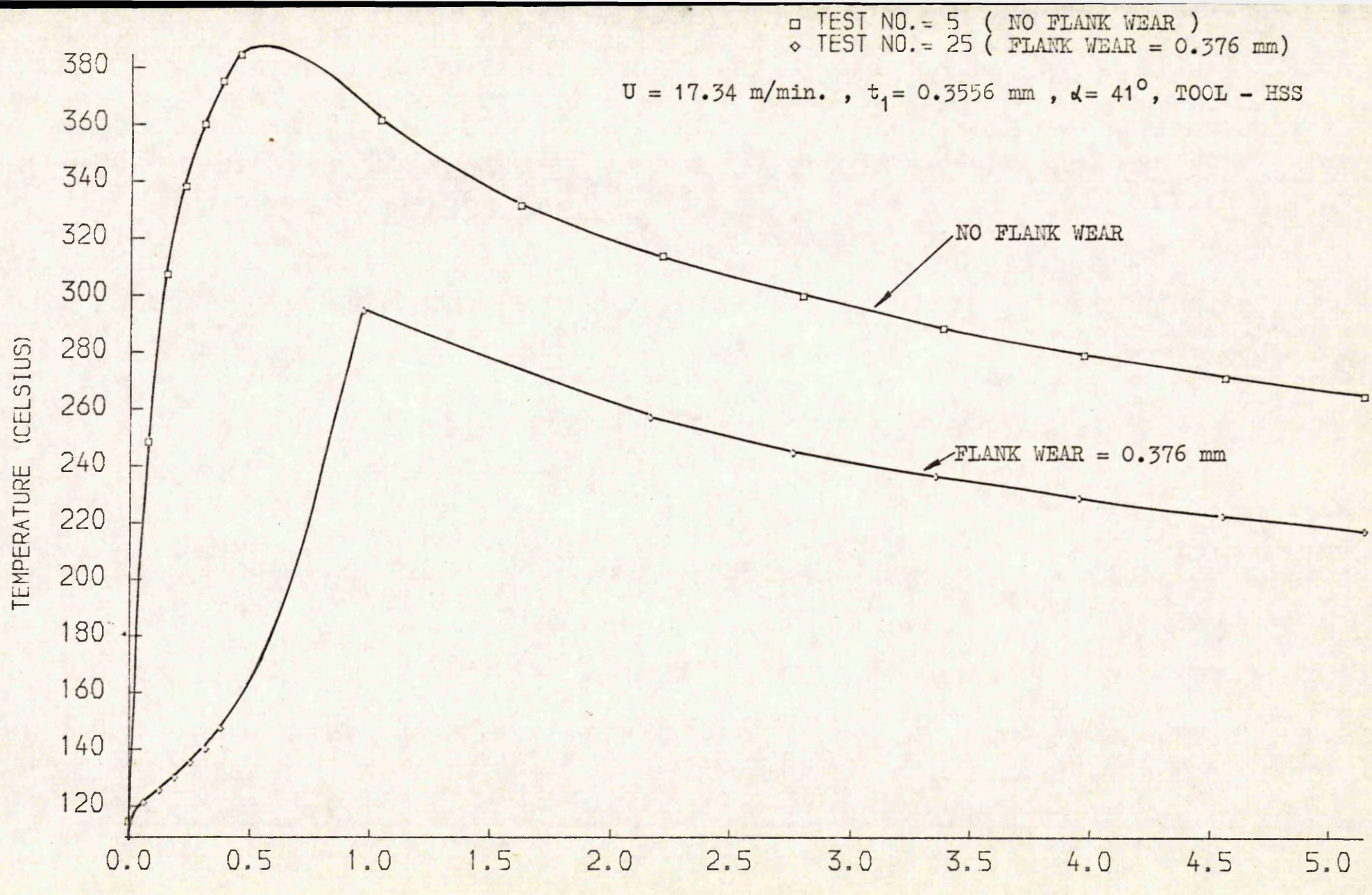

FIG. 5.64 (b) EFFECT OF TOOL FLANK WEAR ON FLANK FACE TEMPERATURES

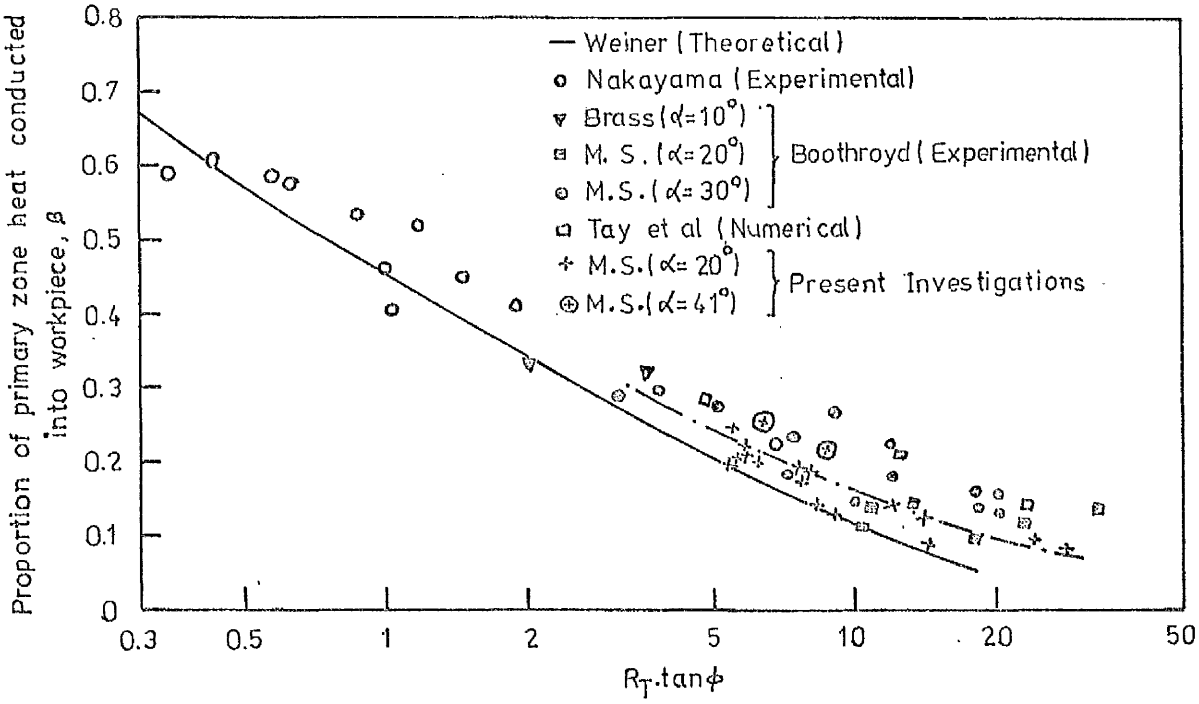

Variation of β with $R_T \tan\phi$, where $R_T = \rho C_p U t_1 / K$

FIG. 5.65

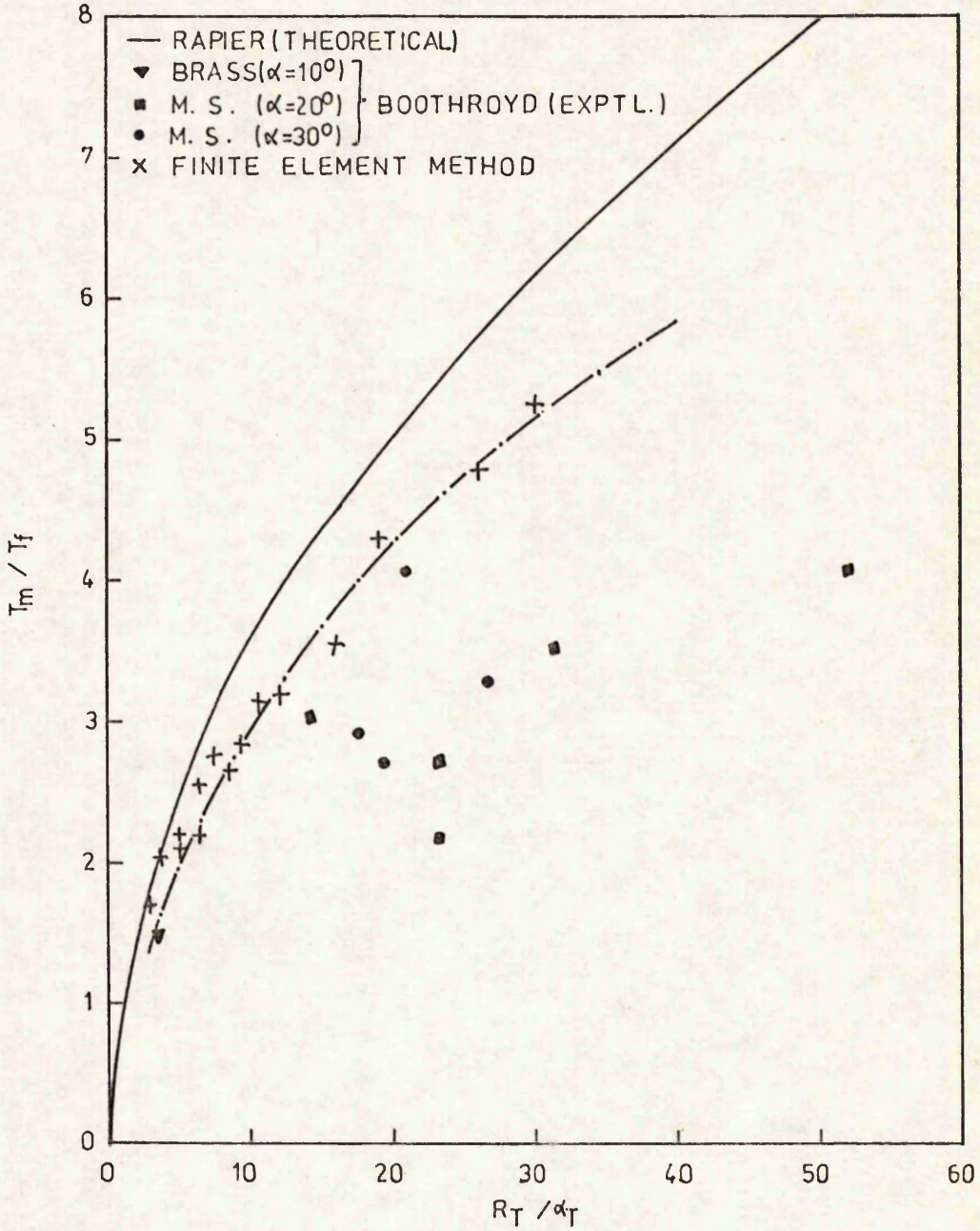

FIG. 5.66

T_m = Maximum rise of temperature in chip

T_f = Mean rise of temperature in chip

$\alpha_T t_2$ = Length of frictional heat source

R_T = Thermal number = $\rho . C_p . V_c . t_2 / K$

APPENDIX I

SIMPLIFICATION OF EQ. (2.9) FOR TRIANGULAR ELEMENTS.

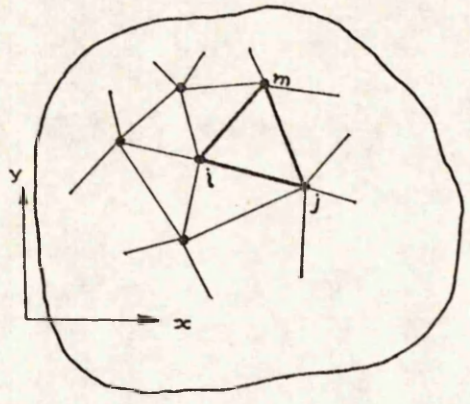

FIG. A1.1 Division of the problem region into elements

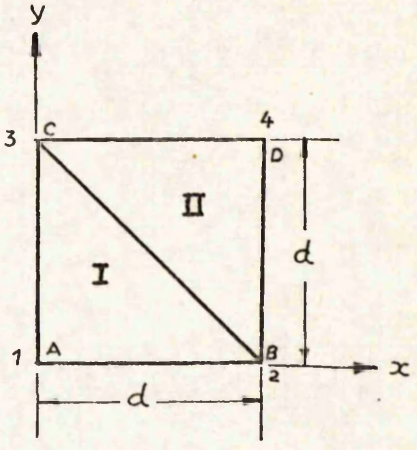

FIG. A1.2 A Typical assembly of two elements

Let the problem region be divided into small triangular elements (Fig. A1.1). For a triangle defined by the nodes i, j, m numbered in an anti-clockwise order, the function T can be uniquely specified within the element by

$$T = \left[N\right] \left\{T\right\}^e$$

$$= N_i T_i + N_j T_j + N_m T_m \qquad \text{(A1.1)}$$

where,

$$N_i = (a_i + b_i x + c_i y)/2\Delta \qquad \text{(A1.2a)}$$

$$N_j = (a_j + b_j x + c_j y)/2\Delta \qquad \text{(A1.2b)}$$

$$N_m = (a_m + b_m x + c_m y)/2\Delta \qquad \text{(A1.2c)}$$

$$a_i = x_j y_m - x_m y_j$$

$$b_i = y_j - y_m \qquad \text{(A1.3)}$$

$$c_i = x_m - x_j$$

With the other coefficients obtained by a cyclic permutation of subscripts in the order i, j, m and

$$2\Delta = \det \begin{vmatrix} 1 & x_i & y_i \\ 1 & x_j & y_j \\ 1 & x_m & y_m \end{vmatrix} = 2 \text{ (area of triangle ijm)} \qquad \text{(A1.4)}$$

Differentiating Eq. (A1.2), the derivatives of the shape functions are

$$\begin{aligned} \frac{\partial N_i}{\partial x} &= b_i/2\Delta & \frac{\partial N_i}{\partial y} &= c_i/2\Delta \\ \frac{\partial N_j}{\partial x} &= b_j/2\Delta & \frac{\partial N_j}{\partial y} &= c_j/2\Delta \\ \frac{\partial N_m}{\partial x} &= b_m/2\Delta & \frac{\partial N_m}{\partial y} &= c_m/2\Delta \end{aligned} \qquad \text{(A1.5)}$$

It can be shown that

$$\iint (a_i + b_i x + c_i y)\, dx\, dy/2\Delta$$

$$= \iint N_i\, dx\, dy = 1/3\ \Delta \qquad \text{(A1.6)}$$

and $$\iint dxdy = \Delta$$

Substituting Eqs. (A1.5) and (A1.6) into Eq. (2.9) and not considering the boundary terms at present, the nodal equation is

$$\left(\frac{Kb_i}{4\Delta} \begin{bmatrix} b_i & b_j & b_m \end{bmatrix} + \frac{Kc_i}{4\Delta} \begin{bmatrix} c_i & c_j & c_m \end{bmatrix} + \frac{\rho C_p u}{6} \begin{bmatrix} b_i & b_j & b_m \end{bmatrix} + \frac{\rho C_p v}{6} \begin{bmatrix} c_i & c_j & c_m \end{bmatrix} \right) \{T\}^e - \frac{Q\Delta}{3} = 0 \qquad \text{(A1.7)}$$

Writing down for the whole element, in matrix form, the element equation is

$$[H]^e \{T\}^e + \{F\}^e = 0 \qquad \text{(A1.8)}$$

where $[H]^e$ is a square matrix, the typical element of which is

$$H^e_{ij} = \frac{K}{4\Delta} (b_i b_j + c_i c_j) + \frac{\rho C_p}{6} (u b_j + v c_j) \qquad \text{(A1.9)}$$

and $$\{F\}^e = -\frac{\dot{Q}\Delta}{3}\begin{Bmatrix}1\\1\\1\end{Bmatrix} \qquad (A1.10)$$

From Eq. (A1.9), the matrix $[H]^e$ can be written as

$$[H]^e = \frac{K}{4\Delta}\begin{bmatrix} b_ib_i & b_ib_j & b_ib_m \\ & b_jb_j & b_jb_m \\ \text{sym.} & & b_mb_m \end{bmatrix} + \frac{K}{4\Delta}\begin{bmatrix} c_ic_i & c_ic_j & c_ic_m \\ & c_jc_j & c_jc_m \\ \text{sym.} & & c_mc_m \end{bmatrix}$$

$$+ \frac{\rho C_p u}{6}\begin{bmatrix} b_i & b_j & b_m \\ b_i & b_j & b_m \\ b_i & b_j & b_m \end{bmatrix} + \frac{\rho C_p v}{6}\begin{bmatrix} c_i & c_j & c_m \\ c_i & c_j & c_m \\ c_i & c_j & c_m \end{bmatrix} \qquad (A1.11)$$

which shows that $[H]^e$ is an asymmetric matrix.

Example.

The example below illustrates the solution procedure for a problem region divided into two elements (Fig. A1.2).

For element I defined by nodes 1 2 3 (always maintaining the anti-clockwise numbering order), the coefficients of Eq(A1.3) are given by

$$\begin{bmatrix} a_1 & a_2 & a_3 \\ b_1 & b_2 & b_3 \\ c_1 & c_2 & c_3 \end{bmatrix} = \begin{bmatrix} d^2 & 0 & 0 \\ -d & d & 0 \\ -d & 0 & d \end{bmatrix} \qquad (A1.12)$$

Using Eq. (A1.11) and the values of the coefficients from Eq. (A1.12) the element matrix is given by

$$\begin{bmatrix} H \end{bmatrix}^I_{1\ 2\ 3} = \begin{bmatrix} H_{11} & H_{12} & H_{13} \\ H_{21} & H_{22} & H_{23} \\ H_{31} & H_{32} & H_{33} \end{bmatrix}^I$$

$$= 1/6 \begin{bmatrix} 6K - s(u+v) & -3K + s.u & -3K + s.v \\ -3K - s(u+v) & 3K + s.u & s.v \\ -3K - s(u+v) & s.u & 3K + s.v \end{bmatrix} \qquad (A1.13)$$

where, $s = \rho C_p \cdot d$ (A1.14)

Similarly, for element II

$$\left[H\right]^{II}_{2\ 4\ 3} = \begin{bmatrix} H_{22} & H_{24} & H_{23} \\ H_{42} & H_{44} & H_{43} \\ H_{32} & H_{34} & H_{33} \end{bmatrix}^{II} = 1/6 \begin{bmatrix} 3K-s.v & -3K+s(u+v) & -s.u \\ -3K-s.v & 6K+s(u+v) & -3K-s.u \\ -s.v & -3K+s(u+v) & 3K-s.u \end{bmatrix} \qquad (A1.15)$$

Assuming that the heat is generated along the surface CD only at the rate of q watts per unit area per unit time, the system heat load vector is given by

$$F = \begin{bmatrix} F_1 & F_2 & F_3 & F_4 \end{bmatrix}^T = \begin{bmatrix} 0 & 0 & -\frac{q.d}{2} & -\frac{q.d}{2} \end{bmatrix}^T \qquad (A1.16)$$

Summing the contributions of both the elements, the nodal equations are

$$T_1/6 \left\{6K - s(u+v)\right\} + T_2/6 \left\{-3K + s.u\right\} + T_3/6 \left\{-3K + s.v\right\} = 0 \qquad (A1.17)$$

$$\frac{T_1}{6} \left\{-3K - s(u+v)\right\} + \frac{T_2}{6} \left\{6K + s(u-v)\right\} + \frac{T_3}{6} \left\{s(v-u)\right\} + \frac{T_4}{6} \left\{-3K + s(u+v)\right\} = 0 \qquad (A1.18)$$

$$\frac{T_1}{6} \left\{-3K - s(u+v)\right\} + \frac{T_2}{6} \left\{s(u-v)\right\} + \frac{T_3}{6} \left\{6K + s(v-u)\right\} + \frac{T_4}{6} \left\{-3K+s(u+v)\right\} = \frac{q.d}{2} \qquad (A1.19)$$

$$\frac{T_2}{6} \left\{-3K - s.v\right\} + \frac{T_3}{6} \left\{-3K - s.u\right\} + \frac{T_4}{6} \left\{6K + s(u+v)\right\} = \frac{q.d}{2} \qquad (A1.20)$$

Boundary Conditions.

(i) The temperature of node 2 is set equal to T_s i.e.,

$$T_2 = T_s \qquad (A1.21)$$

This boundary condition is introduced by setting

$H^{I}_{22} = 1/2$, (Two elements share the node 2)

$H^{II}_{22} = 1/2$,

$H^{I}_{21} = 0$, $H^{I}_{23} = 0$, $H^{II}_{24} = 0$, $H^{II}_{23} = 0$, $F_2 = -T_s$ and as a result Eq. (A1.18) is changed to

$$T_1 \cdot 0 + T_2 + T_3 \cdot 0 + T_4 \cdot 0 = T_s \qquad \text{(A1.22)}$$

(ii) The boundary integral I_B is specified where I_B is given by

$$I_B = - \oint_S N_i \, K \, \frac{\partial T}{\partial n} \cdot ds \qquad \text{(A1.23)}$$

Case I. When the condition

$$\frac{\partial T}{\partial n} = 0 \qquad \text{(A1.24)}$$

is imposed.

As a result of Eq. (A1.24), the boundary integral I_B vanishes and no change takes place in the element matrices.

Case II.

It is given that

$$-K \, \frac{\partial T}{\partial n} = q_s \text{ on surface AC.} \qquad \text{(A1.25)}$$

For this condition, the boundary integral is

$$I_B = - \oint N_i \, K \, \frac{\partial T}{\partial n} \cdot ds = \int_{S_{AC}} N_i \, q_s \, ds \qquad \text{(A1.26)}$$

It can be shown that Eq. (A1.26) contributes to the heat loads at the nodes 1 and 3 only and these additional contributions are given by

$$F_1^+ = q_s \cdot d/2$$

and $$F_3^+ = q_s \cdot d/2 \qquad \text{(A1.27)}$$

Case III.

This is an extension of Eq. (A1.25) when, for a coolant boundary, q_s is expressed in terms of the heat transfer co-efficient h, that is,

$$-K \frac{\partial T}{\partial n} = h(T - T_\infty) \text{ on surface AC} \qquad \text{(A1.28)}$$

and

$$I_B = \int_{S_{AC}} N_i \, h \, (T - T_\infty) \, ds \qquad \text{(A1.29)}$$

Eq. (A1.29) contributes to the element matrix $\left[H\right]^I$ as well as to the heat load vector $\left\{F\right\}^I$ for the boundary nodes only (Eqs. (4.10) and (4.11)). On integration and simplification, these additional contributions can be shown to be

$$\left[H \right]^{I^+}_{1\ 2\ 3} = h \begin{bmatrix} d/3 & 0 & d/6 \\ 0 & 0 & 0 \\ d/6 & 0 & d/3 \end{bmatrix} \qquad \text{(A1.30)}$$

and

$$\left\{ F \right\}^{I+}_{1\ 2\ 3} = \begin{Bmatrix} F_1 \\ F_2 \\ F_3 \end{Bmatrix}^{I^+} = -hT_\infty \cdot \begin{Bmatrix} d/2 \\ 0 \\ d/2 \end{Bmatrix} \qquad \text{(A1.31)}$$

Normally, the boundary conditions of Eq. (A1.25) and of Eq. (A1.28) do not occur together at the same surface. For the above example, hence, the boundary condition of Eq. (A1.25) is not considered.

Combining Eqs. (A1.17), (A1.19), (A1.20), (A1.22), (A1.30) and (A1.31), the nodal equations in the final form are

$$\frac{T_1}{6}\left\{6K - s(u+v) + 2hd\right\} + \frac{T_2}{6}\left\{-3K + s.u\right\} + \frac{T_3}{6}\left\{-3K + s.v + hd\right\} = \frac{hT_\infty \, d}{2} \qquad \text{(A1.32)}$$

$$T_2 = T_s \qquad \text{(A1.33)}$$

$$\frac{T_1}{6}\left\{-3K-s(u+v)+hd\right\} + \frac{T_2}{6}\left\{s(u-v)\right\} + \frac{T_3}{6}\left\{6K+s(v-u)+2hd\right\} + \frac{T_4}{6}\left\{-3K+s(u+v)\right\} =$$

$$d/2\ (q+hT_\infty) \qquad \text{(A1.34)}$$

$$\frac{T_2}{6}\left\{-3K-s.v\right\} + \frac{T_3}{6}\left\{-3K-s.u\right\} + \frac{T_4}{6}\left\{6K+s(u+v)\right\} = q.d/2 \qquad \text{(A1.35)}$$

For illustration, the following numerical values of various quantities are assumed.

$K = 60$ W/m K

$C_p = 300$ J/Kg K

$\rho = 8 \times 10^3$ Kg/m^3

$u = 0.20$ m/sec

$v = 0.30$ m/sec

$d = 1 \times 10^{-4}$ m

$h = 6 \times 10^4$ W/m^2 K

$T_s = T_\infty = 20°C$

$q = 4 \times 10^6$ W/m^2

$s = \rho C_p d = 240$

Substituting the above values into Eqs. (A1.32) - (A1.35), the following set of equations is obtained.

$$252T_1 - 132T_2 - 102T_3 = 360$$

$$T_2 = 20$$

$$-294T_1 - 24T_2 + 396T_3 - 60T_4 = 1560$$

$$-252T_2 - 228T_3 + 480T_4 = 1200$$

Solving the above equations, the resulting nodal temperatures are

$T_1 = 22.199°C$, $T_2 = 20°C$, $T_3 = 25.433°C$ and $T_4 = 25.080°C$.

It can be shown that if no coolant boundary is used (i.e., h = 0)

the temperatures of the nodes 1, 3 and 4 are increased and are given by

$$T_1 = 22.755\,^{\circ}C, \quad T_3 = 26.122\,^{\circ}C \quad \text{and} \quad T_4 = 25.408\,^{\circ}C.$$

APPENDIX II

PROGRAM DATA

A2.1 Input Data.

Input data to the program DATA consists of the following items:

(i) Problem identification and control parameters.

(ii) Material Properties.

(iii) Boundary conditions.

(iv) Elements with heat sources.

(v) Cutting forces.

(vi) Element data.

Input formats are listed below.

(i)	NPRO, NMATL, IELDAT	(16I5)
(ii)	I, CKX(I), CKY(I), ACP(I), AROE(I), AVX(I), AVY(I)	(I8, 6F12.6)
	I = 1, NMATL	
	I, CKXC(I), CKYC(I), ACPC(I), AROEC(I)	(I8, 4F14.8)
	I = 1, NMATL	
(iii)	NBN	(16I5)
	(NBC(I), I = 1,NBN)	(16I5)
	NCON	(16I5)
	(NSE(I), I = 1, NCON)	(16I5)
	(REL(I), I = 1, 7)	(9F8.3)
	(VFLD(I), I = 1, 7)	(9F8.3)
	(ICON(I), I = 1, 7)	(16I5)
	ICOUNT	(16I5)
	(ICON1(I), I = 1 ICOUNT)	(16I5)
	(ELE(I), I = 1, ICOUNT)	(16F5.1)
(iv)	NEPD, NESD, NEFF	(16I5)
	(NPD(I), I = 1, NEPD)	(16I5)

(NSD(I), I = 1, NESD) (16I5)

(NFF(I), I = 1, NEFF) (16I5)

(v) N1R, FV, FH (I5, 6F15.4)

(vi) 1st NTYPE, MATERL, THK, NOV, (JN(I), I=1, NOV) - (2I5,F5.2,13I5)

element (X(I), Y(I), Z(I), I = 1, NOV) (9F8.3)

2nd

element .....

0 (I5) - termination for (vi)

Input Data Glossary.

(i) NPRO indicates the type of problem.

= 1 for a two dimensional problem.

= 2 for a three dimensional problem.

NMATL specifies the number of different types of material in the problem region.

IELDAT indicates the input source of element data.

= 1 for the element data input by cards.

= 2 for the element data input by the disc file no.4.

(ii) CKX An array of thermal conductivity values in x-direction.

CKY An array of thermal conductivity values in y-direction.

ACP An array of specific heat values.

AROE An array of density values.

AVX An array of velocity values in x-direction.

AVY An array of velocity values in y-direction.

CKXC An array of temperature constants for thermal conductivities in x-direction.

CKYC An array of temperature constants for thermal conductivities in y-direction.

ACPC An array of temperature constants for specific heats.

AROEC An array of temperature constants for densities.

(iii) NBN Number of elements with coolant boundary.

NBC An array of coolant boundary elements.

NCON Equal to NBN.

NSE An array indicating the type of coolant surface for each coolant boundary element.

REL An array of relative lengths of coolant surfaces to be used in Renolds equation.

VFLD An array of relative coolant velocities for each coolant surface.

ICON An array indicating the position of first boundary node (in the array of node numbers) for each coolant surface.

ICOUNT Number of constrained boundary nodes with room temperature.

ICON1 An array of constrained boundary nodes with room temperature.

ELE An array indicating the number of elements common to each boundary node with room temperature.

(iv) NEPD Number of elements in the deformation zones.

NESD Number of elements along tool-chip interface (in the chip) subjected to boundary friction.

NEFF Number of elements along work-tool interface(in the tool) subjected to boundary friction.

NPD An array of elements lying in the deformation zones.

NSD An array of elements along tool-chip interface subjected to boundary friction.

NFF An array of elements along work-tool interface subjected to boundary friction.

(v) N1R Test identification number.

FV Cutting force.

FH Feed force.

(vi) NTYPE specifies element type

= 3 for 3-node triangular elements.

= 4 for 4-node quadrilateral elements.

= 5 for 6-node triangular elements.

= 6 for 9-node triangular elements.

= 7 for 8-node quadrilateral elements.

= 8 for 12-node quadrilateral elements.

= 9 for 8-node hexahedron elements.

= --- for new additions.

MATERL Material type of the element.

THK Element thickness - immaterial for 3-dimensional elements.

NOV Number of nodes in the element.

JN An array of element node numbers. The node numbers must be specified in clockwise or anti-clockwise direction.

x,y,z Three separate array of x - y - z co-ordinates in a global system for the whole assemblage of elements. The sets of co-ordinates must be input in the order of their node numbers in JN.

Example.

The sample on the coding sheet is the data input for the Test no. 11 for which the cutting conditions and measured data are given in Table 3.4.

A2.2 Output Data.

The following is the job output (from the program DATA) for

Test No. 11.

A TWO DIMENSIONAL PROBLEM

METAL NO	CONDUCT-IVITY X	CONDUCT-IVITY Y	SPECIFIC HEAT	METAL DENSITY	VELOCITY X	VELOCITY Y
1	.150E-01	.150E-01	.100E+00	.786E-02	.192E+03	-.220E+03
2	.150E-01	.150E-01	.100E+00	.786E-02	.197E+03	0.
3	.970E-02	.970E-02	.110E+00	.817E-02	0.	0.

METAL NO	CKXC	CKYC	ACPC	AROEC
1	-.100E-04	-.100E-04	.138E-03	0.
2	-.100E-04	-.100E-04	.138E-03	0.
3	-.240E-05	-.240E-05	0.	0.

CONSTRAINED NODES FOR STATIONARY TEMPERATURE

1086 1088 1080 1079 1074 1072 1064 1063 1056 1054 1051 1049 1050 1058
1059 1068 1070 1076 1077 1082 1083 1090 1092 1094 1095 1104 1108 1123
1124 1143 1146 1160 1161 1192 1190 1191 1188 1187 1185 1184 1182 1181
1179 1178 1176 1175 1173 1172 1170 1169 1167 1165 1164 1 3 5
9 15 25 29 44 49 70 73 102 106 138 143 181 186
233 236 289 288

NO. OF ELEMENTS CONNECTED TO FIXED TEMP. NODES

1.0 1.0 2.0 1.0 2.0 1.0 2.0 1.0 2.0 1.0 2.0 1.0 2.0 1.0
2.0 1.0 2.0 1.0 2.0 1.0 2.0 1.0 2.0 1.0 2.0 1.0 2.0 1.0
2.0 1.0 2.0 1.0 2.0 1.0 1.0 1.0 2.0 1.0 2.0 1.0 2.0 1.0
2.0 1.0 2.0 1.0 2.0 1.0 2.0 1.0 2.0 1.0 1.0 1.0 1.0 2.0
1.0 2.0 1.0 2.0 1.0 2.0 1.0 2.0 1.0 2.0 1.0 2.0 1.0 2.0
1.0 2.0 1.0 1.0

NO. OF DEGREES OF FREEDOM PER NODE = 1

TOTAL NO. OF ELEMENTS = 359

THE BIGGEST NODE NO. = 1192

THE SMALLEST NODE NO. = 1

BANDWIDTH = 78

TOTAL NO. OF DEGREES OF FREEDOM = 1192

Name

Department

INPUT DATA EXAMPLE FOR PROGRAM "DATA"

Date


```
   1     3     2
         1  0.015          0.015          0.1            0.007858      261.987      -719.805
         2  0.015          0.015          0.1            0.007858      391.650       0.
         3  0.0097         0.0097         0.11           0.008170      0.           0.
         1  -0.00001       -0.00001       0.0001375      0.
         2  -0.00001       -0.00001       0.0001375      0.
         3  -0.0000024     -0.0000024     0.             0.
   0
   0
  74
1086 1088 1080 1079 1074 1072 1064 1063 1056 1054 1051 1049 1050 1058 1059 1068
1070 1076 1077 1082 1083 1090 1092 1094 1095 1104 1108 1123 1124 1143 1146 1160
1161 1192 1190 1191 1188 1187 1185 1184 1182 1181 1179 1178 1176 1175 1173 1172
1170 1169 1167 1165 1164    1    3    5    9   15   25   29   44   49   70   73
 102  106  138  143  181  186  233  236  289  288
1.    1.    2.    1.    2.    1.    2.    1.    2.    1.    2.    1.    2.    1.    2.    1.
2.    1.    2.    1.    2.    1.    2.    1.    2.    1.    2.    1.    2.    1.    2.    1.
2.    1.    1.    1.    2.    1.    2.    1.    2.    1.    2.    1.    2.    1.    2.    1.
2.    1.    2.    1.    1.    1.    1.    2.    1.    2.    1.    2.    1.    2.    1.    2.
1.    2.    1.    2.    1.    2.    1.    2.    1.    1.
  12     5     0
 154  155  156  157  158  159  160  161  162  163  164  165
 160  161  166  167  168
  11 3500.          1560.
```

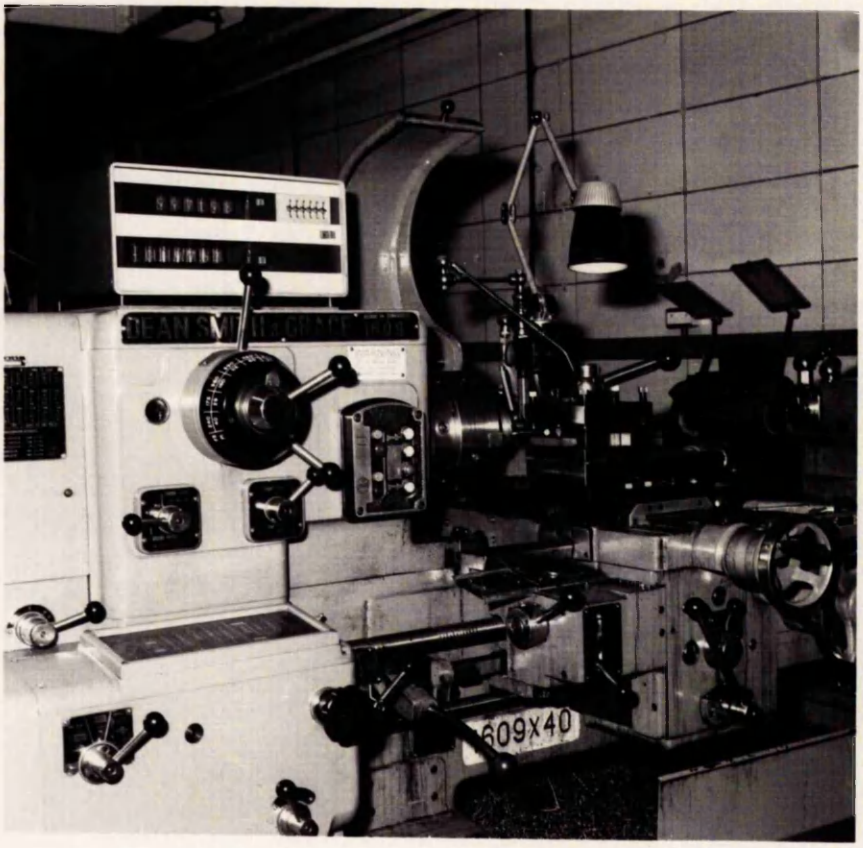

PLATE I

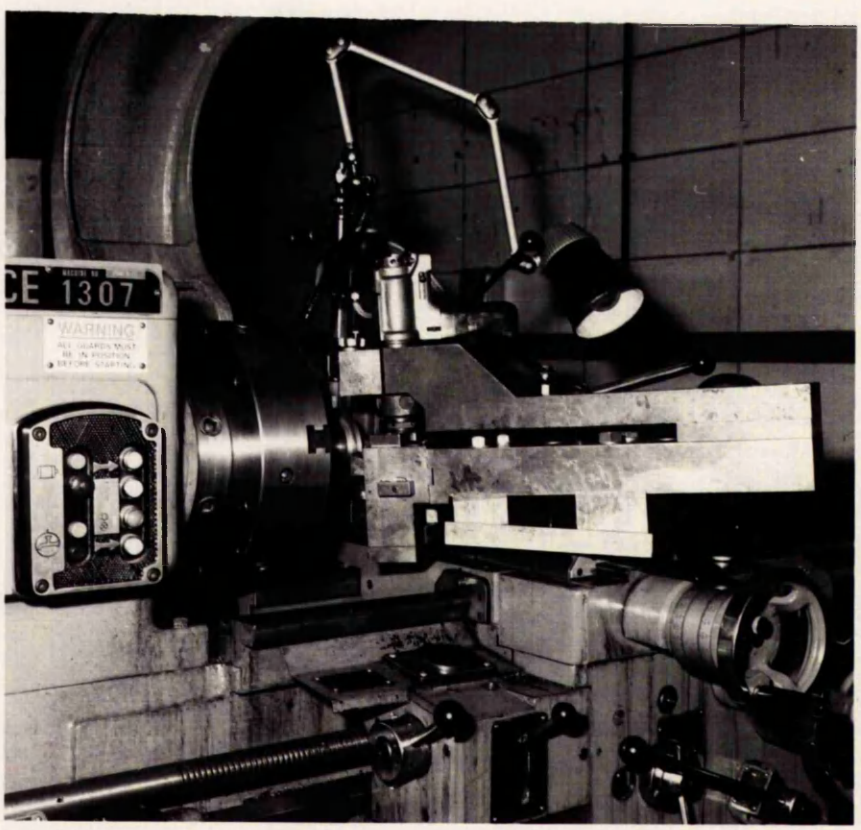

PLATE II

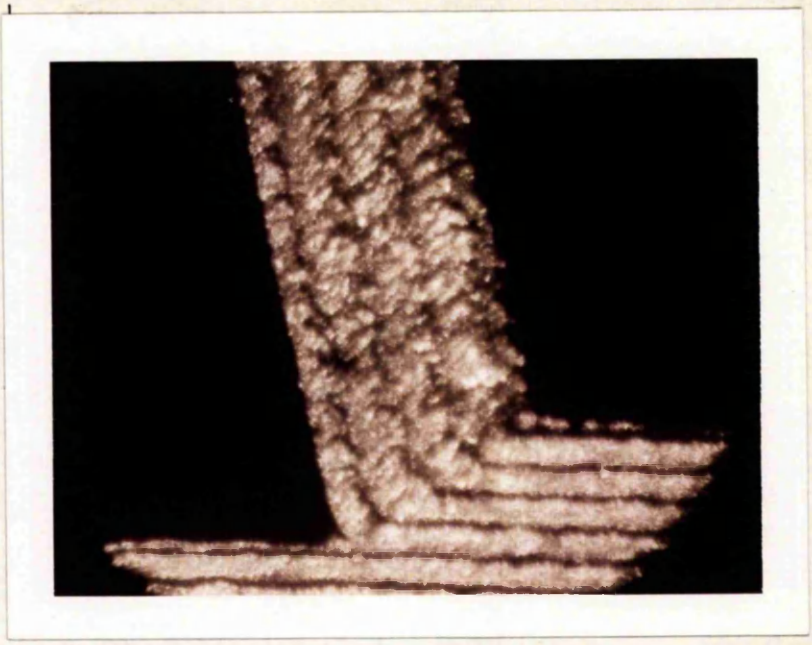

U = 35.2 m/min., t_1 = 0.2845 mm, α = 20°, TOOL - CARBIDE
(a)

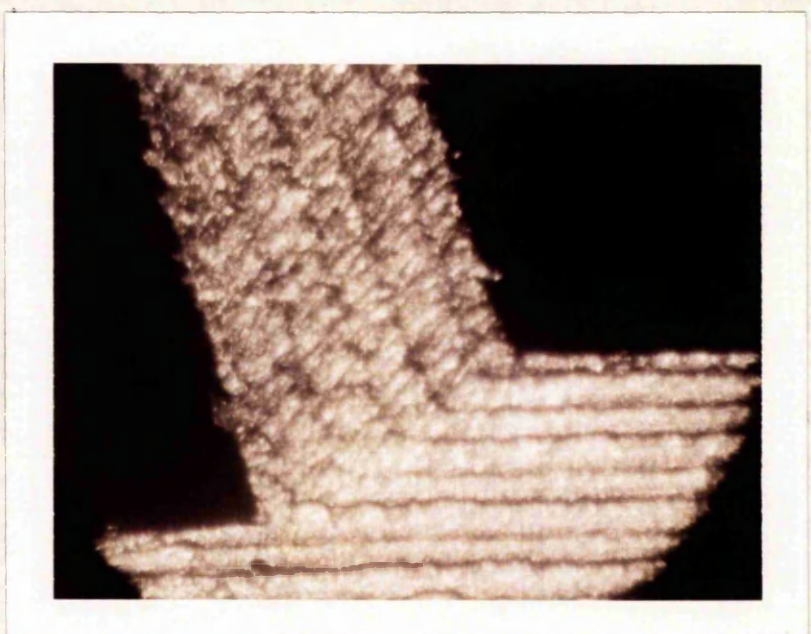

U = 71 m/min., t_1 = 0.3556 mm, α = 20°, TOOL - CARBIDE
(b)

PLATE III Deformed flow lines (contd.)

U = 17.3 m/min., t_1 = 0.3556 mm, α = 41°, TOOL- HSS

(c)

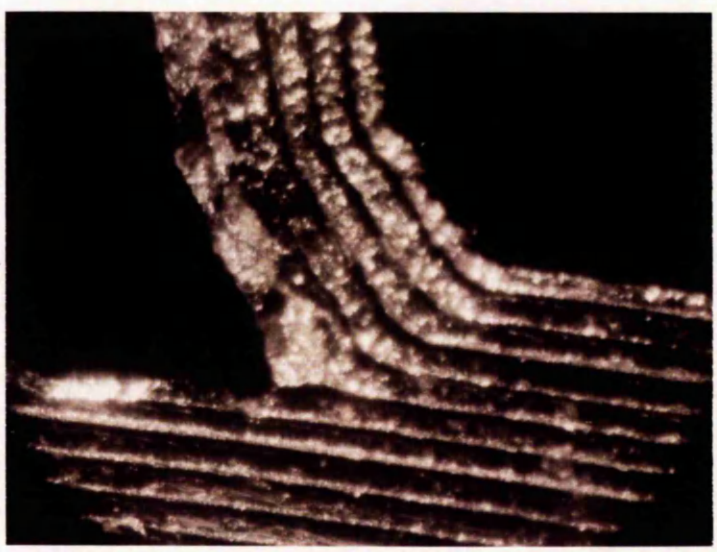

U = 24.8 m/min., t_1 = 0.3556 mm, α = 41°, TOOL- HSS

(d)

PLATE III Deformed flow lines

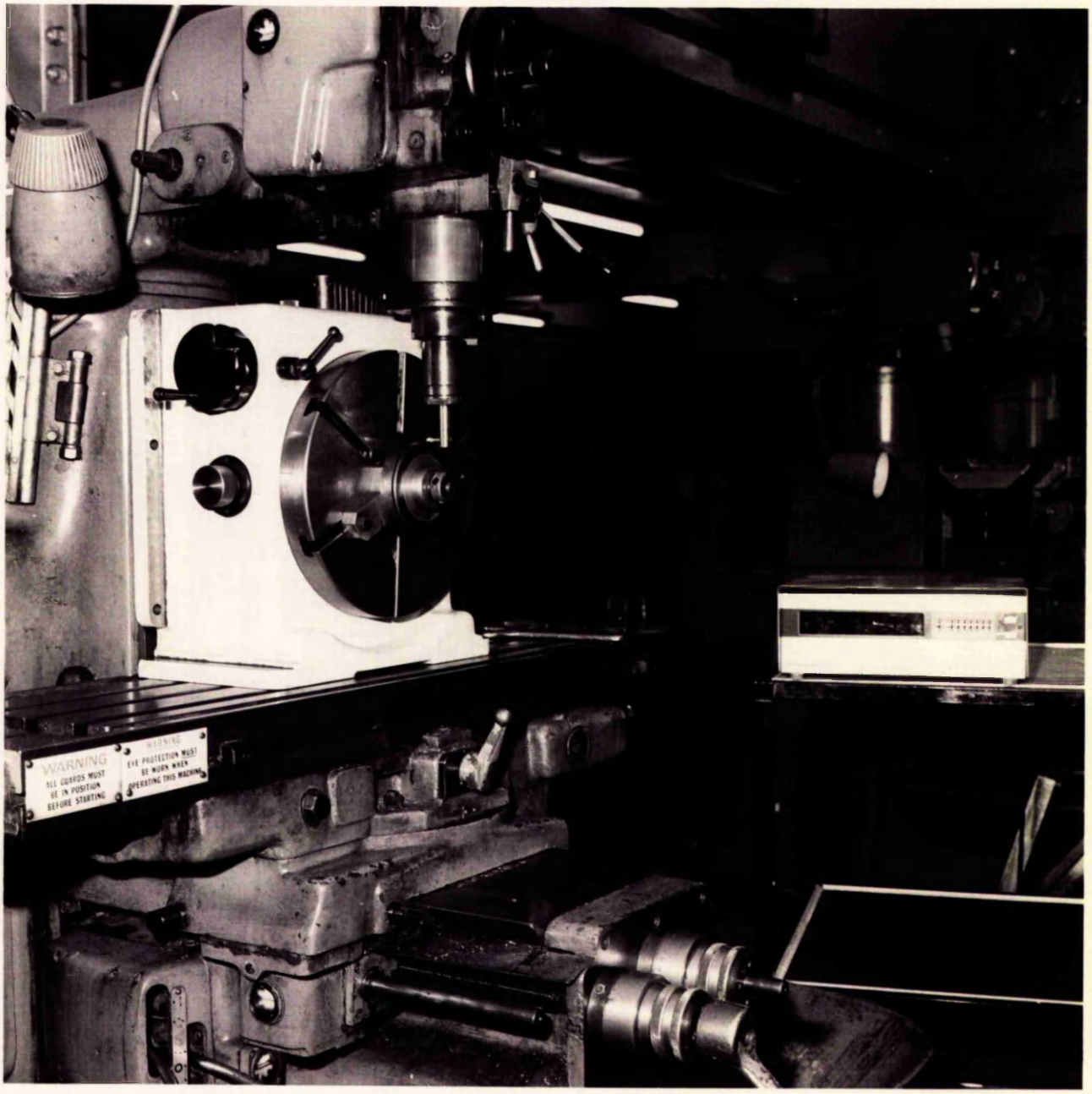
WARNING
ALL GUARDS MUST
BE IN POSITION
BEFORE STARTING
WARNING
EYE PROTECTION MUST
BE WORN WHEN
OPERATING THIS MACHINE

PLATE IV

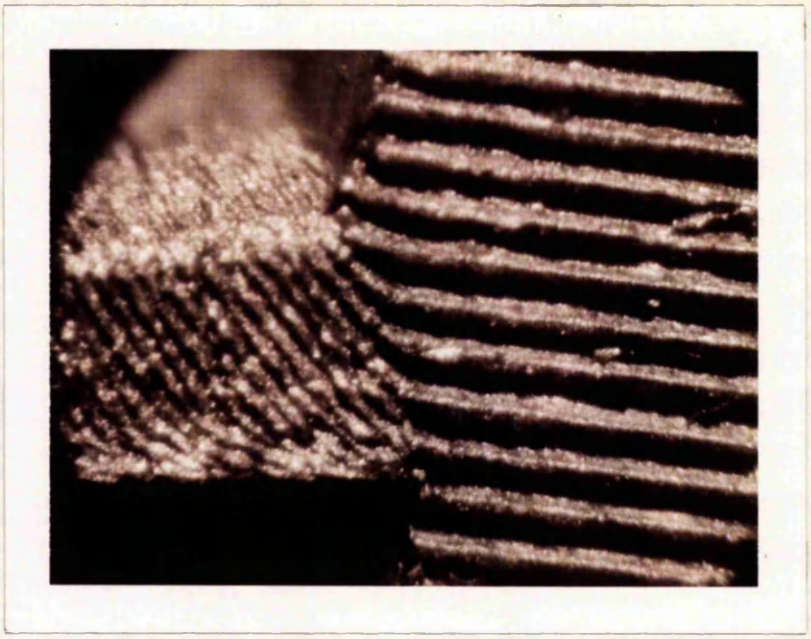

U = 130.7 m/min., t_1 = 0.3556 mm, $\alpha = 20^{\circ}$, TOOL-CARBIDE

(a)

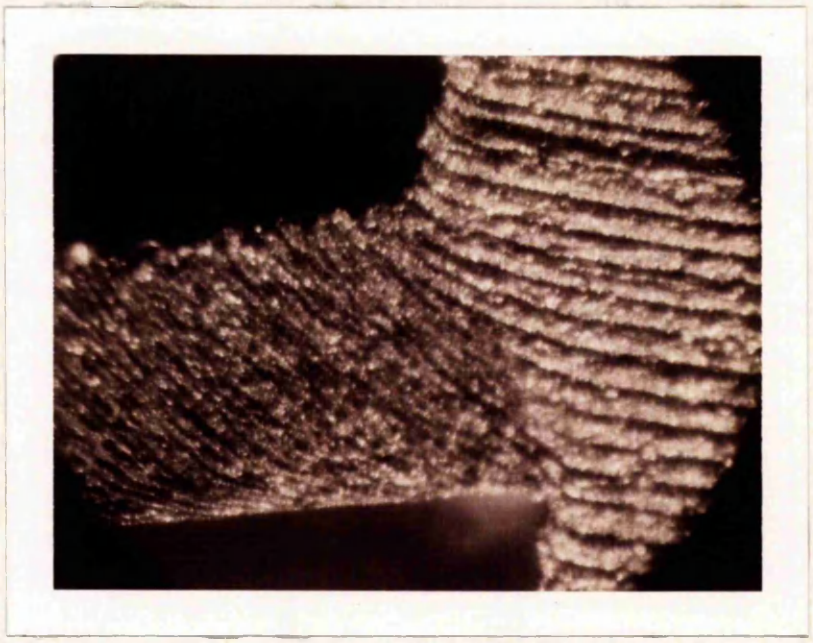

U = 131 m/min., t_1 = 0.3556 mm, $\alpha = 20^{\circ}$, TOOL - CARBIDE, COOLANT - WATER

(b)

PLATE V Secondary chip deformation

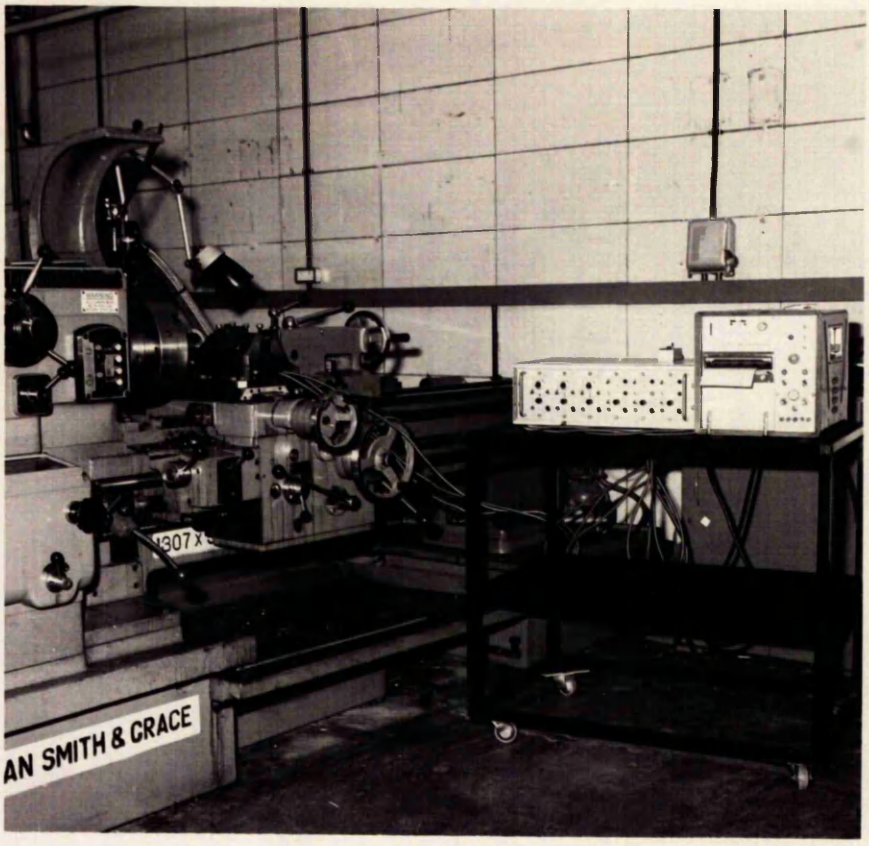

PLATE VI

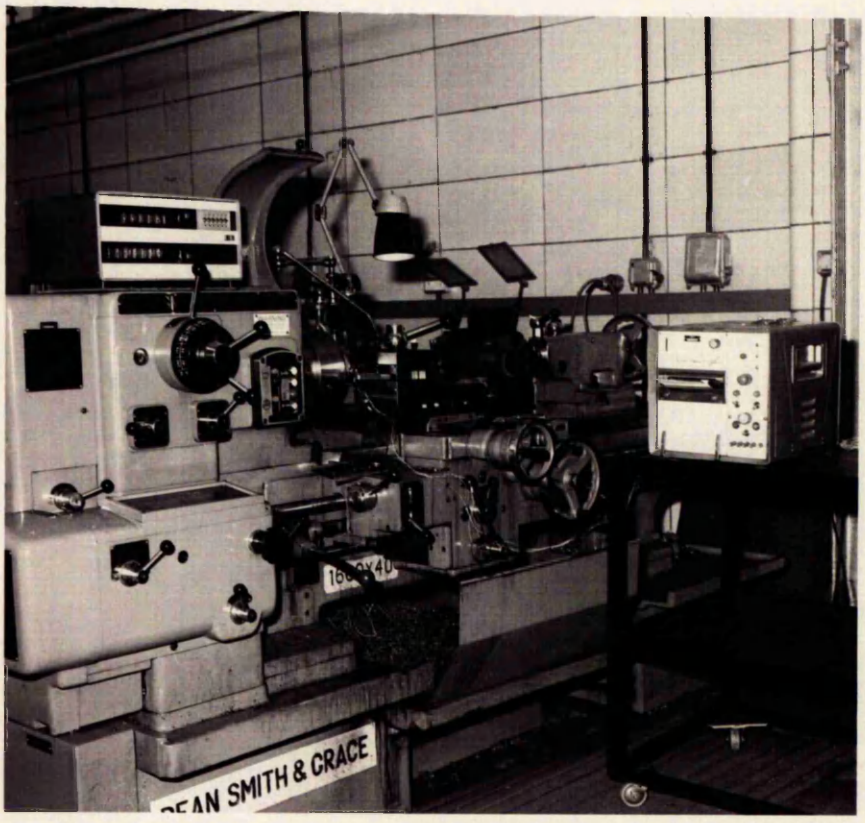

PLATE VII